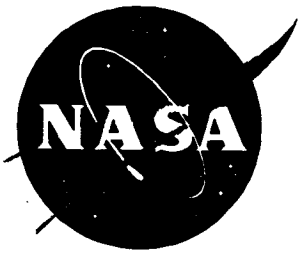

NASA Conference Publication 3311
Part 2

Mechanics of Textile Composites Conference

Edited by
Clarence C. Poe, Jr. and Charles E. Harris

Proceedings of a conference sponsored by the
National Aeronautics and Space Administration,
Washington, D.C., and held in
Hampton, Virginia
December 6–8, 1994

October 1995

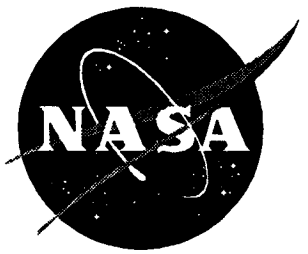

NASA Conference Publication 3311
Part 2

Mechanics of Textile Composites Conference

Edited by
Clarence C. Poe, Jr. and Charles E. Harris
Langley Research Center • Hampton, Virginia

Proceedings of a conference sponsored by the
National Aeronautics and Space Administration,
Washington, D.C., and held in
Hampton, Virginia
December 6–8, 1994

National Aeronautics and Space Administration
Langley Research Center • Hampton, Virginia 23681-0001

October 1995

This publication is available from the following sources:

NASA Center for AeroSpace Information
800 Elkridge Landing Road
Linthicum Heights, MD 21090-2934
(301) 621-0390

National Technical Information Service (NTIS)
5285 Port Royal Road
Springfield, VA 22161-2171
(703) 487-4650

PREFACE

This document is a compilation of papers presented at the Mechanics of Textile Composites Conference in Hampton, Virginia December 6-8, 1994. This conference was the culmination of a three-year program that was initiated by NASA late in 1990 to develop mechanics of textile composites in support of the NASA Advanced Composites Technology Program (ACT). The goal of the program was to develop mathematical models of textile preform materials to facilitate structural design and analysis. Participants in the program were from NASA, academia, and industry.

The use of trademarks or manufacturers' names in this publication does not constitute endorsement, either expressed or implied, by the National Aeronautics and Space Administration.

Clarence C. Poe, Jr.
Charles E. Harris
NASA Langley Research Center

CONFERENCE ORGANIZATION

Sponsored By

Mechanics of Materials Branch
NASA Langley Research Center
Hampton, Virginia 23681-0001

General Chairman	Conference Coordinator and Organizer	Administrative Assistant
Charles E. Harris NASA Langley Research Center	C. C. Poe, Jr. NASA Langley Research Center	Josephine L. Sawyer NASA Langley Research Center

CONTENTS

*Presented under separate cover

Part 2

SESSION 2
STANDARD TEST METHODS

SESSION 3
ANALYTICAL MECHANICS

MODELING AND CHARACTERIZATION OF THROUGH-THE-THICKNESS PROPERTIES OF 3D WOVEN COMPOSITES

Dru Hartranft, Azar Pravizi-Majidi and Tsu-Wei Chou
Center for Composite Materials
University of Delaware
Newark, DE

SUMMARY

The through-the-thickness properties of three-dimensionally (3D) woven carbon/epoxy composites have been studied. The investigation aimed at the evaluation and development of test methodologies for the property characterization in the thickness direction, and the establishment of fiber architecture-property relationships in woven textile structural composites. Three woven architectures were studied: layer-to-layer Angle Interlock, through-the-thickness Angle Interlock, and through-the-thickness Orthogonal. A through-the-thickness Orthogonal woven preform with surface pile was also designed and manufactured for the fabrication of tensile test coupons with integrated grips. All the preforms were infiltrated by the resin transfer molding technique. The microstructures of the composites were characterized along the warp and fill (weft) directions to determine the degree of yarn undulations, yarn cross-sectional shapes, and micro-structural dimensions. These parameters were correlated to the fiber architecture. Specimens were designed and tested for the direct measurement of the through-the-thickness tensile, compressive and shear properties of the composites. Design optimization was conducted through the analysis of the stress fields within the specimen coupled with experimental verification. The experimentally-derived elastic properties in the thickness direction compared well with analytical predictions obtained from a volume averaging model .

INTRODUCTION

Woven and braided composite materials have been the subject of a great deal of research due to the superior through-the-thickness properties and delamination resistance over laminated composites, and the potential for near net shape processing. Numerous predictive models exist for the in-plane and through-the-thickness thermo-elastic properties of braided and woven textile composites. [1-5] Experimental validation of these models has been performed for in-plane properties and good agreement has been observed. However, very limited experimental work has been conducted for through-the-thickness properties due to the difficulty of such experiments and the lack of suitable test methods. The small out-of-plane dimensions of textile composite panels makes the introduction of a uniform tensile, compressive or shear stress field extremely difficult, if not impossible.

This work summarizes the results of an effort by the investigators to study testing and mechanical behavior of 3D woven polymer matrix composites in the thickness direction. The work reported here covers through-the-thickness tension, through-the-thickness compression, interlaminar shear, and transverse (i.e., through-the-thickness) shear testing. In addition, Mode I interlaminar fracture toughness behavior of the composites was also evaluated and the results will be presented in a separate report.

MATERIAL DESCRIPTION

Table 1 summarizes the architectures, thicknesses and tow sizes of the composites used in this investigation. The composites utilized Hercules AS-4 fibers and Shell 1895 epoxy resin. The 3D woven composites had layer-to-layer angle interlock (the LS series), through-the-thickness angle interlock (the TS series), and through-the-thickness orthogonal (the OS series) architectures. The 0.25" thick panels were used for interlaminar shear tests and Mode I interlaminar fracture toughness tests. The 1" thick panels were utilized in the through-the-thickness tensile, compressive and shear tests. All the preforms were woven by Textile Technologies, Inc. (TTI) of Hatboro, Pa. and impregnated by resin transfer molding (RTM) at Boeing of Seattle, WA. In addition to the above materials, a special orthogonal woven composite, the OS-4 panel, was designed and fabricated for through-the-thickness tension testing. This composite had an architecture similar to that of OS-3 except that it contained surface fiber tows attached to the first layer of the warp stuffer tows, forming a 1" long pile on each surface. The surface pile provided for the design of an integrated-grip specimen. The OS-4 panel was impregnated by the investigators using a especially designed mold and RTM processing. Schematics of the layer-to-layer angle interlock, through-the-thickness angle interlock, and orthogonal woven architectures are shown in Figures 1 through 3, respectively. Throughout this work the axes x, y, and z refer to the warp, weft, and thickness directions of the woven composite panels.

Prior to the characterization of the mechanical properties, the fiber volume fraction and microstructure of each panel were determined. This information was required for elastic property modeling. Fiber volume fractions were measured from a minimum of three samples taken from random locations in the panels. Overall fiber volume fractions and void volume fractions were determined using the acid digestion method (ASTM-3171 standard). Directional fiber volume fractions were measured from polished cross sections perpendicular to the warp and weft directions of panels by means of image analysis using NIH 1.54 image analysis software. A summary of the overall and directional fiber volume fractions of each panel is presented in Table 2.

The weave architecture controls the elastic and strength properties of the composite. The repeat structure of the 3D woven materials represents the warp weaver pattern and the weft stacking sequence. Two repeat units are often used to describe the structures of 3D woven materials. A "unit cell" is defined as the smallest segment of the architecture which can be equivalently translated in any direction. This cell does not, however, include the interlacings and surface tow weavers. Therefore, in order to describe the entire structure, a "macro-cell" has been defined. The macro-cell includes the entire thickness thus capturing any surface weavers, as well as the entire weave shifting sequence along the weft tows. Figure 4 illustrates the unit cell and macro-cell for a layer-to-layer angle interlock architecture. The microstructure of each panel was analyzed by microscopy of cross sections perpendicular to the warp and weft directions. Tow sizes and shapes were noted and measured and used to determine the dimensions of the unit cells and macro-cells of each architecture. Tow sizes were measured using NIH 1.54 image analysis software. A summary of the unit-cell and macro-cell dimensions of each composite is presented in Tables 3 and 4, respectively.

In addition to characterizing the dimensions of the repeat structures of each composite, the investigation also revealed the effects of processing on the composite micro structure. The high volume fractions (minimum 60%) desired for the parts requires compacting the dry preforms. The compacting causes distortion of the preform architecture, therefore affecting the composite properties. Several examples of the resulting warp weaver tow distortion for the 1" thick panels are presented in Figure 5. As the figures show, the distortion is quite severe and will obviously have a dramatic effect on the properties of the composite. The effects of the tow distortion on mechanical properties will be discussed in subsequent sections.

ELASTIC PROPERTY MODELING

Numerous schemes have been developed to estimate the thermo-elastic properties of 3D woven and braided materials. Some examples of these models include Yang, Ma and Chou's fiber inclination model [4]; Byun, Du and Chou's macro-cell model [1]; and a modified version of the macro-cell model, which includes more stringent cell boundary conditions, proposed by Pochiraju, Chou and Majidi [8] . These models use micromechanical predictions of tow properties followed by volume averaging of translated tow properties based on tow positions in the unit or macro-cell.

In order to predict the elastic properties of composites used in this work, the macro-cell model of Pochiraju et al. was modified to include the effect of distorted warp weaver tows. These properties were required for the design of the through-the-thickness tensile and compressive specimens, as well as the verification of the experimental results.

The RTM-induced tow distortion was modeled using a simplified sinusoidal path approximation (see Figure 6). The wavelength, λ, of the approximated sinusoidal was determined from the weave parameters of the architecture and the unit or macro-cell dimensions. The amplitude of the path was approximated using fiber volume fraction data, the weave parameters of the composite and macro-cell dimensions. First, the length of each warp weaver tow was determined using Equation (1).

$$L = \frac{4VV_{fz}}{tcz\,N_z\,\pi\,d_f^2} \qquad (1)$$

Where L is the length of the warp weaver tow, V is the volume of the macro-cell, V_{fz} is the volume fraction of warp weaver tows, tcz is the number of carbon fibers in a warp weaver tow, N_z is the number of warp weaver tows in the macro-cell, and d_f is the diameter of a carbon fiber. The length of each warp weaver tow in the macro cell is then used with the following equation to determine A, the amplitude of the distorted tow

$$L = \int_0^{Lzi} \sqrt{1 + \left(\frac{2\pi A}{\lambda} cos\left(\frac{2\pi x'}{\lambda}\right)\right)^2}\, dx' \qquad (2)$$

Where L_{zi} is the straight line distance between warp weaver interlacings, and the x' axis is oriented along the ideal path of the warp weaver tow (Figure 6). The L value from Equation (1) and the calculated value of λ allow the amplitude A to be solved for using an iterative scheme.

After the amplitude of the distorted tow was determined, the micro mechanical properties of the tow were calculated by averaging along the path of the tow, assuming iso-strain condition. The warp weaver, as well as the warp stuffer and weft tows, were assumed to be transversely isotropic bodies with axial and transverse elastic properties determined from the upper and lower bound rule of mixture approximations, respectively. The upper and lower bound approximations of the engineering constants of the warp weaver tow were then assembled into a stiffness matrix following equations presented in [9]. The overall properties of the distorted warp weaver tows were then averaged over the path of undulation by Equation (3)

$$C'_{ij} = \frac{1}{Lzi}\int_0^{Lzi}[T][C][T]^T dx' \qquad (3)$$

Where C'_{ij}'s are the components of the stiffness matrix of the warp weaver tow in the x' y' coordinate system in Figure 6 and [T] is the standard transformation matrix about the z' axis. This matrix can also be found in [9]. This averaging scheme was carried out numerically. The orientation angle along the undulating tow which is used in the [T] matrix is obtained from the slope of the tow by Equation (4)

$$\theta = tan^{-1}\left(\frac{2A\pi}{\lambda}cos\left(\frac{2\pi x'}{\lambda}\right)\right) \qquad (4)$$

Following the averaging scheme of Equation (3), the micro mechanical properties of the distorted tow are transformed to the coordinate system of the composite panel (the x y system in Figure 6) and used in the volume averaging scheme described in [8]. A summary of the predicted elastic properties using the above micro mechanical model and Pochiraju et al's modified macro-cell model is presented in Table 5.

THROUGH-THE-THICKNESS TENSILE TESTING

Specimen Design

A parallel-sided, multi-section specimen consisting of a test section and transition sections was designed for direct through-the-thickness tensile testing. Shan, Majidi, and Chou [7] conducted a detailed 2D stress analysis of the specimen using Boundary Element Analysis (BEA) method in order to optimize the specimen dimensions and reduce stress singularity at the test section/transition section interface. This singularity followed the forms shown in Equations (5) and (6) for displacements and stresses respectively.

$$u_i \propto r^{1-\alpha} \qquad (5)$$

$$\sigma_{ij} \propto r^{-\alpha} \qquad (6)$$

The BEA showed that α was a function of the specimen geometry and the elastic properties of the test and transition sections. The BEA also showed that α became zero for isotropic and orthotropic materials when:

$$\left(\frac{\nu_{ij}}{G_{ij}}\right)_{test} = \left(\frac{\nu_{ij}}{G_{ij}}\right)_{transition} \qquad (7)$$

Therefore, the transition sections must have Poisson's ratio/shear modulus ratio that closely matched that of the test section. Material selection for the transition sections therefore requires reliable predictions of the elastic properties of the composite to be tested.

Besides the dimensional optimizations and property matching, the BEA also showed that notching the transition section above the interface would further reduce α. Figures 7 and 8 show the notched and un-notched bi-material specimens with optimized dimensions, respectively.

Two approaches were followed for the introduction of the transition sections. In the first approach, the transition sections were adhesively bonded to the test section. This specimen configuration was designated the "bi-material specimen" and could be used only for the determination of the elastic properties due to the early failure of the bonded joint. In an effort to delay failure in order to examine the entire stress-strain response, and perhaps obtain the through-the-thickness strength, a second specimen configuration, designated the "integrated-grip specimen" was designed using the OS-4 preform architecture shown in Figure 3a. The surface piles in the OS-4 preform provided for transition sections that were integrally woven to the test section, thus avoiding bonded interfaces in the specimen. Details of the fabrication and testing of the bi-material and integrated-grip specimens are described below.

Specimen fabrication and Testing Procedures

The Bi-Material Specimen Configuration

In order to assess the validity of the bi-material specimen design, three specimen configurations were produced with a TS-3 test section. The first configuration, denoted generation 1, did not use the optimal specimen dimensions or transition/test section material matching. The second specimen configuration, denoted generation 2 (see Figure 7), utilized the optimized specimen geometry and material matching, but did not utilize notches above the interface. The last specimen configuration, denoted generation 3 (see Figure 8), was identical to the generation 2 specimen but utilized notches above the interface as described in the previous section. Only generation 3 specimen was used for tests on LS-3 and OS-3 panels.

The transition sections were 2D glass fabric reinforced epoxy composites fabricated by RTM processing using Shell Epon 862 epoxy resin. The glass fabrics used and their composite properties are shown in Table 6 [10]. These were selected to provide good matching with the predicted elastic properties of Table 5 for the 1" thick (i.e., LS-3, TS-3, and OS-3) woven composites. Table 7 presents the proposed transition and test section combinations for the measurement of E_{33}, ν_{23} and ν_{13} and the predicted α at the corner of the transition section/test section interface.

The test section and transition sections were cut to the proper dimensions and bonded together with American Cyanamid FM-300 film adhesive using a especially designed bonding fixture. The bonding fixture was utilized to assure that constant bonding pressure and specimen alignment were maintained during the cure cycle.

Specimens were cut and prepared along both orientations (i.e., with their wide surfaces parallel to warp or weft directions) in order to measure E_{33} and both ν_{23} and ν_{13}. Electrical resistance strain gages were affixed to both surfaces of each specimen. Tensile testing was carried out on an Instron Model 1125 displacement controlled machine at a displacement rate 0.02"/min. Load and strain gage were recorded using Macintosh based Lab View software.

The Integrated-Grip Specimen Configuration

The integrated-grip specimen was fabricated from the OS-4 composite panel with dimensions given in Figure 9. The interlacing surface pile in the OS-4 preform was woven over polycarbonate spacers. The preform was impregnated by the investigators in 3" x 5" x 2" sections utilizing a especially designed RTM mold. Preform compaction was not utilized in an effort to maintain the orthogonal orientation of the external surface piles. Therefore the fiber volume fraction of the OS-4 composite was similar to that of the preform (i.e., 45%). Following impregnation, void volume calculations according to ASTM D-3171 were performed on several specimens taken from the OS-4 test section. The measurements showed the OS-4 composite to have less than 2% voids which was deemed acceptable. The test section in OS-4 preform had an architecture identical to that of OS-3 preform. However, the actual post-processed architecture and fiber volume fractions of OS-4 composite were somewhat different than those of OS-3 composite due to the lack of compaction when processing the OS-4 composite panel.

The integrated-grip specimens were designed to utilize the same test section dimensions as those used with the bi-material specimen. However, stress singularity reduction by means of test section/transition section property matching or transition section notching were not exercised in the current specimen configuration due to material limitation. Such modifications can be implemented in the specimen design and will undoubtedly improve the results.

The integrated-grip specimens were prepared and tested along the orientations and under the conditions similar to the bi-material specimens.

Results and Discussion

Figure 10 shows a typical stress versus strain plot for a generation 3 bi-material specimen of TS-3 composite. Over 20 specimens were tested for each architecture and the elastic modulus and Poisson's ratio were determined from the initial straight region of each curve. Table 8 summarizes the average elastic properties obtained for the LS-3, TS-3 and OS-3 composites. The Table also lists values of the elastic modulus normalized to 60% fiber volume fraction to facilitate direct comparison of the composites.

Approximately 15 integrated-grip specimens of each orientation were tested and evaluated following the test methods described above. A typical stress versus strain curve for an OS-4 specimen is shown in Figure 11. A summary of the average elastic properties of the OS-4 composite are also presented in Table 8. Again, the measured elastic modulus has been normalized to 60 % fiber volume fraction to facilitate comparison with the properties of the LS-3, TS-3 and OS-3 composite panels.

As Figure 10 indicates, the bi-material specimen reached a maximum stress of only ~1900 psi (13 MPa) due to the failure of the adhesive bond. This failure level was seen to be very repeatable for the generation 3 specimen configuration. In comparison, interface failure levels for generation 2 specimen were typically 1500 psi (10.3 MPa), while generation 1 specimens showed typical interfacial failure stresses of 1200 psi (8.3 MPa). Examination of the generation 3 failure surface consistently showed that failure had occurred at or near the interface, showing evidence of carbon fiber tows having pulled out of the test section. The steady increase in interfacial failure stress from generation 1 to generation 3 specimen configuration shows the success of the singularity reduction scheme.

Direct comparison in Figure 12 of the measured elastic modulus, E33, for the three specimen generations of TS-3 composite shows that while the mean modulus is comparable within 12.8 %, there is a steady decrease in the variation of measured properties from generation 1 to generation 3 configuration. The error bars show one standard deviation range on either side of the mean. The reduction of the scatter in data again shows the effectiveness of interface singularity reduction. Of course some scatter is expected to exist due to experimental variations such as specimen location, local architecture, etc.

Comparing Figures 10 and 11 shows that the integrated-grip specimens failed at approximately 320% higher stress than the TS-3 bi-material specimens. Nevertheless, the OS-4 specimens still failed at the transition section/test section interface or in the grip section, thus preventing a strength measurement. Grip section failures were typically caused by preform imperfections. These imperfections were a result of surface pile tows in the preform interlacing several spacers. This caused the skewing of the spacers and the loss of orthogonality in the transition fiber tows which led to the premature failure within the transition section. In addition to preform imperfections in the transition section, numerous imperfections were observed in the fiber architecture of the OS-4 preforms within the test section. These imperfections are responsible for the large elastic modulus variation noted in the measured properties of the OS-4 composite.

Recommendations for Improvement of the Specimen Design

The failure stress in the bi-material specimen may be increased by using a lap joint configuration at the interface. The lap-joint would offer increased bonding surface over the current configuration and should help prevent premature first-layer fiber pull-out. A schematic of the proposed specimen configuration is presented in Figure 13. Preliminary analyses by the finite element method (FEM) have been performed to study the effects of the lap configuration on the stress field. The predicted through-the-thickness tensile stress profile is presented in Figure 14. The figure shows that the stress field is uniform in the major part of the test section.

The OS-4 preform was the first attempt by TTI at the design. Refining the preforming process in order to eliminate the processing imperfections would improve the failure strength and yield more reproducible data. Improvements in specimen design are also possible. The integrated-grip specimens used in the current investigation did not utilize material property matching between the transition and test sections. In the transition section there was no reinforcement along the warp direction and only polycarbonate spacers existed as "reinforcement" in the weft direction. The drastic in-plane property differences between the test and transition sections obviously resulted in a large stress singularity at the interface corners of the OS-4 specimens. This singularity could be reduced by replacing the polycarbonate spacers with graphite/epoxy laminate spacers of similar elastic properties and fiber volume fraction as the warp reinforcement of the test section.

In addition to including laminates as spacers, the use of stronger pile tows in the transition section than those utilized as through-the-thickness reinforcement in the test section could promote failure in the test section. Additionally, a dog-bone configuration could be utilized as presented in Figure 15. However, further stress analysis is required to determine optimum specimen configuration.

THROUGH-THE-THICKNESS COMPRESSION TESTING

Current Status of Compression Testing of Composite Materials

Compression testing of composite materials with laminated, 2D and 3D architectures has been an area of much research, as well as ambiguity. In general, compression test methods can be split into three categories based on the method of load introduction. The first type, designated indirect or shear loading, introduces a compressive stress field by shear loading the specimen through a fixture. Indirect methods include the IITRI, Celanese, and Lockheed test procedures. The second type, designated direct loading, applies the compressive load directly to the ends of the specimen such as in the NASA, NBS, Rockwell, Wright Patterson, RAE and ASTM-D695 procedures. The direct and indirect methods use both tabbed and untabbed specimens and specimens with lateral support of the gage section. The third specimen type is termed mixed loading and includes flexural test methods of honeycomb sandwich structures. [11]

Several studies comparing compression test methods for advanced composite materials have shown that while measured elastic properties are unaffected by the test method, the strength is strongly dependent on the specimen configuration and method of load application [11,12].

The main goals in the design of a compression specimen are to avoid Euler buckling and to yield a uniform stress field throughout as much of the specimen gage length as possible. Treating the specimen gage length as a homogeneous, orthotropic, simply-supported beam and without the consideration of shear deformations, the critical Euler buckling load [13] is given by

$$P_b = \frac{\pi^2 (w E_{ii} t^3)}{12 l^2 (1 - \upsilon_{ij} \upsilon_{ji})} \qquad \text{with } t < w \qquad (8)$$

where l, w, and t are the length, width, and thickness, respectively, of the specimen within the gage section; E_{ii} is the Young's modulus along the load direction; and ν_{ij} and ν_{ji} are the Poisson's ratios. The i and j subscripts denote directions parallel to the loading axis and perpendicular to the loading axis (i.e., parallel to the thickness direction of the specimen), respectively. When transverse shear deformation of the orthotropic material is included, the critical buckling load has been shown to be given by [14]

$$P_{cr} = \frac{P_b}{1 + 1.2 \cdot \frac{P_b}{A G_{ij}^{eff}}} \qquad (9)$$

Equation (9) represents a check on the measured strength. If the measured strength is close to the Euler buckling load, the specimen design is invalid and the gage length should be shortened. As Equation (9) shows, the critical load is a function of the material properties. Therefore, the required gage length can change with material system.

Specimen gage length also affects the uniformity of the stress field within the specimen test section. An analysis by Horgan [15] gives the following upper bound for Saint Venant's decay length, i.e., the distance from the load application point at which a uniform stress field is obtained

$$\lambda_{sv} = \frac{4.6}{2\pi} t \left(\frac{E_{ii}}{G_{ij}} \right)^{0.5} \qquad \text{for} \quad \frac{E_{ii}}{G_{ij}} >> 1 \qquad (10)$$

A detailed finite element analysis of the IITRI fixture by Bogetti et al. [14] showed the decay length for the specimen to be about 34% of that predicted by Equation (10). Thus the FEM-predicted decay length is approximately

$$\lambda_{fem} = \frac{t}{4} \left(\frac{E_{ii}}{G_{ij}} \right)^{0.5} \qquad (11)$$

From Equation (11), the minimum specimen gage length which will result in a uniform stress field at the midplane of the specimen is $2\,\lambda_{fem}$. This gives the following criterion for minimum gage length based on the stress field uniformity requirement

$$\frac{l}{t} > \frac{1}{2} \left(\frac{E_{ii}}{G_{ij}} \right)^{0.5} \qquad (12)$$

Therefore, Equations (9) and (12) provide the necessary specimen design constraints for valid compression testing.

Three main compressive failure modes have been observed for laminated composites [10,16,17]. These modes are: longitudinal matrix splitting, kink band formation and fiber microbuckling. Fiber microbuckling can occur in shear (in-phase buckling) or extensional modes (out-of-phase buckling). Fiber microbuckling is prominent in composite systems with low-modulus matrix materials. Several analytical models attempt to predict the critical microbuckling load for single fibers embedded in an infinite matrix and for fibers in a composite. Microbuckling loads are obtained by modeling the fibers as two-dimensional columns supported by an elastic foundation. Analyses show that the extensional mode dominates at low fiber volume fractions while the shear mode prevails at fiber volume fractions greater than 30%.

Following the methodology described above, Rosen [18] determined the critical microbuckling stress for the extensional mode to be

$$\sigma_{ce} = 2v_f \left[\frac{E_f E_m v_f}{3(1-v_f)} \right]^{0.5} \qquad (13)$$

where v_f is the fiber volume fraction along the load direction, E_f is the Young's modulus of the reinforcing fiber, and E_m is the Young's modulus of the matrix material. Similarly, the critical microbuckling stress for the shear mode was shown to be:

$$\sigma_{cs} = \frac{G_m}{(1-v_f)} \qquad (14)$$

where G_m is the matrix shear modulus and v_f is the fiber volume fraction along the load direction. Extensions of Rosen's work have been performed to include inelastic microbuckling and initial fiber misorientation [19, 20] .

As the modulus of the matrix material increases the compressive failure mode changes to kink band formation. Typically, kink bands originate at the specimen surface and propagate into the specimen. Kink band formation is random and total failure depends on the merging of the kinked regions. Analyses have shown that fiber kinking strongly depends on the extent of the initial fiber misorientation with respect to the load axis and the matrix yield strength. A detailed thermodynamic analysis by Evans and Adler [21] considers elastic strain energy in the fiber and matrix, plastic work in the matrix, and fiber fracture surface energy to predict kink angles and a failure criterion. A simplification of their analysis presented by Argon [22] shows the critical failure stress in compression to be

$$\sigma_c \approx \frac{\tau_{mys}}{\phi} \qquad (15)$$

where τ_{mys} is the matrix yield shear stress and ϕ is the initial misorientation in radians. The failure criterion offered by Evans and Adler includes statistical flaw distributions and probabilistic fiber fracture parameters.

A limited amount of experimental characterization of the compressive properties of 3D woven composite materials has been performed in the past [23-26]. Cox et al. [25] investigated the in-plane compressive behavior of layer-to-layer and through-the-thickness angle interlock woven carbon/epoxy composites. The failure mode was determined to be kinking of the warp stuffer tows. The final failure of the specimens was seen to be along a shear band. Total failure was assumed to occur at the formation of the second kink band. The critical load was determined from Equation (15) and measured misorintation angles. Good agreement was noted between the predicted critical loads and measured failure loads.

Design and Fabrication of 3D Woven Composite Specimens for Through-the-Thickness Compression Testing

The IITRI specimen configuration was selected for through-the-thickness compression testing of 3D woven composites in this investigation. Compression tests utilized the 1" thick LS-3, TS-3, and OS-3 composites. A bi-material compression specimen was designed following the methodology described above for through-the-thickness tensile testing. The bi-material compression specimen utilized 2D glass fabric reinforced epoxy composite transition sections for the grip area, along with standard glass/epoxy tabs to introduce a uniform compressive stress state into the 1" thick textile composite test coupon. A schematic of the specimen configuration used in the investigation is presented in Figure 16. The specimen thickness and width of 0.25" (6.35 mm) and 0.5" (12.7 mm), respectively, were selected based on the analysis of reference 6. The specimens utilized transition section material matching to minimize the stress singularity which exists at the corners of the test section/transition section interface [7]. Singularity reduction was implemented to ensure that failure occurred in the test section of the specimen and not in the adhesive layer. In order to select a gage length, the critical buckling load (Equation 9) and the critical stress decay length (Equation 11) were calculated using predicted elastic properties. The results are shown in Table 9. Critical lengths and buckling stresses were calculated for both the xz and yz orientations which were used to obtain v_{23} and v_{13}, respectively. These two orientations

required the use of predicted values of G_{23} and G_{13} in Equations (9) and (11). As Table 9 shows, the critical length for stress field uniformity is quite small. The small λ_{cr} is a result of the low degree of anisotropy which exists in the through-the-thickness direction. Since only about 10% of the total fiber volume is oriented in the thickness direction, E_{33} is low and λ_{cr} approaches values for isotropic materials. Since the stress decay length is less than 0.5", which is the recommended gage length for the ITTRI test, a gage length of 0.5" was selected for the specimens to ensure a uniform compressive stress field throughout the specimen gage length.

The test and transition sections were bonded together using American Cyanamid FM-300 film adhesive and a bonding fixture designed and fabricated by the authors. The bonding fixture ensured proper alignment and adequate bonding pressure. The specimens were cured at 350 °F for two hours. Following the adhesive cure, 0/90° strain gages were bonded to the test section of the specimen for strain measurement.

Compression Test Procedure

The bi-material specimens were tested in a displacement-control Instron Model 1125 testing machine at a displacement rate of 0.02 in/min (0.51 mm/min). Load and strain were monitored and stored by Macintosh-based Lab View software. Each specimen was tested until failure. Peak loads were noted and used to calculate the ultimate compressive stress, σ_c^{ult}, for each specimen.

Following the determination of an average σ_c^{ult} for each architecture, a second series of specimens was tested to various load levels to determine the failure mechanisms. Several specimens were loaded to levels near σ_c^{ult}. In the remaining specimens, the maximum load was reduced by steps of 1,000 lb (4.45 kN) to a minimum of 30% of the ultimate strength.

After testing, the surface of each specimen was examined by low-magnification optical microscopy to catalog the surface damage. Following surface inspection, the specimen was cut into four sections along the width direction and the sections were mounted and polished for optical microscopy. Damage modes such as matrix cracks, kink bands and transverse tow cracks were identified and cataloged.

Compression Test Results and Discussion

Elastic Compressive Properties

Elastic properties were obtained from at least five specimens for each architecture and both specimen orientations. Elastic modulus and Poisson's ratios were calculated from the stress-strain curves within the initial 2000 microstrain range. A typical stress-strain curve for an OS-3 specimen is presented in Figure 17. Each specimen tested showed linear behavior up to the maximum strain recorded by the strain gage. The average measured elastic properties for the LS-3, TS-3 and OS-3 composites are presented in Table 10. Measured elastic properties agreed well with the predicted properties presented in Table 5. Comparing the predicted and measured through-the-thickness compressive modulus, E_{33}^c, we find differences of -2.5%, -7.9% and -0.7% for the LS-3, TS-3 and OS-3 composites, respectively. The measured compressive elastic properties compare

favorably with the predicted properties and the measured through-the-thickness tensile elastic properties. The measured Poisson's ratios do not show as favorable an agreement with predictions as the Young's modulus. There are two possible reasons for this. First, the strain gages used to measure the Poisson's properties are much smaller than the dimensions of the macro-cell and are therefore not averaging the mechanical response of the material over an area comparable to that used in the model. Second, the low Poisson's ratios of these materials make accurate measurement of transverse strains extremely difficult.

Compressive Strength and Damage Progression

The peak load was used to calculate σ_c^{ult} for each specimen. The average values of σ_c^{ult} are presented in Table 11. The initial drop after the peak load coincided with splitting of surface warp or weft tows which were oriented perpendicular to the applied load. Beyond the peak load catastrophic failure of the specimen occurred, usually originating at split or damaged surface tows. The final failure appeared to follow the shear band mechanism discussed in the literature for in-plane compression of 3D woven composites [20-22]. However, the failure initiation by transverse surface tow splitting, and not kink band formation in the load bearing tows, made the through-the-thickness compressive failure mechanisms different from the in-plane mechanisms. The measured through-the-thickness strengths show little difference among the architectures. Also, for all architectures the xz specimen orientation produced lower measured strength than the yz orientation. These observations may imply that the failure of the composite is not controlled by the through-the-thickness warp weaver tows, but by the transverse (with respect to the load direction) warp stuffer and weft tows. The xz specimen orientation has the weft tows oriented out of the large 0.5 " (12.7 mm) x 0.5 " (12.7 mm) face (see Figure 16). This orientation has seven unsupported weft tows susceptible to transverse cracking, while the yz orientation has only six unsupported warp stuffer tows.

Microscopic inspections of the failed and damaged specimens indicated that surface tow splitting was the dominant failure mechanism for all three architectures. A summary of the damage progression observations is presented in Tables 12-14 and denotes similarity among the three architectures. Figure 18 documents the damage progression in the surface tows of LS-3 specimens loaded to 110 MPa, 165 MPa, 220 MPa and peak load, respectively. The figures show that damage increases with increased loading, and the orientation of the cracks implies shear damage (approximately ±45° to the loading direction).

As Tables 12-14 show, kink bands in the warp weaver (through-the-thickness) tows were present before the peak load was reached and therefore were not the direct cause of failure. As expected, the number of kink bands observed increased with increasing load. Kink bands are predicted to occur initially at regions of maximum misorientation with the applied load. This supposition was followed in some cases, but the writers observed that existing defects or damage seemed to be more responsible for the initial location and load at which kink bands formed. Several examples of observed kink bands near defects are presented in Figure 19.

In an attempt to ascertain that the observed kink bands were not the dominant failure mode, the critical load values predicted by the kink band model were calculated and compared to the measured values. The load on the warp weaver tows was determined by approximating the warp weaver stacks and the transverse tows as discrete layers. The modulus of the transverse tow layers was approximated by the lower bound rule of mixtures assuming a tow packing fraction of 80%. The warp weaver tow properties were obtained by transforming the axial tow properties with respect to the load axis. The angle of transformation is fixed by the weave architecture. The final load on the warp weaver layers was then calculated by assuming that an iso-stress condition existed in the through-the-thickness direction. Thus

$$\sigma_{33}^{ww} = \frac{\tau_{mys}}{\phi} \qquad (16)$$

at kink-band formation. Using Equation (16) , a matrix yield shear stress of 75 MPa ,and the warp weaver tow orientation, the critical kinking stress for each architecture was calculated and the results are summarized in Table 15. The misorientation angle ϕ was calculated with respect to the z axis and included an average tow distortion component. The tow distortion component was calculated from fiber volume fraction data and an assumed sinusoidal distortion path. As Table 15 shows the predicted kink-band stress corresponds nicely with kink-bands observed during the progressive damage study. The calculations also confirm that the kink-band failure mechanism is not the dominate failure mechanism for overall failure. Additional work is in progress to verify transverse tow failure mechanism as the true dominating failure mechanism.

THROUGH-THE-THICKNESS SHEAR TESTING

Specimen Design and Analysis

Numerous in-plane shear test methods have been developed to characterize the shear properties of composites with laminated and 2D preform architectures [27]. In reviewing these methods to determine the feasibility of modification for use in measuring through-the-thickness shear properties of 3D woven composites it was clear that many of them, including the torsional tube test method, the cross beam method, the Rail Shear method, the Arcan method, and the picture frame method, were unsuitable due to the complex methods of load introduction or the required specimen dimensions. Two test methods, namely the ASTM D-3846 Double Notch Shear (DNS) specimen and the Compact Shear (CS) specimen , appeared viable for utilization.

The Compact Shear specimen, shown in Figure 20, was recently developed by Ifju at Virginia Polytechnic Institute and successfully used to measure in-plane shear properties of cross-ply laminates and 3D woven composites [28]. The original specimen has dimensions of 1.5" x 1.5". However, because of the limited thickness of the composite panels (i.e., 1" for the thick panels in this investigation), the specimen dimensions have to be modified for application to through-the-thickness testing.

The standard ASTM D-3846 DNS specimen, also shown in Figure 20, has primarily been used to measure the interlaminar shear strength of laminated composites. Analysis of the specimen in [27] showed the shear stress field to be extremely nonuniform. Work by Bouette, Cazeneuve and Oytana [29] indicated that overlapping of the machined notches resulted in increased uniformity of the shear stress field in the gage section. Their work included a parametric FEM study to determine the effects of specimen gage length, L, and notch overlap, H, on shear stress field uniformity and tensile opening stresses. As with the CS specimen, the dimensions of the DNS specimen was modified for the measurement of through-the-thickness shear properties of 3D woven composites in this study. FEM analysis was conducted to examine stress distributions in the modified CS and DNS specimens. The results are presented below.

Modification and Analysis of the CS Specimen

Schematics of the two modified CS specimens used in this investigation are shown in Figure 21. The modified specimens are denoted TTIS1, which is used to measure the interlaminar shear properties, and TTIS2 which gives the transverse shear properties. Specimen performance

was judged by comparing the shear stress fields of Ifju's specimen, designated the baseline specimen, and the two modified specimens. Similarly, the transverse tensile stress fields were compared. The goal of the specimen modification was to create a specimen with shear stress field uniformity comparable to the baseline specimen and minimal transverse tensile stresses.

The FEM mesh used to analyze the baseline CS specimen is shown in Figure 22. Eight-node plain stress quadrilateral elements were used throughout the model. Boundary conditions were applied to approximate conditions existing in the fixture. It was assumed that the portion of the specimen clamped in the stationary half of the fixture had zero displacements in the x (or y depending on specimen orientation) and z directions. Similarly, the portion of the specimen clamped in the loaded half of the fixture was assumed to have zero displacements in the x (y) direction. Loading was approximated as a uniform pressure on the upper right arm of the specimen. Computations were performed for an applied pressure giving an average shear stress of 200 psi (1.38 MPa),where

$$P = \frac{\tau_{ij}^{ave} L}{A} \qquad (17)$$

where P is the applied pressure, τ_{ij}^{ave} is the average shear stress at the midplane of the specimen, and L and A are shown in Figure 21.

The FEM mesh was created using the commercial package PATRAN and solutions were obtained with ABAQUS. Normalized shear stress distributions along the gage length are presented in Figure 23 for the midplane (m=0) and planes at distances of m=0.05", m=0.10", and m=0.15" from the midplane. Figure 23 shows the shear stress field to be relatively uniform along the midplane. The magnitude of the stress in this plane is equal to τ_{ij}^{ave} over a z/L range of 0.3 to 0.6.

Figure 23 also presents the normalized transverse tensile stress field in the specimen gage section for the midplane and planes at distances of m=0.05", m=0.10", and m=0.15" from the midplane.. It is shown that the transverse tensile stress field is essentially zero in the majority of the specimen gage section. The results also show that the stress increases with increasing distance from the midplane and as the notches are approached.

Following the analysis of the baseline specimen, stress fields in the TTIS1 and the TTIS2 specimens were examined. The FEM meshes used for TTIS1 and TTIS2 specimens are also displayed in Figure 22. Eight-node plane stress quadrilateral elements and boundary conditions identical to those of the baseline specimen were adopted. The resulting shear and transverse tensile stress fields for a τ_{ij}^{ave} of 200 psi (1.38 MPa) are presented in Figures 24 and 25. The shear stress field for TTIS1 specimen (Figure 24) shows a loss in the symmetry of field compared to the baseline specimen. Conversely, the TTIS2 specimen maintains, if not improves, the field symmetry of the baseline specimen, but exhibits a plateau shear stress of approximately 1.05 times τ_{ij}^{ave} at the specimen midplane. Both specimen configurations displayed similar shear stress decrease with increasing distance from the midplane.

The shear stress fields in the modified TTIS1 and TTIS2 are altered only slightly from those in the baseline specimen. The significant area of the specimen is that covered by the strain gage. The dimensions of the shear gages utilized in this investigation are 0.75" (19 mm) x 0.125" (3.2 mm) for the TTIS1 specimen and 0.5"(12.7 mm) x 0.125" (6.35 mm) for the TTIS2

specimen. In an attempt to quantify the effects of the specimen modification, the average shear stress for planes at a constant distance from the midplane which would be covered by the strain gage was calculated, where

$$\tau_{ij}^{ave} = \frac{1}{L}\int_{L_o}^{L_f} \tau_{ij} dx_j \qquad (18)$$

where i = 3 and j=1,2 for the TTIS1 specimen, while i=1,2 and j=3 for the TTIS2 specimen; L_o and L_f denote the x_j coordinate of the notch tips for the upper notch and the lower notch, respectively. Equation (18) was approximated using nodal shear stress values according to the trapezoidal scheme, where

$$\tau_{ij}^{ave} = \frac{1}{L}\left[\frac{\tau_{ij}^{1}}{2}(x_j^2 - x_j^1) + \sum_{k=2}^{N-1}\tau_{ij}^{k}(x_j^k - x_j^{k-1}) + \frac{\tau_{ij}^{N}}{2}(x_j^N - x_j^{N-1})\right] \qquad (19)$$

where x_j's are the positions of the nodes along the specimen gage length, and N is the total number of nodes along a constant x_j plane. Average stresses were calculated for the specimen midplane and for positions at 0.05" and 0.10" from the midplane. The results of the estimated average stress state on each constant x plane for each specimen is presented in Table 16.

As Table 16 shows, the TTIS1 and TTIS2 specimen modifications only slightly affect the average stress in the specimen gage section. Comparing the two modified specimens with the baseline, the TTIS1 specimen shows a maximum difference with the baseline specimen of approximately 2.0% at the midplane and about 5.1% at 0.10" (2.54 mm) away from the midplane. The TTIS2 specimen shows slightly better agreement at the midplane with a difference of only 1.6% from the baseline specimen. The average shear stress along the midplane of the TTIS2 specimen is, however, closer to the desired average stress of 200 psi (1.378 MPa) than the baseline or TTIS1 specimens. The agreement with the baseline decreases slightly to a 10% difference at 0.10" away from the midplane. All three specimens show approximately a 15% drop in average shear stress at a distance of 0.10" away from the midplane. The analyses also show that for the measurement of strength, failure should occur at the specimen midplane, where

$$\tau_{ij}^{ult} = \frac{F}{LT} \qquad (20)$$

where F is the magnitude of the load applied to the arm of the specimen, L is the specimen gage length at the midplane, and T is the specimen thickness.

Modification and Analysis of the DNS Specimen

The goal of the parametric study was to maximize the degree of uniformity in the shear stress field in the specimen gage section while minimizing the tensile opening stress. The work of Bouette et al. and others has shown that the stress singularity at notch tips is reduced with increasing notch radius. Using this information a notch of radius of 0.03" (0.75mm) was used in the model. Several gage lengths ranging from 0.125" (3.2 mm) to 0.290" (7.4mm) were included in the study. Notch overlap ranges of 0 %, 10%, 20% and 50% of the specimen height of 0.25" (6.35 mm) were investigated.

A typical FEM mesh used in the investigation is shown in Figure 26. Eight-node plane stress quadrilateral elements were used throughout the entire model. The ASTM D-3846 method utilizes a steel clamp, shown in Figure 20, to prevent specimen buckling. However, the small size of the suggested specimen precludes the use of such a clamp here. The specimen is loaded directly in compression between two platens. This loading condition was modeled as zero displacements along the lower platen and as a uniform pressure field at the upper platen.

Following the methodology of the CS specimen analysis, pressure was applied to produce an average shear stress of 200 psi (1.378 MPa) at the midplane of the specimen. The magnitude of the applied pressure is again determined using equation (17) with the dimension A being replaced by the notch spacing L. Models were run for L values of 0.125" (3.2 mm), 0.250" (6.35 mm) and 0.29" (7.4 mm) and H (notch overlap) values of 0%, 10%, 20% and 50% of the specimen thickness for each L condition.

The results, shown in Figure 27, for a gage length of 0.290" are similar to those obtained by Bouette et al. It is seen that increasing the notch overlap improves the symmetry of the stress distribution on each constant x plane, and brings the average shear stress on the midplane closer to the desired τ_{ij}^{ave} of 200 psi. Also, the shear stress profile symmetry decreases with increasing gage length. These trends are quantified in Table 17 which presents the average shear stresses from equation (19) for the specimen midplane and at 0.025" and 0.05" away from the midplane. Table 17 showes that the notch overlap, H, controls the uniformity of the shear stress distribution in the x (y) direction. The distribution is important in elastic property measurement. If the change in average stress between x (y) planes is small, standard strain gages can be effectively used to measure through-the-thickness shear muduli.

In addition to shear stress field uniformity, minimization of tensile opening stresses was desirable to ensure failure in shear. Figure 28 shows the effect of increasing L on the transverse tensile stress distribution at the specimen midplane for H =0%. Increasing L and H increased the maximum tensile stress observed near the notch. raising the H was shown to raise the predicted maximum tensile stress. The maximum opening tensile stress predicted was approximately 4 times the average shear stress, which was seen for the specimen with L=0.290" (7.4 mm) and H=50%.

The FEM analysis revealed the need for the design of two distinct specimen configurations; one for the measurement of the elastic shear properties and the other for the determination of shear strength. In an attempt to capture as much of the through-the-thickness repeat structure as possible for elastic property measurement, the final dimensions of the elastic property specimen were selected as L=0.290" (7.4 mm) and H=50%. The strength specimen required minimizing L to reduce transverse tensile stresses. However, as with the elastic property measurement, testing of the entire repeat structure was desirable. Therefore, it was decided that several specimens with different gage lengths would be used, all with H=20%. The H value of 20% was used to ensure that the average shear stress in the specimen midplane was in fact the desired stress as calculated by equation (20). Schematics of the final specimen dimensions are presented in Figure 29.

Shear Specimen Fabrication and Testing Procedures

Both the TTIS1 and TTIS2 specimen configurations were utilized in testing for through-the-thickness properties of the LS-3 composite panel. Due to lack of material, only the TTIS1 specimen configuration was used with the TS-3 and OS-3 panels. Each specimen was prepared and tested in two orientations to measure the various through-the-thickness shear properties. Table

18 lists the specimen orientations and the properties determined for each specimen and orientation . The orientation was defined by the plane on which the shear stress was applied (See Figure 21). The TTIS2 specimen configuration gives the transverse shear properties while the TTIS1 configuration yields the interlaminar shear properties.

Specimens were cut from the composite panels using a water-lubricated, diamond-coated cut-off wheel. Following the cutting procedure, notches were machined into each coupon using a 0.25" (6.35 mm) diameter endmill. Next, strain gages were bonded to the surface of each specimen as shown in Figure 21. Both TTIS1 and TTIS2 specimens were tested in the fixture developed by Ifju. The fixture was designed to accommodate 1.5" (38 mm) x 1.5" (38 mm) specimens. Since the TTIS2 specimen is only 1" (25.4mm) long in the load direction composite spacers were fabricated and used to support the specimen in the fixture.

Due to lack of material, the modified DNS specimen was used only for the OS-3 composite to determine G_{13} and τ_{13} properties. coupons, 0.50"x 0.50"x1.0", were cut from the OS-3 panel in the yz orientation. Notches were machined into each specimen using a slot grinding machine fitted with a diamond-coated wheel. Following the notching procedure, 0.0625" (1.6 mm) shear strain gages were bonded onto the specimen at the center of the gage length as shown in Figure 29. The strain gages covered approximately 80% of the specimen gage section.

In addition to the 1" thick composites, interlaminar shear strength tests were also performed on the 0.25" thick LS-1, LS-2, TS-1 and TS-2 panels. Shear strengths were measured using standard ASTM D3846-79 specimens shown in Figure 20. Two specimen orientations were tested to obtain shear strengths τ_{31} and τ_{32}. The τ_{31} was obtained by imparting a compressive load along the warp tows, while the τ_{32} was measured by applying a compressive load along the weft tows.

All shear tests were conducted in an Instron 1125 displacement-controlled machine at a displacement rate of 0.02"/min (0.71 mm/min). Load and strain were monitored and stored using Macintosh supported Lab View software.

Shear Test Results and Discussion

Elastic Shear Properties

Summaries of measured elastic shear moduli for each composite architecture and specimen configuration are presented in Table 19. Representative stress vs. strain plots obtained from the TTIS1 and TTIS2 specimen configurations are shown in Figures 30 and 31, respectively. The materials tested typically showed large regions of linear response followed by non-linear response.

Comparing measured elastic moduli for the LS-3 composite in Table 19, it is noted that for identical shear couples the moduli are nearly equivalent. A statistical analysis, using t-test with a confidence level of 95%, was performed on the raw data to check for the equivalency of measured G_{13} and G_{23} (TTIS2 configuration) with G_{31} and G_{32} (TTIS1 configuration). The following null and alternative hypothesis were proposed:

$$H_0: G_{13}^{TTIS2} = G_{31}^{TTIS1}$$
$$H_1: G_{13}^{TTIS2} \neq G_{31}^{TTIS1} \qquad (21)$$

and

$$H_0: G_{23}^{TTIS2} = G_{32}^{TTIS1}$$
$$H_1: G_{23}^{TTIS2} \neq G_{32}^{TTIS1} \quad (22)$$

The values of t were calculated using equation (16) shown below.

$$t = \frac{\overline{X_1} - \overline{X_2}}{\sqrt{\frac{s_1^2}{n_1} + \frac{s_2^2}{n_2}}} \quad (23)$$

where $\overline{X_1}$ and $\overline{X_2}$ are the means of the measured properties, s_1, and s_2 are the standard deviations of the measured properties and n_1 and n_2 are the number of samples in each population. The critical t value obtained from standard statistical tables is 1.79. [30] Inserting the statistical data for the LS-3 composite for each orientation, the calculated t values were 0.40 and 0.29 for the G_{13}/G_{31} and G_{23}/G_{32} pairs, respectively. Since both these values are less than the critical t value the proposed hypotheses in equations (21) and (22) are accepted showing equivalent measured properties for the TTIS1 and TTIS2 specimen configurations.

A similar statistical analysis was performed on the measured G_{13}/G_{31} properties for the OS-3 composite. The G_{13} data were obtained with the modified DNS specimen while the G_{31} data were determined from the TTIS1 specimen. A t-test on the difference in measured means was again performed against the following null and alternative hypothesis

$$H_o: G_{13}^{DNSS} = G_{13}^{CSS}$$
$$H_1: G_{13}^{DNSS} \neq G_{13}^{CSS} \quad (24)$$

A 95% confidence level was utilized leading to a critical t value of 1.79. The value of t from equation (23) is 0.404 which again is less than the critical level indicating that the measured G_{13} and G_{31} are statistically equivalent.

From a testing standpoint, the modified CS specimens were easier to fabricate and to use. The modified CS specimen fabrication procedure involved only cutting 1.0" (25.4 mm) x 1.5" (38 mm) coupons and milling the notches. Conversely, the modified DNS specimens involved the use of a milling machine to notch the sample which resulted in less accurate specimen dimensions and increased fabrication times. Additionally, less of the stress-strain curve of the material was obtained with the modified DNS due to specimen bending which resulted in touching of the opposite notch surfaces. The specimen bending was due to the large notch overlap required in the DNS specimen for a uniform shear stress field. Also, the composite through-the-thickness stiffness is extremely low which allows bending of the DNS specimen ligaments and subsequent notch closure. For elastic property measurement the modified CS specimen showed superior performance and ease of fabrication and is therefore recommended over the modified DNS specimen.

Shear Strengths

Strength data were successfully obtained from the TTIS1 specimen (interlaminar shear strength) but not the TTIS2 or the modified DNSS specimen configurations (transverse shear strength). The TTIS2 specimens failed prematurely in the specimen arm. The modified DNS

specimens also failed prematurely in bending in the ligament directly under the notch. As described earlier, notch overlaps of H=20% were utilized to ensure uniform shear stress fields. This specimen configuration allowed ligament bending and subsequent touching of the notch faces. Specimens with no notch overlap (H=0%) were fabricated, despite the non-uniform stress distribution, and tested in attempts to obtain some indication of the through-the-thickness shear strength. However, strength values were still not obtained due to notch closure. The inability of the DNS specimen to yield strength was due to the low through-the-thickness stiffness of the composite panels. The through-the-thickness stiffness of each panel is under 2 Msi (13.8 GPa) which allows the opposite faces of the notches to touch prior to failure in the gage section of the specimen. The notch closure problem could possibly be eliminated with the fabrication of a compatible restraining jig similar to the one used in the standard DNS specimen.

The failures observed in the TTIS1 specimen configuration followed tow interfaces in the specimen gage section . In fact, if tows fell along the midplane of the specimen failure would still occur at the tow interfaces away from the specimen midplane. The interlaminar shear strengths (τ_{31} and τ_{32}) obtained from the TTIS1 specimen configuration are summarized in Table 20.

The failure of the modified specimens to measure transverse shear strength components was due in part to the fiber/matrix interfacial properties. Failure in through-the-thickness shear required failure of fibers in the warp and weft tows while the interlaminar failure merely involved interfacial failure between the matrix and tows.

A summary of the interlaminar shear strengths of the 0.25" composite panels is presented in Table 21. For all of the four architectures tested the shear strength τ_{31} is greater than τ_{32}. Also, the TS architecture provides a higher interlaminar shear strength than the LS architecture. These trends follow the expectation. The τ_{31} shear strength is larger because the loading direction is parallel to the warp weaver tows. Similarly, the TS architectures provide superior strength since the entire thickness of the plate is interlaced by the warp weaver tows, not just the adjacent layers as in the LS architecture.

Shear failure mechanisms were similar in all architectures. Failure initiated at the notch tips and propagated throughout the remainder of the test region along the interface of warp and weft tow stacks. Typical failures showed the through-the-thickness reinforcement to remain intact and bridge the failed interface regions. The bridging, however, did not provide any load transfer. Thus, despite the through-the-thickness reinforcement, the interlaminar strength was still a matrix dominated property.

Comparison of the interlaminar shear strengths measured from the 0.25" panels and the 1" panels shows comparable performance between the 1" and 0.25" panels. Table 22 presents the measured interlaminar shear strengths for all the architectures normalized to 60 % overall fiber volume fraction.

CONCLUSIONS

Characterization of the composites microstructures revealed significant distortion of the architecture due to compaction during the RTM processing. Distortion of the through-the-thickness tows was particularly severe in the OS-3 composite and is believed to be the primary reason for the lower through-the-thickness Young's modulus of this composite compared to LS-3 and TS-3 panels. The volume averaging model used in this investigation for the prediction of the composite elastic moduli was modified to include the effect of the processing-induced tow

undulations. Without such modification the model significantly over-predicted the elastic properties.

A bi-material specimen, consisting of a test section and transition sections, was designed and evaluated for the direct measurement of through-the-thickness tensile behavior of 3D textile composites. This specimen utilized 1" thick composite panels (i.e., LS-3, TS-3, and OS-3). Design optimizations obtained from a Boundary Element Analysis were implemented and proven successful. The adhesively-bonded bi-material specimen with optimized configuration was effective in providing the through-the-thickness elastic moduli but its early failure at the bonded joint rendered it unsuitable for strength measurement. The experimentally determined Young's modulus, E_{33}, and Poisson's ratios, ν_{13} and ν_{23}, agreed reasonably well with predicted values. An orthogonal woven preform with surface pile was designed which allowed the fabrication of a bi-material specimen with integrally woven transition sections. This specimen resulted in over 300% improvement in the failure stress over the bonded specimen, however, premature failure still occurred near the grip region due to architectural imperfections in the preform and no attempt to optimize the transition section properties or the specimen geometry. Recommendations for improvements of the bonded and integrated-grip tensile specimens have been proposed.

The bi-material specimen was also used for through-the-thickness compression testing using the ITTRI compression fixture. Both, through-the-thickness compressive strength and elastic moduli were measured. The compressive elastic modulus and Poisson's ratios agreed well with those obtained from tensile tests as well as the predicted values. Investigation of the compressive failure mechanisms showed that although kink bands occurred, they were not responsible for the composite final failure. Final failure was due to transverse tow splitting.

Two modified Compact Shear and a modified Double Notch Shear specimens were used for the determination of both transverse and interlaminar shear strengths and elastic moduli. These specimens utilized 1" thick composite panels. Both specimen configurations proved successful for the determination of the through-the-thickness shear elastic moduli. The experimental values of shear moduli agreed well with theoretical predictions. While both specimen configurations will provide accurate elastic properties, the modified CS configurations are recommended due to the ease of fabrication and the ability of the specimen to measure a wider range of the stress-strain curve.

The interlaminar shear strength was successfully determined from the modified CS specimen (TTIS1). But neither the modified CS (TTIS2) nor the modified DNS specimens could provide a measurement of the transverse shear strength. The TTIS2 specimens failed in the specimen arm while the modified DNS specimens exhibited premature failure under the notches due to specimen bending. Strength properties could possibly be obtained using the modified DNS specimen with the use of a restraining jig, or by incorporating tabbing material onto the arms of the TTIS2 specimen.

Interlaminar shear strengths were also determined for the 0.25" woven panels (i.e., LS-1, LS-2, TS-1, and TS-2) using the modified DNS specimen. Comparable performance was observed between the 0.25" and the 1" composite panels. For all the composites tested, the τ_{31} strength was larger than the τ_{32} strength. Also, the through-the-thickness angle interlock architecture gave superior interlaminar shear strength than the layer-to-layer angle interlock architecture.

ACKNOWLEDGMENT

This work was supported by NASA Langley Research Center under contract Number NAG-1-1383. The authors would like to thank Dr. Peter Ifju of the University of Florida for supplying the fixture for compact shear testing.

REFERENCES

[1] Byun, J. H., Leach, B. S., Stroud, S. S. and Chou, T. W.: Structural Characteristics of Three-Dimensional Angle-Interlock Woven Fabric Preforms. in Processing of Polymers and Polymeric Composites, ASME, MD-, vol. 19, American Society for Mechanical Engineers, New York, 1989, p. 177.

[2] Chou, T. W. and Yang, J. M.: Structure-Performance Maps of Polymeric Metal and Ceramic Matrix Composites. *Metall. Trans. A,* vol. 17, 1986, pp. 1547-9.

[3] Ma, C. L., Yang, J. M. and Chou, T. W.: Elastic Stiffness of Three-Timensional Braided Textile Structural Composites. in Composite Materials, Testing and Design (Seventh Conference), ASTM STP 893, American Society for Testing and Materials, Philadelphia, PA, 1986, pp. 404-21.

[4] Yang, J. M., Ma, C. L. and Chou, T. W.: Fiber Inclination Model of Three-Dimensional Textile Structural Composites. *J. Comp. Mat.,* Vol. 20, No. 5, 1986, pp. 472-84.

[5] Majidi, A. P., Yang, J. M., Pipes, R. B. and Chou, T. W.: Mechanical Behavior of Three-Dimensional Woven Fiber Composites. in Proceedings of the Fifth International Conference on composite Materials, The Metallurgical Society of AIME, Warrendale, PA, 1986, pp. 1247-65.

[6] Pochiraju, K., Majidi, A. P. and Chou, T. W.: Theoretical and Experimental Characterization of 3-D Woven and Braided Textile Composites. ICCE-1, New Orleans, LA, 1994.

[7] Shan, H. Z., Majidi, A. P. and Chou, T. W.: Numerical Analysis for Design of Composite Specimens for Through-the-Thickness Tensile Measurements. *J. Comp. Mat.*, Vol. 28, 1994, pp. 1032-56.

[8] Byun, J. H.: Process-Microstructure-Performance Relationships of Three-Dimensional Textile Composites. Ph.D Thesis, University of Delaware, Newark, DE, 1991.

[9] Hull, D.: An Introduction to Composite Materials. Cambridge University Press. Cambridge, 1981, pp. 103-121.

[10] Steenkamer, D.: The Influence of Preform Design and Manufacturing Issues on the Processing and Performance of Resin Transfer Molded Composites. Ph. D. Thesis, University of Delaware, Newark, DE, 1993.

[11] Camponesch, E. T., and K. O'Brien: Compression of Composite Materials: a Review. *ASTM STP 1110* , American Society for Testing and Materials, Philadelphia, PA, 1991, pp. 550-578

[12] Haberle J. G., and Matthews F.L.: The Influence of Test Method on the Compressive Strength of Several Fiber-Reinforced Plastics. *J. of Advanced Mat.,* Oct. 1993, pp. 35-45.

[13] Timoshenko, S.P., Theory of Elastic Stability, 1st edition, McGraw-Hill, New York, New York, 1936.

[14] Bogetti, T. A., Geillespie, J. W. and Pipes, R. B.: Evaluation of the IITRI Compression Test Method for Stiffness and Strength Determination. *Composites Science and Technology* , Vol 32, No. 1, 1988, pp. 57-76.

[15] Horgan, C. O.: Some Remarks on Saint-Venant's Principle for Transversely Isotropic Composites, *Journal of Elasticity,* Vol. 2, 1972, pp. 335-9.

[16] Hahn, H. T., Williams, J. G., and J. M. Whitney, Ed.: Compression Failure Mechanisms in Unidirectional Composites. *Composite Materials: Testing and Design (Seventh Conference), ASTM STP 893.* American Society for Testing and Materials, Phiadelphia, PA, 1986, pp. 115-39.

[17] Greszczuk, L. B.: Compressive Strength and Failure Modes of Unidirectional Composites. *Analysis of the Test Methods for High Modulus Fibers and Composites ASTM STP 521*, American Society for Testing and Materials, Philadelphia, PA, 1973, pp. 192-217.

[18] Rosen, B. W.: in *Fiber Composite Materials*, American Society of Metals, Metals Park, Ohio, 1965, Chapter 3.

[19] Schurerch, H.: *American Institute of Aeronatucs and Astronautcs Journal.,* Vol. 4, No. 1, 1966, pp. 102-6.

[20] Slaughter, W. S. and Fleck, N. A.: Viscoelastic Microbuckling of Fiber Composites. *Journal of Applied Mechanics, Trans. of the ASME,* Vol. 60, No. 4, 1993, pp. 803-806.

[21] Evans, A.G. and Adler, W. F.: Kinking as a Mode of Structural Degradation in Carbon Fiber Composites. *Acta. Metallurgica* , Vol. 26, 1978, pp. 725-738.

[22] Argon, A. S.: Fracture of Composites. *Treeatise of Materials Science and Technology*, Vol 1., Academic Press, New York, 1972. pp 106-114.

[23] Guess, T. R. and Reedy E. D.: *J. Comp. Tech Res.*, Vol. 7, 1986, p. 136.

[24] Guess, T. R. and Reedy E. D.: *J. Comp. Tech Res.,* Vol. 8, 1986, p. 163.

[25] Cox, B.N., Dadkhah, M.S., Inman R. V., Morris, W. L. and Zupon, J.: Mechanisms of Compressive Failure in 3D Composites. *Acta metall .mater.,* Vol. 40, No. 12., 1992, pp. 3285-3298.

[26] Weaver, C.W. and Williams J., G.: Deformation of a Carbon-Epoxy Composite Under Hydrostatic Pressure. *Journal of Materials Science.,* Vol. 10, 1975, pp. 1323-1333.

[27] Chaterjee, S., Adams, D. and Oplinger D. W.: Test Methods for Composites a Status Report. DOT/FAA/CT Report-93/17, III. June 1993.

[28] Ifju, P. NASA Textile Mechanics Workgroup Progress Report. July 1993.

[29] Bouette, B.; Cazeneuve, C.; Oytan, C.: Effect of Strain Rate on Interlaminar Shear Properties of Carbon/Epoxy Composites. *Composite Sciece and Technology*, Vol. 45, No. 4, 1992, pp 313-324.

[30] Hogg, R. V. and Ledolter, J., *Engineering Statistics* , Macmillan Publinshing Company, New York, 1987, p. 397.

Table 1 - Descriptions of the Fiber Architectures

Desig.	Architecture	Nominal Thickness in (mm)	Tow Size K		
			Warp Stuffer	Warp Weaver	Weft
LS-1	Layer-to-layer angle interlock	0.25 (6.35)	24	6	12
LS-2	Layer-to-layer angle interlock	0.25 (6.35)	12	3	6
LS-3	Layer-to-layer angle interlock	1.00 (25.4)	60	6	24
TS-1	Through-the-thickness angle interlock	0.25 (6.35)	24	6	12
TS-2	Through-the-thickness angle interlock	0.25 (6.35)	12	3	6
TS-3	Through-the-thickness angle interlock	1.00 (25.4)	60	6	24
OS-2	Through-the-thickness orthogonal	0.25 (6.35)	12	3	6
OS-3	Through-the-thickness orthogonal	1.00 (25.4)	60	6	24
OS-4	Through-the-thickness orthogonal	1.00 (25.4)	60	6	24

Table 2 - Overal and Directional Fiber Volume Fractions

Architecture	Overall Fiber Vol. %	Warp Stuffer %	Weft %	Warp Weaver %
LS-1	57.80±0.78	32.5	20.4	4.9
LS-2	60.29±1.72	33.2	24.7	2.4
LS-3	58.95±0.68	27.8	18.6	12.6
TS-1	60.69±1.82	33.6	18.9	8.1
TS-2	58.05±0.40	29.4	21.8	7.0
TS-3	62.30±1.12	33.3	20.9	8.1
OS-3	63.10±2.36	30.4	16.6	16.1
OS-4	44.50±1.50	21.4	11.7	11.4

Table 3 - Unit Cell Dimensions

Composite	a (mm)	b (mm)	c (mm)
LS-1	4.26	9.00	1.39
LS-2	3.12	14.31	1.04
LS-3	4.20	2.13	2.81
TS-1	11.18	12.34	5.72
TS-2	12.34	1.78	5.72
TS-3	2.00	2.14	2.85
OS-3	2.42	2.24	2.90

Table 4 - Macro-Cell Dimensions

Composite	a (mm)	b (mm)	c (mm)
LS-1	9.52	9.00	5.72
LS-2	8.89	14.31	5.72
LS-3	8.41	2.13	25.40
TS-1	22.36	8.90	5.76
TS-2	24.68	10.68	5.75
TS-3	16.44	2.14	25.40
OS-3	4.84	2.24	25.40

Table 5 - Predicted Elastic Properties Using Volume Averaging Method

Composite	E_{11} (GPa)	E_{22} (GPa)	E_{33} (GPa)	G_{23} (GPa)	G_{13} (GPa)	G_{12} (GPa)	ν_{23}	ν_{13}	ν_{12}
LS-1	90.2	55.8	9.6	6.2	6.4	6.2	0.054	0.039	0.030
LS-2	87.3	65.4	10.1	6.5	6.7	6.5	0.048	0.041	0.028
LS-3	79.1	53.5	12.0	6.3	6.7	6.3	0.051	0.047	0.040
TS-1	86.1	53.3	13.4	6.6	6.9	6.6	0.053	0.038	0.035
TS-2	75.8	59.3	12.2	6.2	6.4	6.2	0.046	0.40	0.051
TS-3	84.9	59.1	12.5	6.8	7.0	6.8	0.050	0.051	0.036
OS-3	85.4	49.9	13.4	6.9	7.7	6.9	0.058	0.061	0.033

Table 6 - Glass Fabric/Epoxy Mechanical Property Data

Fabric Type	Test Direction	Weight Fraction	E_{11} (GPa)	ν_{12}
Continuous Strand Mat.	Warp	0.281	7.16	0.30
Continuous Strand Mat.	Warp	0.367	8.41	0.31
Continuous Strand Mat.	Warp	0.431	9.57	0.29
0/90/C	Warp	0.645	21.56	0.18
0/90/C	Warp	0.774	28.89	0.17
0/90	Warp	0.617	21.42	0.18
0/90	Warp	0.672	24.46	0.16
0/90	Warp	0.707	28.87	0.13
45/C	Warp	0.616	14.67	0.42
45/C	Warp	0.704	17.77	0.39

Table 7- Transition Section/Test Section Combinations for Bi-Material Specimen

Composite	Orientation	Transition Section Material	α
LS-3	XZ	0/90 (W_f=0.707)	0.011
LS-3	YZ	0/90 (W_f=0.707)	0.009
TS-3	XZ	0/90 (W_f=0.707)	0.011
TS-3	YZ	0/90 (W_f=0.707)	0.013
OS-3	XZ	0/90 (W_f=0.707)	0.015
OS-3	YZ	0/90 (W_f=0.707)	0.012

Table 8 - Summary of Measured Through-the-Thickness Tensile Properties

Architecture	E_{33} (GPa)	Normalized To 60% E_{33} (GPa)	ν_{13}	ν_{23}
LS-3	11.62±2.28	11.82	0.050±0.011	0.101±0.023
TS-3	12.18±2.28	11.73	0.083±0.012	0.186±0.015
OS-3	11.11±3.84	10.56	-	0.0698±0.021
OS-4	8.58±5.49	11.56	0.0341±0.0078	0.1040±0.032

Table 9 - Critical Stress Decay Length and Critical Buckling Stress

Specimen	E_{33} (GPa)	G_{13} (GPa)	G_{23} (GPa)	λ_{cr} (mm)	l (mm)	σ_{cr} (MPa)
LS3-XZ	12.0	6.75	6.34	4.37	12.7	1697
LS3-YZ	12.0	6.75	6.34	4.23	12.7	1731
TS3-XZ	12.6	7.23	6.86	4.30	12.7	1801
TS3-YZ	12.6	7.23	6.86	4.19	12.7	1831
OS3-XZ	13.4	7.65	7.03	4.33	12.7	1863
OS3-YZ	13.4	7.65	6.95	4.16	12.7	1912

Table 10 - Summary of Measured Compressive Elastic Properties

Composite	E_{33} (GPa)	ν_{13}	ν_{23}
LS-3	12.3 ± 2.8	0.038 ± 0.005	0.122 ± 0.041
TS-3	13.6 ± 1.8	0.059 ± 0.031	0.070 ± 0.030
OS-3	13.3 ± 3.2	0.043 ± 0.017	0.185 ± 0.074

Table 11 - Summary of Measured Ultimate compressive Strengths.

Composite	Orientation	σ_c^{ult} (MPa)
LS-3	XZ	374.9 ± 22.9
LS-3	YZ	412.5 ± 19.0
TS-3	XZ	345.8 ± 1.62
TS-3	YZ	402.5 ± 11.4
OS-3	XZ	361.6 ± 25.4
OS-3	YZ	411.2 ± 26.9

Table 12 - Damage Progression in LS-3 Composite

Applied Stress (MPa)	% of Average Failure Stress	Observed Damage
110	26.7	• Several matrix cracks originating at voids noted • Matrix cracks concentrated near bi-material interface
165	40.1	• Density of matrix cracks increased greatly • Kink bands noted in several warp weaver tows • Several cracks oriented at approximately ±45° noted in surface warp stuffer tows
220	53.5	• Matrix crack density and kink band density increased • Degree of cracking in surface warp stuffer tows increased.
Peak	100	• Matrix crack density and kink band density increased • Total splitting of surface warp stuffer tow observed

Table 13 - Damage Progression in TS-3 Composite

Applied Stress (MPa)	% of Average Failure Stress	Observed Damage
220	54.7	• Several matrix cracks originating at voids noted. • No kink bands observed in any of the viewed cross-sections. • Cracks starting to form in surface warp stuffer tows.
275	68.6	• Density of matrix cracks increased greatly. • Kink bands noted in several warp weaver tows. • Significant cracking seen in surface warp stuffer tows.
330	82.3	• Matrix crack density and kink band density increased • Degree of cracking in surface warp stuffer tows increased.
Peak	100	• Matrix crack density and kink band density increased • Total splitting of surface warp stuffer tow observed

Table 14 - Damage Progression in OS-3 Composite

Applied Stress (MPa)	% of Average Failure Stress	Observed Damage
165	40.1	• Matrix cracks noted • Preliminary kink bands noted
275	67.1	• Density of matrix cracks increased greatly • Kink bands noted in several warp weaver tows • Several cracks oriented at approximately $\pm 45^{o}$ noted in surface warp stuffer tows
330	80.0	• Numerous kink bands in through-the-thickness tows • Cracking in warp surface tows increased
Peak	100	• Matrix crack density and kink band density increased • Total splitting of surface warp stuffer tow observed

Table 15 - Critical Stresses Predicted from Kink Band Model

Composite	ϕ (radians)	σ_c (MPa)
LS-3	0.61	124.0
TS-3	0.574	130.7
OS-3	0.496	151.2

Table 16 - Average Stresses Along Planes at Different Positions for Baseline and Modified CS Specimens

Specimen	Midplane psi (MPa)	Midplane+0.05" psi (MPa)	MidPlane+0.10" psi (MPa)
Baseline	204.2 (1.407)	199.0 (1.371)	174.7 (1.203)
TTIS1	208.3 (1.435)	199.2 (1.372)	165.7 (1.142)
TTIS2	201.0 (1.385)	199.8 (1.377)	157.0 (1.082)

Table 17 - Average Stresses Along Planes at Different Positions for Modified DNS Specimen

Gage Length (L) (in/mm)	Notch Overlap (H) %	$\tau_{i\,3}^{ave}$ x=0.000 psi (MPa)	$\tau_{i\,3}^{ave}$ x=0.025" psi (MPa)	$\tau_{i\,3}^{ave}$ x=0.050" psi (MPa)
0.125 / 3.2	0	134.7	121.4	70.9
0.125 / 3.2	10	176.1	132.1	87.3
0.125 / 3.2	20	200.6	150.8	106.5
0.125 / 3.2	50	199.8	199.5	191.8
0.250 / 6.35	0	148.8	129.2	96.1
0.250 / 6.35	10	188.3	141.8	104.1
0.250 / 6.35	20	198.5	165.1	121.4
0.250 / 6.35	50	199.9	199.8	187.0
0.290 / 7.4	0	148.9	131.5	98.1
0.290 / 7.4	10	189.9	143.1	105.4
0.290 / 7.4	20	199.5	165.6	122.8
0.290 / 7.4	50	199.7	199.9	181.7

Table 18 - Test Matrix for Modified CS Specimens

Specimen	Orientation	Measured Elastic Property	Measured Strength Property
TTIS1	XY	G_{31}	τ_{31}
TTIS1	YX	G_{32}	τ_{32}
TTIS2	XZ	G_{23}	τ_{23}
TTIS2	YZ	G_{13}	τ_{13}

Table 19 - Summary of Measured Properties Using Modified CS Specimens

Composite	G_{13} Msi (GPa)	G_{31} Msi (GPa)	G_{23} Msi (GPa)	G_{32} Msi (GPa)
LS-3	1.01±0.26 (6.96±1.8)	1.07±0.30 (7.37±2.06)	0.836 ± 0.11 (5.76 ±0.75)	0.815 ± 0.14 (5.61± 0.98)
TS-3	-	0.761 ± 0.06 (5.24 ± 0.42)	-	0.900 ± 0.06 (6.2 ± 0.42)
OS-3	-	0.895±0.03 (6.17 ± 0.17)	-	0.846± 0.05 (5.83 ± 0.36)

Table 20 - Summary of τ_{31} and τ_{32} Strength Data Obtained with TTIS1 Specimen Configuration

Composite	τ_{31} psi (MPa)	τ_{32} psi (MPa)
LS-3	3820 ± 310 (26.3 ± 2.1)	3365 ± 273 (23.2 ± 1.9)
TS-3	4270 ± 750 (29.4 ± 5.2)	3830 ± 345 (26.4 ± 2.4)
OS-3	4980 ± 927 (34.3 ± 6.4)	5370 ± 693 (37.0 ± 4.8)

Table 21 - Interlaminar Shear Strength Data from 0.25" Panels

Architecture	Shear Strength Tested	Measured Shear Strength psi (MPa)
LS-1	τ_{31}	4230±695 (29.0±4.8)
LS-1	τ_{32}	3400±430 (23.0±3.0)
LS-2	τ_{31}	5480±515 (37.8±3.5)
LS-2	τ_{32}	5270±515 (36.3±3.5)
TS-1	τ_{31}	6050±250 (41.7±1.7)
TS-1	τ_{32}	4095±330 (28.2±2.3)
TS-2	τ_{31}	5905±270 (40.7±1.9)
TS-2	τ_{32}	3510±450 (24.2±3.1)

Table 22 - Interlaminar Shear Strength Data from 0.25" Panels Normalized to 60% Fiber Volume Fraction

Architecture	Shear Strength Tested	Measured Shear Strength psi (MPa)
LS-1	τ_{31}	4390 (30.2)
LS-1	τ_{32}	3530 (24.3)
LS-2	τ_{31}	5450 (37.6)
LS-2	τ_{32}	5210 (35.9)
LS-3	τ_{31}	3890 (26.8)
LS-3	τ_{32}	3425 (23.6)
TS-1	τ_{31}	5980 (41.2)
TS-1	τ_{32}	4030 (27.8)
TS-2	τ_{31}	6100 (42.0)
TS-2	τ_{32}	3630 (25.0)
TS-3	τ_{31}	4115 (28.4)
TS-3	τ_{32}	3690 (25.4)
OS-3	τ_{31}	4735 (32.6)
OS-3	τ_{32}	5450 (37.6)

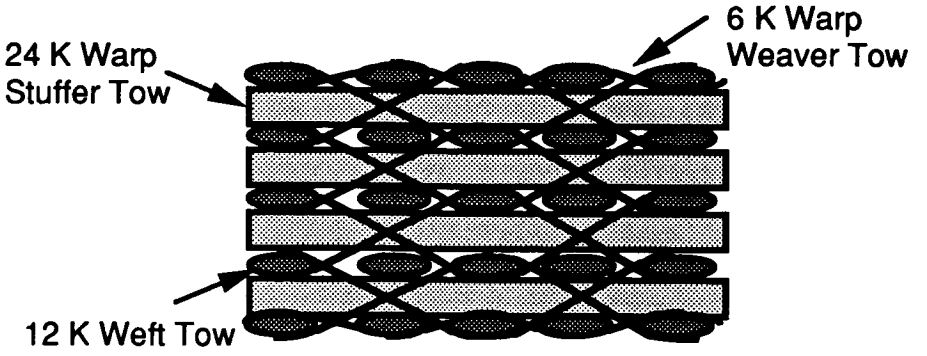

(a) LS-1

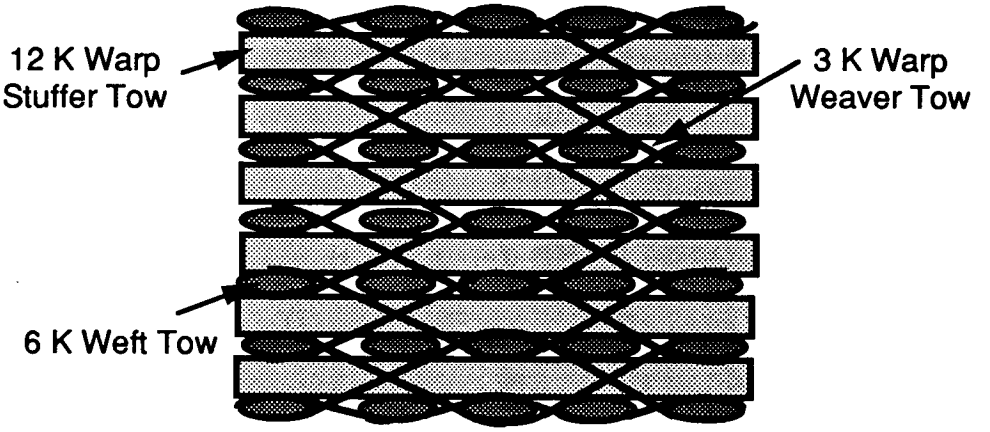

(b) LS-2

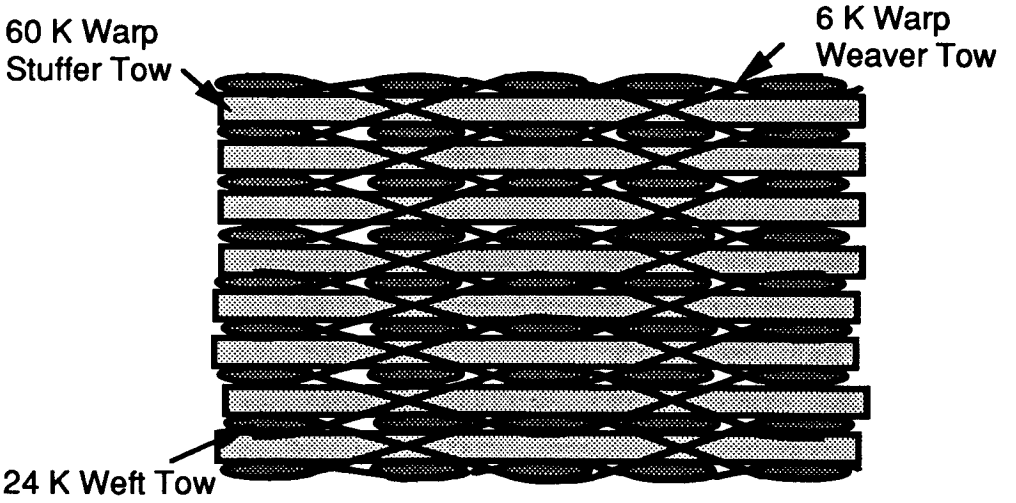

(c) LS-3

Figure 1 - Schematics of layer-to-layer angle interlock preform architectures

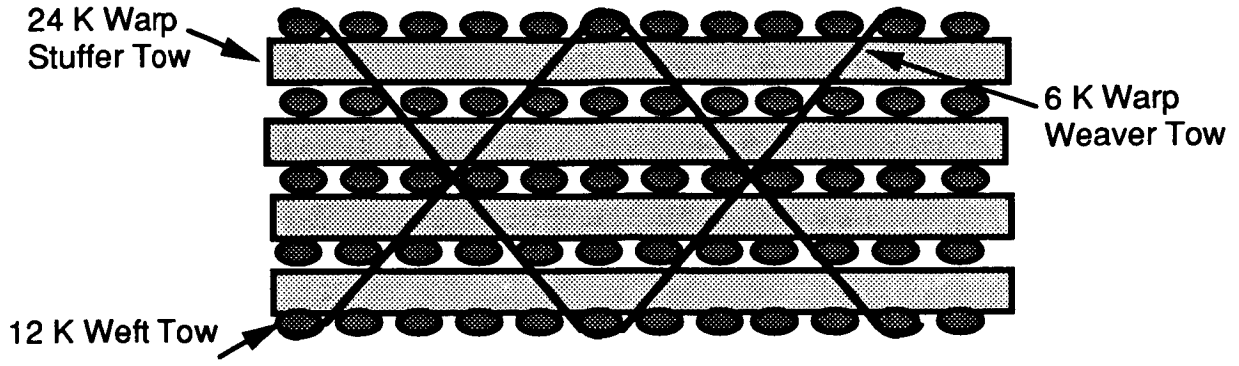

(a) TS-1

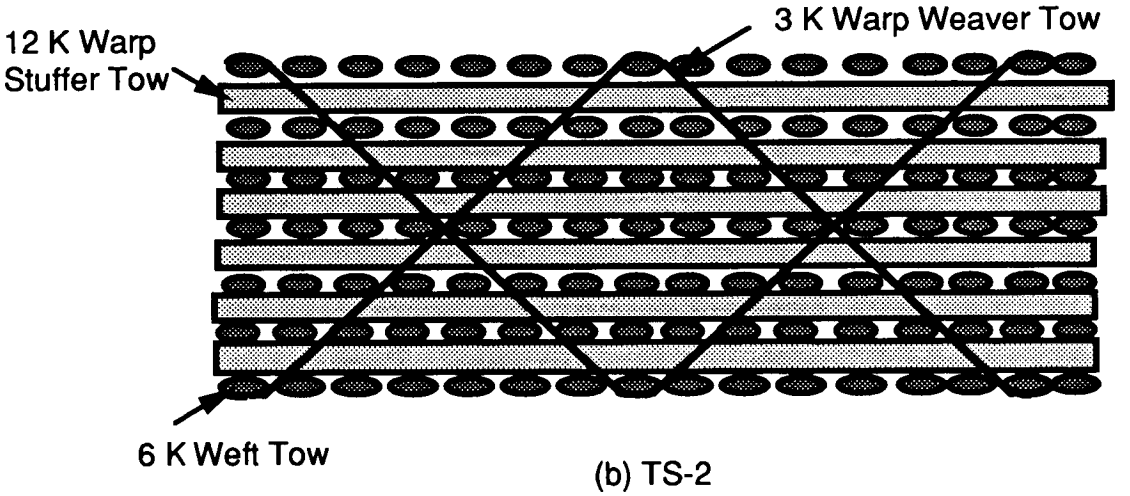

(b) TS-2

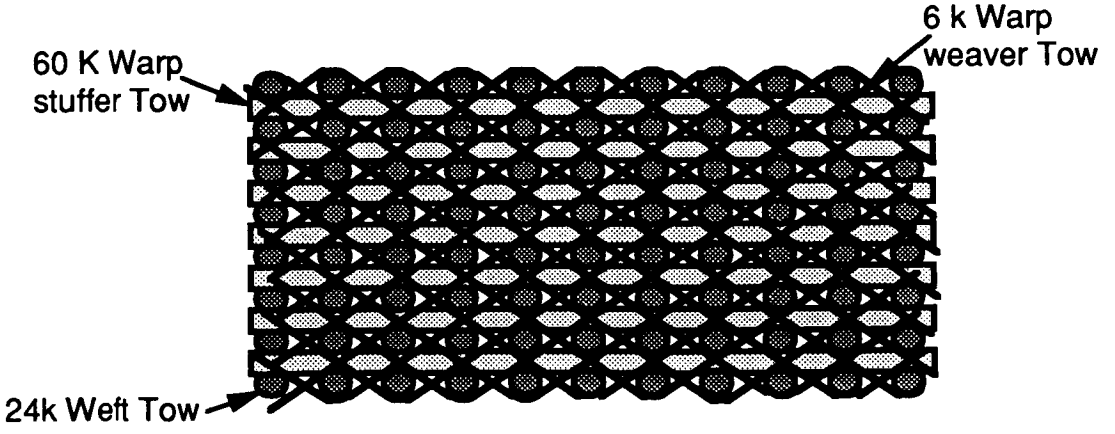

(c) TS-3

Figure 2 - Schematics of throught-the-thickness angle interlock architectures

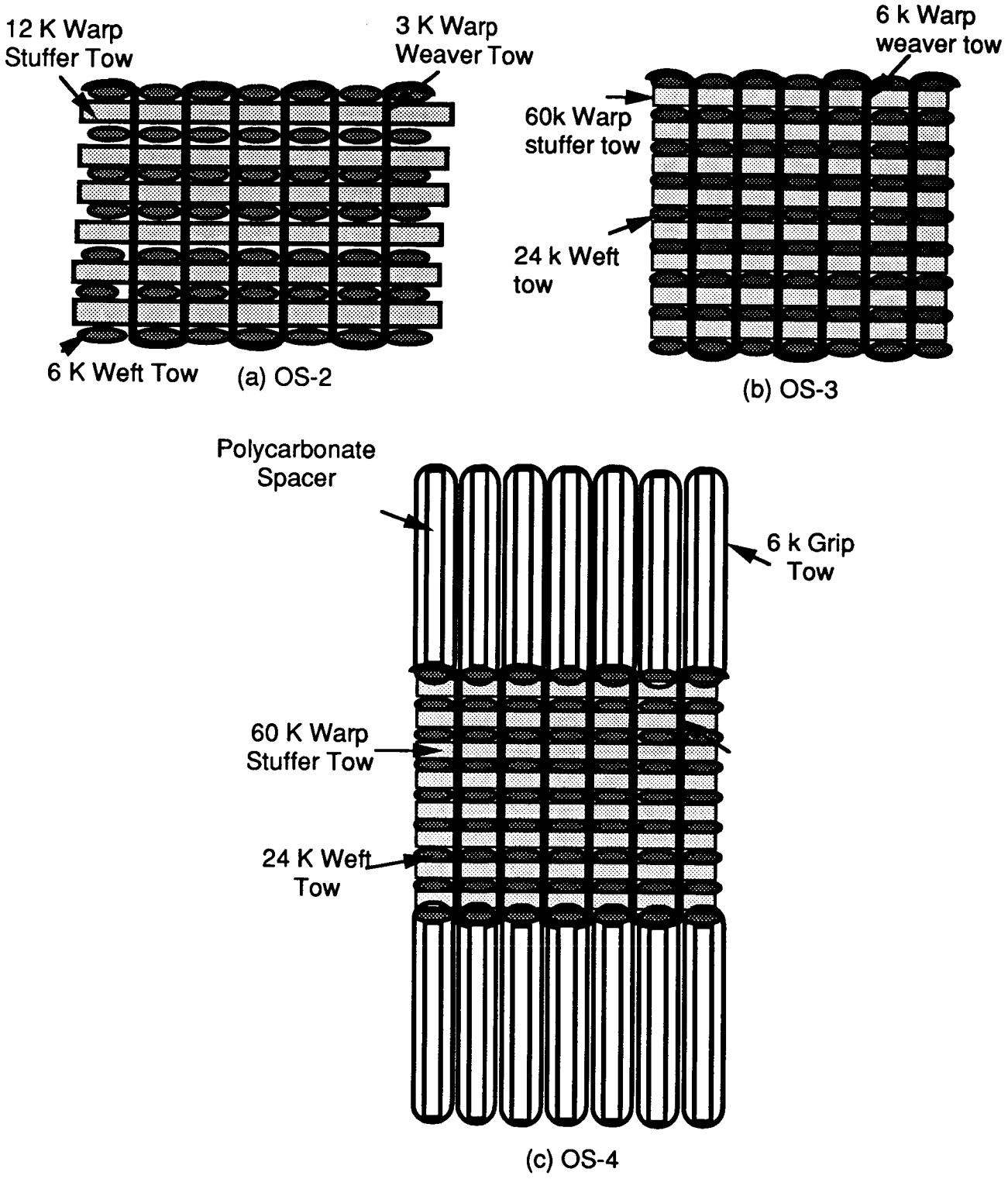

Figure 3 - Schematics of through-the-thickness orthogonal weave architectures

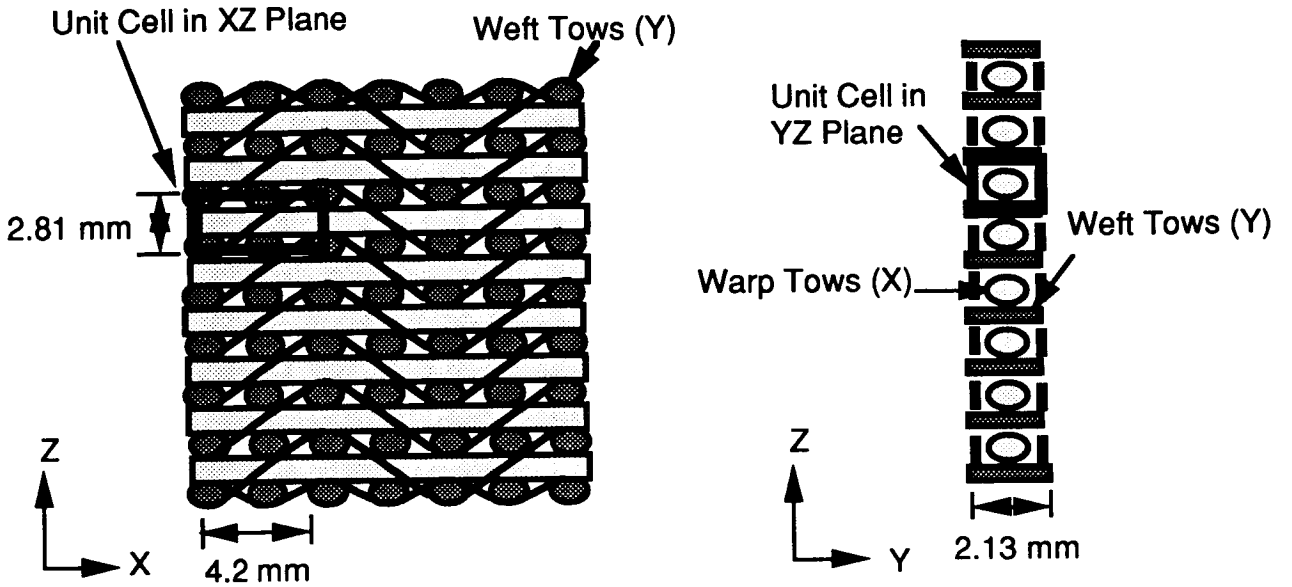

(a)

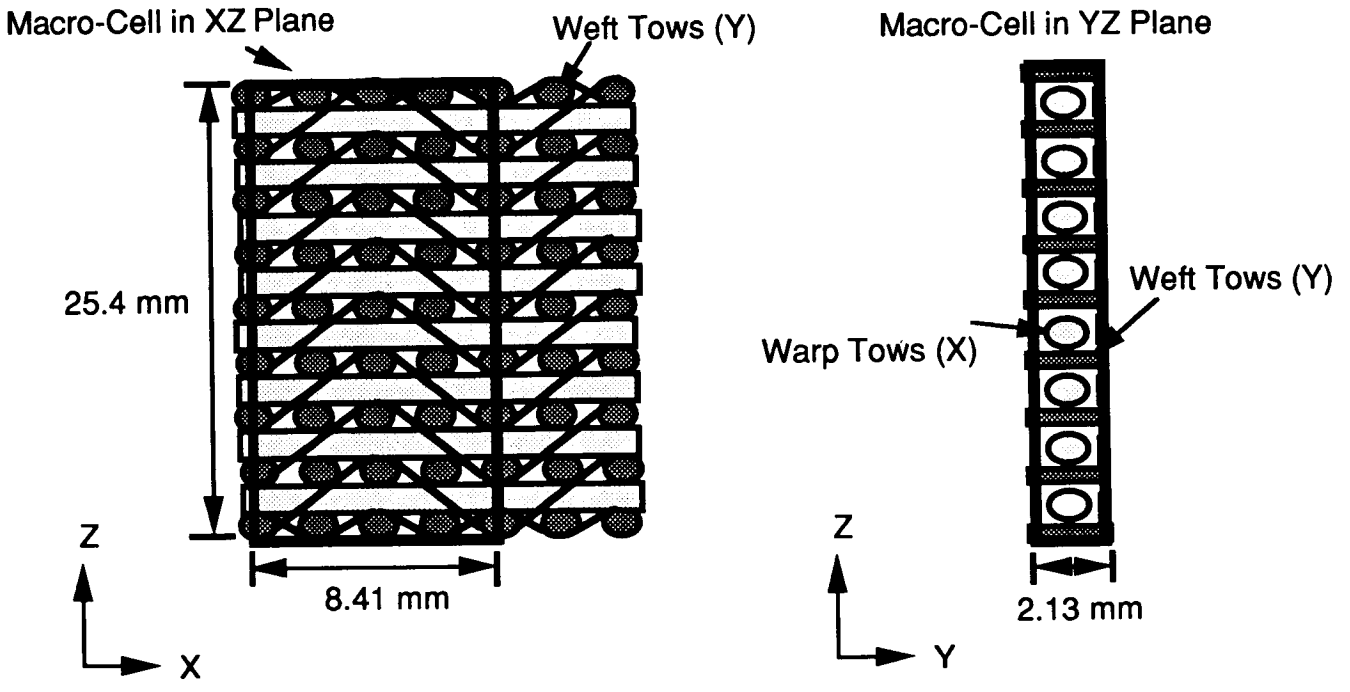

(b)

Figure 4 - Schematics of (a) a unit cell and (b) a macro-cell for a LS-3 architecture.

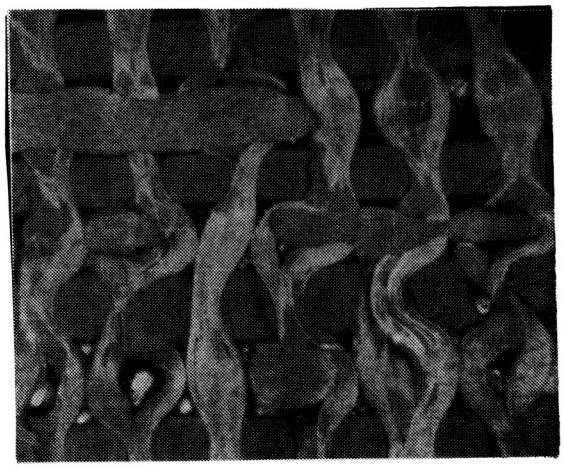

(a)

(b)

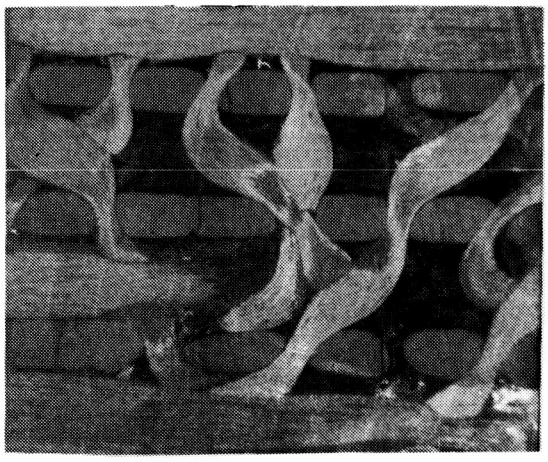

(c)

Figure 5 - Examples of RTM-induced tow distortions for (a) OS-3 composite, (b) LS-3 composite, and (c) TS-3 composite.

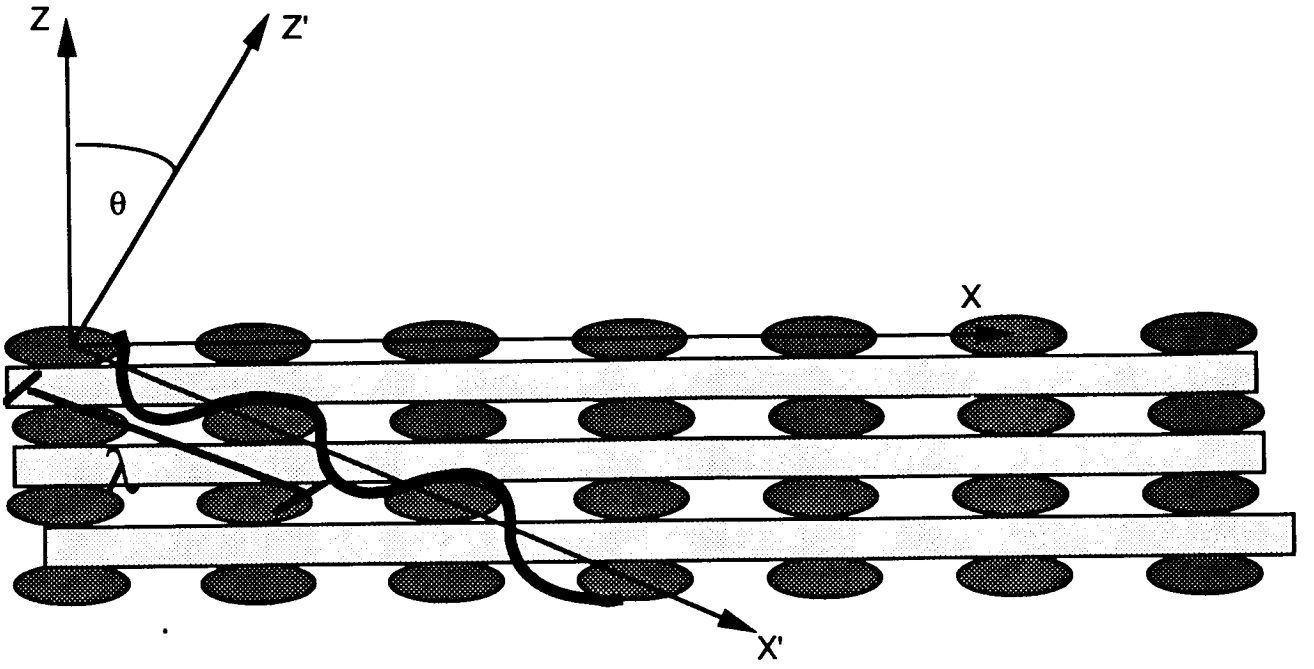

Undulation aprroximated by sinusodial path

$$Z' = A \cdot \sin\left(\frac{2\pi X'}{\lambda}\right)$$

Figure 6 - Simplified model of distorted warp weaver tow.

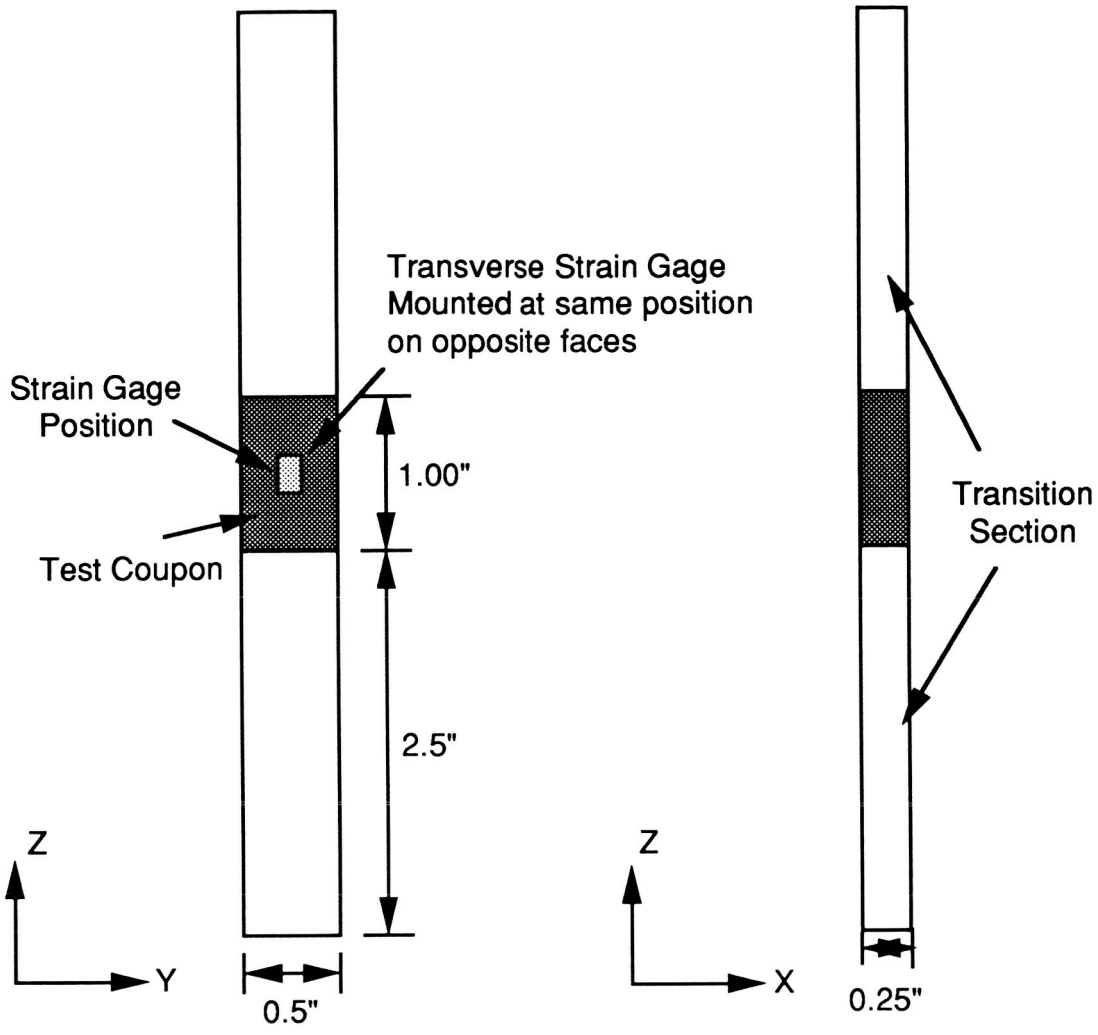

Figure 7 - Dimensions of Generation 2 bi-material tensile specimen.

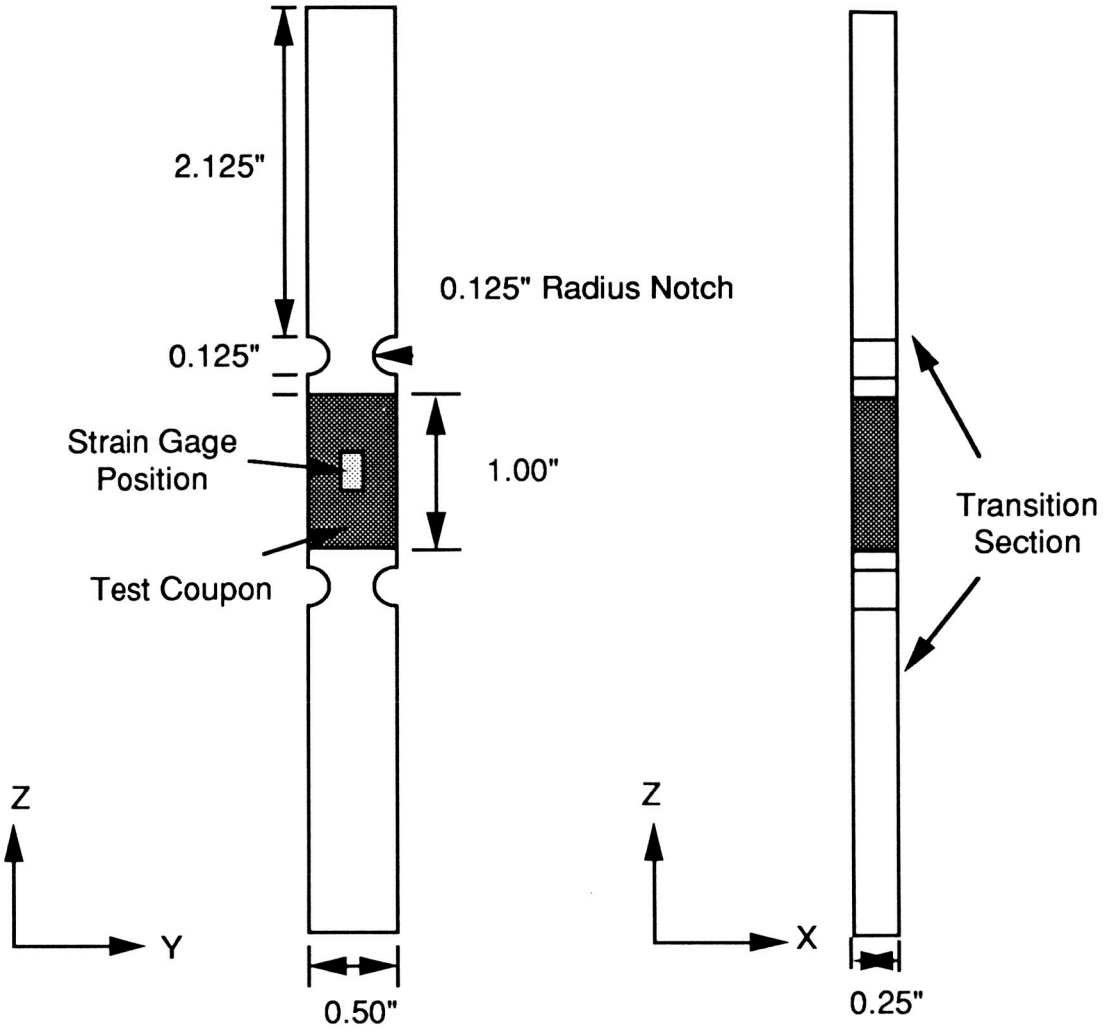

Figure 8 - Dimensions of Generation 3 bi-material tensile specimen.

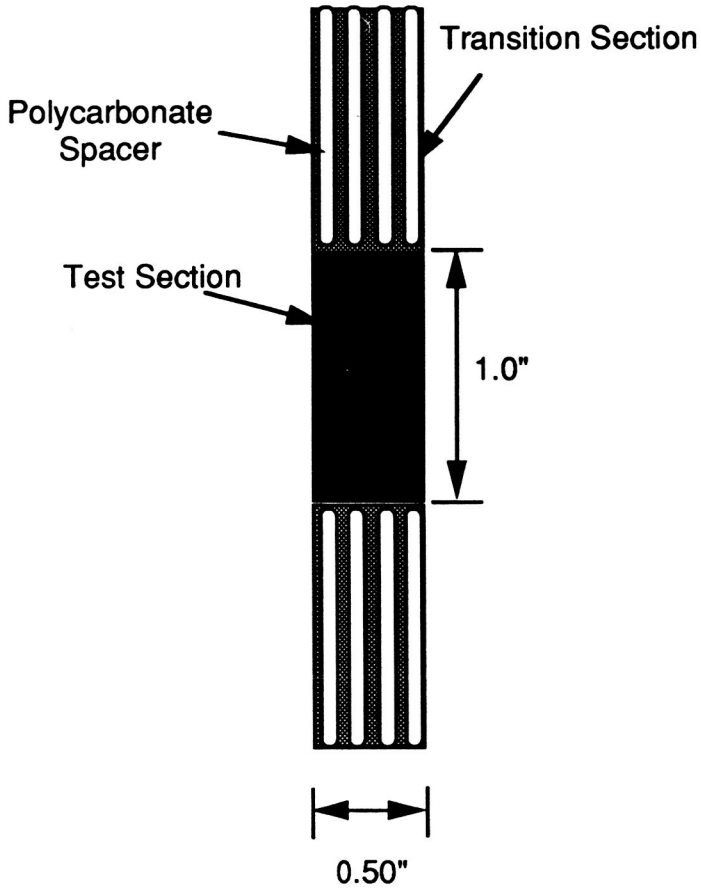

Figure 9 - Schematic of the integrated-grid tensile specimen using the OS-4 architecture.

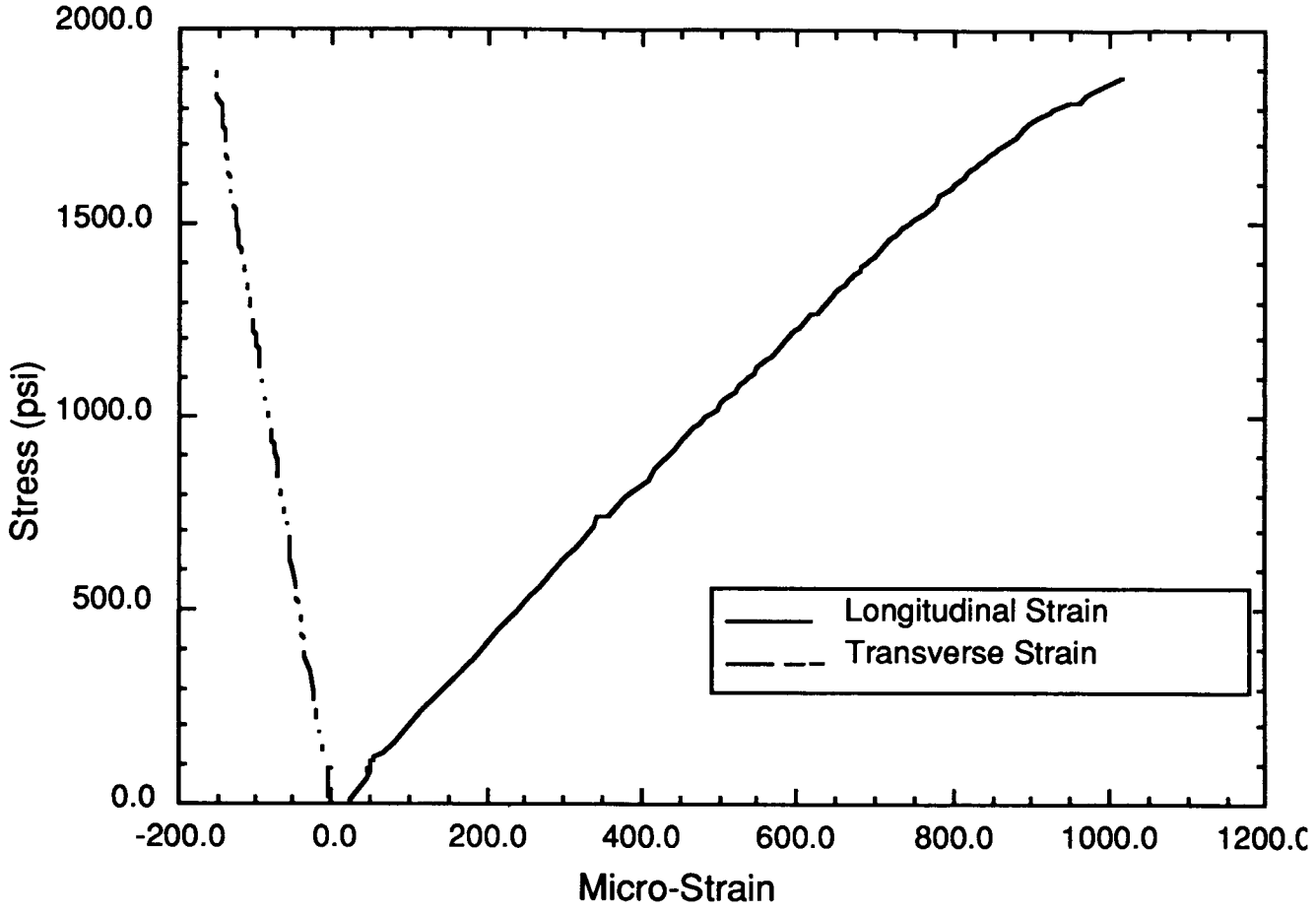

Figure 10 - Typical tensile stress-strain curve for generation 3 specimens of TS-3 composite

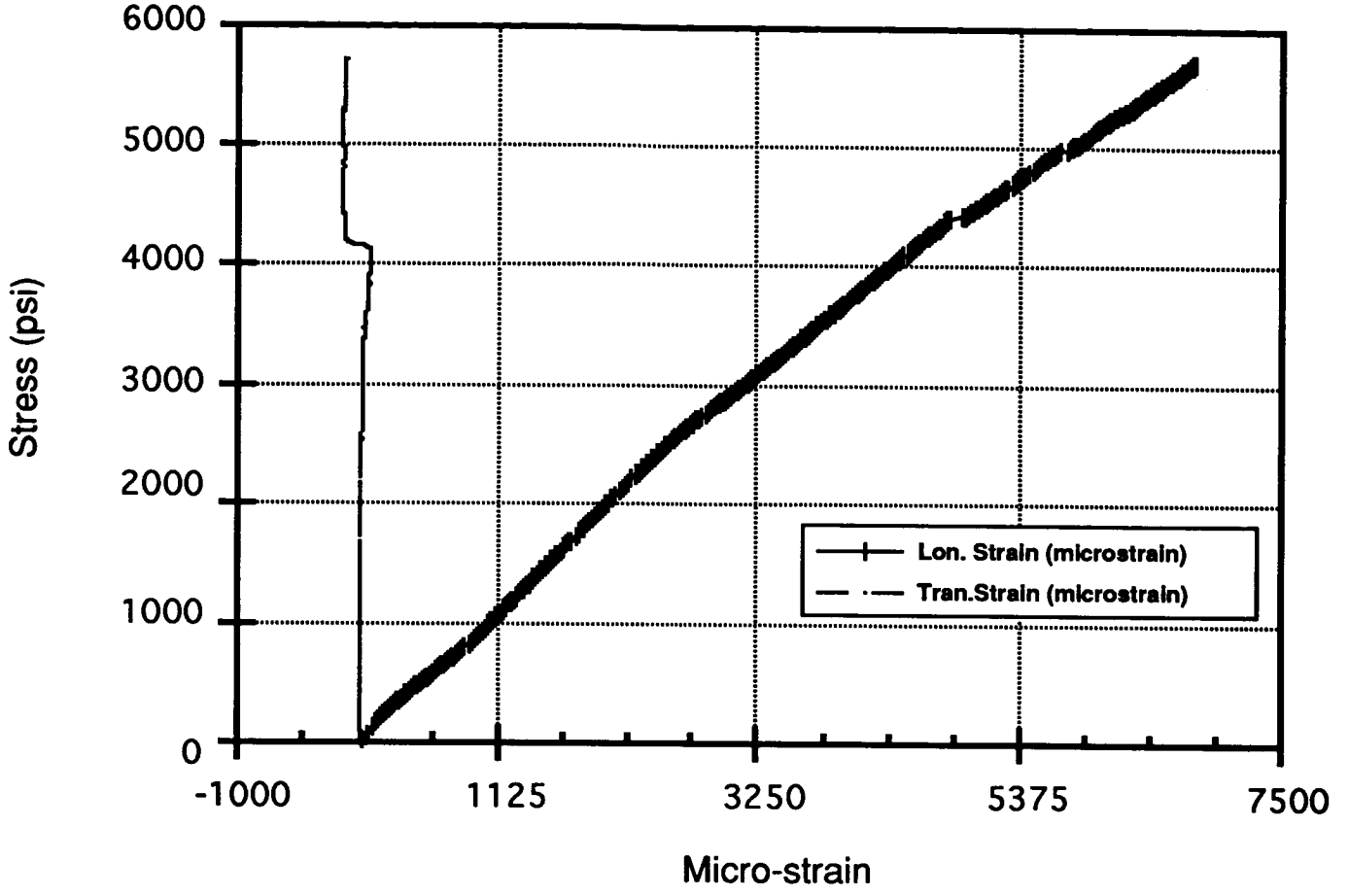

Figure 11 - Typical tensile stress-strain plot for OS-4 integrated-grip specimen.

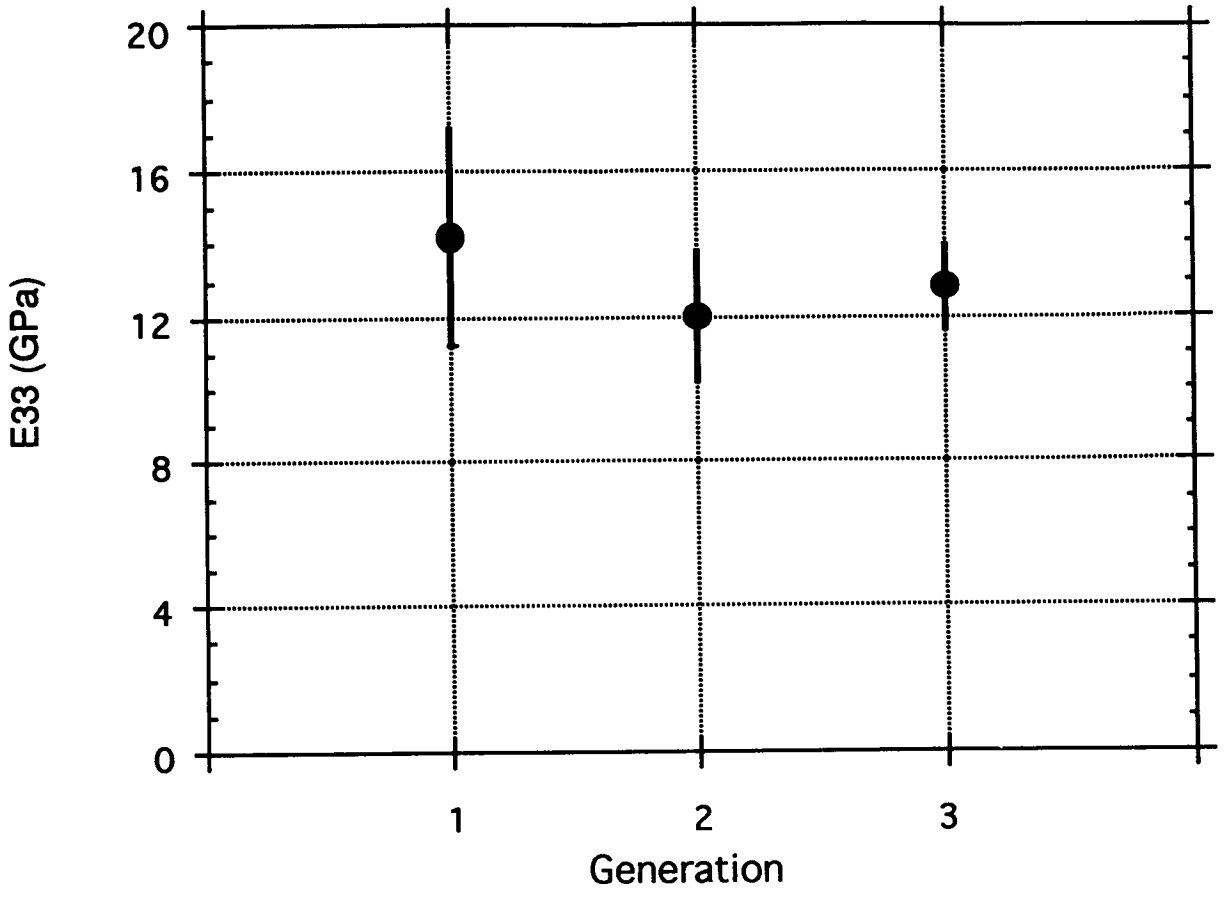

Figure 12 - Improvement in data reproducibility with specimen generation.

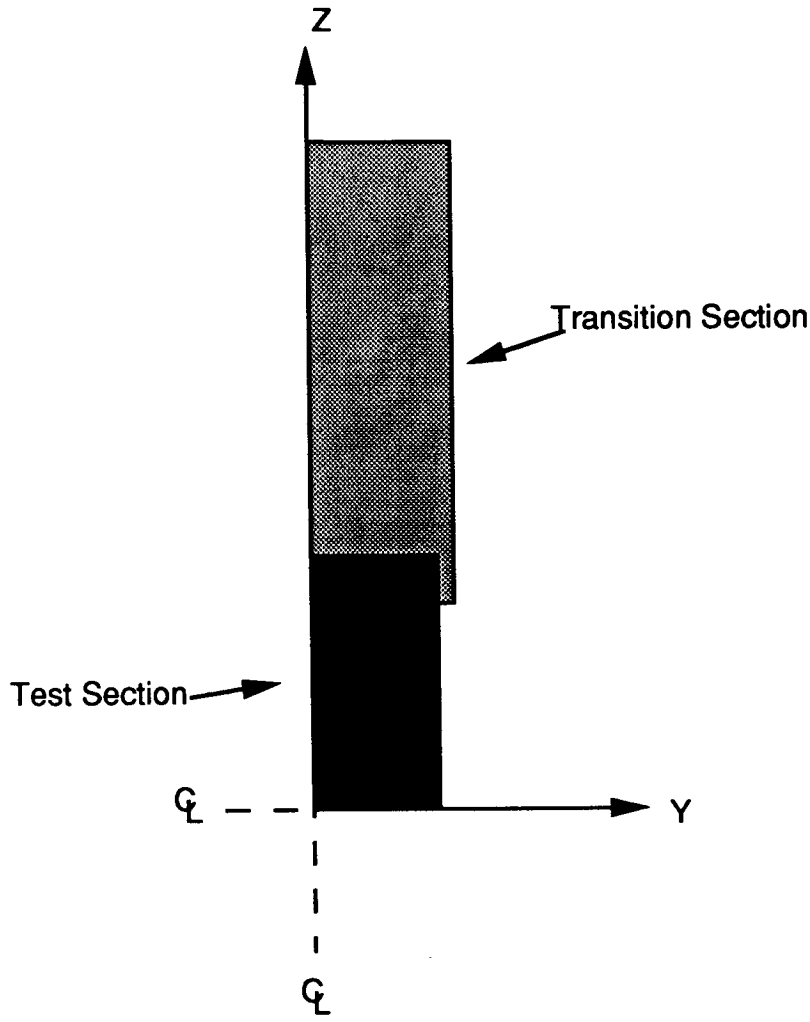

Figure 13 - Quarter schematic of proposed lap-joint specimen configuration.

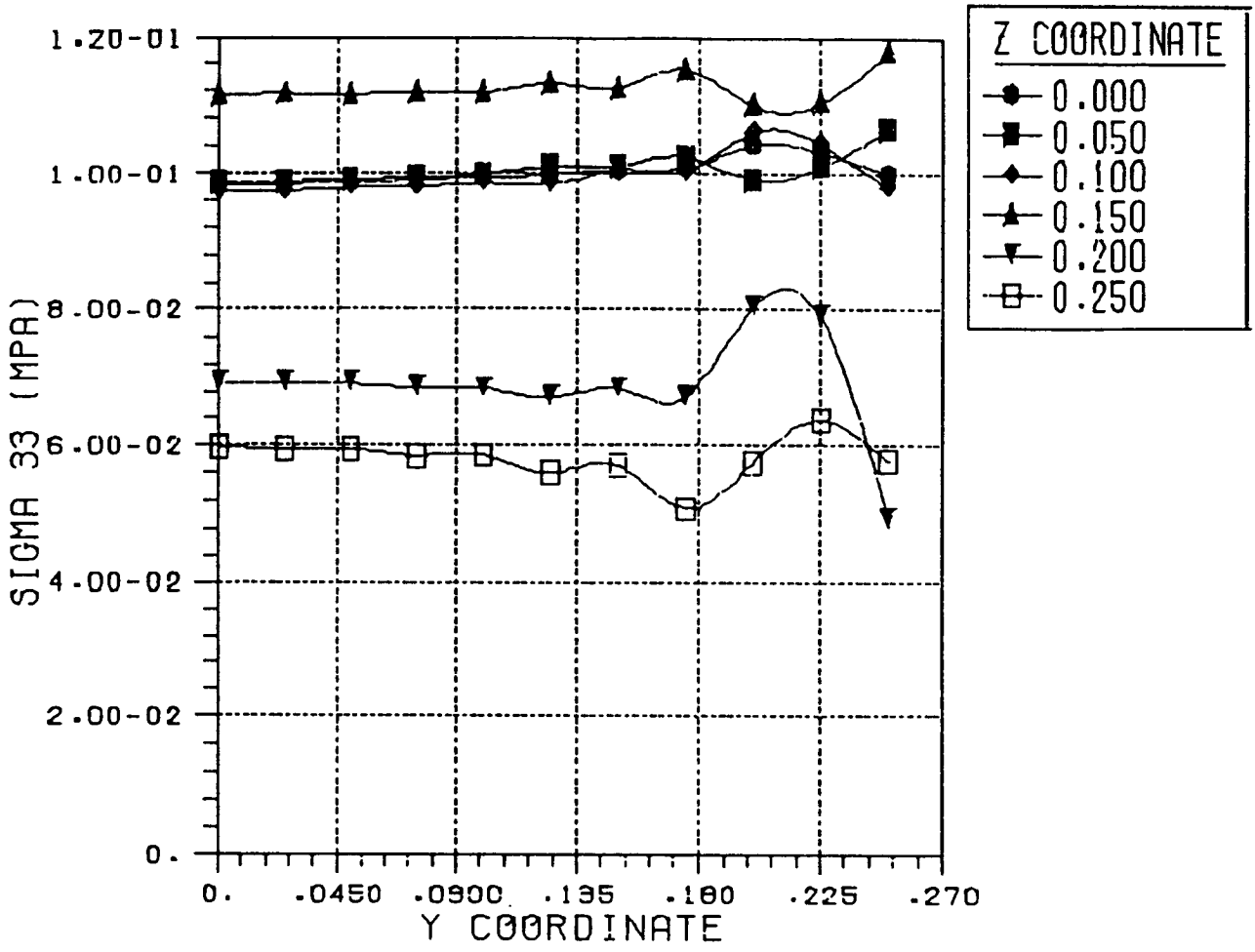

Figure 14 - Predicted through-the-thickness tensile stress field for lap-joint specimen configuration.

Figure 15 - Proposed integrated-grip dogbone tensile specimen.

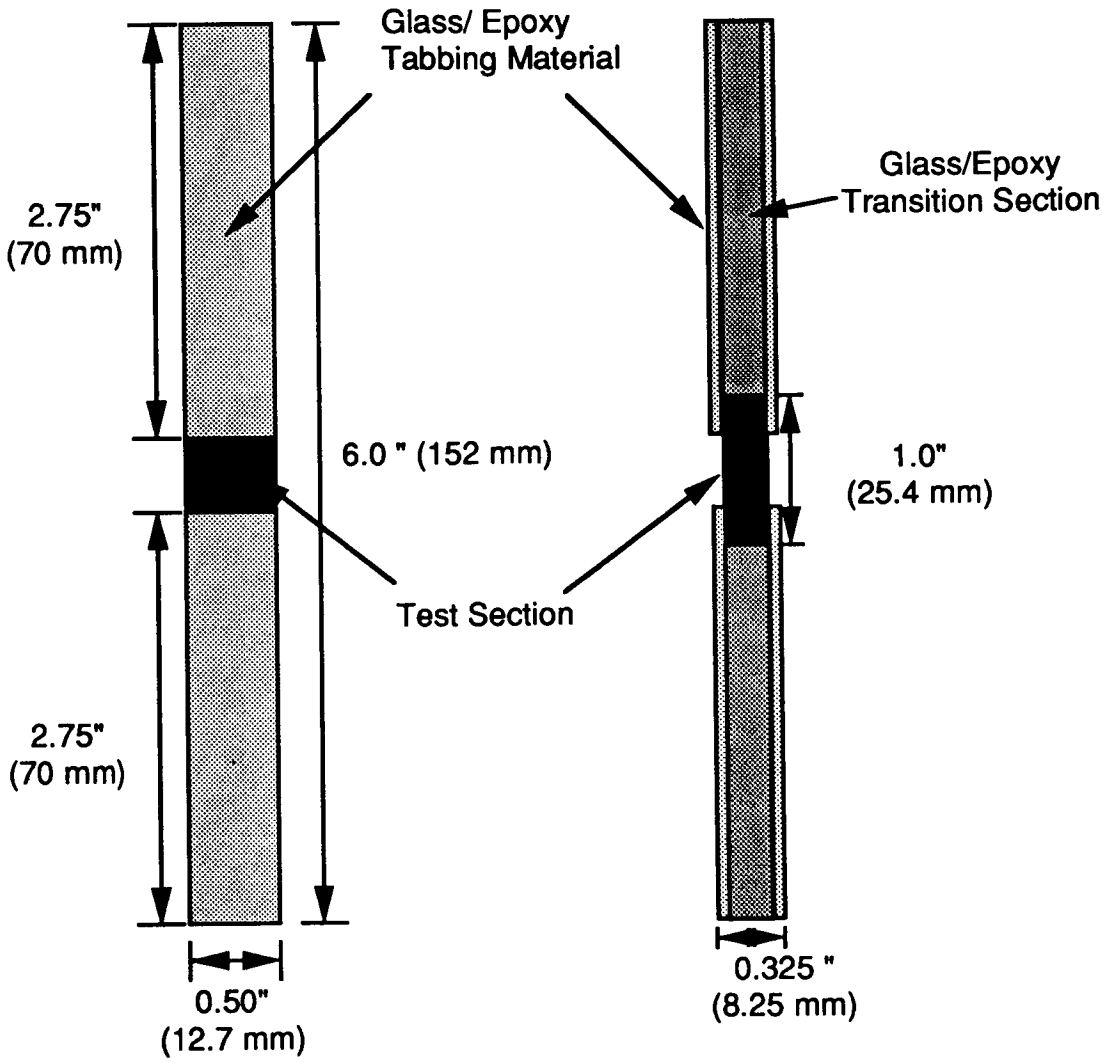

Figure 16 - Schematic of through-the-thickness compression specimen.

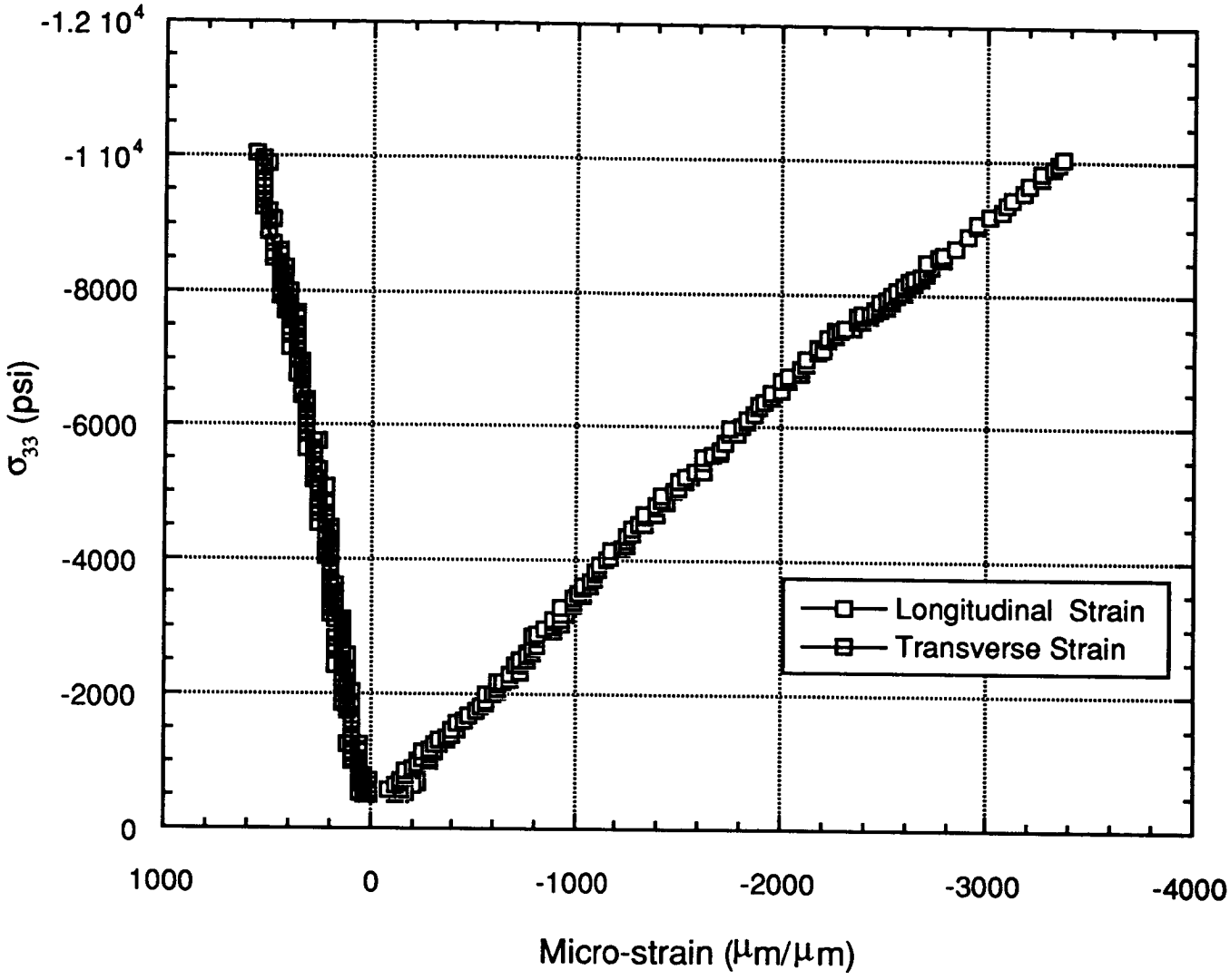

Figure 17 - Typical compressive stress-strain curve for OS-3 composite.

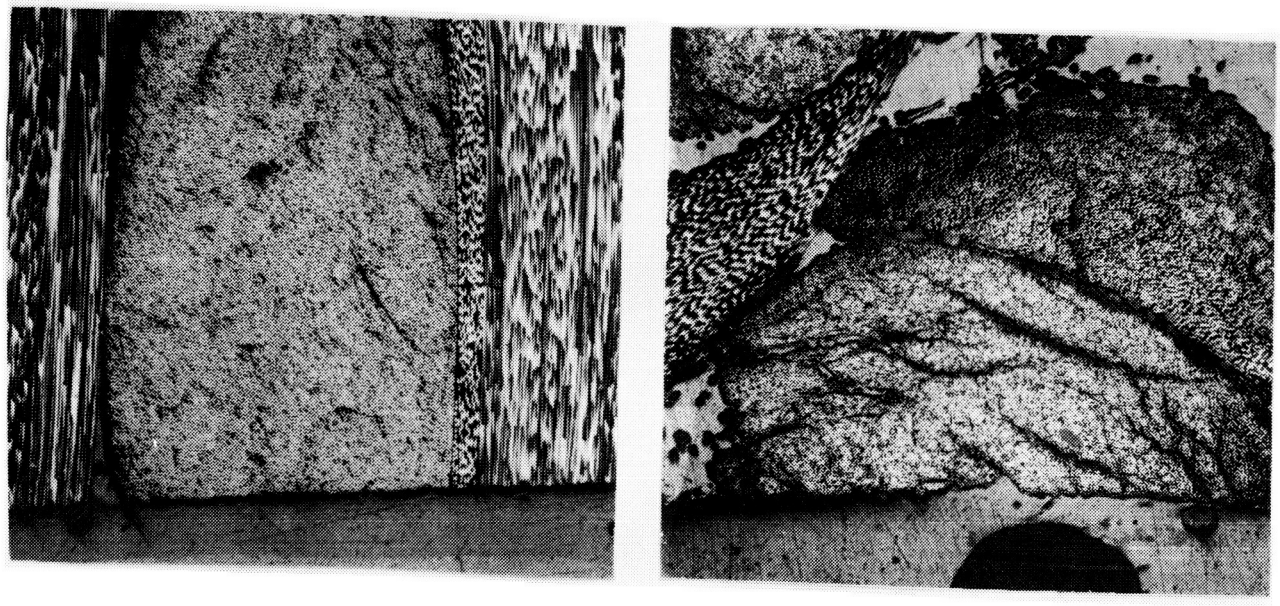

(a) (b)

(c) (d)

Figure 18 - Compressive damage progression in the surface weft tows of LS-3 specimen loaded to (a) 110 MPa, (b) 165 MPa, (c) 220 MPa and (d) Peak Load.

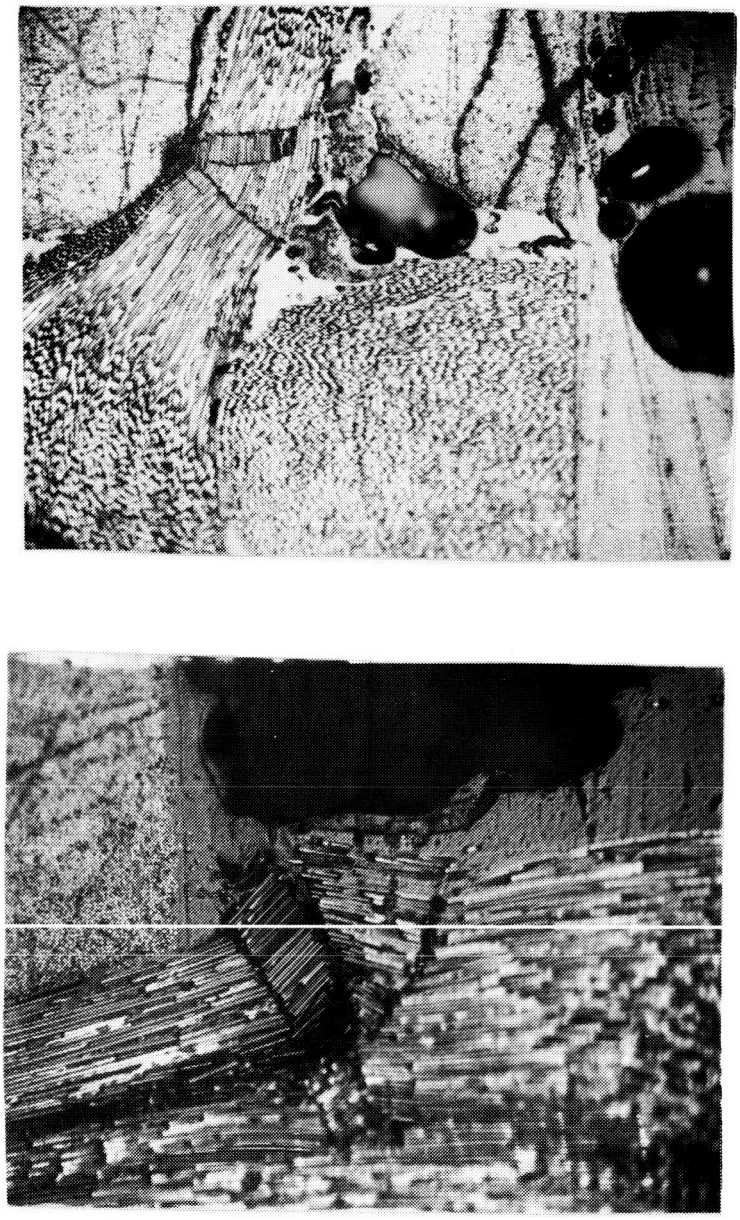

Figure 19 - Examples of kink bands near voids.

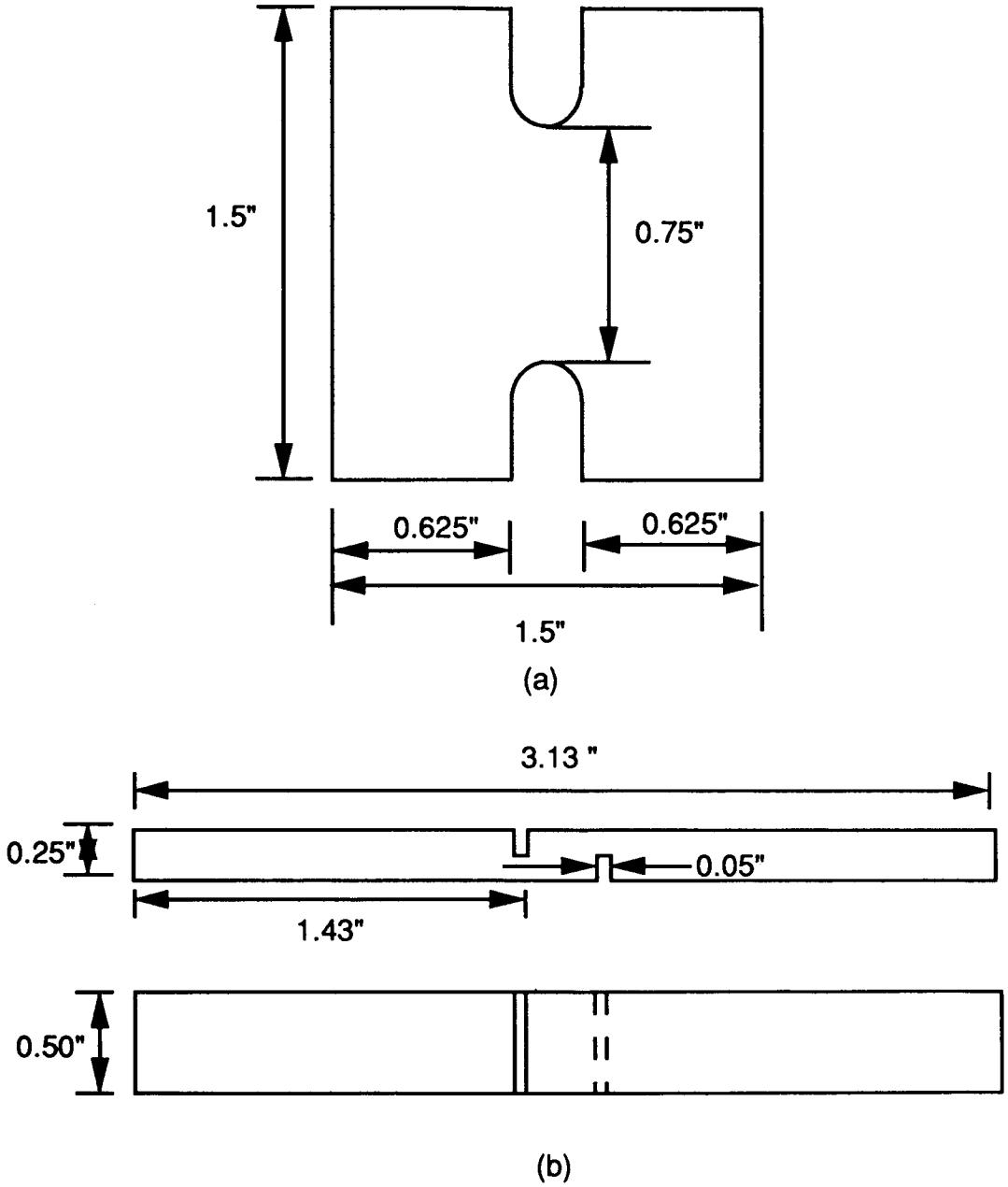

Figure 20 - Schematics of (a) baseline Compact Shear (CS) specimnen, and (b) Standard ASTM D3846-79 Double Notch Shear (DNS) specimen.

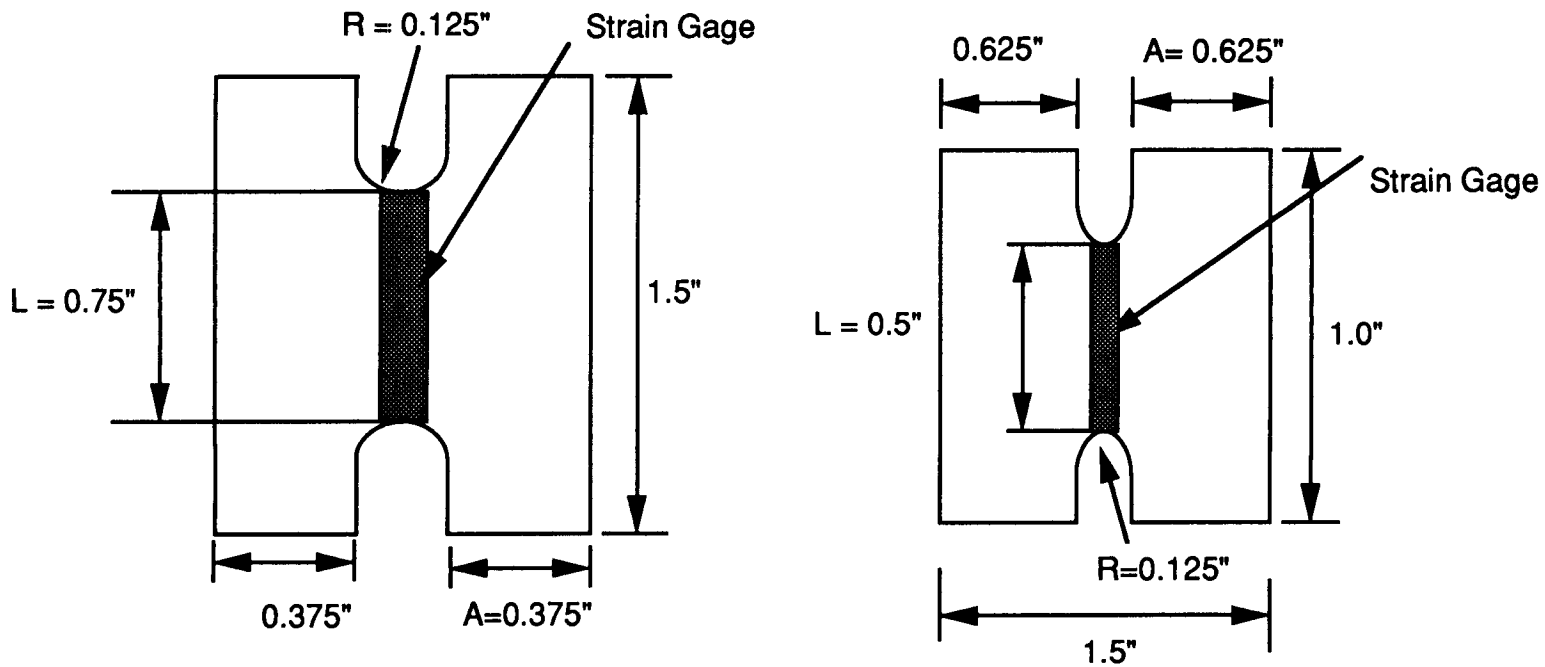

(a) TTIS1

(b) TTIS2

Figure 21 - Schematics of the two modified CS specimens for (a) interlaminar (TTIS1) and (b) transverse(TTIS2) shear testing.

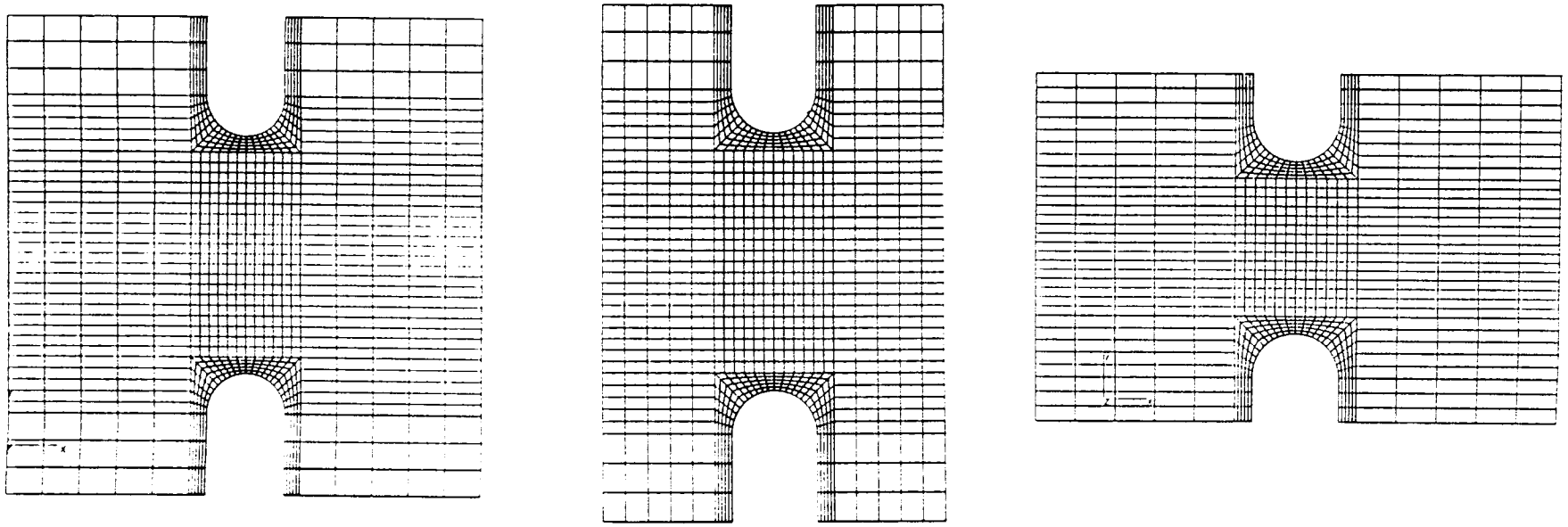

(a) (b) (c)

Figure 22 - FEM meshes for (a) baseline CS, (b) TTIS1, and (c) TTIS2 specimens.

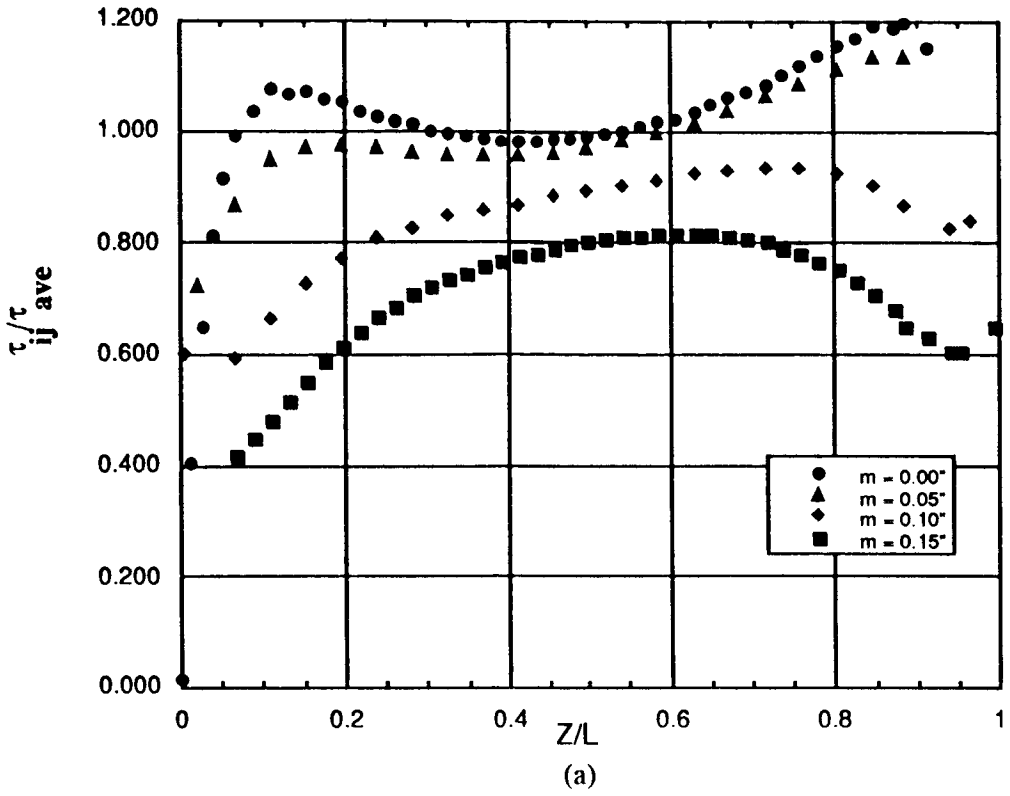

(a)

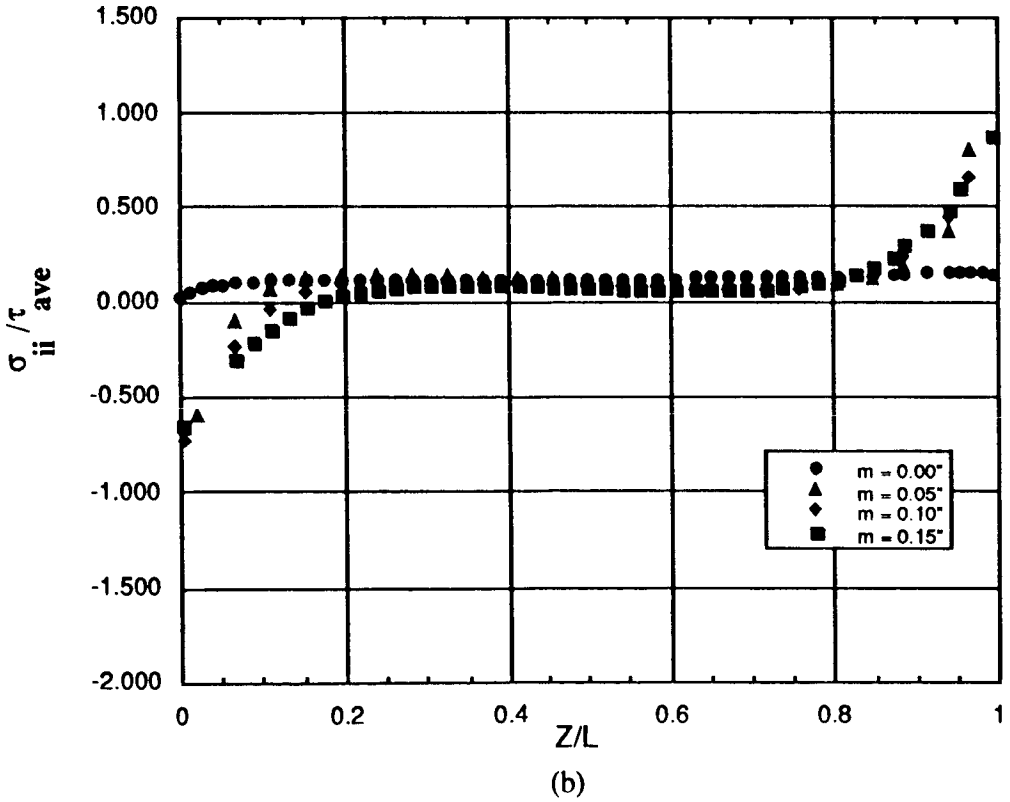

(b)

Figure 23 - Normalized stress distruibutions from FEM analysis for baseline CS specimen; (a) shear stress (b) transverse tensile stress.

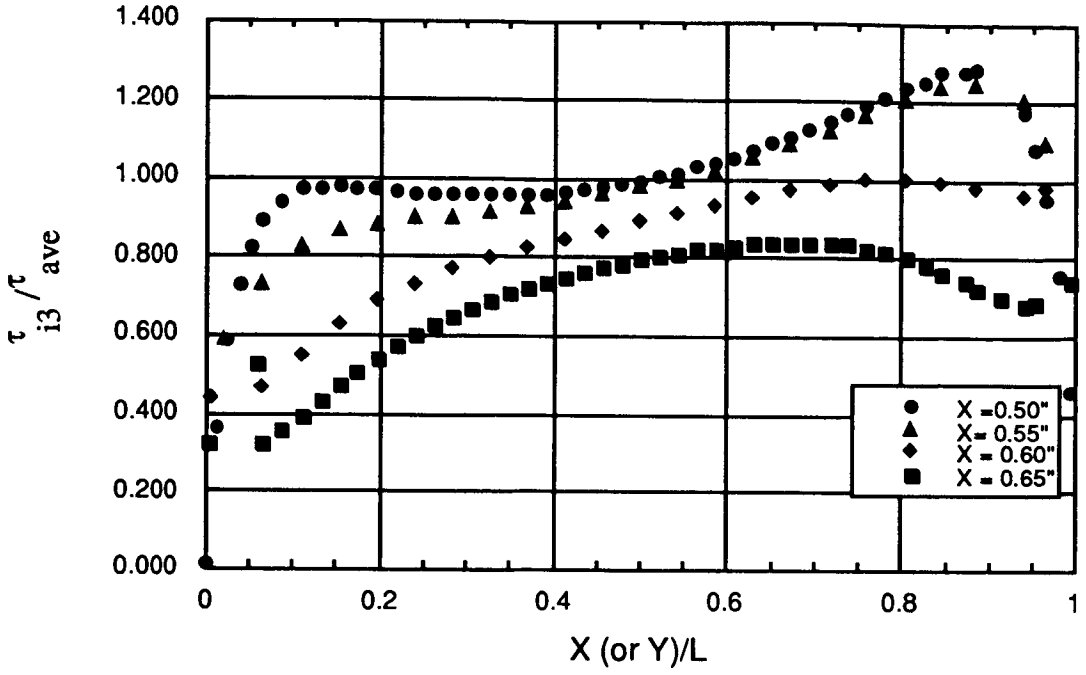

(a)

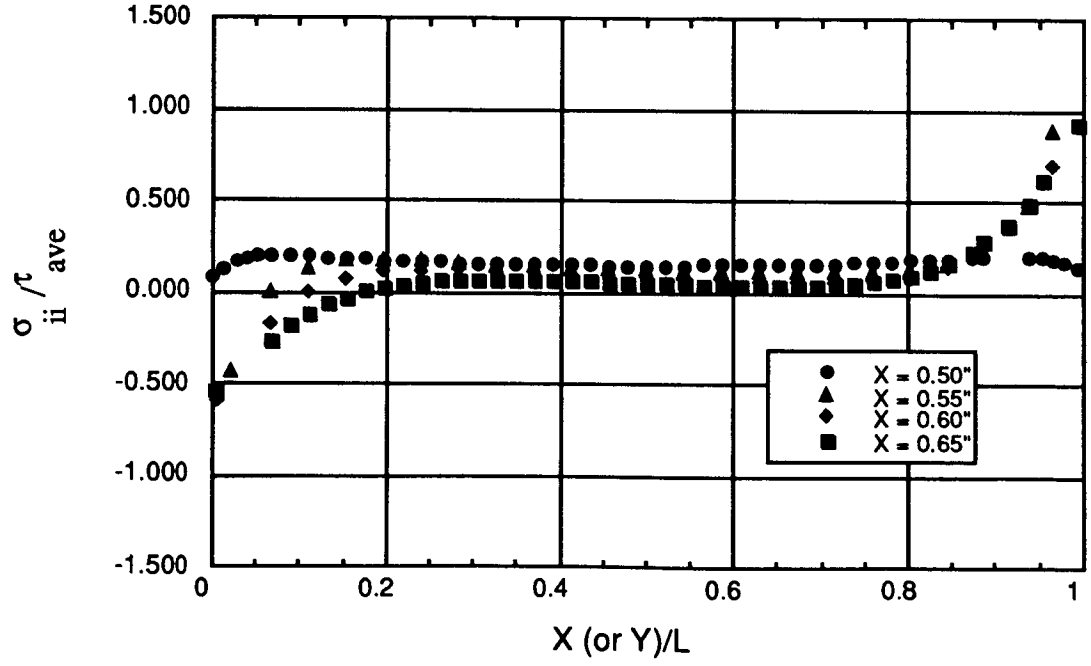

(b)

Figure 24 - Normalized stress distruibutions from FEM analysis for TTIS1 specimen; (a) shear stress (b) transverse tensile stress.

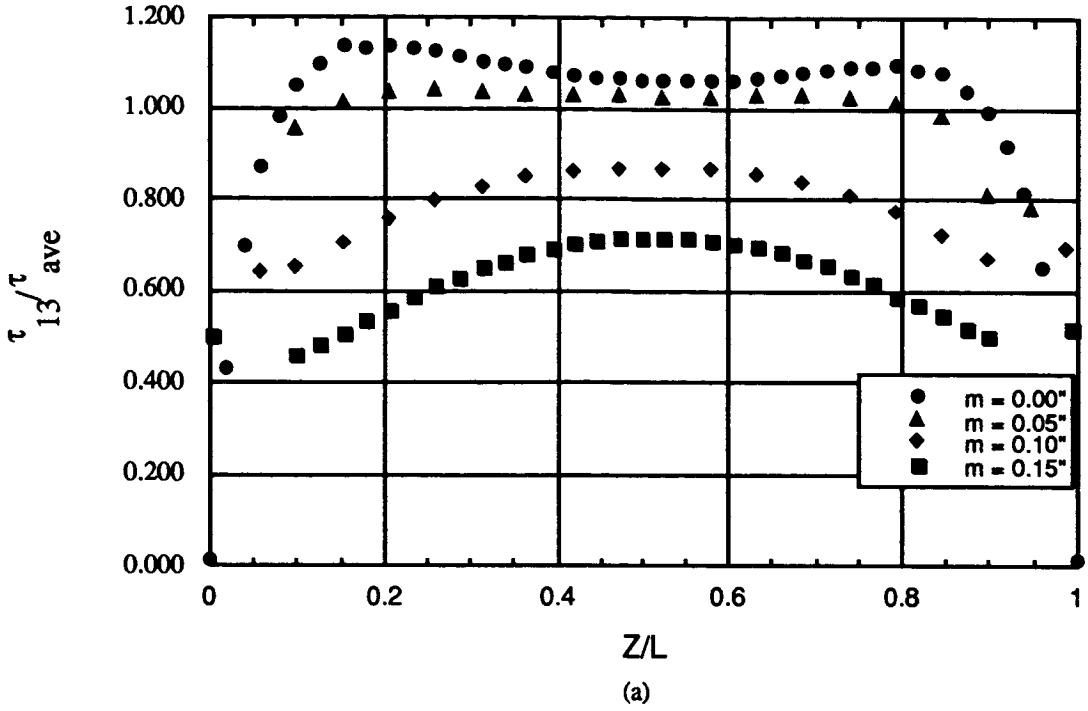

(a)

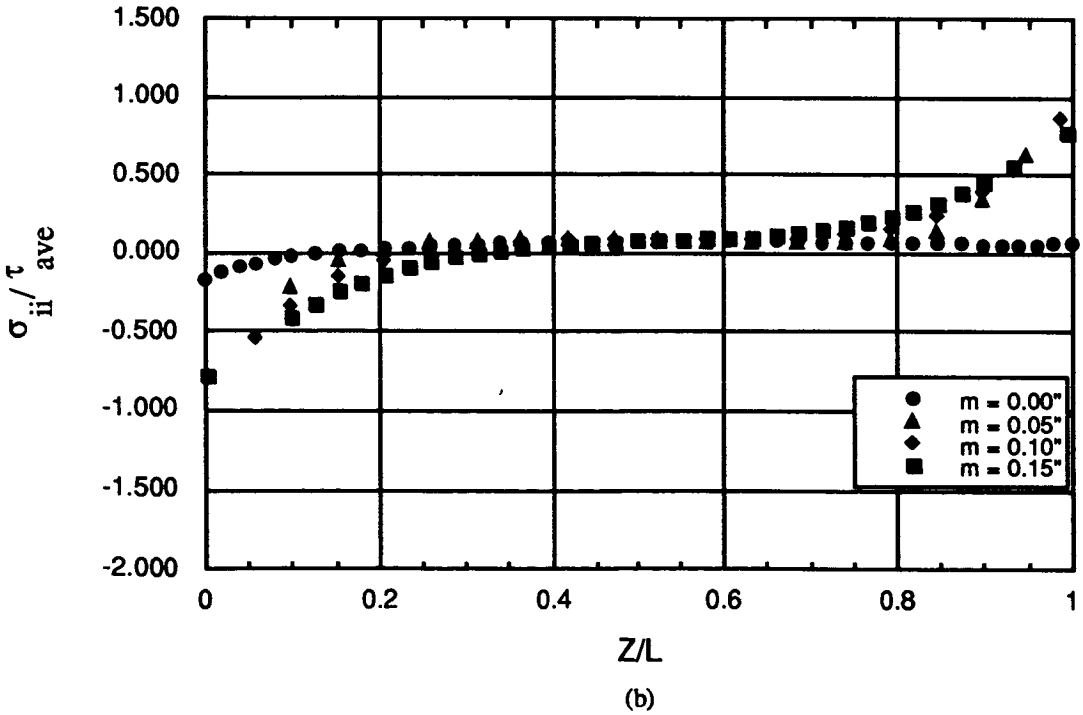

(b)

Figure 25 - Normalized stress distruibutions from FEM analysis for TTIS2 specimen; (a) shear stress and (b) transverse tensile specimen.

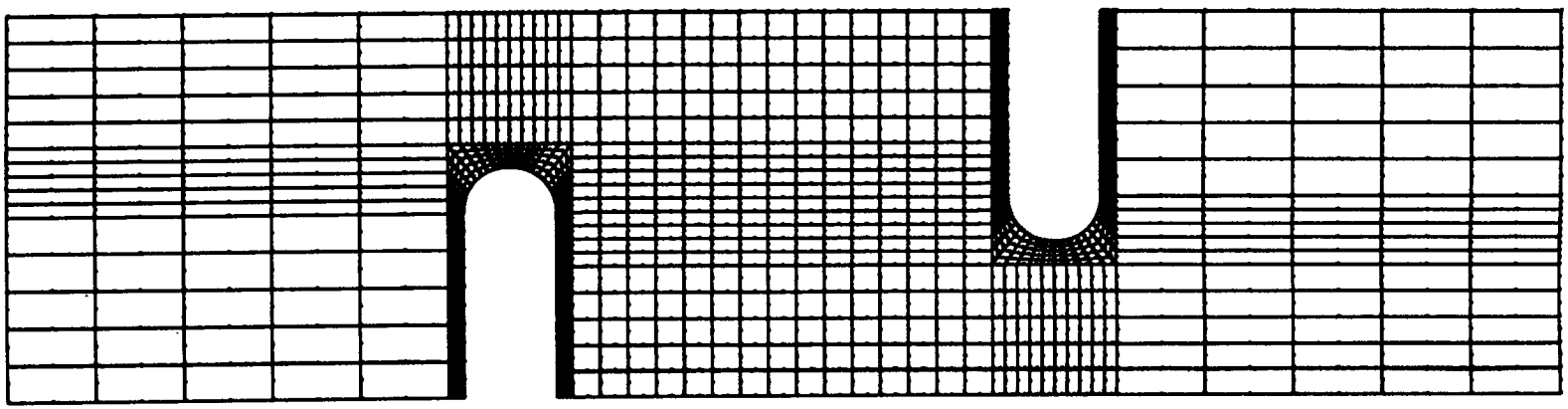

Figure 26 - FEM mesh for the modified DNS specimen.

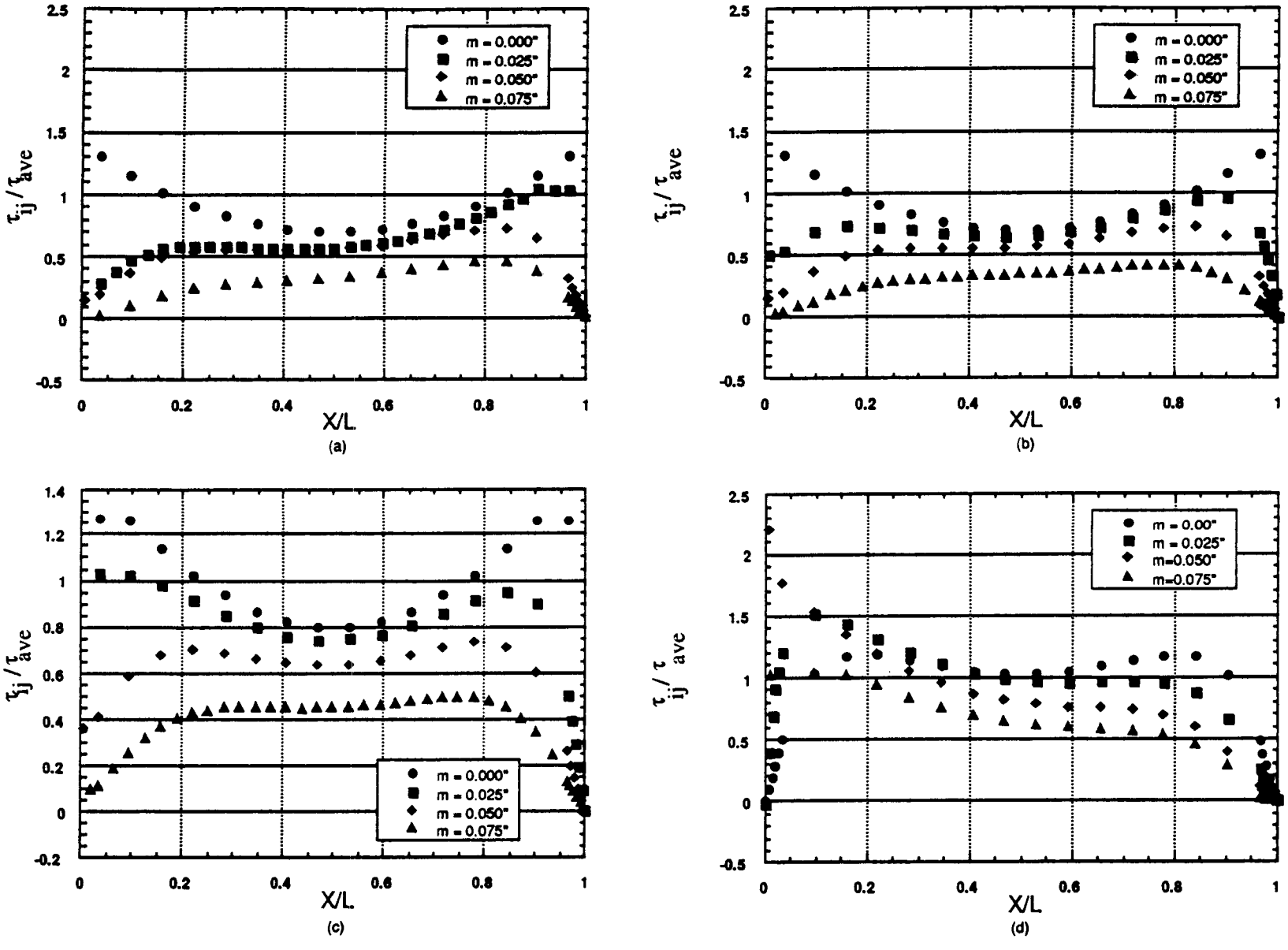

Figure 27 - Normalized shear stress distributions for modified DNS specimen with (a) L=0.290" H=0%, (b) L=0.290" H=10%, (c) L=0.290" H=20%, and (d) L=0.290" H=50%

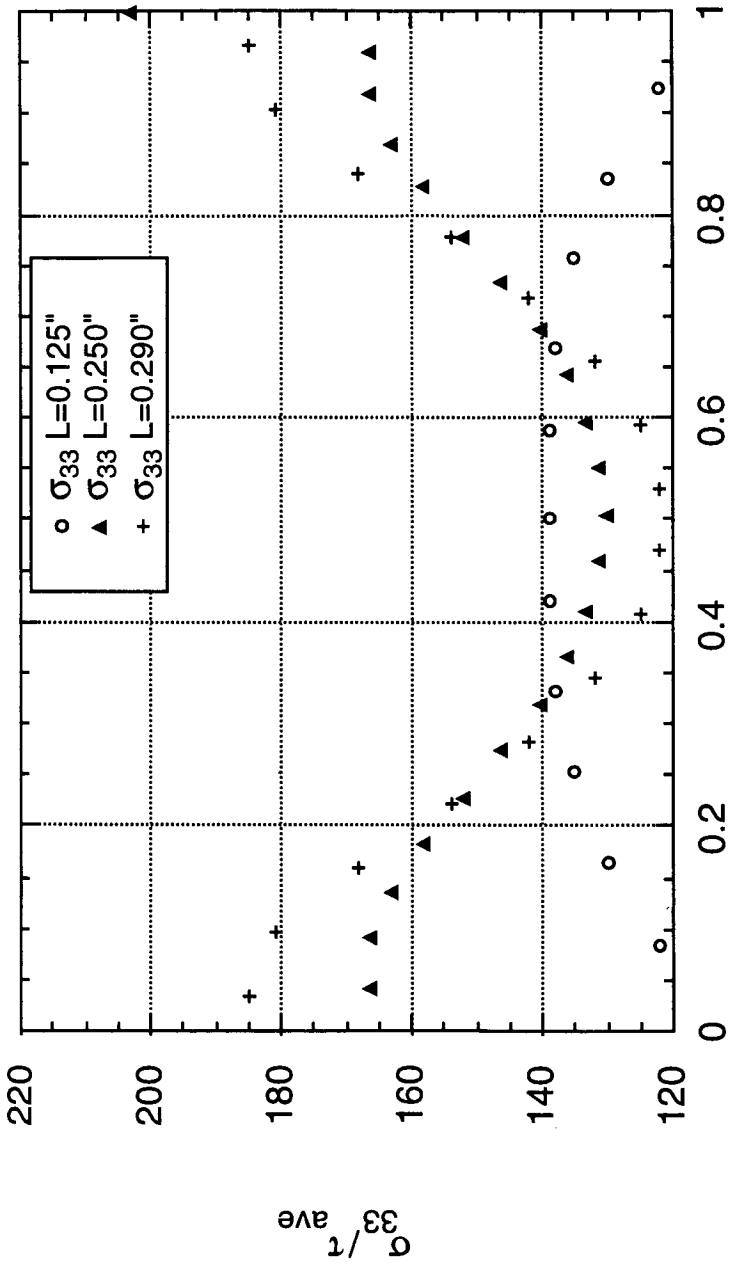

Figure 28 - Transverse tensile stress distributions for modified DNS specimens with H=0% and different L values.

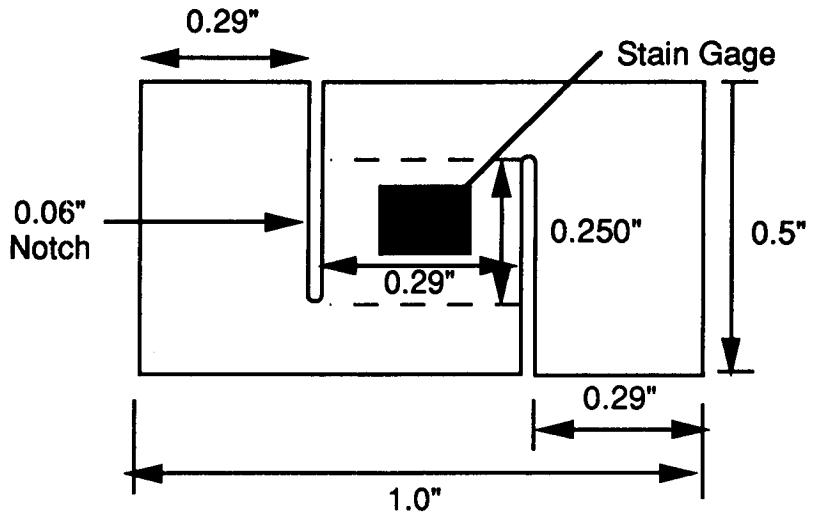

(a)

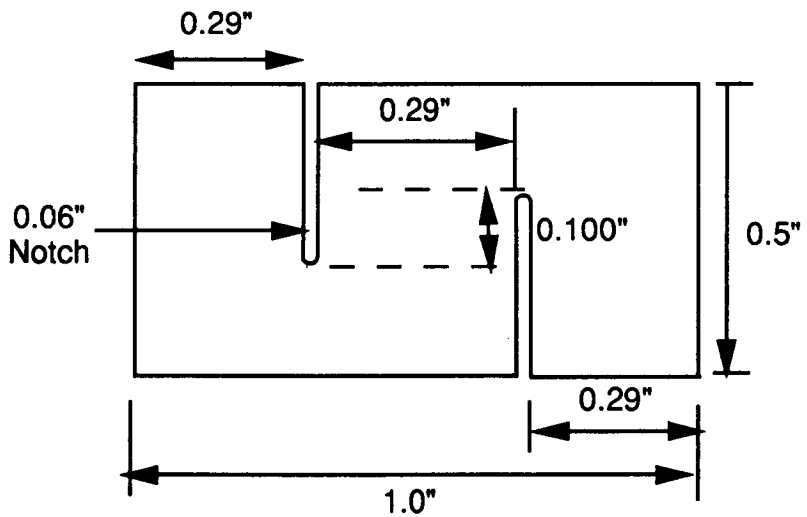

(b)

Figure 29 - Schematics of modified DNS specimens for (a) shear elastic modulus and (b) shear strength measurements.

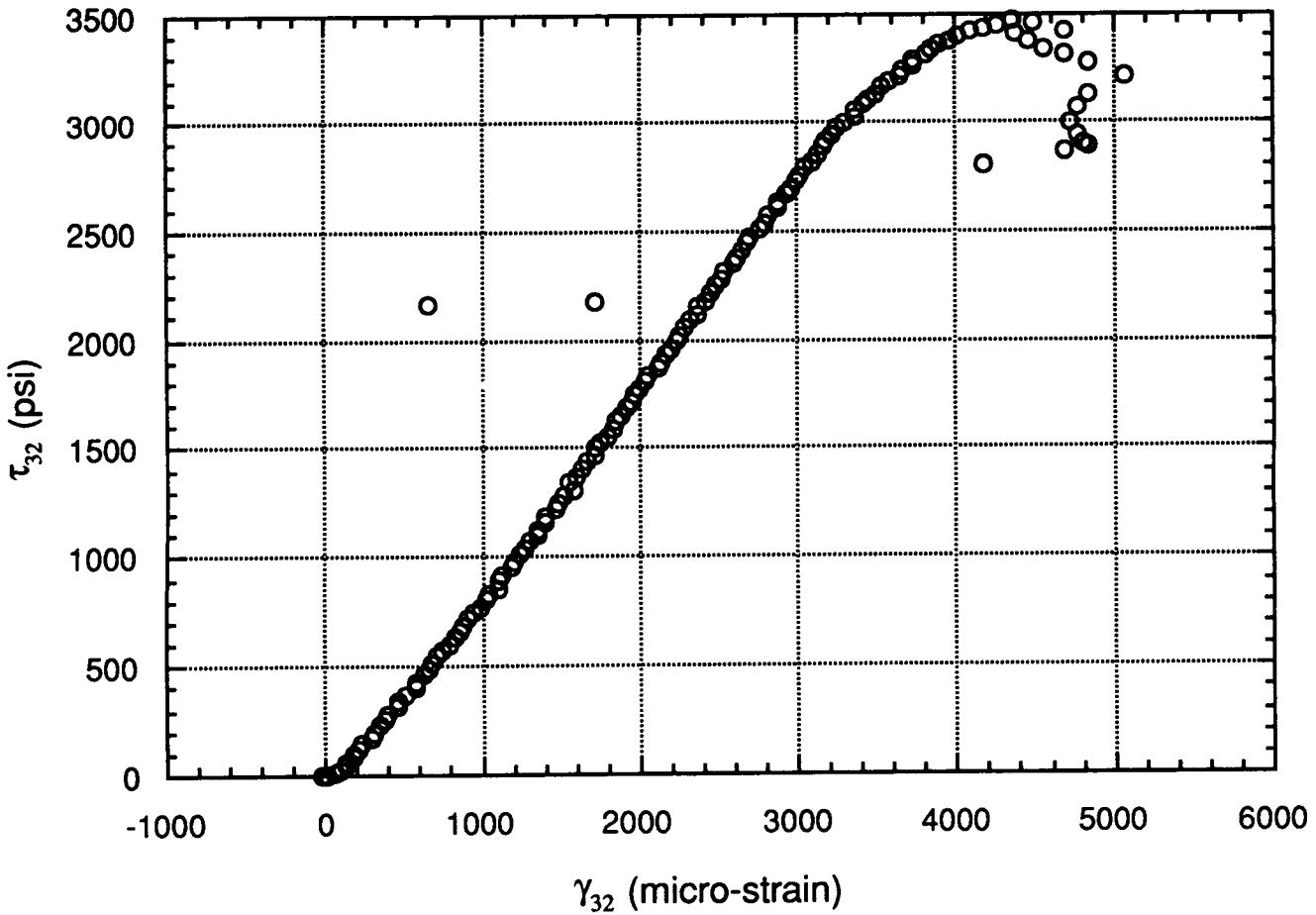

Figure 30 - Shear stress-strain curve obtained for LS-3 composite using modified TTIS1 specimen configuration.

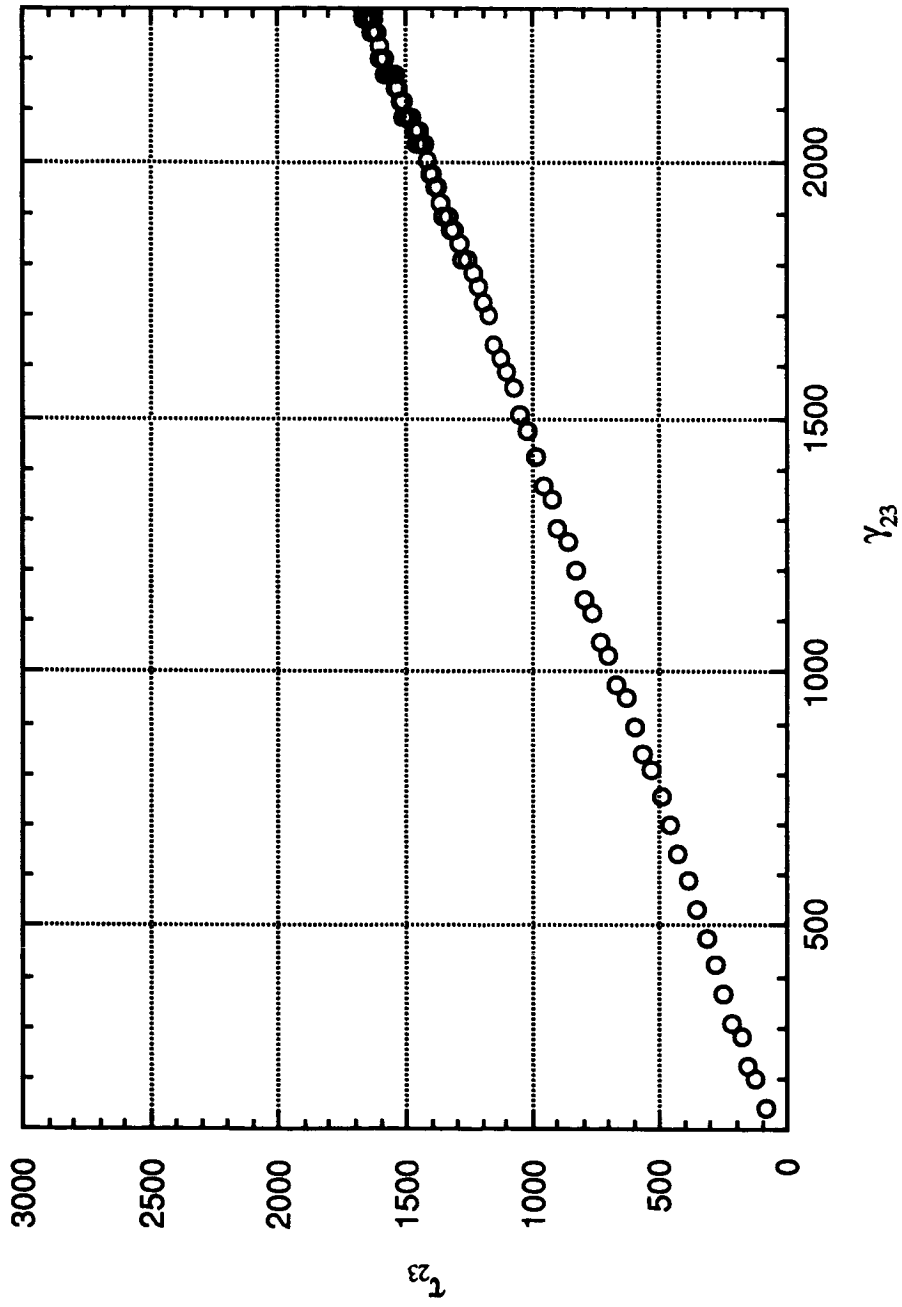

Figure 31 - Stress-strain curve for LS-3 composite using modified TTIS2 specimen configuration.

Out-of-Plane Properties

Wade C. Jackson
Vehicle Structures Directorate (ARL)

Marc A. Portanova
Lockheed Engineering & Science

Abstract

This paper summarizes three areas of research which were performed to characterize out-of-plane properties of composite materials. In the first investigation, a series of tests was run to characterize the through-the-thickness tensile strength for a variety of composites that included 2D braids, 2D and 3D weaves, and prepreg tapes. A new test method based on a curved beam was evaluated. Failures were significantly different between the 2D materials and the 3D weaves. The 2D materials delaminated between layers due to out-of-plane tensile stresses while the 3D weaves failed due to the formation of radial cracks between the surface plies caused by high circumferential stresses along the inner radius. The strength of the 2D textile composites did not increase relative to the tapes. Final failure in the 3D weaves was caused by a circumferential crack similar to the 2D materials and occurred at a lower bending moment than in the other materials. The early failures in the 3D weaves were caused by radial crack formation rather than a low through-the-thickness strength. The second investigation focused on the development of a standard impact test method to measure impact damage resistance. The only impact tests that currently exist are compression after impact (CAI) tests which incorporate elements of both damage resistance and damage tolerance. A new impact test method is under development which uses a quasi-static indentation (QSI) test to directly measure damage resistance. Damage resistance is quantified in terms of the contact force to produce a unit of damage where the metric for damage may be area in C-scan, depth of residual dent, penetration, damage growth, etc. A final draft of an impact standard that uses a QSI test method will be presented to the ASTM Impact Task Group on impact. In the third investigation, the impact damage resistance behavior of a variety of textile materials was studied using the QSI test method. In this study, the force where large damage initiates was measured and the delamination size as a function of force was determined. The force to initiate large damage was significantly lower in braids and weaves. The delamination diameter - impact force relationship was quantified using a damage resistance parameter, Q*, which related delamination diameter to impact force over a range of delamination sizes. Using this Q* parameter to rate the materials, the stitched uniweaves, toughened epoxy tapes, and through-the-thickness orthogonal interlock weave were the most damage resistant.

Through-the-Thickness Tensile Strength of Textile Composites

Textile composite materials have the potential for better through-the-thickness properties than traditional laminated composites. Traditional laminated composites are very susceptible to delamination from out-of-plane loads that may occur from impact loading or around structural details such as curved geometry, ply drops, or fasteners. With improved through-the-thickness properties, the susceptibility to damage from out-of-plane loads should be greatly reduced.

Textile composites may have a 2D construction where discrete layers are stacked to produce a desired thickness or a 3D construction where a single layer is manufactured to a desired thickness. In the 2D materials, the preform layers are expected to nest snugly together to improve the through-the-thickness properties. In the 3D materials, reinforcement in the thickness direction was specifically included to directly improve these properties.

Through-the-thickness tensile strength is an important material property but is a difficult property to quantify. In laminated composite materials, the through-the-thickness tensile strength can be approximated by the transverse-width strength measured from flat 90° specimens [1]. In textile composites, however, the architecture of the preform is three dimensional with significantly different properties in all directions. In this study, two test methods that incorporate a specimen with a curved test section were used. Through-the-thickness tension is induced in the test section by a moment which attempts to open the curve. One of these test methods uses a curved beam in four-point bending to measure the strength [2]. This method was developed for this test program and was evaluated as part of this investigation

Using these two test methods, a series of tests was run to characterize the through-the-thickness strength for a variety of composites made from textile preforms. Specimens were made from four different 2D braids, six 3D weaves, prepreg fabrics, and from unidirectional tape specimens. For both loading configurations, the data were reduced using an elasticity solution for anisotropic curved beams.

Materials

A variety of textile and prepreg tape materials were used in this investigation. All specimens were manufactured with Hercules AS4 carbon fibers and similar resins. For comparison purposes, a toughened epoxy (8551-7) was also used to make tape specimens. All tape specimens were manufactured using prepregs of AS4/3501-6 (24 & 48 ply) or AS4/8551-7 (25 & 48 ply). The 2D braided and 3D woven preforms were impregnated with Shell RSL-1895/W epoxy resin using the resin transfer molding (RTM) process [3]. The 1895/W system was developed for RTM and has similar properties to 3501-6 epoxy.

The 2D braids were formed on cylindrical mandrels and incorporated longitudinal yarns to create a triaxial construction with a $0°/\pm\theta°$ orientation (Fig. 1). Four different braid geometries were manufactured [3]. The braid angle, the yarn sizes, and the longitudinal yarn content were varied to determine sensitivity to these parameters. The desired thickness was obtained by overbraiding layers. Since all specimens had the same nominal thickness of 6.35 mm, the number of layers decreased with increasing yarn bundle size.

Type	Braid angle	Braider size	% 0° yarns
$[0_{30k}/\pm70_{6k}]_8$	±70	6k	46
$[0_{75k}/\pm70_{15k}]_6$	±70	15k	46
$[0_{36k}/\pm45_{15k}]_6$	±45	15k	46
$[0_{6k}/\pm45_{15k}]_{10}$	±45	15k	12

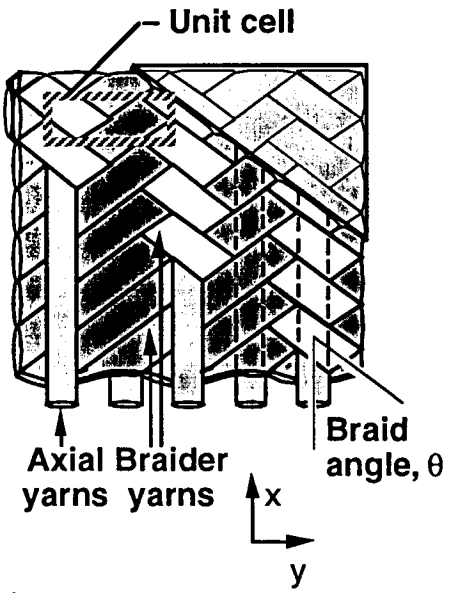

Figure 1. 2D triaxial braid architecture

The 2D-woven fabrics included a plain weave and two 5-harness satin weaves. One of the 5-harness satin weaves was made with 3k tows (AW280-5H), and one was made with 6k tows (AW370-5H). The plain weave (AW193PW) was used to make two panels of 12 and 16 layers. The panels made from the satin weaves were 12 layers thick. The 3D weaves were all interlock woven fabrics where yarns are woven through the thickness to provide direct resistance to delamination. The interlock tows ran parallel to the warp (0°) yarns and wrapped around the weft (90°) yarns. Three different weave architectures were investigated: through-the-thickness orthogonal interlock (OS), through-the-thickness angle interlock (TS), and layer-to-layer angle interlock (LS). The weave architectures are shown schematically in Fig. 2. For each

architecture, one panel was woven using small fiber bundles (-2), and one panel was woven using large fiber bundles (-1).

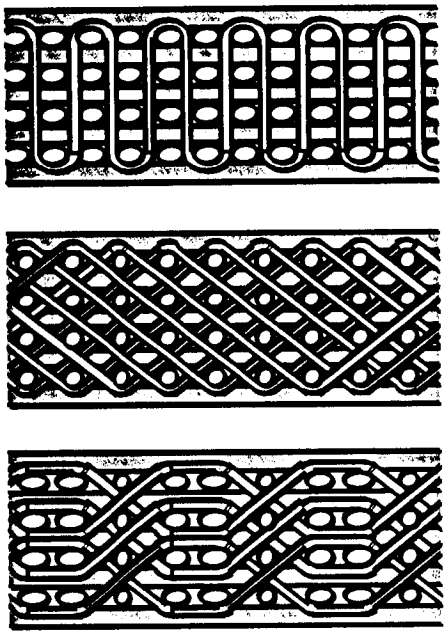

Through-the-thickness orthogonal interlock (OS)

Through-the-thickness angle interlock (TS)

Layer-to-layer interlock (LS)

	Warp		Weft		Weaver
Code	#	size	#	size	size
-1	4	24k	5	12k	6k
-2	6	12k	7	6k	3k

Figure 2. 3D weave architecture

Test Configuration and Data Reduction

Two different test configurations, shown schematically in Fig. 3, were used to measure strength. A new test method was evaluated which used a four-point-bending (4PB) fixture where the specimens were loaded by rollers to create a force couple on each loading arm [2]. Because of the geometry of the 4PB fixture, the specimens were self aligning. The second configuration used a steel hinged loading mechanism (HLM) which was aligned and clamped on to the specimen's loading arms [1]. This test method had been used previously to measure the strength of unidirectional laminates. This loading fixture allowed the specimen to be tested in a tension testing machine. The displacement was controlled at 0.2 in/min (0.5 mm/min) during loading for both test methods. Loads and displacements were digitally recorded. To aid in detecting failure location, the edges of each specimen were painted white with a water-based typewriter correction fluid.

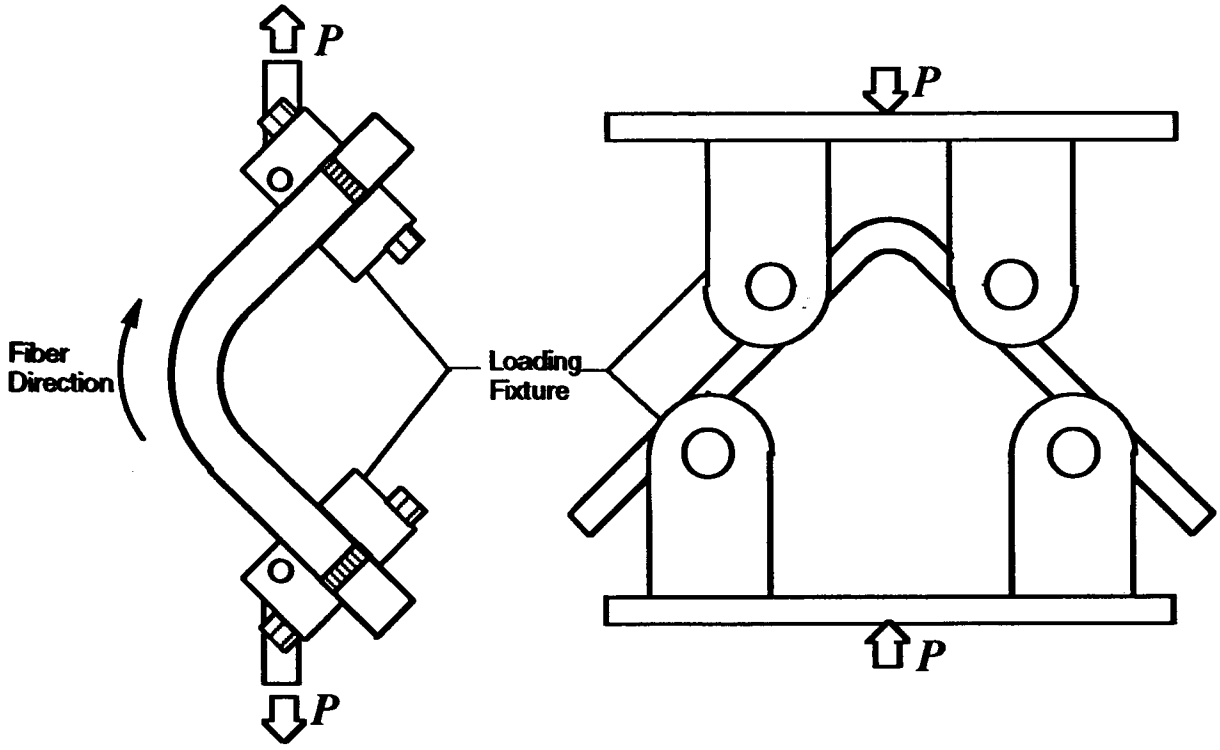

Hinged Loading Mechanism Test Method (HLM)

4-Point Bend Test Method (4PB)

Figure 3. Test configurations

The loads on the test section were calculated for both test configurations prior to analysis. To calculate stresses in the curved segment, the applied loads had to be translated to the ends of the curved segment. For the 4PB configuration, the applied moment on the curved section of the specimen is simply the product of the force exerted by one of the cylindrical loading bars and the distance between two bars along a loading arm (Fig. 4). The bar force and distance were calculated from the total load and the geometries of the loading fixture and test specimen [2]. Since a force couple acts on the loading arm, the resultant force is zero. For the HLM test configuration, a similar procedure was followed to calculate the loading [1]. The resultant force, however, is nonzero for this case ($P \neq 0$). These results are shown schematically in Figure 4.

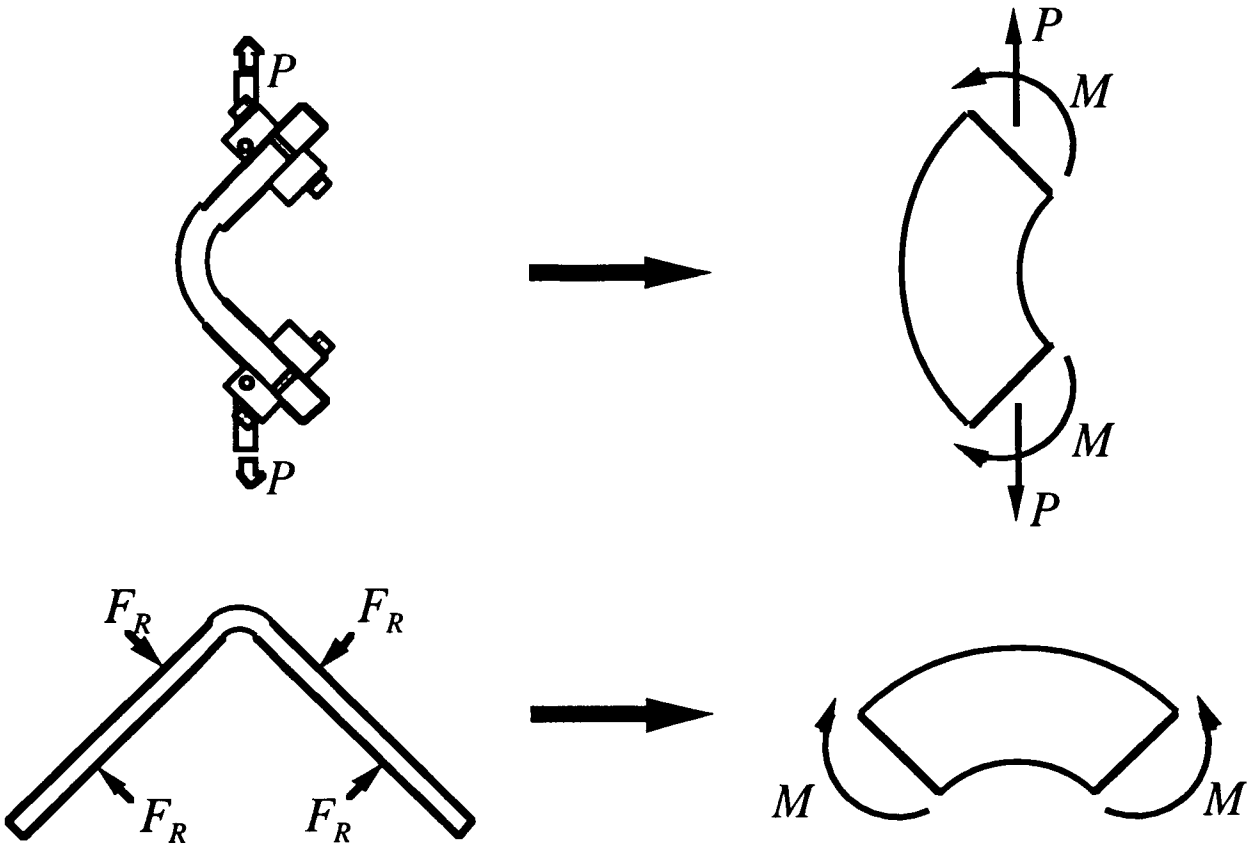

Figure 4. Translation of forces

Solutions were developed by Lekhnitskii for the stresses in a curved beam segment with cylindrical anisotropy [4]. Using the translated loads at the ends of the curved segment, the stresses were calculated using the Lekhnitskii stress equations. For the hinged test configuration, the stress equations become more complex since the stresses produced by the moment and the end force must be superimposed [1]. Also, because of the end force, the stresses become a function of angular position. However, in the four-point-bending test configuration, the curved segment is under a state of pure bending. Consequently, the closed-form stress analysis is much simpler and independent of angular position [2]. Nevertheless, the stress fields produced in the curved region are only slightly different for the two different loading methods. Typical radial and tangential stress distributions, σ_r and σ_θ, along the centerline of the specimen are shown in Figure 5. The radial stress, σ_r, reaches a maximum at approximately 35% of thickness from the inner radius and is zero at both free edges. The tangential stress, σ_θ, ranges from tension on the inner radius to compression at the outer radius.

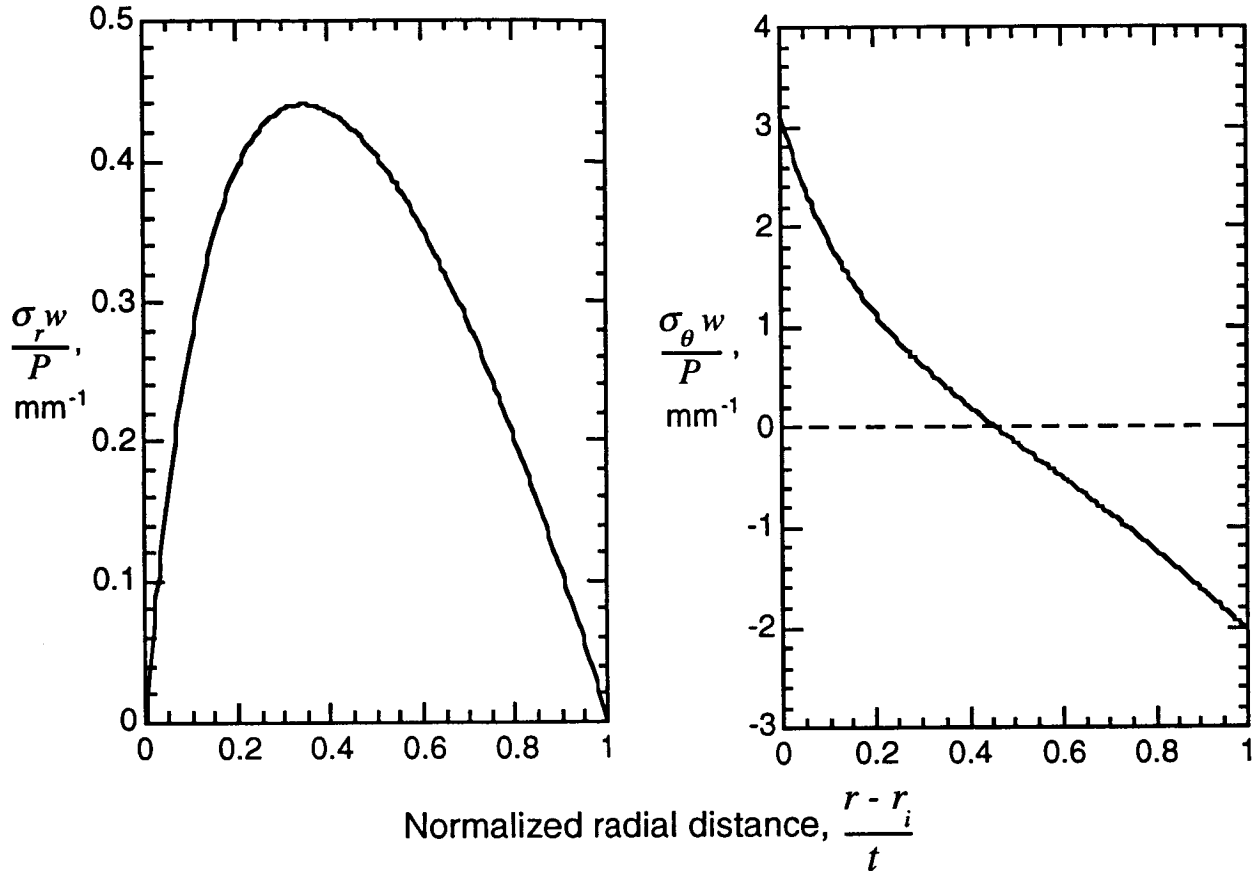

Figure 5. Typical stress distribution for a curved beam under bending

Experimental Results

Each specimen was loaded to failure using either the four-point-bending fixtu (4PB) or the hinged loading mechanism (HLM). A typical load history to failure is shown in Figure 6 for a 48-ply AS4/8551-7 specimen using the 4PB fixture. At failure the load drops sharply due to the stiffness loss caused by the unstable formation of circumferential delaminations.

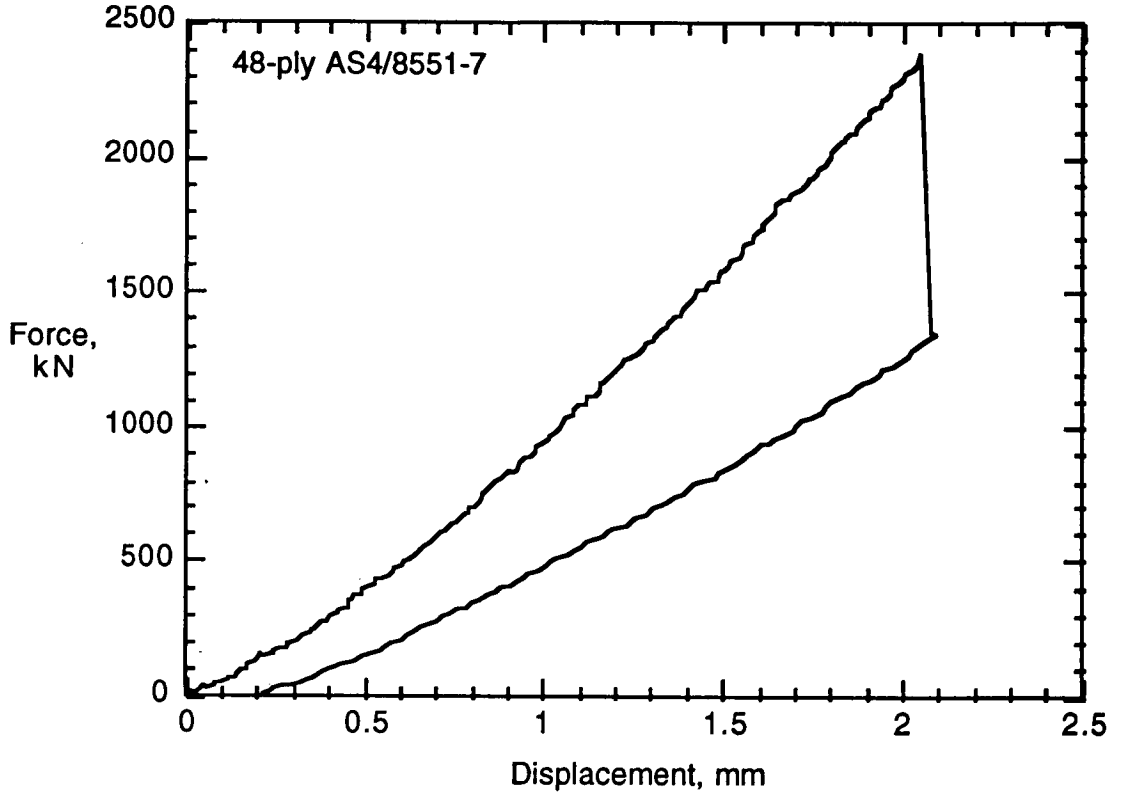

Figure 6. Typical load history

Failures were significantly different between the 2D materials and the 3D weaves (Fig. 7). Moiré fringe patterns provided an excellent method of detecting and documenting damage [1,5]. All the 2D materials (tapes, fabrics, and triaxial braids) simply delaminated between layers due to the out-of-plane tensile stresses. No damage was detected prior to delamination. Often, subsequent delaminations were also formed due to load redistribution into the sublaminates. The delaminations in the 2-D braids often followed a tortuous path due to the nested layers. In the 3D weaves, damage began accumulating very early in the loading. During loading, the specimens emitted a crackling noise which was produced by radial cracks forming between the 90° (weft) surface plies in the inner radius caused by the tensile circumferential stress. Matrix cracking around the interlock tows was also observed. The radial cracks

extended across the entire width of the specimen. Some of the radial cracks extended a third of the way into the thickness. Despite the through-the-thickness reinforcement, circumferential cracks similar to the 2D materials eventually formed. The OS-2 weave, however, never formed a circumferential crack. Since the cracks in the inner radius significantly alter the stresses in the bend, a through-the-thickness stress at failure could not be calculated for the 3D weaves.

Failure Modes

Layered Material (Tapes, 2-D Weaves, 2-D Braids)

Non-Layered Material (3-D Weaves)

Figure 7. Typical failure modes

A summary of the average strengths (maximum σ_r at the onset of damage) along with the high/low data is shown in Fig. 8 for all the 2D materials. In general, the 2D textile materials had very similar strengths with the range of strengths overlapping for each of the material systems. However, the through-the-thickness strength was generally lower than in the tape materials. The 48-ply AS4/3501-6 tape material had a similar strength to the 2D textiles but had a low fiber volume fraction. The through-the-thickness strengths of the specimens made from the prepreg materials, and possibly the RTM materials, decreased rapidly with decreasing fiber volume fraction.

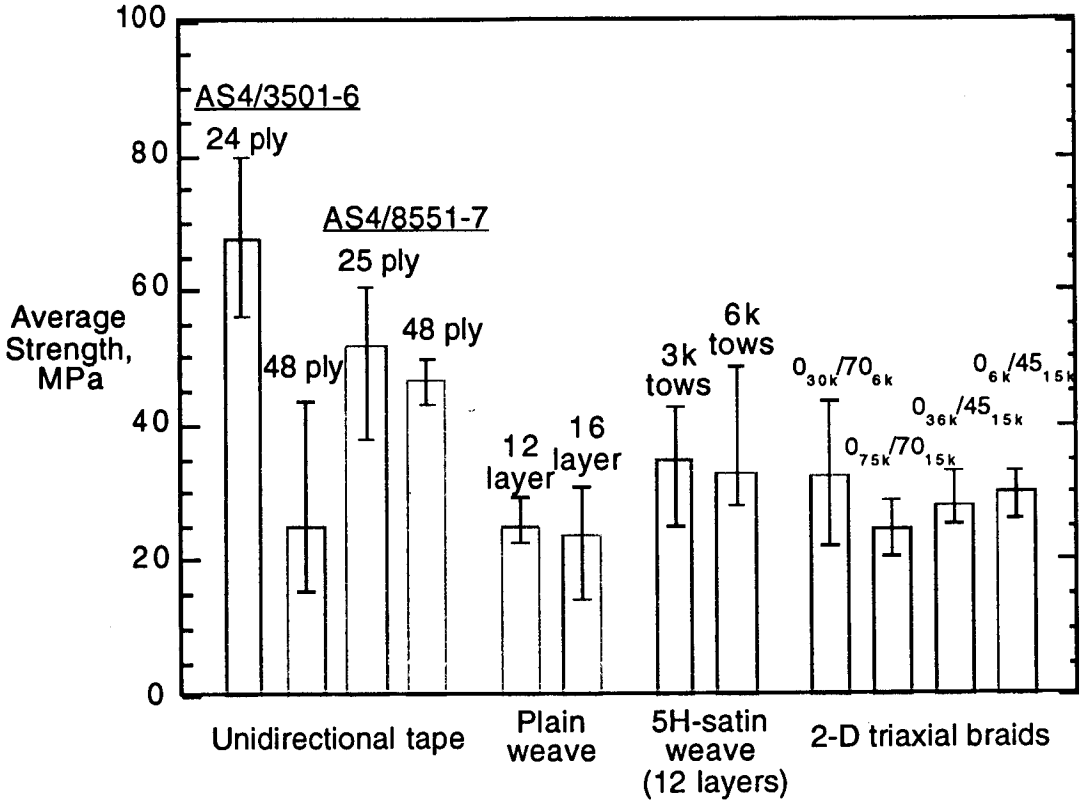

Figure 8. Average strengths of 2D materials

For the AS4/3501-6, the 24-ply strength was significantly higher than the 48-ply strength but had a much higher fiber volume fraction (Fig. 9). Excluding volumetric effects, the through-the-thickness strength should be independent of thickness. The average ply thickness in the bend was 0.165 mm in the 48-ply specimens and 0.133 mm in the 24-ply specimens. In previous tests, a strong correlation was found between ply thickness and strength. Therefore, the large strength difference may be a result of the 24% increase in ply thickness (decrease in fiber volume). The average

ply thicknesses of the 25 and 48-ply AS4/8551-7 specimens were nearly identical at 0.157 and 0.156 mm, respectively. Accordingly, the strengths were also close and within the scatter of data. The manufacturer's product data sheet for AS4/3501-6 lists a ply thickness of 0.13 mm to achieve a 62% fiber volume fraction. Since the AS4/3501-6 and AS4/8551-7 materials had identical fiber areal weights (149 g/m^2), identical ply thicknesses represent identical fiber volume fractions. Consequently, the strengths between the two material systems were only compared for similar fiber volume fractions. The average ply thicknesses of the 48-ply 3501-6 specimens and all the 8551-7 specimens were within 6%. For this case, the 8551-7 has nearly twice the strength of the 3501-6 material.

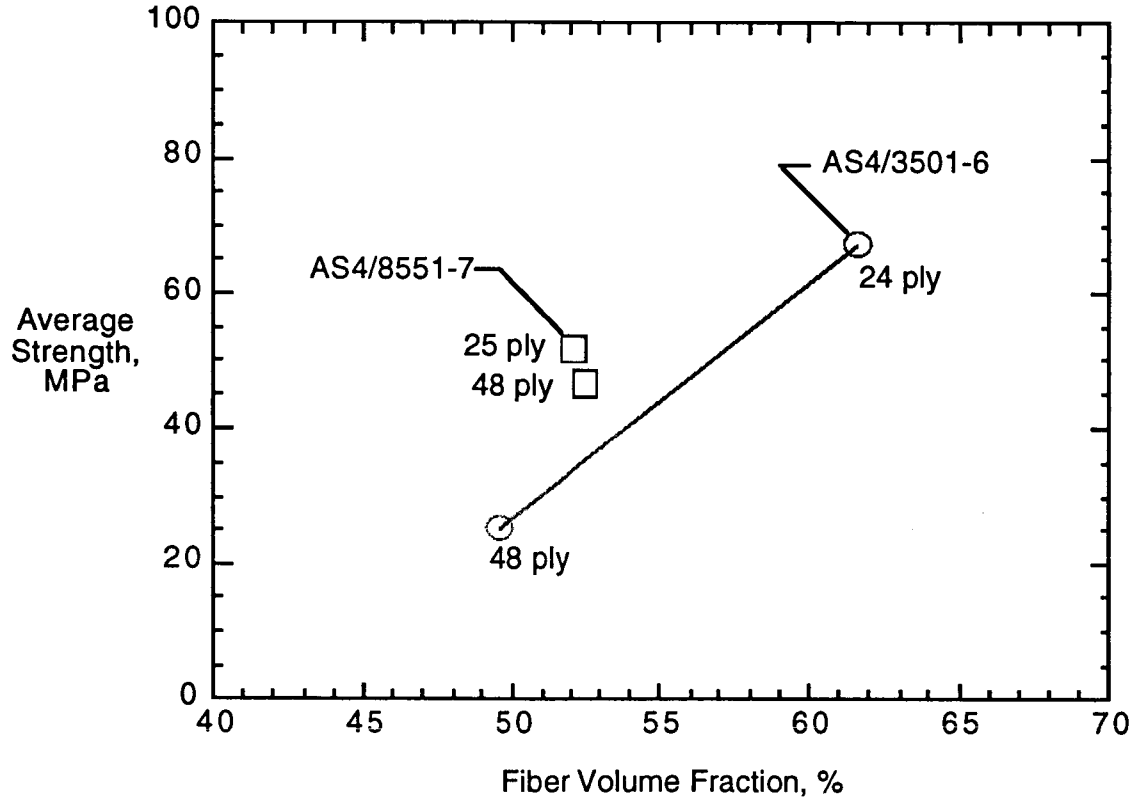

Figure 9. Effect of fiber volume fraction

The strengths of the 12- and 16-layer plain weaves were nearly identical. The average layer thickness in the bend was 0.208 mm for both thicknesses. The average layer thicknesses in the loading arms were 0.180 and 0.178-mm for the 12- and 16-layer specimens, respectively. The manufacturer's product data sheet lists a ply thickness of 0.18 mm for a 62% fiber volume fraction. Therefore, these strengths may increase with higher compaction. The two 5H-satin weaves also had nearly identical strengths. For the weave with 3k tows, the average layer thickness was 0.301 mm in the bend whereas the product data sheet lists a thickness of 0.25 mm for a 62% fiber

volume fraction. For the weave with 6k tows, the average layer thickness was 0.347 mm in the bend and the corresponding value on the data sheet was 0.34 mm for a 62% fiber volume fraction. Therefore, for equal fiber volume fractions, the 3k weave may have a higher strength.

Since stresses in a damaged material cannot be readily calculated, the moment at failure was calculated for the 3D weaves. The failure load was defined as the load where circumferential cracks formed. The circumferential cracks reduced the bending stiffness and caused a small drop in load. The average bending moment at failure is shown in Fig. 10 for tests using the 4PB fixture. Many of the 2D materials are also included for comparison. The OS-2 weave is not shown since circumferential cracks did not form. The bending moment was normalized by the width and thickness of each specimen for comparison. The 3D weaves all failed at significantly lower bending moments than all of the 2D materials. This 3D architecture failed at lower loads due to the radial cracking between the 90° (weft) surface plies along the inner radius. For the six 3D weave architectures, the bending moments at failure were all within 20% of each other. When analyzed in terms of the bending moment, the 2D materials had relative rankings nearly identical to the strength analysis.

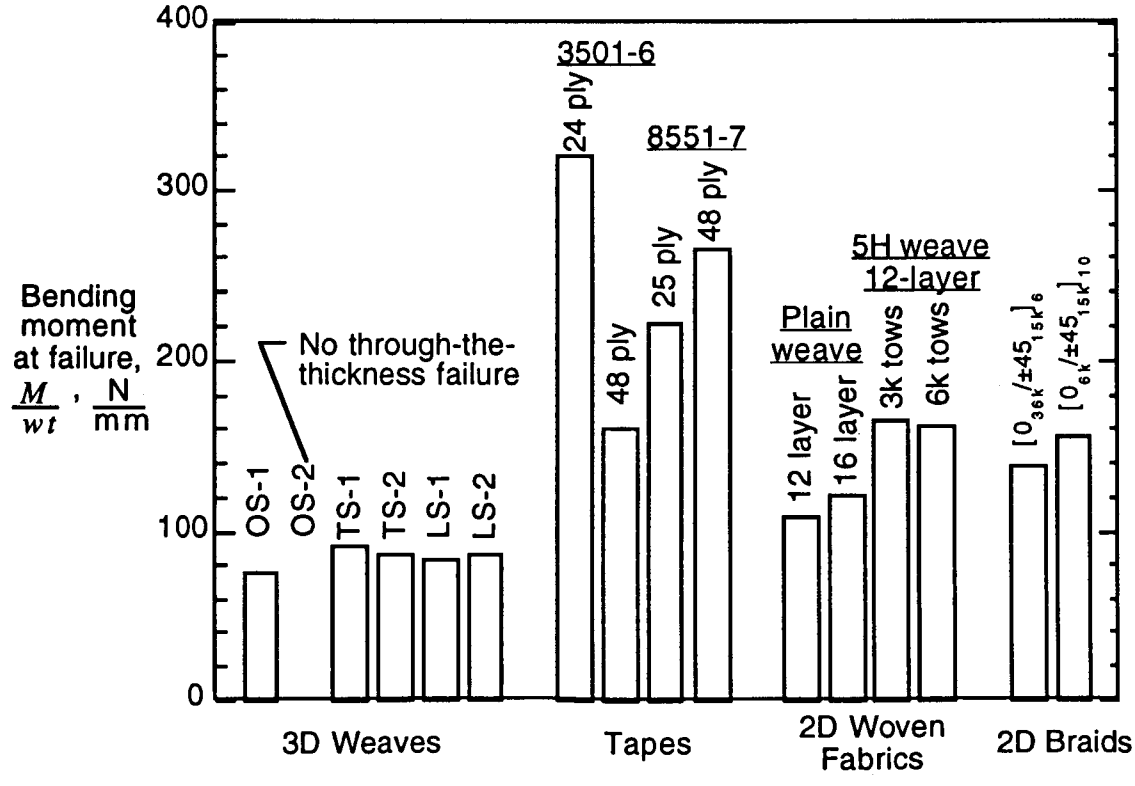

Figure 10. Average bending moment at failure

Specimens taken from the same panel were tested using both test methods to determine the effects on strength. A comparison of strengths measured using the two different test methods is shown in Fig. 11 for seven panels which represent all the 2D material types. The range of strengths, indicated by symbols, is also shown in the figure. For most of the materials, the average strengths were quite close considering the scatter in the data. Some differences may arise because of variations in specimen quality since specimens for each test method came from opposite sides of the same panel. Consequently, if the quality of the panel varied from side to side, a disparity in strengths would be exhibited between the two test methods. In the 16-layer plain weave panel, the two adjacent specimens that were tested using different test methods had identical strengths yet the overall averages differed by 24%. Also, less scatter was expected using the 4PB test since the specimens were self aligning while, in the HLM test, the hinges must be precisely positioned by hand. However, the scatter in the data was similar between the two methods.

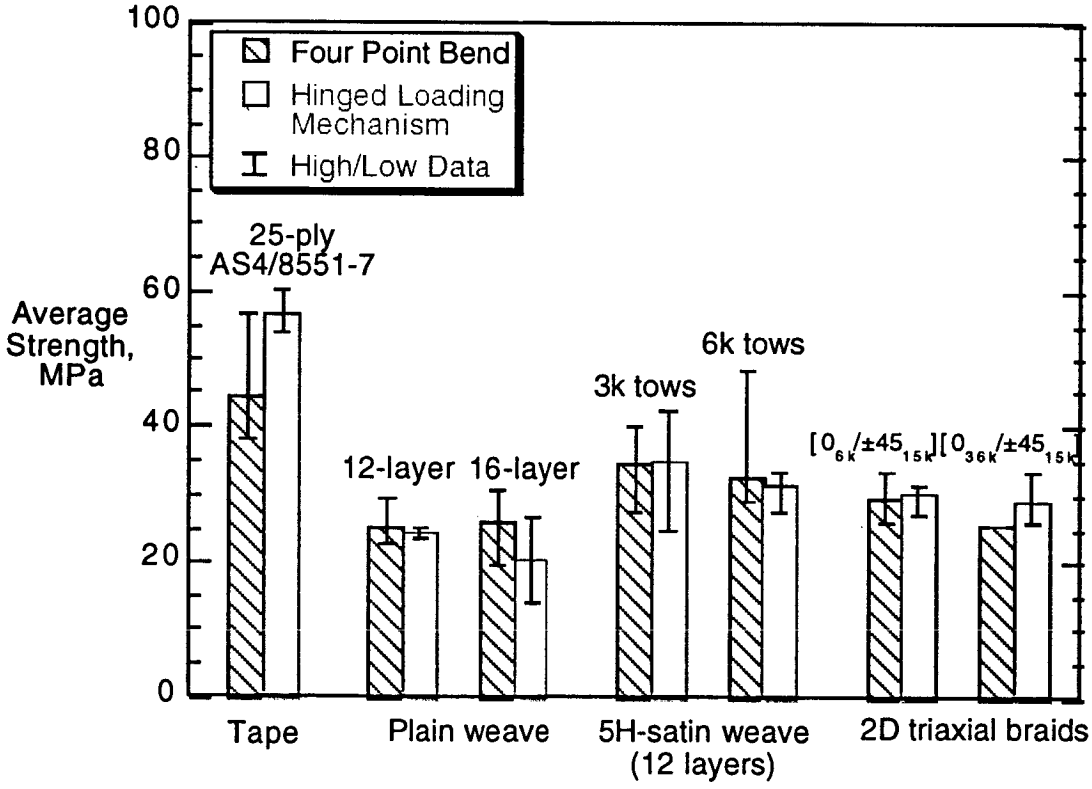

Figure 11. Comparison of strength data from the two test methods

Summary - Through-the-Thickness Strength

Curved beams made from a variety of 2D and 3D composites were tested to determine the through-the-thickness strength. A new test configuration that used a four-point-bending fixture was evaluated and compared to a configuration that used a hinged loading mechanism. Both test methods produced identical failures at nearly identical stresses. However, the four-point-bend test method was the preferred test method since it was self-aligning and did not require laborious positioning and clamping of hinges onto the specimen. In addition, the strength analysis was greatly simplified since a constant moment was produced in the test section.

Failures were significantly different between the 2D materials and the 3D weaves. The 2D materials delaminated between layers due to out-of-plane tensile stresses. At failure, the sublaminates formed by the initial delamination would often delaminate to form more sublaminates. The delaminations between braided layers followed a more tortuous path than the other 2D materials. Initial damage in the 3D weaves occurred very early in the loading and was made up of a series of radial cracks caused by the tensile circumferential stress along the inner radius. Final failure was caused by the formation of circumferential cracks around the test section similar to the 2D materials. Circumferential cracks did not form in the OS-2 weave, however. Due to the radial cracks, a through-the-thickness strength could not be calculated for the 3D weaves.

The strength of the 2D textile composites was lower than the tapes. The through-the-thickness strength was found to decrease significantly with decreasing fiber volume fractions. Final failure in the 3D weaves occurred at a lower bending moment than the other materials. The early failures were caused by the formation of radial cracks due to bending rather than a lower through-the-thickness strength.

Standard Impact Test Method Development

This investigation focused on the development of a standard impact test method to measure impact damage resistance. Existing impact test methods were first evaluated to determine their suitability. Since a suitable test was not found, a new test was developed to isolate damage resistance. Working through standards organization such as ASTM and Mil-Handbook 17, the new test method is being further developed and promoted for adoption. New research in this program is going to focus on the development of "rules" for damage tolerance testing.

Existing Impact Test Methods

The only impact tests that currently exist are compression after impact (CAI) tests which incorporate elements of both damage resistance and damage tolerance. The only results typically reported from CAI tests are compression strengths. Since the compression strength is a function of both damage resistance and damage tolerance, the user is unable to determine which properties were improved or not improved. An improvement in CAI strength could even be caused by an improvement in damage

resistance but a decrease in damage tolerance. In addition, all CAI test results are based on impacter kinetic energy. Consequently, the amount of damage is a function of target and impacter configuration (i.e., plate size, BC's, indenter diameter, etc.) [6]. Several CAI test methods are commonly used which all have different target and impacter configurations (Boeing, SACMA, and NASA). Consequently, results from one test method cannot be compared with results from a different method. In addition, since the results are configuration dependent, the results from coupon test cannot be easily scaled to plate of different sizes and boundary conditions. A typical impact test method is shown in Figure 12.

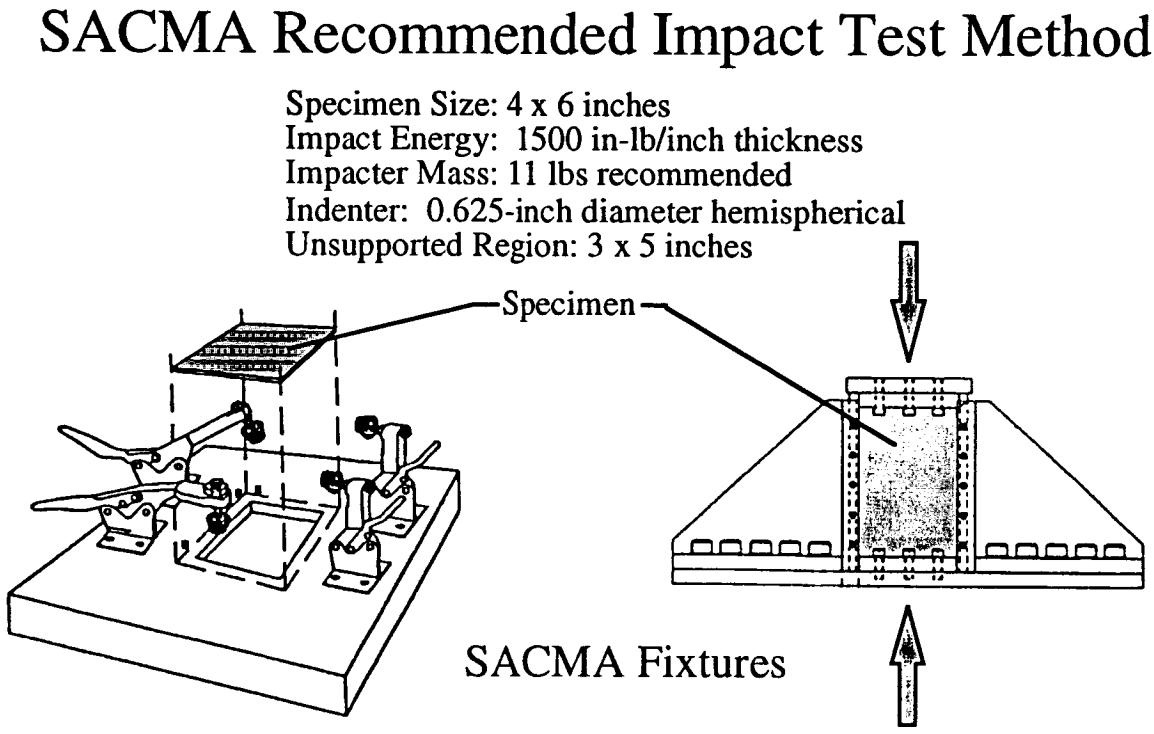

Figure 12. Typical CAI impact test

Impact tests can be performed with a large range of impacter mass and velocity combinations. Depending on these combinations, the impact specimen can respond in various manners. Commonly used impact methods are shown in Figure 13. A quasi-static indentation (QSI) test uses a universal test stand to slowly apply a transverse load. A falling weight impact test typically uses a large mass dropped from relatively low heights. The air gun impact test uses a small mass projectile fired down a barrel. It has been shown for many cases that a relatively small plate impacted by a large mass will deform in a quasi-static manner [6-8].

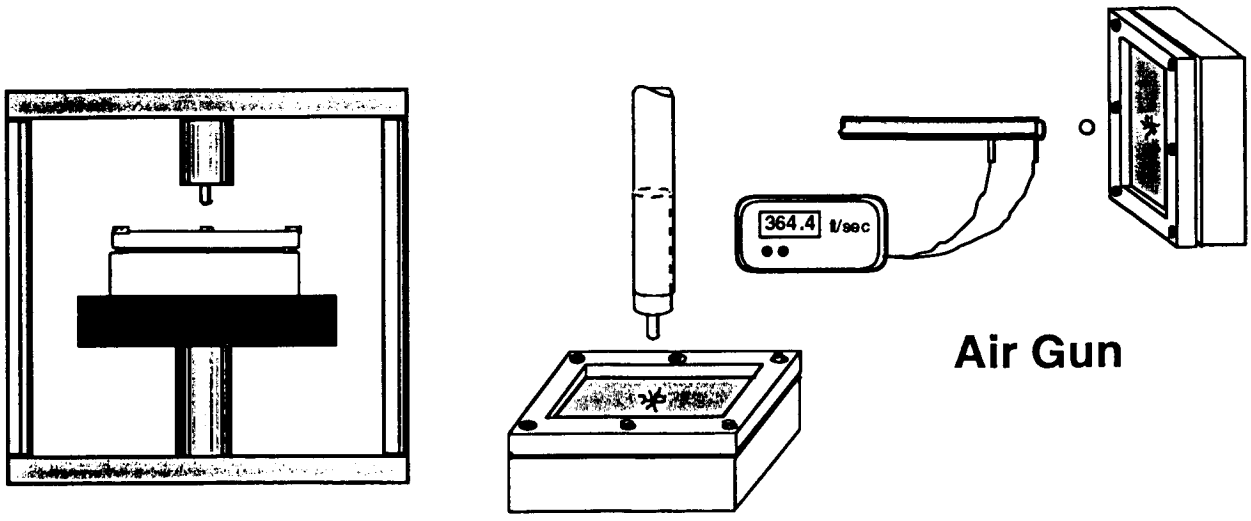

Figure 13. Impact methods

The quasi-static indentation (QSI) test was selected for development to measure damage resistance. This test method is the easiest of the three methods to use since it requires no special testing equipment. In addition, the force is applied very slowly under displacement control which allows for additional measurements during the test. Since a quasi-static deformation occurs, the test closely simulates the falling-weight impact test in many cases. By using impact force rather than impact energy, the damage is much less dependent on the impact configuration. Damage resistance is quantified in terms of the contact force to produce a unit of damage where the metric for damage may be damage diameter in C-scan, depth of residual dent, penetration, damage growth, etc. Some of these parameters (C-scan damage diameter and dent depth) are a function of the applied force. Consequently, the QSI tests must be done in increments if these parameters are to be monitored. A typical c-scan of impact damage in a 48-ply quasi-isotropic carbon/epoxy laminate is shown in Figure 14.

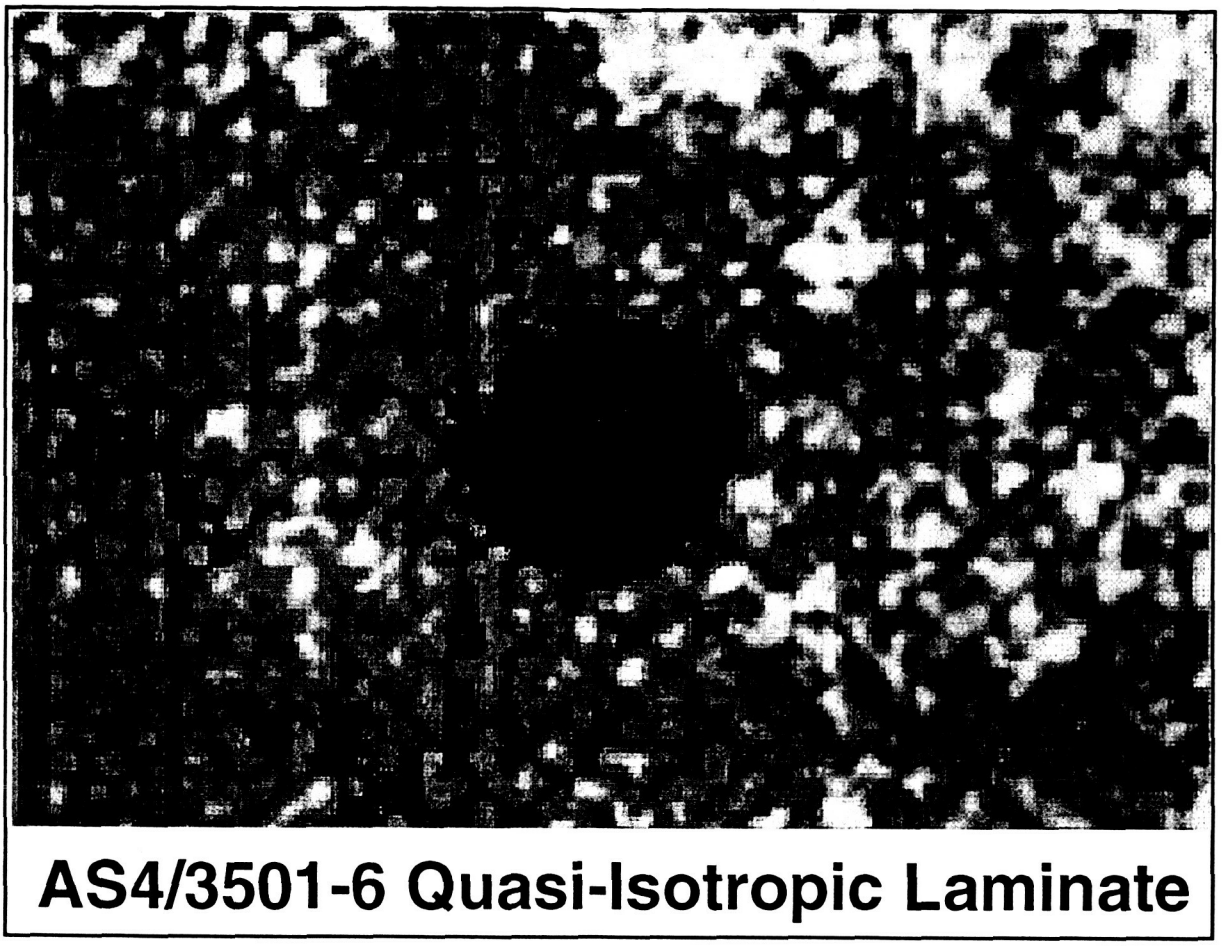

Figure 14. A typical c-scan of impact damage

A final draft of an impact standard that uses a QSI test method will be presented to the ASTM Impact Task Group (D30.02.06) at the May 1995 meeting. In this document, the impact test will be run quasi-statically under displacement control. A 6.0-inch-square specimen will be simply supported on a 5-inch-diameter ring. Many post-impact compression tests use a 4.0- x 6.0-inch square specimen. By using a 6.0-inch-square specimen, the edges can be trimmed to perform this damage tolerance test in an existing fixture. A 32-ply quasi-isotropic laminate has been specified for the impact specimen. The specimen will be indented using a 0.5-inch-hemispherical steel indenter. The force where damage first affects the force-displacement behavior (termed "F_1"), dent depth, and maximum force are specified to be recorded. The delamination size could not be included in this standard since ASTM does not currently have an NDE standard.

Quasi-Static Indentation Tests on Textile Composite

To improve the weight saving benefits of carbon/epoxy materials, there is a need to improve the damage tolerance and delamination resistance of these materials. Composites made from textile materials may significantly improve these properties. In this investigation, the impact damage resistance behavior of a variety of textile materials was studied using the quasi-static indentation (QSI) test method. The force where large damage initiates was measured and the delamination size as a function of force was determined. The delamination diameter - impact force relationship was quantified using a damage resistance parameter, Q*, which related delamination diameter to impact force over a range of delamination sizes.

Test Procedure

The QSI tests were performed in a servo-hydraulic load frame under stroke control at a ramp rate of 0.02 in/min. All specimens were clamped firmly in an aluminum test fixture during testing. An instrumented tup attached to a 0.5-in-diameter hemispherical indenter was used to measure load. The tup was mounted in the grips of the load frame such that the indenter traveled normal relative to the face of the specimen. The indentation load and stroke output were recorded at a rate of one data point per second throughout the loading history using a digital data storage oscilloscope. The relevant damage and test parameters were measured and recorded after each test. Many of the test coupons were indented more than one time. Initially, each specimen was loaded to a pre-determined force and then unloaded. The damage and test parameters were then measured and recorded. After this initial series of measurements was taken, the specimen was then reloaded to a higher force and the series of measurements was repeated. This process was repeated at approximately 2.22 kN (500 lbf) increments until the delaminations had grown close to the edge of the test fixture.

Materials

As in the through-the-thickness strength testing, a variety of textile and prepreg tape materials were used in this investigation. The same 2D triaxial braids (four different braid geometries), 3D interlock weaves (three architectures), and prepreg tape materials (AS4/3501-6 and AS4/8551-7) were used as in the previous investigation. Tape equivalents of the $[0_{6k}/\pm45_{15k}]$ triaxial braid and the TS-2 through-the-thickness angle interlock weave were also made from AS4/3501-6 for comparison purposes.

In addition to these materials, stitched and nonstitched uniwoven composite materials were evaluated. Stitched laminates were not used in the through-the-thickness testing since tightly curved stitched panels could not be manufactured. Four laminate thicknesses were manufactured with quasi-isotropic lay-ups of $[45°/0°/-45/90°]_{nx}$ where n = 2, 3, 4, and 6. These laminates were made from layers of dry uniweave carbon fabric which consisted of 97% Hercules AS4 carbon fibers and 3% fiberglass fill yarn by weight. The fill yarns were 225-denier fiberglass and were

woven normal to the carbon tows to hold the fibers together while stitching. The preforms for the stitched laminates were lock stitched at 8 penetrations per inch with a 1250 yd/lb fiberglass yarn. All stitching was in the 0° direction with 1/8-inch row spacing. The preforms were impregnated with Hercules 3501-6 epoxy by Douglas Aircraft Company using the resin transfer molding (RTM) process. After manufacture, all laminates were ultrasonically c-scanned to ensure that the panels were of high quality and free from manufacturing defects.

Initial Delamination Growth

To gain a better understanding of the impact damage mechanics, particular damage events were related to the impact force where the event occurred. The force (F_1) where large damage initiates is one measure of impact damage resistance. This force was defined as the force at which the contact force versus indenter displacement curve changes because of damage formation or growth. At this force, a sharp load drop often occurs which is associated with unstable delamination growth. This unstable delamination growth typically causes a sudden loss of transverse stiffness and an audible "pop." The unstable delamination growth was used because of its ease of identification. Some matrix cracks and small delaminations may form just prior to the F_1 force. A comparison of F_1 forces for all of the materials was made.

Stitched and Nonstitched Uniweaves

Each of these coupons was 4.00-in. square and contained in a fixture with a 3.00-in. square opening. The force - indenter displacement is shown for 16-ply stitched and nonstitched uniweaves in Figure 15. The stitched laminates could not be compacted to the same thickness as the nonstitched laminates. Consequently, the stitched laminates were slightly stiffer because of this increased thickness. The value of F_1 was approximately 10% higher in the stitched laminates than in the nonstitched. This slightly larger value of F_1 was attributed to the greater thickness of the stitched panels. For these thin specimens, a sharp load drop did not occur at F_1.

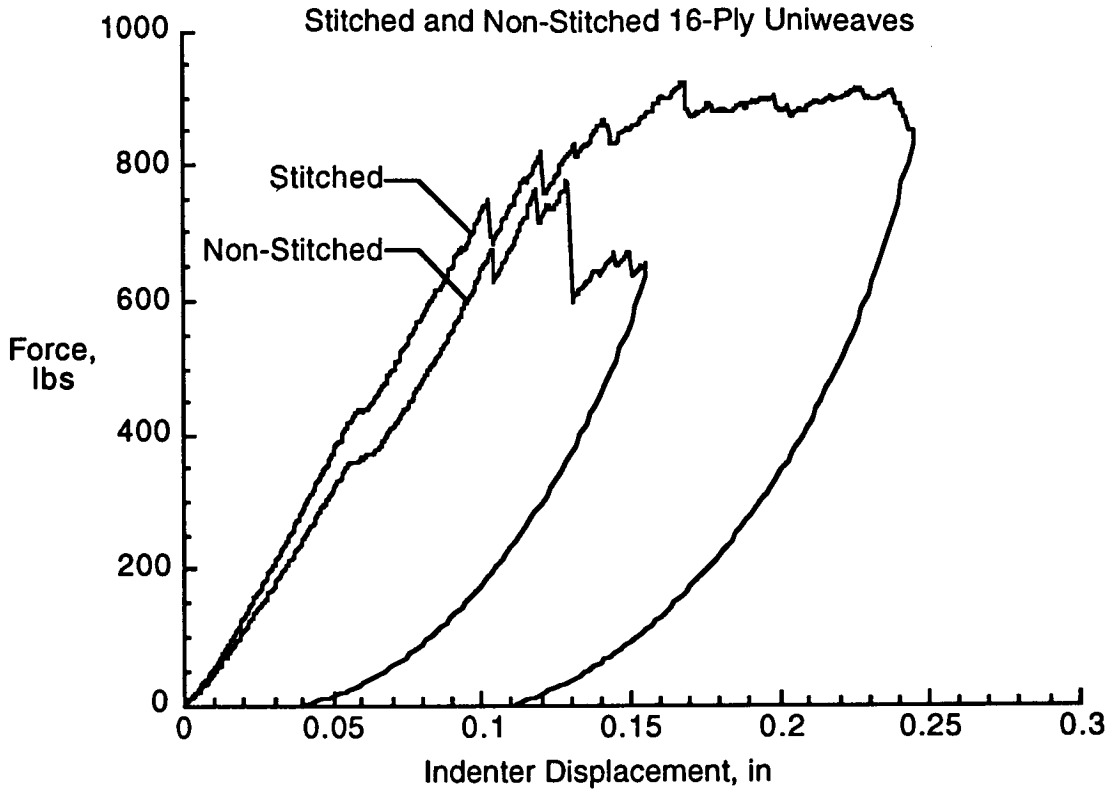

Figure 15. Quasi-static indentation of 16-ply stitched and non-stitched uniweaves

A similar plot of the force - indenter displacement is shown in Figure 16 for the 48-ply stitched and non-stitched laminates. Both of these laminates have similar transverse stiffnesses. The value of F_1 is approximately 20% lower for the stitched case. The nonstitched laminate has a sharp load drop at F_1 associated with unstable delamination growth. Stitching, however, appears to prevent this initial unstable delamination growth.

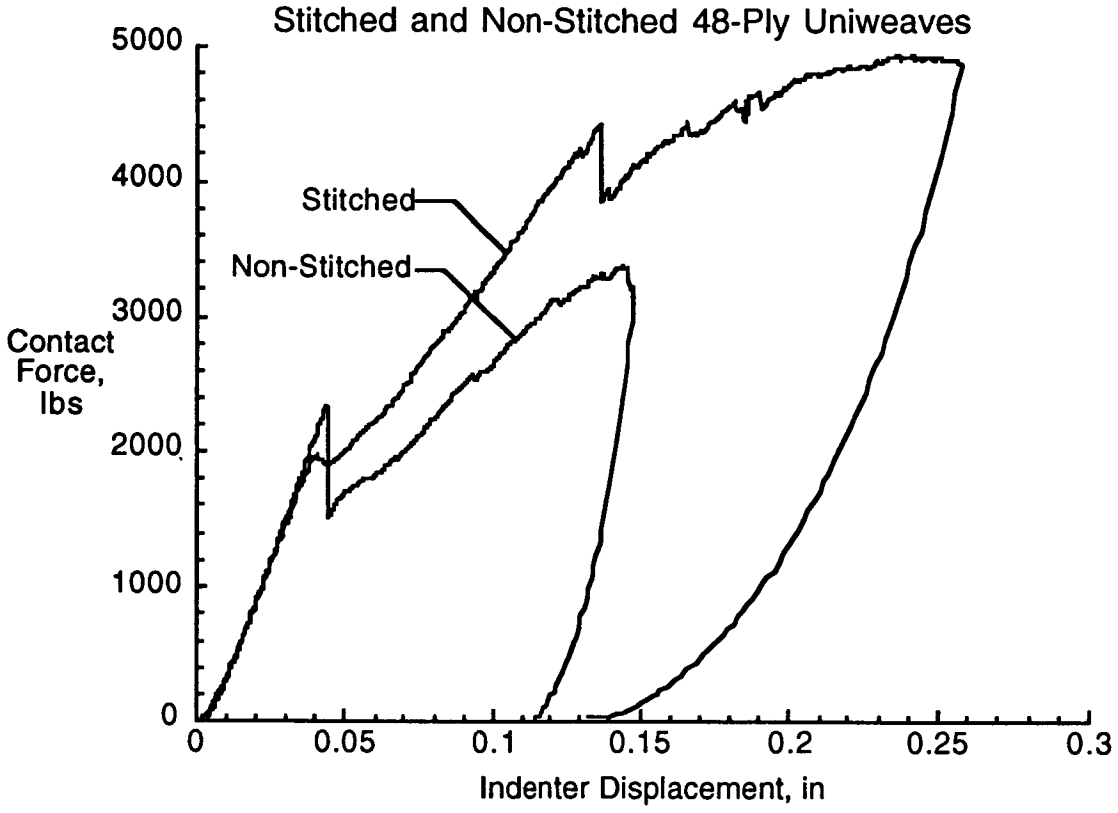

Figure 16. Quasi-static indentation of 48-ply stitched and non-stitched uniweaves

A summary of the average values of F_1 for the four different thicknesses of stitched and nonstitched laminates is shown in Figure 17. The initiation force decreased with decreasing plate thickness. For the 16-, 24-, and 32-ply laminates, stitching did not affect the value of F_1 by more than 10 %. However, for the 48-ply laminates, the value of F_1 was approximately 17% lower for the stitched laminates.

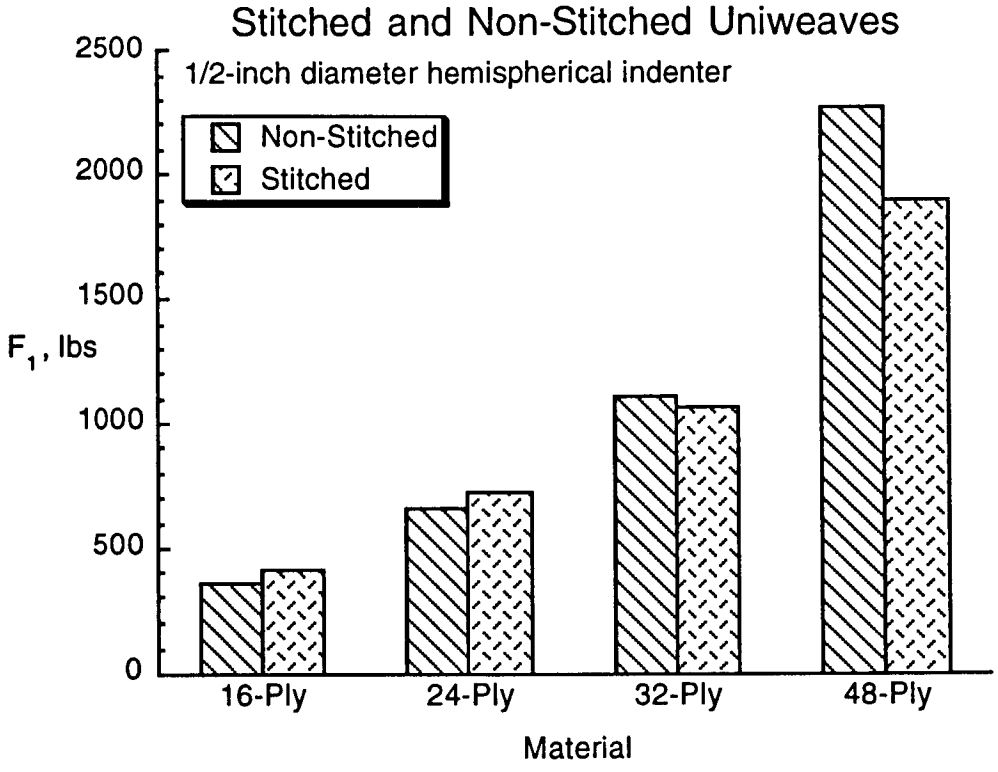

Figure 17. Average values of F_1 for stitched and non-stitched laminates

2D Triaxial Braids

Each of these coupons was 3.00-in. square and contained in a fixture with a 2.00-in. square opening. A smaller specimen had to be used due to a shortage of material. Previous studies have shown that the value of F_1 was independent of plate size. The force - indenter displacement is shown for three braids and a tape equivalent braid in Figure 18. The differences in stiffness between the different braids reflect the different fiber architectures which result in different flexural properties. All the braided panels were cured to the same thickness. The value of F_1 was easily identifiable since the layers of braided preform delaminate similarly to tape composites. However, there was no sharp drop in force when F_1 was reached. The tape equivalent laminate had a sharp load drop similar to the quasi-isotropic tape laminates.

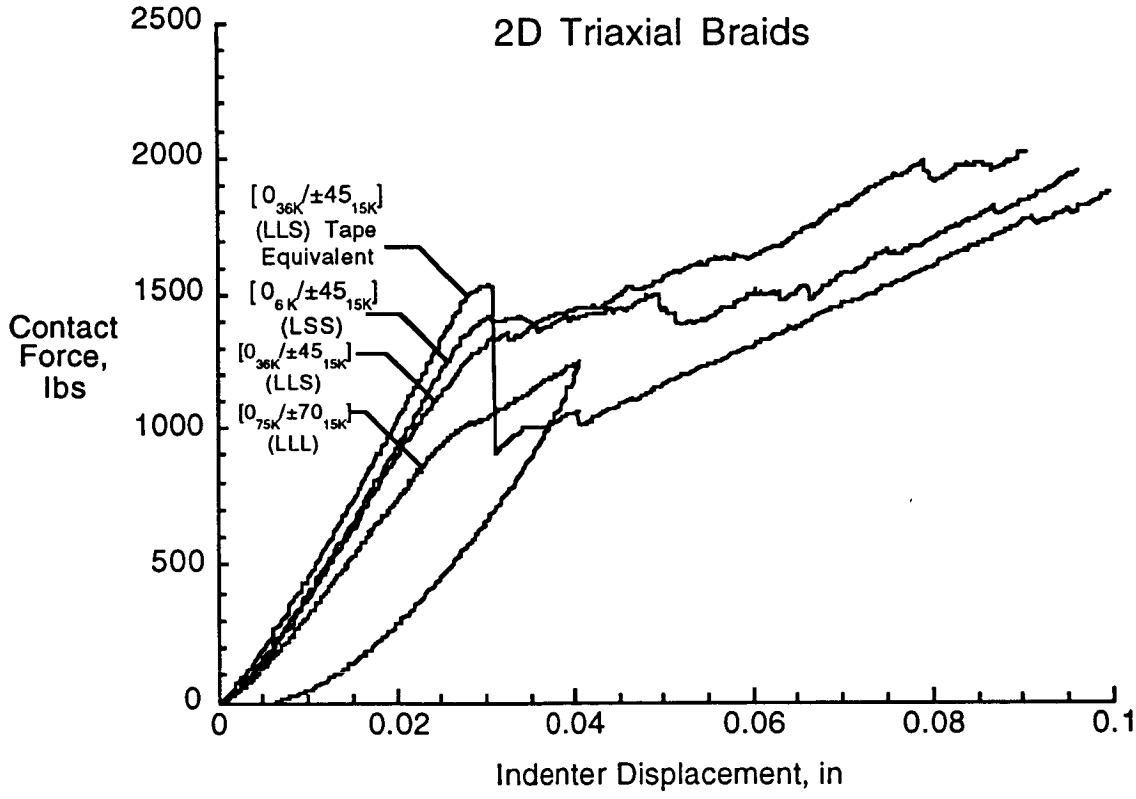

Figure 18. Quasi-static indentation of 2D triaxial braids.

A summary of the average values of F_1 for the 2D triaxial braids and a tape equivalent is shown in Figure 19. The [$0_{75K}/\pm70_{15K}$] (LLL) braid had a lower value of F_1 (lower by a minimum 17% in all cases) than the other three braids. This lower value may be caused by the large 75k fixed yarns. The tape equivalent laminates had an average F_1 that was more than 25% greater than the actual braid.

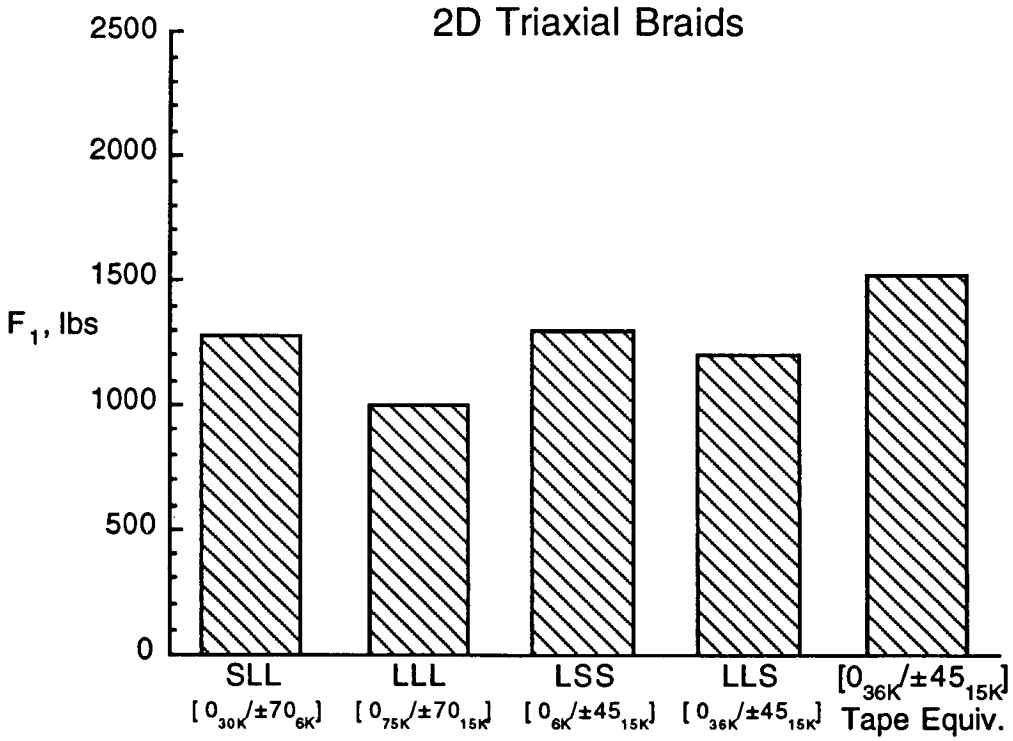

Figure 19. Average values of F_1 for 2D triaxial braids.

C-2.

3D Interlock Weaves

Again, small 3.00-in. square coupons contained in a fixture with a 2.00-in. square opening were used due to a shortage of material. The loading history is shown for three of the weaves and a tape equivalent weave in Figure 20. All woven panels were cured to the same thickness and, consequently, the differences in stiffness reflect the different textile architectures. The value of F_1 was not easily identifiable in several of the weaves. In the OS-2 weave, this point could not be identified at all since the material gradually lost stiffness. The OS-2 weave is also the only weave that did not delaminate in the through-the-thickness strength testing. Only the tape equivalent laminates showed a sharp drop in force when F_1 was reached.

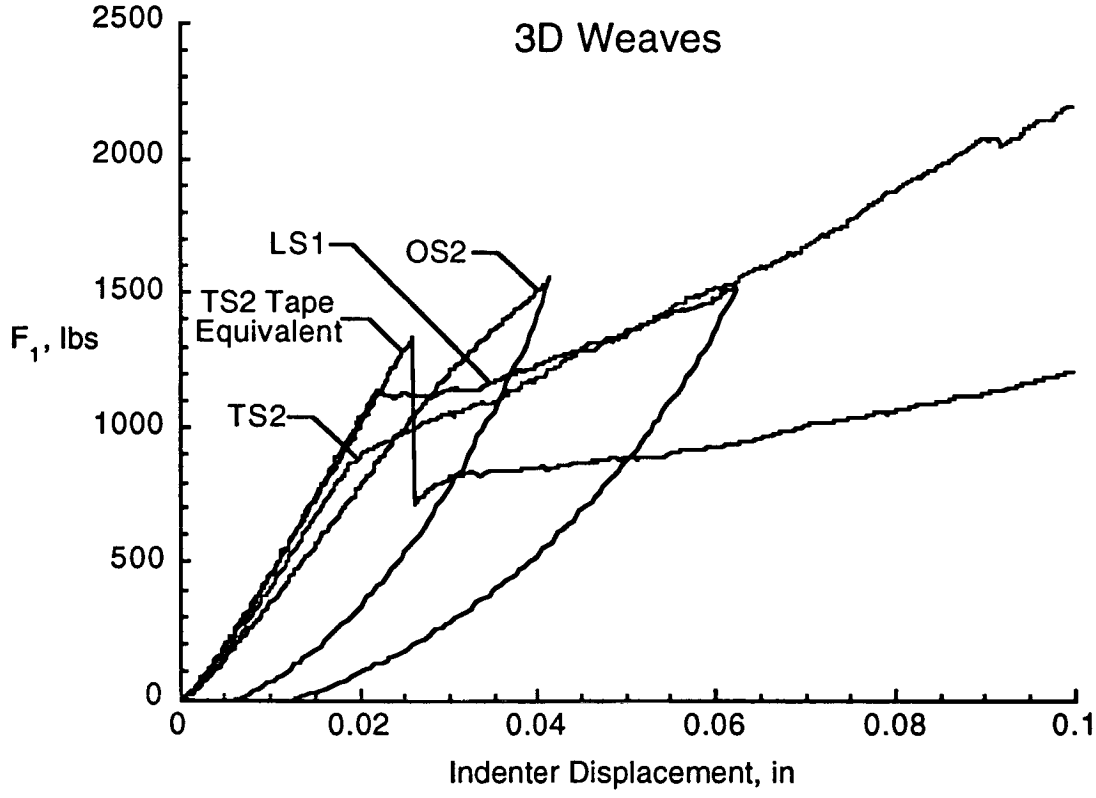

Figure 20. Quasi-static indentation of 3D weaves.

A summary of the average values of F_1 for the 3D weaves and a tape equivalent is shown in Figure 19. The LS and TS weaves have very similar values of F_1. The OS-1 weave has a slightly lower value of F_1 than the other weaves. Again, a distinct value of F_1 could not be identified for the OS-2 weaves. The TS-2 tape equivalent laminate had a 35% larger value of F_1 than the actual weave. The tow size did not affect the F_1 values for the LS and TS weaves. However, the smaller tows in the OS weave may have significantly reduced delaminations.

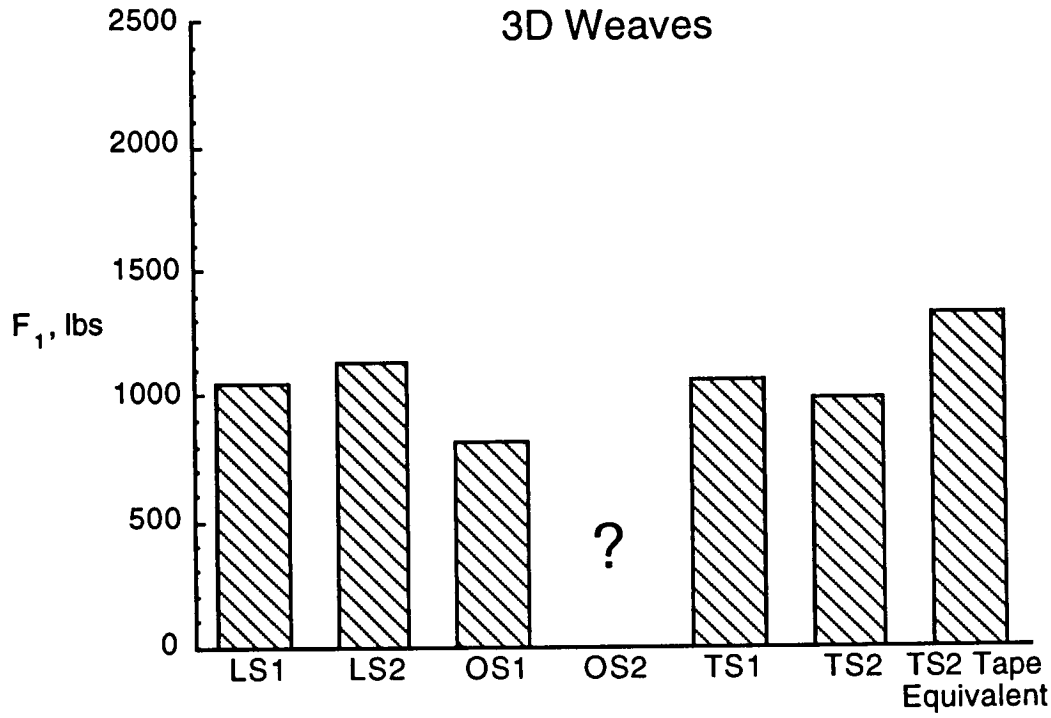

Figure 21. Average values of F_1 for 3D weaves.

An overall comparison of average F_1 values is shown in Figure 22 for all the different material systems. All of the comparison materials have a nominal thickness of 0.25 inches. In general, the tape materials performed significantly better than the weaves and the braids. The toughened tape (8551-7) had much higher values of F_1 than the non-toughened tape (3501-6). Stitching lowered the F_1 value relative to the nonstitched material. The tape equivalent laminates had lower values of F_1 than the quasi-isotropic tape laminates because multiple layers of tape were stacked on top of one another in the same orientation to simulate the thick layers of the braids and weaves.

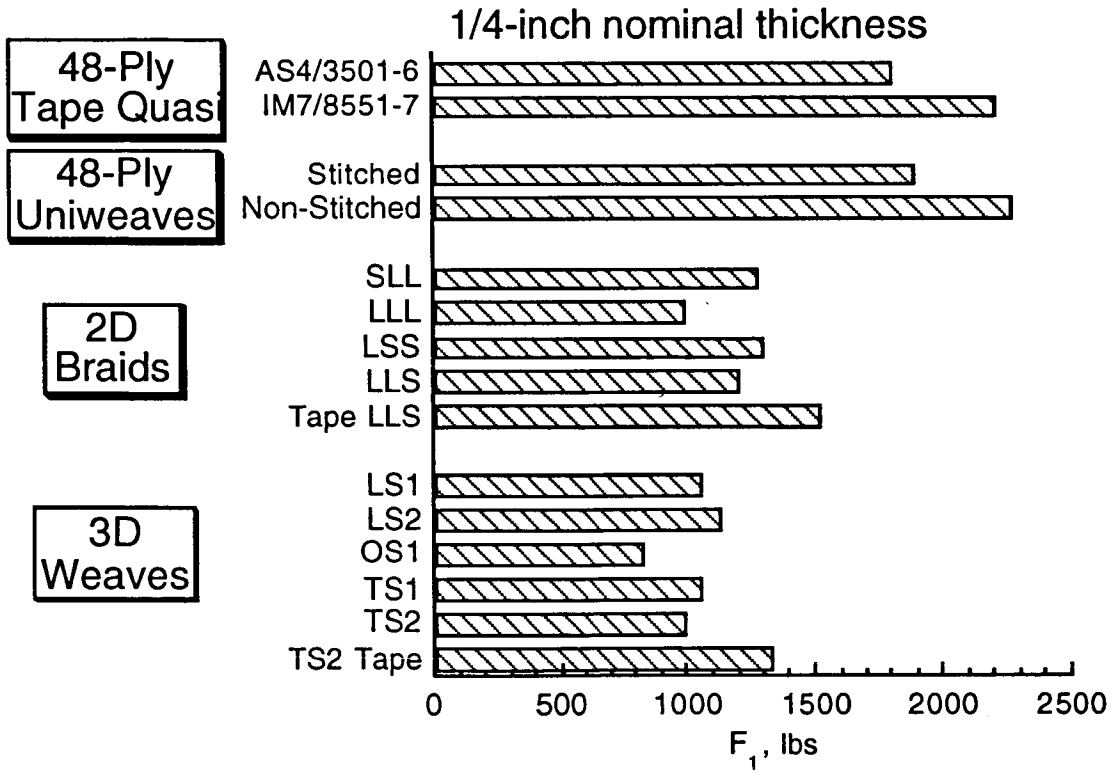

Figure 22. Overall comparison of average F_1 values for all material forms.

Q* Damage Resistance Parameter

One objective of this study was to measure the damage resistance of different material forms over a range of damage sizes. CAI tests are generally performed at a single impact energy representing a single damage size. To quantify damage resistance over a range of damage sizes, a new method was used that relates damage size to impact force. In this method [6], a single damage resistance parameter called "Q*" provides a means to quantitatively rank the damage resistance. The analysis used to develop Q* was based on experimental observations involving impacts of quasi-isotropic plates. The Q* parameter represents the average transverse shear force per unit length associated with the edge of the delamination (Fig. 23). This parameter was observed to be constant between initial delamination growth and indenter penetration for quasi-isotropic laminated composites. By making Q* calculations, each materials ability to resist damage development or growth can be assessed.

To calculate Q*, the relationship between impact force and maximum delamination diameter, d_o, was determined . Q* is then calculated from the slope of the force - delamination diameter line between delamination initiation and indenter penetration (Fig. 23). The extent of the delamination was determined ultrasonically using c-scans. A c-scan provides a projection of all the various regions of delamination. The delamination area was calculated using image analysis and converted to diameter assuming a circular delamination area.

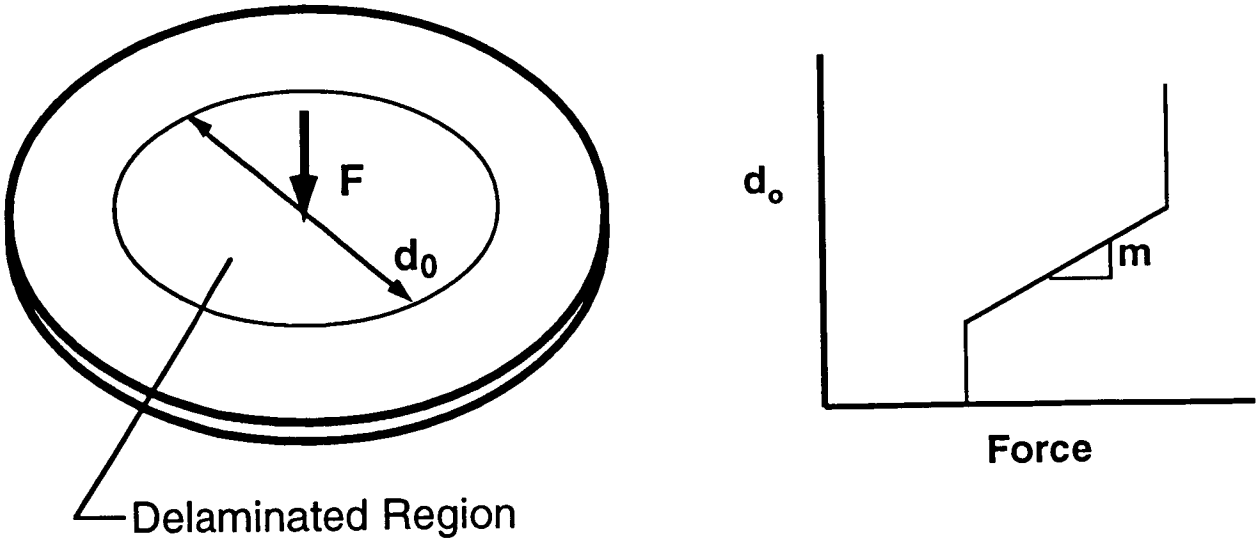

From equilibrium:

$$Q_r^* = \frac{F}{\pi d_0}$$

$$Q_r^* = \frac{1}{\pi m}$$

Figure 23. Calculation of the Q* damage resistance parameter.

An example of an impact force - delamination diameter plot is shown in Figure 24 for a 48-ply AS4/3501-6 quasi-isotropic laminate. A Q* of 75.0 kN/m was calculated from the slope of the line. There were no significant effects on the delamination diameter between running single tests per specimen versus multiple tests per specimen.

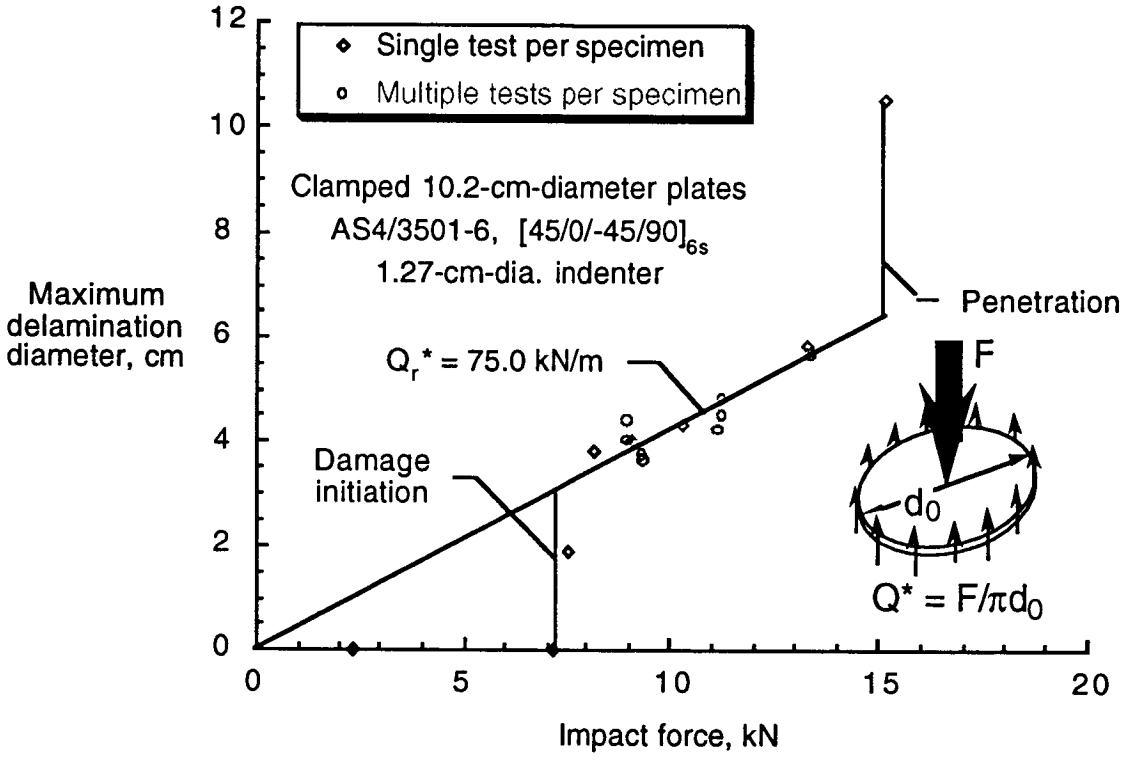

Figure 24. Delamination diameter as a function of impact force for AS4/3501-6.

The results of the Q* calculations for the stitched and nonstitched uniweaves are shown in Figure 25. Stitching increased the damage resistance as measured by Q* in all cases. The value of Q* increased with increasing plate thickness. For each material thickness, the improvement in Q* due to stitching also increased with plate thickness. The 48-ply plates showed the greatest improvements with a 90% increase in the Q* value while the 16-ply materials showed only a 23% increase.

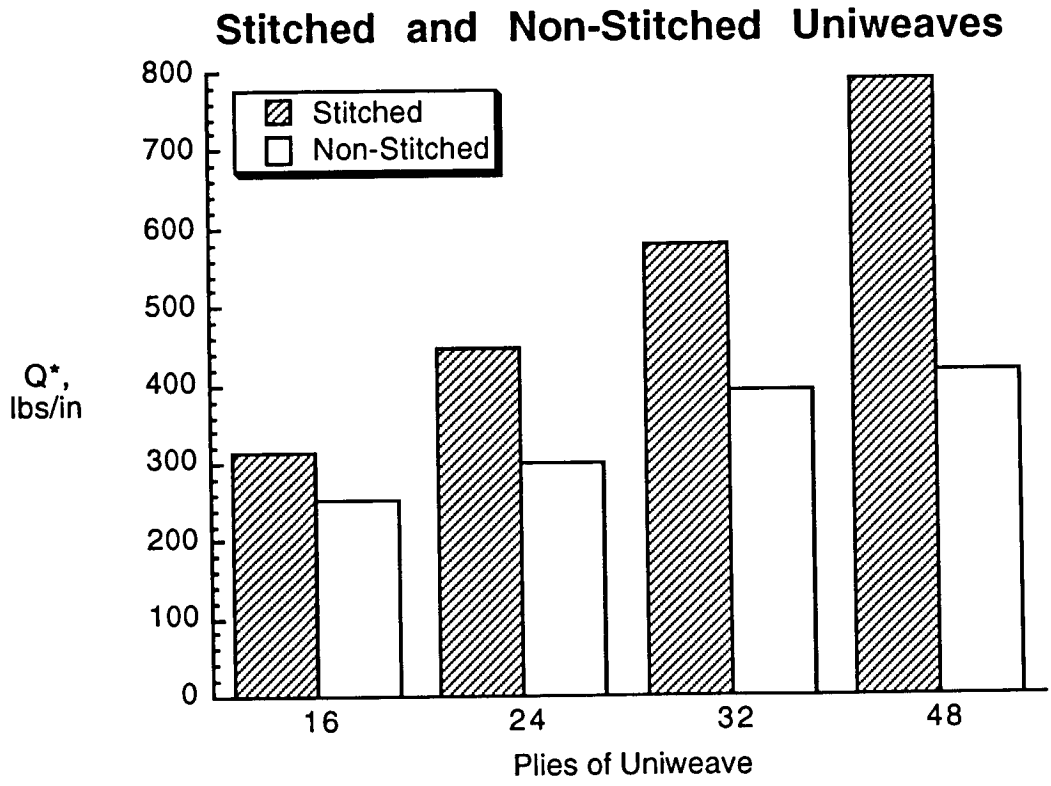

Figure 25. Comparison of Q* for stitched and nonstitched uniweaves.

In Figure 26, the results of the Q* calculations for the 2D triaxial braids are shown. All the braids except the LLL braid have Q* values within 1% of one another. The Q* value of the LLL was approximately 25% lower than the other braids. The nesting of the braided layers may have increased the damage resistance since the LLS tape equivalent laminate had a 22% lower value of Q* than the actual LLS braid.

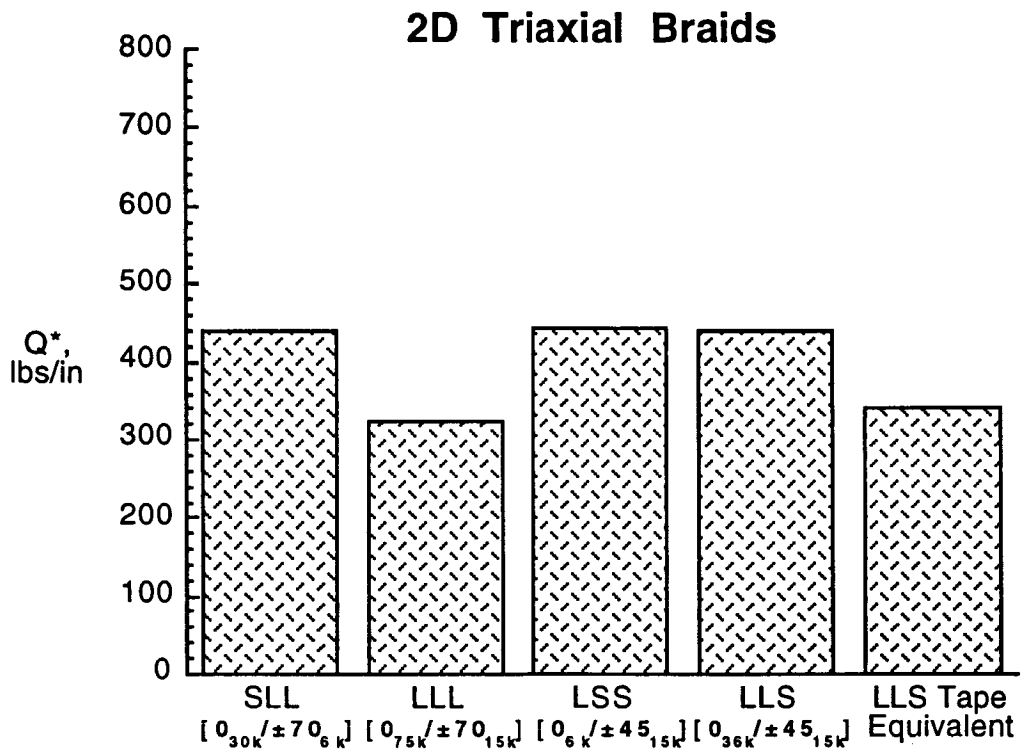

Figure 26. Comparison of Q* for 2D triaxial braids.

In Figure 27, the results of the Q* calculations for the 3D weaves and a tap equivalent weave are shown. In the LS and TS weaves, there was no significant effe on Q* as a result of using the smaller tows. However, in the OS weave, Q* increase by more than a factor of two as a result of using the smaller tows. The OS-1 weav (larger tows) had Q* values comparable to the other weaves. The LS weave ha approximately 25% lower values of Q* than the TS weave. The TS2 tape equivale laminate performed worse than the TS2 weave by about 50% showing that th through-the-thickness reinforcement was effective relative to a non-reinforce laminate.

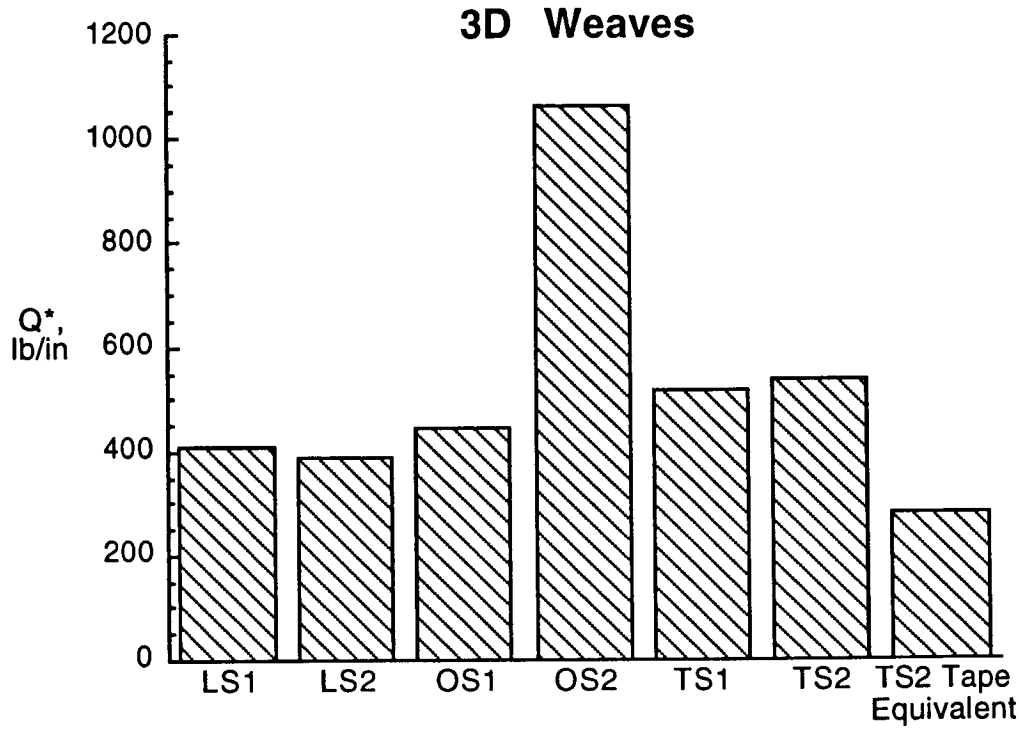

Figure 27. Comparison of Q* for 3D weaves.

An overall comparison is made in Figure 28 for all the 1/4-inch nominal thickness materials. The best performing materials were the toughened tape (IM7/8551-7), the stitched uniweave, and the OS-2 through-the-thickness orthogonal interlock weave. The delamination resistance of the braids (excluding the LLL braid) and the weaves (excluding the OS2 weave) was very similar to the quasi-isotropic tape (AS4/3501-6) and nonstitched uniweave laminates. The tape equivalent laminates and the LLL braid were the least resistant to delamination.

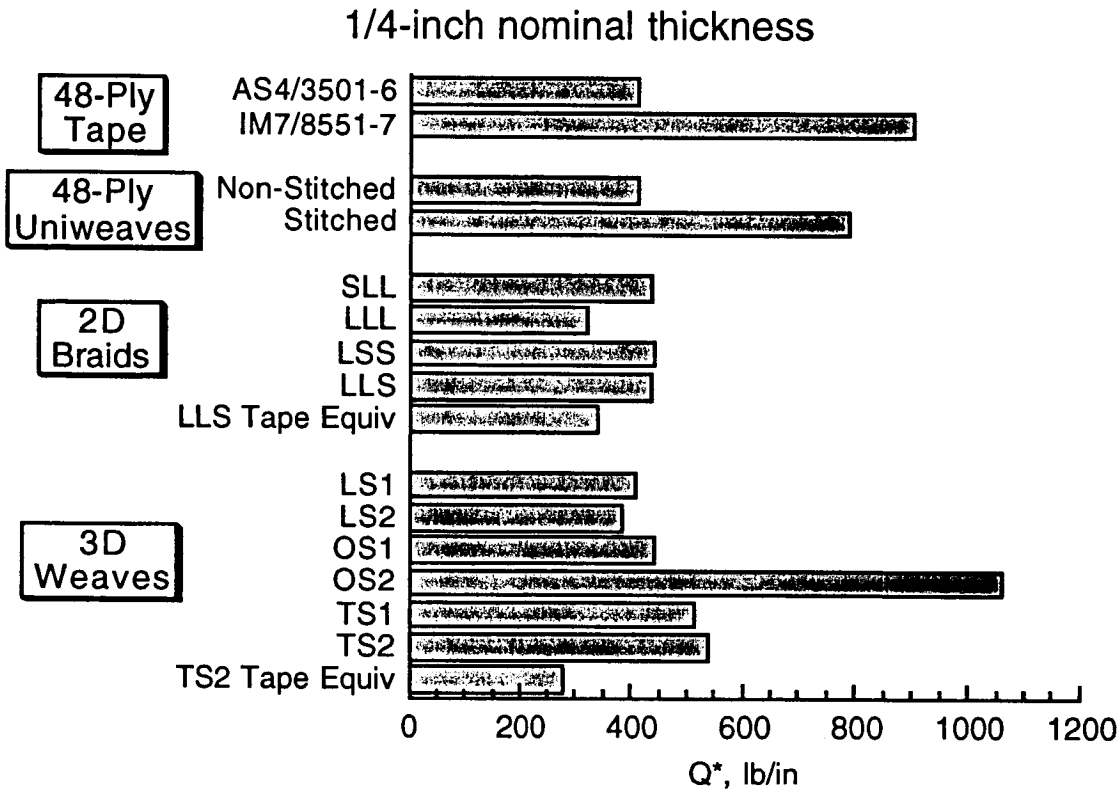

Figure 28. Overall comparison of Q* for all materials.

Summary - Quasi-Static Indentation Tests on Textile Composite

In braided and woven textile composites, the force to initiate delaminations (F_1) was significantly lower than in the tape or uniweave materials. The lower initiation forces may be due to the thicker layers used in these materials. Similarly, the tape equivalent laminates which had plies of the same direction grouped together also had lower values of F_1 relative to the 48-ply quasi-isotropic materials. Likewise, the LLL braid which had large 75k axial yarns had the lowest values of F_1. The equivalent laminates, however, had a higher value of F_1 than the textile which may indicate that fiber waviness also plays a roll in the low values of F_1. Except in the 48-ply laminates, stitching did not significantly affect the value of F_1. The damage resistance of these

materials, however, was significantly improved by stitching (smaller damage size for a given force). In general, the thicker plates showed the greatest improvements in damage resistance (Q*) due to stitching.

The OS-2 weave was the only material where a distinct value of F_1 could not be determined. This material also had the best performance in terms of Q* of all the materials tested. Moreover, through-the-thickness strength testing failed to produce a delamination in this material. Using this Q* parameter to rate the materials, the stitched uniweaves, toughened epoxy tapes, and OS-2 through-the-thickness orthogonal interlock weave were the most damage resistant.

References

[1] Jackson, W. C. and Martin, R. H., "An interlaminar Tensile Strength Specimen," Composite Materials: Testing and Design (Eleventh Volume), ASTM STP 1206, E. T. Camponeschi, Jr., Ed., American Society for Testing and Materials, Philadelphia, December 1993, pp. 333-354.

[2] Jackson, W. C. and Ifju, P. G. "Through-the-Thickness Tensile Strength of Textile Composites," *Composite Materials: Testing and Design (Twelfth Volume), ASTM STP,* C. R. Saff and R. B. Deo, Eds., American Society for Testing and Materials, Philadelphia. (submitted for publication)

[3] Falcone, A., Dursch, H, Nelson, and Avery, W., "Resin Transfer Molding of Textile Composites," NASA CR 191505, July 1993.

[4] Lekhnitskii, S.G., "Anisotropic Plates," Gordon and Breach Science Publishers, New York, 1968, pp. 95-101.

[5] Ifju, P. G.; Masters J. E.; and Jackson W. C. "Using Moire Interferometry to Aid in Standard Test Method Development for Textile Composite Materials," submitted for publication to Journal of Composites Science and Technology.

[6] Jackson, W. C. and Poe, C. C. Jr., "The Use of Impact Force as a Scale Parameter for the Impact Response of Composite Laminates," *Journal of Composites Technology & Research*, Vol. 15, No. 4, Winter 1993, pp. 282-289.

[7] Sjöblom, Peter: Simple Design Approach Against Low-Velocity Impact Damage. 32nd International SAMPE Symposium, April 6-9, 1987, pp. 529-539.

[8] Elber, W.: Failure Mechanics in Low-Velocity Impacts on Thin Composite Plates. NASA TP 2152, May 1983.

Effects of Preform Architecture on Modulus and Strength of 2-D Triaxially Braided Textile Composites

John E. Masters
Lockheed Engineering and Science

Rajiv A Naik
Analytical Services and Materials, Inc.

Pierre J. Minguet
Boeing Defense & Space
Helicopters Division

The following pages contain annotated copies of the figures presented at the Mechanics of Textile Composites Symposium held in December 1994 at NASA Langley Research Center. The figure presented at the meeting will be reproduced at the top of each page; comments on important points in the figure will be added at the bottom.

Outline of Presentation :

- Introduction
  - Objective
  - Materials
- Experimental Results
- Analytical Results
- Summary

Figure 1. Outline of Presentation.

Laminates formed using braided fibrous preforms have been extensively investigated during the course of the past few years as alternatives to unidirectional prepreg tape systems. This paper focused on one aspect of that work. It defined the role of the fibrous preform architecture in controlling a laminate's mechanical properties. The presentation was divided into four sections as the outline listed above illustrates. The presentation began with a brief introduction which defined the objectives of the study and detailed the materials studied. This was followed by a review of empirical test results. The materials' moduli and strengths were measured in both tension and compression. Their shear moduli were also experimentally determined. The review of the empirical data comprised the bulk of the presentation. A comparison of the experimental data to results predicted analytically was then presented. The presentation concluded with a few summary remarks.

TRIAXIAL BRAID PATTERN: DESCRIPTION OF MATERIAL TESTED

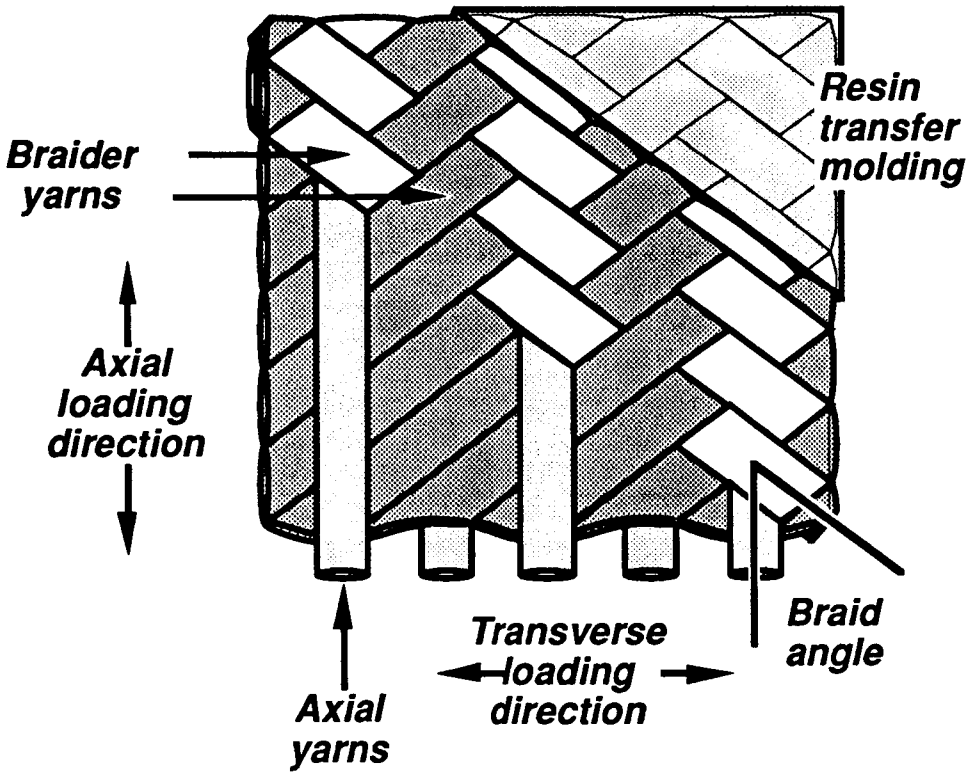

Figure 2. Triaxial Braid Pattern.

The specimens studied in this investigation featured 2-D triaxially braided AS4 graphite fiber preforms impregnated with Shell 1895 epoxy resin. In a triaxially braided preform three yarns are intertwined to form a single layer of 0°/ ± Θ° material. In this case, the braided yarns are intertwined in a 2 x 2 pattern. Each + Θ yarn crosses alternatively over and under two - Θ yarns and vice verse. The 0° yarns were inserted between the braided yarns. This yields a two dimensional material. The figure above schematically illustrates the fiber architecture and establishes the nomenclature used in the paper.

The yarns were braided over a cylindrical mandrel. The desired preform thickness was achieved by overbraiding layers; there are no through-the-thickness fibers. After braiding, the preforms were removed from the mandrel, slit along the 0° fiber direction, flattened, and border stitched to minimize fiber shifting. The resin was introduced via a resin transfer molding process.

Objective :

Measure the Effects of
Primary and Secondary Braid
Parameters on Laminate Response

Figure 3. Objective of Study.

Simply stated, the objective of this work was to define the role of the fibrous preform architecture in controlling laminate response. The results reviewed in this paper, as indicated above, measure the effects of a variety of primary and secondary braid parameters on laminate mechanical properties. The properties examined in this paper include the materials' Young's moduli and strength in both the longitudinal and the transverse directions and their shear moduli. The longitudinal and transverse properties were measured in both tension and compression.

BRAIDING PARAMETERS INVESTIGATED

Primary Braid Parameters :

Yarn Size

Braid Angle

Axial Yarn Content

Secondary Braid Parameters :

Axial Yarn Spacing

Braid Yarn Crimp Angle

0° Yarn Crimp Angle

Figure 4. Braiding Parameters Investigated.

An examination of the schematic of the preform architecture shown in an earlier figure suggests four parameters that can be altered to change the preform's properties. They are the axial yarn size, the braider yarn size, the braid angle, and the axial yarn spacing. Several braids were designed to isolate the effect of these individual parameters. The objective was to directly measure their effect on the materials' elastic properties and strength.

As the table above indicates, the parameters were divided into primary and secondary categories. The primary parameters were expected to have the greatest effect on the material. Based on experience with laminate prepreg tape composites, they are the parameters that would be considered first when a material is being designed for a particular application.

The three primary preform parameters listed are braid angle, yarn size, and 0° yarn content. As defined in an earlier figure, the braid angle is the angle the braider yarns make with the axial yarns. Braid angles typically range from 15° to 75°. Yarn size is expressed in terms of the number of filaments per yarn. The AS4 fibers used in these materials have a nominal diameter of 7 microns. The last parameter listed, axial yarn content, is typically expressed as a percentage of 0° yarns. It is the volumetric proportion of longitudinal yarns to total yarn content and is a function of braid angle and yarn size. Although it is not an independent parameter, the axial yarn content is typically defined for each preform because it provides valuable insight into the material response.

The table also lists three parameters as secondary braid parameters. The first two, axial yarn spacing and braider yarn crimp angle, are controlled by the specifics of the braiding machinery used. Axial yarn spacing is a function of the mandrel diameter and the number of yarn carriers used to make the braid. The braider yarn crimp angle in the angle that the braider yarns make out-of-the-plane of the preform as they pass over and under other braider and axial yarns. The braider yarn crimp angle is a function of the axial yarn size and spacing. The third parameter listed as a secondary braid parameter, 0° yarn crimp, may be thought of as a material defect. In theory, the axial yarns are not crimped when they are inserted between the braider yarns.

TEST METHODS AND PROCEDURES

Primary Braid Parameters. These test results were obtained as a part of a program to develop standard test methods for textile composites [1]. The program evaluated a number of straight-sided tensile test specimen geometries and concluded that width and length effects were minimal. The axial tension data presented in this paper are the average of the eighteen values in that study. Specimen widths ranged from 25.4 mm (1.0 in) to 63.5 mm (2.5 in) and their lengths ranged from 90 mm (3.5 in) to 220 mm (8.75 in). The specimens used to measure the braids' transverse tension properties measured 50.8 mm (2.0 in) by 180 mm (7.0 in). Three replicate test values were averaged to determine these data. All specimens featured 57 mm (2.25 in) long, 1.25 mm (0.05 in) thick beveled fiberglass tabs.

The tensile specimens were ramped to failure in displacement control at a loading rate of 1.25 mm/min (0.05 in/min). They were instrumented with 12.7 mm (0.500 in) square strain gages (Measurements Group Inc. gage EA-06-500AE-350) which were mounted in both the longitudinal and transverse directions. The specimens' moduli were calculated by performing a linear regression of stress versus axial strain. The axial strain range used in the calculation was 1000 to 3000 microstrain.

The compression data presented in this paper were obtained using a modified IITRI test specimen. Unbeveled fiberglass tabs were mounted to the straight-sided specimen. The baseline test section used was 6.35 mm (0.25 in) thick, 38 mm (1.5 in) wide, and 38 mm (1.5 in) long. Instead of using the special IITRI loading fixture, the specimen is gripped in the test machine with hydraulic grips. Special attention was taken in machining the tabs to insure that the tab surfaces are parallel. Strain gages were mounted on the front and back of the specimens to monitor specimen stability and to insure that bending did not occur.

Secondary Braid Parameters: Similar specimen geometries and test procedures were used to measure the tensile properties of these specimens. The longitudinal tension specimens were 40 mm

(1.5 in) wide and 255 mm (10.0 in) long in these tests. The transverse tension specimens measured 40 mm (1.5 in) by 175 mm (7.0 in). All specimens had 57 mm (2.25 in) long fiberglass tabs bonded to each end.

These tests were conducted in displacement control at a ramp rate of 0.254 mm/min (0.01 in/min). The longitudinal tension specimens used 12.7 mm (0.500 in) by 4.6 mm (0.180 in) wide strain gages (Measurements Group Inc. gage CEA-06-500UW-350) to measure both the axial and transverse strains. The transverse tension test specimens were instrumented with 2.54 mm (1.0 in) long gages (EA-13-10CBE-120) in the load direction; 12.7 mm (0.500 in) gages (CEA-06-500UW-350) were used to measure the specimens' Poisson's contraction. Moduli and Poisson's ratios were again computed via linear regression to the data gathered as the specimens were loaded from 1000 to 3000 microstrain.

Shear Testing: The Compact Shear Specimen developed by Ifju [2] was used to measure the shear moduli of all seven braids tested. This 40 mm (1.5 in) by 40 mm (1.5 in) square specimen features a 20 mm (0.750 in) test section. Strain gages (Measurements Group Inc. gage EA-06-500AE-350), developed specifically for these specimens, were mounted to the front and back of the specimens. The two strain measurements were averaged together and used to compute the shear moduli. Moduli were again computed over the 1000 to 3000 microstrain range.

Normalization: All the data presented in this paper were normalized to 60% fiber volume to facilitate comparison of results.

PROPOSED SHORTHAND NOTATION:

A shorthand notation, similar to the practice used to define the stacking sequence of laminates formed of uni-directional prepreg tape, was introduced to define the braid architecture. It is based on the nomenclature defined in the figure.

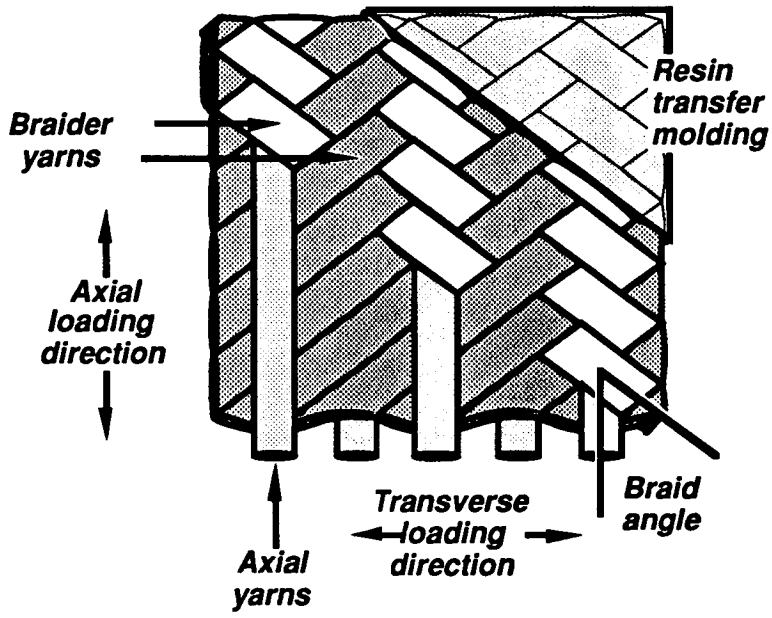

[0° xk / ± Θ° yk] N% Axial

where: Θ indicates the braid angle,

x indicates the number of fibers in the axial yarn bundles,

y indicates the number of fibers in the braided yarn bundles,

k indicates thousands, and

N indicates the percentage by volume of axial yarns in the preform

Figure 5. Proposed Shorthand Notation for 2-D Triaxial Braids.

Table I. Braids Developed For Primary Braid Parameter Study

Braid	Comparison
[0 30k / ± 70 6k] 46% Axial [0 75k / ± 70 15k] 46% Axial	<u>Yarn Size Effect:</u> Yarns Scaled by Factor of 2.5
[0 75k / ± 70 15k] 46% Axial [0 36k / ± 45 15k] 46% Axial	<u>Braid Angle Effect:</u> Angle Changed from 70° to 45° *Axial Yarns Differ by Factor of 2*
[0 36k / ± 45 15k] 46% Axial [0 6k / ± 45 15k] 12% Axial	<u>Axial Yarn Content:</u> Content Changed from 46% to 12% *Axial Yarns Differ by Factor of 6* *Braider Yarn Crimp Angle Changes (11° to 6.5°)*

COMMENTS ON THE BRAID ARCHITECTURES: PRIMARY BRAID PARAMETER STUDY

Four braid architectures were designed to isolate the effects of the primary braid parameters on the laminate response. They are listed in Table I in the shorthand notation defined earlier.

The most straightforward way to analyze the data to be presented is to consider the four braids as three sets of pairs. The table groups the braids in this manner and compares their preforms. It lists the primary braid parameter to be considered when the data are compared. The first two architectures listed, for example, were designed to define the effects of yarn size on mechanical properties. In this case, both the axial and braider yarns have been scaled by a factor of 2.5; the braid angle and the axial yarn content were held constant. Unfortunately, it was not possible to vary only a single braid architecture parameter in the other two pairs of laminates. The comparisons given for these laminates identify the primary braid parameter that was varied by design (underlined and in regular text); the other parameters that were varied by necessity are shown in italics.

It should be noted that these architectures were chosen to define the extremes of the family of 2-D triaxial braids. Emphasis was given in their design to providing a wide range of mechanical properties to support analytical model development.

EFFECT OF YARN SIZE ON TENSILE PROPERTIES

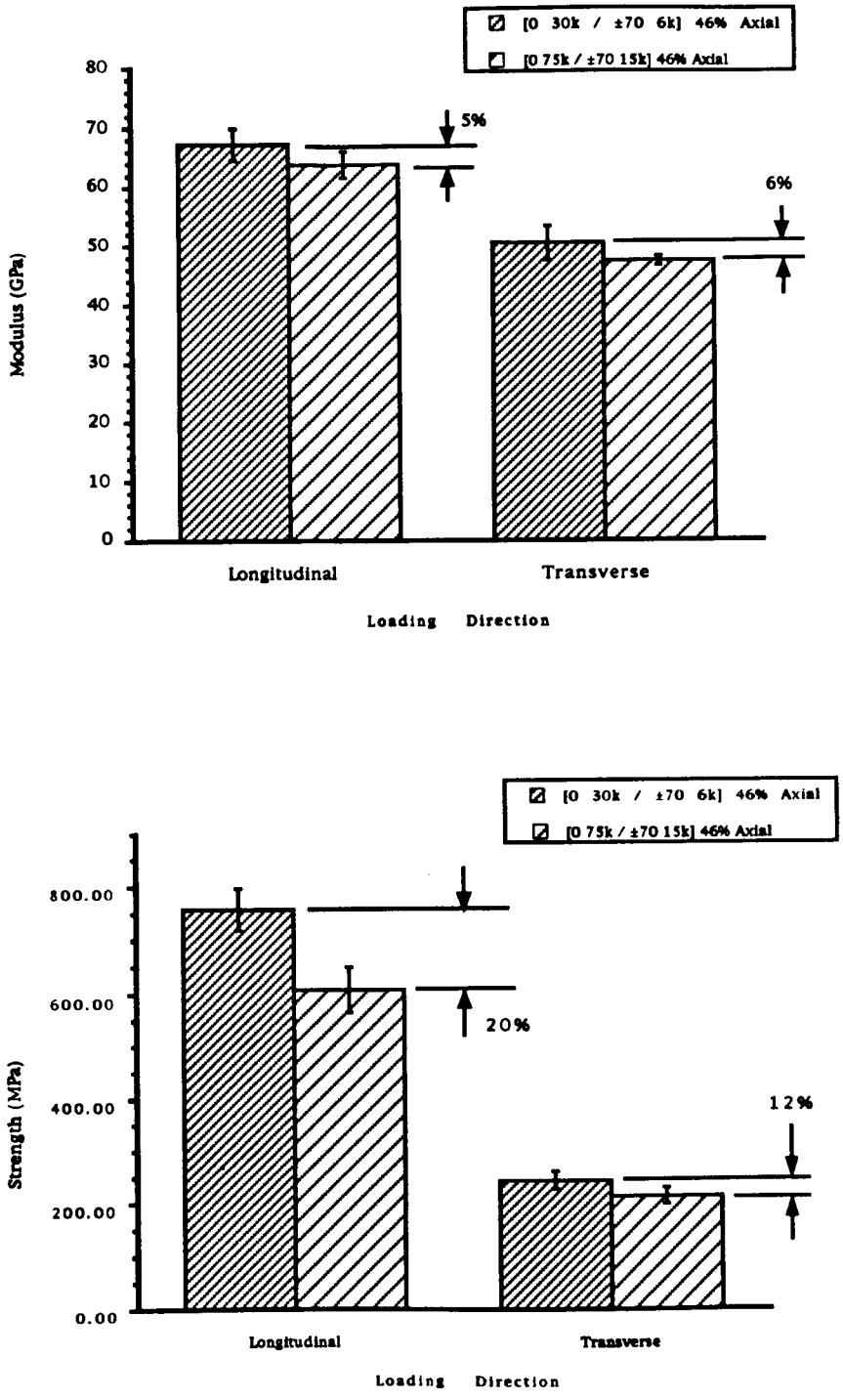

Figure 6. Effect of Yarn Size on Tensile Modulus and Strength.

EFFECT OF YARN SIZE ON COMPRESSION PROPERTIES

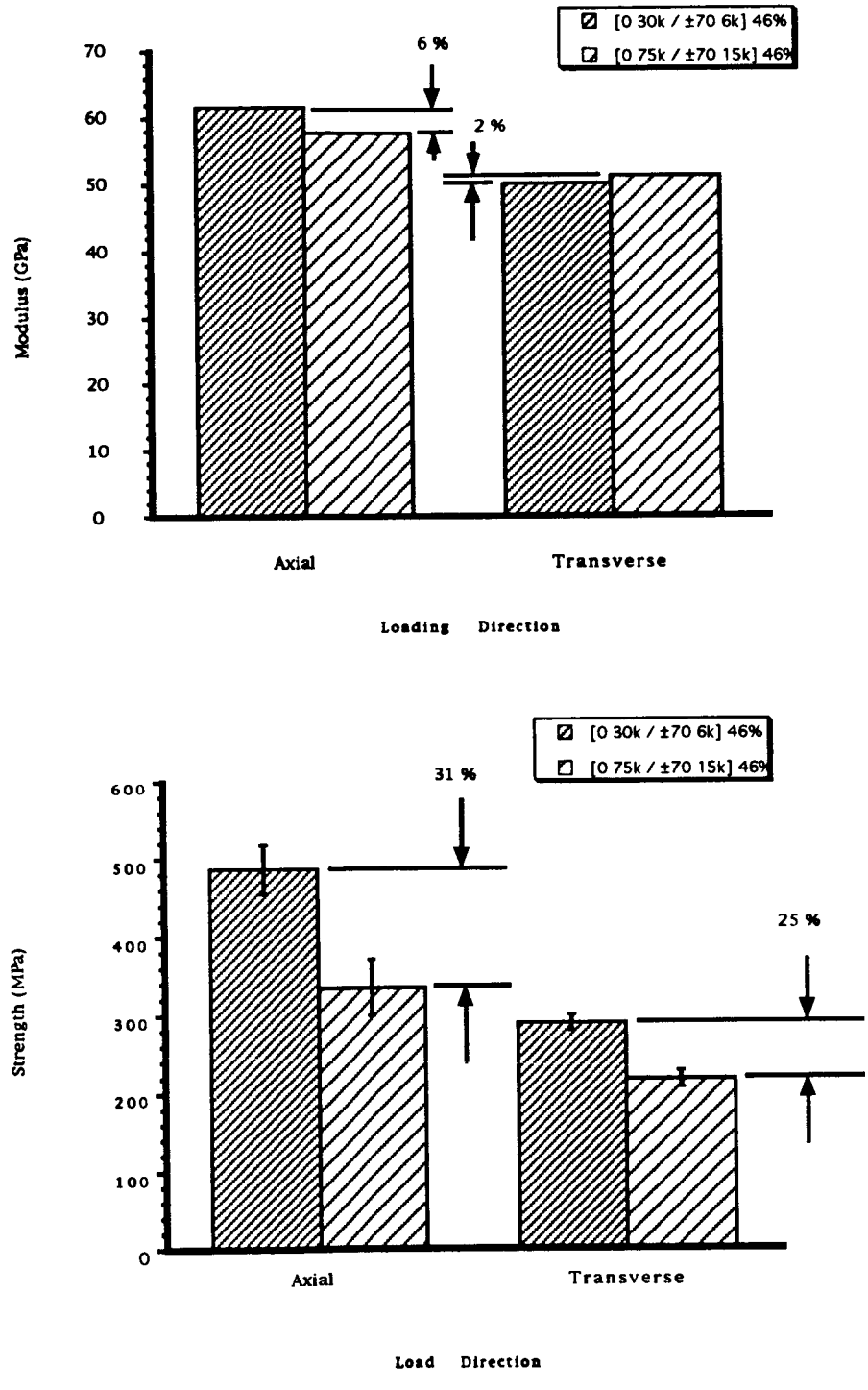

Figure 7. Effect of Yarn Size on Compression Modulus and Strength.

EFFECT OF BRAID ANGLE ON TENSILE PROPERTIES

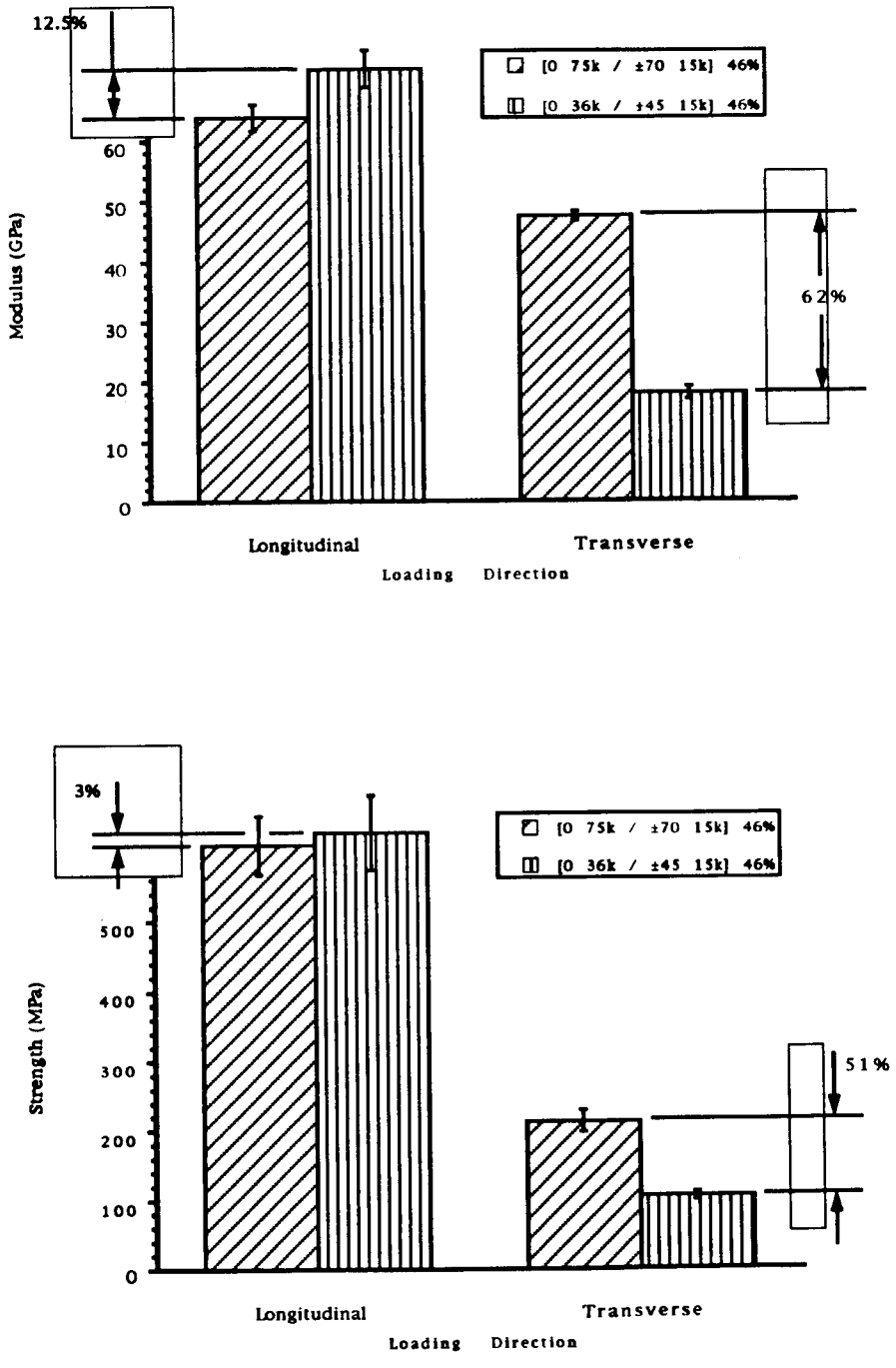

Figure 8. Effect of Braid Angle on Tensile Modulus and Strength.

EFFECT OF BRAID ANGLE ON COMPRESSION PROPERTIES

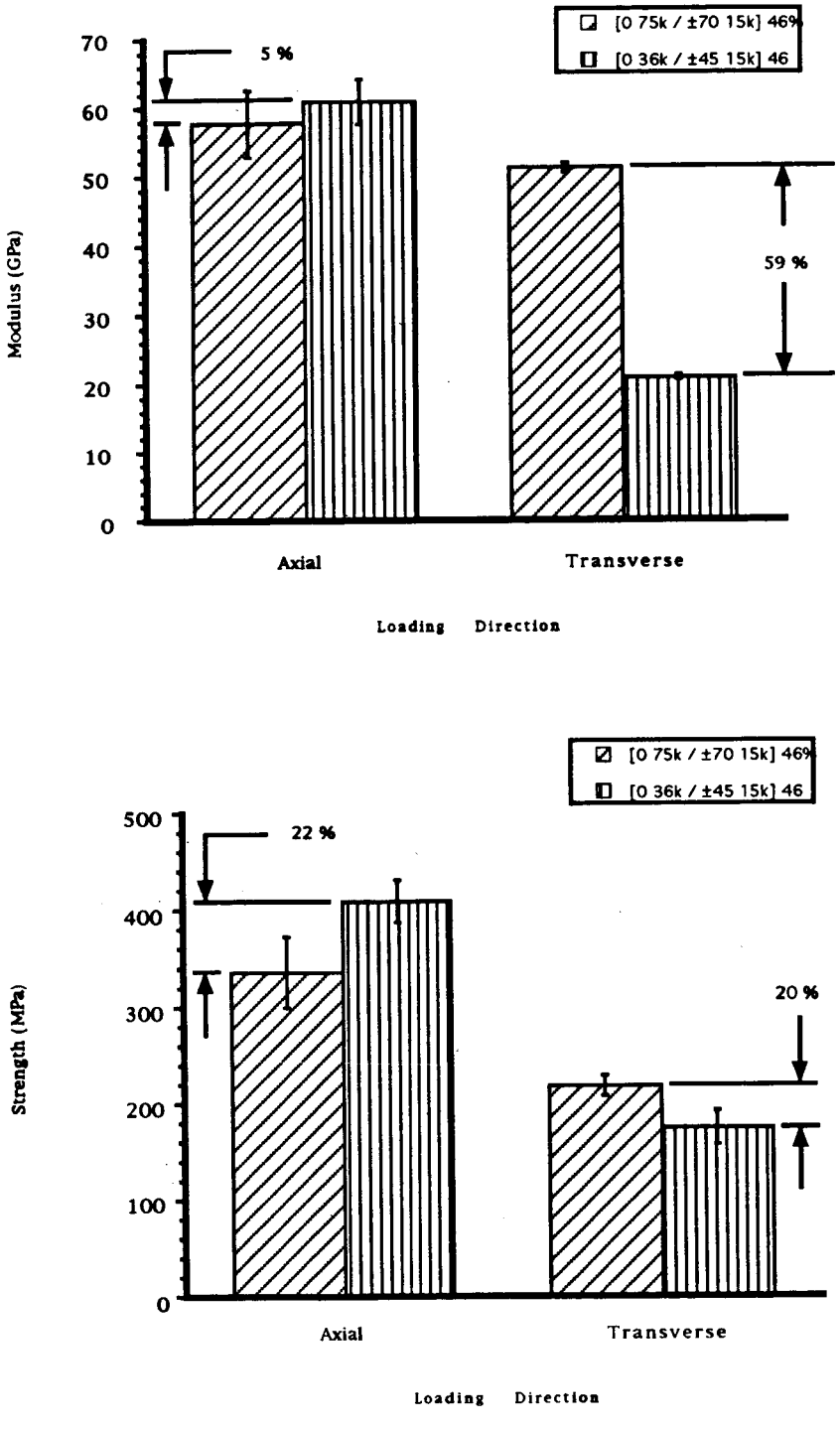

Figure 9. Effect of Braid Angle on Compression Modulus and Strength.

EFFECT OF AXIAL YARN CONTENT ON TENSILE PROPERTIES

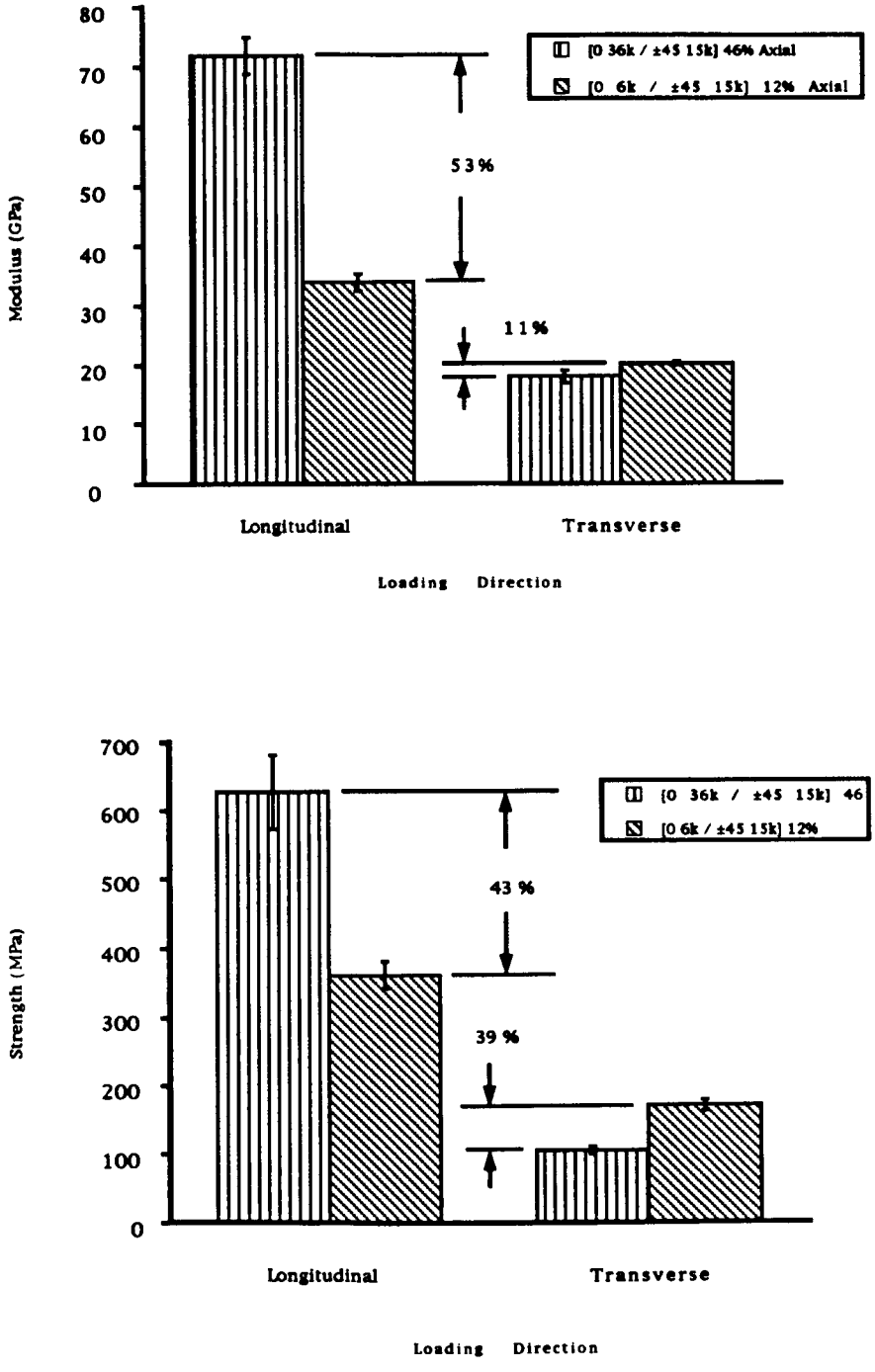

Figure 10. Effect of Axial Yarn Content on Tensile Modulus and Strength.

EFFECT OF AXIAL YARN CONTENT ON COMPRESSION PROPERTIES

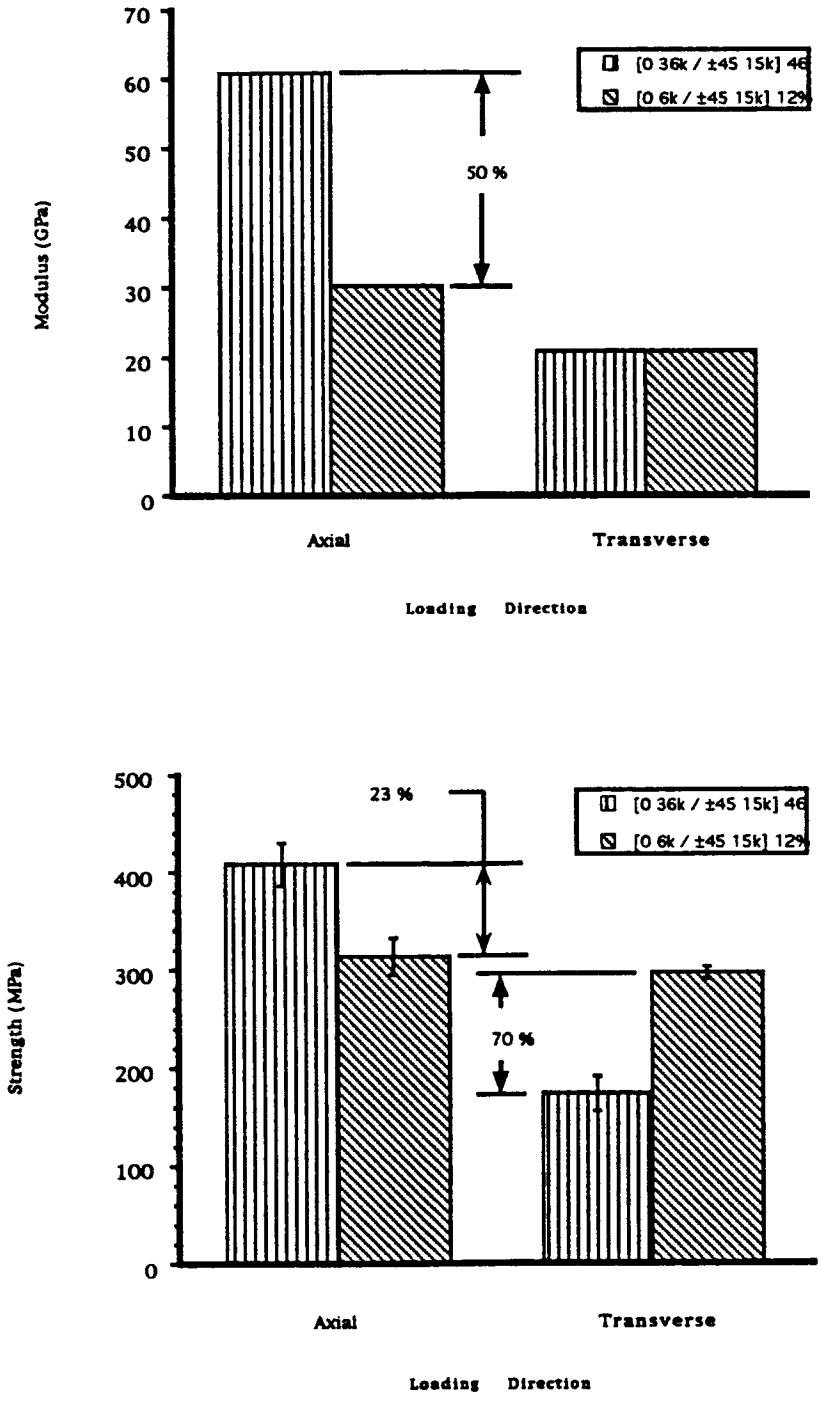

Figure 11. Effect of Axial Yarn Content on Compression Modulus and Strength.

EFFECT OF PRIMARY BRAID PARAMETERS ON LAMINATE SHEAR MODULUS

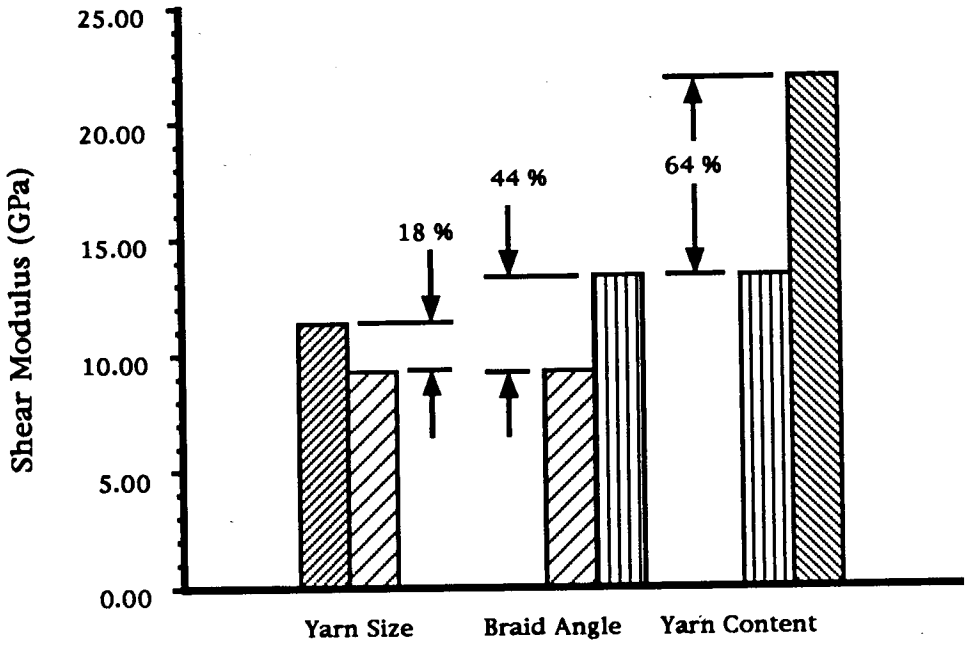

Figure 12. Effect of Primary Braid Parameters on Shear Modulus.

PRIMARY BRAID PARAMETERS & LAMINATE RESPONSE: OBSERVATIONS

Yarn Size Effects

A comparison of results obtained for the [0_{30k}/±70_{6k}] 46% Axial and [0_{75k}/±70_{15k}] 46% Axial architectures (Figures 6 and 7) indicates that a size effect is evident in these braided laminates. The axial and braider yarn tow sizes have been increased by a factor of 2.5 in these laminates. The data indicate that the materials' tensile and compression moduli showed slight decreases as yarn size increased. The changes in longitudinal and transverse moduli ranged from 2% to 6% and were within the scatter in the data. In contrast to the tensile and compression moduli, the shear modulus (Figure 12) decreased sharply as the yarn size increased.

Although the changes in elastic tensile and compression moduli were comparable to the scatter in the data, material strength was measurably lowered as yarn size increased. The longitudinal tensile strength decreased by 20% and the transverse tensile strength was reduced by 12%. As the figures indicate, the reductions in compression strength were even greater.

These results indicate that a size effect exists in textile composites. An analogous effect has been noted in composites fabricated of laminated unidirectional prepreg tape. The decreases in strength and toughness in those materials are often attributed to increases in interlaminar stresses which accompany increases in layer thickness. Increased waviness in the axial yarns of the courser braids was initially suspected to be a contributing factor in the braided laminates strength reductions. An investigation of crimp in the axial yarns was conducted. These results will be presented in a later section of this paper.

Braid Angle Effects

The effect of braid angle on material properties is seen when the data obtained for the [0_{75k}/±70_{15k}] 46% Axial and the [0_{36k}/±45_{15k}] 46% Axial architectures are examined (Figures 8 and 9). These effects were most pronounced in the materials' transverse and shear properties since the laminate response in the axial direction was dominated by the 0° yarns which constituted 46% of the preform. The axial tensile modulus showed a 12.5% increase as the braider yarns were rotated 25° in the longitudinal direction; the longitudinal compression modulus increased by only 5%. The axial tensile strengths of the two materials were also essentially equal. Their compression strengths, however, differed by 22%; strength increased with the change in braid angle.

By comparison, all the transverse properties measured decreased as the braid angle changed from 70° to 45°. This is, of course, an expected result since, when loaded in this direction, the laminates tested are effectively 90/±20 and 90/± 45. The braider yarns play a more prominent role in these laminates

and the effect of the braid angle changes are more evident. The tensile and compression moduli decreased by 62% and 59%, respectively. The transverse strengths were reduced by 51% in tension and 20% in compression. The shear modulus, on the other hand, increased by 45% as the braid angle changed from 70° to 45° (Figure 12). Rotating the braider yarns from ±70° to ± 45° has more effectively aligned these yarns with the principal stress directions in the shear test.

The changes measured in the braids' elastic properties are comparable to those typically seen in laminated tape composite systems. As has been previously demonstrated [3], classical laminated plate theory does reasonably well in predicting braided laminate elastic properties even when the braider yarn crimp effects are not recognized. These predictions are most accurate for the longitudinal modulus. Their accuracy decreases for the transverse and shear moduli since braider yarn crimp plays a more dominant role in these responses. The moduli of tape laminates with fiber contents and orientations equivalent to those of the two braids discussed above were predicted using classical laminated plate theory as a comparison. Laminated plate theory predicted a 7% change in longitudinal tensile modulus and a 62% change in transverse tensile modulus. The predicted change in shear modulus was, however, far greater than the measured value; 82% versus 45%.

Axial Yarn Content Effects

The final set of data to be considered feature results measured for the $[0_{36k}/\pm45_{15k}]$ 46% Axial and $[0_{6k}/\pm45_{15k}]$ 12% Axial architectures. They were designed to measure braid sensitivity to axial yarn content. In contrast with the results noted in the previous section, the longitudinal properties were most effected in these data. This is, of course, to be expected since the axial yarn content was reduced by 34% as the axial yarn size was reduced 6 fold. As the data in Figures 10 and 11 indicate, the longitudinal tensile modulus was reduced by 53% and the tensile strength in that direction diminished by 43%. Similar changes were noted for the laminates loaded in compression. Increases in the transverse tensile and compression properties and in the shear response of the material were also anticipated since decreasing axial yarn content has, in effect, increased the ±45° braider yarn content (from 54% to 88%). Although the transverse moduli showed only a moderate increase, the large increases in transverse tensile and compression strengths are of note. Increasing the ±45° braider yarn content had a large effect on the shear modulus (Figure 12); it increased by 64%. A greater portion of the fibers in the $[0_{6k}/\pm45_{15k}]$ 12% Axial laminate are now aligned in the direction of the principal stresses due to the increased ±45° yarn content.

Laminated plate theory was again used to predict the moduli of equivalent tape laminates. The measured changes in the braids' elastic properties noted above are similar to those anticipated for laminated tape materials. Plate theory predicts, for example, a 54% decrease in longitudinal modulus and a 46% increase in shear modulus.

BRAIDS DEVELOPED FOR SECONDARY BRAID PARAMETER STUDY

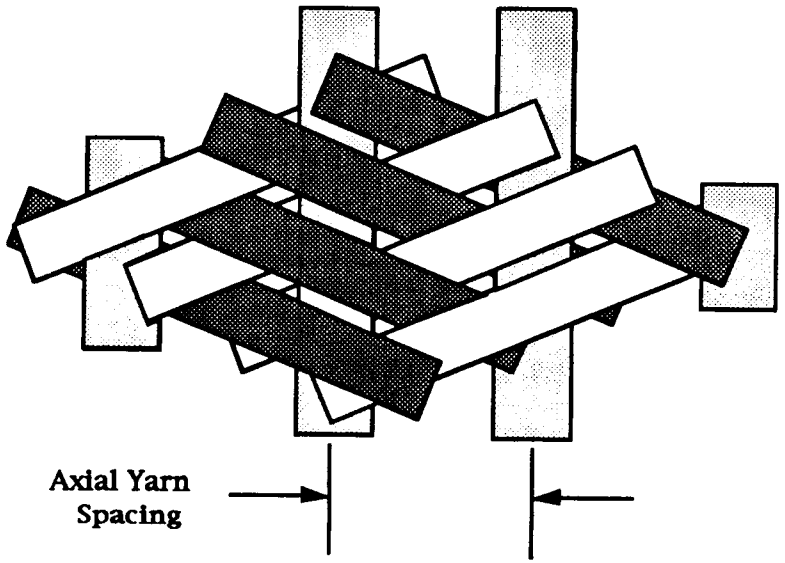

Table II. 0° Yarn Spacing and Braider Yarn Crimp of Laminates Tested in Secondary Braid Parameter Study.

Material Type	0° Yarn Density Nominal (Yarn / cm)	0° Yarn Density Measured (Yarn / cm)	0° Yarn Spacing (mm)	Braider Yarn Crimp Angle (°)
[0 18k/ ± 66.5 6k] 38% Axial	1.64	1.57 ± 0.03	6.37	10.7 ± 3.7
[0 18k/ ± 66.5 6k] 38% Axial	1.88	1.94 ± 0.05	5.15	13.9 ± 3.8
[0 18k/ ± 66.5 6k] 38% Axial	2.07	2.09 ± 0.09	4.78	16.8 ± 4.1

COMMENTS ON THE BRAID ARCHITECTURES: SECONDARY BRAID PARAMETER STUDY

Three braids were studied to determine the effects of the two secondary braid parameters on laminate response. The three braids had the same yarn sizes, braid angles, and axial yarn contents. They featured the [0 18k / ± 66.5 6k] 38% Axial braid architecture which was designed by Boeing for fuselage frame applications as a part of NASA's Advanced Composites Technology Program. The three architectures' featured different axial yarn spacing and braider yarn crimp angles, however. This was accomplished by changing the diameters of the mandrels on which the fibrous preforms were braided. Increasing the mandrel diameter increased the longitudinal yarn spacing since the total number of yarn carriers was held constant.

The yarn spacing and braider yarn crimp angles of the three braids tested in this program are listed in Table II. The table provides two measures of the interval between axial yarns : Yarn Density and Yarn Spacing. The former is expressed in terms of the number of yarns per unit length of fabric. The nominal and average measured Yarn Densities of the three architectures tested are listed in the table. The textile community typically expresses yarn spacing in these terms. The authors believe, however, that the inverse of these values, defined here as the Yarn Spacing, provide a more intuitive representation. These values are equivalent to the distance between axial yarn centerlines, as shown in the figure.

As the data in the table indicates, axial yarn spacing ranged from 4.78 to 6.37 mm. The figure shows a repeatable unit of the braid architecture that is sometimes referred to as the braid's natural unit cell. Increasing the yarn spacing to this degree will increase the unit cell's area by 64%. This opens the braid since the yarn sizes were held constant. Increasing the yarn spacing will also change the braider yarn's crimp angle significantly. The data also indicate that changing yarn spacing from 4.78 to 6.37 mm significantly increased the braider yarn crimp angle.

BRAIDER YARN CRIMP ANGLE vs. AXIAL YARN SPACING

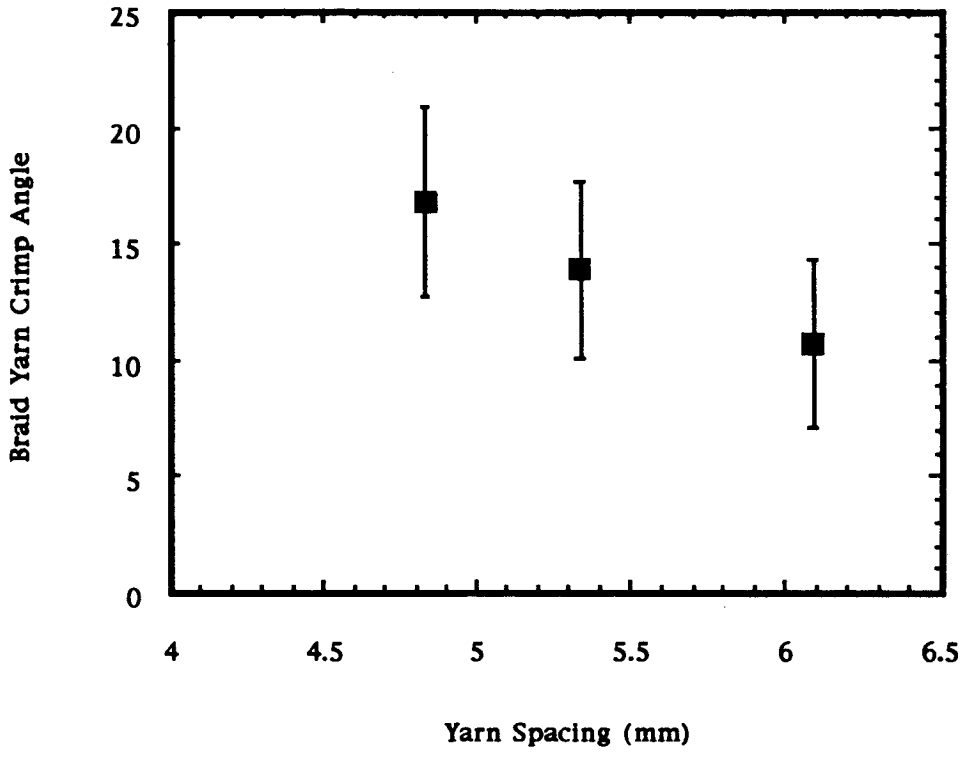

Figure 13. Empirical Data Demonstrate the Effect of Axial Yarn Spacing on Braider Yarn Crimp Angle.

As indicated earlier, the braider yarn crimp angle is a function of the axial yarn size and spacing. This figure plots the experimentally measured braider yarn crimp angles vs. axial yarn spacing for the three braids investigated in this phase of the study. Although there is wide scatter in the measured values, the crimp angle appears to be a linear function of the axial yarn spacing over the ranges studied.

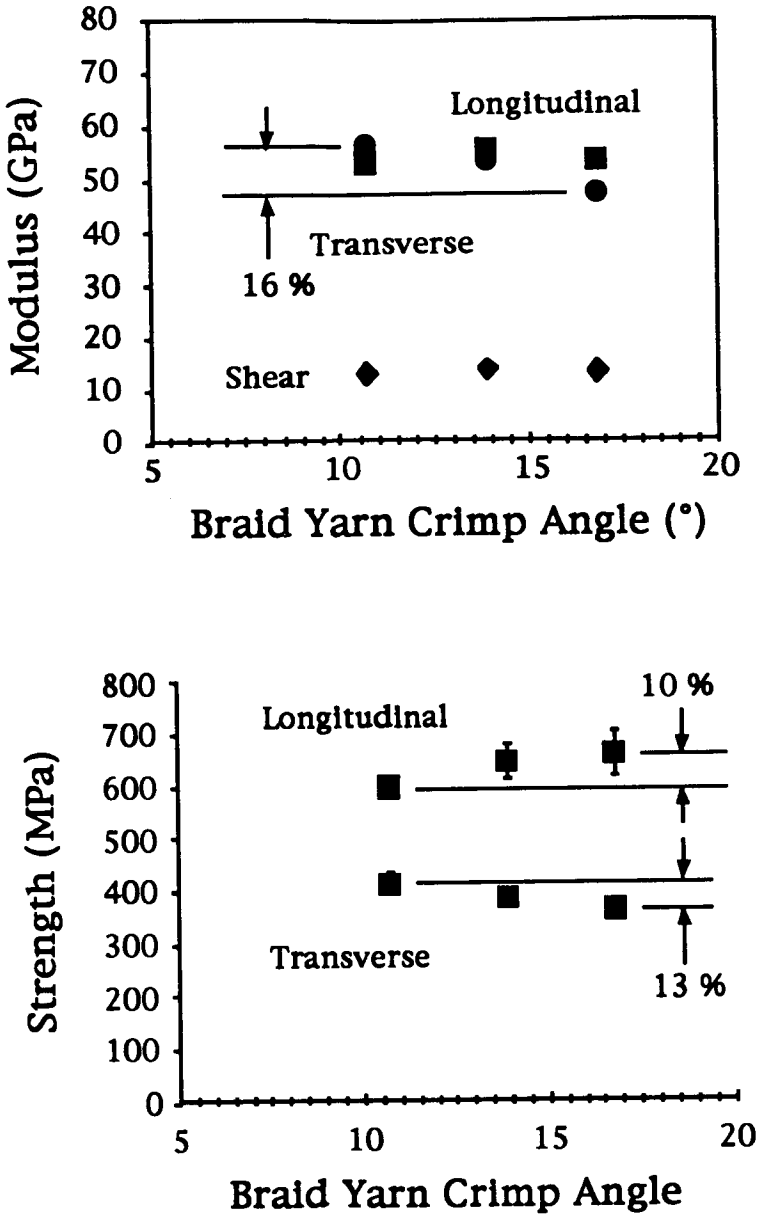

Figure 14. Braider Yarn Crimp vs. Tensile Modulus and Strength.

A review of the test results indicates that the braider yarn crimp had only a small effect on the longitudinal and shear moduli. The transverse modulus, on the other hand, decreased steadily as the braider yarn crimp increased. A 16% reduction was noted over the range tested. Changes in the laminates' strengths were not as marked. As the data in the lower figure indicates, the transverse strength, like the transverse modulus, decreased with increasing crimp in the braider yarns. Axial strength, on the other hand, increased only slightly. The total change in axial strength, however, was comparable to the scatter in the data.

MEASURED AND PREDICTED TENSILE MODULI:
PRIMARY BRAID PARAMETER STUDY

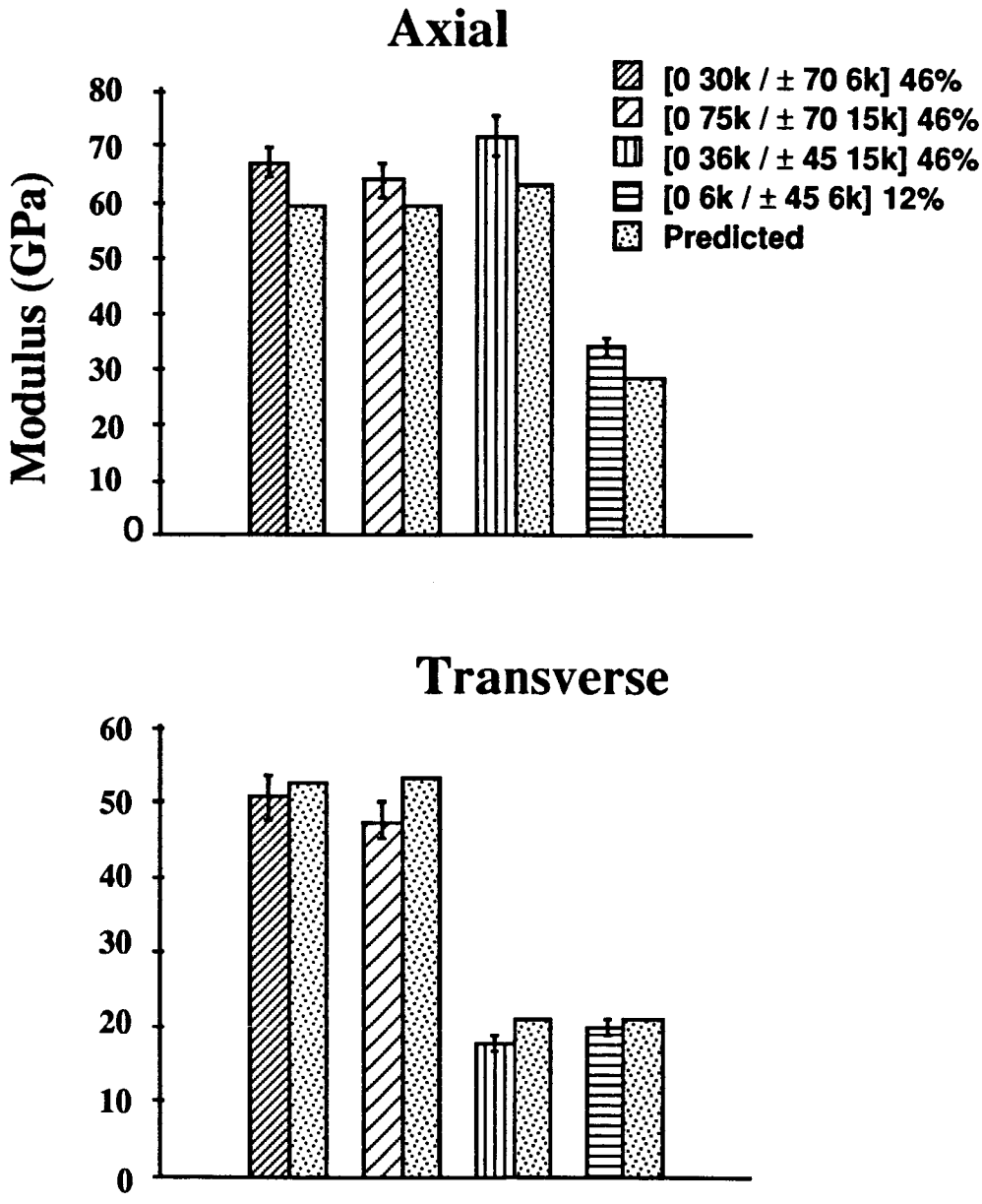

Figure 15. Measured and Predicted Tensile Moduli.

The TEXCAD analysis developed by Naik [4] was used to predict the elastic response of the four materials tested to define the effects of the primary braid parameters on laminate response. The measured and predicted results are shown in the figures. The model accurately predicted each architecture's longitudinal and transverse moduli.

Table III. 0° Yarn Crimp: Measured Values

Braid	0° Yarn Crimp
[0 30k / ± 70 6k] 46% Axial	2.85 ± 2.5
[0 75k / ± 70 15k] 46% Axial	3.10 ± 2.0
[0 36k / ± 45 15k] 46% Axial	4.00 ± 3.5
[0 6k / ± 45 15k] 12% Axial	3.20 ± 2.2

As was noted earlier, the reduction in strength noted in the [0 75k / ± 70 15k] 46% Axial laminates was initially attributed to crimp in the axial yarns. An investigation of axial yarn crimp for all the braid types investigated was conducted. Several samples of each braid type were sectioned in the longitudinal direction and metallurgically polished. Photomicrographs of these cross-sections were assembled and scanned into the computer. A series of short lines were electronically drawn tangent to the axial yarns in a piece-wise linear manner. The angle that each individual line segment made with the surface of the specimen was then measured.

The results of the measurements made for the four braid architectures investigated in the primary braid parameter study are summarized in Table III above. They indicate that significant degrees of axial yarn crimp were evident in all architectures. The data also indicate that the [0 30k / ± 70 6k] 46% Axial and [0 75k / ± 70 15k] 46% Axial laminates had comparable degrees of crimp in their 0° yarns. This latter observation, of course, indicates that the differences in the strengths of the two braids is not attributable to axial yarn crimp.

STRENGTH PREDICTIONS

In addition to its ability to predict a textile composite's modulus, TEXCAD is also capable of predicting laminate strength. The analysis was applied to the braid architectures investigated in the primary braid parameter study. The measured and predicted tensile and compression strengths of these four materials are plotted in Figure 16. The analysis was conducted twice for each architecture; first assuming no axial yarn crimp; and then with the crimp included. A 95 percentile "worst-case" scenario was modeled in the latter instance. Assuming the 0° yarn crimp measurements described above fit a normal distribution, the axial yarn crimp angle input to the model was calculated to be the mean value plus two times the standard deviation of the measurements. This in effect models the case in which all the axial yarns display this extreme defect. The two predicted values, therefore, provide an upper and lower bound on the laminate strength.

MEASURED AND PREDICTED STRENGTHS:
PRIMARY BRAID PARAMETER STUDY

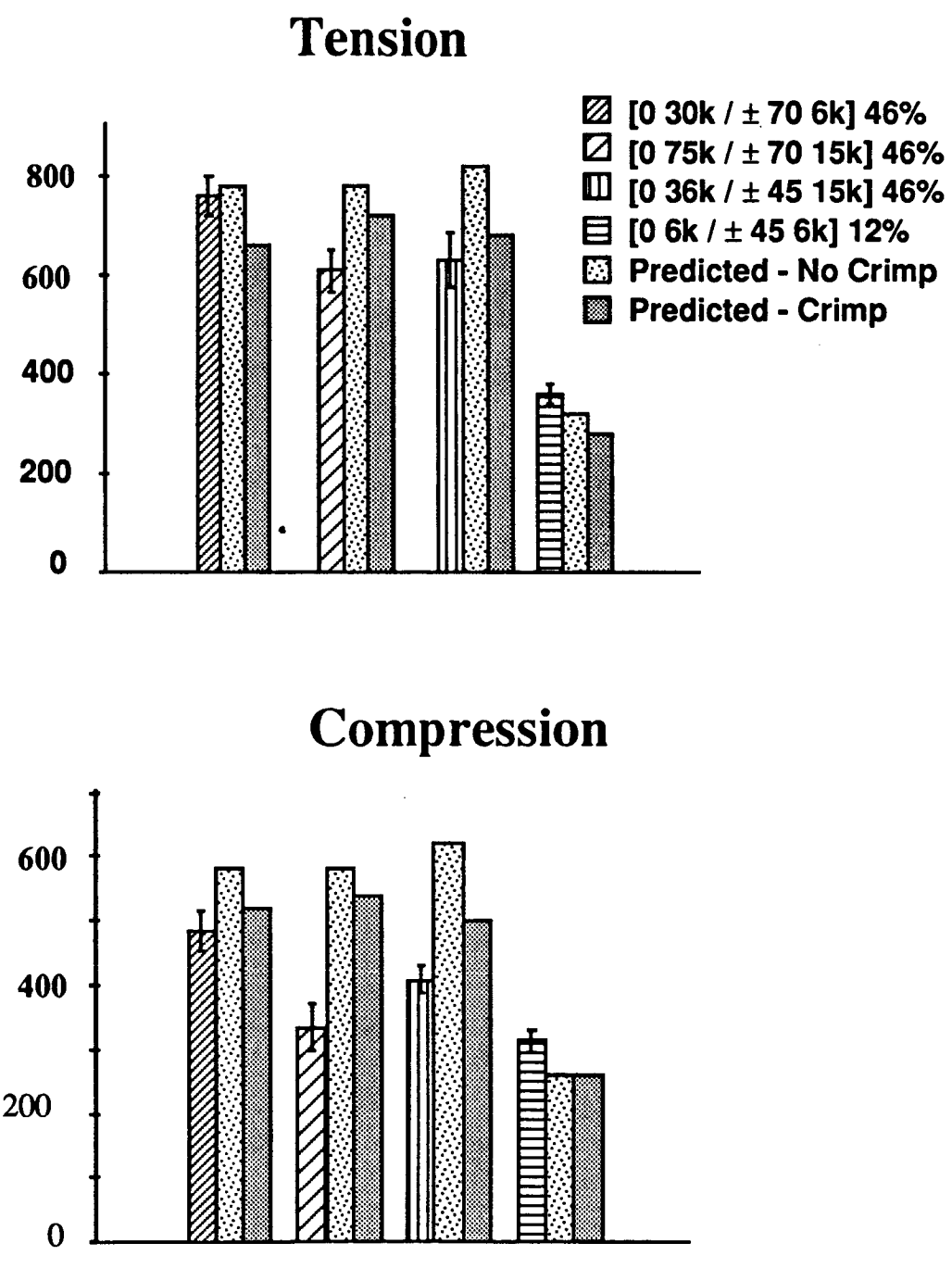

Figure 16. Measured and Predicted Tensile and Compression Strengths.

Summary:

Experimental Results

Effects of Architecture on Mechanical Response Measured

Yarn Size Effect Evident

Sensitivity to Braid Angle and Axial Yarn Content Similar to Tape Laminates

Braider Yarn Crimp and Axial Yarn Spacing Effects Minor

Significant 0° Yarn Crimp Present

Figure 17. Summary of Experimental Results.

The key points of the experimental work reported in this paper are summarized above.

The data indicate that a yarn size effect was evident in the material. Longitudinal and transverse strengths of the [0 75k / ± 70 15k] 46% Axial laminates were significantly lower than the strengths of [0 30k / ± 70 6k] 46% Axial laminates in both tension and compression. A mechanism that would explain this effect has not been identified. Increased axial yarn crimp in the courser braid, which was believed to be a contributing factor, does not appear to explain the results.

The test data also indicated that the sensitivities of braided laminates to changes in braid angle and axial yarn content are similar to those seen in laminates made of unidirectional prepreg tape. Applying classical laminated plate theory to tape laminates with equivalent fiber contents and orientations provides a reasonable approximation of the trends seen in the braided laminates.

The investigation of secondary braiding parameters indicated that the longitudinal tensile and shear properties of the braided laminates tested were not significantly effected by changes in the axial yarn spacing and braider yarn crimp. Their transverse moduli and strengths did, however, decrease as braider yarn crimp increased.

Finally, significant degrees of axial yarn crimping were measured in all four architectures investigated in the primary braid parameter study. It was not possible, however, to define a trend in the data; comparable degrees of crimp were measured for each architecture. Further investigation of this phenomenon is recommended. This should include examination of additional samples and a more rigorous statistical treatment of the data. In addition, several potential refinements to the yarn crimp measurement technique were suggested during discussions at the symposium.

Summary:

Analytical Results

TEXCAD Successfully Predicted Mechanical Properties

Effects of Braid Angle and Yarn Content Changes on Modulus and Strength Predicted

Effects of 0° Yarn Crimp on Laminate Strength Predicted

Figure 18. Summary of Analytical Results.

The TEXCAD analysis was used to predict the elastic response of the four materials tested to define the effects of the primary braid parameters on laminate response. The model accurately predicted each architecture's longitudinal and transverse moduli. The analysis also accurately depicted the braided laminates' sensitivity to changes in braid angle and axial yarn content.

TEXCAD's ability to predict a textile composite's strength was also exercised. It was again applied to the four braid architectures investigated in the primary braid parameter study to define the sensitivity of the materials' tensile and compression strengths to axial yarn crimp.

References:

1. Minguet, P. J., Fedro, M. J., and Gunther, C. K., "Test Methods for Textile Composites," NASA Contractor Report 4609, 1994.

2. Ifju, P. G., "The Shear gage and Compact Shear Specimen for Shear Property Measurements of Composite Materials," Ph.D. Dissertation, Virginia Polytechnic Institute and State University, June 1992; Virginia Polytechnic Institute Center for Composite Materials and Structures report 92-19, July 1992.

3. Masters, J. E., Foye, R. L., Pastore, C. M., and Gowayed, Y. A., "Mechanical Properties of Triaxially Braided Composites: Experimental and Analytical Results," *Journal of Composites Technology & Research*, JCTRER, Vol. 15, No. 2, Summer 1993, pp. 112 - 122.

4. Naik, R. A., Ifju, P. G., and Masters, J. E., "Effect of Fiber Architecture Parameters on Deformation Fields and Elastic Moduli of 2-D Braided Composites," *Journal of Composite Materials*, Vol. 28, No. 7/1994, pp. 656 - 681.

A COMPARISON OF GRAPHITE/EPOXY TAPE LAMINATES AND 2-D BRAIDED COMPOSITES MECHANICAL PROPERTIES*

Pierre J. Minguet
Boeing Defense & Space Group, Helicopters Division
Philadelphia, PA

ABSTRACT

A comparison of the mechanical properties of unidirectional composite tape laminates and of 2-dimensional triaxially braided composite was conducted. The tape laminate layups were designed to match the percentage of axial fibers and the angle of the bias tows in the braided composite. The material system used for the laminates is AS4/3501-6 which was chosen as the closest available match to AS4/1895 used for the braids. The strength and stiffness properties measured here include tension, open-hole tension, filled-hole tension, compression and open-hole compression, all of these in both the longitudinal and transverse direction.

Results show that the longitudinal modulus of both material forms is quite similar, but that the transverse modulus of the braids is lower. In terms of strength, the longitudinal unnotched strength of the braids is lower than that of the laminates, while the transverse strength is significantly lower. For both strength and stiffness, the crimp in the bias tows of the braid is probably the main cause for reduced properties. On the other hand, a very significant increase in open-hole and filled-hole tension strength was observed for the braids compared to the tape laminates. However, this was not observed in compression where all the braid properties are lower than for the laminates.

INTRODUCTION

Carbon/Epoxy composites made from textile fiber preforms manufactured with a Resin-Transfer-Molding (RTM) process have some potential for reducing costs and increasing damage tolerance of aerospace structures. One form of textile preform which is under consideration is a 2-dimensional triaxially braided fabric. A large amount of test data has been generated recently to quantify the mechanical properties of various 2-D braided configurations loaded in tension, with and without holes, compression, with and without holes, shear and bolt bearing [1].

The key question is then to determine and quantify the benefits and drawbacks of this material form. Because of the nature of the triaxial fabric (e.g., no 90° fibers), little data which could be used for a direct comparison of mechanical performance is available for more conventional material forms (i.e. tape or biaxial fabric laminates). Therefore, tape laminates with the same ply orientation and percentage of 0° fibers as the previously tested braided composites were manufactured and tested. More detailed results of the effort reported here can be found in Reference 2.

* Work done under contract NAS1-19247

TEST PROGRAM DESCRIPTION

Four configurations of 2-D braided composite were extensively tested in a previous investigation as reported in Reference 1. The 2-D braided fabric contains two types of tows, the longitudinal (axial, or 0°) tow and the braided (or bias) tows oriented at angle θ of the axial tow. The braid pattern used is 2X2 pattern, meaning that each braided tow goes over and under two tows at a time. As shown in Table 1, the first three architectures contain a large percentage of axial fiber typical of a composite optimized for a predominantly longitudinal loading. The first architecture, SLL, was braided with small tows to provide a fine architecture, while the third one, LLL, was braided with 2.5 times larger tows, thus allowing to examine the influence of tow sizes. The second architecture, LLS was braided with a 45° bias angle, thus allowing one to examine the influence of braid angles. For practical applications, braid angles will often be limited to the 45° to 70° range, and the comparison of LLS and LLL allows one to examine both upper and lower bounds on that parameter. Finally, the fourth architecture, LSS, contains a larger amount of ±45° tows more typical of a composite optimized for shear loading.

Three laminates were designed to match the bias angle and percentage of axial fibers of these braids. Two of the braids, SLL and LLL, have the same layup with different tow sizes and thus will be compared with the same laminate. The material system used is AS4/3501-6 (4.4 oz/yd^2) which closely matches the AS4/1895 system used for the braids. The following laminates were used:

Laminate 1: $[(45/0/-45/0)_2/45/0/-45]_s$
22 Plies Total, 10 0° Plies (45.4%), 12 45° Plies, to match LLS.

Laminate 2: $[(70/0/-70/0)_2/70/0/-70]_s$
22 Plies Total, 10 0° Plies (45.4%), 12 70° Plies, to match SLL and LLL.

Laminate 3: $[(\pm45)_2/0/(\pm45)_3/0(\pm45)_3/0/(\pm45)_2]_t$
23 Plies Total, 3 0° Plies (13.0%), 20 45° Plies, to match LSS.

Table 1 Description of 2-D braid architectures

Name	Longitudinal Tow Size	Braided Tow Size	% Longitudinal Tow	Braid Angle [°]	Unit Cell Width [in]	Unit Cell Length [in]
SLL	30 K	6 K	46	70	0.458	0.083
LLS	36 K	15 K	46	45	0.415	0.207
LLL	75 K	15 K	46	70	0.829	0.151
LSS	6 K	15 K	12	45	0.415	0.207

Three specimens were used for each test configuration. Standard size specimen, 12" long and 1.5" wide, were used for the tension tests. Modified IITRI specimens, 1.5" long by 1.5" wide test section, were used for the compression tests. The laminate thickness was doubled for the compression specimen to insure specimen stability. A hole diameter of 0.188" was mistakenly used in the compression test instead of the standard 0.250".

The same approach used in Reference 1 was used here to make all results directly comparable. **All results are normalized to a 60% fiber volume fraction**. Fiber volume fraction and thickness were measured on all manufactured panels. After averaging these data over all panels, a nominal ply thickness of **0.0054"** was calculated. All stiffness moduli and Poisson's

coefficients are the initial value of these properties and were measured with a linear regression between 0.001 and 0.003 strain levels. Wherever a nominal strain is reported, it is equal to the strength divided by the initial modulus. Actual strain is the last reading obtained from a strain gage prior to failure. Strength is always calculated as load divided by actual width and nominal thickness.

Open-hole and filled-hole strength results were corrected to infinite plate width with the following formula for a hole diameter d, a nominal thickness t_{nom} and a plate width w :

$$\sigma_{\infty} = \left[\frac{2 + \left(1 - \frac{d}{w}\right)^3}{3\left(1 - \frac{d}{w}\right)} \right] \cdot \frac{P}{w\ t_{nom}}$$

TENSION PROPERTIES

Tension properties for all laminates were measured in both the longitudinal (0°) and transverse (90°) directions. Properties included stiffness modulus, Poisson's coefficient, open-hole strength (01.88" and 0.250" diameters) and filled-hole strength using a fully-torqued 0.25" titanium hilock fastener. All the tension properties measured in the longitudinal (0°) direction are shown in Table 2, while all the properties measured in the transverse (90°) direction are shown in Table 3.

Table 2 Laminate Longitudinal Tension Properties

Property	Laminate 1	Laminate 2	Laminate 3
Modulus [msi]	10.33	9.63	4.92
CoV [%]	0.8	2.8	0.5
Poisson's Coefficient	0.663	0.157	0.713
CoV [%]	2.3	3.7	0.8
Unnotched Strength [ksi]	131	132	63
Nominal Strain [μs]	12,690	13,750	12,840
CoV [%]	12.5	6.3	1.8
Actual Strain [μs]	12,300	13,400	15,200
0.188" OHT Strength [ksi]	72	66	42
OHT Nom. Strain [μs]	6,960	6,860	8,460
CoV [%]	4.4	1.0	2.0
0.250" OHT Strength [ksi]	69	66	40
OHT Nom. Strain [μs]	6,640	6,820	8,080
CoV [%]	3.8	3.6	1.2
0.250" FHT Strength [ksi]	60	49	42
FHT Strain [μs]	5,820	5,090	8,560
CoV [%]	2.1	1.8	2.7

Note: Laminate 1 $[(45/0/-45/0)_2/45/0/-45]_s$
Laminate 2 $[(70/0/-70/0)_2/70/0/-70]_s$
Laminate 3 $[(\pm45)_2/0/(\pm45)_3/0/(\pm45)_3/0/(\pm45)_2]_t$

Coefficients of variation were generally quite low and well within the typical values obtained when testing composites. The only exception was the unnotched 0° strength of L1 for which one specimen failed prematurely. If that data point was excluded, L1 strength would be 141 ksi (13,600 μs). Laminate 1 and 2 were linear to failure, as indicated by the fact that actual and nominal strains are virtually equal, while laminate 3 (with a high percentage of ±45° plies) had a softening behavior with the actual strain much higher than nominal. Failure for L1 and L2 occurred close to the tabs. L3 exhibited a large amount of delamination.

Somewhat different failure modes were observed in the 90° unnotched tension tests. Laminates 1 and 2 exhibited a clean straight break well inside the test section. Laminate 3 also failed inside the test section and showed mostly an in-plane shear failure mode, along with some visible edge delaminations. Laminate 1 and 3 had a softening behavior because of their 45° ply angle. The strain levels in L2 were much below that in the 0° tests, indicating that pure fiber fracture was not the dominant failure mode.

All laminates but L3 show a strong sensitivity to the presence of a fully torque fastener in the longitudinal tension test. Strength reductions were 13% for L1, 26% for L2. In the transverse direction, the influence of the fastener was quite different. A strength increase was observed for L1 (+18%) and L2 (+3%), while a strength decrease was observed for L2 (-10%). Note that the strength increase was observed for the two laminates with a low transverse modulus.

Table 3 Laminate Transverse Tension Properties

Property	Laminate 1	Laminate 2	Laminate 3
Modulus [msi]	3.37	8.96	3.48
CoV [%]	0.9	0.6	1.5
Poisson's Coefficient	0.225	0.147	0.513
CoV [%]	9.4	3.9	1.1
Unnotched Strength [ksi]	35	72	35
Nominal Strain [μs]	10,480	8,020	10,030
CoV [%]	1.8	3.3	0.9
Actual Strain [μs]	15,600	8,300	14,800
0.188" OHT Strength [ksi]	31	59	33
OHT Nom. Strain [μs]	9,210	6,580	9,520
CoV [%]	1.2	3.5	0.6
0.250" OHT Strength [ksi]	28	53	32
OHT Nom. Strain [μs]	8,359	5,910	9,140
CoV [%]	2.7	3.4	0.8
0.250" FHT Strength [ksi]	33	50	33
FHT Strain [μs]	9,660	5,580	9,430
CoV [%]	2.3	3.1	0.5

Note: Laminate 1 $[(45/0/-45/0)_2/45/0/-45]_s$
Laminate 2 $[(70/0/-70/0)_2/70/0/-70]_s$
Laminate 3 $[(\pm45)_2/0/(\pm45)_3/0/(\pm45)_3/0/(\pm45)_2]_t$

The first comparison, shown in Figure 1, is for longitudinal modulus. Minimal differences were found between braids and tape laminates: +0.4% for SLL, -4.6% for LLL, -0.9% for LLS, and -0.6% for LSS. Considering experimental scatter and the slight differences in percentage of 0°, it is fair to say that there is no difference between longitudinal moduli for the two material forms. The slight reduction for LLL is probably due to the additional tow waviness introduced by the use of large tow sizes.

The comparison is quite different for the transverse modulus. As shown in Figure 1, the braided material is substantially less stiff: -19% for SLL, -24% for LLL, -22% for LLS, and -16% for LSS. The primary cause for this reduction is the crimp in the bias tows.

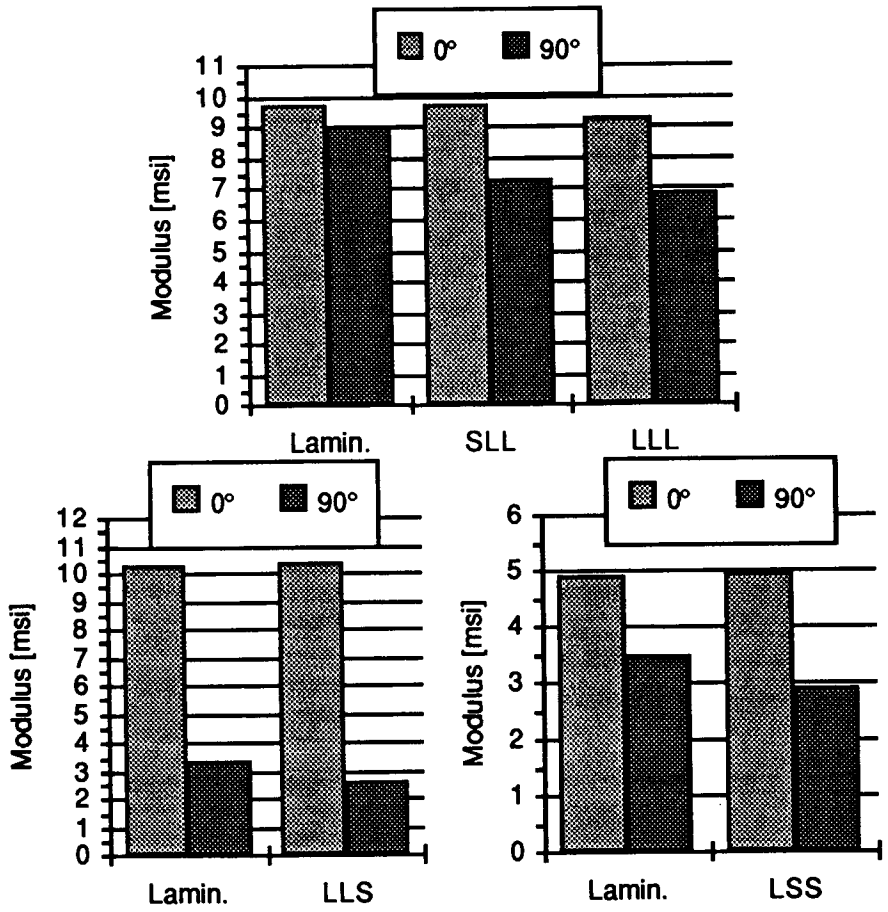

Figure 1 Comparison of Longitudinal and Transverse Tension Modulus.

The comparison for unnotched longitudinal tension strength is show in Figure 2.a to 2.c. A notably lower strength was obtained for all the braids: -17% for SLL, -34% for LLL, -31% for LLS, and -16% for LSS. Once again, the tow waviness is a probable contributor to this loss of strength. However, it is somewhat surprising that there was so little difference in modulus and such difference in strength. Another possible contributor is the matrix material. Although 1895 and 3501-6 are rather similar epoxys, it is possible that 1895 is more brittle or has a lower strain to failure than 3501-6.

The open-hole tension strength comparison is based on the standard 1/4" diameter hole which is often used in developing material allowables. In Reference 1, several hole diameters were tested for each braided material. A log-log best fir curve of strength versus hole diameter was then calculated. This procedure showed that the data at some of the hole diameters did

not follow the overall trend due to experimental scatter. This was the case for the 1/4" hole in the SLL and LLS architecture. Thus, instead of using the data for the 1/4" hole, the strength is calculated with the following best fit equations:

SLL: $\sigma = 72.2 * d^{-.165}$ LLL: $\sigma = 53.0 * d^{-.315}$

LLS: $\sigma = 61.3 * d^{-.208}$ LLS: $\sigma = 28.8 * d^{-.265}$

Results in Figure 2 show a clear strength advantage for the braided materials. The relative differences between braid and laminate strength were +37% for SLL, +24% for LLL, +20% for LLS, and +4% for LSS. Since moduli are quite similar for each braid and equivalent laminate, the differences in term of nominal strain are about the same.

This strength difference is further magnified in the filled-hole tension test. As mentioned above, the laminated material was quite sensitive to the presence of a fastener, while the data in Ref. 1 showed that the braids were not. The relative differences in term of strength were: +72% for SLL, +47% for LLL, and +19% for LLS (no data is available for LSS).

Post-failure examination of the braided specimens revealed extensive matrix failure between the axial and bias tows which would tend to reduce the stress concentration for axial yarns. On the other hand, examination of the laminated specimen showed a fairly clean fracture surface across the specimen net section. Because these are such significant differences and because this is such an important property in terms of design, this topic would warrant further work to confirm these experimental results and explain this apparent advantage of braids over tape laminate.

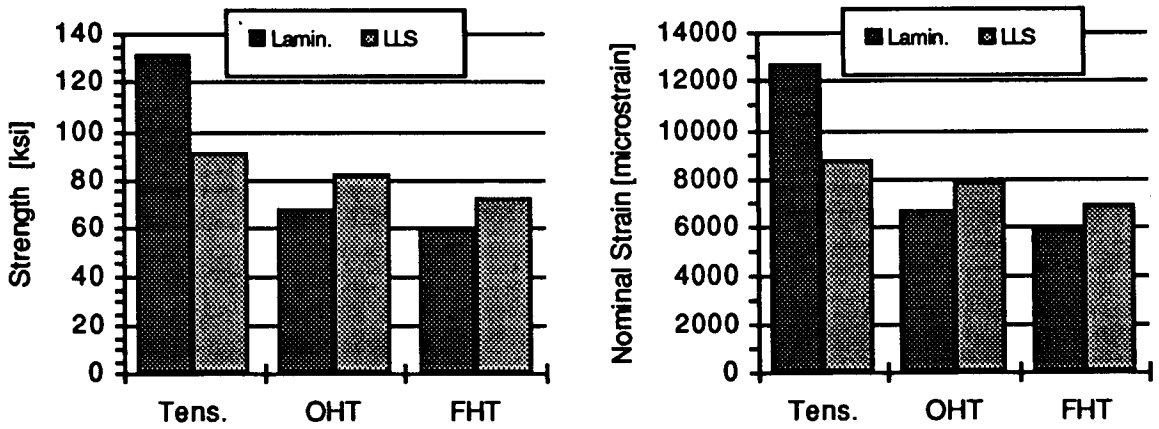

Figure 2.a Comparison of 0° Tension Strength for Tape Laminate 1 and LLS.

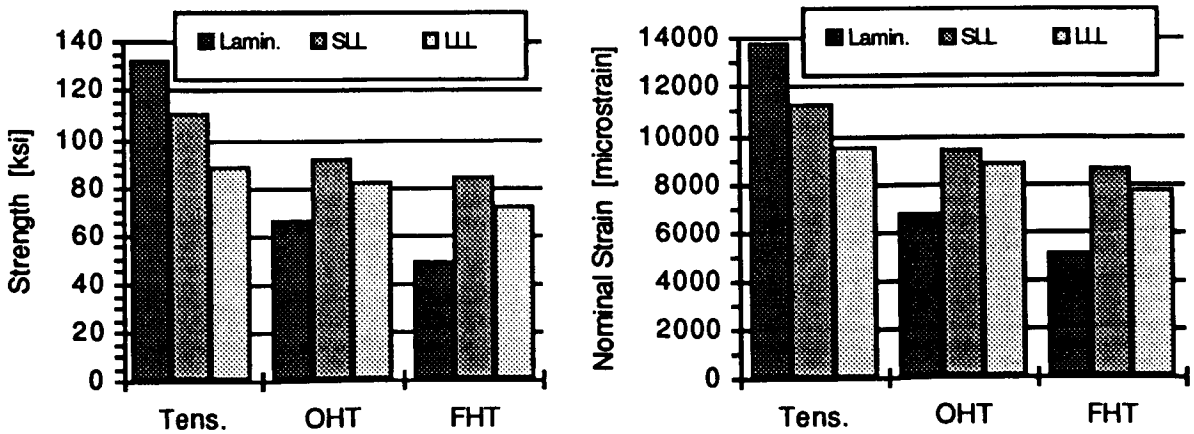

Figure 2.b Comparison of 0° Tension Strength for Tape Laminate 2, SLL and LLL.

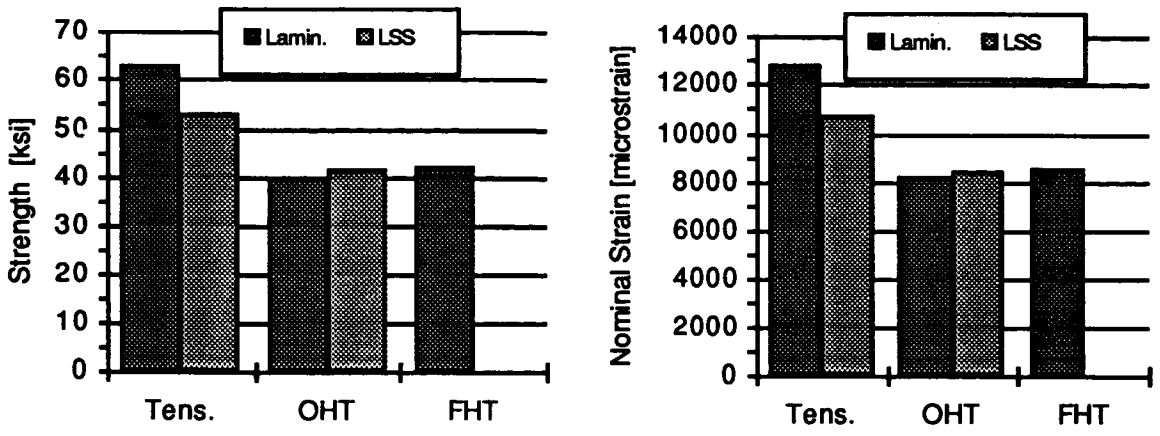

Figure 2.c Comparison of 0° Tension Strength for Tape Laminate 3 and LSS.

Strength measured along the transverse direction for these materials is shown in Figure 3.a to 3.c. For the unnotched case, the braided material show a severe strength reduction compared to the tape laminates: -51% for SLL, -57% for LLL, -57% for LLS, and -29% for LSS. Once again, the crimp in the bias tows is the likely cause for the strength reduction.

Only a limited set of data is available for the transverse open-hole tension strength of the braided material. A single hole size of 1/4" was tested and is used for comparison. Somewhat surprisingly, these materials exhibited no notch sensitivity, and in some cases, the strength was slightly higher than that for the unnotched case. The data is probably too limited at this point to draw any definite conclusion. The tape laminates did show some notch sensitivity, and thus the differences in strength between the two material forms are reduced compared to the unnotched case: -36% for SLL, -43% for LLL, -46% for LLS, and -16% for LSS.

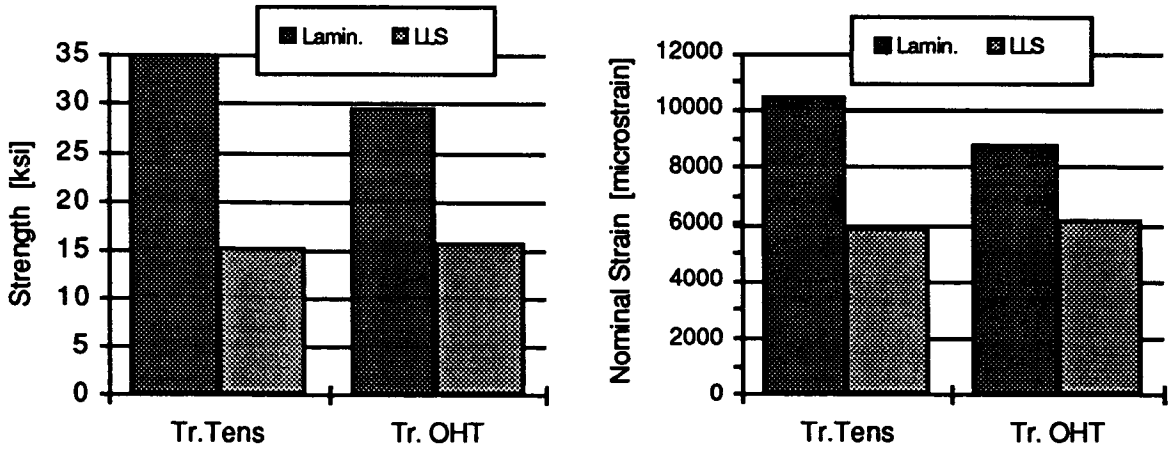

Figure 3.a Comparison of 90° Tension Strength for Tape Laminate 2 and LLS.

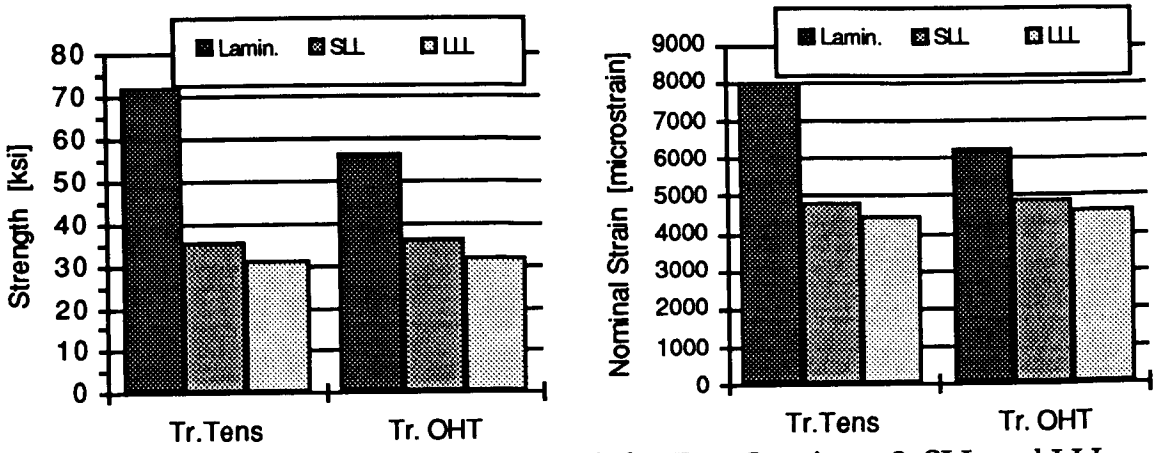

Figure 3.b Comparison of 90° Tension Strength for Tape Laminate 2, SLL and LLL.

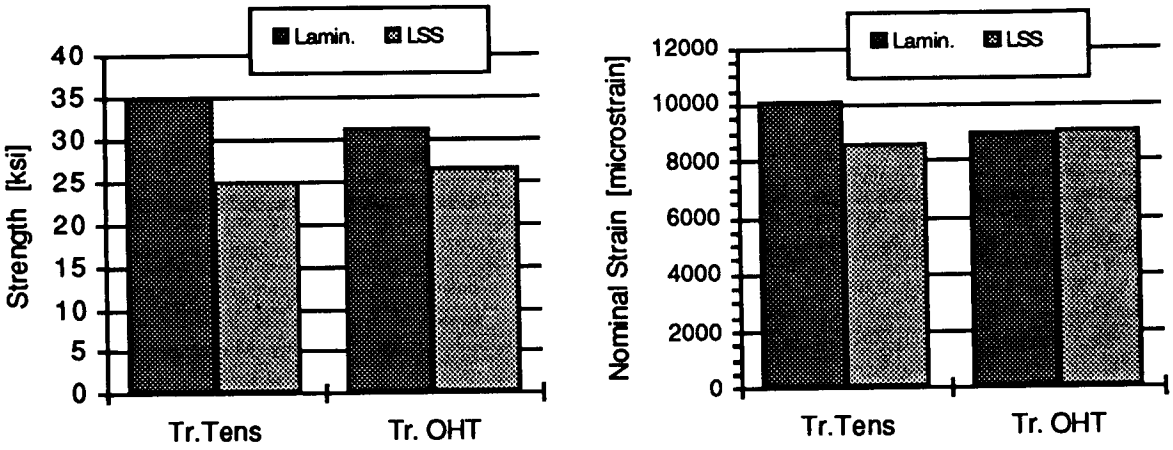

Figure 3.c Comparison of 90° Tension Strength for Tape Laminate 3 and LSS.

COMPRESSION PROPERTIES

Compression properties for all four laminates were also measured in both the longitudinal (0°) and transverse (90°) directions. Properties included stiffness modulus, Poisson's coefficient and open-hole strength (0.188" diameter). A modified IITRI test specimen [1] with a test section of 1.5" by 1.5" was used for all tests.

All the compression properties measured in the longitudinal (0°) direction are shown in Table 4, while all the properties measured in the transverse (90°) direction are shown in Table 5. Coefficients of variation were generally quite low and well within the typical values obtained when testing composites. Some of the exceptions were the unnotched 0° strength of L1, notched 90° strength of L1 and unnotched 90° strength of L2. The nominal strains reported in this section were always calculated with the compression modulus. When comparing the compression moduli to the ones measured in tension, significant differences were observed, 17% lower for L1, 13% for L2 and 16% for L3. A similar observation can me made for the transverse modulus: 8% lower for L1, 14% for L2 and 13% for L3. Although it is typical for composites to be softer in compression, these differences are slightly higher than expected. The test specimen itself, with a short and wide test section, is believed to be partly responsible for this effect. Longitudinal fiber strains at failure were fairly typical of this type of material,

ranging from 0.95% to 1.1%. High strains to failure were measured wherever there was large percentage of ±45° fibers, such as in the 0° and 90° test of L3 and in the 90° test of L1.

Table 4 Laminate Longitudinal Compression Properties

Property	Laminate 1	Laminate 2	Laminate 3
Modulus [msi]	8.84	8.53	4.25
CoV [%]	1.0	2.1	1.6
Poisson's Coefficient	0.704	0.172	0.712
CoV [%]	3.0	1.8	3.2
Unnotched Strength [ksi]	84	82	58
Nominal Strain [μs]	9,500	9,640	13,560
CoV [%]	9.9	5.5	5.1
0.188" OHT Strength [ksi]	65	75	43
OHT Nom. Strain [μs]	7,330	8,770	10,210
CoV [%]	1.5	2.0	1.4

Note: Laminate 1 $[(45/0/-45/0)_2/45/0/-45]_s$
Laminate 2 $[(70/0/-70/0)_2/70/0/-70]_s$
Laminate 3 $[(\pm45)_2/0/(\pm45)_3/0/(\pm45)_3/0/(\pm45)_2]_t$

Table 5 Laminate Transverse Compression Properties

Property	Laminate 1	Laminate 2	Laminate 3
Modulus [msi]	3.13	7.84	3.08
CoV [%]	0.6	1.3	1.5
Poisson's Coefficient	0.237	0.151	0.525
CoV [%]	2.1	6.7	2.5
Unnotched Strength [ksi]	50	70	48
Nominal Strain [μs]	15,880	8,930	15,720
CoV [%]	4.9	12.3	1.5
0.188" OHT Strength [ksi]	42	61	44
OHT Nom. Strain [μs]	13,520	7,830	14,220
CoV [%]	7.6	1.3	0.4

Note: Laminate 1 $[(45/0/-45/0)_2/45/0/-45]_s$
Laminate 2 $[(70/0/-70/0)_2/70/0/-70]_s$
Laminate 3 $[(\pm45)_2/0/(\pm45)_3/0/(\pm45)_3/0/(\pm45)_2]_t$

The first comparison, shown in Figure 4, is for modulus. Small differences were found between braids and tape laminates for the longitudinal modulus, +4.6% for SLL, -1.9% for LLL, -0.2% for LLS, and 3.1% for LSS, and for the transverse modulus, +7.5% for SLL, -5.4% for LLL, -3.2% for LLS, and -1.6% for LSS. The differences for the transverse modulus are less than those observed in the tension case. Based on these observations, it would appear that the modulus measured in the laminated specimen might be somewhat under-estimated, although no precise cause was found for this effect.

The comparison for unnotched longitudinal compression strength is shown in Figure 5.a to 5.c. As anticipated, a lower strength was obtained for all the braids: -14% for SLL, -28% for

LLL, -31% for LLS, and -16% for LSS. Once again, the tow waviness is a probable contributor to this loss of strength. Unlike in the tension case, the notched strength of the braids came in lower than that of the tape laminates in all cases. The comparison of the transverse strength shown in Figure 6.a to 6.c reveals the same poor performance of the braids that was also observed in the tension case. A strength reduction of up to 57% for the case of the LLL architecture was measured.

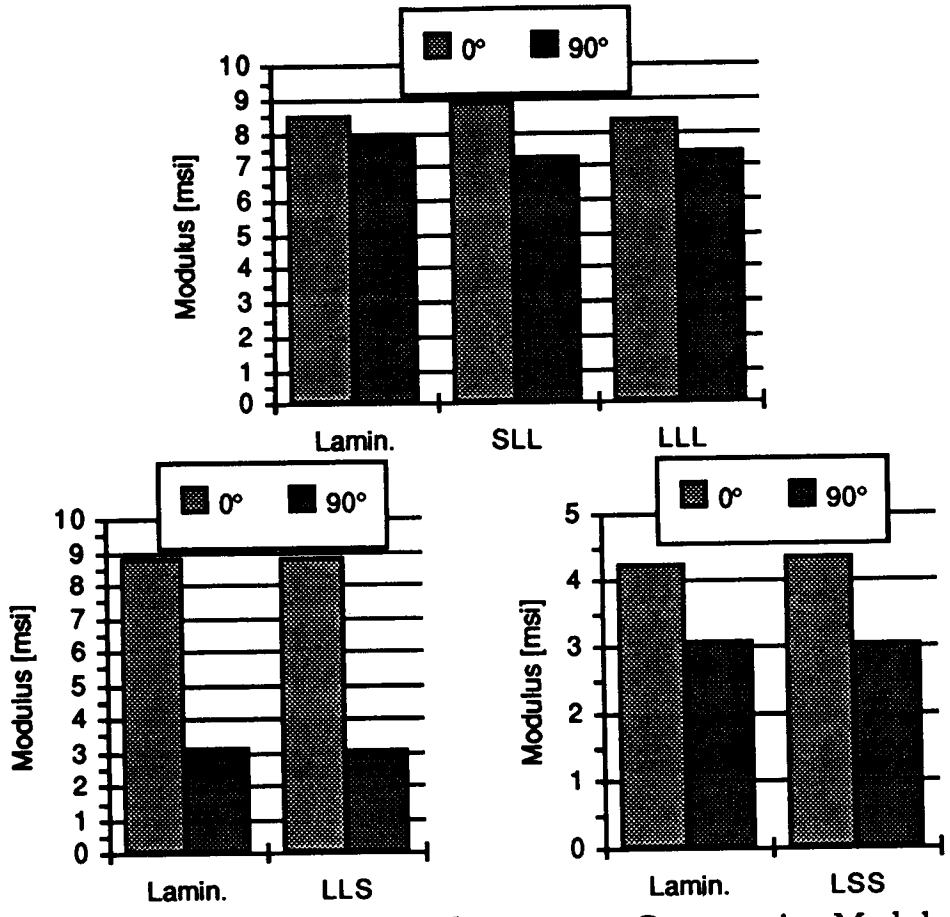

Figure 4 Comparison of Longitudinal and Transverse Compression Modulus.

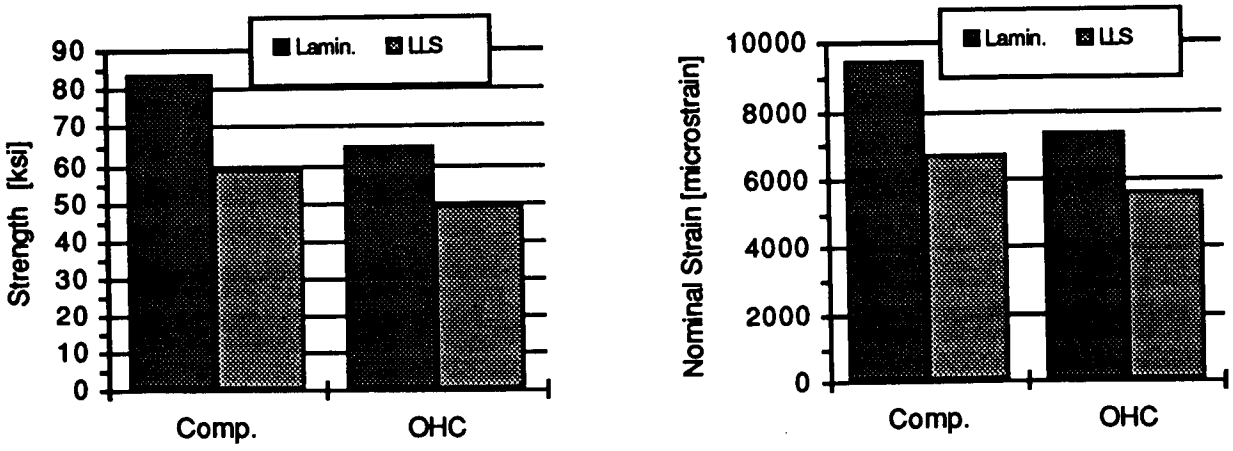

Figure 5.a Comparison of 0° Compression Strength for Tape Laminate 1, LLS.

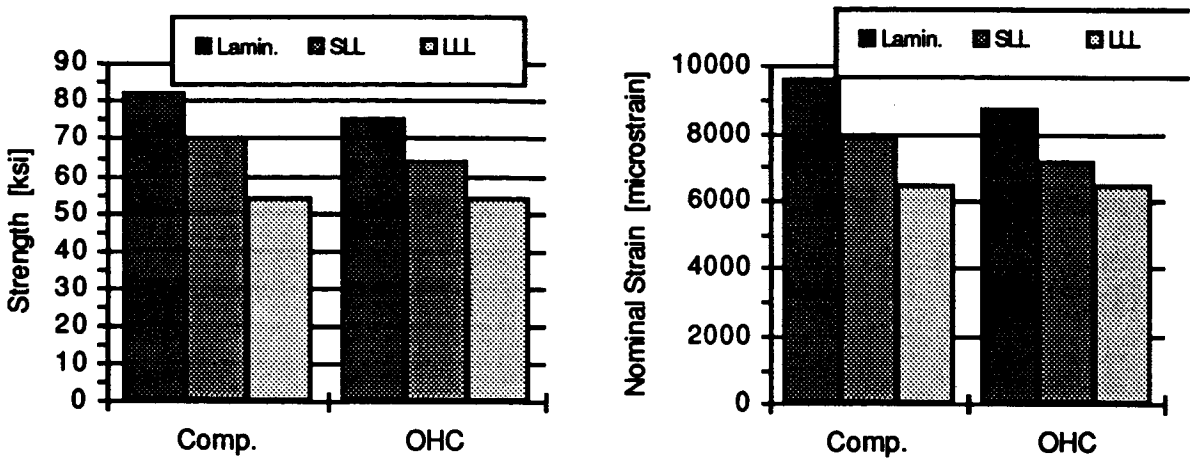

Figure 5.b Comparison of 0° Compression Strength for Tape Laminate 2, SLL and LLL.

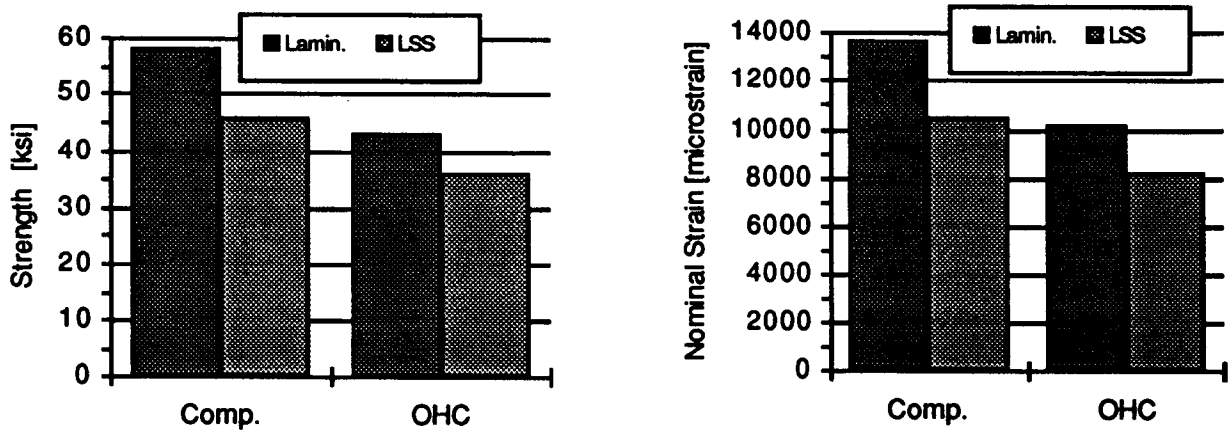

Figure 5.c Comparison of 0° Compression Strength for Tape Laminate 3, LSS.

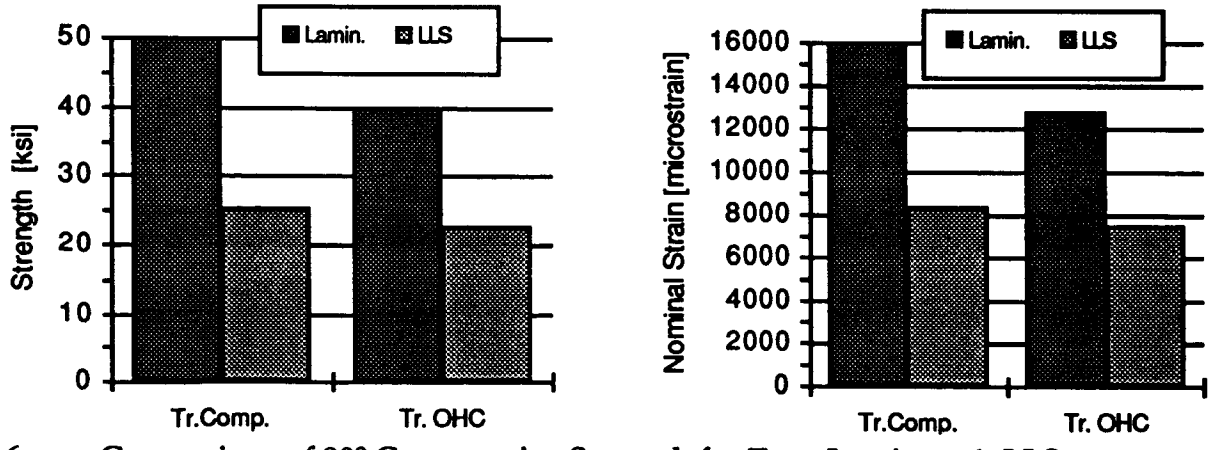

Figure 6.a Comparison of 90° Compression Strength for Tape Laminate 1, LLS.

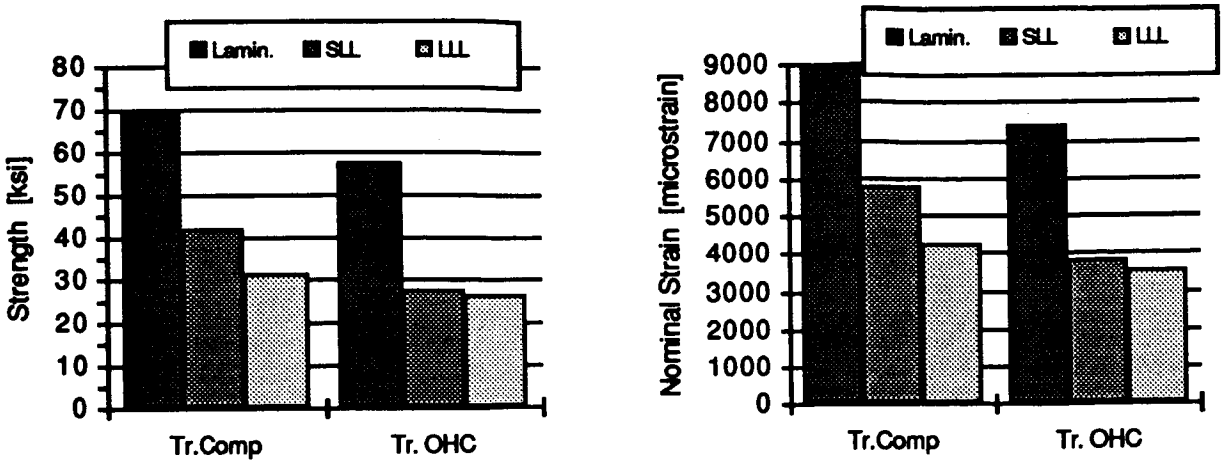

Figure 6.b Comparison of 90° Compression Strength for Tape Laminate 2, SLL and LLL.

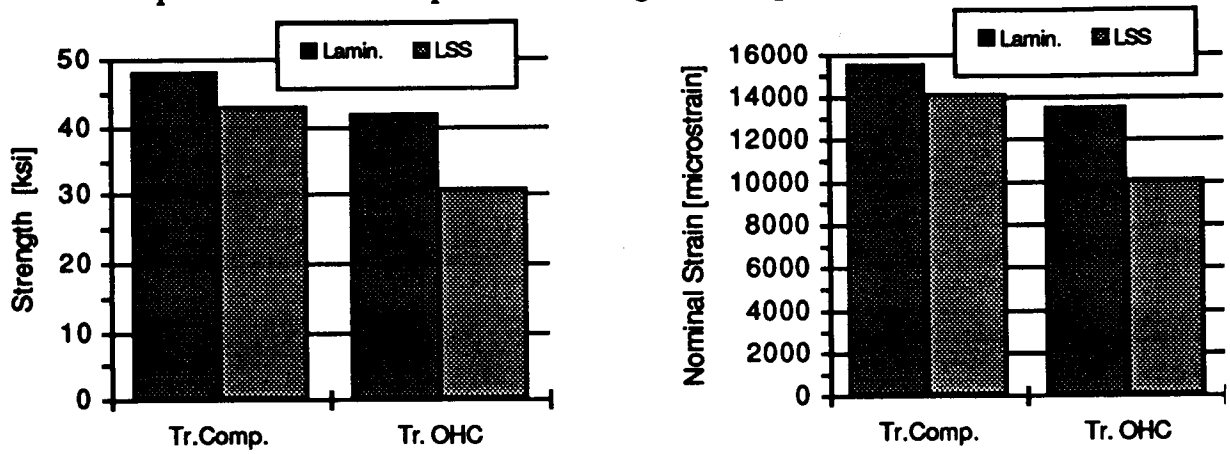

Figure 6.c Comparison of 90° Compression Strength for Tape Laminate 3, LSS.

SUMMARY

Results of the comparison between the two material forms show that the longitudinal modulus of both material forms is quite similar, but that the transverse modulus of the braids is lower. In terms of strength, the longitudinal unnotched strength of the braids is lower than that of the laminates. On the positive side, a very significant increase in open-hole and filled-hole tension strength was observed for the braids compared to the tape laminates. However, this was not observed in compression where all the braid properties are lower than for the laminates. The very low strength of the braids should be considered in more details and could be a concern depending on the type of structural application.

REFERENCES

1. Minguet, P.J., Fedro, M.J., Gunther, C.K., "Test Methods for Textile Composites", NASA CR-4609, July 1994.

2. Minguet, P.J., Gunther, C.K., "A Comparison of Graphite/Epoxy Tape Laminates and 2-D Braided Composites Mechanical Properties", NASA CR-4610, July 1994.

IMPACT TESTING OF TEXTILE COMPOSITE MATERIALS

by

Marc Portanova
Lockheed Engineering & Science

Presented at:
Textile Mechanic Working Group Meeting

December 6 - 8, 1994

OUTLINE

Objective

Approach

Description of Materials

Test Specimen Configurations

Test Methods

Results
- Damage Resistance
  - C-Scan Damage Area
  - Impact Force
- Damage Tolerance
  - Compression & Tension After Impact
  - Residual Strength

Summary of Findings

Objectives:

To evaluate the Impact Damage Resistance & Damage Tolerance of various Textile Composite Materials.

Program Methodology

Static Indentation Tests

- Perform Repeated Static Indentation tests to obtain various amounts of damage.
- Document the Damage Resistance of each of the material forms.
- Calculate the falling weight impact energies to produce the same amounts of damage.

Falling Weight Impact Tests

- Impact coupons at the energy levels calculated from the Static Indentation tests.
- Document the Damage Resistance of each of the material forms.

Compression & Tension After Impact Tests

- Measure and compare the residual strength after impact of these materials.
- Document the Damage Tolerance of each of the material forms.

Stitched & Unstitched Uniweaves

Stitched & Unstitched Uniweave Constructed From AS4/3501-6 Carbon/Epoxy.

A 225 denier fiberglass yarn was woven in the fill direction to hold the fibers together while stitching.

Stitching was done with a 1250 yd/lb fiberglass yarn at 8 penetrations per inch, each spaced 1/8 inch apart.

Four quasi-isotropic layups:

		Avg. Thickness, in.	
		Stitched	Unstitched
48 ply	$[45°/0°/-45°/90°]_{6s}$	0.297	0.262
32 ply	$[45°/0°/-45°/90°]_{4s}$	0.203	0.178
24 ply	$[45°/0°/-45°/90°]_{3s}$	0.155	0.135
16 ply	$[45°/0°/-45°/90°]_{2s}$	0.102	0.091

2-D Triaxial Braid Configurations

Material	Braid Code	Braid Yarn Size	Percent 0° Yarns	Braid Pattern	0° Yarn Size	Avg. Thickness, in.
SLL	[030K/±706K]46	6K	46	0±70	30K	0.225
LLL	[075K/±7015K]46	15K	46	0±70	75K	0.220
LLS	[036K/±4515K]46	15K	46	0±45	36K	0.251
LSS	[06K/±4515K]12	15K	12	0±45	6K	0.220

[0XXK / ±TXXK] Y % Axial

Where: XX indicates the yarn size, K indicates thousands
Y indicates the percentage of axial yarns in the preform.

3-D Woven Preform Configurations

TS1 & TS2 Through-the-Thickness Angle Interlock

LS1 & LS2 Layer-to-Layer Angle Interlock

OS1 & OS2 Through-the-Thickness Orthogonal Interlock

Avg. Specimen Thicknesses, in.

TS1	0.229	LSI	0.223	OS1	0.225
TS2	0.222	LS2	0.227	OS2	0.231

Basically:
"1" have Larger Yarns with Fewer Yarns/in. and Fewer Layers Than "2".
Yarn % Areal Wt. was about equal between the 1 & 2 configurations.

SPECIMEN CONFIGURATIONS

Static Indentation & Falling Weight Coupons

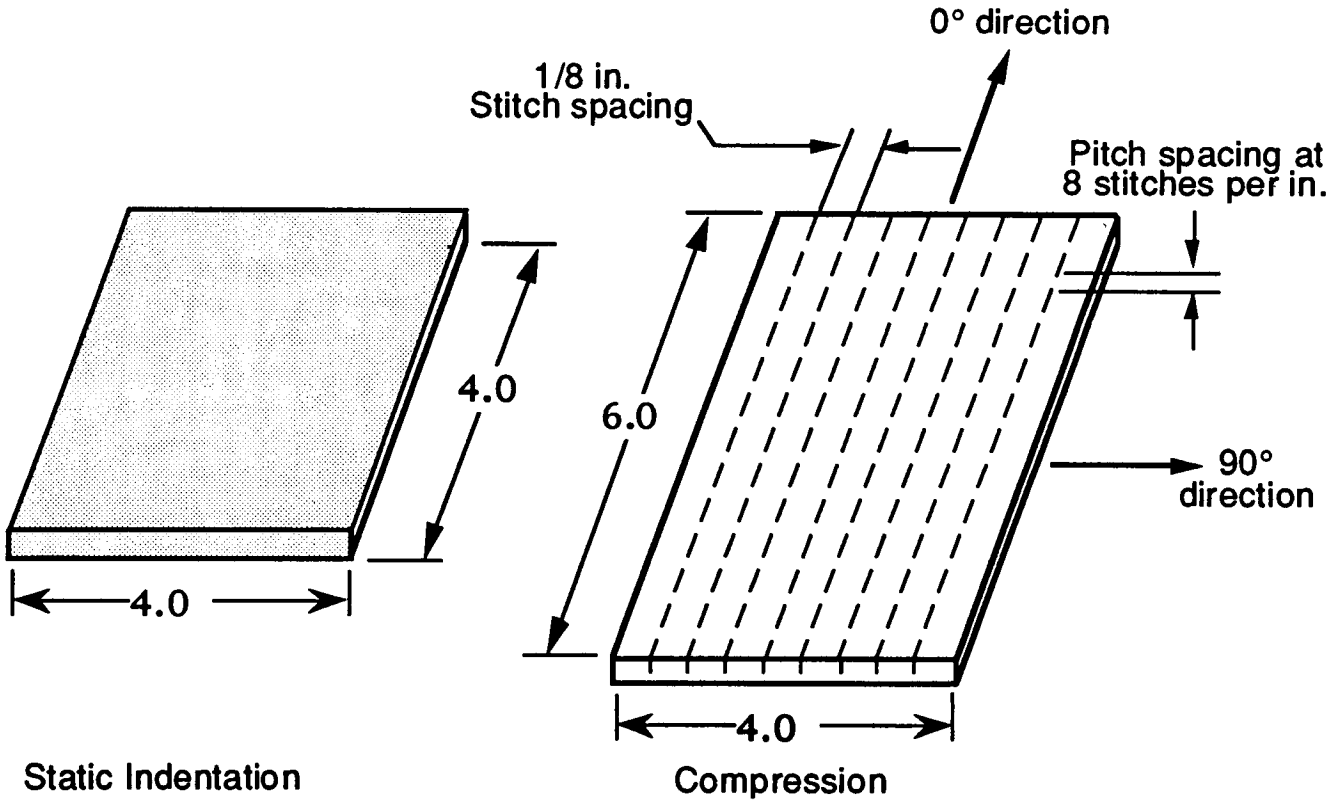

Test Specimen Configurations were as shown. The static indentation coupons were 4.0 in. square. The CAI & TAI were 4.0 in. wide and 6.0 or 10.0 inch long, respectively.

Impact Methods

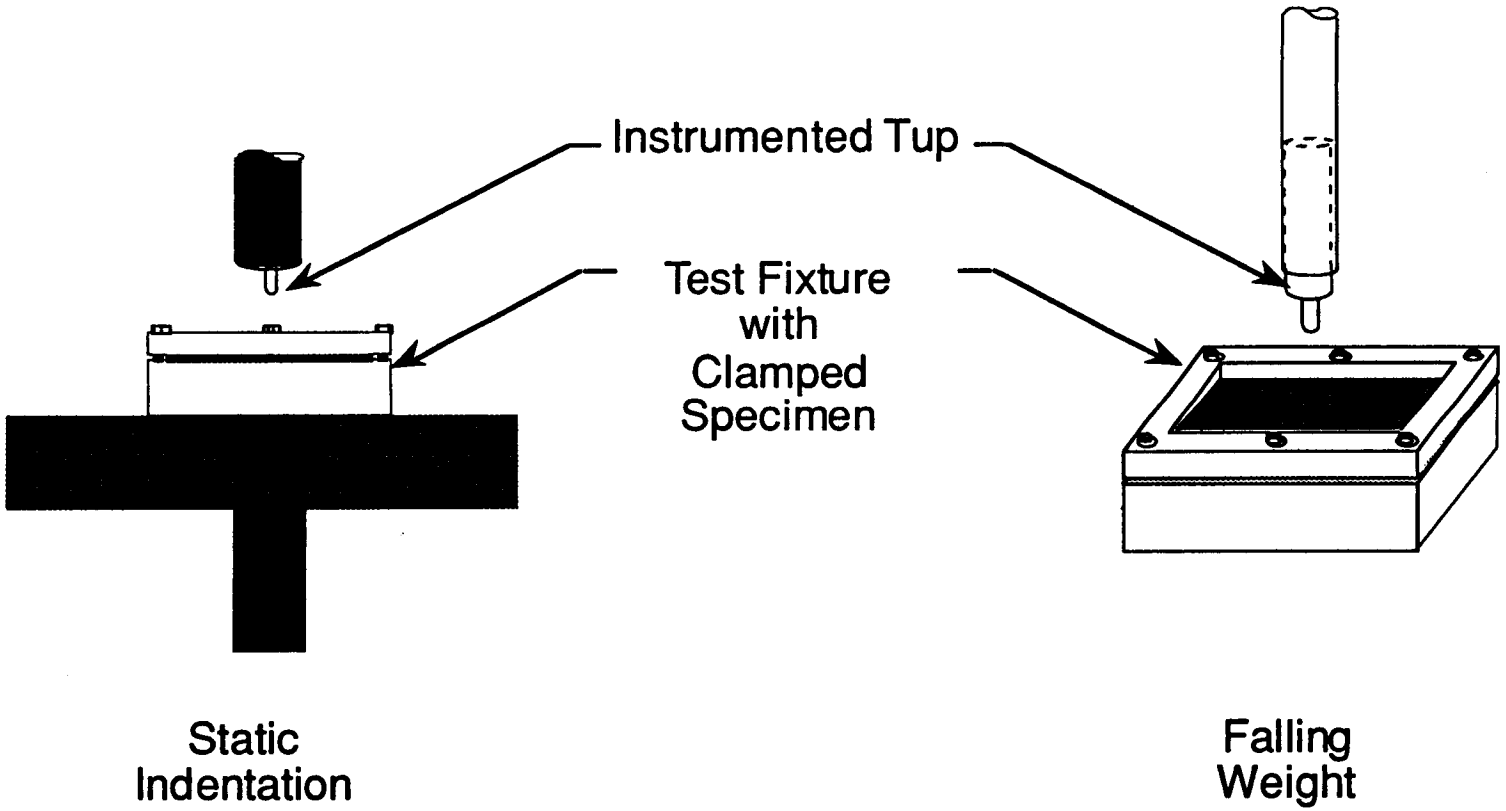

Both Static Indentation and Falling Weight Impacts were performed. Both testing methods used the same instrumented tup, 1/2" diameter tip, and clamped aluminum test frames.

Static Indentation Tests
32 ply Unstitched Uniweave

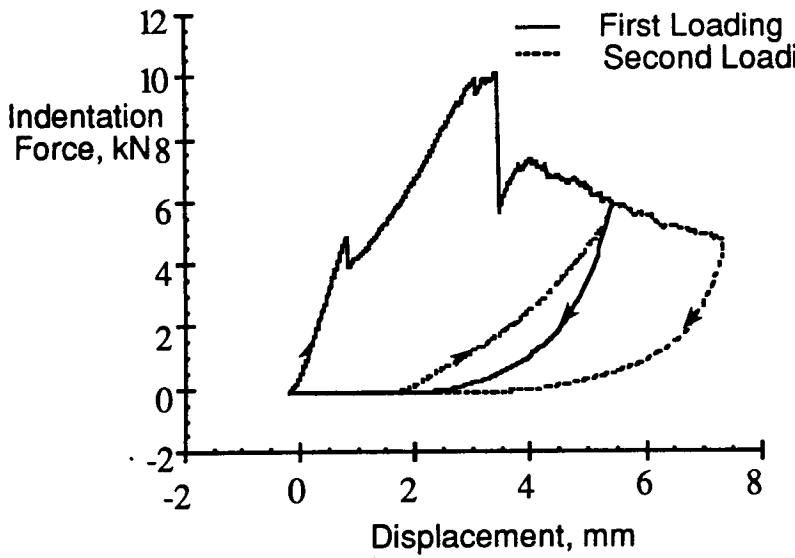

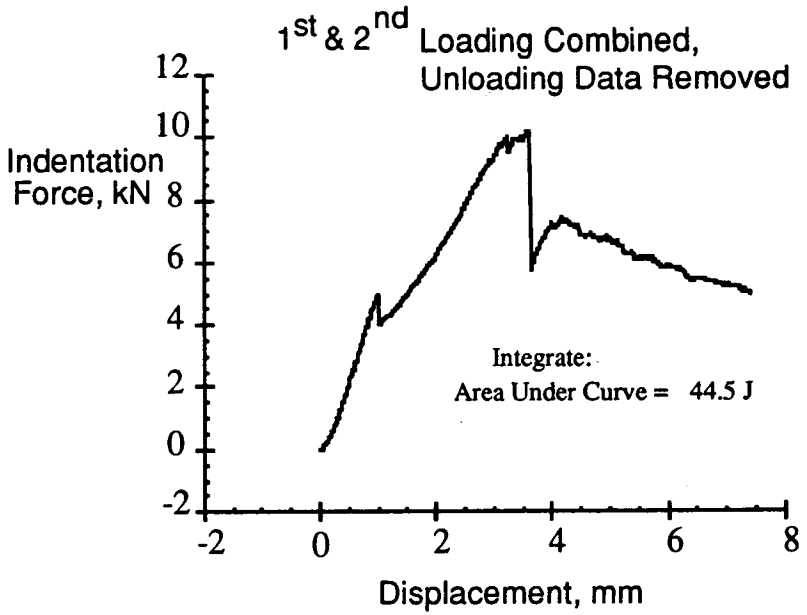

Data, taken from static indentation tests such as these, were used to determine the falling weight energies required to produce pre-determined amounts of damage in the Uniwoven materials. Energies were calculated to produce on average both 0.10 inch dent depths and a barely measurable surface dent, dents on the order of a few thousands of an inch. For the purpose of this presentation, the terms "Severe Impact Damage" refers to impacts sufficient to produce average dent depth in the uniweaves of 0.10 inch. The term "Barely Visible Damage" refers to impact energies sufficient to produce damage barely measurable by C-Scan. The average dent depths for each of the impact energies used on each of the various material architecture's are given elsewhere.

Falling Weight Impact Energies For Uniweaves

	BVD	Mean	SID
48 ply Stitched 48 ply Unstitched	15.39 ft•lbs	39.12 ft•lbs	62.86 ft•lbs
32 ply Stitched 32 ply Unstitched	7.29 ft•lbs	18.77 ft•lbs	30.26 ft•lbs
24 ply Stitched 24 ply Unstitched	5.48 ft•lbs	13.29 ft•lbs	21.11 ft•lbs
16 ply Stitched 16 ply Unstitched	3.00 ft•lbs	7.43 ft•lbs	11.87 ft•lbs

BVD : Barely Visible Damage, Dent depths ≈ 0.005 in.
Mean : Mean Impact Damage, Dent depths ≈ 0.04 in.
SID : Severe Impact Damage, Dent depths ≈ 0.10 in.

In order to isolate the effect of stitching, impact energies were kept constant between the stitched and unstitched specimens for each of the different ply counts.

Falling Weight Impact Energies For Braids & Weaves

	BVD	SID
2-D Braids	15.39 ft•lbs	62.86 ft•lbs
3-D Weaves	15.39 ft•lbs	62.86 ft•lbs

BVD: Barely Visible Damage, Dent depths ≈ 0.009 in.
SID: Severe Impact Damage, Dent depths ≈ Penetration.

The 2-D Braids and 3-D Weaves had an average plate thickness only slightly thinner than that of the 48 ply Unstitched Uniweaves. In order to make a comparison of the Impact Damage Resistance & Impact Damage Tolerance of these materials with that of the Uniweaves, impact energies were kept the same as what was used on the 48 ply Uniweaves. The "Barely Visible Damage" energy lever resulted in average dent depths slightly larger that obtained with the Uniweaves. The "Severe Impact Damage" energy level resulted in plate penetration in most cases.

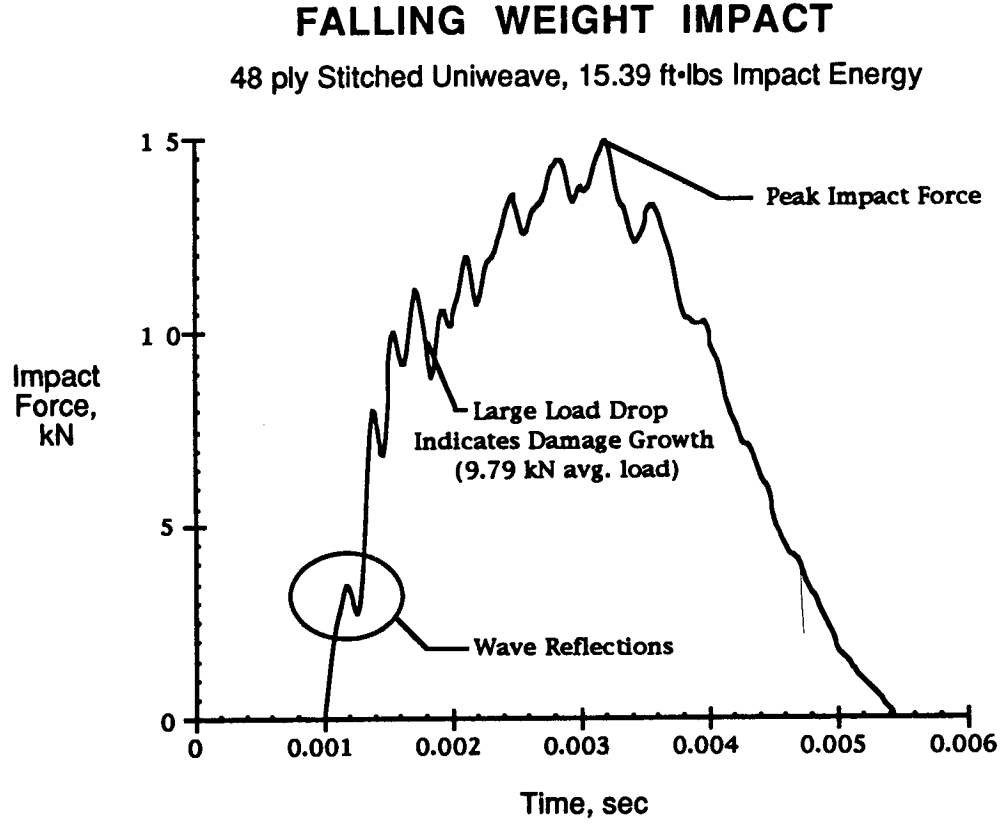

This a plot of Impact Force -vs- Time for a typical stitched uniweave. The amount of peak force obtained is a function of the extent of damage to the test coupon from the impact event. Lower peak energies imply that energy was absorbed by damage growth.

Compression After Impact Test Fixture

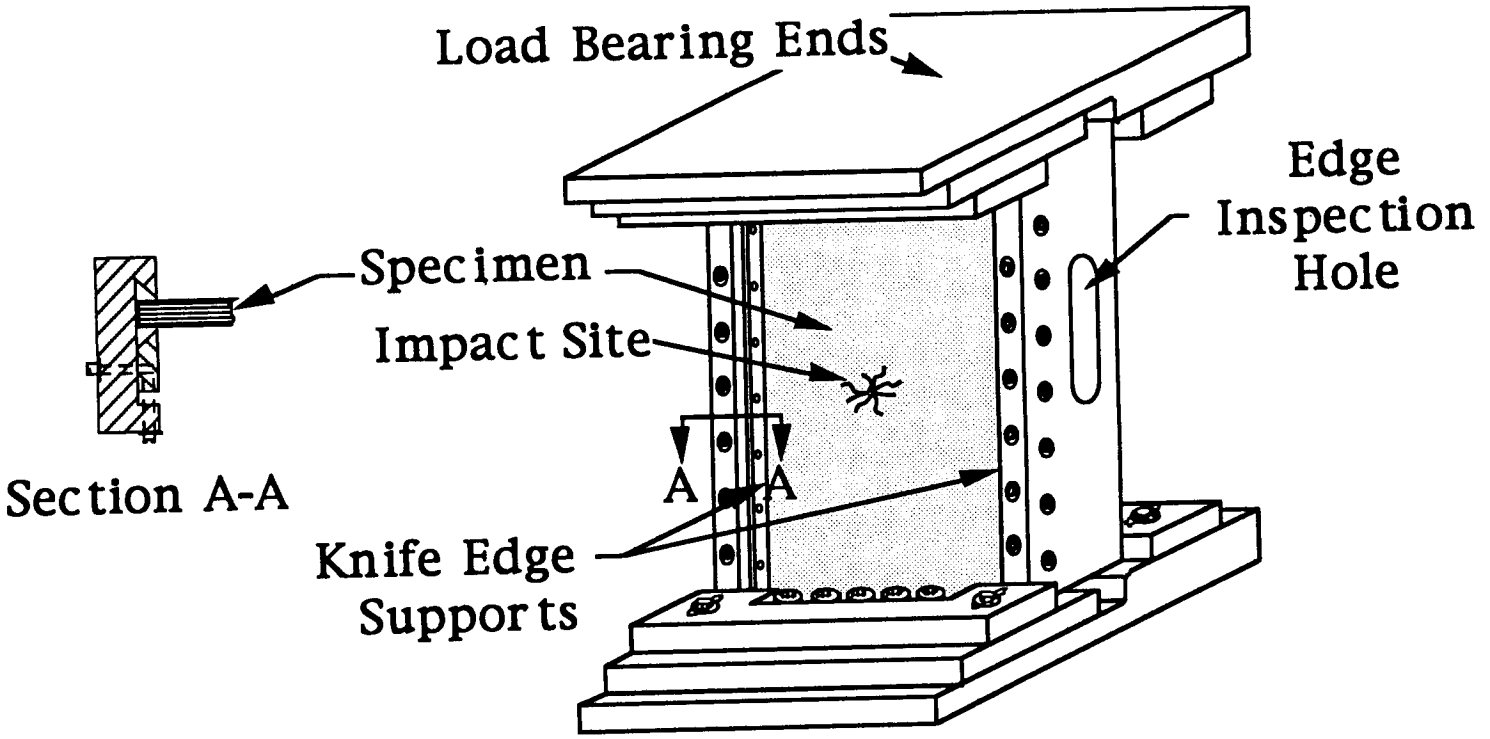

This standard NASA compression after impact test fixture was used to prevent buckling in the test coupon during loading. Obvious buckling was observed in the 16 ply coupons and some of the 24 ply coupons. Thus, the reported failure strengths will be lower than expected.

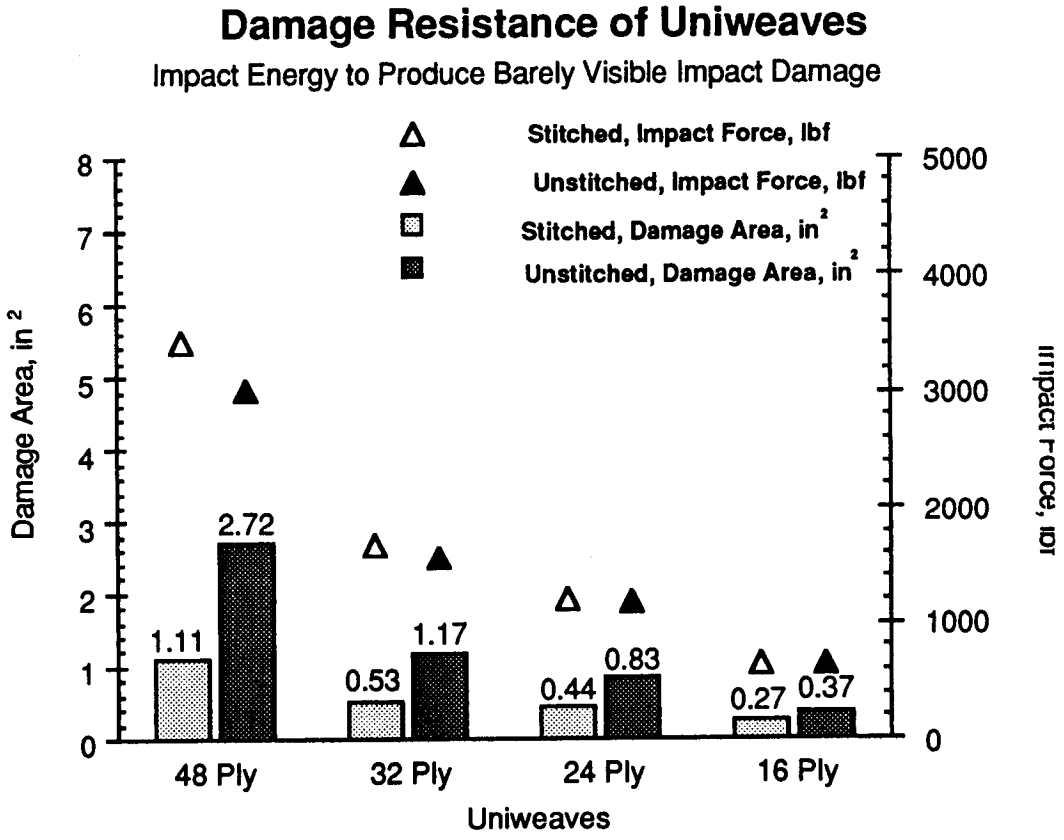

This is a plot of Damage Area and Impact Force versus each material type for both stitched and unstitched uniweaves impacted at an energy sufficient to produce "Barely Visible Impact Damage". Four different thicknesses are shown. Investigation of this figure shows that damage area was always larger without stitching. It is also observed that the peak impact force, obtained during the actual impact event, is always lower for the unstitched materials. Implying that damage growth increases with decreasing peak force. Thus, stitching has improved the materials Damage Resistance.

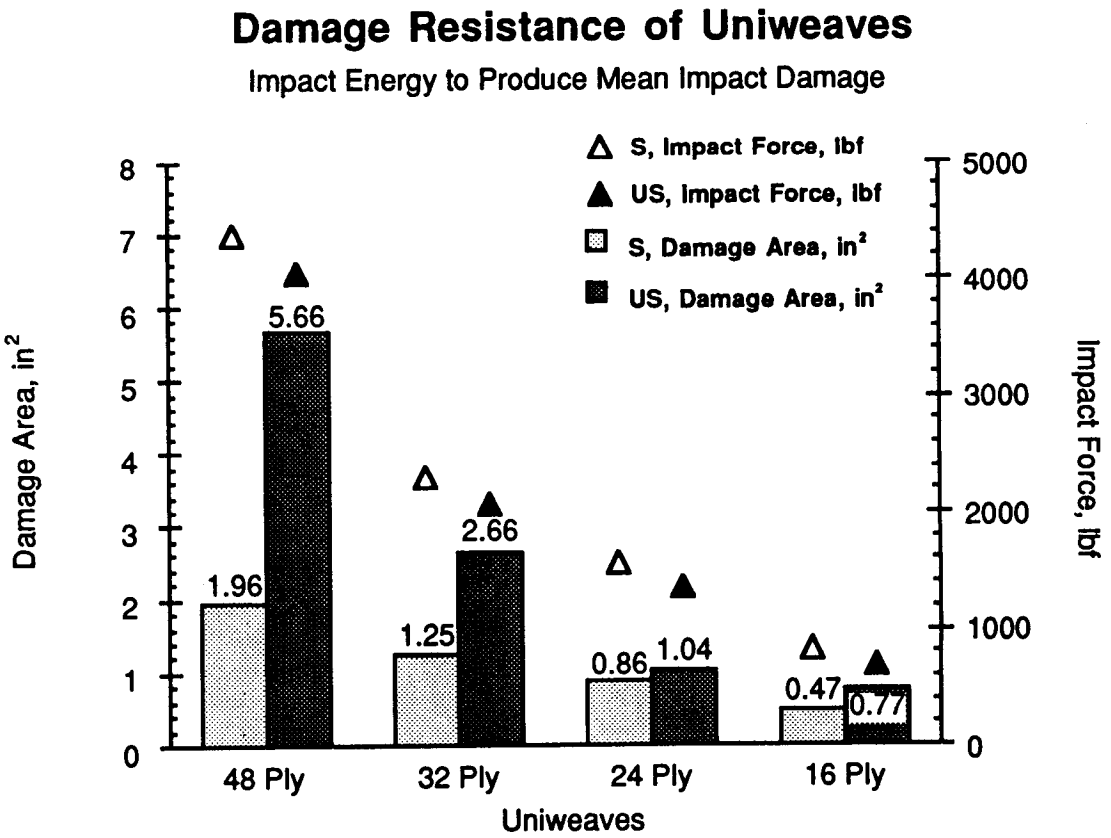

This is a plot of Damage Area and Impact Force versus each material type for both stitched and unstitched uniweaves impacted at an energy sufficient to produce "Mean Impact Damage". All four ply thicknesses are shown. Again the damage resistance is improved by stitching. Damage areas are smaller and peak impact energies are higher in all cases. In this figure there is also a plate thickness effect shown. As the plate thickness increases, so does the improvement in damage resistance.

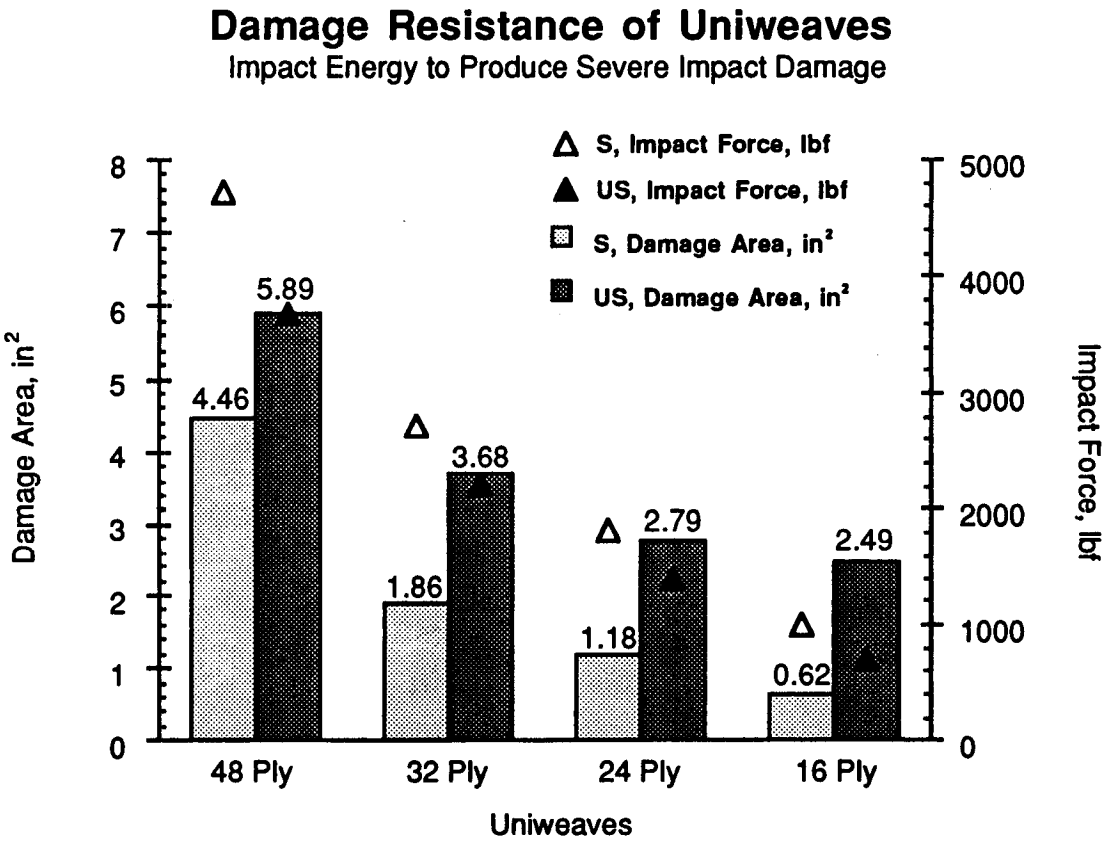

This is a plot of Damage Area and Impact Force versus each material type for both stitched and unstitched uniweaves impacted at an energy sufficient to produce "Severe Impact Damage". All four ply thicknesses are shown. Damage resistance is again improved by stitching. Damage areas are smaller and peak impact energies are higher for the stitched materials in all cases. Comparing this figure to the "Barely Visible Impact" energy level you will find that damage area increased almost 300% in the unstitched materials but only about 200% with the stitched uniweaves.

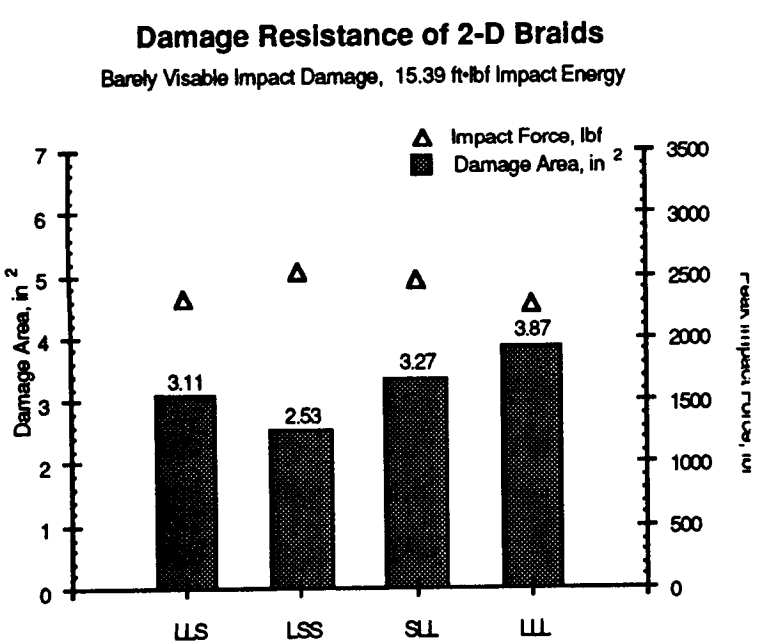

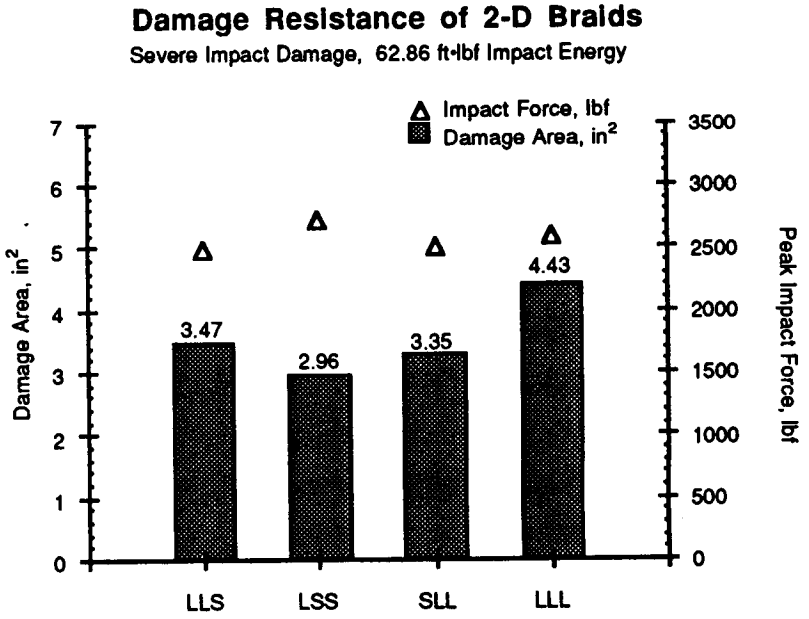

The figure on the left is a plot of Damage Area and Impact Force versus each material type for the 2-D Braids impacted at an energy sufficient to produce "Barely Visible Impact Damage". The figure on the right is the same as the first figure but at the elevated impact level to produce "Severe Impact Damage". All four braid types are compared. Damage areas were large as compared with the other material forms at the lower impact level but damage area only increased 11% between the BVD and SID energy levels. There were no obvious improvements in Damage Resistance by varying the braiding perimeters. The LSS architecture, which contained the smaller sized tows, did show the most resistance to damage growth but the extent of damage was still fairly severe.

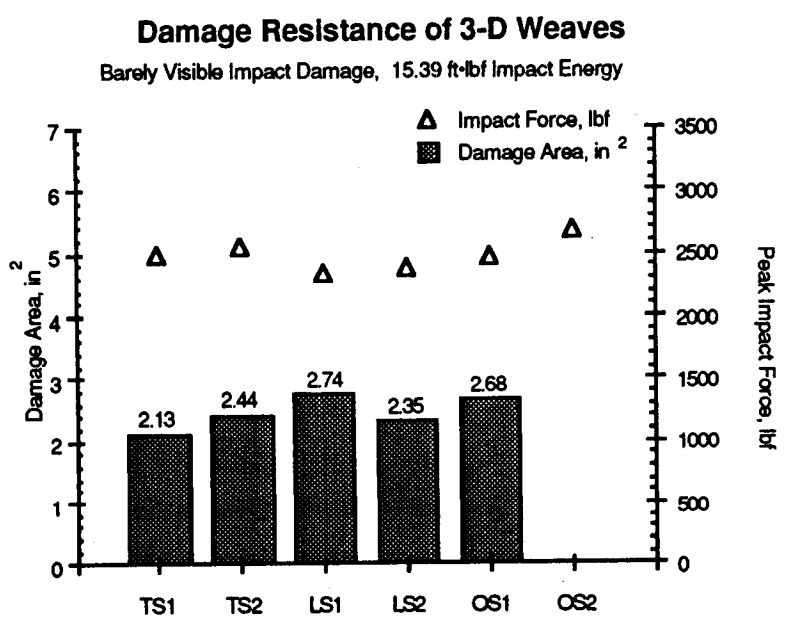

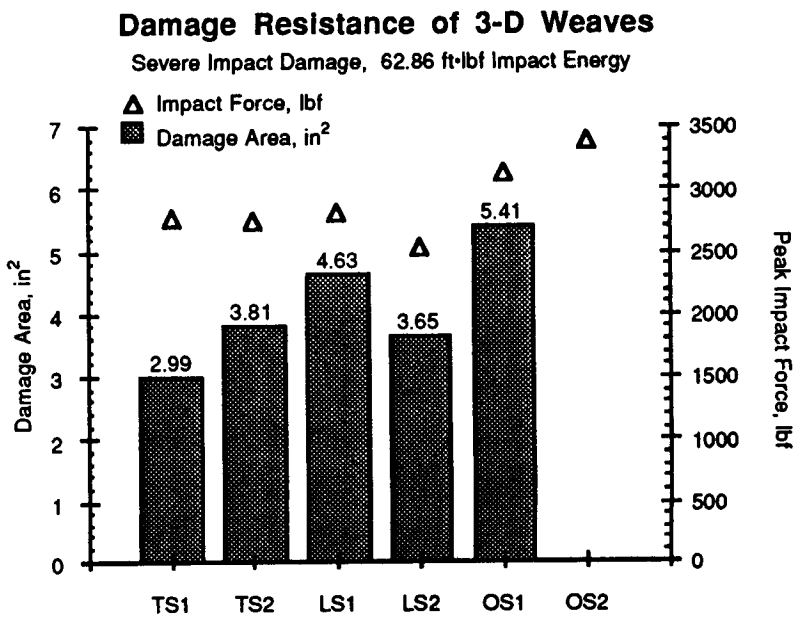

These are plots of Damage Area and Impact Force versus each material type for the 3-D Weaves impacted at the "Barely Visible Impact Damage" level on the left and the "Severe Impact Damage" level on the right. Five of the six weave types are compared. The OS2 material is absent due to the inability to acquire c-scan data on this material form. Damage resistance was improved over the Braids and Unstitched Uniweaves but not over the Stitched Uniweaves. There was a 64% increase in damage area between these two figures on the average. There appears to be an improvement in Damage Resistance with the TS# materials while the OS1 displays the worst response. It will later be shown that this trend reverses itself in a comparison of Damage Tolerance between these same two architecture's.

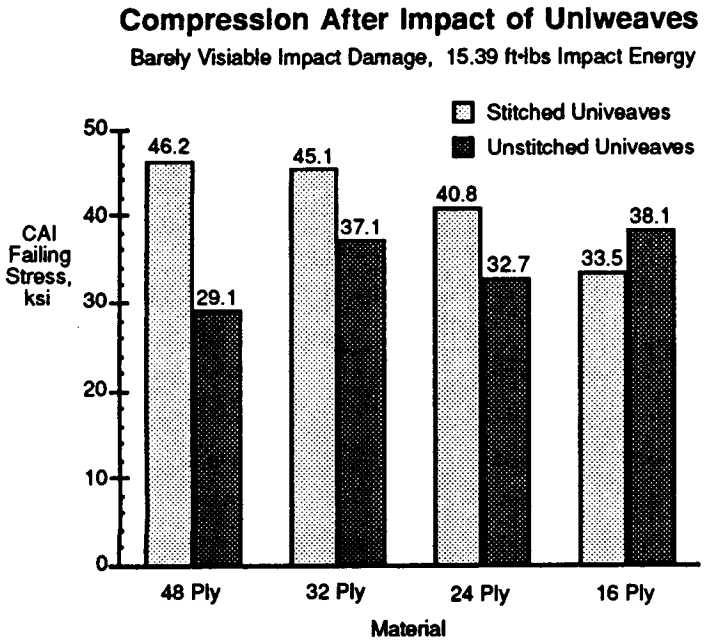

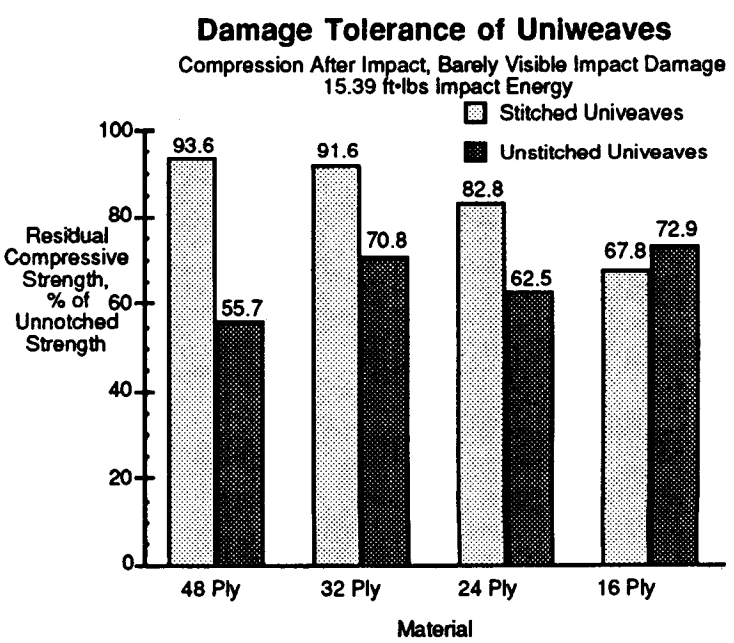

These two figures show an evaluation of the Compression Response of the Stitched & Unstitched Uniweaves, impacted at the lower "Barely Visible Impact Damage" energy level. On the left is a plot of the Compression after Impact (CAI) Strength versus each of the material forms and on the right is a plot of the residual strength where the CAI data has been normalized by it's unnotched strength. Noticeable bending was present in the 16 ply and some 24 ply specimens during loading thus, the failure strengths for these tests are low. Stitching appears to enhance this materials damage tolerance. An average of better than 91% retention in strength was had with the 48 ply materials. Compression strengths averaged better than 40 ksi demonstrating the ability to exceed current design criteria for commercial aircraft. Residual strength appears to improve with increasing plate thickness.

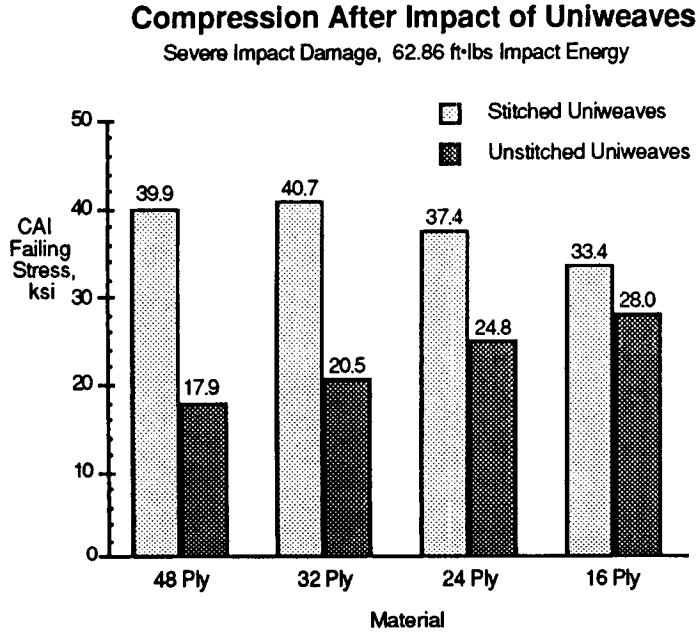

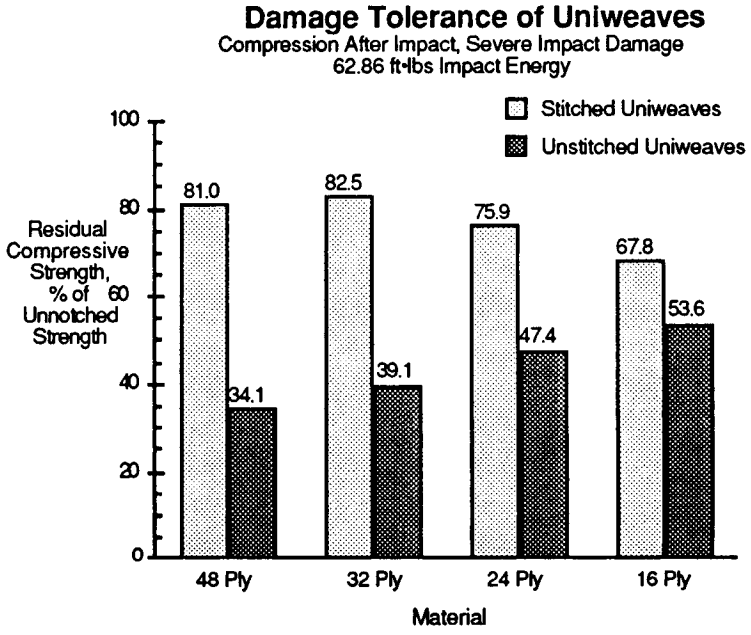

These two figures allow an evaluation of the Compression Response of the Stitched & Unstitched Uniweaves, impacted at the higher "Severe Impact Damage" energy level. On the left is a plot of the Compression after Impact (CAI) Strength versus each of the material forms and on the right is a plot of the residual strength where the CAI data has been normalized by it's unnotched strength. Stitching continues to enhance the damage tolerance capability of this material form. Even at this severe impact energy level, compression strengths were around the 40 Ksi threshold for design standards. Again, damage tolerance tended to improve with increasing plate thickness. Residual strengths were around 80% of the unnotched strength for the thicker 48 & 32 ply specimens but dropped with the thinner plates. The percent improvement in damage tolerance with stitching was greater at the higher impact energy level than that obtained at the lower impact energy.

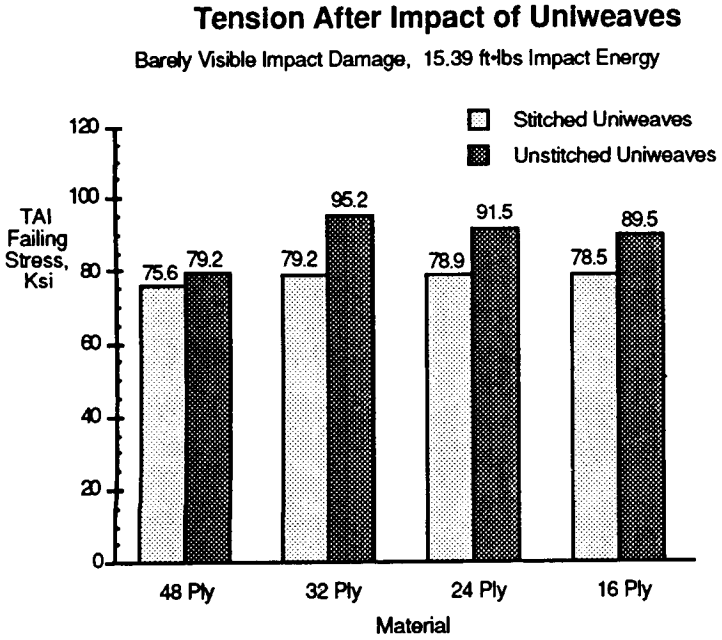

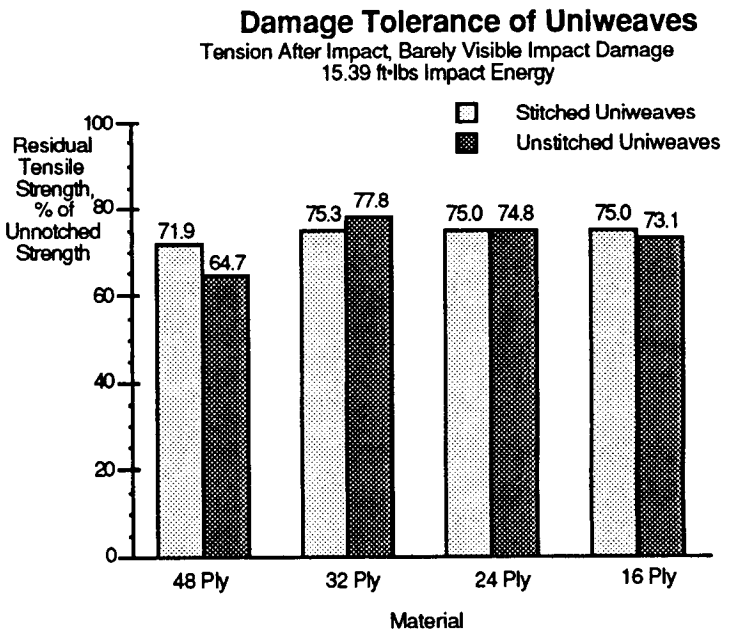

These two figures show an evaluation of the Tension Response of the Stitched & Unstitched Uniweaves impacted at the lower "Barely Visible Impact Damage" energy level. On the left is a plot of the Tension after Impact (TAI) Strength versus each of the material forms and on the right is a plot of the residual strength where the TAI data has been normalized by it's unnotched strength. Stitching didn't appear to enhance the TAI strength but did tend to improve the strength retention. The unstitched uniweaves had an average failure strength of 78 ksi and an average of 74 % strength retention while the stitched averaged 89 ksi failure strength and only 73% retention of unnotched strength. Thus, even though the failure strengths were lower, the strength retention was equal or slightly better.

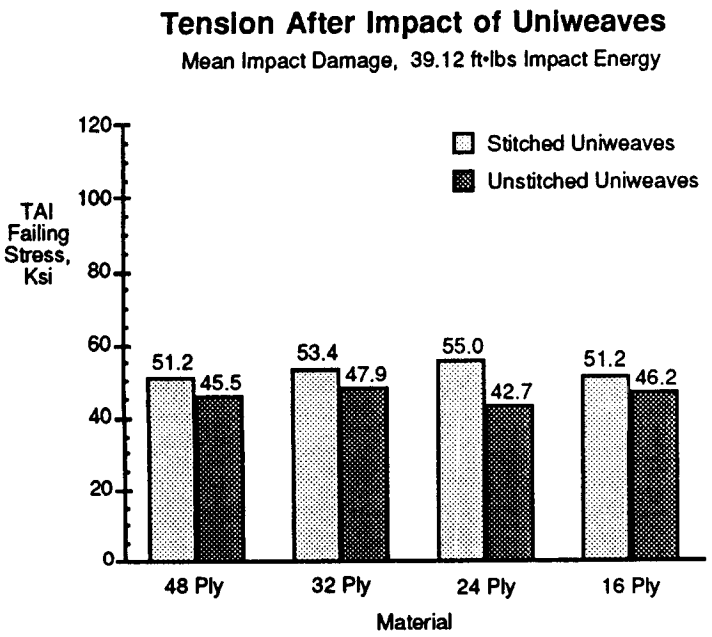

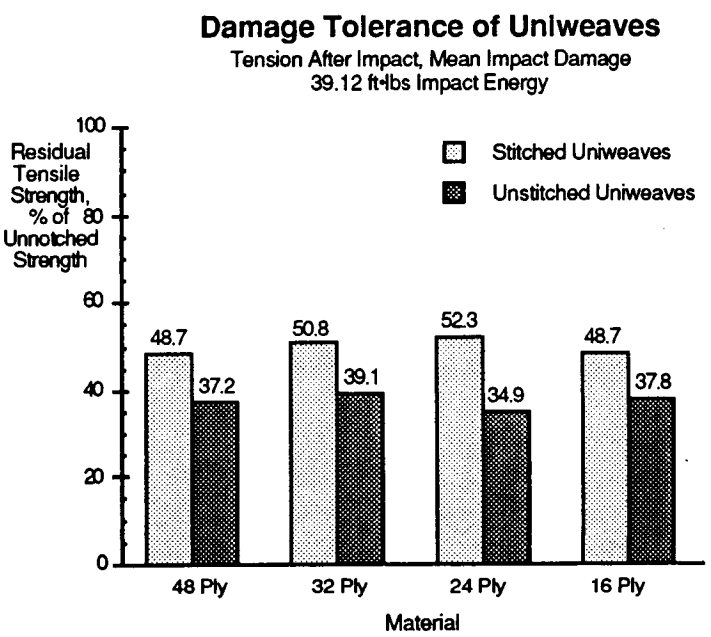

These two figures show an evaluation of the Tension Response of the Stitched & Unstitched Uniweaves impact at the "Mean Impact Damage" energy level. On the left is a plot of the Tension after Impact (TAI) Strength versus each of the material forms and on the right is a plot of the residual strength where the TAI data has been normalized by it's unnotched strength. At this median impact energy, stitching tended to improve both the TAI and residual strength of this material. With all ply counts, failing stresses were greater for the stitched uniweaves than the unstitched. In tension, these failure strengths were all well above the 40 ksi design allowable imposed by the commercial airframe manufactures. The percent residual strengths were also larger at this higher impact energy level. This implies that stitching may offer an improvement at the more extreme damage states while providing little or no improvement to specimens with little or no damage.

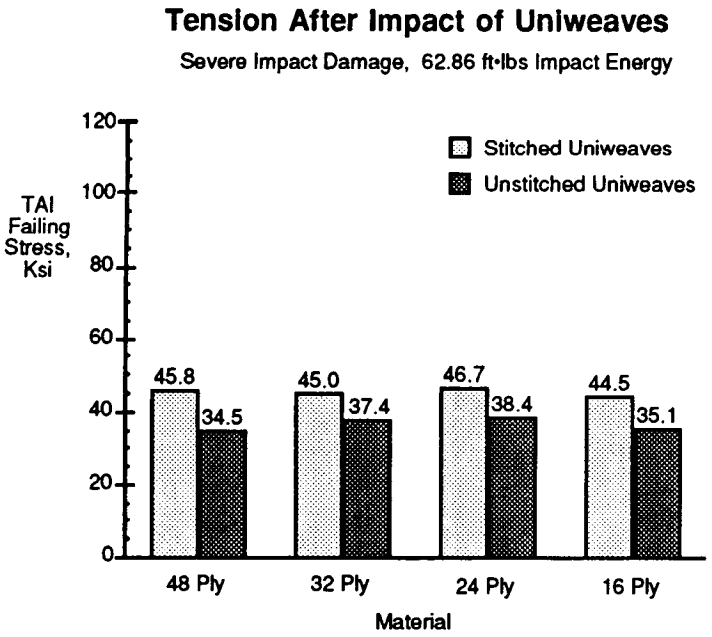

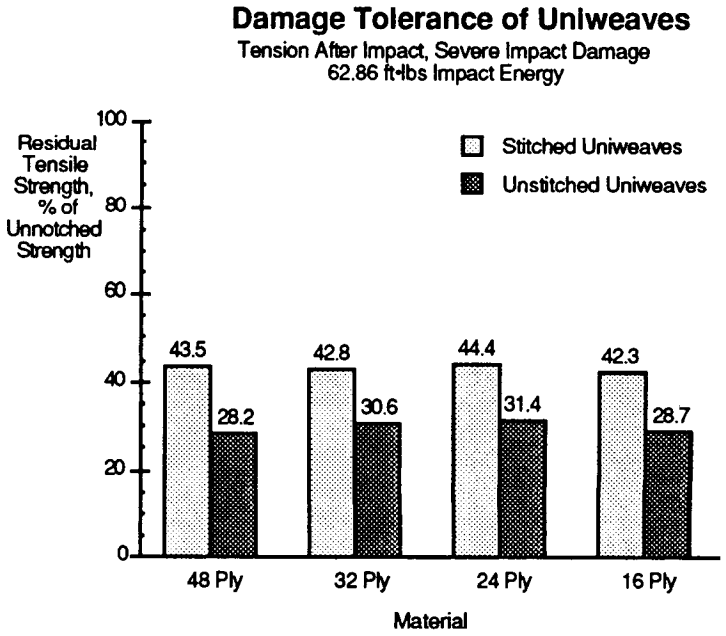

These two figures show an evaluation of the Tension Response of the Stitched & Unstitched Uniweaves impacted at the higher "Severe Impact Damage" energy level. On the left is a plot of the Tension after Impact (TAI) Strength versus each of the material forms and on the right is a plot of the residual strength where the TAI data has been normalized by it's unnotched strength. At the highest impact energy, stitching tended to improve both the TAI and residual strength of this material. Again failing stresses were greater for the stitched uniweaves than the unstitched. These failure strengths were all above the 40 ksi design allowable for the stitched materials. The percent of residual strength was also better with the stitched material. It is important to recall that stitching improved the CAI strength & compression Damage Resistance dramatically. In tension, stitching has not been shown to offer such improvements.

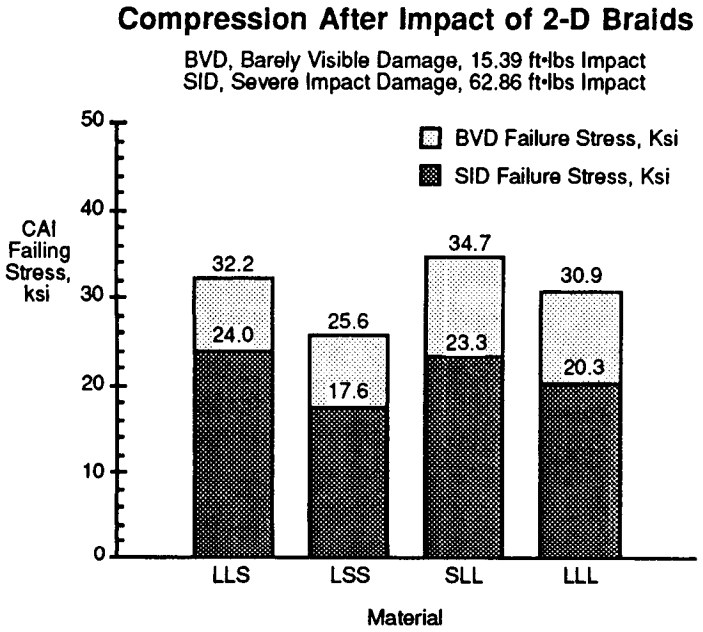

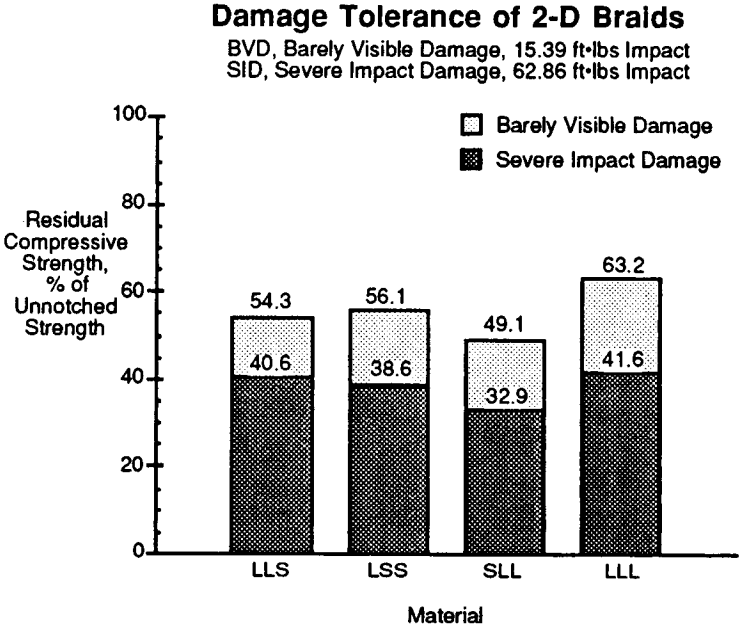

Compression After Impact (CAI) strength is plotted on the left while Residual Strength as a percent of unnotched strength is shown on the right for each of the four 2-D Braided architectures. Data for both the lower "Barely Visible Impact Damage" level and the upper "Severe Impact Damage" level are shown in each figure. Examination of these figures shows that the LSS architecture, which had the best Damage Resistance of the braids, has the least CAI strength. None of the 2-D Braids performed exemplary in either failing strength or percent of unnotched strength retention. Failing strengths, even at the lower impact energy, were all below the commercial airframe design allowable of 40 ksi. The residual strengths were also rather poor. The best residual strength performance was from the LLL architecture which coincidentally, had the worst Damage Resistance of the Braids. It retained only 63% of it's unnotched strength.

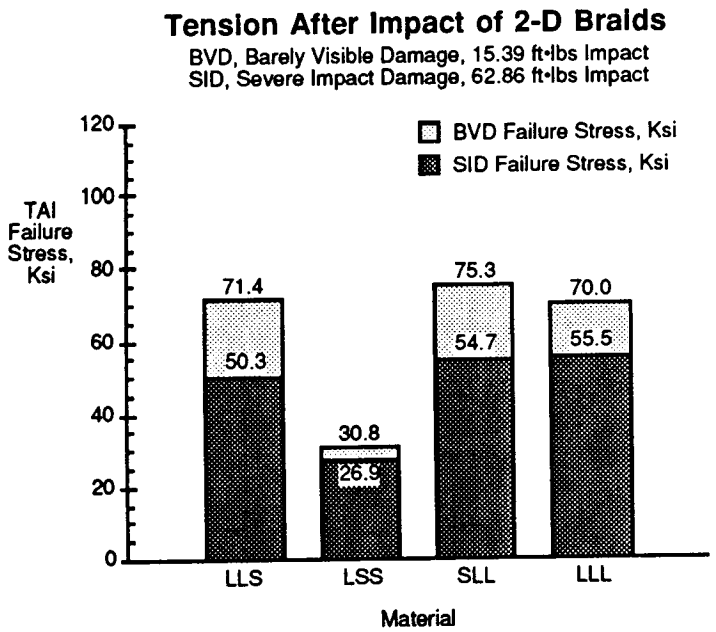

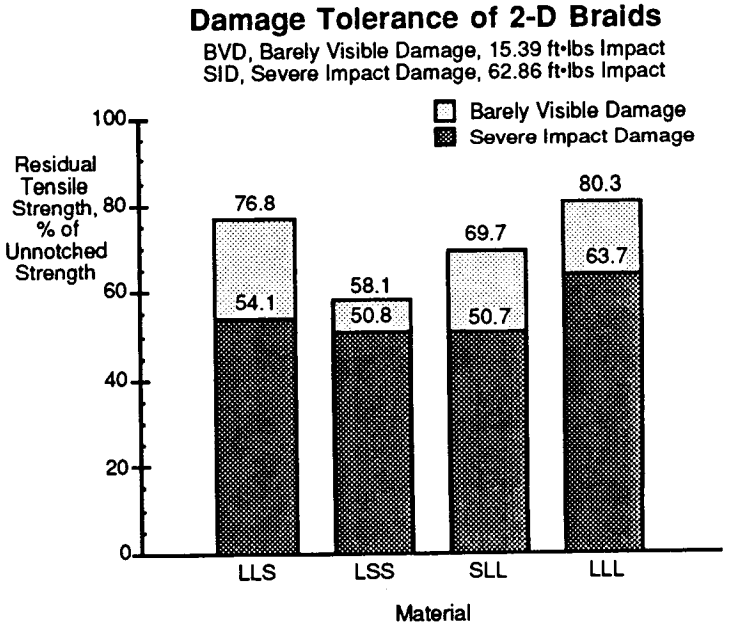

Tension After Impact (TAI) strength is plotted on the left while Residual Strength as a percent of unnotched strength is shown on the right for each of the four 2-D Braided architectures. Data for both the lower "Barely Visible Impact Damage" level and the upper "Severe Impact Damage" level are shown in each figure. Again the LSS has the lowest TAI strength but recall that while the other three architecture's have 46% axial yarns, the LSS has only 12%, thus accounting for the significantly lower failing stress. Also, the LLL again has the greatest percent retention of unnotched strength. Although the 2-D Braids performed significantly better in tension that in compression, there overall strength is still rather low. At the "Severe Impact Damage" impact energy, the average percent residual strength is only 16% less than at the lower impact energy level.

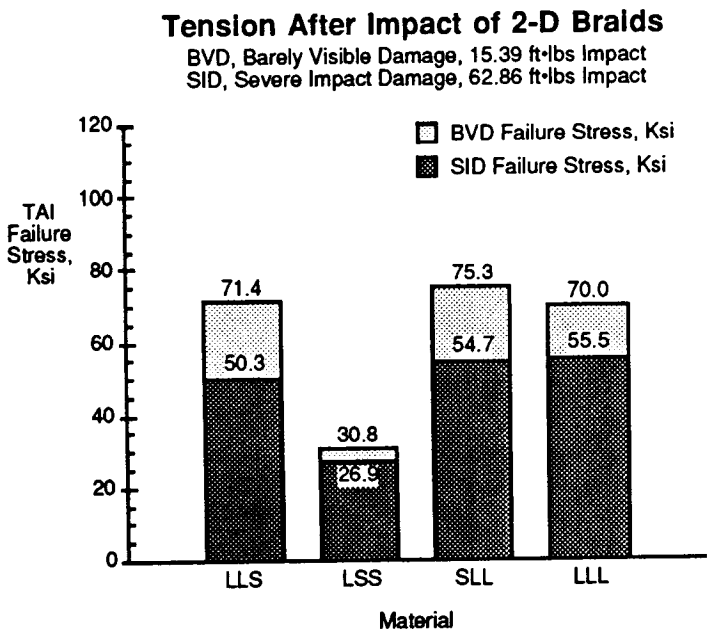

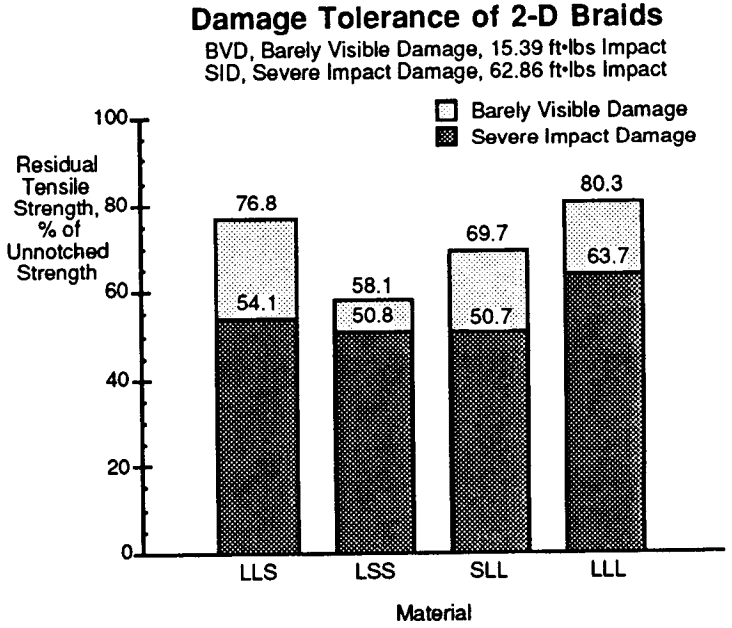

Tension After Impact (TAI) strength is plotted on the left while Residual Strength as a percent of unnotched strength is shown on the right for each of the four 2-D Braided architectures. Data for both the lower "Barely Visible Impact Damage" level and the upper "Severe Impact Damage" level are shown in each figure. Again the LSS has the lowest TAI strength but recall that while the other three architecture's have 46% axial yarns, the LSS has only 12%, thus accounting for the significantly lower failing stress. Also, the LLL again has the greatest percent retention of unnotched strength. Although the 2-D Braids performed significantly better in tension that in compression, there overall strength is still rather low. At the "Severe Impact Damage" impact energy, the average percent residual strength is only 16% less than at the lower impact energy level.

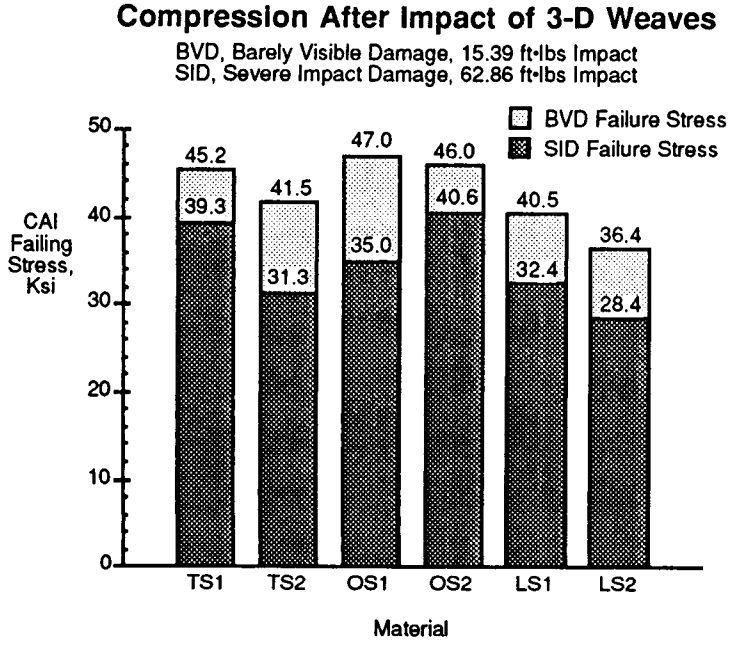

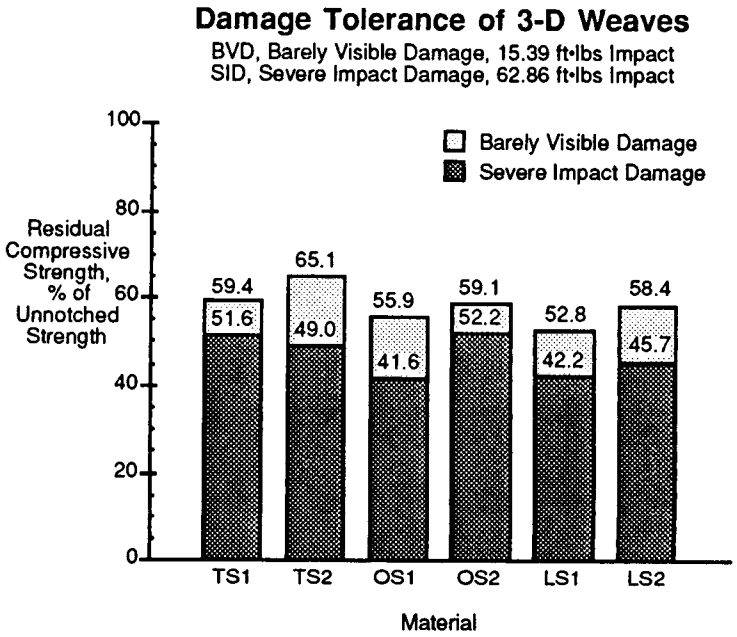

Compression After Impact (CAI) strength is plotted in the left figure and Residual Strength as a percent of unnotched strength is shown on the right figure for each of the six 3-D Weaves. Data from both the lower "Barely Visible Impact Damage" level and the upper "Severe Impact Damage" level are shown in each figure. The weaves outperformed the 2-D Braids and the Unstitched Uniweaves at both impact energy levels in compression. They compared about equally with the Stitched Uniweaves, having an a failing stress of greater that 40 ksi with the OS1 architecture at the highest impact energy. Recall that the OS1 architecture also demonstrated the best Damage Resistance of the 3-D Weaves. Residual strengths were better that those of the 2-D Braids, regardless of the impact energy level. The Unstitched Uniweaves retained a higher percentage of their unnotched strength than the 3-D Weaves at the lower impact energy level but not at the more severe level. The Stitched Uniweaves outperformed the 3-D Weaves in compression, regardless of the impact energy level compared.

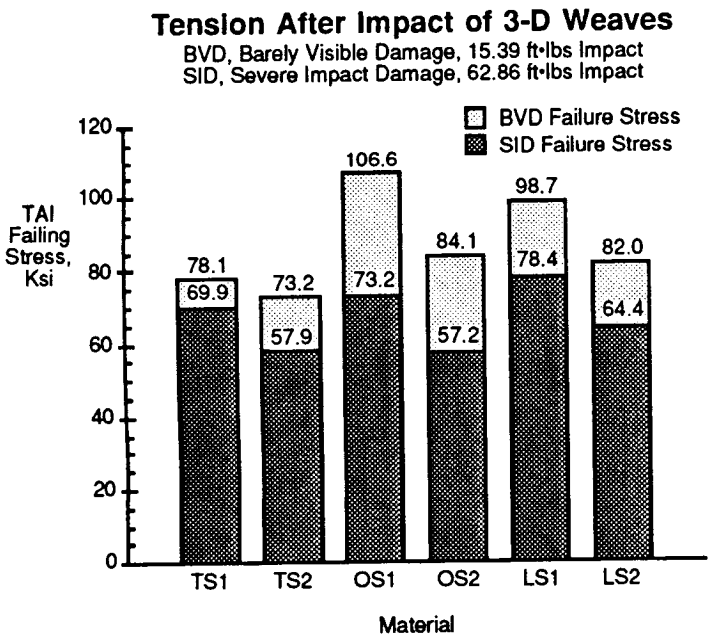

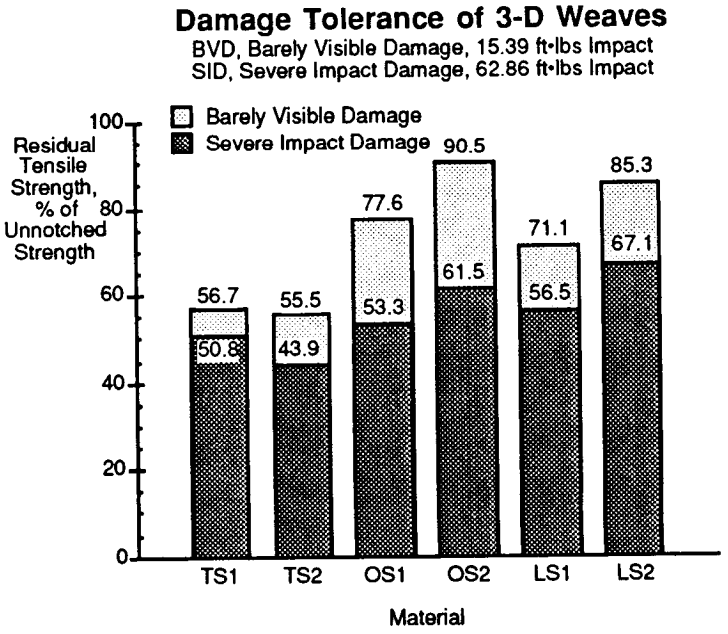

Tension After Impact (TAI) strength is plotted in the right left and Residual Strength as a percent of unnotched strength is shown on the right figure for each of the six 3-D Weaves. Data from both the lower "Barely Visible Impact Damage" level and the upper "Severe Impact Damage" level are shown in each figure. The 3-D Weaves tended to exhibit there best performance in tension. Although the extent of damage from impact was generally higher than that of many of the other material architecture's, the failing stresses obtained from these materials were typically higher. Failing stresses for the OS1 specimens averaged 106.6 ksi, far better that any other material form. Only the 32 ply Stitched Uniweave came within 10% of this value. The best performing 2-D Braid offered 30% less load carrying capability at the "Barely Visible Damage" impact level. With the residual strength comparison, the OS2 material retained better that 90% of it's unnotched strength. Again, outperforming any other architecture evaluated in tension.

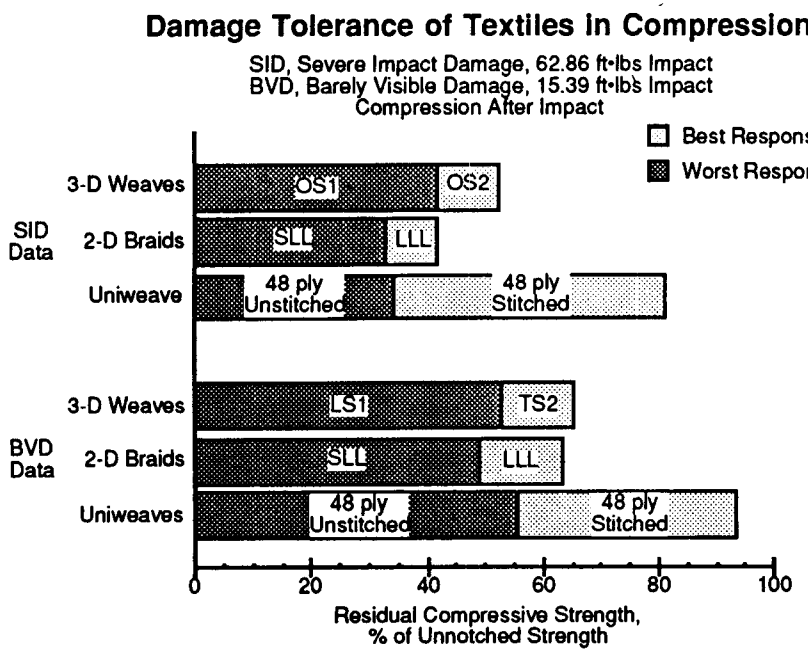

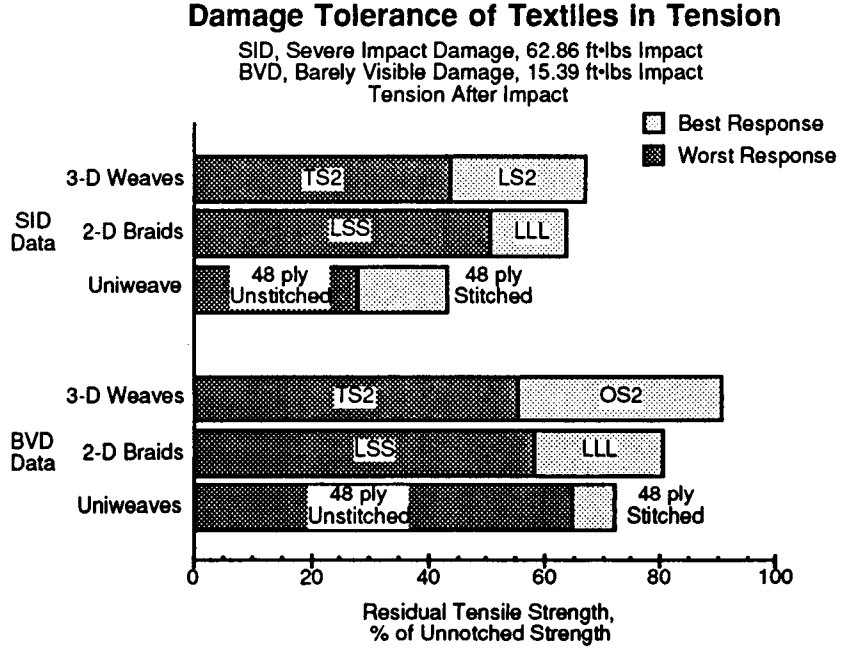

These two figures allow a comparison of the best and worst response to damage tolerance for all of the material architecture's in both tension and compression. The figure on the left shows the results from compression testing while the figure on the right is for the tension data. Both figures display results at both the "Severe Impact Damage" and "Barely Visible Damage" impact levels. Examination of these figures shows that stitching, which excels at reducing damage growth in compression, does not appear to enhance damage tolerance in tension. Overall, the 2-D Braids offer little tolerance to impact damage in compression but have moderately good response in tension. The 3-D Weaves, which offer reasonably good damage tolerance in compression, outperform all the other textile architecture's compared in tension. This result is surprising, given the poor damage resistance of these material forms.

Summary - Damage Resistance

Stitched & Unstitched Uniweaves

- Stitched Materials Had Less Damage Area and Higher peak Impact Force than Unstitched.
- Damage Resistance Increased with Plate Thickness.
- Unstitched 48 ply Had 189% More Damage Area Than Stitched 48 ply With Mean Impact Damage.

2-D Braids

- No Significant Difference Produced By Varying Any Of The Braiding Parameters.
- LLL Had 53% More Damage Area Than LSS with SID.

3-D Weaves

- No Significant Difference At Low Impact Energies.
- OS1 Had 53% More Damage Area Than TS1 with SID.

Summary - Damage Tolerance

Stitched & Unstitched Uniweaves

- Stitching: Improved CAI Strength at All Energy Levels.
  Improved TAI strength at Mean & SID levels.
- Stitching Improved Damage Tolerance in All Cases.
- Damage Tolerance Increased with Plate Thickness.
- Stitched 48 ply CAI retained 94% of unnotched strength.
- Stitched 48 ply TAI retained 72% of unnotched strength.

2-D Braids

- Residual Strength Better in Tension Than Compression.
- LLL retained 63% of Unnotched CAI strength with BVD.
- LLL retained 80% of Unnotched TAI strength with BVD.

3-D Weaves

- Residual Strength Better in Tension Than Compression.
- TS2 retained 65% of Unnotched CAI strength with BVD.
- OS2 retained 90% of Unnotched TAI strength with BVD.

DAMAGE TOLERANCE OF TEXTILES IN COMPRESSION

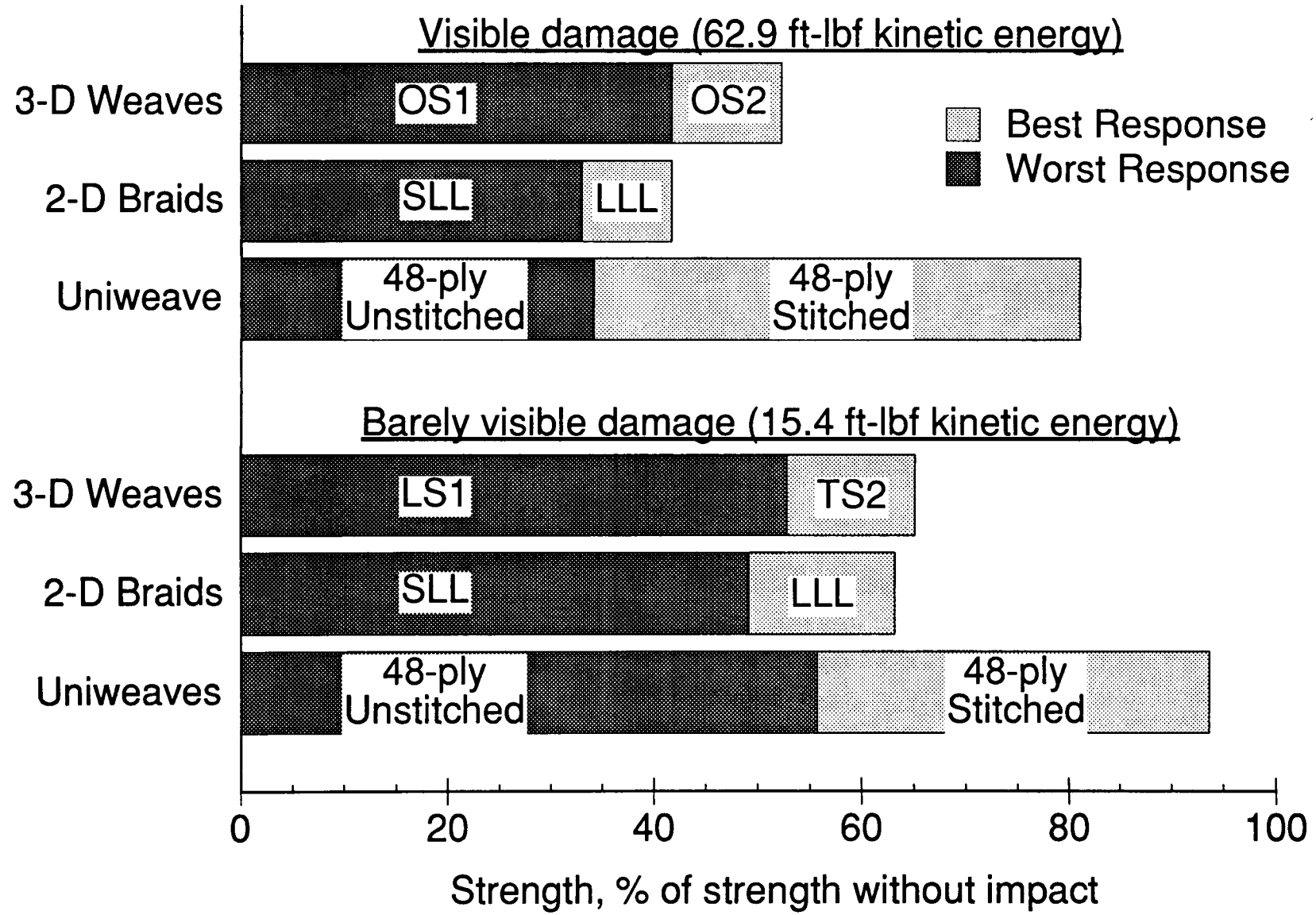

Plot BVD & SID % Residual CAI

DAMAGE TOLERANCE OF TEXTILES IN TENSION

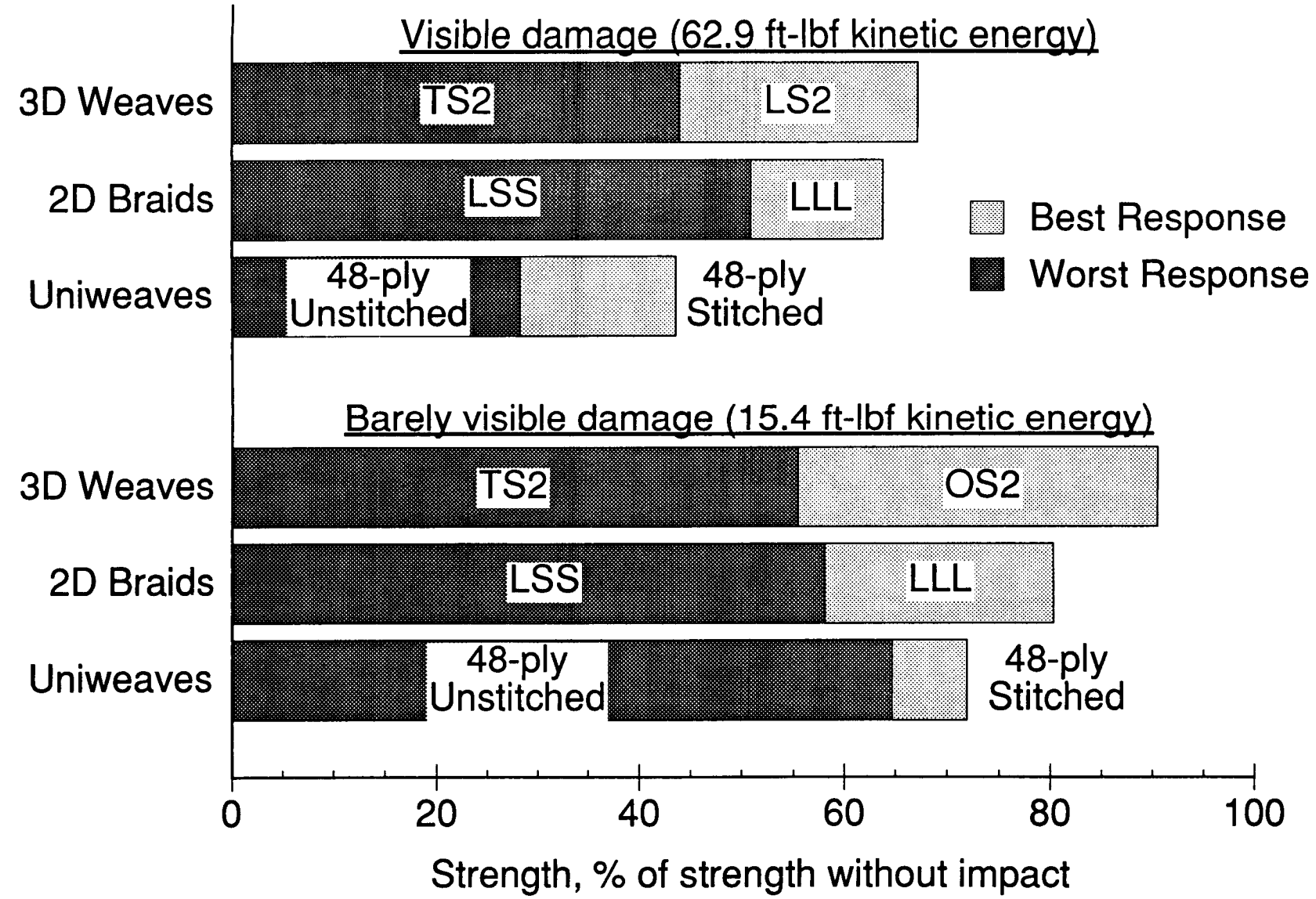

Plot BVD & SID % Residual TAI

Lockheed

Textile Technology Development

Textile Mechanics Conference
NASA Langley Research Center
Hampton, VA
December 6-9, 1994

Bharat M. Shah
Lockheed Aeronautical Systems Company
Marietta, GA 30063-0648

ASM 12/4/94 01 BMS

Lockheed

Introduction

Advanced Composite Structural Concepts and Materials Technologies for Primary Aircraft Structures.
NASA/LaRC Contract No. NAS1-18888

NASA COTR : Randall C. Davis

LASC Program Mgr. : A. C. Jackson

TEAM :

Ron Barrie	(Engr. Manager)
R.L. Chu	(Design)
Bharat Shah	(Structural Methods/Mechanics/Analysis)
Jay Shukla	(Materials and Processes)
Dan Skolnik	(Manufacturing)

Lockheed

Presentation Agenda

- Program Scope / Overview
  - ACT Tasks Accomplishments
- Mechanics of Textile Composites
  - Scope
  - Preform Architectures
  - Design Properties and Database
  - Performance Prediction Modeling
  - Impact Response Analysis
  - Bolted Joint Strength Prediction
  - Summary / Conclusions

Advanced Composite Structural Concepts and Materials Technologies for Primary Aircraft Structures

NASA / LaRC Contract No. NAS1-18888 / LASC Program Mgr: A.C. Jackson

CRITICAL TECHNOLOGY

Automated Manufacturing of Fuselage Primary Structures

- Woven and Braided Preforms
- Resin Transfer Molding (RTM)
- Powder Coated Tows

OBJECTIVES

- Evaluate and Select Resin Systems for RTM and Powder Towpreg Material
- Develop/Evaluate Advanced Textile Processes
  - Compare 2-D and 3-D Braiding for Frame Applications
  - Develop Window Belt and Side Panel Structural Design Concepts
- Evaluate Textile Material Properties
- Develop Low Cost Manufacturing Processes/ Tooling

9656-13 LASC
02-24-94
Opt-34B

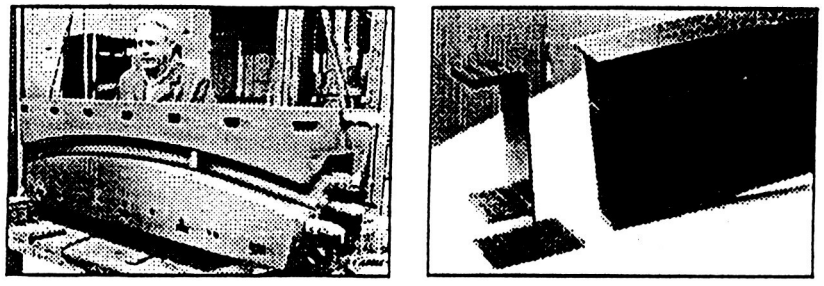

Braided "F" Frame (RTM Process)

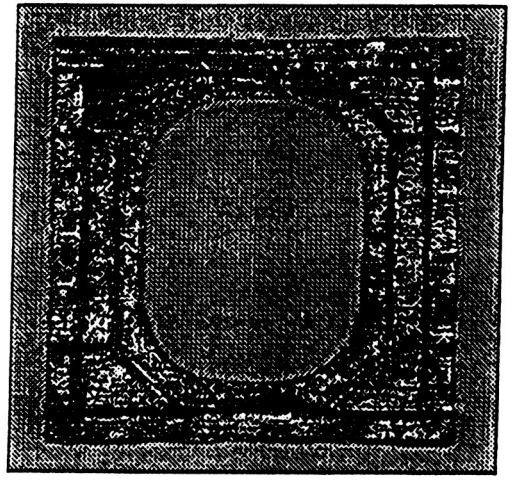

Powder Coated Tow Preform
(Window Belt Reinforcement)

Advanced Composite Structural Concepts and Materials Technologies for Primary Aircraft Structures

Task 1 - Advanced Resin Systems for Textile Preforms

- Evaluate Resin Systems for Resin Transfer Molding (RTM) & Powder Towpregging

ACCOMPLISHMENTS

- Evaluated Three RTM Resins
  - PR-500 (3M)
  - RSL-1895 (Shell)
  - E905L (BP)
- Selected PR-500 Resin

- Evaluated Three Powder Coated Towpregs
  - PS-501 (3M)
  - RSS-1952 (Shell)
  - CET-3 (Dow)
- Selected PS-501 Powder Coated Towpreg (Now Called AMD-0036)

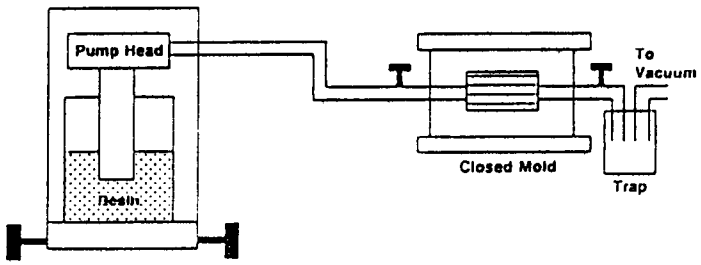

RTM Process

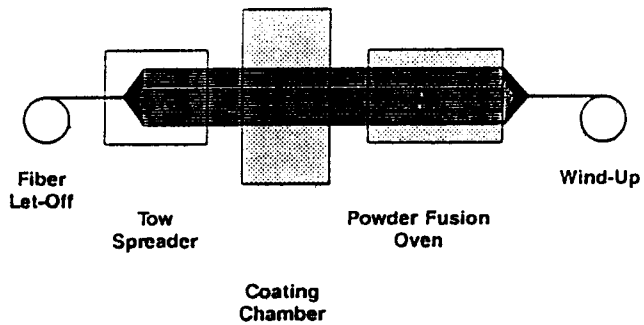

Powder Coating Process

Advanced Composite Structural Concepts and Materials Technologies for Primary Aircraft Structures

Task 2 - Preform Development and Processing

- Evaluate Textile Preforms and Develop Preliminary Data Base On Resin Transfer Molded (RTM) and Powdered Towpreg Materials

ACCOMPLISHMENTS

- Evaluated Seven Woven, Braided and Knitted Textile Processes
- Evaluated 3-D Woven and Braided Preform for Preliminary Data Base
- Resin Transfer Molding (RTM) Flat Panel Preforms and Preliminary Data Base
- Evaluated Flat Panel Preform Micro-Structures and Physical Properties
- Established Criteria and Limitations of Textile Processing for Advanced Design Concepts for Fuselage Structures
- Evaluated Powder Towpreg in Weaving Braiding and Knitting Processes

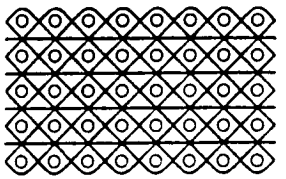

Through the Thickness Weaving

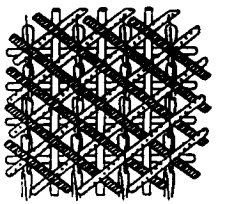

Multi-Axial Knitting/Stiching

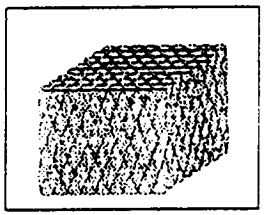

3-D Through the Thickness Braiding

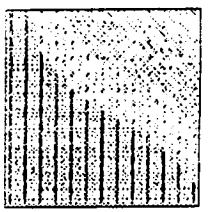

Multi-Axial "Weaving" Process

9656-31 LASC
12-05-94
Opt 34b

Advanced Composite Structural Concepts and Materials Technologies for Primary Aircraft Structures

Task 3.1 - Fuselage Frame Development

- Conduct Trade Studies to Select Braiding Approach for Side Panel Circumferential Frames

ACCOMPLISHMENTS

- Developed 2-D and 3-D Braided Frame Concepts
- Costs Trades Indicate 2-D Braid Less Costly Than Metals
- Testing Complete, 2-D Frames Meet or Exceed all Requirements

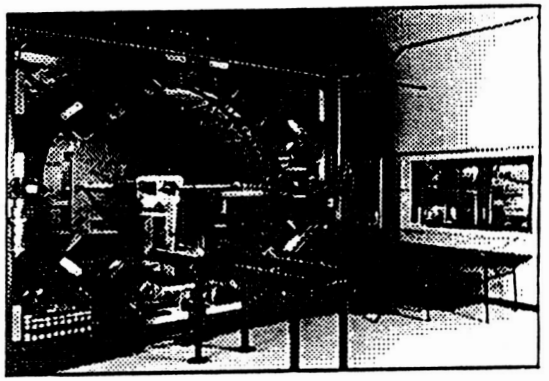

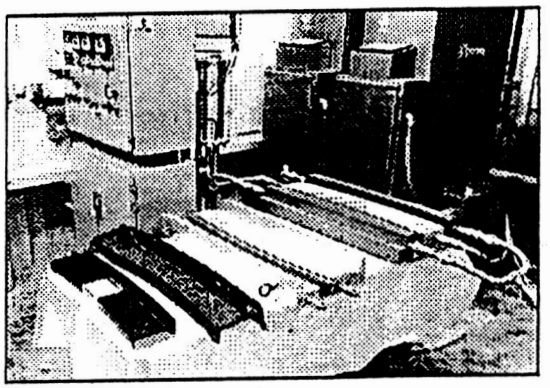

9656-32 LASC
02-24-94
Opt 34b

Advanced Composite Structural Concepts and Materials Technologies for Primary Aircraft Structures

Task 3.2 - Fuselage Window Belt Development

- Develop Advanced Textile Concept for Fuselage Window Belt

ACCOMPLISHMENTS

- Developed Woven & Warp Knitted Concepts
- Completed Cost Analysis
- Woven Concept Shear Panel Test Completed
- Test Correlation In Progress
- Knitted Concept Dropped
  - Poor Performance in Knitting Trials

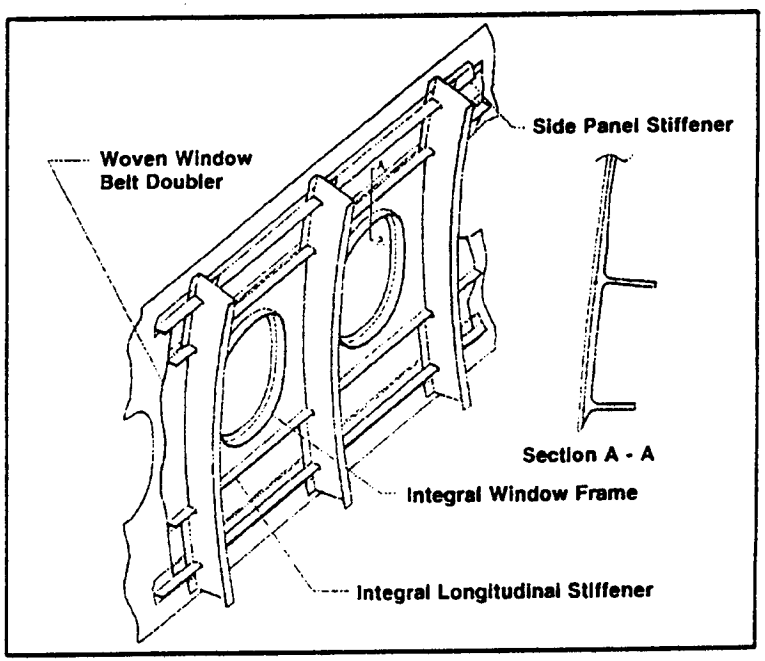

C-3

9656-33 LASC
12-05-94
Opt 34b

Advanced Composite Structural Concepts and Materials Technologies for Primary Aircraft Structures

Task 3.3 - Keel Frame

- Develop Keel Frames for Boeing Test Components

ACCOMPLISHMENTS

- Twenty four (24) "J" Section 2-D Triaxially Braided / RTM Frames Shipped to Boeing
- 12 Frames Successfully Co-Bonded Into Aft Keel Test Panel (Boeing)
- 12 Frames Remain to be Co-Bonded in the Next Test Panel (Boeing)
- Frames for Forward Keel Currently Being Planned

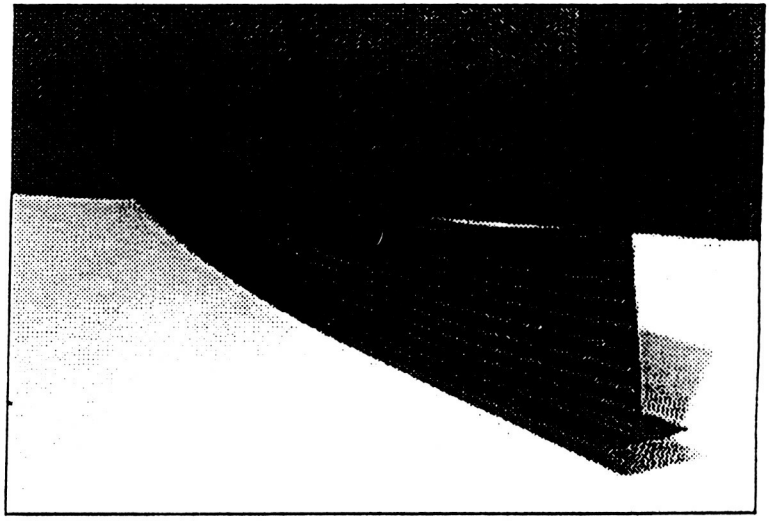

9656-34 LASC
02-23-94
Opt 45a

Advanced Composite Structural Concepts and Materials Technologies for Primary Aircraft Structures

Task 3.4 - Benchmark Side Panel Common Structural Test Component

- Develop 100% Textile Side Panel Concepts
- Fabricate Benchmark Test Panel for Testing at NASA

ACCOMPLISHMENTS

- Four Advanced Textile Side Panel Concepts Designed for Relative Cost & Weight Savings and Structural Performance

- Down Selected to Two Promising Concepts for Detail Design and Structural Testing
  1. 3-D Woven (Techniweave) Integral Stringers and Window Frames
  2. Conventional 3-D Woven Pultruded Stiffeners Braided Window Frame

Task 3-4 To Be Redirected

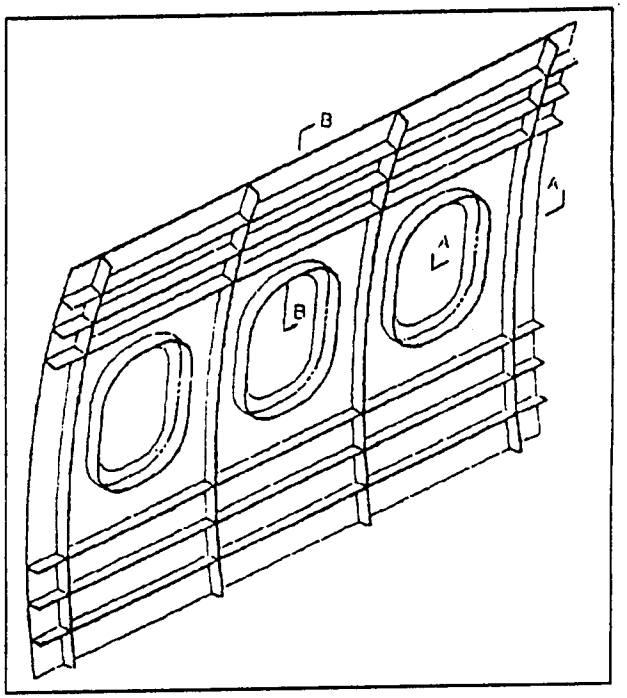

9658-35 LASC
02-23-94
Opt 45a

Advanced Composite Structural Concepts and Materials Technologies for Primary Aircraft Structures

Task 3.4 - Sandwich Fuselage Panel

- Develop Fuselage Side Panel Including Window Belt Using ATP Honeycomb and Braided RTM

ACCOMPLISHMENTS

- Two Design Concepts Evaluated for Manufacturing Feasibility and Cost

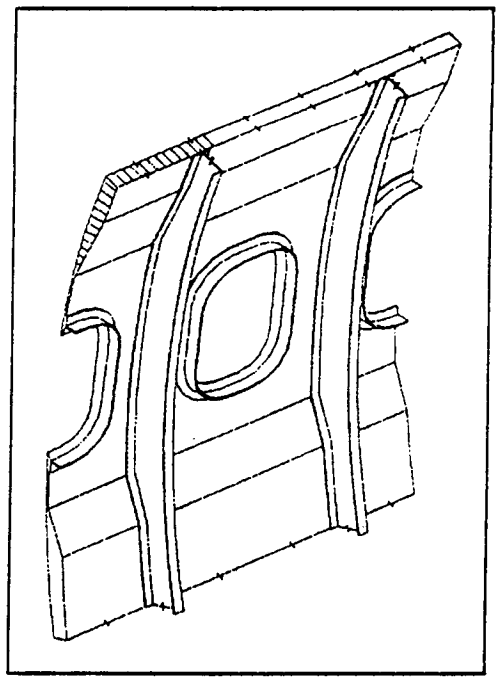

9656-35 LASC
12-05-94
Opt 45a

Advanced Composite Structural Concepts and Materials Technologies for Primary Aircraft Structures

Task 3.5 - Analytical Methods Development and Validation

- Develop Design-to-Properties
- Predict Textile Composite Strength & Stiffness
  - Model Development & Verification
- Develop Impact Response Method
- Conduct Bolted Joint Test and Analysis

ACCOMPLISHMENTS

Textile Composite Properties Obtained by Test

- Strength Threshold High

Process-Microstructure-Performance Relationship

- Stiffness & Strength Prediction Models Developed
  - Currently Being Validated

Impact Response Method Development

- Finite Element Based Code - "3DIMPACT"
- Progressive Damage Criteria / Enhancement Incorporated

Bolted Joints Tests Completed

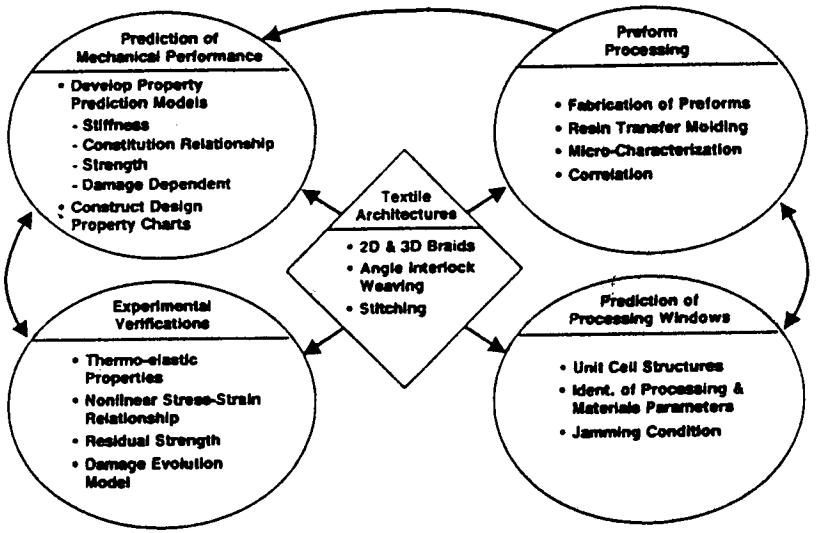

9656-36 LASC
12-05-94
Opt 45a

Advanced Composite Structural Concepts and Materials Technologies for Primary Aircraft Structures

Task 4.0 - Low Cost Fabrication Methods

- Develop Methods of Fabricating Composite Materials Using Low Cost Textile Preforms

ACCOMPLISHMENTS

- Fabricated Flat Panels for Mechanical Property Testing Using RTM and Powder Towpreg Technologies
- Developing Methods to Debulk and Cure Components in a Cost Effective Manner
- Currently Debugging LIMS (Resin Flow Simulation)

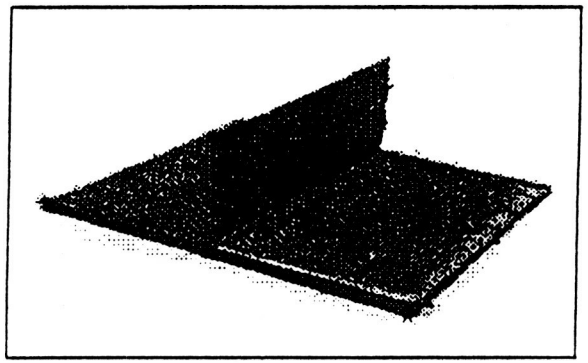

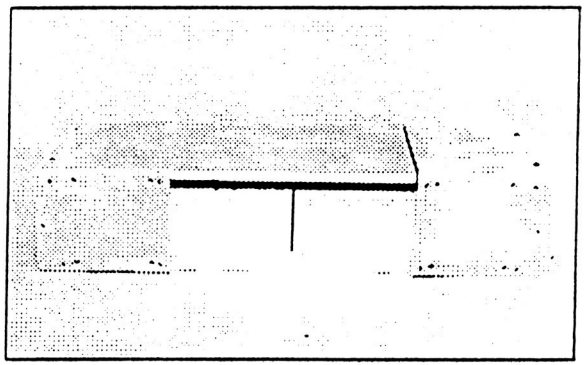

9650-37 LASC
02-24-94
Opt-45a

Lockheed

Objective/ Scope

- Develop " Design-to-Properties " of Textile Composites
- Establish the Material Level Damage Mechanisms
- Establish Damage Progression Characteristics
- Develop Performance Prediction Models
  - Stiffness Model(s)
  - Strength Model(s)
  - Damage-dependent Model
  - Impact Response Analysis Methodology
  - Bolted Joint Strength Prediction

Textile Architectures

3-D Braid(TTT)

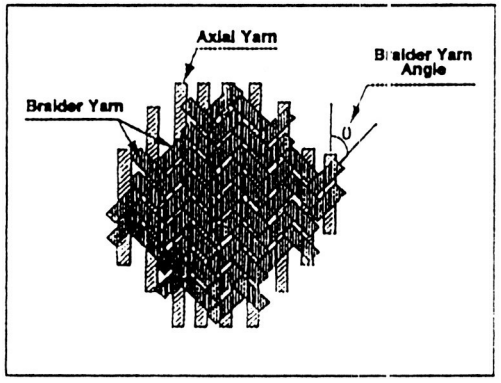

Pattern I

	.12" thick	.16" thick	θ°
Axial	6K(30.3%)	6K(30.9%)	0
Braider	6K(69.7%)	6K(69.1%)	60

Pattern II

	.12" thick	.16" thick	θ°
Axial	18K(56.3%)	18K(57.2%)	0
Braider	6K(43.7%)	6K(42.8%)	60

3-D Woven(LTL)

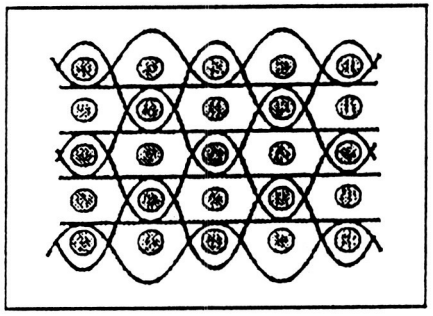

Pattern I

	Tow Size	Approx. Yarn Distribution(%)
W(0°)	6K	45.7
F(90°)	6K	46.1
z	3K	8.2

Pattern II

	Tow Size	Approx. Yarn Distribution(%)
W(0°)	12K	46.3
F(90°)	6K	45.6
z	3K	8.1

3-D Woven(TTT)

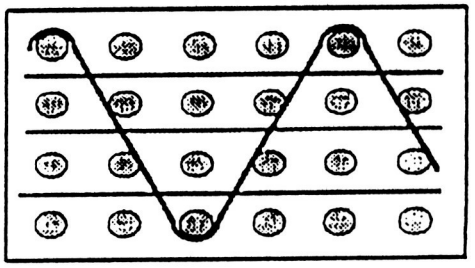

Pattern II

	Tow Size	Approx. Yarn Distribution(%)
W(0°)	12K	47.7
F(90°)	6K	44.4
z	3K	7.9

i717-07
6-02-93
Opt-36b

Lockheed

Longitudinal Tension Strength

3D Textile Composite [AS4/PR500]

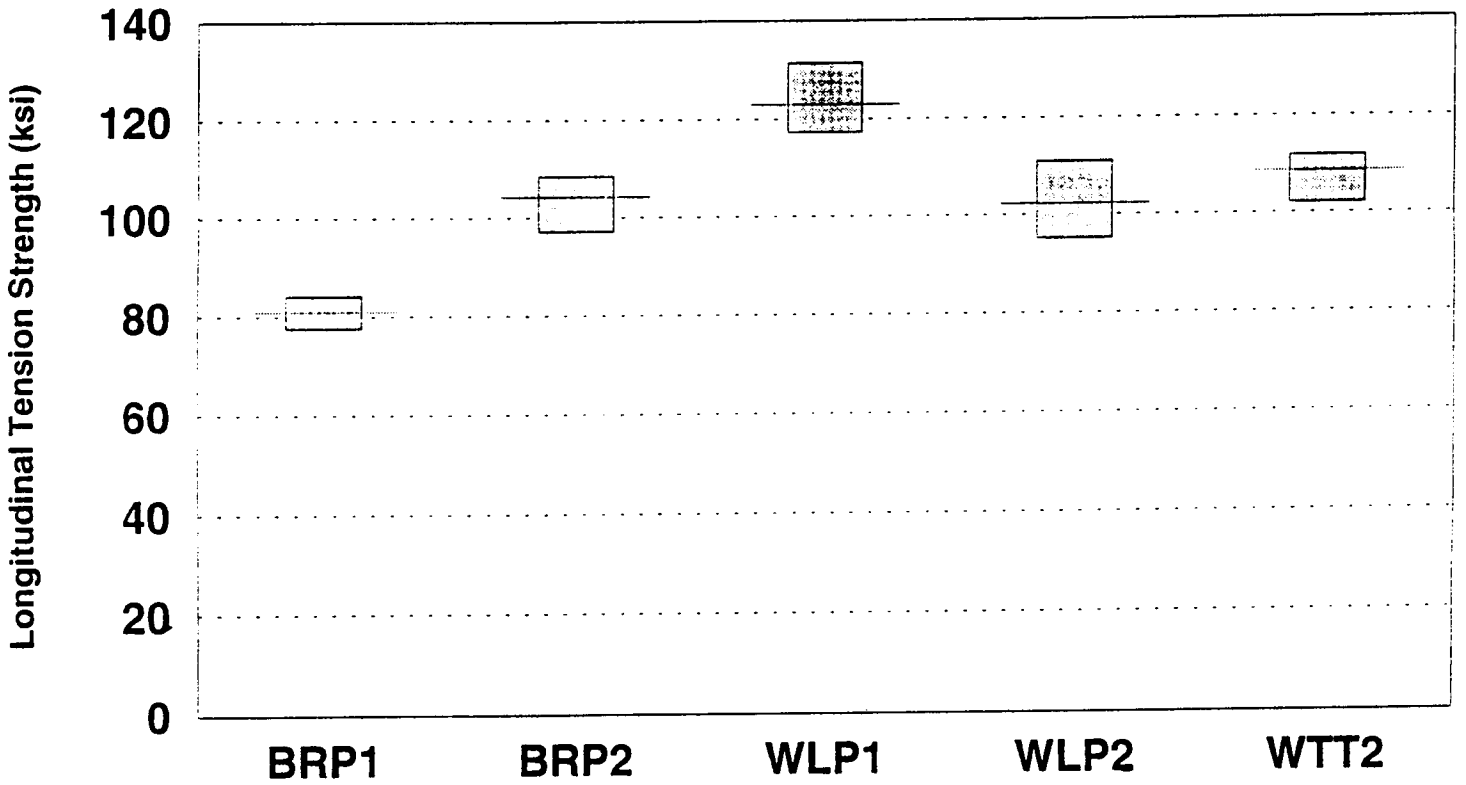

ASM 12/4/94 01 BMS

Lockheed

Longitudinal Compression Strength

3D Textile Composites [AS4/PR500]

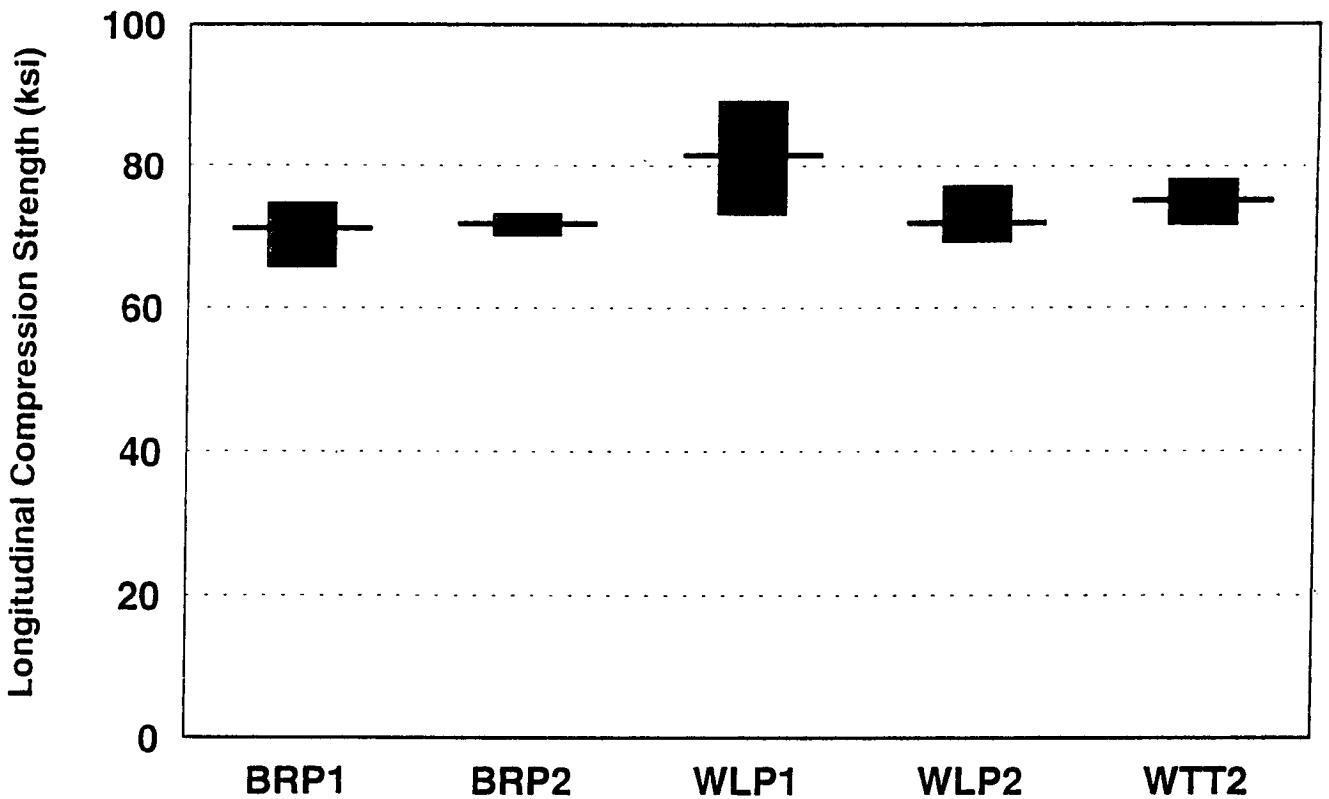

ASM 12/4/94 01 BMS

Lockheed

Longitudinal Tension Modulus

3D Textile Composite [AS4/PR500]

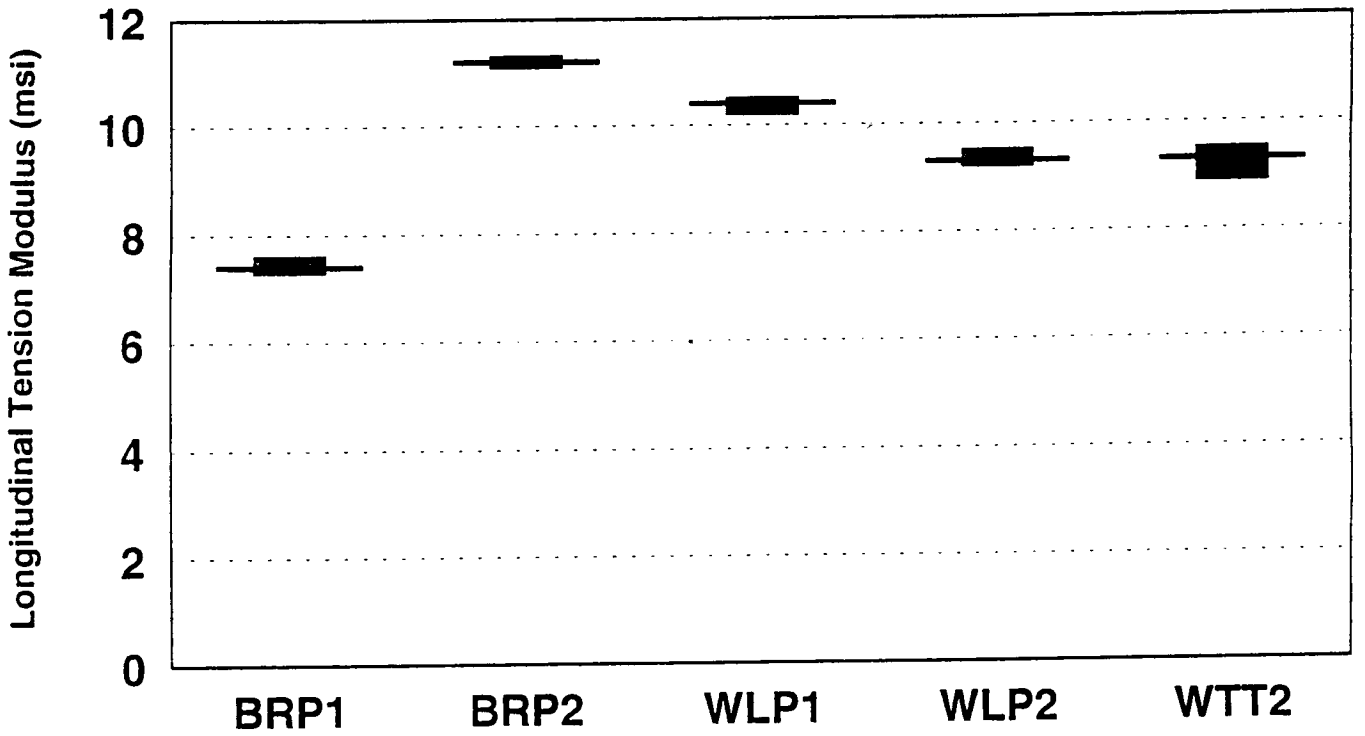

Lockheed

Longitudinal Compression Modulus

3D Textile Composite [AS4/PR500]

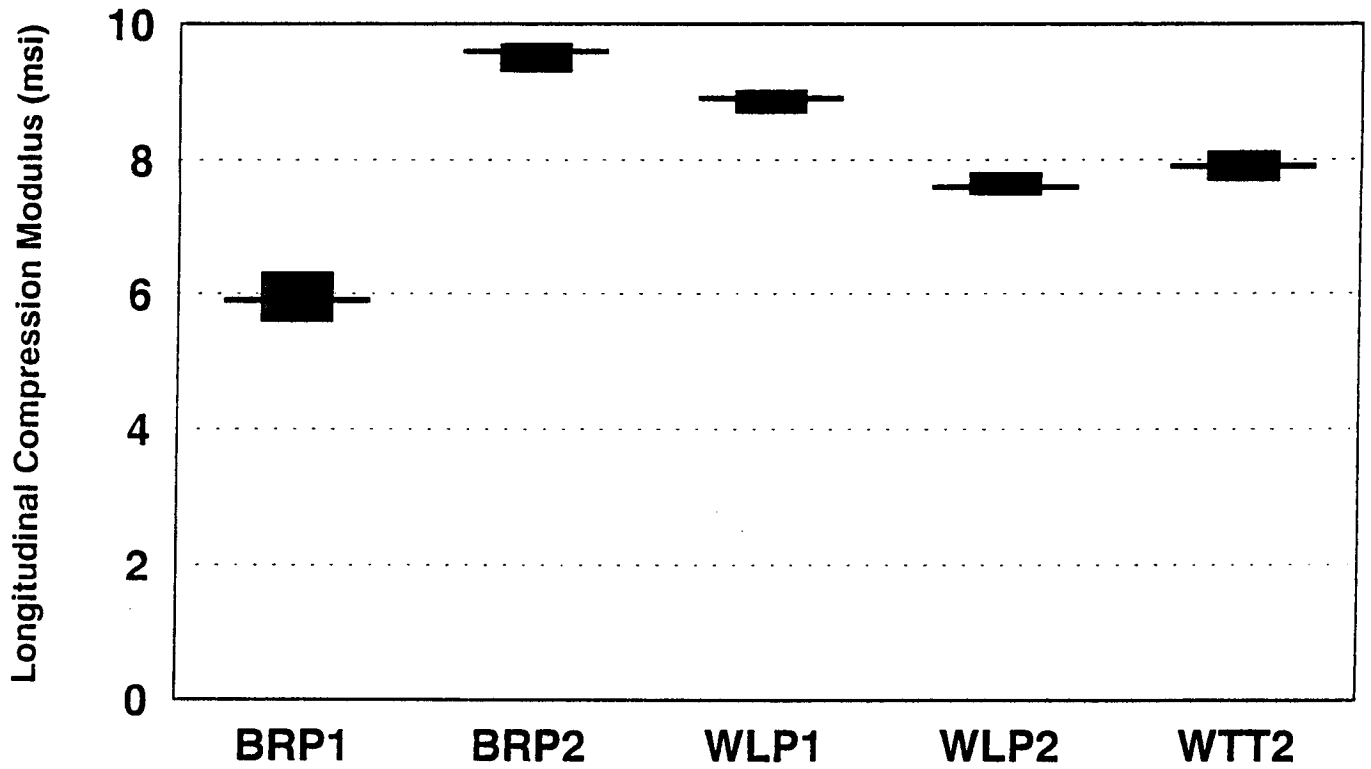

Lockheed

Open-Hole Fatigue Characteristic

3D Textile Composite (AS4/PR500)

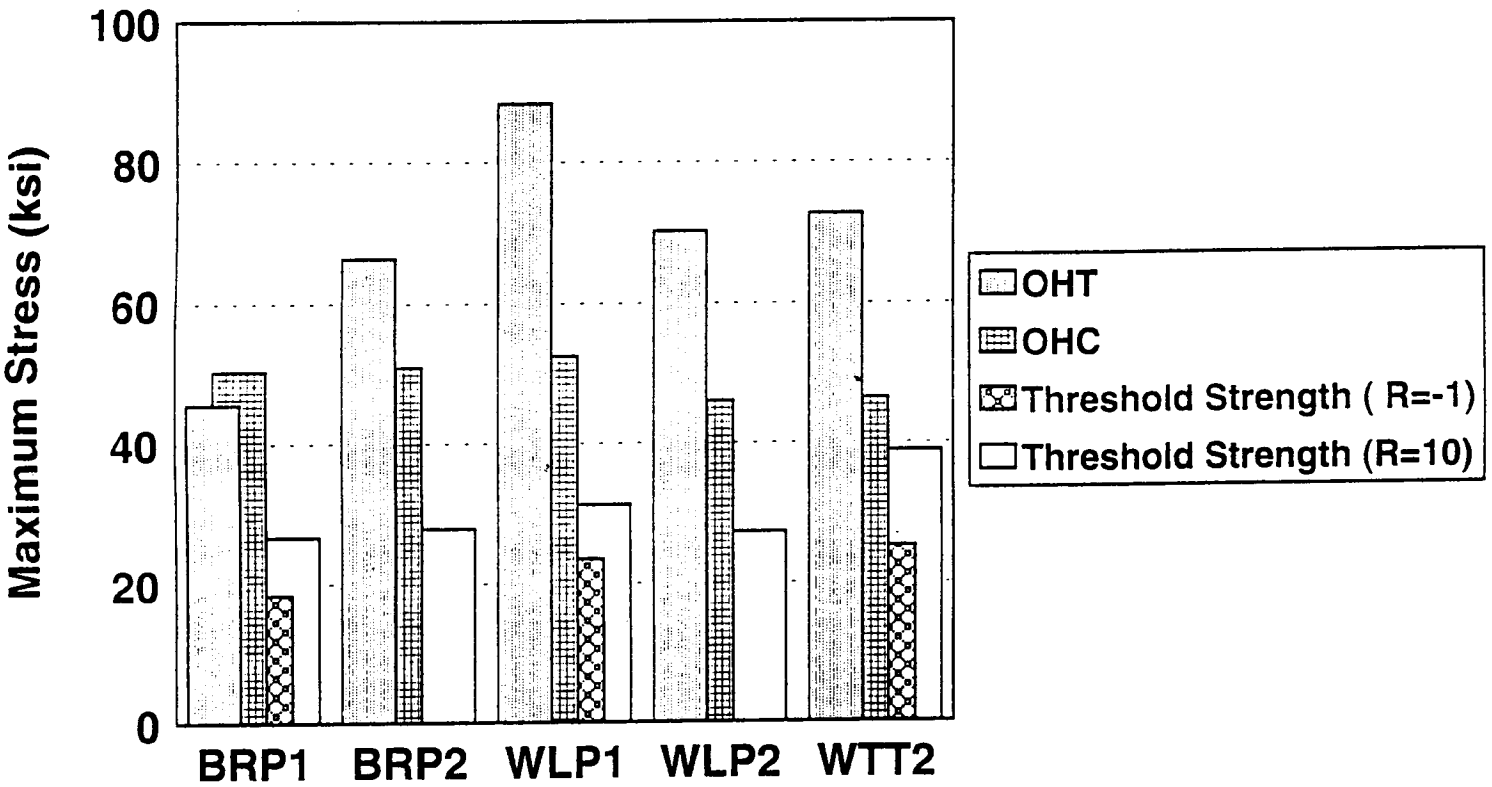

Lockheed

Experimental Textile Database

AS4/PR500 [RTM]

Elastic Constant	UNT [L/T]	UNC [L/T]	Fatigue	OHT	OHC	Bolt Bearing	FHT	FHC	CAI	ILT
				3D	Weave	LTL				
x	x/x	x/x	x	x	x	x	x	x	x	x
				3D	Weave	TTT				
x	x/x	x/x	x	x	x	x	x	x	x	x
				3D	Braids					
x	x/x	x/x	x	x	x	x	x	x	x	x
				2D	Braids					
x	x	x		x	x				x	
			Multi	Axial	Warp	Knit				
x	x	x		x	x				x	
				8HS	Fabric					
x	x	x		x	x				x	

Lockheed

Experimental Textile Database

AS4/ AMD0036 [Powdered Towpreg]

Elastic Constant	UNT [L/T]	UNC [L/T]	CAI	OHT	OHC	Bolt Bearing
	2D Triaxial Braids [$0°_{6k}$, +/- $60°_{6k}$] 33% Axials					
x	x/x	x/x	x	x	x	x
	2D Triaxial Braids [$0°_{18k}$, +/- $60°_{6k}$] 50% Axials					
x	x/x	x/x	x	x	x	x
	3D Weave (Techniweave) [(+/- $45°_{6k}$, $0°_{6k}$, $90°_{6k}$) , Z_{3k}]$_{NS}$					
x	x/x	x/x	x	x	x	x
	3D Multi-layered Weave [(+/-$45°_{6k}$, Z_{3k}) , ($0°/90°_{6k}$, Z_{3k})]$_S$					
x	x	x	x	x	x	x

Lockheed

Experimental Textile Database

Bolted Textile Joints

Bearing / Bypass 2 Ratios	Single Lap Shear Tension t=.12in.	Single Lap Shear Tension t=.16 in.	Double Lap Shear Tension	Double Lap Shear Compression	Double Lap Shear Trans. Tension	Fastener Push Through
		2D Triaxial Braids [0°_{12k}, +/- 60°_{6k}] 33% Axials				
X	X	X	X	X		X
		3D Braids [0°_{6k}, +/- 60°_{6k}] 33% Axials				
X	X	X	X	X	X	X
		3D Weave (Techniweave) [(+/- 45°_{6k}, 0°_{6k}, 90°_{6k}) , Z_{3k}]$_{NS}$				
X	X	X	X	X		X
		3D Multi-layered Weave [(+/-45°_{6k}, Z_{3k}) , (0°/90°_{6k}, Z_{3k})]$_S$				
X	X	X	X	X		X

Bearing Bypass Interaction

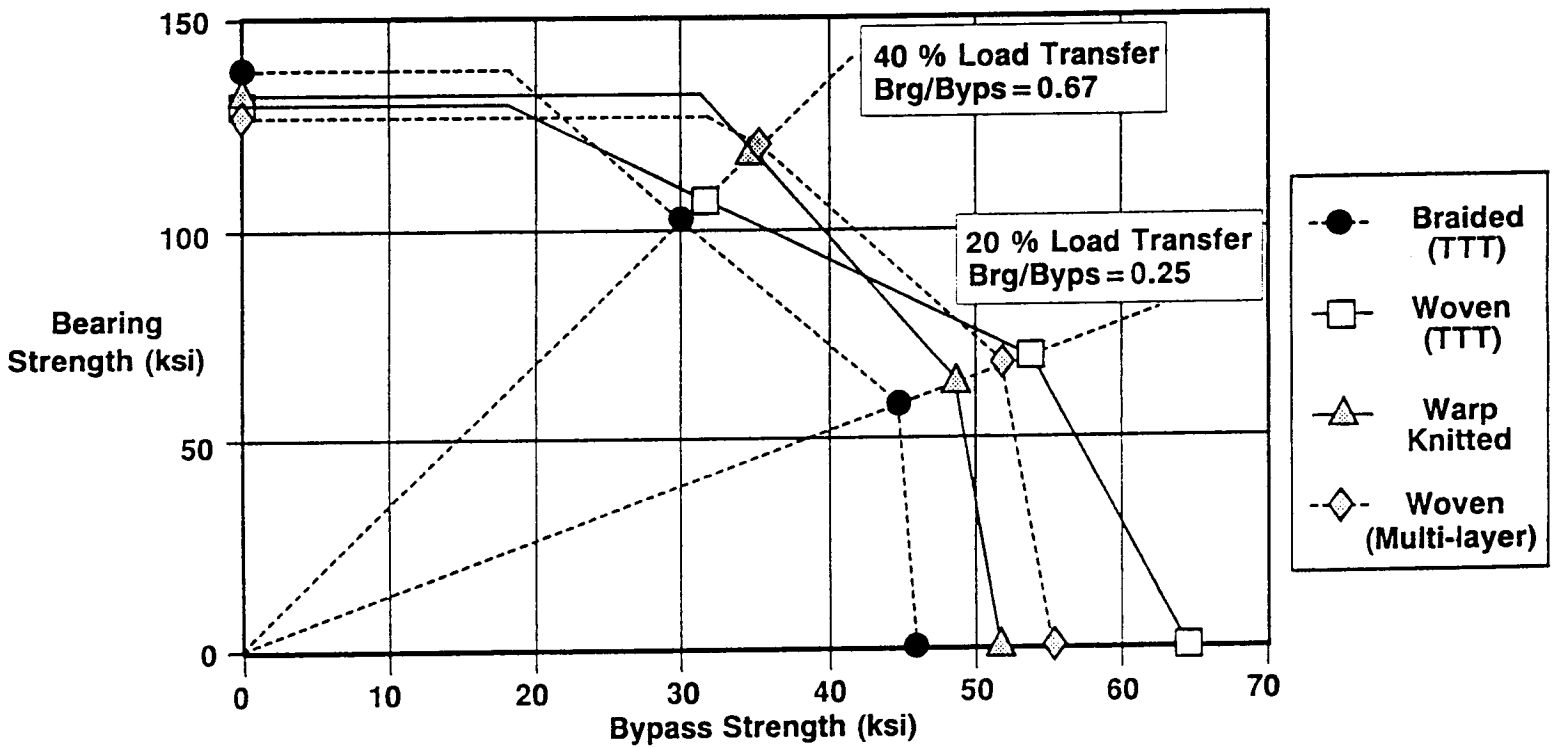

9942-24
12-05-94

Material Properties Database

M/VISION Implementation

- Approach
  - Employ Existing Client-Server Workstation Network
  - Store All Results in an Electronic Databse
    - Automate Data Reduction Methods
    - Improve Accessibility to Test Data
    - Difficult-to-Predict Material Behavior can be Examined Empirically
    - Rapid Comparative Property Evaluation

Lockheed

M/Vision Implementation

Database System Flow

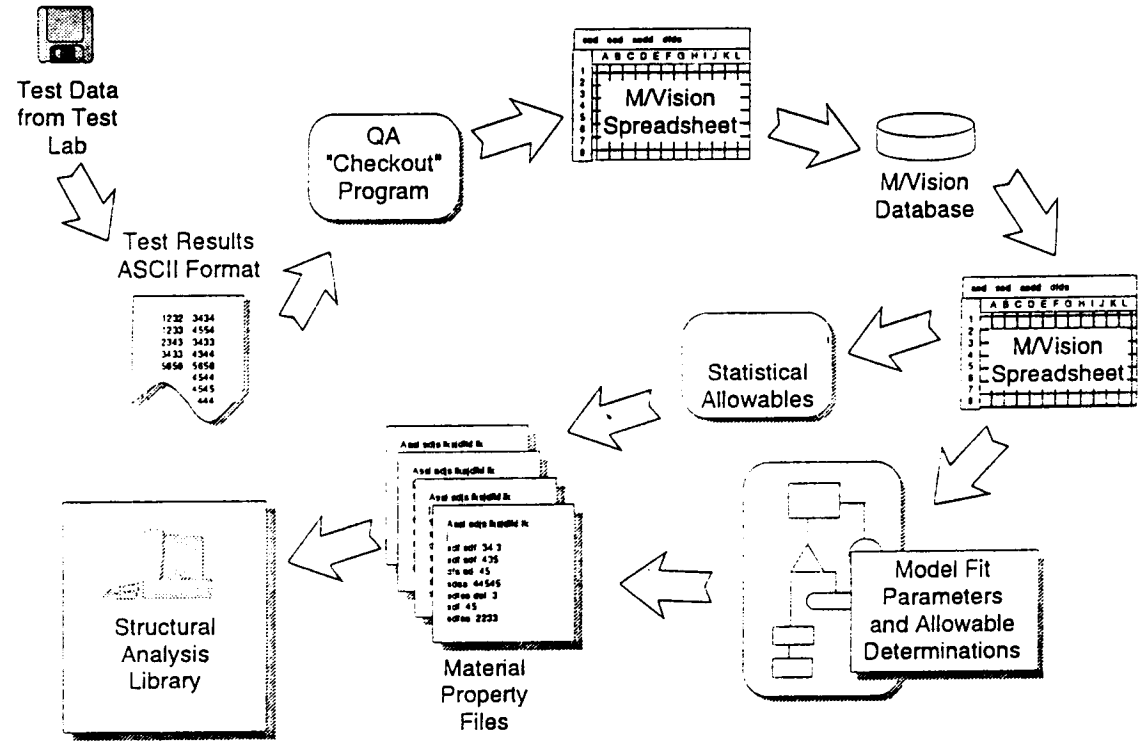

UNCLASSIFIED

Lockheed

Textile Performance Modeling

Preform	Elastic Constant	CTE's	UNT Strength L/T	UNC Strength L/T	Shear Strength	Joint Strength	Impact Resistance	Impact Tolerance
3-D Weave	x	x	x	x	x	x	x	x
3-D Braids	x	x	x	x	x	x	x	x
2-D Braids						x	x	x

Lockheed

Performance Prediction Modeling

University of Delaware Effort

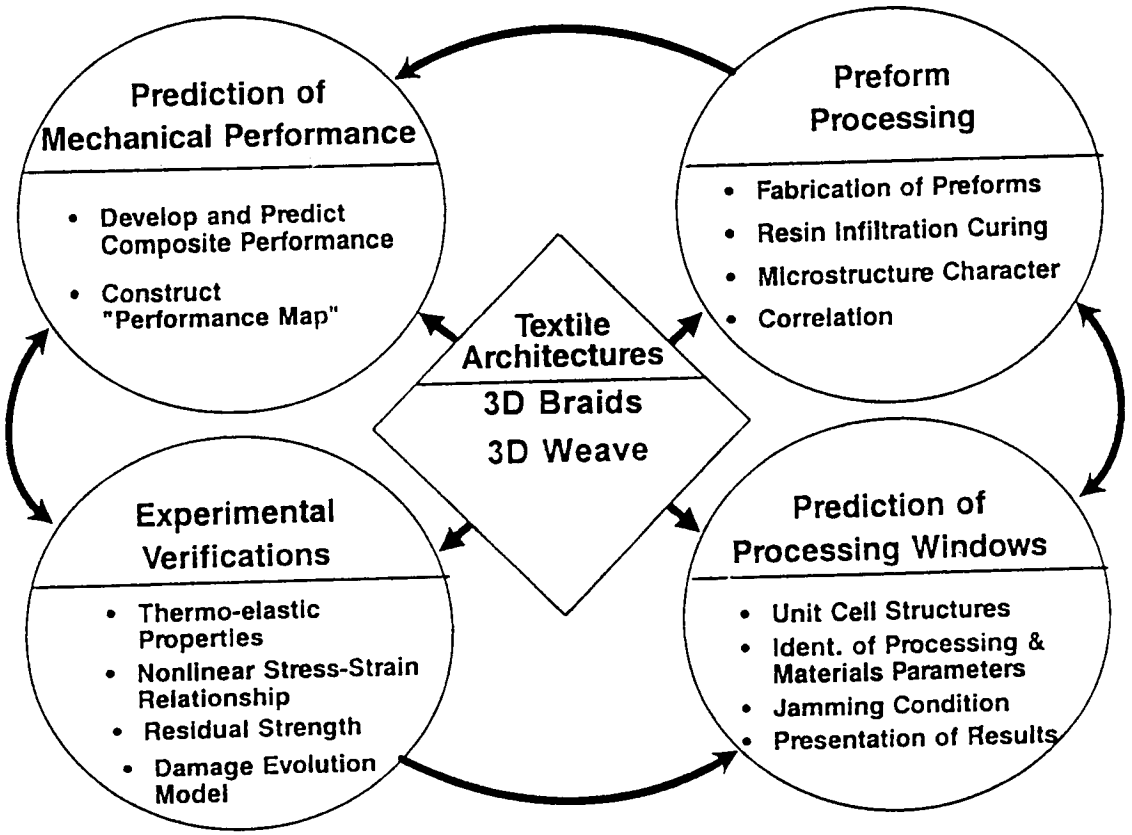

Lockheed

Properties Prediction Modeling

- Geometrical modeling of 3D textile composites
- Stiffness computation modeling
  - stiffness averaging approach
  - homogeneous boundary approximation
- Strength modeling
  - tensile strength : volume fraction approach
  - compressive strength: shear mode buckling analysis
  - shear strength : Sun's single param. yield criteria
  - off-axis strength : one parameter yield curve
- Bending response modeling
  - Ambursumyan's model
  - Jone's model
- Damage modeling with multi -scale-multi-grid method
- Bolted textile joints analysis - "BOLTEX"

Lockheed

Impact Response Analysis Methodology

3DIMPACT - Code

- Existing Capabilities
  - 3D Transient Finite Elements Code
  - Low Velocity Impact of Laminated Composite
  - In-Plane and Out-of-Plane Stresses
  - Extent of Delamination
- Capabilities Update
  - Contact Force Distribution
  - Laminated and Textile Composites
  - Progressive Damage Model
  - Residual Strength Prediction

Lockheed

Summary / Conclusions

- Textile Composites Properties Characterization completed
  - Longitudinal properties goals were met
  - Out-of-plane property goal was not met
  - Transverse properties of 3D-braided composite are poor
  - Shear strength of 3D-braided composite is good
  - Bearing strength of 3D- composites lower than fabrics
  - Powdered towpreg textile composite properties characterization is in-work
  - Textile properties database (MVISION] established
- 3D- textile composites strength and stiffness models shows very good results
- Impact response analysis method developed
  - Impact resistance and tolerance prediction capability installed
  - Predictions for laminated composite very good
  - Predictions for textile composite needs improvement
- Textile joint strength prediction method developed
- Methods improvement issues
  - Limited test data
  - Out-of-plane properties unavailability
  - Damage mechanisms and mechanics

Development Of A Stitched/RFI Composite Transport Wing

Yury Kropp
McDonnell Douglas Aerospace-Transport Division
Long Beach, CA

Abstract

Development of a composite wing primary structure for commercial transport aircraft is being undertaken at McDonnell Douglas under NASA contract. The focus of the program is to design and manufacture a low cost composite wing which can effectively compete with conventional metal wing structures in terms of cost, weight and ability to withstand damage. These goals are being accomplished by utilizing the stitched/RFI manufacturing process during which the dry fiber preforms consisting of several stacks of warp-knit material are stitched together, impregnated with resin and cured. The stitched/RFI wing skin panels have exceptional damage tolerance and fatigue characteristics, are easily repairable, and can carry higher gross stress than their metal counterparts. This paper gives an overview of the program, describes the key features of the composite wing design and addresses major issues on analysis and manufacturing.

Introduction

The development of transport aircraft composite primary wing structure has been under study at McDonnell Douglas since 1975. The original design concept was based on the prepreg tape material designed to the ultimate micro-strain level of 4500 for damage tolerance. However, it become evident that this conventional prepreg approach was not likely to lead to a cost effective application of composite materials to primary wing structure. The stitched dry preform/resin film infusion process was selected as having the best potential for achieving target weight and cost goals.

In the S/RFI process the dry fiber preforms arranged in stacks are stitched through the thickness with a multi-needle machine, are impregnated with resin and cured in an autoclave (Figure. 1). Besides improving damage resistance and tolerance of the cured part, stitching also provides the compaction necessary for the assembly of inner mold line (IML) tooling, enhances the flow of resin in the infusion process, and virtually eliminates stiffener separation and other secondary failure of an interlaminar nature.

A primary objective of the "Innovative Composite Aircraft Primary Structure" (ICAPS) program is to develop the technology to allow the incorporation of an all-composite wing on a commercial transport aircraft. The baseline aircraft selected for this study is a new McDonnell Douglas MD-XX advanced technology twin-engined aircraft (Figure 2). The aircraft configuration is designed to carry 192 passengers in a two-class arrangement. Composites will make up 39% of the airframe weight (Figure 3), a significant increase from the MD-11 or MD-80/90 series aircraft.

A key feature of the MD-XX aircraft is the high aspect ratio composite wing which is aerodynamically more efficient than the comparable metal wing (Figure 4). The more efficient and lighter wing will require smaller control surfaces, smaller engines and lighter support structure. The entire aircraft resized will weigh 7300 lb less than its metal wing counterpart. The combined effect of a lighter and more efficient aircraft is to reduce the direct operating cost (DOC) by 2.1 percent, translating into more than 100 percent profit increase for the airlines.

A study was performed to predict production costs of the composite and metal wing aircraft (Figure 5). Learning curves applied to the metal boxes were based on industry history related to the amount of automation used. A less advantageous learning curve, having a constant value of 87 percent, was applied to the S/RFI process because of its highly automated nature. The study proved that the application of composite primary structure to the wing box of the MD-XX will result in a cost-effective solution.

Semi-Span Wing Design

The baseline wing configuration is given in Figure 6. The wing is a two spar, multiple rib structure. The skin is reinforced with blade stiffeners. The 41-foot wing segment, denoted the semi-span wing, was selected to be designed and tested under the current program. This length

was determined as being the maximum that could be comfortably accomodated within a conveniently available company autoclave.

The components of the structural test box shown in Figure 7 consist of upper and lower cover panels, front and rear spars, ribs, bulkheads, and attach fittings for the main landing gear and the engine pylon. The cover panels are the major components and account for approximately 75 percent of the total box weight. The skins, stringers, the intercostal clips and the spar webs are made with S/RFI manufacturing process. The rest of the components are made from conventional prepreg tape material.

The skin preforms are manufactured in the form of discrete stacks each containing nine unidirectional layers (Figure 8). The upper skin stacks utilize the low-cost Hercules AS4 fiber system. Since higher open hole tension allowables are required in the lower cover in order to increase the gross stress level, the decision was made to substitute higher-strength IM7 fibers for AS4 in the 0^0 direction.

The wing skins, being part of the aerodynamic profile, have contoured double curvature surfaces (Figure 9). These curvatures are more severe on the lower skin where the stringers have to be made in the form of curved triaxially woven braided socks stitched together. The other benefit of braiding is that it is a more automated, and therefore more cost effective manufacturing process. Double curvature of the lower skin presented another problem from a design point of view. Since the individual stack pieces would not follow the surface without wrinkling, the skin will be made in two individual stitched parts which will be spliced longitudinally prior to curing.

Design Requirements and Allowables

The effort to design an all-composite wing is based on the "building block" approach to engineering. Under this approach, the wing structure is subdivided into a number of simple subcomponent structures which are then designed, analyzed and tested. This allows us to fine-tune and validate the analysis techniques, to record valuable lessons learned during the process and, as the sufficient experience is gathered, to move on to larger, more complex structures. In many instances, the purpose of the subcomponent tests is simply to derive an allowable stress or load. Numerous subcomponents have been tested to date, Ref. 8, some of which are shown in Figure 10.

One of the central tasks in designing a new structure such as the S/RFI wing is to formulate the appropriate design and failure criteria which would guarantee the structural integrity of the component, and at the same time not incur an unnecessary weight penalty. The following design criteria (Figure 11) have been selected on the basis of past design experiences, Federal Aviation Regulations (FAR-25) and the FAA Advisory Circulars, Ref. 4-5.

- Discrete Source Damage. This type of damage occurs in flight or on the ground and is a result of collision with a foreign object such as another aircraft, building, bird or vehicle.

Severe in-flight damage might be encountered after a major engine disintegration. For the purposes of this program, the extent of the discrete source damage is to include a completely severed stringer and the skin on either side up to the flanges of the adjacent stringers. Since the aircraft exposed to such damage will be immediately repaired, it is extremely unlikely that peak loads of the flight envelope would be encountered in the time interval between the described event and landing. A structure with discrete source damage must therefore be able to withstand only 70 percent of the design limit load (DLL) without catastrophic failure and only flight conditions must be considered.

- Detectable (visible) Damage. When a structure is damaged to a lesser extent than during the discrete source damage event, the damage may remain undetected during the regular inspection intervals. During such time the structure is required to carry 100 percent of DLL. To be detectable, the indentation due to damage must be at least 0.1 inches in depth. Once the damage is detected, the damage site is repaired.

- Non-Detectable Damage. When the impact event produces no visible symptoms or a dent depth of less than 0.1 inches, damage is considered to be non-detectable, and the structure must be able to survive full design ultimate load (DUL). The impact energy up to 100 ft-lb for the exterior surfaces and up to 20 ft-lb for the interior surfaces must considered in the stress analysis of every structural component. It is conceivable that the 100 ft-lb impact, sometimes even a lower energy impact, may produce a detectable dent in thin laminates. In such cases, the impact energy level must be reduced until the level which produces a 0.1" dent is found.(Recall that dents deeper than 0.1" are classified as detectable). Conversely, a 100 ft-lb impact rarely produces detectable damage in thick laminates, while higher impact energies being unlikely events should not be considered.

- Reparability If a structure is exposed to damage of such an extent that the damage can be detected by visual inspection, the affected structural site will be repaired. The structure in the repaired configuration is required to withstand the same set of loads as in the unrepaired state. The repairs must therefore be designed to carry the design ultimate load (DUL).

As part of the subcomponent analysis phase of the program, work was performed to determine all of the required material and structural allowables which would satisfy the applicable design criteria listed above. Whenever possible, testing was preceded by analysis to predict the structural response and to calculate the final failure loads. Based on the comparison of analysis and test, analytical models were either validated, or improved to match the test data. In some cases, as in the case of analysis for the discrete source damage, the analytical models produced results so different from test that they were found to be of limited usefulness. In such cases, the decision was made to derive the allowable stresses on the basis of test alone.

In order to design a wing structure for the effects of the discrete source damage, it was postulated that the result of this type of damage would most likely be a completely severed stringer including the skin on either side. The total length of the through crack was taken to be seven inches. To differentiate between the upper and lower covers, tension and compression cases were examined separately, Figure 12. Shown in this figure also are panels used for

measuring the panel residual strength after a 100 ft-lb impact event. Figure 13 gives the photograph of the test panel instrumented with strain gages in which damage was simulated by a seven inch saw cut through the middle stringer.

The analytical model for the discrete source damage analysis was based on the classical point stress criterion (Ref. 10). A fine grid finite element model was constructed to determine the stress distribution in the vicinity of the crack tip. The calculated initial crack propagation stress closely matched the test data. Although the model was able to predict a stable crack growth as the crack extended towards the adjacent stringer flanges, the calculated final failure stress was off by a factor of 2. The difference was attributed to the fact that the point stress criterion in its original form does not adequately describe the entire range of different crack lengths without the help kind of empirical correction factors. These, for example, can be defined such as to make the characteristic distance a function of the crack size. The other reason for the discrepancy could be the complex nature of the stress state in the configuration where the crack is extended all the way to the flanges of the adjacent stringers. Detailed 3-D FEM analysis utilizing fracture mechanics techniques appears to be the most promising tool for solution of such problems.

It is interesting to note that the discrete source damage tension and compression panels showed a very different structural response during test, Ref. 2. In the tension panel, Figure 14, the crack propagated to the flanges and, as the load increased, changed the direction and extended along the side of the flange. The panel ultimately failed at the grips, never reaching its full structural potential. The crack in the compression panel, on the other hand, never changed its course and grew under the flange of the stringer causing failure of the panel, Figure 15. Both panels demonstrated that stitching helped prevent skin-to-stiffener disbonds which is a typical failure mode of the conventional pre-preg composites.

The gross area stress ultimate design allowables derived from test were 50.8 ksi and 80.6 ksi for the upper and lower covers respectively. The tested tension panel was made up of AS4 fiber. The wing lower cover is made from the higher strength IM7/AS4 hybrid material which makes it possible that even higher residual strength may be attained. Overall, such high values of the gross stress allowables make the discrete source damage design criterion less critical relative to other structural criteria such as reparability and tolerance to non-detectable damage.

The tests have confirmed the theory that stringers play a major role in arresting one- or two-bay cracks resulting from a discrete source impact. The crack arrestment capability of a panel can best be described in terms of a stiffening ratio, the ratio of stiffness of a stringer to that of a bay. The stiffening ratio of the tested panel was 35%. All the cover panels of the semi-span wing are being sized to this stiffening ratio. Since the exact mechanisms of the crack arrestment phenomenon are still not completely understood, an additional design requirement is imposed on the wing stringer geometry. The ratio of the flange thickness to the combined thickness of skin and flange is being kept at approximately 40% to match that of the tested panel.

As was mentioned earlier, tests have shown that the wing reparability requirements are by far the most important criteria governing the selection of the maximum working stress level in the covers of the semi-span wing. Operational requirements dictate the need for a capability for

installing rapid and inexpensive repairs in the wing covers under austere field conditions. There is also an additional requirement that the repairs can be accomplished with conventional non-perishable materials. A design solution utilizing bolted-on metal patches was rated as the most promising repair concept for the semi-span wing, Ref. 2.

Two different repair scenarios were formulated. The first scenario addresses the repair of wing skin with detectable or discrete source damage sufficiently localized so that the stringers adjacent to the damage site remain unaffected. To avoid a potential long term material degradation and to prevent possible fuel leaks, the material around the damaged area must be removed. The shape of the clean-up area was determined from a finite element analysis optimization study. An elliptical hole with the major axis aligned with the longitudinal direction and with its minor axis spanning the distance between the adjacent stringers was selected as causing the minimum local stress concentrations. Although the structure in the clean-out configuration retained a sufficient amount of ultimate strength, the installation of a mechanically fastened doubler was nevertheless necessary in order to meet the aerodynamic and the fuel containment requirements of the wing. The repair was demonstrated on a four stringer panel with an elliptical cut-out (1:2 eccentricity ratio) covered by a .125-in. 7075-T6 aluminum doubler fastened with .375 in. titanium bolts.

The second repair scenario involves repairs of a damaged or completely severed stringer. As before, the affected site is cleaned out by introducing an elliptical cutout. The removed part of the damaged stringer is replaced by an aluminum substitute, and the entire area is covered with a metal doubler attached to the skin by means of mechanical fasteners. The repairs of this type were investigated on a five-stringer panel. A typical wing cover location for such panel is shown in Figure 16.

The tests of the five-stringer and the four-stringer (Figure 17) repair panels verified the required ultimate capacity of the repaired structures in terms of the allowable gross stress level. The upper cover is currently being designed to withstand 40 ksi of gross ultimate compression stress. The lower cover, being composed of a superior strength hybrid material with IM7 fiber, is designed to 50 ksi gross ultimate tension stress. Although the above stress allowables are assumed to apply universally to any location within the wing, further work may be required to investigate whether any fine-tuning or modifications in the proposed repair concept are required for some local regions in the wing such as spar caps and access doors, or for any other locations where loading or the geometry are drastically different from the tested configurations. Some of this work is being planned for the later phases of the wing development project.

The current status of stress allowables corresponding to various structural design criteria and compared to the required structural capacity is given in Figure 18. The figure demonstrates that all the structural design goals set for the development of the semi-span wing are being met successfully.

The gross allowable stress of 40 ksi and 50 ksi for the upper and lower covers respectively in general satisfy only the reparability requirement of the wing. It has been observed that the undetectable damage criterion is more restrictive than the reparability condition when moderately thin laminates are considered. Predicting the residual strength of a composite structure subjected

to impact is a complex task which is still a topic for much of the ongoing research within the stress community. Many of the proposed solutions requiring an intensive computational effort, such as a progressive failure model, are clearly unacceptable for a production type of design effort. In response to the need for a simple, yet effective theory, NASA has developed a parametric damage model, Ref. 6.

The parametric damage model assumes that the residual strength of a structure depends on a single damage parameter. It has been found that the damage parameter giving the best fit to the experimental data is a maximum impact force divided by the square of the laminate thickness, Figure 19. The impact force is calculated from an energy balance equation and should include the stiffness and inertial characteristics of the impacted structure. The parametric damage model makes it possible to apply the information gathered from coupon testing for prediction of the compression-after-impact strength (CAI) of an actual structure by relating both to the same parameter.

It is important to note that for the same level of impact energy and the same thickness, the residual strength of a structure will typically be higher than that of a coupon, because coupons, being stiffer, usually develop higher impact forces. This observation allows us to conservatively utilize the CAI strength obtained from coupons and apply the methods of the parametric damage model only to those locations in the wing which operate at low safety margins. This simplifies the design process by allowing the construction of a single stress allowable curve applicable to a wide range of laminate thicknesses, Figure 20. A similar curve is currently being prepared for the lower cover laminates except that, besides the CAI strength, it also addresses the tension-after impact allowable strength (TAI).

In addition to the structural design criteria whose function is essentially to prescribe the allowable stress level within the wing, there are a number of manufacturing requirements which have to be addressed in the design process. The maximum depth of the stringer plus skin is set at 4.0 in to satisfy the stitching machine constraint shown in Figure 21. The maximum number of skin stacks which can be stitched by a multi-needle machine is currently nineteen (each stack is .054 in. thick). In order to be able to utilize a multi-needle machine for stitching of the upper cover blades, the blade thickness must be limited to a maximum of ten stacks. Skin stack drop-offs must accomplished one at a time to minimize the joggle of the stringer blade, Figure 22.

The design of a real wing structure which eventually will be flown on an actual airplane is a complex and involved process which requires a careful consideration of all the various design issues. Many of these issues, which have been omitted in this paper due to its limited scope, can be found in Ref. 1. Among these are the tooling development, design for lightning protection, fuel and other systems issues.

Analysis Methodology

Reliable analysis methods are required in order to minimize the risk associated with the development of a new all-composite wing. The analysis methodologies developed during the

preliminary phases of the project and used for the analysis of the semi-span wing will be ultimately validated when the wing box is tested at NASA Langley. Many of the techniques have already been validated during the subcomponent tests phase of the project. Among these are the modified lamination theory, composite joint analysis techniques, the parametric damage model.

The development of the modified lamination theory was necessitated by the fact that the ultimate strength and stiffness of a stitched warp-knit material are affected by crimping of the load carrying fibers. The problem was solved by assuming that the extent and the effect of the crimping was a function of the fiber orientation. The material properties of each layer within a stack were assigned based on the layer's direction relative to the stitching path. Table 1 lists the laminae properties which were derived from test.

Table 1. Stitched Lamina Material Properties

Lamina Properties	0-degree	45-degree	90-degree
E_l (msi)	18.0	17.7	17.5
E_t (msi)	1.62	1.62	1.62
G_{lt} (msi)	.80	.80	.80
ν	.34	.34	.34
F_{lt} (ksi)	225.	200.	185.
F_{lc} (ksi)	145.	140.	135.
F_{tt} (ksi)	5.	5.	5.
F_{tc} (ksi)	31.	31.	31.
F_{sh} (ksi)	17.5	17.5	17.5

The unnotched strength properties of a laminate are rarely used in the strength analysis of a composite component, because it is the notched allowables and the CAI strength which are the critical parameters governing the load carrying capability of the component. The unnotched laminate properties are nevertheless important for defining the reference strength in the off-axis directions. This off-axis strength is used for establishing the open- and loaded-hole strength of the wing laminates. The method for calculating these is based on the stress concentration theory of J. Hart-Smith, Ref. 9.

The theory, originally developed for uniaxially loaded composite holes and recently generalized to include the effect of biaxial loading, is based on a postulate that the degree of stress relaxation at the surface of a hole is linear with the stress concentration factor acting on the net section. The theory is functionally equivalent to the point stress method (Ref.10), and in fact reduces to it in the case of an infinitely wide plate. Unlike the point stress method, Hart-Smith theory cannot account for the hole size effect and for the effect of the off-axis loading. An extensive testing program was therefore undertaken to fully characterize the wing cover laminates by considering

all the various hole sizes and load orientations. The results of the test were cast in terms of the stress reduction coefficients referred to as the C-factors.

Although the C-factor approach does require more coupon testing than the point stress method, the method has some definite advantages over the point stress method, especially in situations when the bearing-bypass interaction type of analysis is required. It has been observed that the loaded hole analysis based on the characteristic distance derived from tests of the open hole coupons does not correlate well with the test results. Since in the C-factor theory the stress reduction coefficients are defined for the separate loaded - and open-hole problems, a better match to the experimental data can be obtained. This improved accuracy was especially important when the repairs of the wing cover, the root splice area and the Main Landing gear attachment were analyzed. The analysis of the latter presented a particular challenge since the directions of the by-pass and bearing loads, as well as the material direction of the skin laminate were all misalligned relative to each other.

The methodology of analysis for damage tolerance is based on the parametric damage model described earlier. In the course of the stress analysis of the lower cover access holes, a limitation in the application of the parametric damage model method was encountered. High stress concentrations on the surface of an access hole make it very conservative to directly utilize the TAI allowable stress which is by definition a measure of the far field failure stress. Improvements to the method are being studied.

To determine the internal load distributions in the wing, a FEM model of the semi-span wing , Figure 23, has been constructed in PATRAN 3.0 and executed in NASTRAN This model serves as the global element in the global-local analysis process. Some of the local fine-grid FEM models representing the critical subcomponents are shown in Figure 24. The global FEM model of the wing will be used to perform global buckling analysis, once sizing of all the wing components is completed. According to the design criteria, neither the global nor local buckling modes are permitted to occur in any structural component of the semi-span wing. Since the stringers are designed to have stable cross-sections, they are analyzed as continuous multi-span beam-columns deflected laterally to match the wing deflected configuration. Failure of a stringer is assumed to occur when the combined axial and bending stress at the edge of a blade exceeds the CAI allowable stress.

Conclusions

The development effort to design and build an all-composite wing structure has been presented. It is demonstrated in this paper that all the cost and weight targets which make the all-composite wing an attractive alternative to a conventional metal wing are being met. The success of the program is largely due to the outstanding damage tolerance characteristics and low cost associated with the S/RFI process. Up to this point in the wing development program, no major problems have been encountered in design, analysis or manufacturing. The program successfully passed the preliminary design review (PDR) with NASA in March 1994, and a full development

effort is underway now to prepare for the critical design review (CDR) to be held in August 1995.

Acknowledgments

The author would like to express his appreciation to Arthur Hawley and Jay Sutton for their technical guidance and their invaluable help in preparing this document.

References

1. Hawley, A. V.: Preliminary Design of a Transport Aircraft Composite Wing, Fifth NASA/DoD Advanced Composites Technology Conference, Aug. 1994

2. Sutton, J.O, Jegley, D., Kropp, Y., and Banister-Hendsbee, D. L.: Design, Analysis, and Test of Composite Primary Wing Structure Repairs, Fifth NASA/DoD Advanced Composites Technology Conference, Aug. 1994

3. Hawley, A. V. and Sutton, J. O.: Design and Analysis Consideration for Stitched/RTM Composite Wing Structure, NASA CP 3229, 1993

4. Department of Transportation, FAA, Federal Aviation Regulations Part 25 - Airworthiness Standards: Transport Category Airplanes

5. "Damage Tolerance and Fatigue Evaluation of Structure", FAR Advisory Circular, AC 25.571-1a, March 5, 1986

6. Jackson, W. C., and Poe, Jr. C. C.: The Use of Impact Force as a Scale Parameter for the Impact Response of Composite Laminates, NASA TM 104189, January 1992.

7. Hinrichs, S. , Chen, V., Jegley, D, Dickenson, L.C., Kedward, K.: Effect of Impact on Stitched/RFI Compression Panels, Fifth NASA/DoD Advanced Composites Technology Conference, Aug. 1994

8. Burwasser, J. T., and Stewart, T. Z.: Composite Wing Verification Subcomponents, Fifth NASA/DoD Advanced Composites Technology Conference, Aug. 1994

9. Nelson, W. D., Bunin, B. L., and Hart-Smith, L. J.: Critical Joints in Large Composite Aircraft Structure, NASA CR-158902-2, July 1978

10 Deaton, J. W., Dexter, H. B., Markus, A. M., and Rohwer, K. M.: Evaluation of Braided Stiffener Concepts for Transport Aircraft Wing Structures, Fifth NASA/DoD Advanced Composites Technology Conference, Aug. 1994

10. Whitney, J. M. and Nuismer, R. J. : Stress Fracture Criteria for Laminated Composites Containing Stress Concentrations, J. of Composite Materials, Volume 8, July 1974

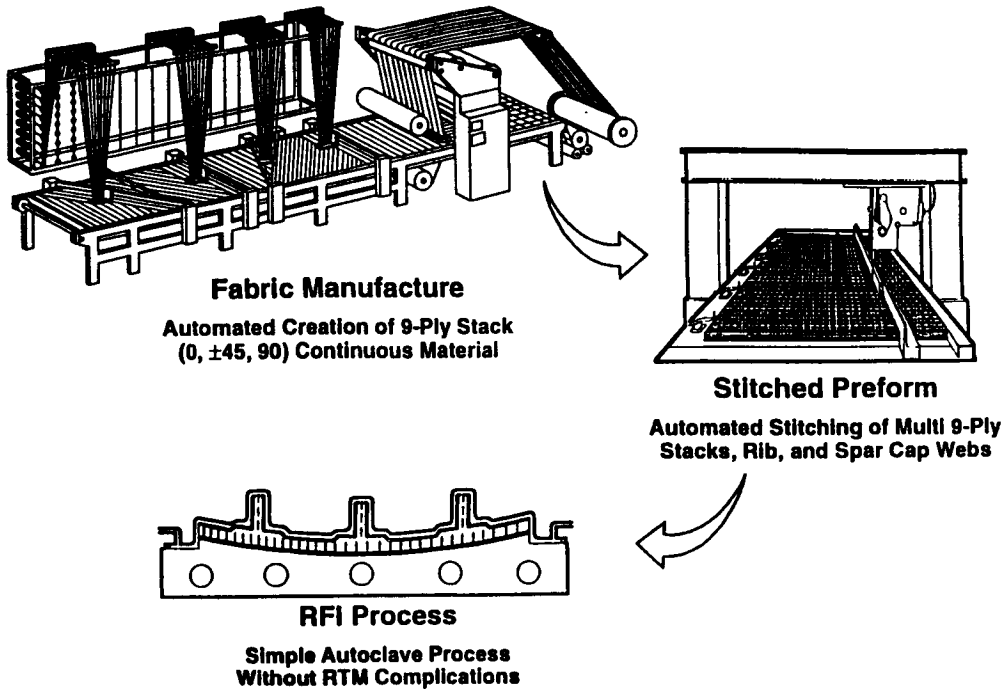

Figure 1. Stitched RFI Manufacturing Process

MD-XX Transport Aircraft
D-3308-4 configuration
192 passengers
Wing span = 129 ft. 4.5 in.
Wing area = 1385 sq. ft.
Wing aspect ratio = 12.1

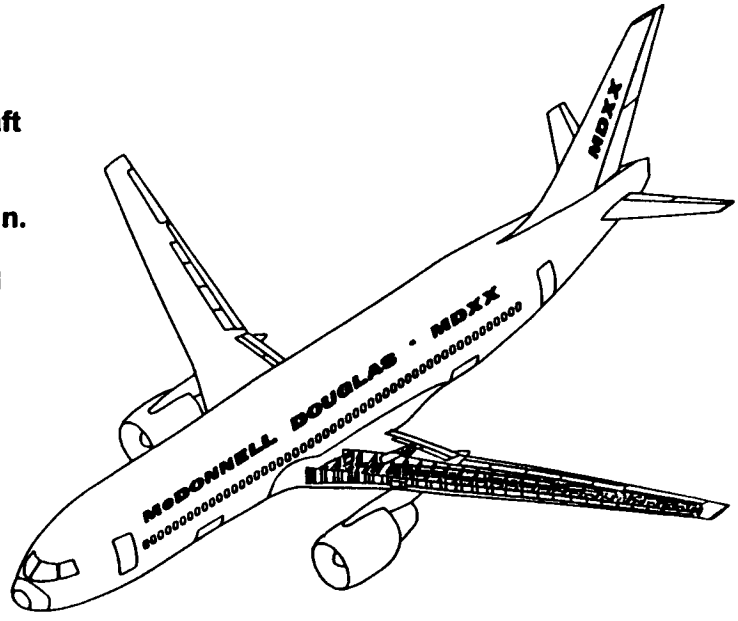

Figure 2. Baseline Aircraft

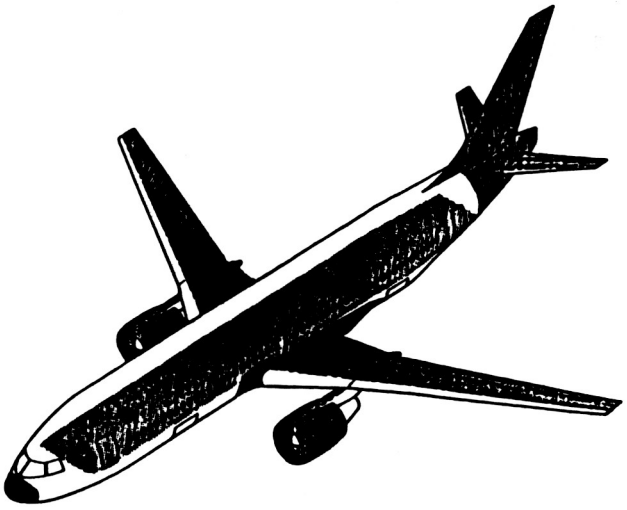

Radome
Tailcone
Fairings
Nacelles
Fuselage Floor
Stabilizers
Control Surfaces
L/G Doors
Wing Box

Figure 3. MD-XX Composite Applications

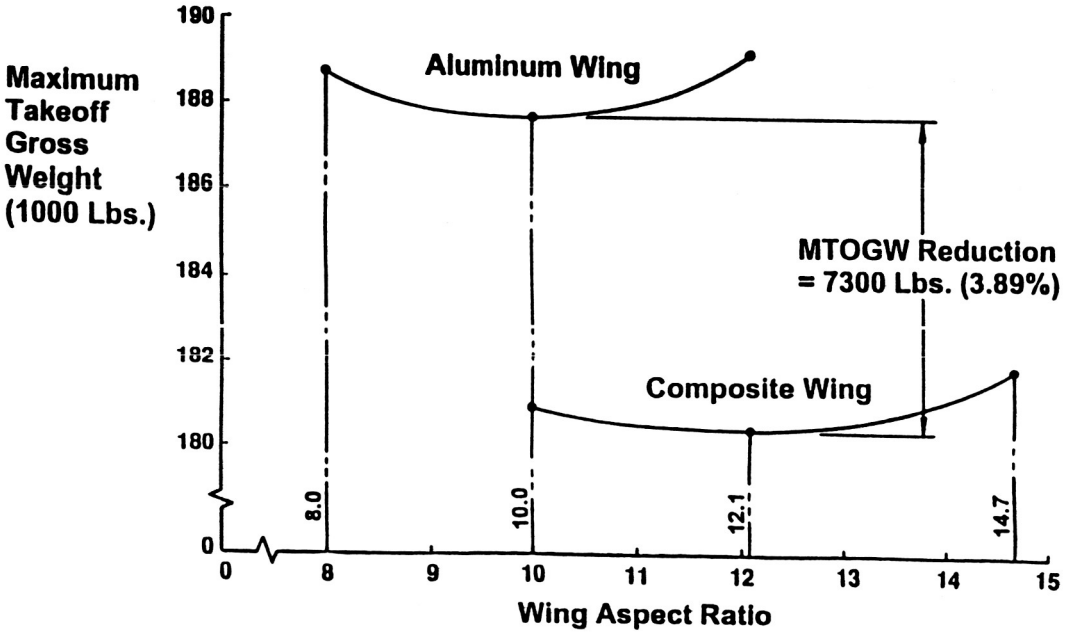

Figure 4. Aircraft Aspect Ratio Study

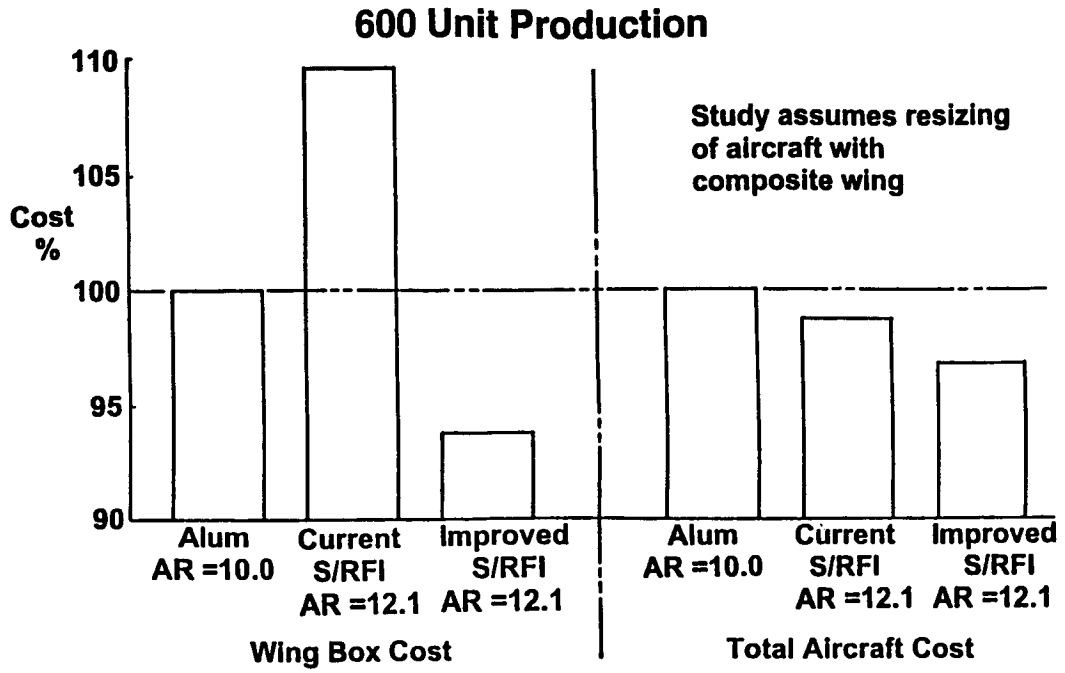

Figure 5. Aircraft Cost Study

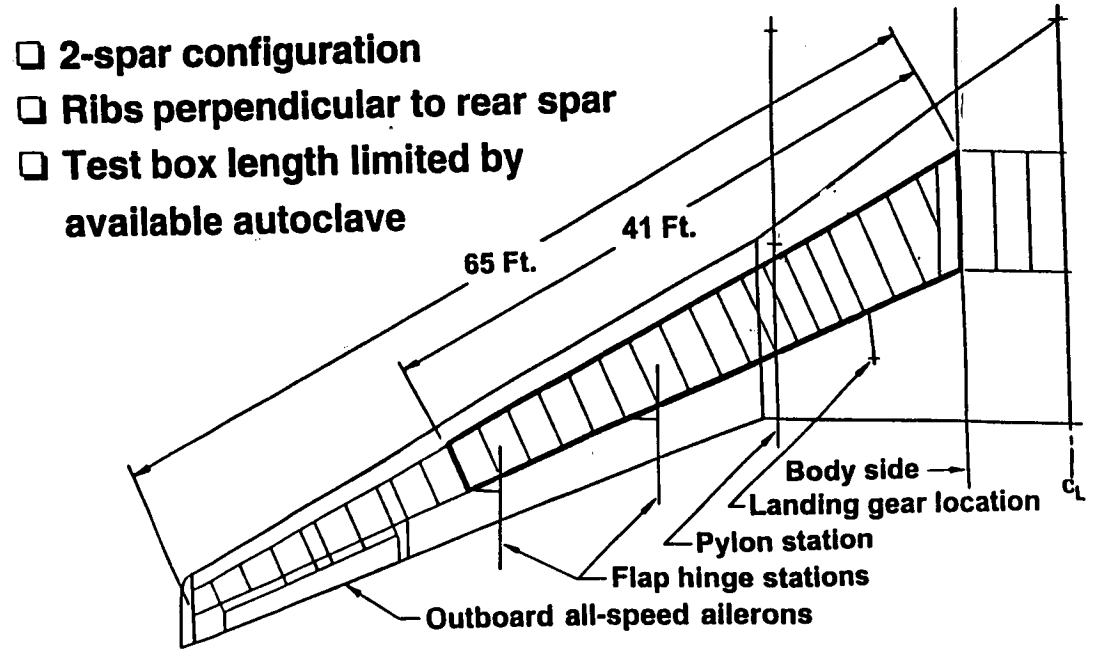

Figure 6. Baseline Wing Configuration

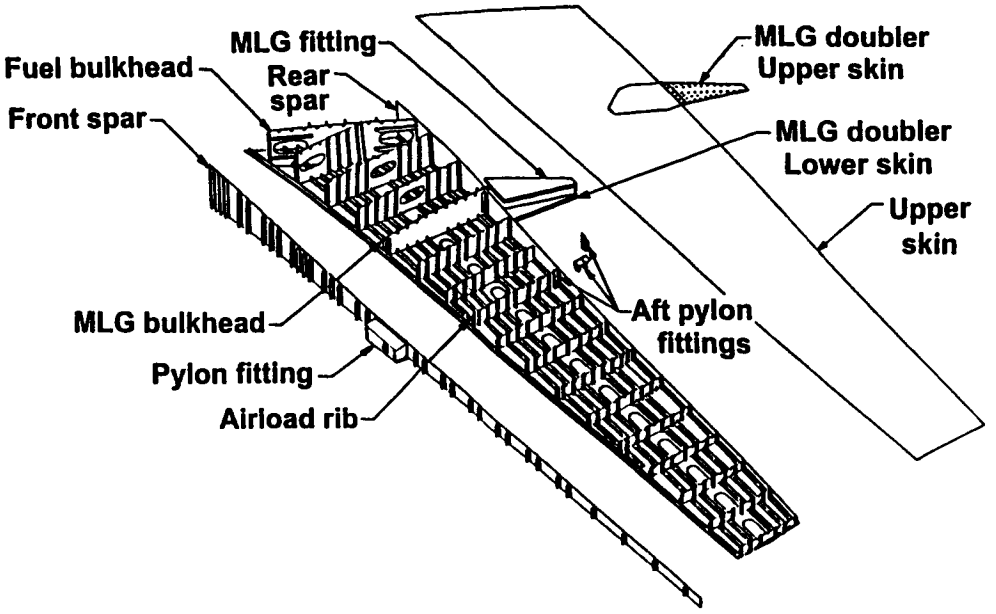

Figure 7. Structural Wing Box Components

LAYER DIRECTION	AREAL WEIGHT (g/m^2)	FIBER MATERIAL	
		TYPE 1 (UPPER)	TYPE 2 (LOWER)
45	153	AS4	AS4
-45	153	AS4	AS4
0	320	AS4	IM7
0			
90	173	AS4	AS4
0	320	AS4	IM7
0			
-45	153	AS4	AS4
45	153	AS4	AS4
TOTAL	1425		

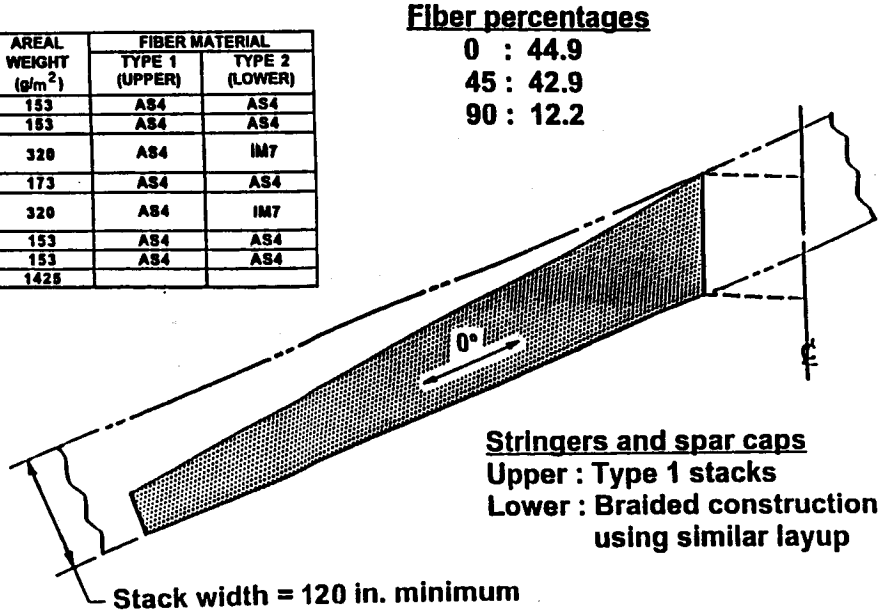

Figure 8. Preplied Laminate Stack

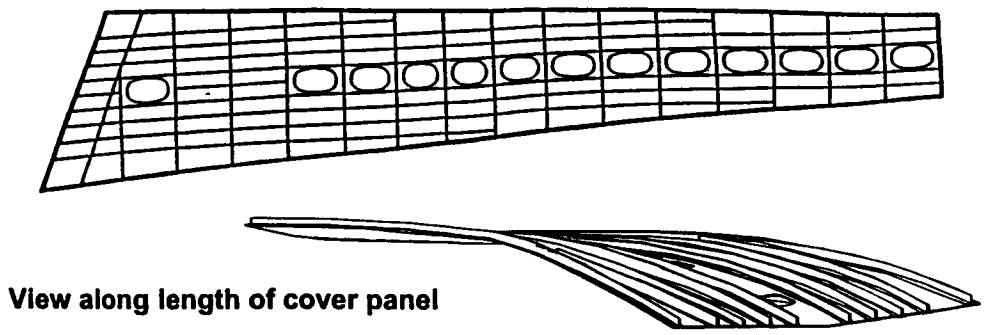

- Twisted double curvature surface
- Fuel access holes midway between spars
- Stringer planes determined by door locations

Figure 9. Wing Lower Cover

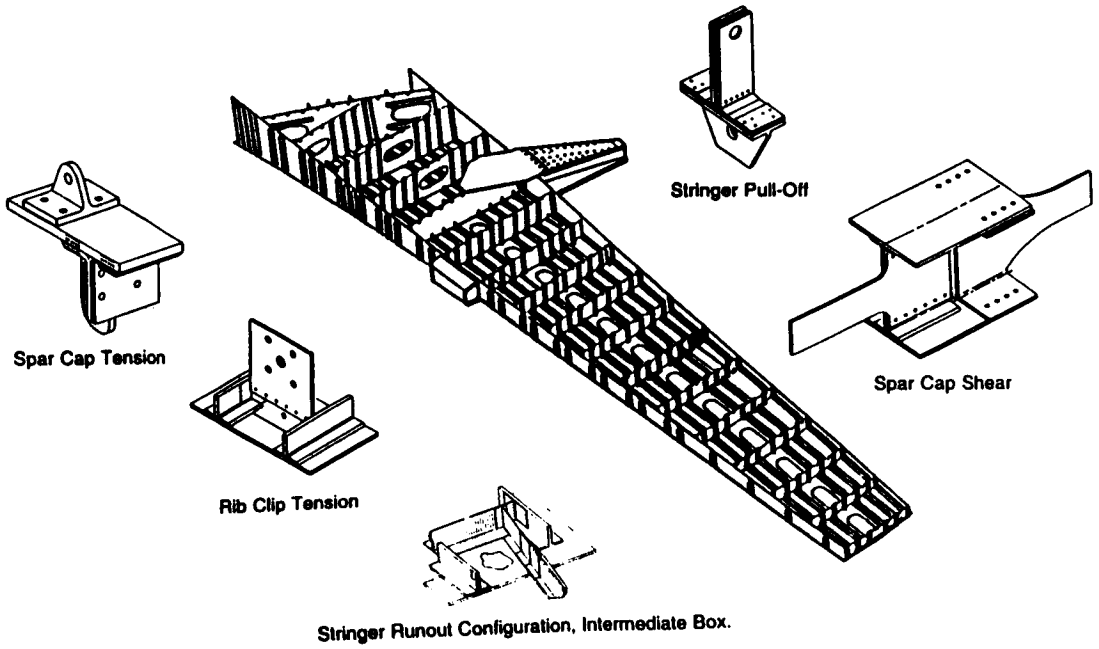

Figure 10. Subcomponent Test Program

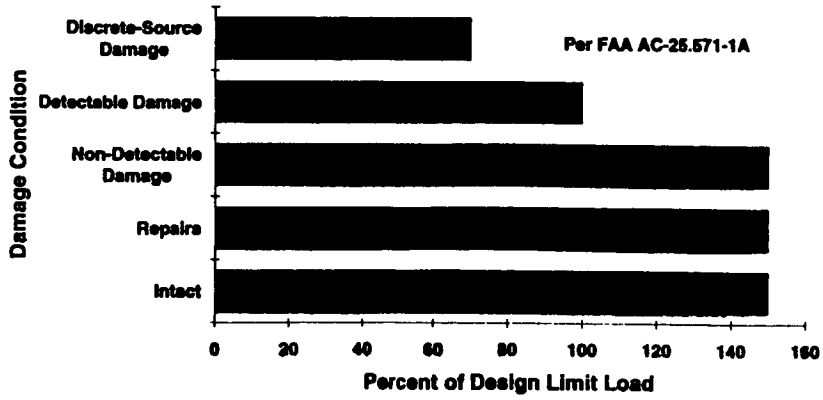

Figure 11. Composite Wing Design Criteria

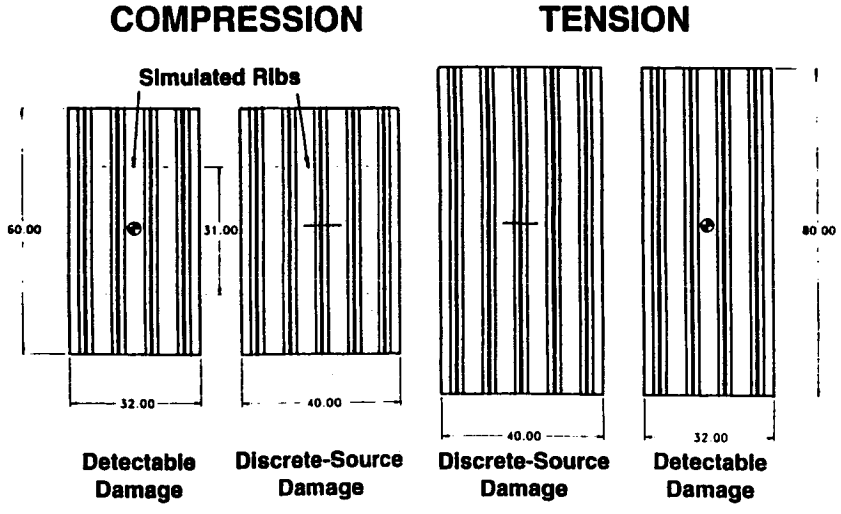

Figure 12. Wing Cover Damage Tolerance Test Panels

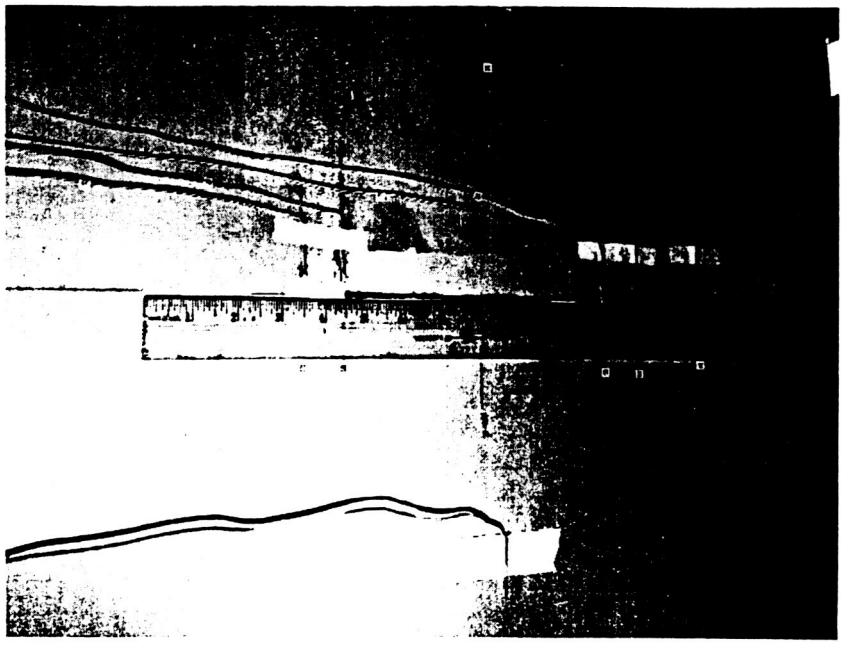

Figure 13. Panel with Discrete Source Damage

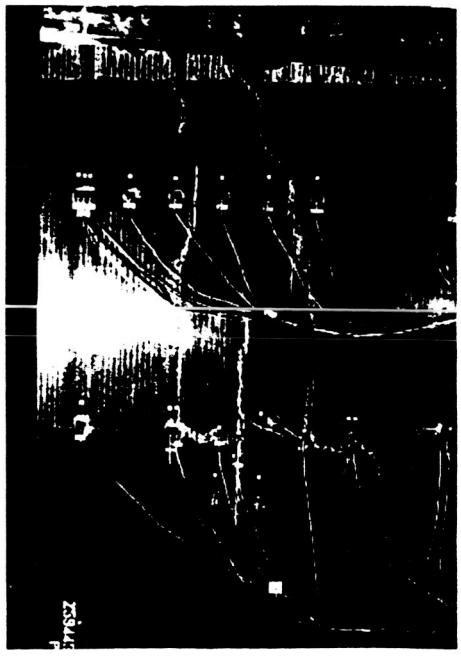

Figure 14. Failure of Discrete Source Damage Tension Panel

Figure 15. Failure of Discrete Source Damage Compression Panel

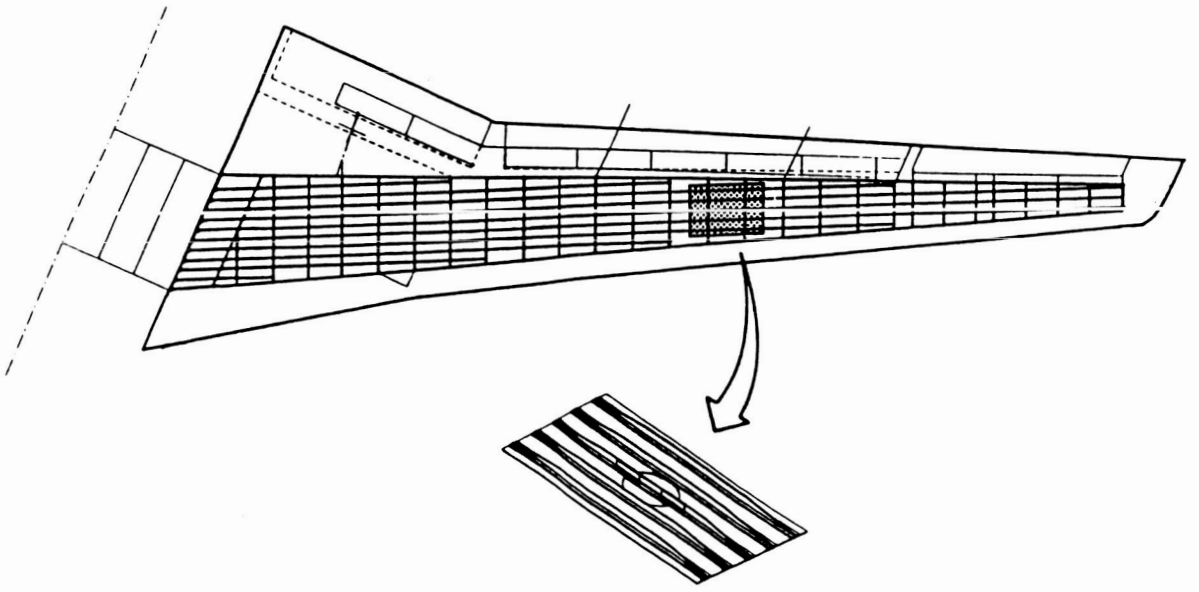

Figure 16. Location of Test Repair Panel

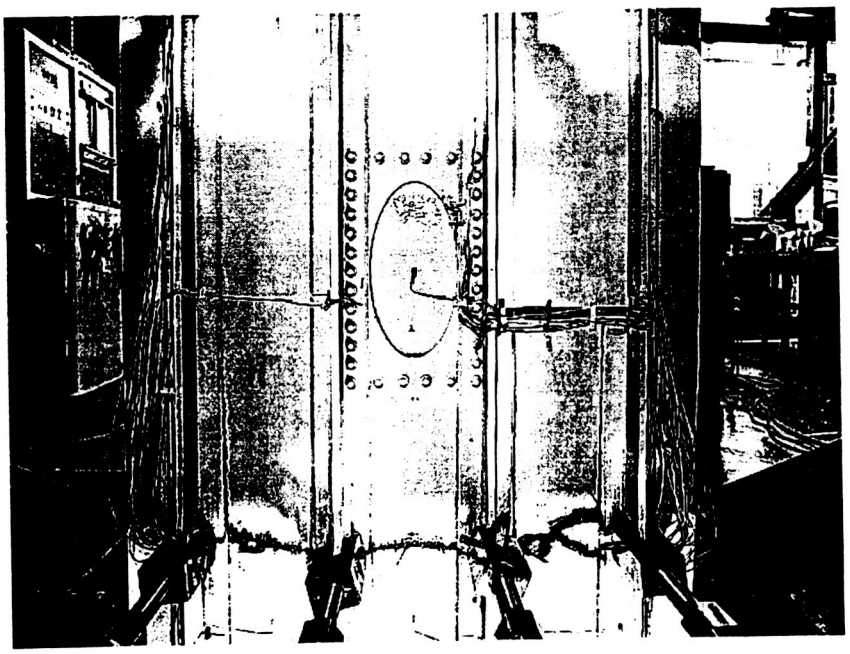

Figure 17. Failure of Repaired Compression Panel

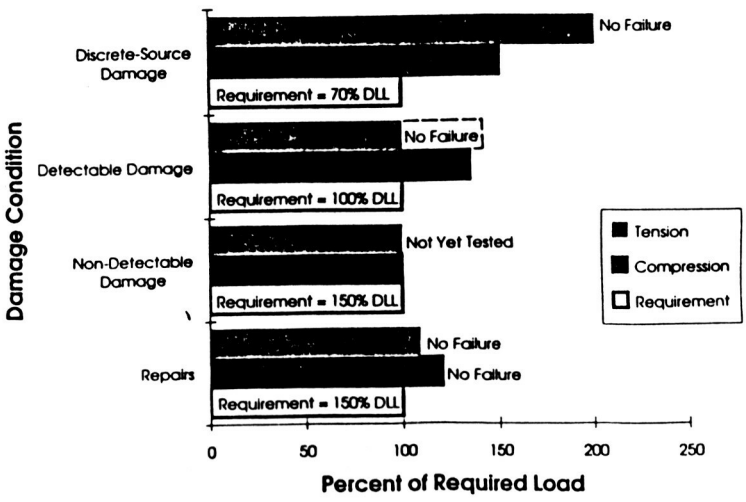

Figure 18. Design Criteria vrs Test for the Semi-Span Wing

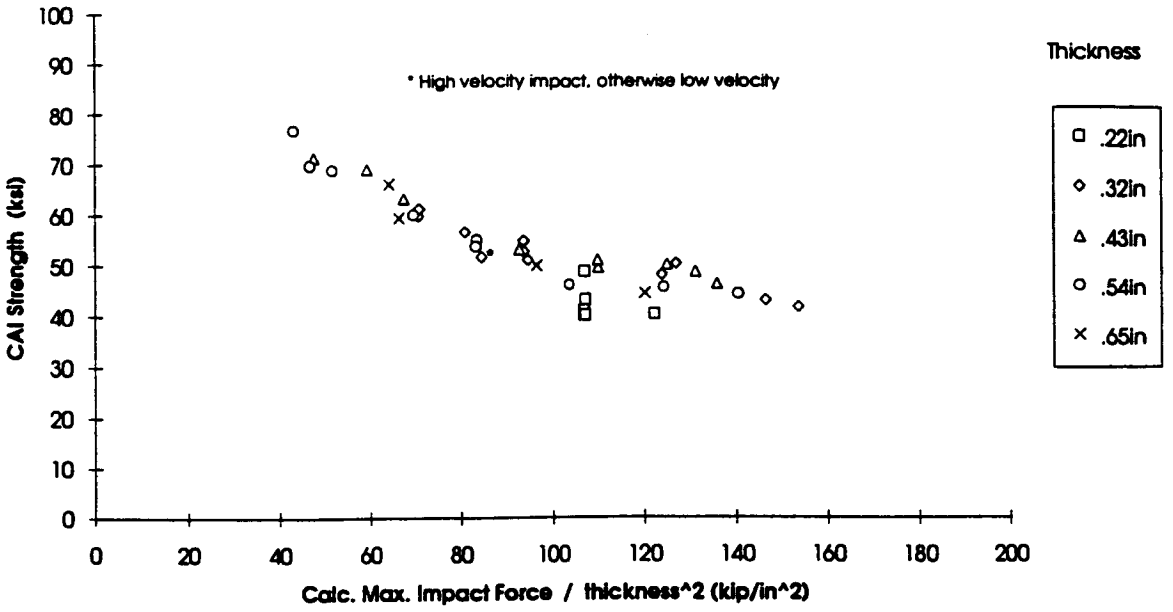

Figure 19. CAI Strength For Wing Upper Cover

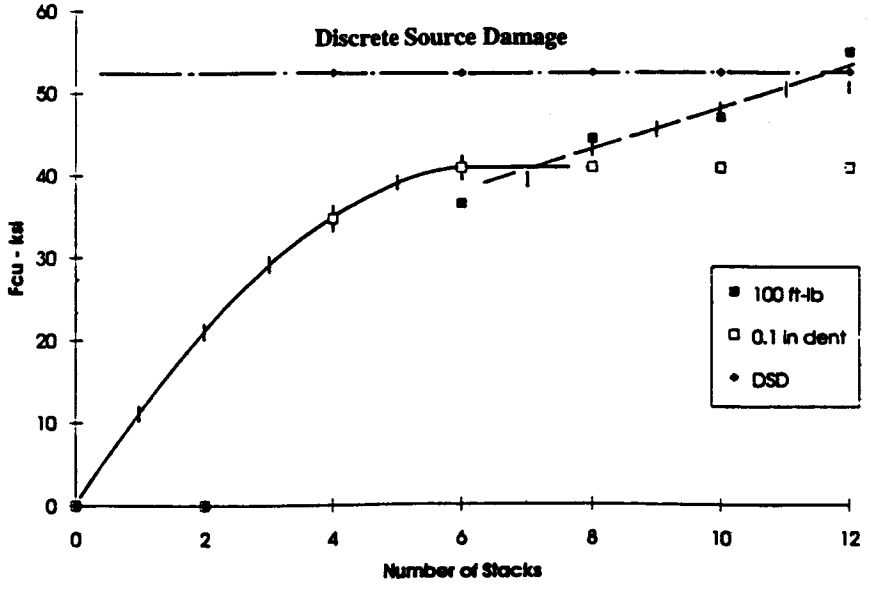

Figure 20. Upper Cover Allowable Stress for Damage Tolerant Design

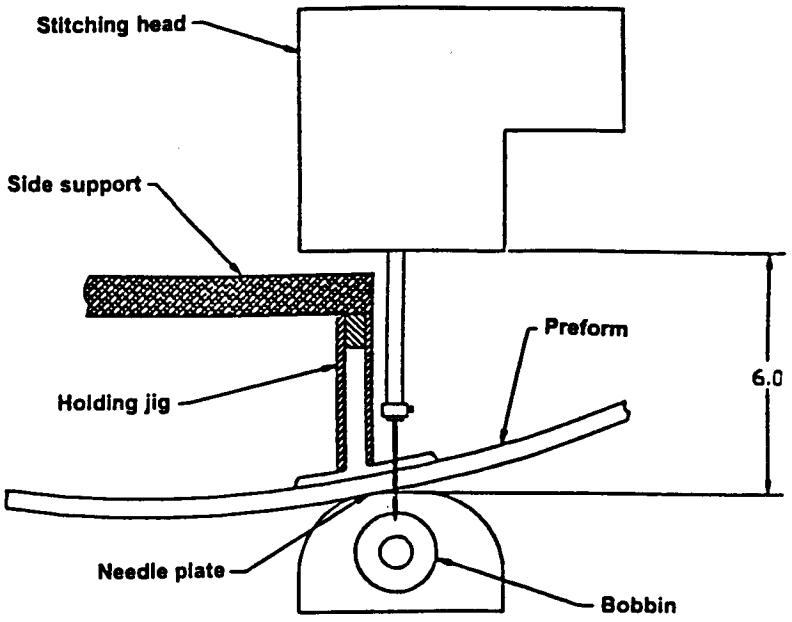

Figure 21 Stitching Head Clearance Constraint

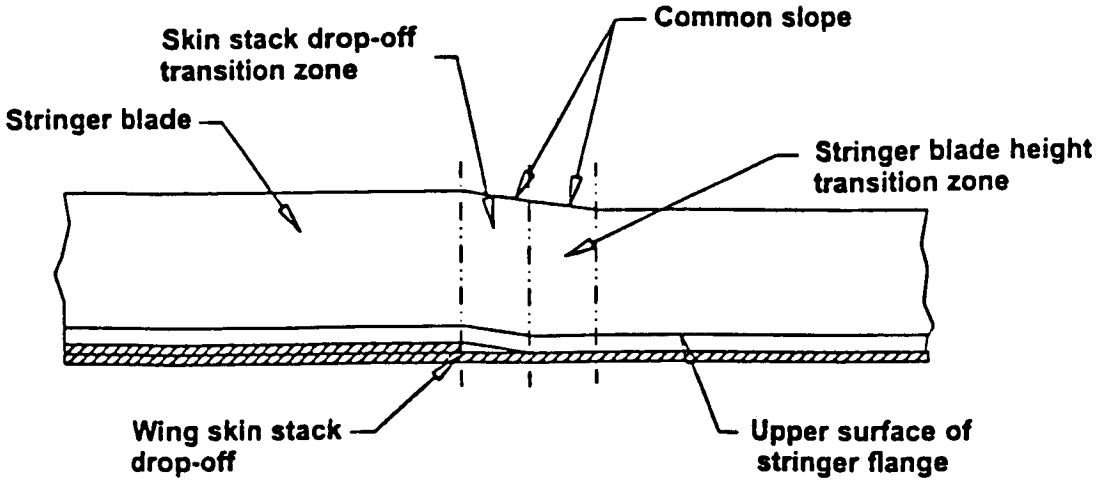

Figure 22 Stringer Height Transitions

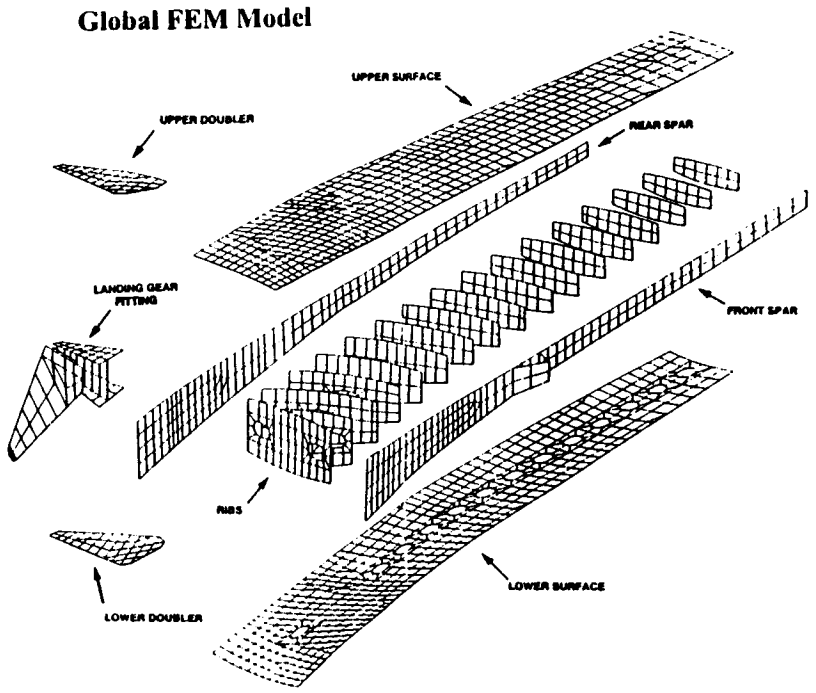

Figure 23 Global FEM Model of the Semi-Span Wing

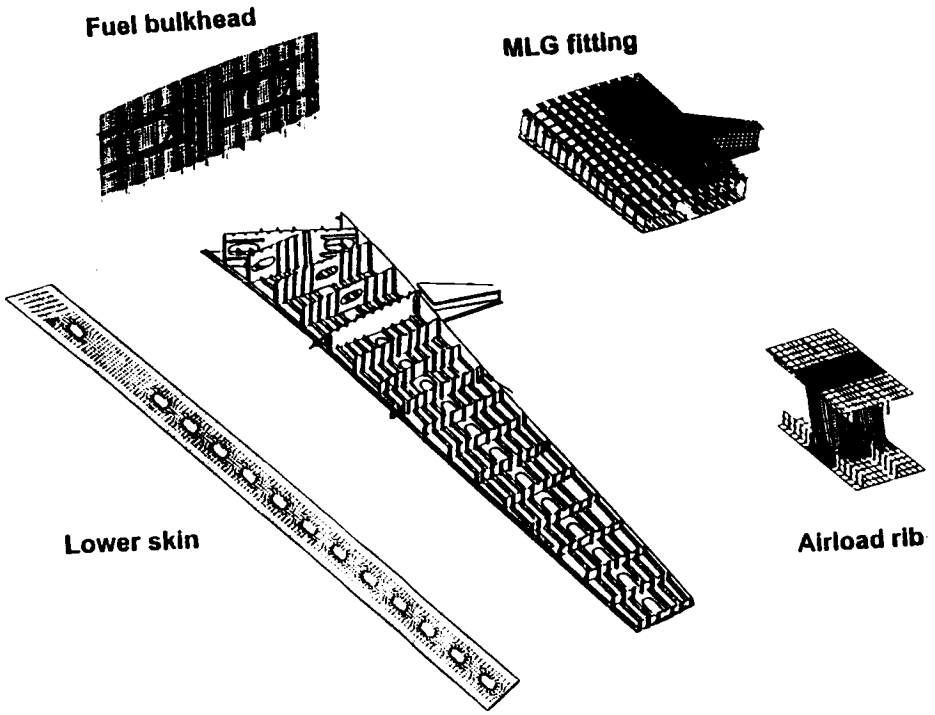

Figure 24 Global/Local Analysis of Critical Components.

EFFECTS OF STITCHING ON FRACTURE TOUGHNESS OF UNIWEAVE TEXTILE GRAPHITE/EPOXY LAMINATES*

Bhavani V. Sankar
and
Suresh K. Sharma
Center for Studies of Advanced Structural Composites
University of Florida
Gainesville, FL

SUMMARY

The effects of through-the-thickness stitching on impact damage resistance, impact damage tolerance, and Mode I and Mode II fracture toughness of textile graphite/epoxy laminates were studied experimentally. Graphite/epoxy laminates were fabricated from AS4 graphite uniweave textiles and 3501-6 epoxy using Resin Transfer Molding. The cloths were stitched with Kevlar® and glass yarns before resin infusion. Delamination were implanted during processing to simulate impact damage. Sublaminate buckling tests were performed in a novel fixture to measure Compression After Impact (CAI) strength of stitched laminates. The results show that CAI strength can be improved up to 400% by through-the-thickness stitching. Double Cantilever Beam tests were performed to study the effect of stitching on Mode I fracture toughness G_{Ic}. It was found that G_{Ic} increase 30 times even for a low stitching density of 16 stitches/square inch. Mode II fracture toughness was measured by testing the stitched beams in End Notch Flexure tests. Unlike in unstitched beams crack propagation in stitched beams was steady. The current formulas for ENF tests were not found suitable for determining G_{IIC} for stitched beams. Hence two new methods were developed - one based on crack area measured from ultrasonic C-scanning and the other based on equivalent crack area measured from the residual stiffness of the specimen. The G_{IIc} was found to be at least 5 -15 times higher for the stitched laminates. The mechanisms by which stitching increases the CAI strength and fracture toughness are discussed.

INTRODUCTION

Though the unidirectional laminated composites have high strength in fiber direction, they lack through-the-thickness reinforcement. Hence, they have poor interlaminar fracture toughness and are susceptible to delaminations. One of the ways to reinforce a laminate through the thickness is stitching. The idea of stitching the textile preform fits well within the realm of existing textile technology. Mignery et al. [1] investigated use of stitching by

*Work done on grant at the University of Florida, NAG-1-1226.

Kevlar® yarn to suppress delamination in unidirectional graphite/epoxy laminates. The results showed stitches effectively arrest delamination. Dexter and Funk [2] investigated characterization of impact resistance and interlaminar fracture toughness of quasi-isotropic graphite-epoxy laminates made of unidirectional Thornel 300-6K fibers/Hercules 3501-6 resin and stitched with polyester or Kevlar® yarns. They experimented with stitch parameters and found significant drop in damage areas of stitched laminates compared to unstitched laminates for the same impact energy. The Mode I fracture toughness, characterized by the critical strain energy release rate, G_{Ic} , was found to be about 30 times higher for the stitched laminates. Effect on Mode II fracture toughness was not investigated in this study. Ogo [3] investigated effect of through-the-thickness stitching of plain woven graphite/epoxy laminates with Kevlar® yarn. The study showed manifold increase in G_{Ic} values at the expense of slight drop of in-plane properties. However, his results did not show any significant increase (8%) in Mode II fracture toughness as characterized by the critical strain energy release rate, G_{IIc}. Pelstring and Madan [4] developed semiempirical formulae relating damage tolerance of a composite laminate to stitching parameters. Mode I critical strain energy release rate was found to be 15 times over the unstitched laminates, and the critical strain energy release rates decreased exponentially with increase in stitch spacing. Correlation of toughness characteristics shows that predictable trend existed between strain energy release rate, damage area, and CAI strength. Byun et al. [5] conducted a finite element analysis on 3-D woven double cantilever beam (DCB) specimen and evaluated Mode I critical strain energy release rate to investigate the influence of through-the-thickness fibers on crack driving force on crack length. Chen et al. [6] proposed effective critical strain energy release rate to measure Mode I fracture toughness of stitched laminates using a finite element model. Recently, Jain and Mai [7] have analytically modeled Mode I delamination toughness of stitched laminated composites.

It is evident from above studies that through-the-thickness stitching significantly improves Mode I fracture toughness in laminates made of unidirectional tapes or plain woven fabric cloth of graphite and epoxy resin. However, effect on Mode II fracture toughness needs to be fully investigated. Further, variations of stitch density, stitch failure mechanisms and their contribution to Mode I and Mode II fracture toughness are not completely understood.

EXPERIMENTAL PROGRAM

An experimental program was conducted to understand the effects of stitching on Mode I and Mode II fracture toughness. To measure critical strain energy release (G_{Ic}) in Mode I crack propagation mode, Double Cantilever Beam (DCB) tests were performed on stitched and unstitched laminates in stroke control mode. Similarly, to measure the critical strain energy release rate in Mode II fracture (G_{IIc}), End Notched Flexure (ENF) tests were conducted. Material system for both types of tests were same as described in the following section. At least 3 and up to 12 specimens were tested for each category of specimen to study stitch failure mechanisms and ensure statistically consistent data. Guidelines suggested by Carlsson [8] were used to perform the tests. Energy-Area method was used to compute G_{Ic}. New methods to compute G_{IIc} have been explored for the stitched laminates and are presented

in a later section.

Effects of stitch yarn, stitch density and yarn denier on G_{Ic} were studied. Stitch damage mechanisms in Mode I tests were investigated using Photomicrography and Scanning Electron Microscopy (SEM). Effects of stitch yarn, stitch density, yarn number, starter crack length, crack surface and contact roller pin friction and unstitched length on G_{IIc} were studied. The unstitched length is defined as the distance of starter crack from the first stitch. Stitch damage mechanisms in Mode II tests were investigated using X-Radiography, Ultrasonic C-Scanning and Photomicrography.

MATERIAL SYSTEM

Uniweave graphite fabric preforms of 24 plies were stitched and Resin-Transfer-Molded (RTM) with epoxy 3501-6 resin to fabricate plates from which the specimens were machined. A modified lock stitch was used. This lock ensures the position of needle and bobbin stitch interlock on top surface of the laminate. Three bobbin yarns of different denier , each with two different stitch densities of 4×1/4" and 8×1/8" were used for stitching. A denier is a measure of linear density in grams per 9000 meters of the yarn. This can also be represented by yarn number which is given by yards/lb for the yarn. Further, we define stitch density in a composite laminate by the number of stitches per square inch and represent this density by the stitching pattern as: (Number of stitches per inch) × (Spacing between two stitch lines), e.g., 8×1/8" means a stitch density of 64 where pitch is 8 stitches per inch and distance between two adjoining stitch rows is 1/8". Needle stitching yarn used in all the cases was Kevlar®-29 made by E.I. du Pont de Nemours and Co., Inc.. Top and bottom plies of the uniweave preform were covered by one layer of plain weave fiberglass cloth to act as retainer cloth for the stitches. The details of the stitch yarns used are given in Table 1. For the purposes of this document, the three bobbin stitch yarns will be referred to as: Kevlar-2790, Glass-1250 and Glass-750. In addition, one unstitched plate for each type of testing was processed for control specimens. Thus, seven plates (#24 to 30) were processed for Mode I and Mode II Fracture Toughness Tests as per details shown in Table 2 and Fig. 1. The plates were Ultrasonically C-Scanned for quality and location of teflon inserts. A schematic diagram of the DCB and ENF specimens is shown in Fig. 2 and Fig. 3 respectively.

DOUBLE CANTILEVER BEAM TESTS: RESULTS AND ANALYSIS

G_{Ic} of the Unstitched and 4×1/4" Stitched Laminates

Stitch Failure Mechanism

Crack propagation during the DCB test in case of the unstitched laminates was gradual and steady, while it was observed to be intermittent and dynamic in the case of the stitched

laminates. Crack front always proceeded ahead leaving the unbroken stitches in the wake. The stitches first debond from the matrix and subsequently break as the crack continues to propagate. The failure of stitches always occurred at the position of bobbin and needle yarn stitch lock in case of Kevlar-2790 and Glass-1250. In both of these types of stitch yarns, the bobbin yarn broke at the stitch lock and not the needle yarn *like* splitting into two reinforcing stems of bobbin yarn. However, in case of the thicker Glass-750 bobbin yarn, the needle yarn failed leaving the bobbin yarn intact. Breaking of the needle yarn in such a case created a hole on the top surface where the stitch lock was located. Broken bobbin stitch yarns prevented the crack to close completely during the unloading as also indicated by a slight compressive load seen in the typical P-δ curves of a DCB test given in Fig. 4.

Increase in G_{Ic} due to Stitching

The critical strain energy release rate using energy-area approach is given by:

$$G_{Ic} = \frac{\Delta W}{\Delta A} \qquad (1)$$

where, ΔW is the work done during the each incremental crack propagation and ΔA is the new incremental crack surface area created. It was assumed that the crack front follows a near straight line path and propagates in a self-similar manner. The increase in the Mode I critical strain energy release rates for various laminates are compared in Fig. 5. Increase in the Mode I fracture toughness due to a low stitch density of 4×1/4" is outstanding. The average increase in Mode I fracture toughness due to stitching is at least an order higher than the unstitched laminates. The use of Kevlar-2790 as stitching yarn improved the fracture toughness by about 15 times, use of Glass-1250 improved it by about 30 times, and the Glass-750 increased the toughness by about 21 times. The G_{Ic} value for the unstitched laminates was 302.6 J/m^2.

G_{Ic} of the 8×1/8" Stitched Laminates

Six different hinge installation methods were tried out to make the hinge bond strong enough so that the crack propagates well before the failure of the hinge bond. Details of these methods are given in [9]. Integrally machined hinges shown in Fig. .6a worked satisfactorily. However, the fracture toughness of 8×1/8" stitched specimens was found to be so high that the specimen failed in bending about 1/4" away from the initial starter crack front line. In order to strengthen the specimen, new integrally machined tabs of steel as shown in Fig. 6b were bonded over the entire surface of the specimen. Guenon [10] has studied Mode I interlaminar fracture toughness of 3-D woven composites using a "tabbed specimen" which is similar to this one. However, it was found that this type of tabbing is not suitable for stitched laminates due to holes being created by the failure of the needle yarn as explained earlier. Therefore, it was not possible to experimentally determine G_{Ic} for 8×1/8" stitched specimens of this study using this type of DCB test. The specimens would have to be made thick enough to prevent bending failure. It is conjectured that the G_{Ic} values for these high stitch density laminates may be more by about 100 times over the unstitched laminates.

END NOTCH FLEXURE TESTS: RESULTS AND ANALYSIS

Current Method of Computing G_{IIc} and its Applicability for Stitched Laminates

A typical P-δ curve for an unstitched and a stitched laminate is shown in Fig. 7. The existing literature uses the well known formula to calculate the critical strain energy release rate [3,8] as given in the following equation:

$$G_{IIc}=\frac{9P^2Ca^2}{2w(2L^3+2a^3)} \qquad (2)$$

where, a is starter crack length, L is half length of specimen, C is compliance, w is the width of the specimen and P will be the critical load at the time of crack propagation. The average value obtained by this method was 670.72 J/m^2. An energy-area approach similar to the one described earlier for calculation of G_{Ic} was also used to compare the G_{IIc} values obtained from the formula. An average G_{IIc} of 672.77 J/m^2 was obtained indicating excellent correlation between the two approaches.

While the crack propagation in an unstitched laminate is unsteady as is also indicated by the sudden drop in load on the P-δ curve, the crack propagation in the stitched specimens was observed to be steady. The P-δ curves for all the stitched laminates were observed to follow same nonlinear pattern during the loading. There is no sudden drop in load as the crack starts propagating. Compliance of the specimen gradually changes as the crack propagates. Therefore, the use of beam theory formula using nonlinear P_c and linear C as suggested by Ogo [3] will not give a correct estimate of G_{IIc} in case of stitched laminates. Two new methods to calculate G_{IIc} for the stitched laminates are presented in the following section. Preliminary photomicrographic studies of tested stitched specimens also suggested that the crack length can not be measured accurately from the visual inspection of the side edge. Then, C-Scans were taken and it was found that actual crack propagation was much more than the visually observed. Hence, the values of crack propagation measured by C-Scans were used in computations for the first of the two new methods presented.

New Methods to Determine G_{IIc} of Stitched Laminate

Two new methods have been developed for computing the Mode II fracture toughness as afunction of crack length in ENF tests. They are: (1) Area Method using C-Scan; (2) Equivalent Area Method using Compliance of the Unloading Curve.

The procedure for computing G_{IIc} using the C-scan method can be described by the following steps:

- Ensure starter crack at first stitch line
- Ensure crack propagates to at least few stitches during test
- Calculate work done (ΔW) from P-δ curve

- Find area of crack surface (ΔA) using C-scan
  G_{IIc}= (ΔW)/(ΔA)

The equivalent area method involves the following steps:

- Calculate EI from linear compliance (C) of the loading curve
- Calculate compliance of unloading curve (C') at 500 N line (i.e., a 20% less load than the P_c of linear loading curve)
- Calculate effective crack length (a_{eff}) using C' and the following formulae:

  For $a < L$

$$C' = \frac{(2L^3 + 3a_{eff}^3)}{96EI} \tag{3}$$

  For $a > L$

$$C' = \frac{-(2L - a_{eff})^3}{32EI} + \frac{L^3}{12EI} \tag{4}$$

- Select appropriate a_{eff} out of the two calculated above
- Calculate crack surface area (ΔA) using the selected a_{eff}
- G_{IIc} = (ΔW)/(ΔA)

Effect of Stitching on G_{IIc}

The G_{IIc} values using all the three methods described above, were calculated and the average values of the data are plotted in a bar chart given in Fig. 8. The figure also brings out the comparison of G_{IIc} values using beam theory formula and the two new methods presented above. The crack had propagated up to about center line in all these tests as found by the C-Scans i.e., about the same extent as that of the unstitched laminates. As expected, the values of G_{IIc} obtained from using beam theory formulation do not show any appreciable increase, indicating that the intrinsic Mode II critical strain energy release rate of the material remains the same. However, the stitching does significantly improve the effective or apparent G_{IIc} as indicated by the values obtained from using both of the new area methods. The energy required to propagate the crack is apparently more due to the stitches. This is because not all the energy imparted during the test directly goes to the crack front, a good amount of the energy now is also being used in other stitch damage mechanisms. The stitched laminate appears to behave more like a structure.

The area method using C-scan seems to give the upper bound of G_{IIc} values while the equivalent area method using compliance of the unloading curve gives the lower bound. The increase in apparent G_{IIc} values is very impressive regardless of the stitch yarn. It is about 5-15 times that of the unstitched laminates using the conservative lower bound values. It appears that the crack length detected by the C-Scanning is smaller than the effective crack

propagation length. With each stitch yarn the apparent G_{IIc} increases with increase in the stitch density except for Glass-750, where the change is insignificant due to increased stitch density, pointing towards a possible optimum. Thus it can be concluded that stitching significantly improves the Mode II fracture toughness. The possible stitch failure mechanisms observed are discussed in a later section which further explain the rise in G_{IIc}.

Variation of G_{IIc} with Increase in Crack Length

The slope of the nonlinear loading part of the P-δ curve can be very useful in predicting some of the material properties. This curve represents gradually changing compliance as the crack length increases. Variation in G_{IIc} as the crack propagates was investigated using this part of the curve. Mode II fracture toughness at each data point of the acquired signal was calculated using the energy area method ($\Delta W/\Delta A$). The ΔW is work done from the P-δ curve to propagate the crack length by a total increment of Δa. The total increment of propagated crack length is a_{eff} minus the initial starter crack length a_o. The a_{eff} at each point was computed by using Equ. 3, wherein the C' would be the nonlinear compliance at that point. The variation of G_{IIc} with the crack length for all the stitch yarns used in this study is shown in Fig. 9. The effect of stitching on Mode II fracture toughness can be studied from this curve. Initially, there is very little effect of the stitches and the value of G_{IIc} is about the same as that of an unstitched laminate. As the crack starts propagating, more and more stitches start becoming effective by added energy dissipation due to matrix deformation, thereby, making the material system tougher. The rate of rise of the G_{IIc} for all the 4×1/4" stitch density is less than 8×1/8" density laminates.

The variation of G_{IIc} was also studied in one more way by calculating the ΔW for each of the two successive load increments and dividing this incremental work done by the corresponding incremental increase of ΔA between only those two successive points. A typical curve in case of Glass-750 is shown in Fig. 10 and represents instantaneous variation of G_{IIc} with crack length.

Stitch Failure Mechanisms

Stitch yarn contribution towards increase in Mode II fracture toughness and the associated failure mechanisms were investigated. The crack space is very narrow in the ENF tests of these laminates and visual resolution is much less than the actual extent of crack front propagation. Therefore, the technique of painting side edges with white paint does not work accurately. Ultrasonic C-Scanning did reveal the crack length but as we have seen in the preceding section that this technique seems to measure less than the effective crack length. X-Radiography of crack surface was also attempted. X-Ray opaque fluid solutions of Zinc Iodide, Barium Chloride and Conray® were tried in varying concentrations. The capillary action does not seem to be adequate to obtain good contrast. Variation in X-Ray intensity were also conducted using the facilities at the University's Medical Center. Changes in the distance of the specimen, soaking time for capillary action, X-Ray exposure times, and different photographic films were tried without satisfactory results. Primary problem appears to be the inability of the X-ray opaque dye to penetrate into the extremely narrow crack space or the relative opening of the crack was not sufficient so that opaque solution was

concentrated enough. Future experimental work may explore a more accurate method.

However, physically cutting the specimens in small incremental steps starting from the undamaged end confirmed that even the first stitch line did not break though the crack as seen from the C-scan had propagated at least up to center line of the specimen. The type of stitches used in this study did not break or at best, it is conjectured that perhaps first one or two stitches may have partially broken. The crack front appears to have travelled around the stitch yarn. Due to the uniweave architecture of the fabric there was no additional resistance except that of the matrix and the glass fill yarn (2.5%) typically used in the uniweave cloth during fabric manufacture. This is analogous to stitch yarn "ploughing" through the matrix. The "ploughing" represents plastic or elastic-plastic deformation of the matrix. This explains about the same amount of fracture toughness increase by Kevlar-2790 and Glass-1250 which are closer to each other in diameter, while the Glass-750 being the thicker yarn gives higher rise in fracture toughness for 4×1/4" stitch density. The thicker the yarn, the more there was deformation of the matrix. Also the fracture toughness increases with increase in stitch density indicating increased matrix deformation, except for Glass-750. In the case of 8×1/8" Glass-750, the fracture toughness in fact drops compared to 4×1/4" Glass-750, this may be due to excessive density of this thick yarn making the available matrix volume easier to "plough". This also indicates that there is a possible optimum stitch density for desired fracture toughness and design loading requirements.

EFFECT OF STITCHING ON SUBLAMINATE BUCKLING OF DELAMINATED UNIWEAVE TEXTILE GRAPHITE/EPOXY LAMINATES

Sublaminate Buckling Tests

Sublaminate buckling is an important failure mode in fiber composite laminates that affects compression-after-impact (CAI) strength [11]. This study investigated effects of stitching on sublaminate buckling behavior which is expected to correlate with the CAI strength. Specimens with different stitch densities and known delaminations were subjected to compression loading. The delaminations simulate the impact damage and were created by inserting teflon film strips during the processing in between various ply interfaces in the 48 ply $[(45/0/45)_s]_{4s}$ uniweave textile graphite/epoxy laminates as shown in Fig. 11. Five different types or degrees of damage were simulated (serially #zero to 4, where #zero is the control specimen without any damage), stitch yarns and the variation in stitch densities were same as that for the fracture toughness tests described earlier. The specimens of a gage length of 2.4 or 2.9" and a width of 1.5" were cut from these plates. The loading ends were machined flat and parallel. Back-to-Back strain gages were mounted to study global instabilities. The University of Florida Compression-After-Impact (UF-CAI) test fixture was used for the tests. The fixture allows end compression loading and can be adapted for different gage lengths as shown in Fig. 12. The fixture evolved from an existing NASA post-impact compression fatigue test fixture at the Center for Studies of Advanced Structural Composites, University of Florida. The design considerations and its experimental validation are given in [9]. A typical

stress-strain curve of the test is shown in Fig. 13. A total of 131 specimens were tested.

Effect of Stitching on CAI Strength

The average values of CAI strength normalized for 2.4" gage length are given in Table 3. The variation in CAI strength data was not exceeding 5% in 90 specimens out of the 126 valid tests, and it did not exceed 10% in the remaining showing good consistency in test results. Variation of CAI strength with different types of damage for the unstitched laminates is plotted in Fig. 14. The CAI strength drops significantly with increase in delaminations for unstitched laminates. The effect of stitching with different yarns of 4×1/4" stitch density is shown in Fig. 15. The effect of increased stitch density 8×1/8" can be observed from Fig. 16. The CAI strength of delaminated stitched laminates showed excellent improvement over the delaminated unstitched laminates. The improvement in case of the worst delaminated specimens (Damage type #4) stitched with high stitch density like 8×1/8" was as much as 400% over the unstitched laminates. It is also clear from the CAI strength data and the above mentioned graphs that all the three different stitch yarns seem to improve the CAI strength to about the same extent when their stitch densities are equal. This may be due to the fact that any through-the-thickness stitch yarn with sufficient breaking strength and stiffness is able to restrain buckling of the sublaminates by holding them together. More evidence of this is discussed in next section on the sublaminate buckling failure mode. To study a comparative trend of the improvement in CAI strength data due to stitch density, the data were curve fitted using a locally weighted linear regression (Axum software) and the curves are plotted in Fig 17. Here, it was assumed that the different delaminated states (i.e., Damage types #Zero to 4) simulate impact damage of an increasing order.

Effect of Stitching on Sublaminate Buckling Failure Mode

It was observed that the damaged unstitched laminates tended to fail by buckling of the sublaminates. This could be seen from the white painted side edge surfaces. The painted surface opens up at the teflon inserted interplies and the laminate buckles, but the laminate regains its geometry after the unloading. This failure mode is sketched in Fig. 18. However, stitching tends to hold the sublaminates together thus prevent buckling. The stitch yarns will be subjected to tensile loading in the process of trying to restraint sublaminate buckling. Therefore, the failure mode is drastically changed to typical small kink zone formation and subsequent fiber fracture. This also explains the impressive gains in CAI strength due to 8×1/8" stitch density as compared to 4×1/4" density. This type of failure is schematically shown in Fig. 19.

IMPACT DAMAGE RESISTANCE AND DAMAGE TOLERANCE OF THIN PLAIN WEAVE STITCHED GRAPHITE/EPOXY LAMINATES

Static Indentation tests

The static indentation-flexure (SIF) test can be used to study impact damage response due to impact of large masses at very low velocities [12,13]. These tests simulate quasi-static impact conditions. In addition, they offer greater opportunity to study progressive damage propagation during the impact event. These tests were conducted on unstitched and stitched 16 ply plain weave graphite fabric/epoxy (Hercules A193-P/ 3501-6) laminates. The processing of plates for the specimens was done at Center for Studies of Advanced Structural Composites, University of Florida, and is given in [9]. The specimens were 3.6 mm (0.140") nominally thick square plates i.e., about half the thickness of the uniweave laminates used for sublaminate buckling tests. The stitch densities of 5×1/4" and 8×1/4" with Kevlar-2790 as stitch yarn only were processed. The laminates were simply supported on circular support rings of different diameters. The specimens were statically indented and unloaded at three different contact force levels in order to assess damage progression. Load-displacement data was gathered. Effect of stitching on indentation damage area for a given contact force and damage propagation were studied. Subsequently, residual compression strength of each specimen was measured by performing the CAI test using the UF-CAI test fixture. Ultrasonic C-Scans were taken to assess damage area. The effect of varying support ring diameters used to provide the simple support conditions was also studied.

Impact Damage Resistance of Thin Laminates as Characterized by Impact Force

A representative comparison of the low velocity impact damage response as simulated through static indentation tests for the 8×1/4" stitched and the unstitched laminates at different loading steps and with different support ring diameters can be seen in Figs. 20. It is noted that there is no significant difference in the contact force required to initiate damage in the stitched and unstitched plates, indicating that the stitch does not seem to have an affect on the impact resistance in these thin plates as far as impact force is concerned. Apparently, the through-the-thickness reinforcement does not become very effective for small thicknesses. There is a slight increase in the ultimate load in the stitched plates, but that could be due to increased thickness also. This insignificant affect of stitching on the impact damage resistance of thin laminates as characterized by impact force agrees with the findings of Jackson and Portanova [14] who report increase in improvement of the impact resistance of the stitched laminates as the thickness of laminate is increased. Increase in support ring diameter decreases the maximum peak failure load.

Impact Damage Resistance of Thin Laminates as Characterized by Impact Damage Area

The effect of stitching on the indentation damage area due to different contact force levels for the unstitched and the 5×1/4" stitched laminates is shown in Fig. 21. The stitched specimens demonstrated about 40% less damage area compared to unstitched specimens for the same load. Thus, impact damage resistance improved significantly due to stitching considering that these were thin laminates and the stitch density is not very high. Thus it can be inferred that though the damage initiation for the unstitched and the thin stitched laminates is likely to occur at the same loading conditions, but further propagation of the damage can be significantly restricted by stitching. The damage area reduces with increase in support ring diameter for both the unstitched and the stitched laminates.

Compression-After-Impact (CAI) Strength of Thin Laminates

The CAI strength of the statically indented specimens was measured using the UF-CAI test fixture. The compressive strength is known to increase with reduction in gage length of the specimen [15]. The 8×1/4" stitched specimens were primarily processed to study stitching, processing and impact damage with varying support ring diameters (meaning different gage lengths in a CAI test), their numbers in each category were insufficient to study the CAI data to observe the effect of stitching with other variables remaining constant. Therefore, effect of stitching for 5×1/4" stitched specimens (all of them had the same gage length = 2.4") is presented. The residual post-impact strength as measured by the CAI test for the specimens is plotted against the impact damage area in Fig. 22. The stitched and the unstitched laminates were loaded up to same levels in each indenting event to cause the impact damage. The stitched specimens showed about 25% higher CAI strength than the unstitched laminates for the maximum contact force.

CONCLUSIONS

Mode I Fracture Toughness of Stitched Uniweave Laminates

1. The Mode I fracture toughness characterized by G_{Ic} increases at least by an order higher. In case of 4×1/4" stitch density laminates, Kevlar-2790 (1600 denier) stitch yarn increased it by about 15 times, Glass-1250 (3570 denier) by about 30 times and Glass-750 (5952 denier) increased it by about 21 times. The Mode I critical strain energy release rate for the unstitched was 302.6 J/m^2.

2. The Mode I fracture toughness of 8×1/8" stitch density laminates could not be measured experimentally as the specimen failed in bending before the crack could propagate any distance. In order to find the G_{Ic} for these high stitch density laminates, thicker specimens

need to be made. This illustrates the impressive rise in Mode I fracture toughness.

3. The crack propagation in unstitched laminates is gradual and steady. The crack propagation in the stitched laminates is intermittent and unsteady. The stitches first debond from the matrix after the crack front passes ahead. The stitches always fail at or near the stitch lock. The bobbin yarns failed in case of Kevlar-2790 and Glass-1250 stitch yarns The needle yarn failed in the case of the stronger bobbin Glass-750 yarn. This indicates the role a needle yarn may play in further improving G_{Ic}. In general, both bobbin and needle yarn may be of approximate equal strength to avoid a weaker linkage.

Mode II Fracture Toughness of Stitched Uniweave Laminates

1. Stitching significantly improves Mode II fracture toughness. The increase in apparent G_{IIc} was 5 to 15 times when the crack was allowed to propagate up to about center line of the laminates.

2. As the crack surfaces do not open during the ENF test, and hence it is difficult to estimate the crack length by any method such as visual, X-radiography or Ultrasonic C-Scan. The Ultrasonic C-Scan underestimates it. Two new methods to calculate apparent G_{IIc} have been developed: one using work done by the area under the P-δ curve and the C-Scan area of the crack surface; second method uses compliance of the unloading curve.

3. The critical strain energy release rate increases with increase in crack length. This is because not all energy imparted to the laminate goes directly to the crack front. Part of it is used in stitch and other matrix failure mechanisms as more stitches become effective in the passage of the crack propagation. The stitched laminate seems to behave more like a structure rather than a material. The stitches did not break during these tests. The stitch yarn seems to plough through the matrix causing elastic and elastic-plastic deformation. Therefore, as the crack starts propagating, the ploughing resistance increases resulting in increased Mode II fracture toughness.

Effect of Stitching on Sublaminate Buckling Failure Mode, and CAI Strength

1. The improvement in the CAI strength of the stitched laminates with 8×1/8" stitch density was as high as 400% compared to the unstitched laminates for the worst case of delamination studied. Stitching was observed to effectively restrict sublaminate buckling failure of uniweave laminates with teflon implanted delaminations.

2. The CAI strength increases rapidly with increase in stitch density. It reaches a peak CAI strength that is very close to the original compression strength of the material. For the highest stitch density studied i.e., 8×1/8", the CAI strength of the stitched uniweave laminates for the worst damage case was about 65 ksi as compared to about 70 ksi of the undamaged

stitched control specimens.

3. The effect of different type of stitch yarn is not noticeable. All the stitch yarns investigated demonstrated very close performance in improving the CAI strength. It appears that any stitch yarn with adequate breaking strength and stiffness successfully restricts the sublaminate buckling.

Effect of Stitching on Thin Stitched Plain Weave Laminates

The damage progression during a static indentation test in stitched textile laminates is similar to yielding in ductile materials. This is unlike in most unstitched laminates where a delamination initiates suddenly during a static indentation test. In case of thin laminates though the impact damage resistance as characterized by impact force did not change significantly, the impact damage area for the stitched laminates was about 40% less compared to that of the unstitched laminates. These results agree well with other studies where stitching shows increasing improvement in impact damage resistance with increase in the thickness of laminates. It may be because through-the-thickness reinforcement is not fully effective in thin laminates.The CAI strength of thin stitched laminates (5×1/4") was about 25% higher than the unstitched laminates for the same maximum impact force.

Development of a New CAI Test Fixture

A new CAI test fixture designated as the University of Florida CAI test fixture (UF-CAI) has been developed and experimentally validated.

REFERENCES

[1] Mignery, L.A., Tan, T.M. and Sun, C.T.: The use of stitching to suppress delamination in laminated composites, ASTM STP 876, 1985, pp. 371-385.

[2] Dexter, H.B. and Funk, J.G.: Impact resistance and interlaminar fracture toughness of through-the thickness reinforced graphite/epoxy, AIAA paper 86-1020-CP, 1986.

[3] Ogo, Y.: The effect of stitching on in-plane and interlaminar properties of carbon-epoxy fabric laminates, CCM Report Number 87-17, Center for Composite Materials, University of Delaware, Newark, May 1987, pp 1-188.

[4] Pelstring, R. M. and Madan, R.C.: Stitching to improve damage tolerance of composites, 34th International SAMPE Symposium, May 1989, pp 1519-1528.

[5] Byun, J., Gillespie, J.W. and Chow, T.: Mode I delamination of a three-dimensional fabric composite, *Journal of Composite Materials*, Vol 24, May 1990, pp 497-518.

[6] Chen, V.L., Wu, X.X. and Sun, C.T.: Effective interlaminar fracture toughness in stitched laminates, Proceedings of the 8th Annual Technical meeting of the American Society of Composites, Cleveland, OH, 1993, pp 453-462.

[7] Jain, L. K. and Mai, Y.: On the effect of stitching on Mode I delamination toughness of laminated composites, *Composites Science and Technology*, 51 (1994), pp 331-345.

[8] Carlsson, L.A. and Pipes, R.B.: *Experimental characterization of advanced composite materials*, Prentice-Hall. Inc., publication, 1987, pp 157-193.

[9] Sharma, S.K.: Effects of through-the-thickness stitching on impact and interlaminar fracture properties of textile graphite/epoxy laminates, M.S. thesis, University of Florida, Gainesville, FL32611-6250.

[10] Guenon, V.A.E.: Interlaminar fracture toughness of three dimensional composites, M.S. Thesis, University of Delaware, Dec 1987, pp 1-116.

[11] Suemasu, H.: Effects of multiple delaminations on compressive buckling behavior of composite panels, *Journal of Composite Materials*, Vol. 27, No. 12/1993, pp 1172-1192.

[12] Kwon, Y.S. and Sankar, B.V.: Indentation-flexure and low-velocity impact damage in graphite/epoxy laminates, NASA CR 187624, University of Florida, March 1992, pp 1-58 (also published in ASTM *Journal of Composites Technology and Research*, 1993, Vol 15 (2), pp 101-111.)

[13] Sankar, B.: Scaling of Low-Velocity Impact of Symmetric Laminates, *J. of Reinforced Plastics and Composites,* 1992, Vol 11 (3), pp 296-309.

[14] Poe, C.C. Jr., Jackson, M.A., Portanova, M.A. and Masters, J.E.: Damage tolerance of textile composites, The Proceedings of the fourth NASA/DoD conference, Salt Lake City, June 7-11, 1993.

[15] Reeder, J.: Comparison of the compressive strength for stitched and toughened composite systems, NASA TM 109108, Apr 94, pp 1-44.

Table 1: Details of stitch yarns used

STITCH YARN	BREAKING STRENGTH (Newton)	BREAKING STRENGTH (lbf)
Kevlar (1600 denier ≈ 2790 yd/lb) bobbin yarn	347	78
Glass (3570 denier ≈ 1250 yd/lb) bobbin yarn	262	59
Glass (5952 denier ≈ 750 yd/lb) bobbin yarn	436	98
Kevlar (400 denier ≈ 11160 yd/lb) needle yarn	53	12

Table 2: Material system for Mode I and Mode II Fracture Toughness Tests

PLATE #	LAY UP	STITCH DENSITY	STITCH YARN	YARN NUMBER (yards/lb)	DENIER (gm/9000 meters)	AVERAGE THICKNESS OF PLATES (mm)
24	Uni-directional 24 plies†	4×1/4"	Kevlar	2790	1600	3.683
25		8×1/8"	Kevlar	2790	1600	4.191
26		4×1/4"	Glass	1250	3570	3.810
27		8×1/8"	Glass	1250	3570	4.191
28		4×1/4"	Glass	750	5952	4.318
29		8×1/8"	Glass	750	5952	4.445
30		None	-	-	-	3.556

† Each ply is AS4 uniweave graphite fabric. The stitching is in 0° fiber direction. A 26"×2.5"×0.0005" thick teflon crack starter film is located at the midplane along the edge as shown in Figs. 1. No stitching is within 1/2" of the film. Top and bottom plies are covered by plain weave fiberglass cloth to retain the stitches.

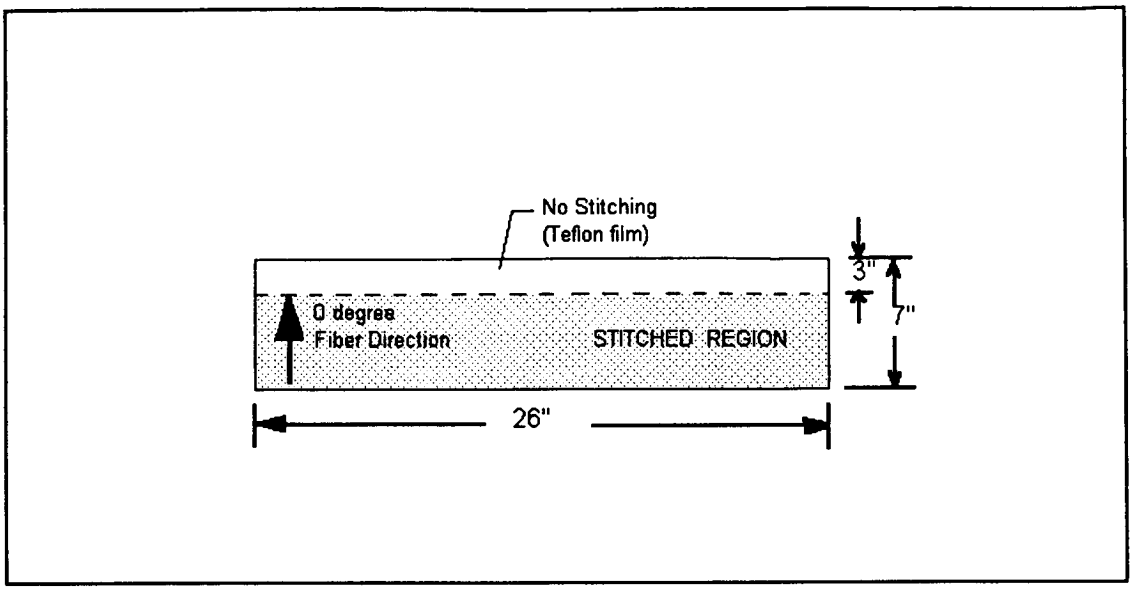

Figure 1: A schematic of typical stitched RTMed plate for interlaminar fracture toughness test specimens

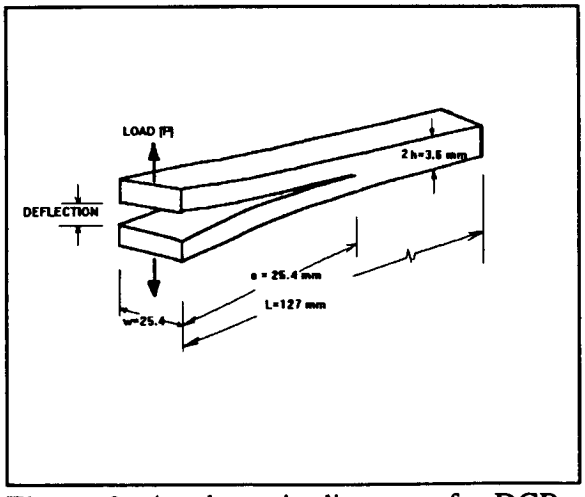

Figure 2: A schematic diagram of a DCB specimen cut from the RTMed plates

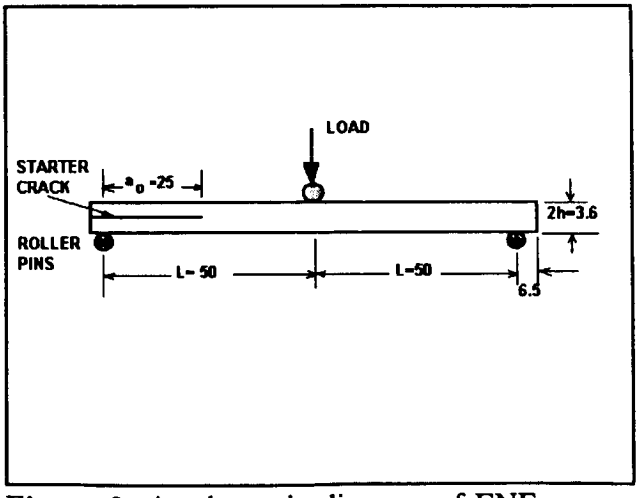

Figure 3: A schematic diagram of ENF specimen (dimensions are in mm).

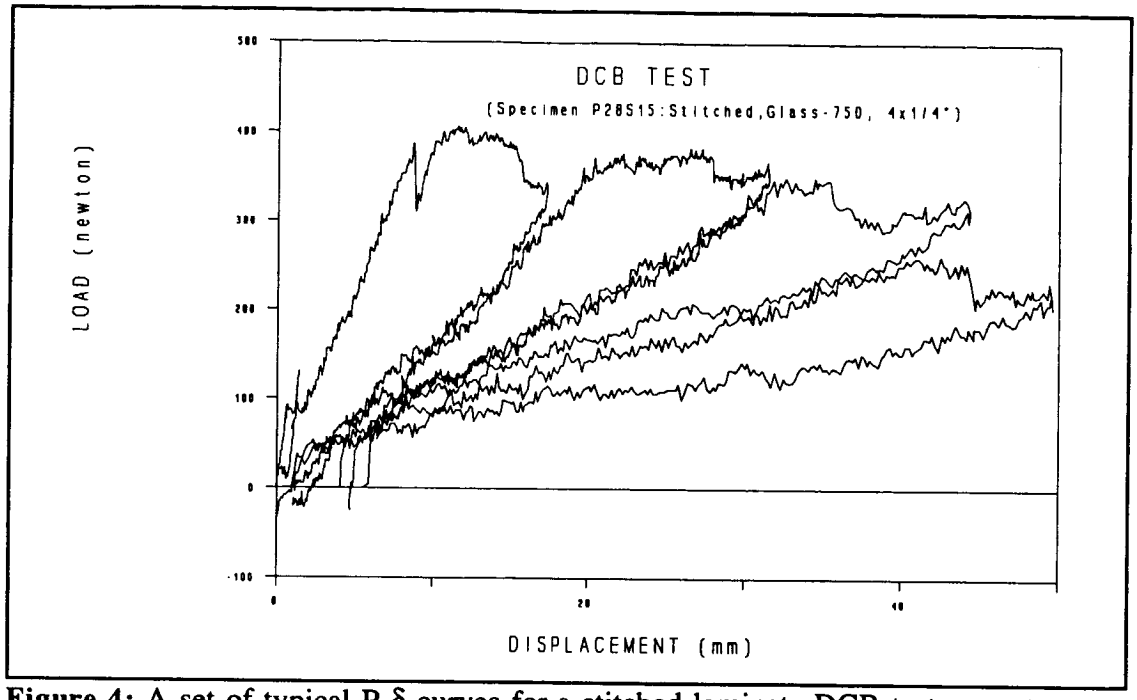

Figure 4: A set of typical P-δ curves for a stitched laminate DCB test

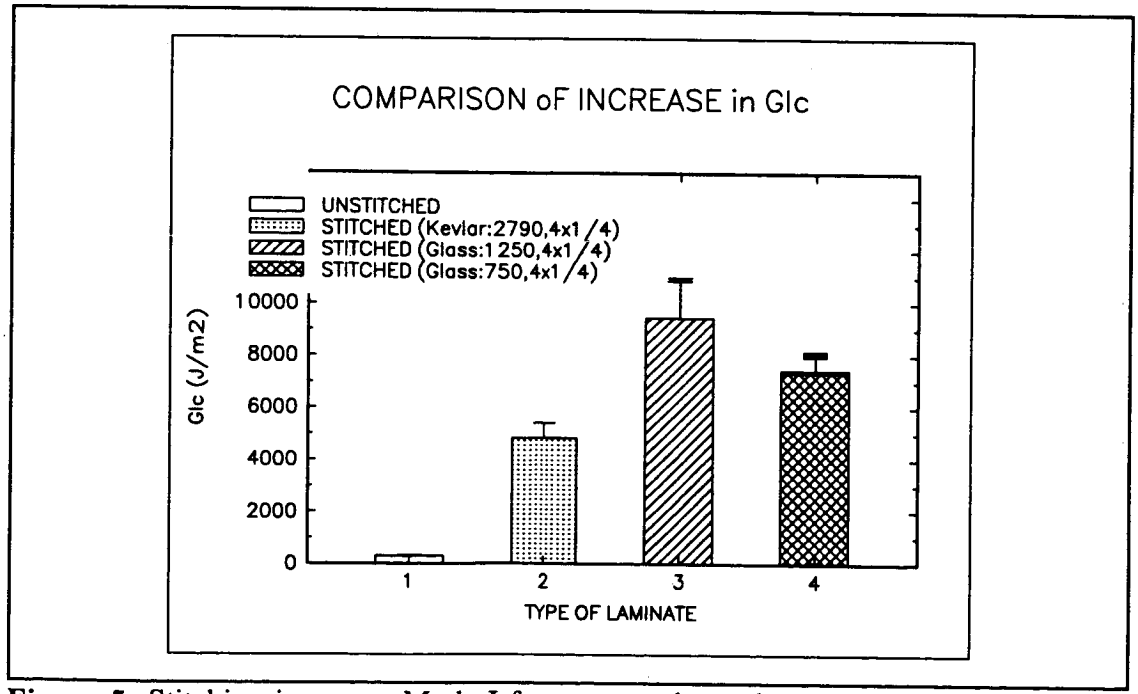

Figure 5: Stitching increases Mode I fracture toughness by 15-30 times for 4x1/4" stitch density laminates.

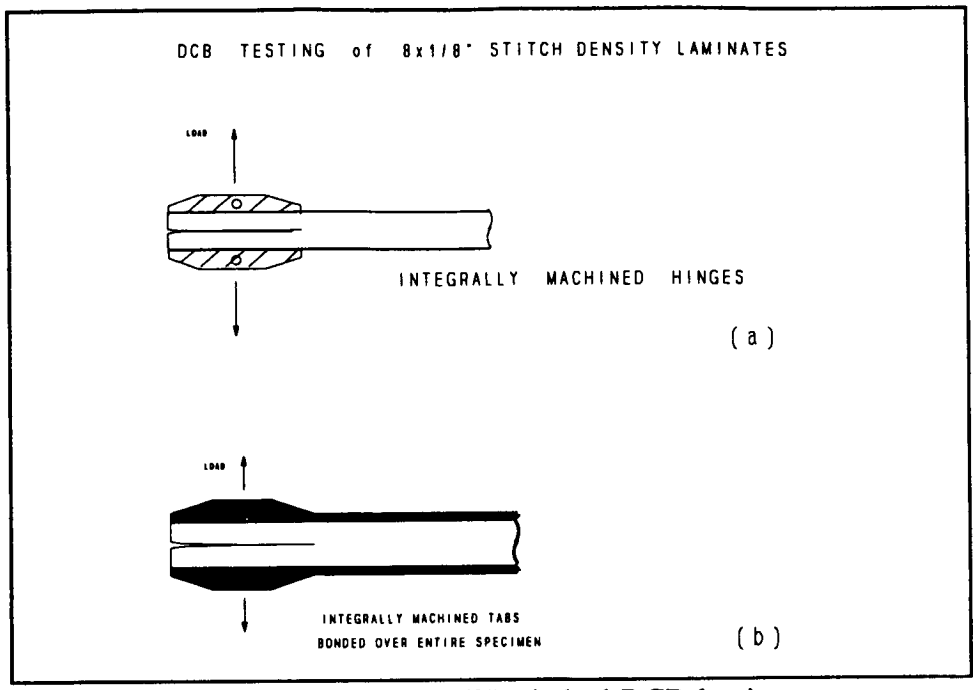

Figure 6: Hinges used to test 8×1/8" stitched DCB laminates

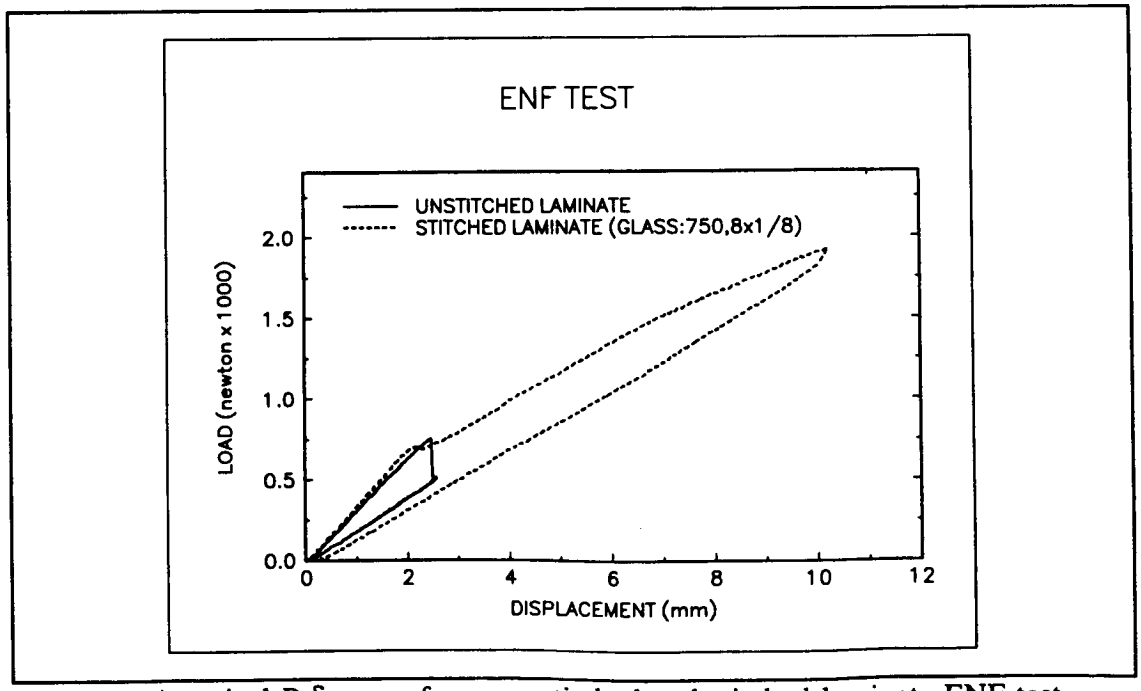

Figure 7: A typical P-δ curve for an unstitched and stitched laminate ENF test

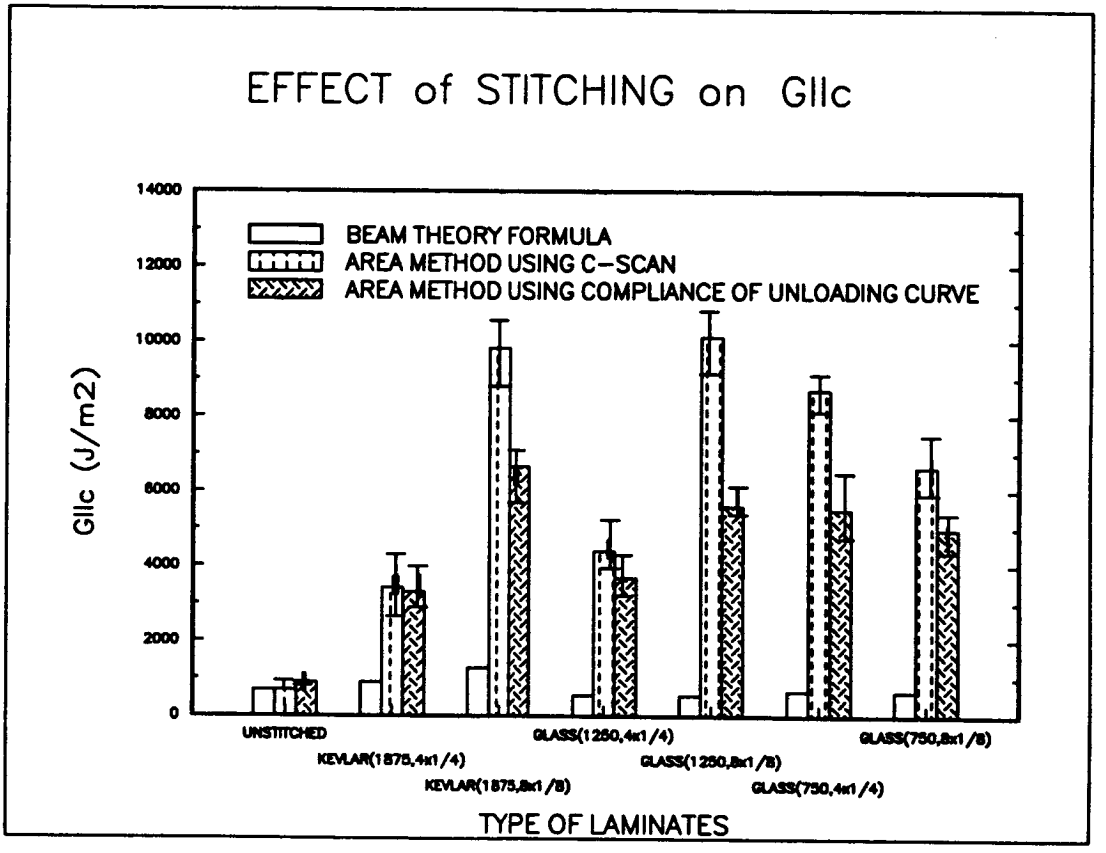

Figure 8: Effect of stitching on G_{IIc}. The crack propagated up to about center line ($\Delta a=0.5\times L$) in all cases.

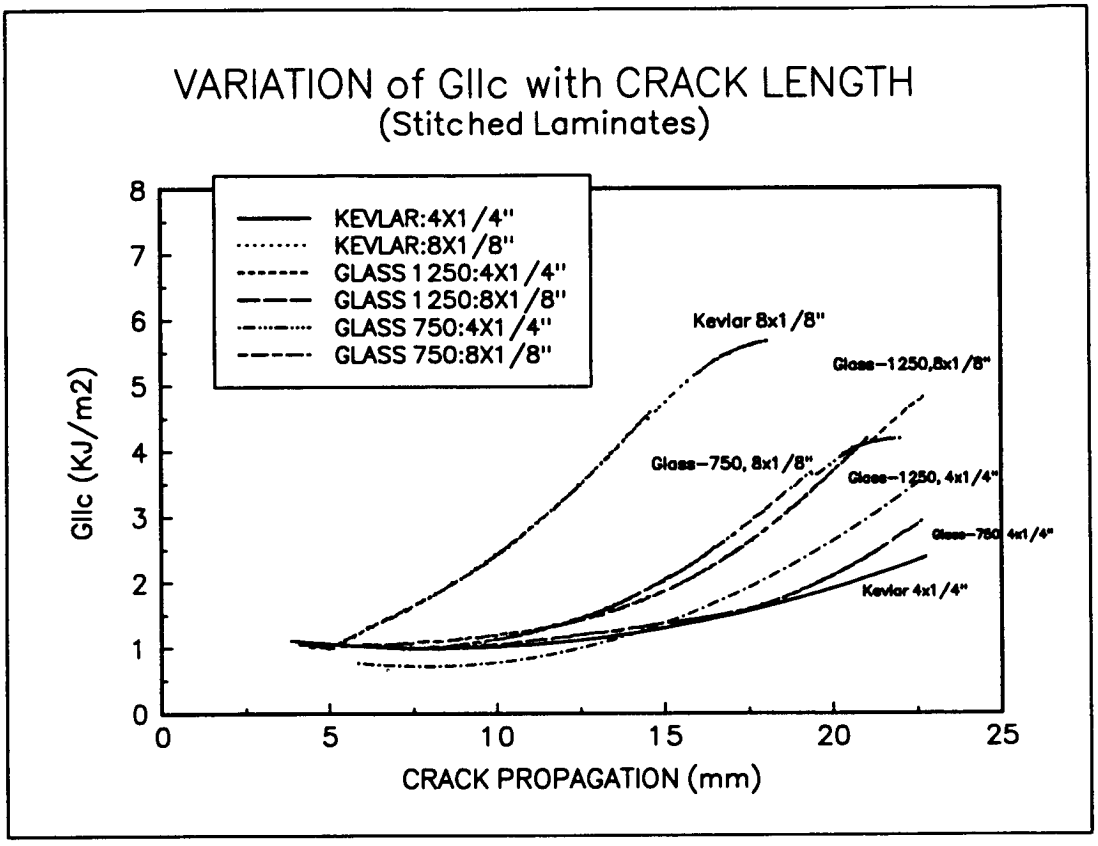

Figure 9: Variation in G_{IIc} with increase in crack length of stitched laminates

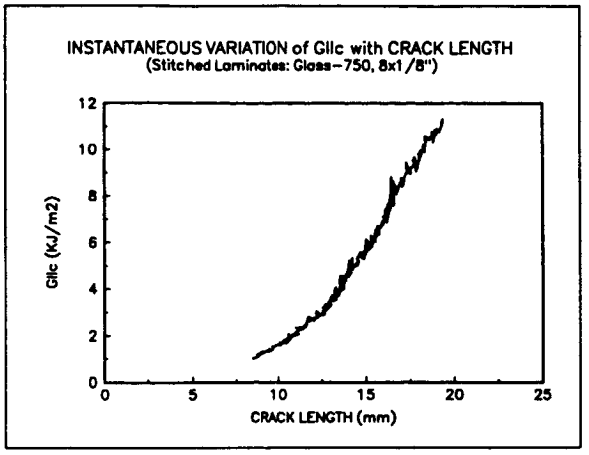

Figure 10: A typical variation of G_{IIc} at each time interval (instantaneous) with increase in crack length of stitched laminates.

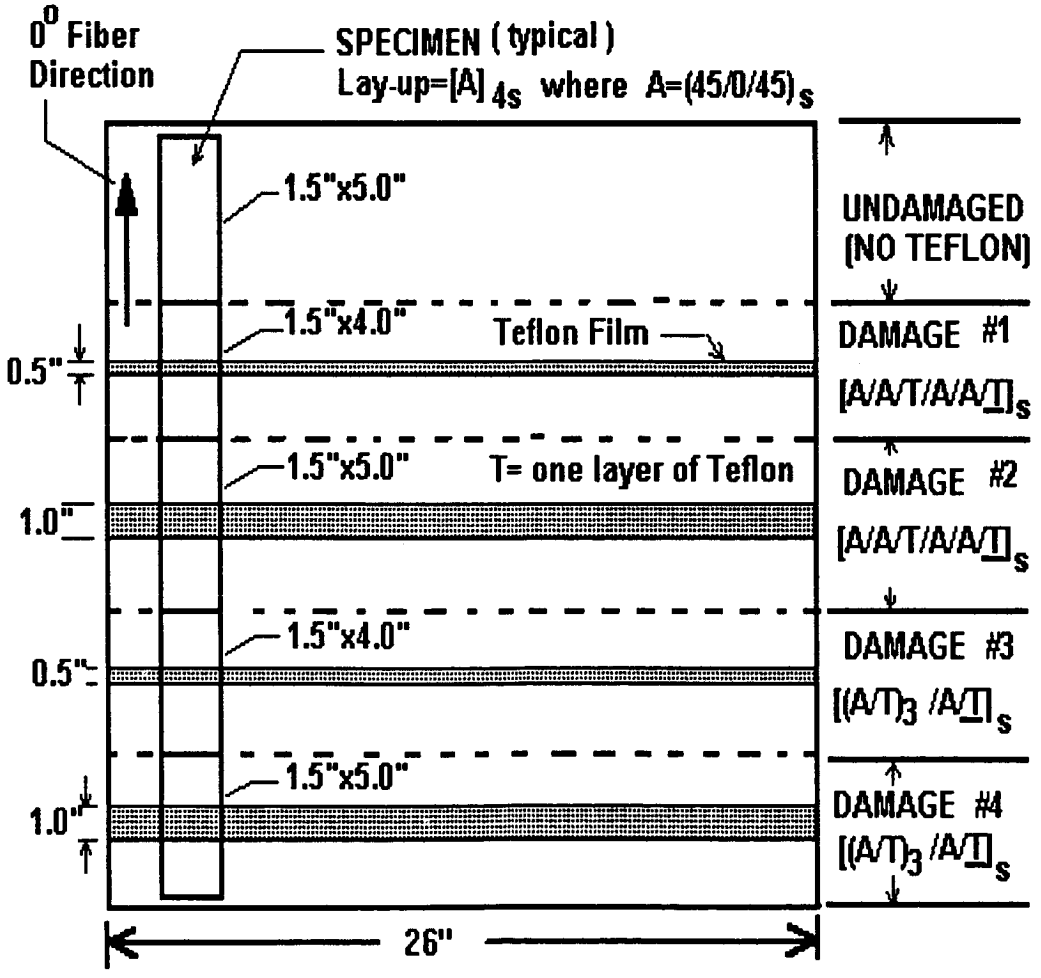

Figure 11: Details of a typical RTMed plate for Sublaminate Buckling Test specimens

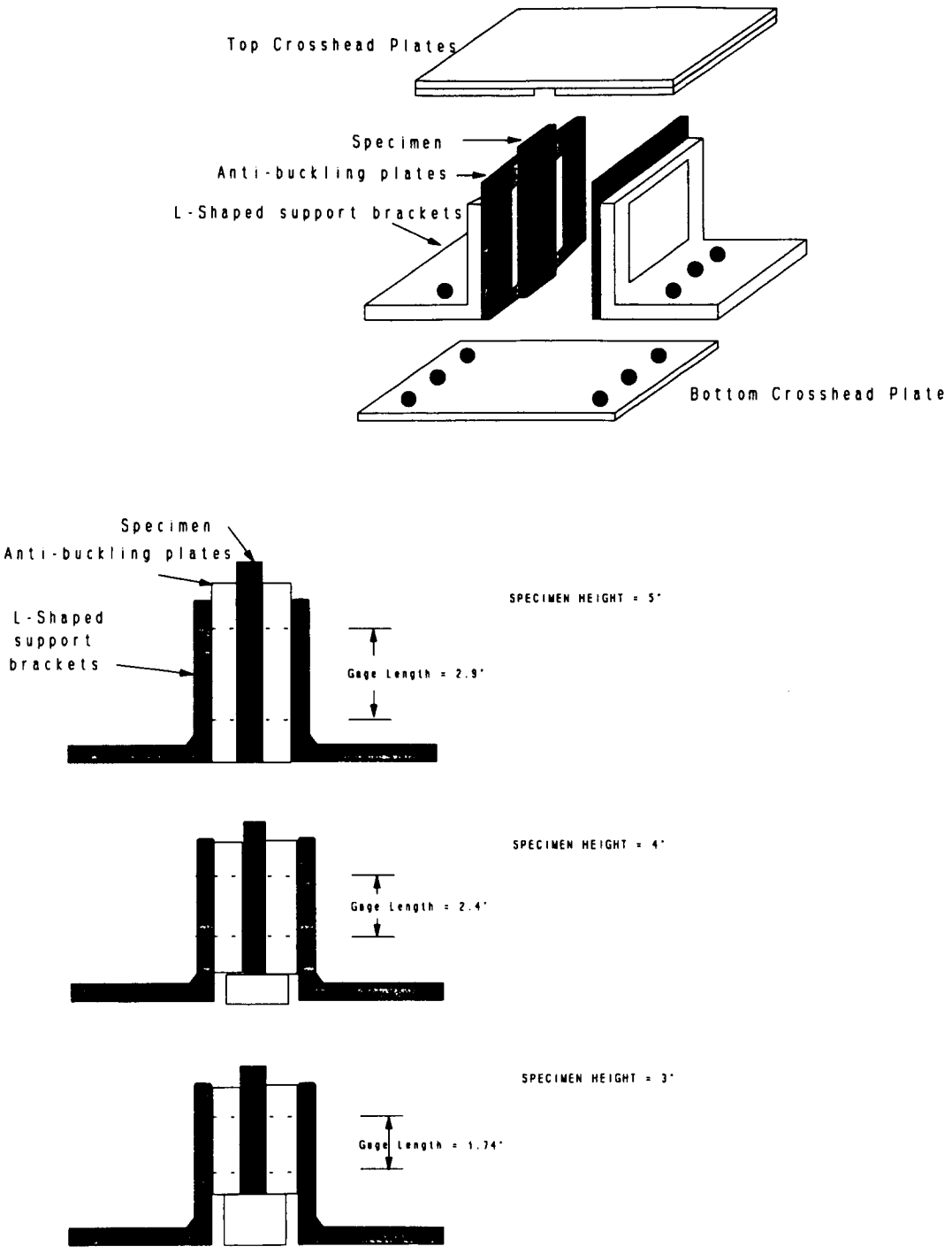

Figure 12: A sketch of the University of Florida Compression-After-Impact (UF-CAI) test fixture along with adaptations required for different specimen heights

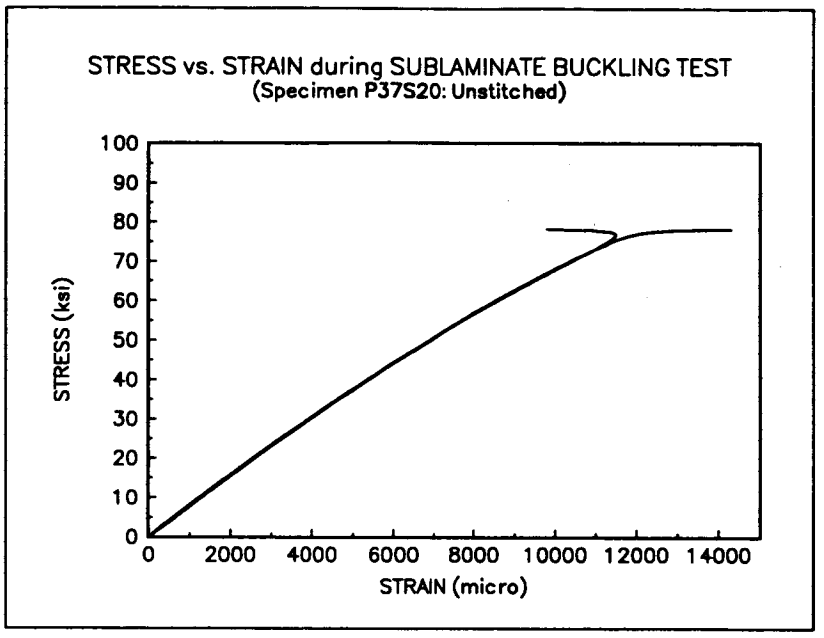

Figure 13: A typical stress-strain response for an unstitched laminate.

Table 3: Effect of Stitch Yarn and Stitch Density on CAI strength

Type of Damage†	CAI (ksi) Plate #31, Stitched: Kevlar 2790,4x1/4	CAI (ksi) Plate #32, Stitched: Kevlar 2790,8x1/8	CAI (ksi) Plate #33, Stitched: Glass 1250,4x1/4	CAI (ksi) Plate #34, Stitched: Glass 1250,8x1/8	CAI (ksi) Plate #35, Stitched: Glass 750,4x1/4	CAI (ksi) Plate #36, Stitched: Glass 750, 8x1/8	CAI (ksi) Plate #37, Un-stitched
Zero (No Damage)	72.88	69.24	75.04	69.72	73.53	71.53	80.92
1	71.28	68.79	68.33	60.51	66.58	58.77	76.36
2	54.44	63.96	56.86	69.51	54.68	62.91	48.76
3	43.27	65.11	47.65	62.22	45.71	57.24	41.7
4	33.37	60.04	39.46	69.54	38.82	64.01	16.9

† Damage Type #1 = 3 teflon film inserts, each of 0.5" height running through the entire width of the specimen and located at $[A/A/T/A/A/\underline{T}]_s$ where A = $(45/0/45)_s$ and T is a teflon insert. Thickness of teflon film in all cases was 0.0005".
Damage Type #2 = same as Damage Type #1 but the teflon film inserts are of 1.0" height each.
Damage type #3 = 7 teflon film inserts, each of 0.5" height and located at $[(A/T)_3\ /A/\underline{T}]_s$.
Damage Type #4 = same as Damage Type #3 but the teflon film inserts were of 1.0" height each.

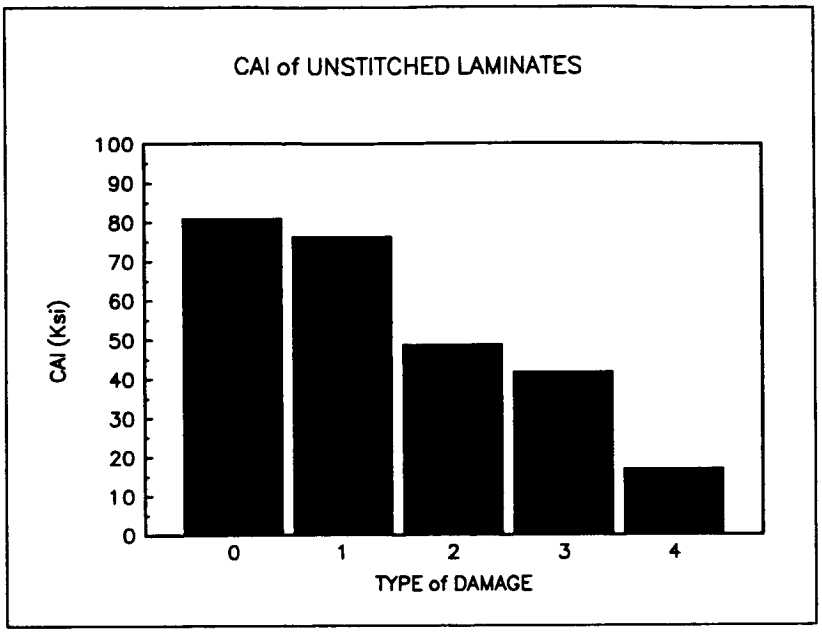

Figure 14: Drop of compression strength in unstitched laminates with different types of damages.

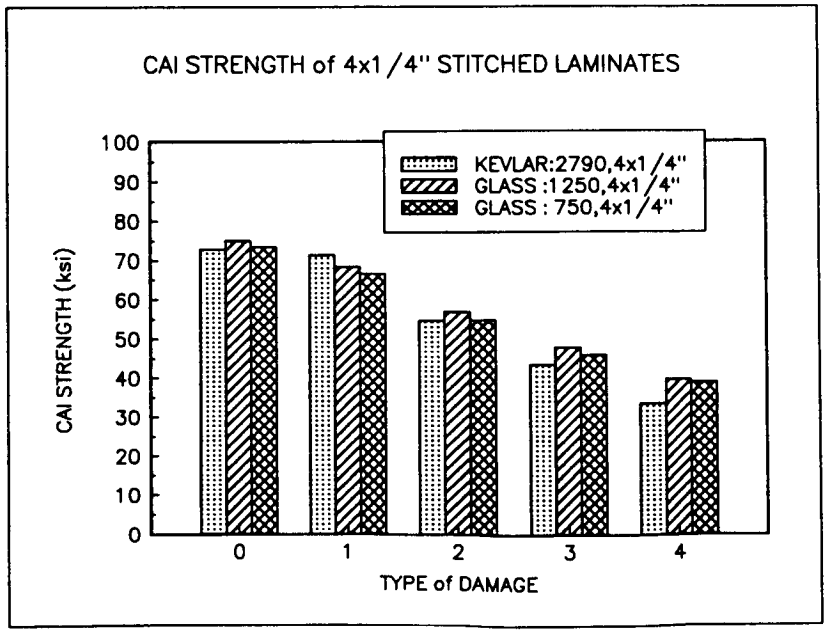

Figure 15: Effect of 4x1/4" stitch density yarns on CAI strength

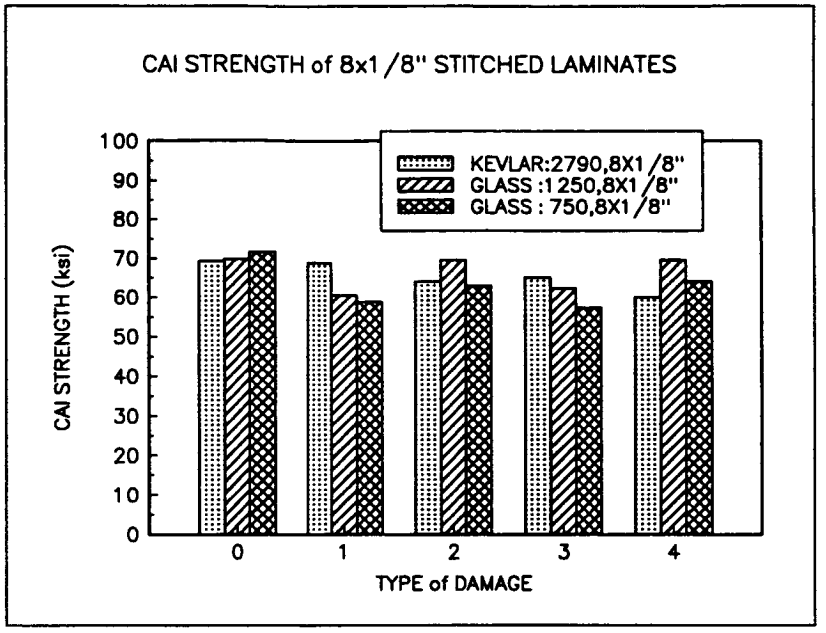

Figure 16: Effect of 8×1/8" stitch density yarns on CAI strength

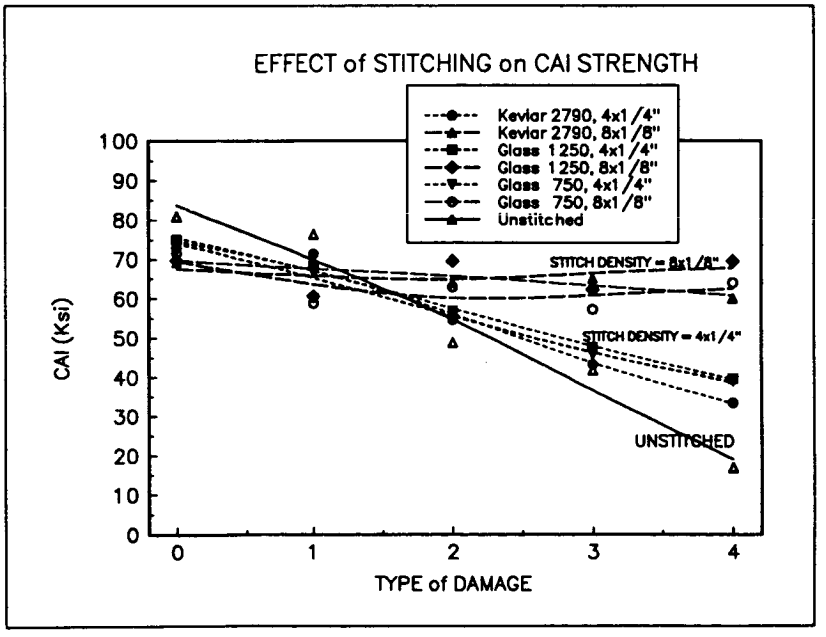

Figure 17: A trend of the effect of stitch density on CAI strength

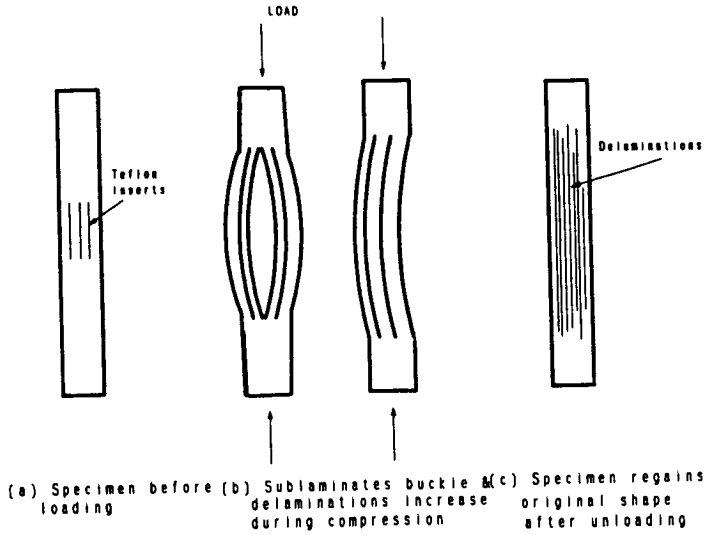

Figure 18: A sketch of the typical sublaminate buckling failure mode of delaminated unstitched specimens

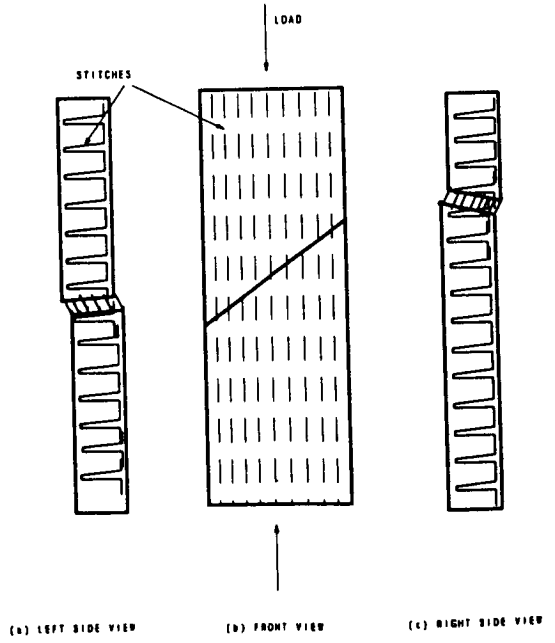

Figure 19: A sketch of a typical stitched sublaminate buckling failure mode

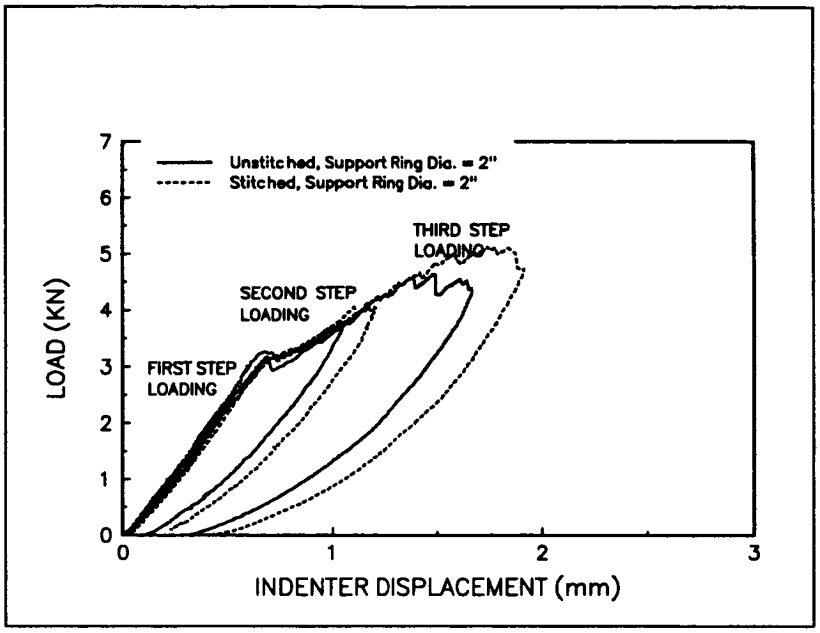

Figure 20: Indentation response; 2" support ring diameter

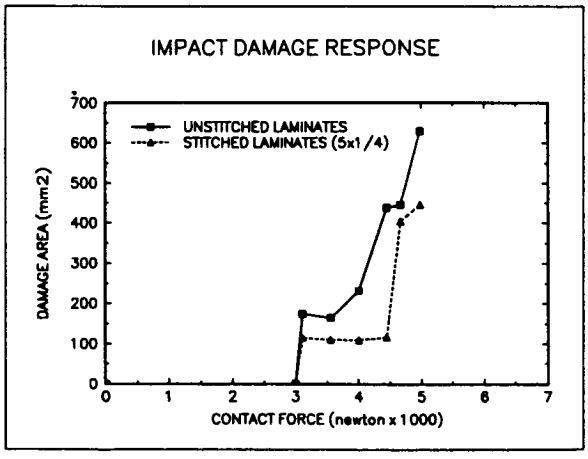

Figure 21: Damage Area is 40% less for the 5×1/4" stitched laminates

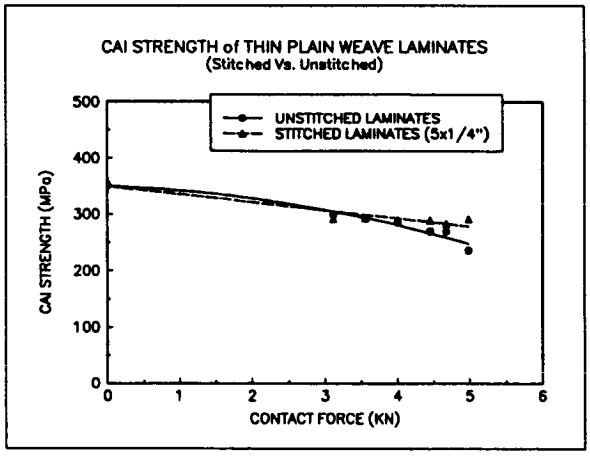

Figure 22: Stitching improves the CAI strength of thin plain weave laminates by about 25%.

IMPACT DAMAGE IN COMPOSITE PLATES

BY

I. Shahid, S. Lee, and F.K. Chang
Dept. of Aeronautics and Astronautics
Stanford University
and

B.M. Shah
Lockheed Aeronautical Systems Company
Marietta, GA

SPONSORED BY ARO AND LOCKHEED

INTRODUCTION

Computer Code: PDCOMP

Progressive damage analysis for laminated composites.

Ref: Shahid and Chang," An accumulative damage model for tensile and shear failures of laminated composite plates" (1994, JCM).

Computer Code: 3DIMPACT

Prediction of the extent of delaminations in laminated composites resulting from a point impact load.

Ref: Choi and Chang, "A model for predicting impact damage of graphite/epoxy laminated composites due to point-nose impact" (1992, JCM).

PDCOMP CODE

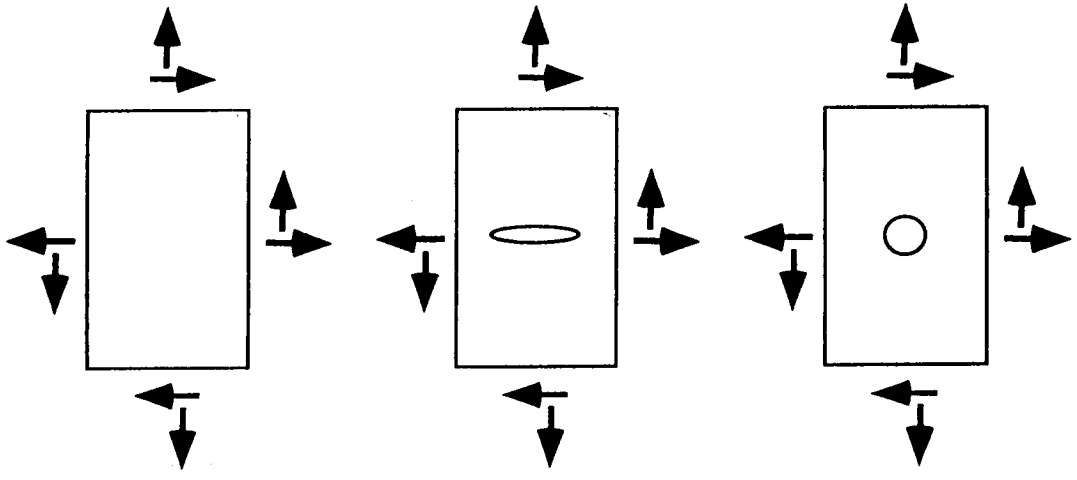

- Predict damage accumulated inside composites as a function of applied loads.
- Estimate residual ply properties as a function of damage state and failure mode.
- Limited to symmetric laminates.
- Ignore the edge effect.

3DIMPACT CODE

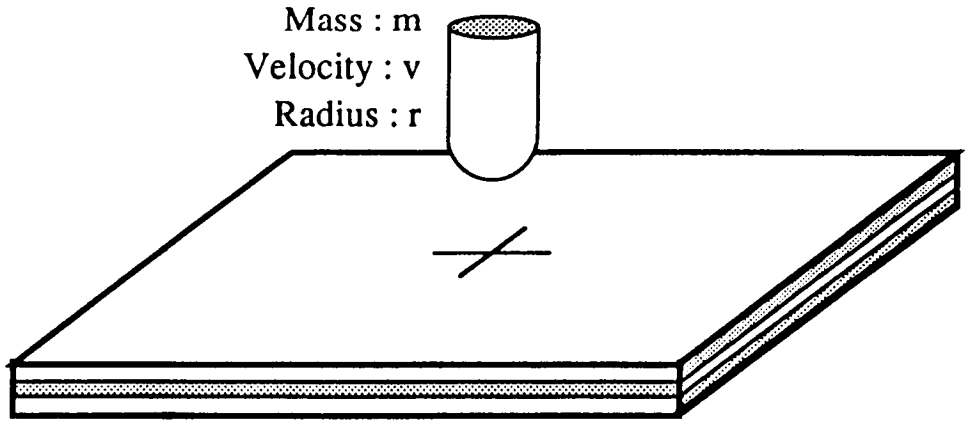

Laminated Composite Plate

- **Predict impact velocity threshold.**
- **Estimate the extent of delaminations in laminates resulting from low-velocity impact.**
- **Limited to symmetric laminates.**
- **Applied to point-nose impact.**
- **No material degradation considered.**
- **Needs to determine an empirical parameter Da.**

OBJECTIVE

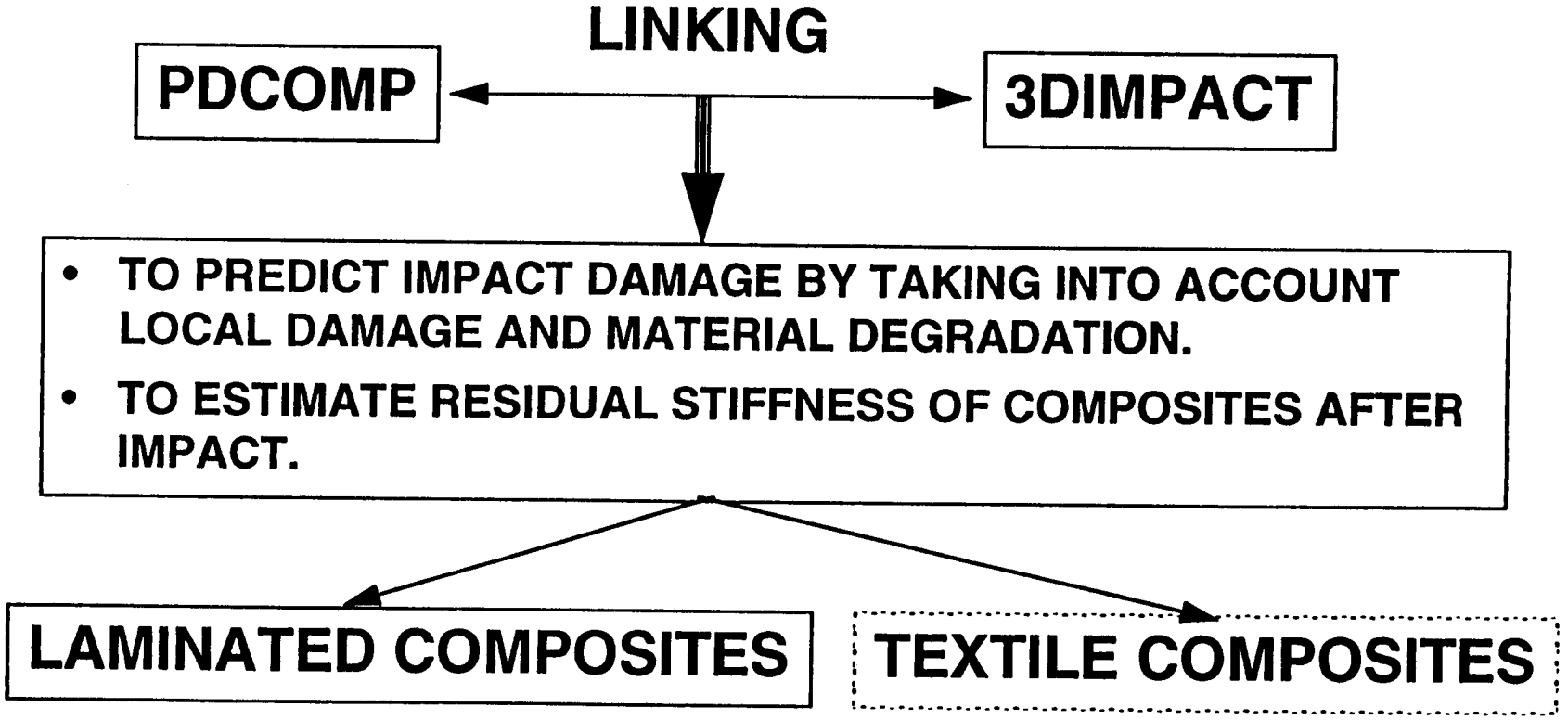
LINKING
PDCOMP
3DIMPACT
• TO PREDICT IMPACT DAMAGE BY TAKING INTO ACCOUNT LOCAL DAMAGE AND MATERIAL DEGRADATION.
• TO ESTIMATE RESIDUAL STIFFNESS OF COMPOSITES AFTER IMPACT.
LAMINATED COMPOSITES
TEXTILE COMPOSITES

MAJOR MODIFICATION OF THE 3DIMPACT CODE

FOR LAMINATED COMPOSITES

1. Failure Criteria

matrix cracking

delamination

fiber breakage

2. Material Degradation

- Material properties as a function of failure mode and the extent of the damage (from PDCOMP).

3. Hertzian Contact Law ($F = k \alpha^{\beta}$)

- Modify contact stiffness k as a function of damaged material properties.
- Apply to both loading and unloading paths.
- Contact area may vary during impact.

LOCAL DAMAGE EFFECT ON FORCE RESPONSE

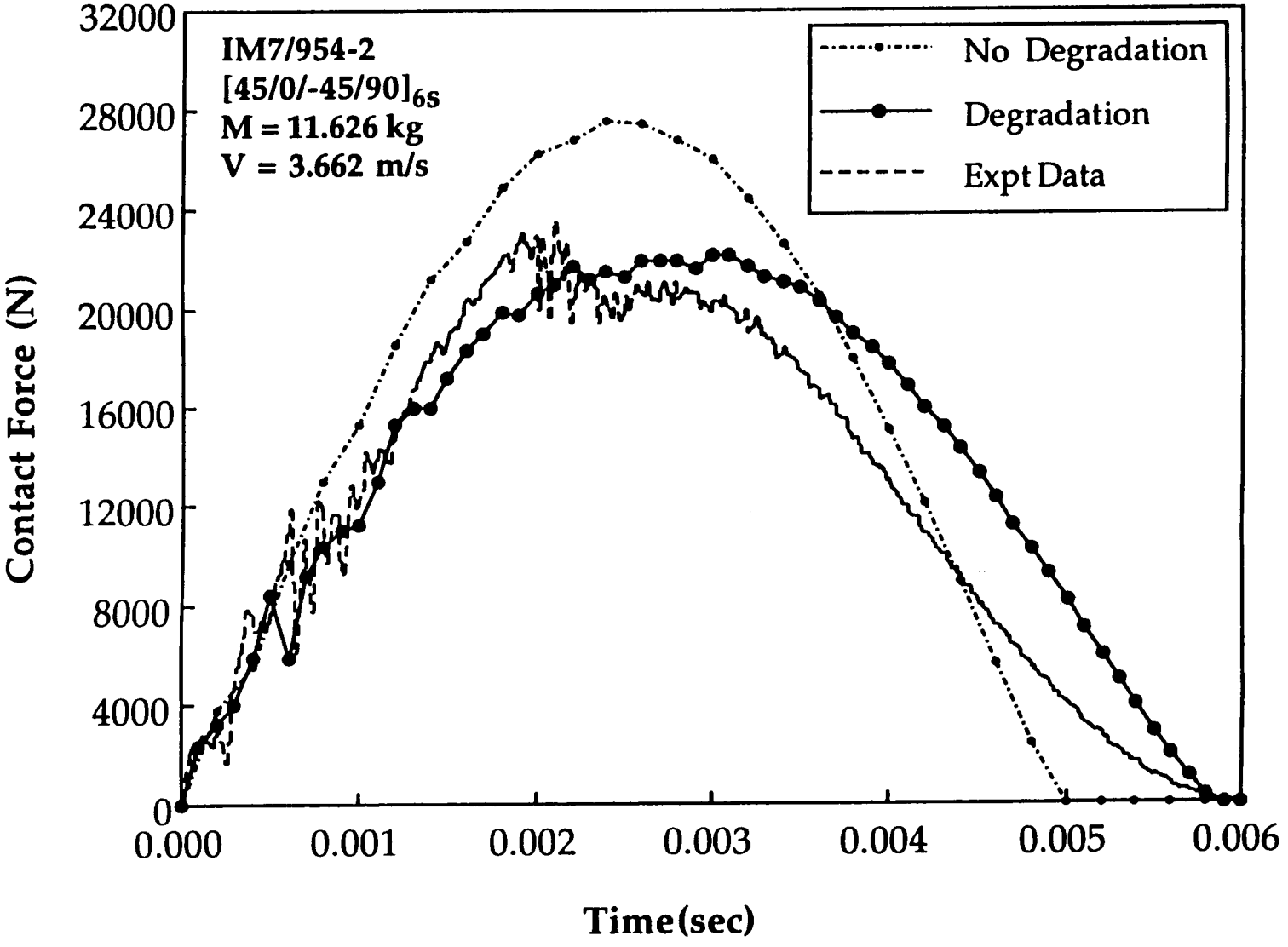

Impact force distribution as a function of time for IM7/954-2 graphite/epoxy composites. Comparison between the predictions with and without material degradation and the test data.

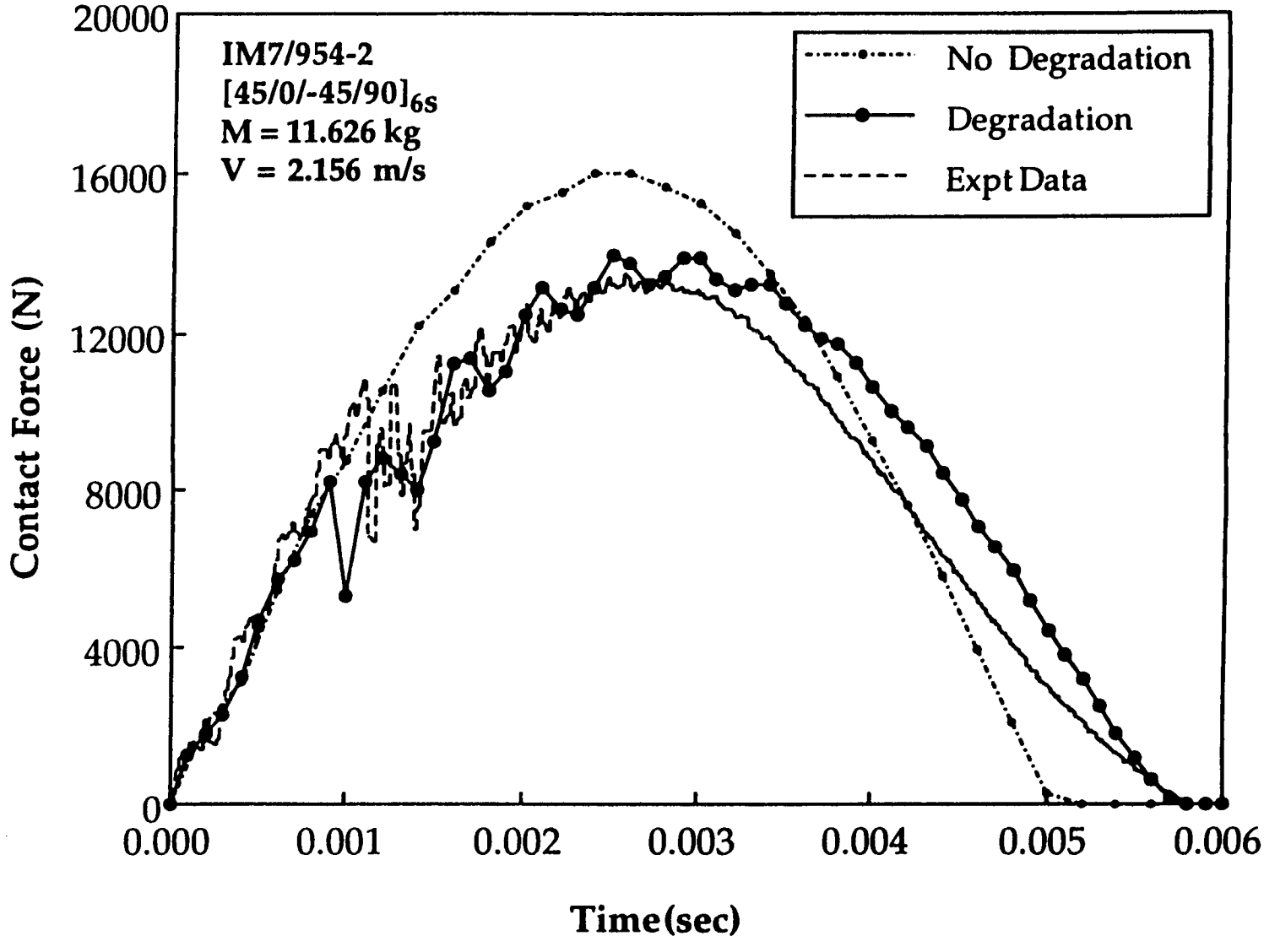

Impact force distribution as a function of time for IM7/954-2 graphite/epoxy composites. Comparison between the predictions with and without material degradation and the test data.

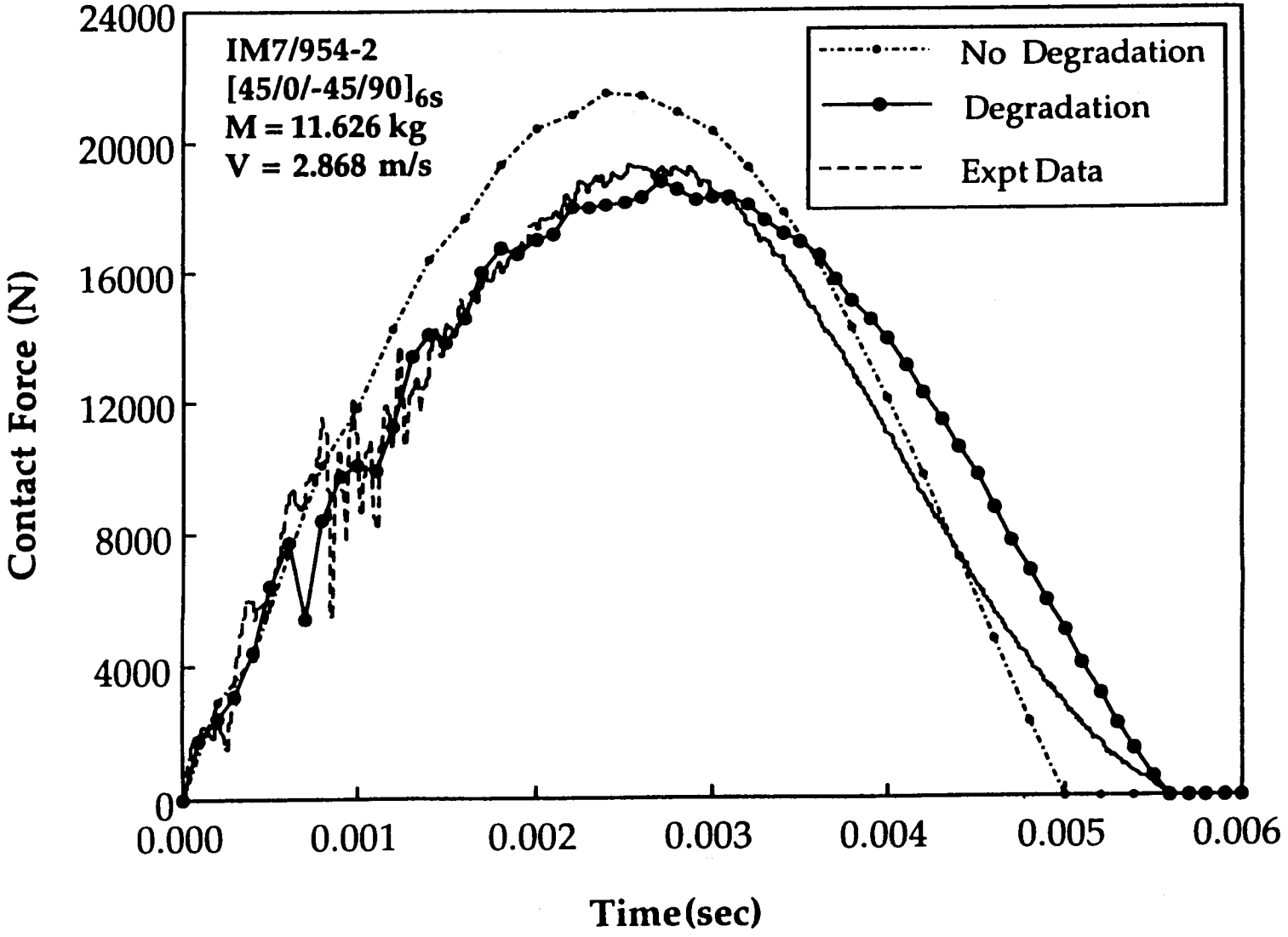

Impact force distribution as a function of time for IM7/954-2 graphite/epoxy composites. Comparison between the predictions with and without material degradation and the test data.

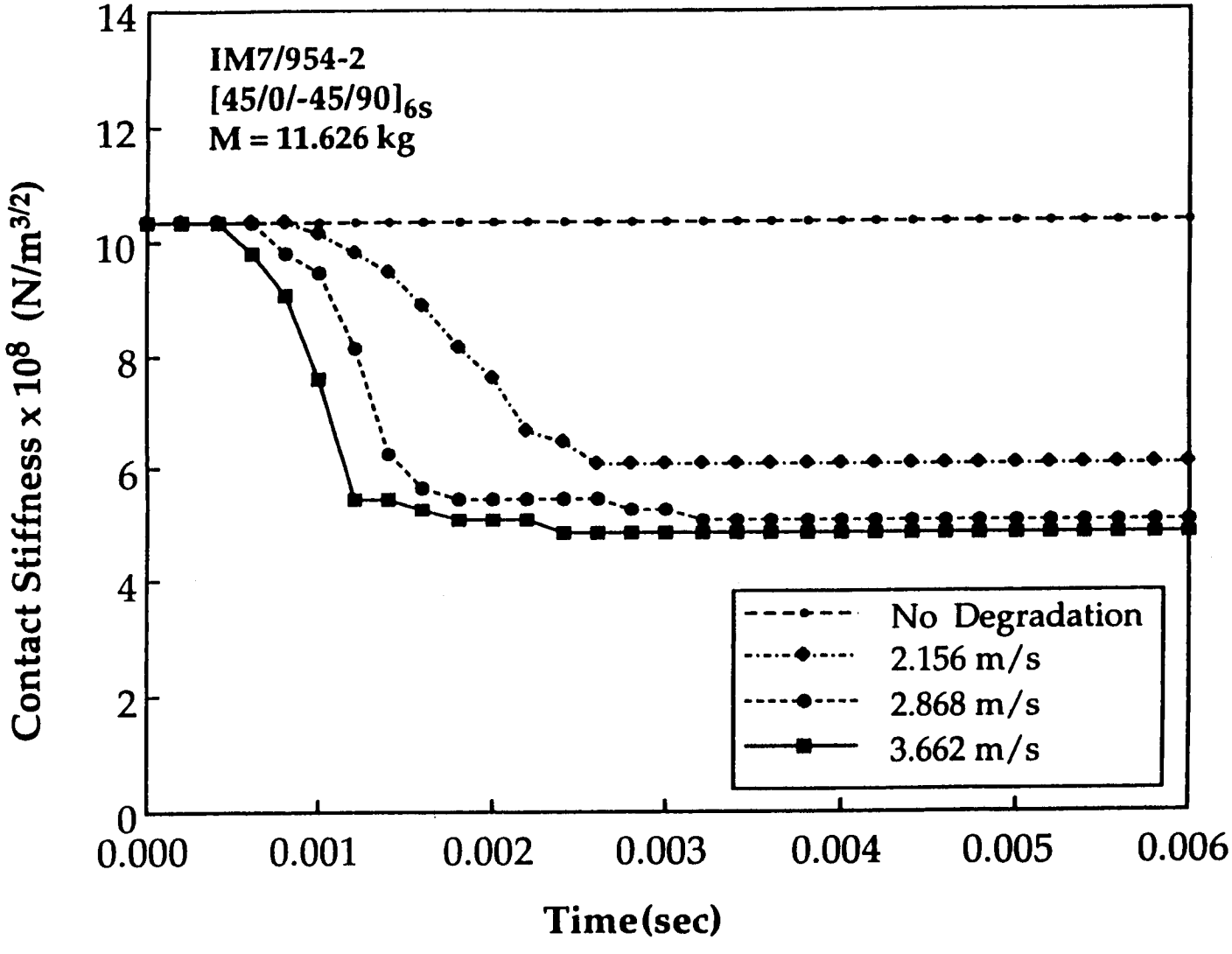

The distribution of the contact stiffness as a function of time during impact on IM7/954-2 graphite/epoxy composites for an impactor at three different velocities.

MASS EFFECT (AT SAME IMPACT ENERGY)

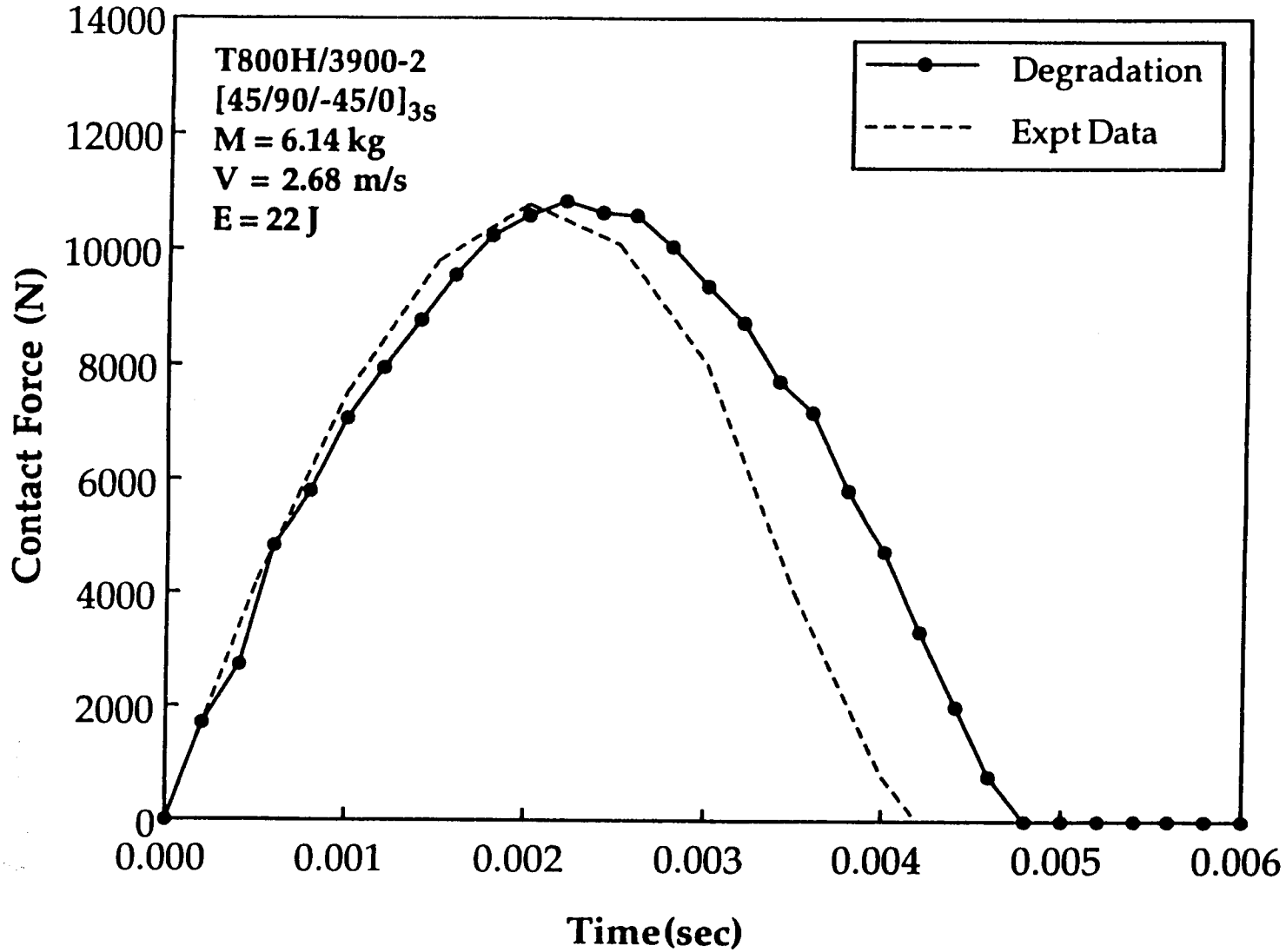

Impact force distribution as a function of time for T800/3900-2 graphite/epoxy composites. Comparison between the predictions based on the present model and the test data

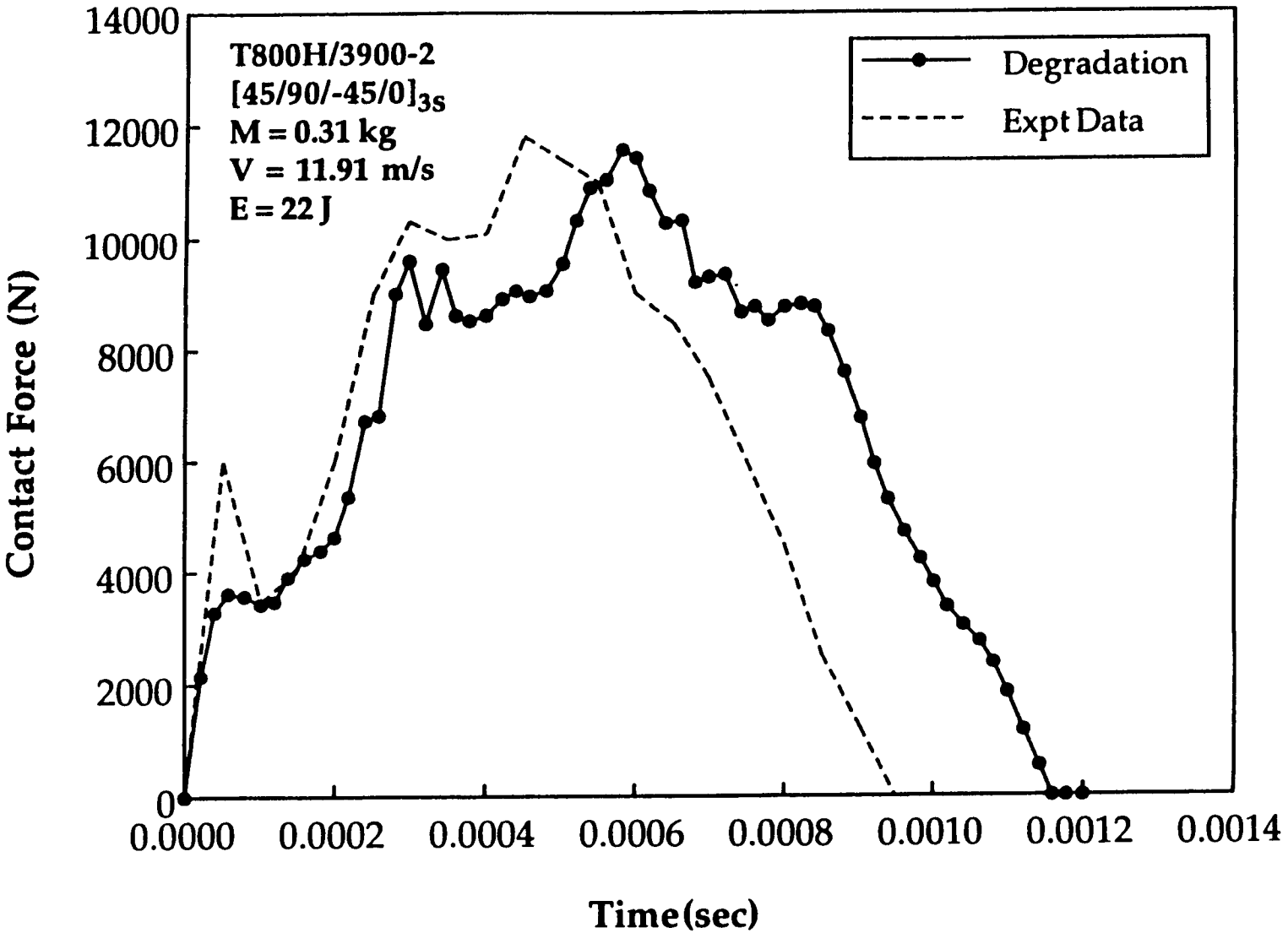

Impact force distribution as a function of time for T800/3900-2 graphite/epoxy composites. Comparison between the predictions based on the present model and the test data

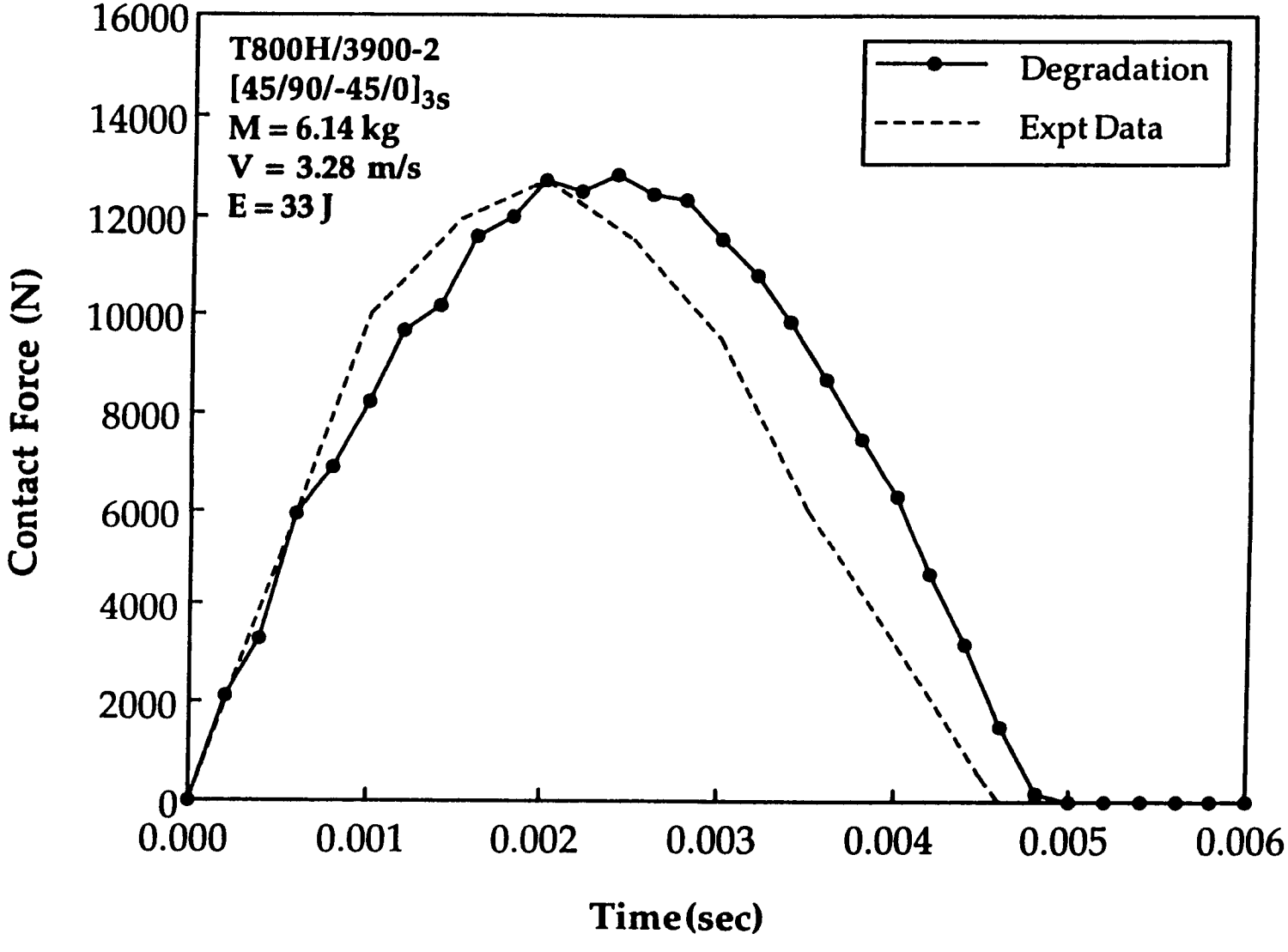

Impact force distribution as a function of time for T800/3900-2 graphite/epoxy composites. Comparison between the predictions based on the present model and the test data

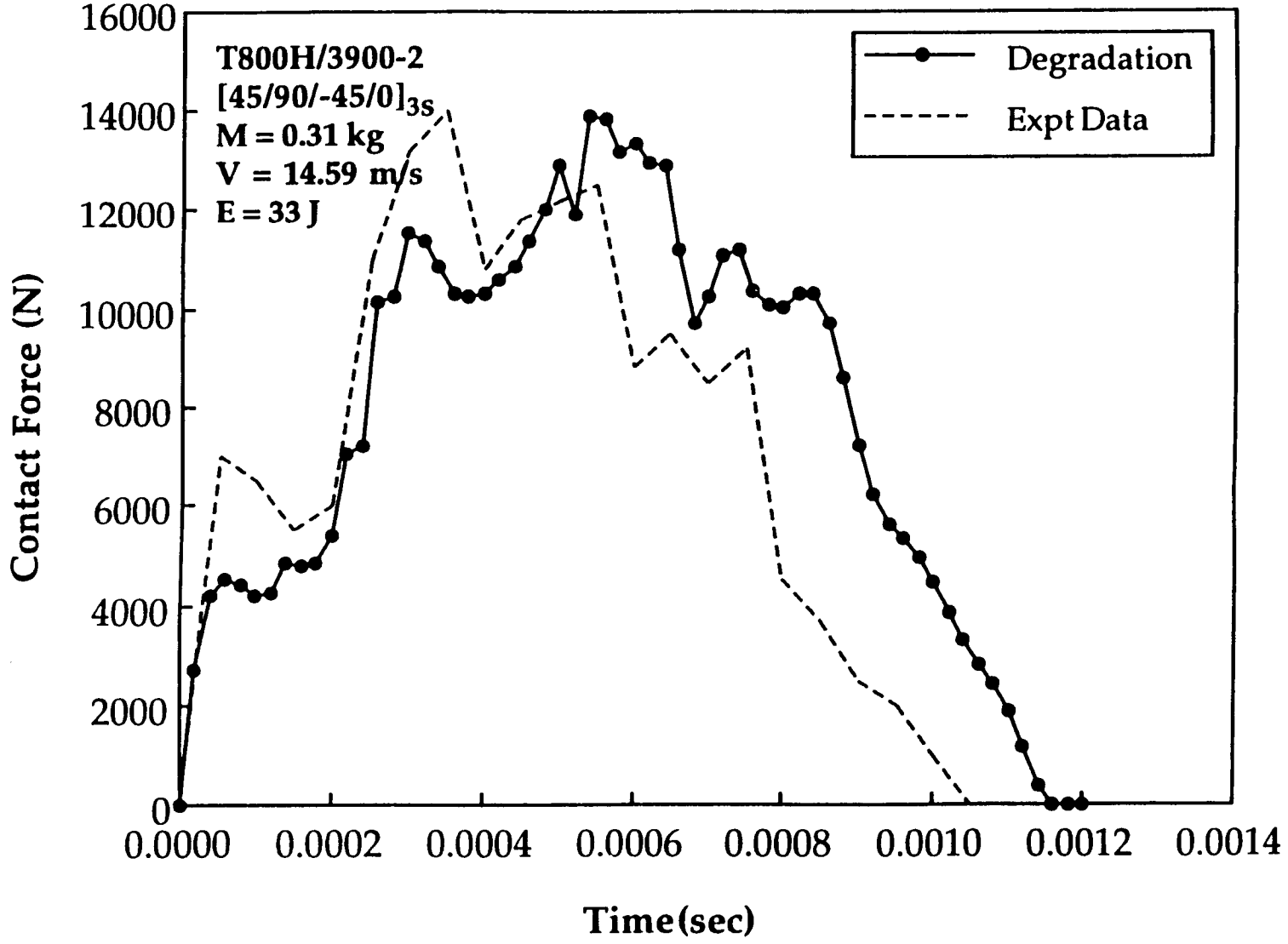

Impact force distribution as a function of time for T800/3900-2 graphite/epoxy composites. Comparison between the predictions based on the present model and the test data

INTERFACIAL STRENGTH EFFECT (WITH AND WITHOUT INTERLEAVES)

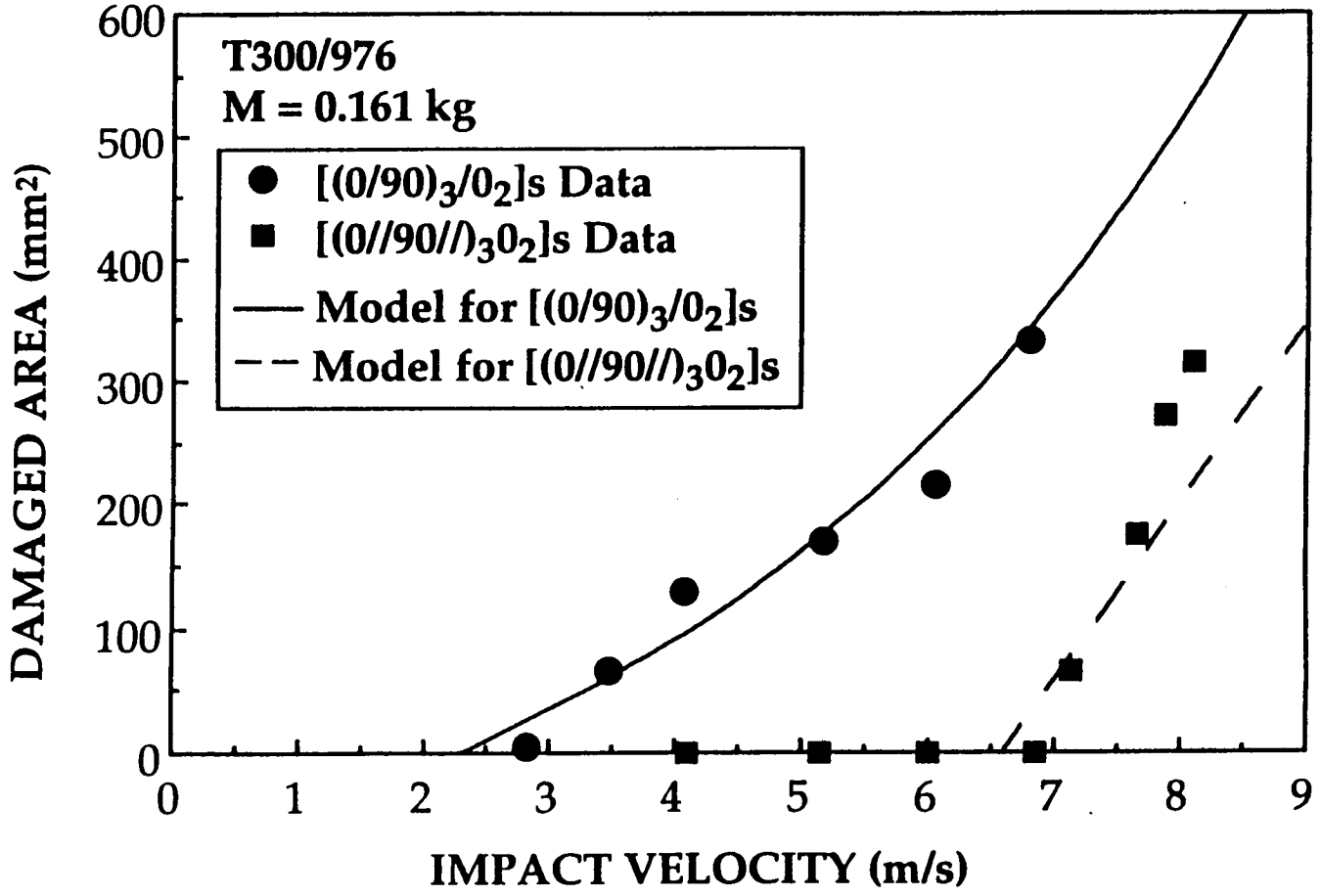

Impact damage area as a function of the impact velocity for composites with and without interleaves. Comparison between the predictions and the test data.

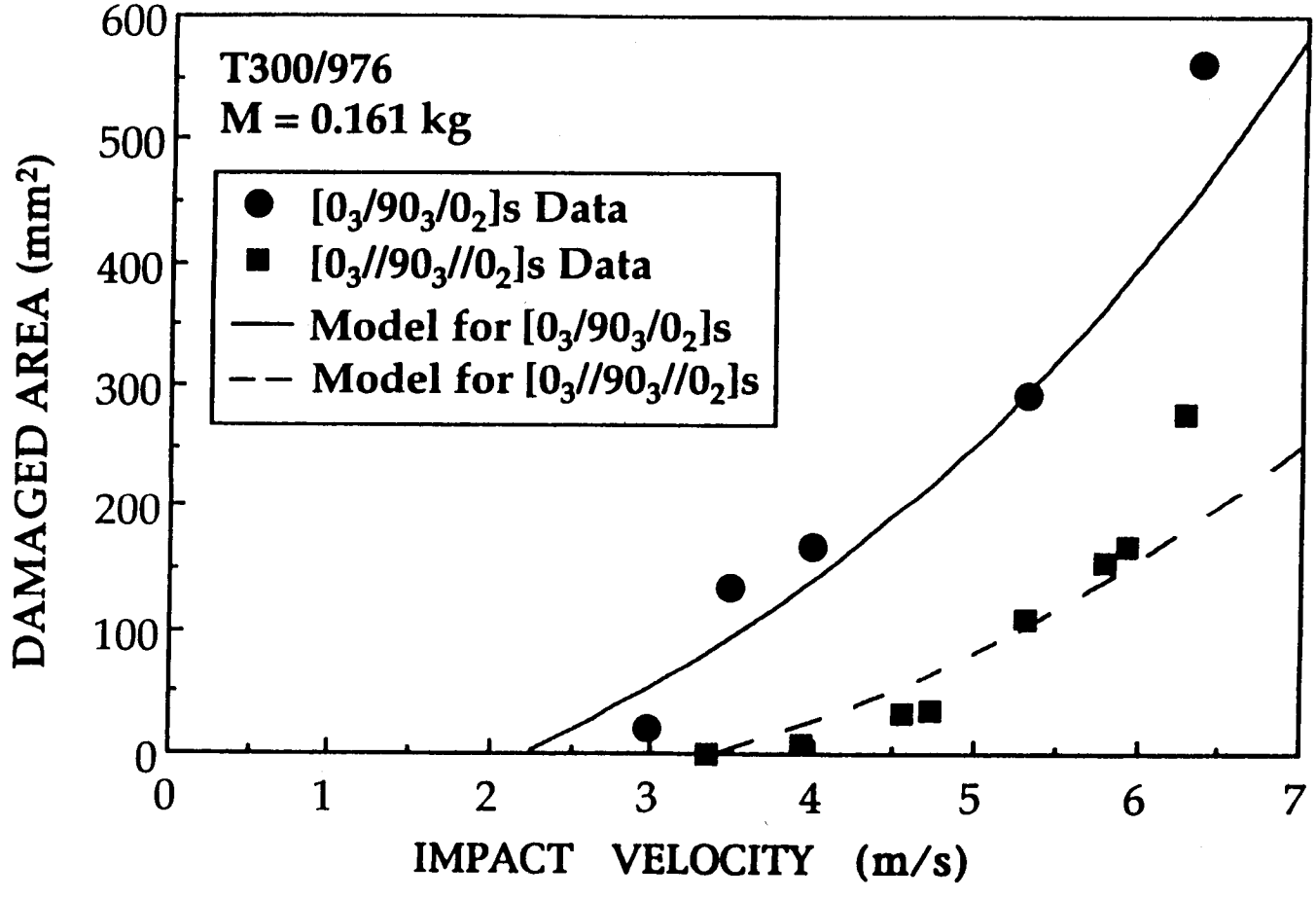

Impact damage area as a function of the impact velocity for composites with and without interleaves. Comparison between the predictions and the test data.

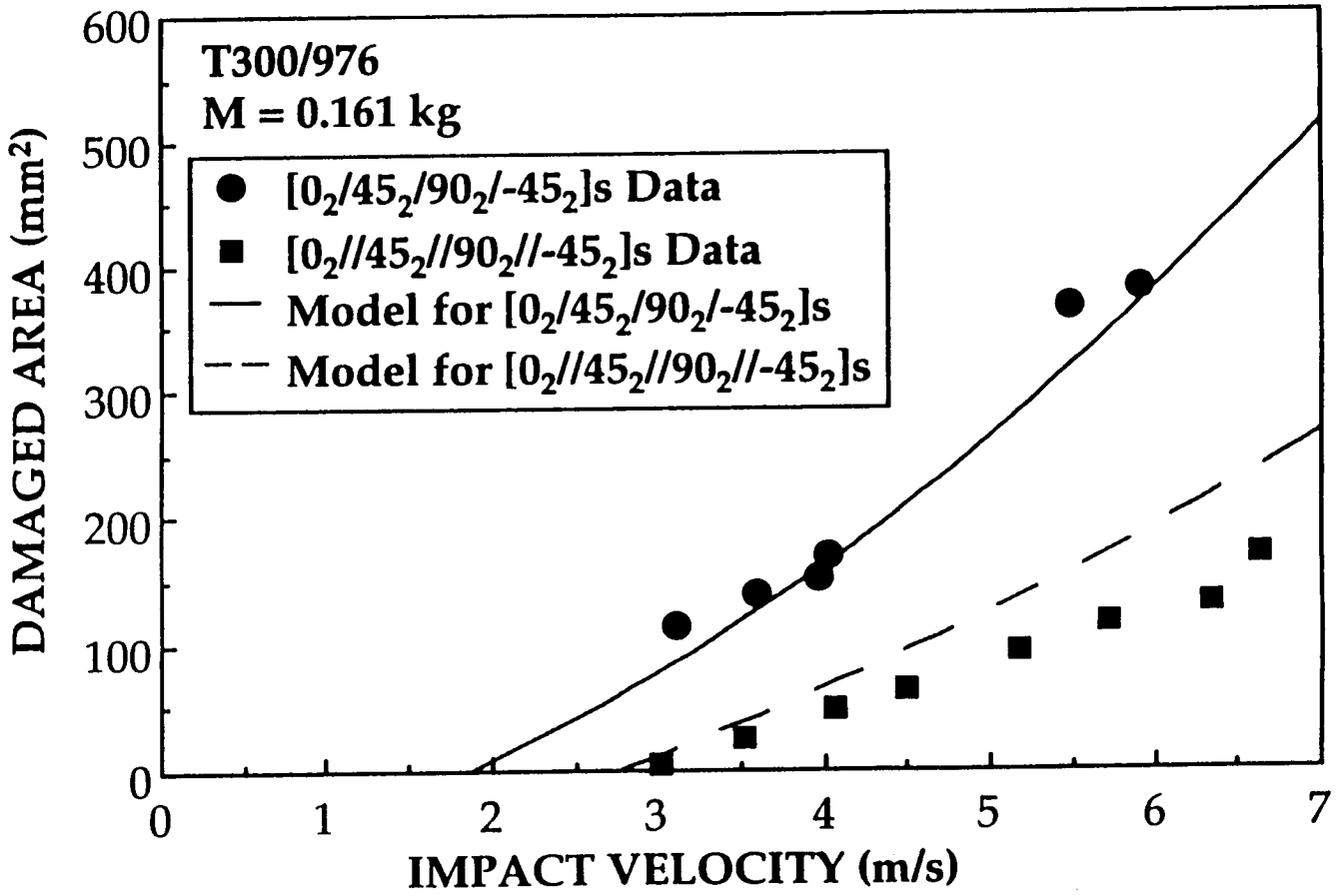

Impact damage area as a function of the impact velocity for composites with and without interleaves. Comparison between the predictions and the test data.

THE MAJOR INCLUSION IN 3DIMPACT CODE

FOR TEXTILE COMPOSITES

1. Material Properties

- Homogeneous and anisotropic media

2. Failure Criteria

- Modified Tsai-Wu 3-D failure criterion

  Mode I: inplane failure dominated along a principal axis

  Mode II: inplane failure dominated along the second principal axis.

  Model III: out-of-plane failure.

3. Material Degradation

- Material properties as a function of failure mode; a 0.1 degradation factor applied to the engineering properties associated with the failure mode.

4. Modified Hertzian Contact Law ($F = (k)\ \alpha\ \beta$)

C-4

Lockheed

Impact and CAI test conditions

Code	Material Form	Pattern	Laminate Thickness (in.)	Ply Thickness (in.)	Impact Energy (in.-lb)
L1	Braids	2	0.151	0.0377	146
L2	"	1	0.165	0.0413	146
L3	Woven(LTL)	2	0.162	0.0405	146
L4	"	1	0.162	0.0405	146
L5	Woven(TTT)	2	0.171	0.0425	146
L6	Braids	2	0.175	0.0437	240
L7	"	1	0.161	0.0403	240
L8	Woven(LTL)	2	0.164	0.041	240
L9	"	1	0.165	0.0413	240
L10	Woven(TTT)	2	0.169	0.0422	240
N1*	Braids	1	0.181	0.0453	240
N2*	"	1	0.172	0.043	192
N3*	"	1	0.178	0.0445	72
N4*	"	1	0.179	0.0447	96
N5*	Woven(LTL)	1	0.175	0.0437	72
N6*	"	1	0.168	0.042	96
N7*	"	1	0.173	0.0432	240

Impactor mass 13.2 lbf; * 9.8 lbf. ; Nose radius 5/16 in.

MATERIAL PROPERTIES USED IN THE CALCULATIONS

	Impactor velocity(in/s)	Exx(msi)	Eyy(msi)	Ezz(msi)	Vxy	Vxz	Vyz	Gxy(msi)	Gxz(msi)	Gyz(msi)	Xt (ksi)	Yt (ksi)
1	92.43	11.180	4.420	4.420	0.4000	0.4000	0.5700	1.630	1.630	1.578	104.34	29.11
2	92.43	7.410	4.380	4.380	0.3920	0.3920	0.5600	2.170	2.170	1.573	80.94	55.48
3	92.43	11.420	10.040	1.575	0.0528	0.4778	0.3892	0.976	1.743	1.250	102.31	90.41
4	92.43	10.820	9.843	1.544	0.0515	0.4813	0.3761	0.937	1.852	1.227	123.04	83.56
5	92.43	10.710	9.995	1.523	0.0578	0.4094	0.3711	0.910	1.450	1.207	108.47	93.45
6												
7	118.51	11.180	4.420	4.420	0.4000	0.4000	0.5700	1.630	1.630	1.578	104.34	29.11
8	118.51	7.410	4.380	4.380	0.3920	0.3920	0.5600	2.170	2.170	1.573	80.94	55.48
9	118.51	11.420	10.040	1.575	0.0528	0.4778	0.3892	0.976	1.743	1.250	102.31	90.41
10	118.51	10.820	9.843	1.544	0.0515	0.4813	0.3761	0.937	1.852	1.227	123.04	83.56
11	118.51	10.710	9.995	1.523	0.0578	0.4094	0.3711	0.910	1.450	1.207	108.47	93.45
12												
13	137.54	7.410	4.380	4.380	0.3920	0.3920	0.5600	2.170	2.170	1.573	80.94	55.48
14	123.00	7.410	4.380	4.380	0.3920	0.3920	0.5600	2.170	2.170	1.573	80.94	55.48
15	75.36	7.410	4.380	4.380	0.3920	0.3920	0.5600	2.170	2.170	1.573	80.94	55.48
16	87.00	7.410	4.380	4.380	0.3920	0.3920	0.5600	2.170	2.170	1.573	80.94	55.48
17												
18	75.36	10.820	9.843	1.544	0.0515	0.4813	0.3761	0.937	1.852	1.227	123.04	83.56
19	87.00	10.820	9.843	1.544	0.0515	0.4813	0.3761	0.937	1.852	1.227	123.04	83.56
20	137.52	10.820	9.843	1.544	0.0515	0.4813	0.3761	0.937	1.852	1.227	123.04	83.56

	Xc (ksi)	Yc (ksi)	Rail S (ksi)	Interlaminar Tension (ksi)
1	71.84	32.75	23.60	7.65
2	71.11	54.29	24.40	6.85
3	71.94	55.25	13.10	5.15
4	81.56	53.66	12.30	5.36
5	75.06	57.86	18.90	3.70
6				
7	71.84	32.75	23.60	7.65
8	71.11	54.29	24.40	6.85
9	71.94	55.25	13.10	5.15
10	81.56	53.66	12.30	5.36
11	75.06	57.86	18.90	3.70
12				
13	71.11	54.29	24.40	6.85
14	71.11	54.29	24.40	6.85
15	71.11	54.29	24.40	6.85
16	71.11	54.29	24.40	6.85
17				
18	81.56	53.66	12.30	5.36
19	81.56	53.66	12.30	5.36
20	81.56	53.66	12.30	5.36

Lockheed

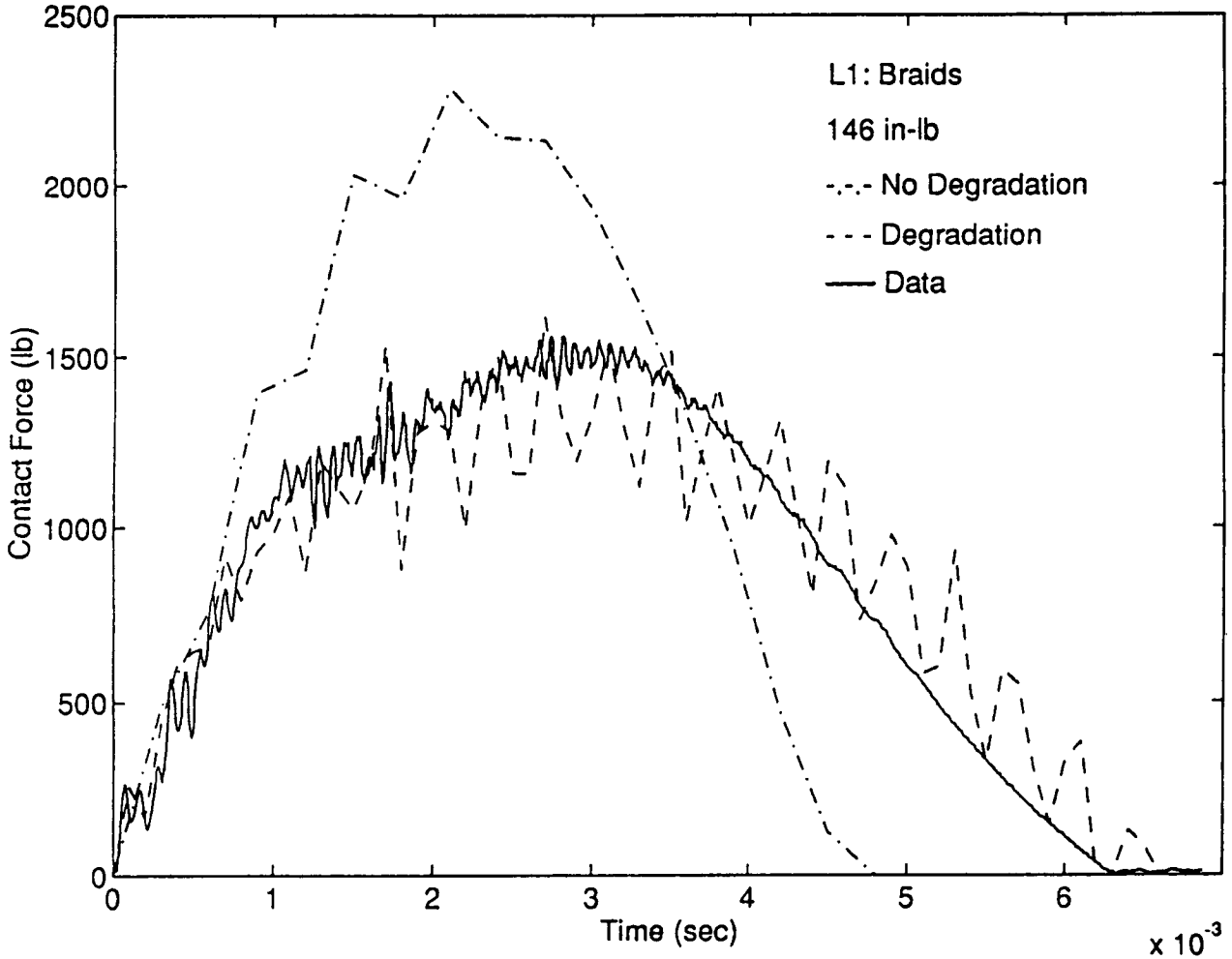
L1: Braids
146 in-lb
-.-.- No Degradation
- - - Degradation
—— Data
Contact Force (lb)
Time (sec)
x 10^-3
0
500
1000
1500
2000
2500
0
1
2
3
4
5
6

Lockheed

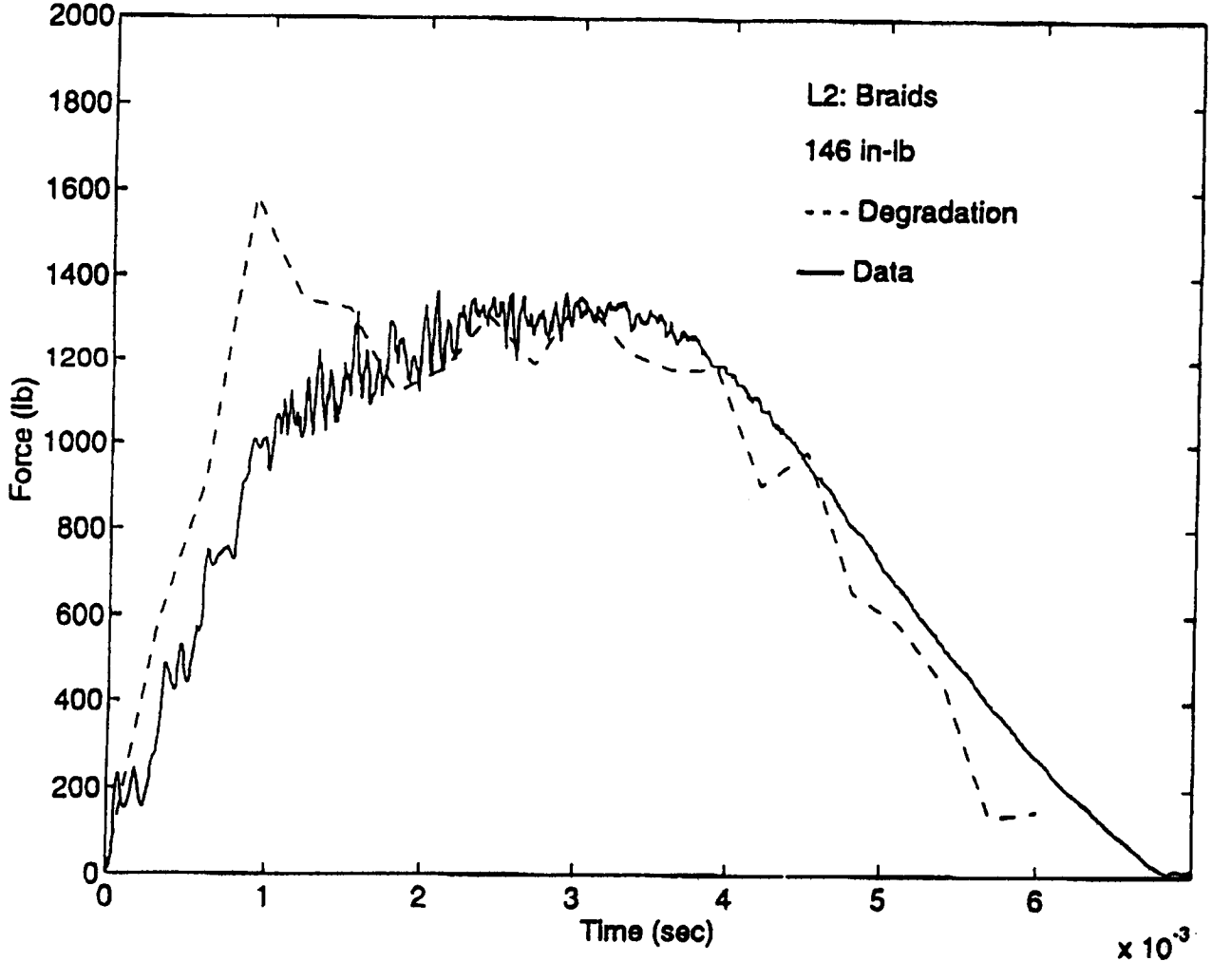
L2: Braids
146 in-lb
Degradation
Data
Force (lb)
Time (sec)
x 10^-3
2000
1800
1600
1400
1200
1000
800
600
400
200
0
0
1
2
3
4
5
6

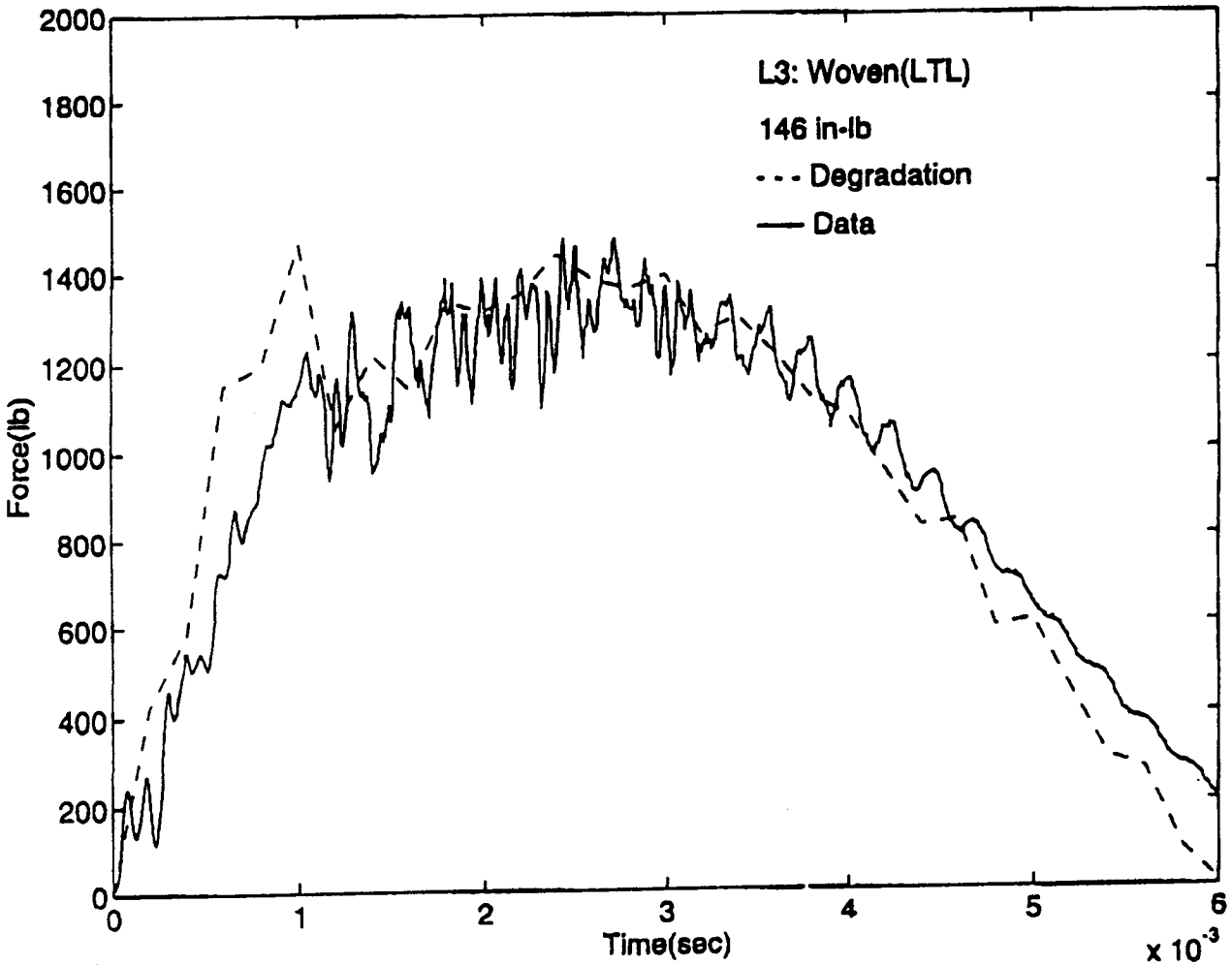
L3: Woven(LTL)
146 in-lb
- - - Degradation
— Data
Force(lb)
Time(sec)
x 10^-3
2000
1800
1600
1400
1200
1000
800
600
400
200
0
0
1
2
3
4
5
6

Lockheed

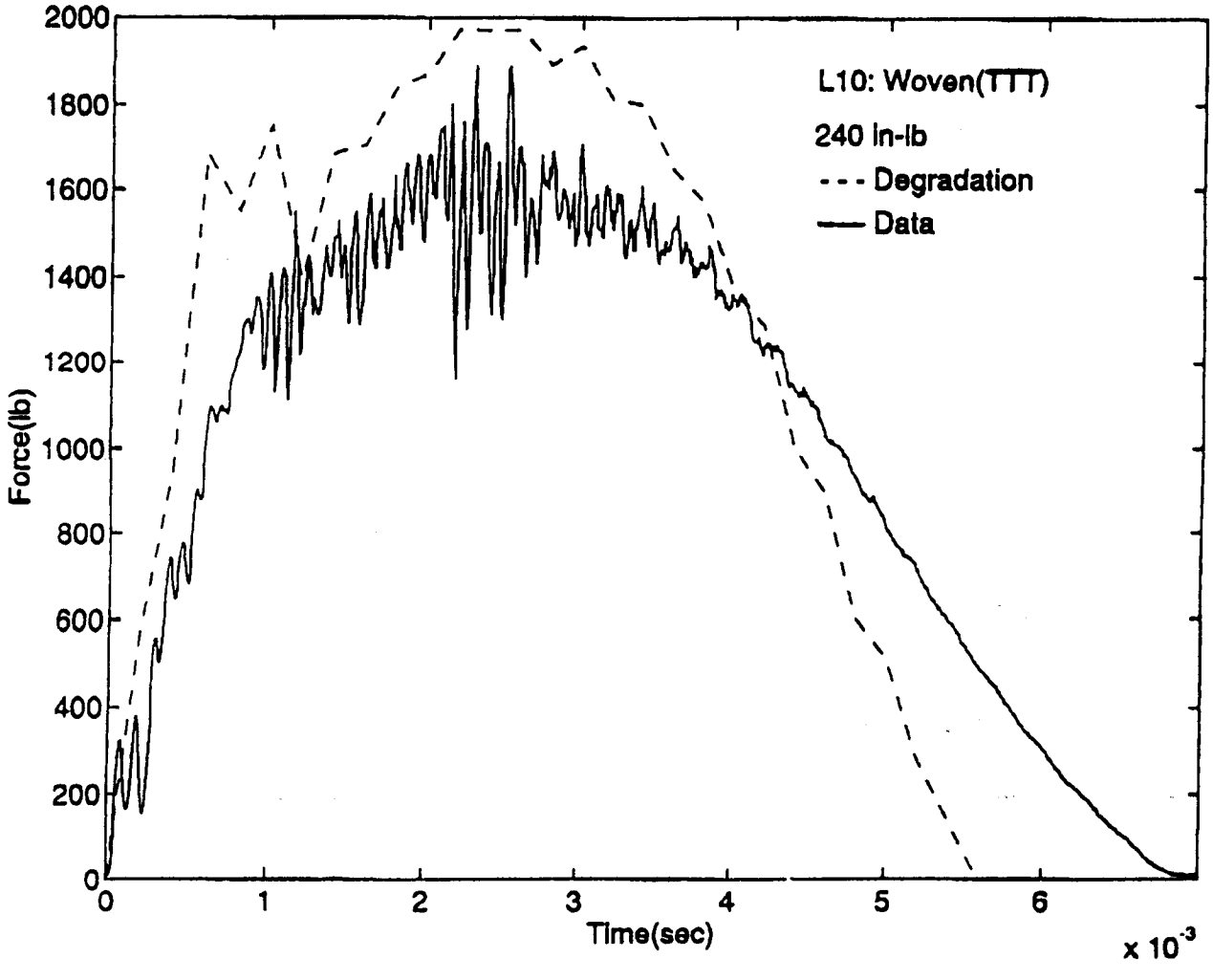
L10: Woven(TTT)
240 in-lb
- - - Degradation
— Data
Force(lb)
Time(sec)
x 10^-3
0
200
400
600
800
1000
1200
1400
1600
1800
2000
0
1
2
3
4
5
6

Lockheed

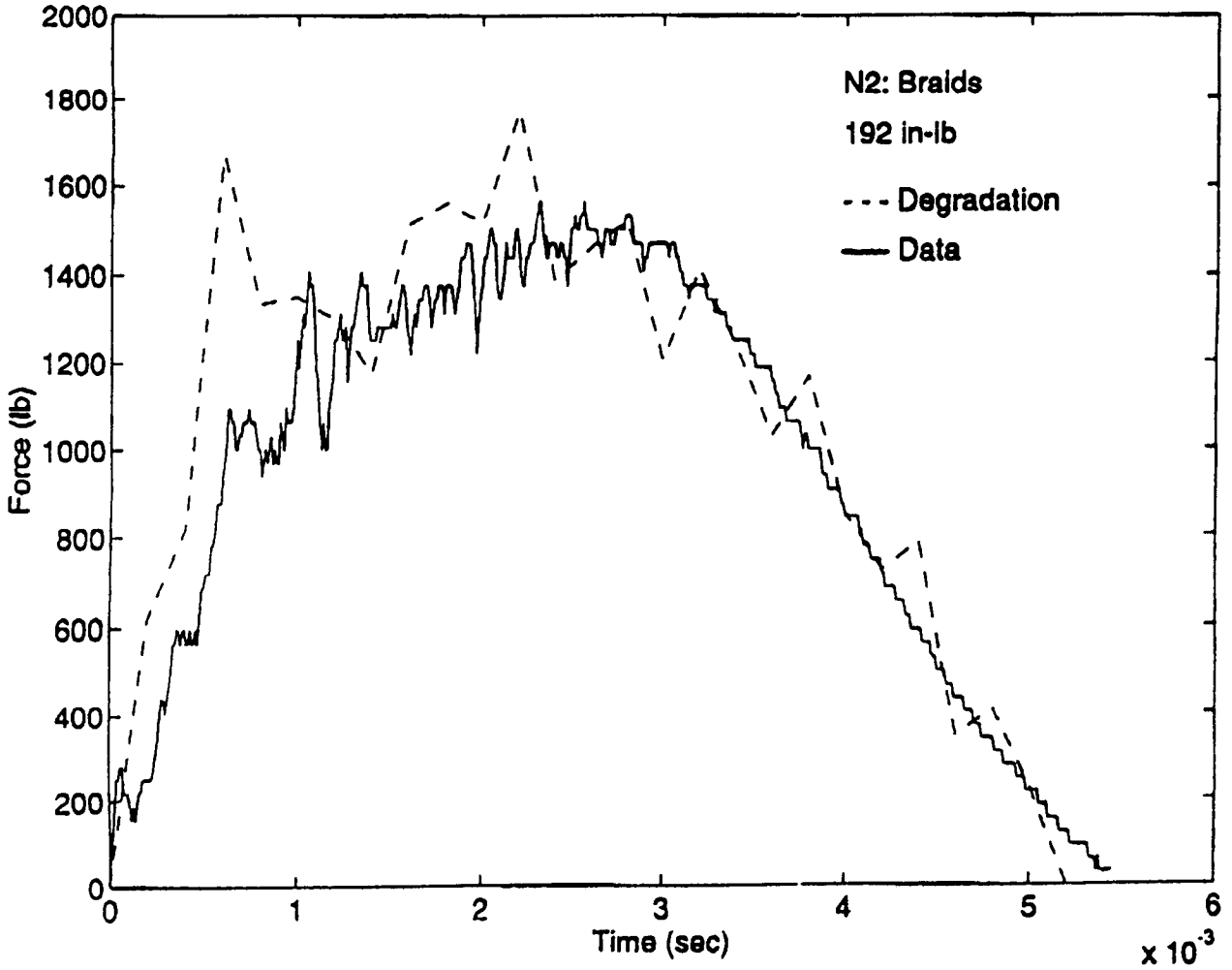
N2: Braids
192 in-lb
- - - Degradation
— Data
Force (lb)
Time (sec)
x 10^-3
0
200
400
600
800
1000
1200
1400
1600
1800
2000
0
1
2
3
4
5
6

Lockheed

Results Comparison - Analysis vs. Test

Code	Expt.Dent Depth(in.)	Pred. Dent Depth (in)	Damage Area(sq.in.)	Pred. Damage (sq. in.)	Expt. CAI (kips)	Pred. CAI (kips)
L1	0.011	0.026	0.99	1.196	29.8	23.5
L2	0.011		0.95		23.9	
L3	0.012	0.023	0.89	0.7	22.8	27.5
L4	0.015	0.024	1.13	0.551	23.5	13.5
L5	0.012	0.019	1.67	0.504	26.8	23.5
L6	0.014		1.67		26.2	
L7	0.058		1.35		19.1	
L8	0.018	0.029	1.42	0.74	21.2	16.5
L9	0.023	0.037	1.82	0.71	23.5	23
L10	0.023	0.025	2.24	0.627	26.3	22.5

CONCLUSION

- The modified 3DIMPACT code could predict more accurately the impact damage in laminated composites than the earlier version.
- Local damage could have a significant effect on the response of the target and the force-time history of the impactor.
- The predictions of the code for textile composites were promising.
- More work needs to be done on characterization of material properties of textile composites containing damage.
- Hertzian contact law is not good for unloading and for simulating impact damage; the impactor should be included in the finite element modeling.

PARAMETRIC STUDIES OF STITCHING EFFECTIVENESS FOR PREVENTING SUBSTRUCTURE DISBOND

Gerry Flanagan
Materials Sciences Corporation
Fort Washington, PA

Keith Furrow
Lockheed Engineering & Sciences Co.
Hampton, VA

INTRODUCTION

A methodology is desired that will allow a designer to select appropriate amounts of through-thickness reinforcement needed to meet design requirements. The goal is to use a relatively simple analysis to minimize the amount of testing that needs to be performed, and to make test results from simple configurations applicable to more general structures. Using this methodology, one should be able to optimize the selection of stitching materials, the weight of the yarn, and the stitching density.

The analysis approach is to treat substructure disbond as a crack propagation problem. In this approach, the stitches have little influence until a delamination begins to grow. Once the delamination reaches, or extends beyond a stitch, the stitch serves to reduce the strain-energy-release-rate (G) at the crack tip for a given applied load. The reduced G can then be compared to the unstitched material toughness to predict the load required to further extend the crack. The current model treats the stitch as a simple spring which responds to displacements in the vertical (through-thickness) direction. In concept, this approach is similar to that proposed by other authors. See Ref. 1 for example. Test results indicate that the model should be refined to include the shearing stiffness of the stitch.

The strain-energy-release-rate calculations are performed using a code which uses interconnected higher-order plates to model built-up composite cross-sections. When plates are stacked vertically, the interfacial tractions between the plates can be computed. The plate differential equations are solved in closed-form. The code, called SUBLAM, was developed as part of this

section in one dimension. Because of this limitation, rows of stitches are treated as a two-dimensional sheet. The spring stiffness of a row of stitches can be estimated from the stitch material, weight, and density. One unknown in the analysis is the effective length of the spring, which depends on whether the stitch is bonded to the surrounding material. This issue was examined in Ref. 4. As a practical and conservative approach, we can assume that the stitch is bonded until a crack passes the stitch location. After the crack passes, it is fully debonded.

A series of tests were performed to exercise the methodology outlined above. The test incorporated an attached flange such that the sudden change in thickness initiated a delamination. Two load conditions were used (3-point and 4-point bending) so that ratio of shear load to moment load could be varied. The analysis was used to estimate the material's critical G from the unstitched specimens. With this data, a prediction was made for the load required to delaminate the stitched specimens.

Using the methodology, design charts have been created for simplified geometries. These charts give stitch force, along with G_I and G_{II} as a function of the stitch spring stiffness. Using the charts, it should be possible to determine the stitch spring stiffness and strength required to reduce the G to a desired level. From these parameters, the actual stitching material, weight, and density can be computed. The results have been nondimensionalized for wider applicability.

VERIFICATION TEST

Specimen Fabrication

The two test specimen configurations are shown in Fig. 1. The specimens were fabricated from dry, AS4 uniweave fabric preforms that were resin film infusion molded (RFI) with 3501-6 resin. Uniweave fabric consists of unidirectional Hercules AS4 carbon fiber tows woven together with 225 denier glass fibers. The weave fibers made up a small portion (~2%) of the weight of the fabric. Each configuration had a stitched and unstitched version.

The stitched flanges were attached to the skin before molding by laying up the skin and flange together and mounting them in a 34 inch by 34 inch sewing frame. Then 4 inch or 2 inch wide rows of 1600d Kevlar 29 lock stitching secured the flanges to the skin. The stitch rows were 0.2 inches apart , with a 0.125 inch step. After stitching, the excess flange material was cut away.

During the RFI process, the dry textile preforms were placed on top of a pre weighed film of degassed 3501-6 epoxy resin lying in the bottom of the metal mold. The mold cover had a cavity in the shape of the flange. Holes vented the excess resin. After closing the mold and sealing it around the edges, the entire mold was placed in a hot press and evacuated at 30 mm Hg. Platens at 285°F heated the preform to reduce the viscosity of the resin and mechanical pressure (100 psi) from the platens forced the resin into the fabric preform. Raising the platen temperatures to 350°F and holding for 2 hours fully cured the composite panels.

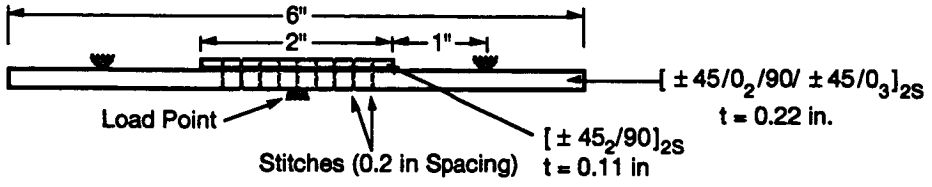

Figure 1. Three-point bending specimen with stitched attached flange.

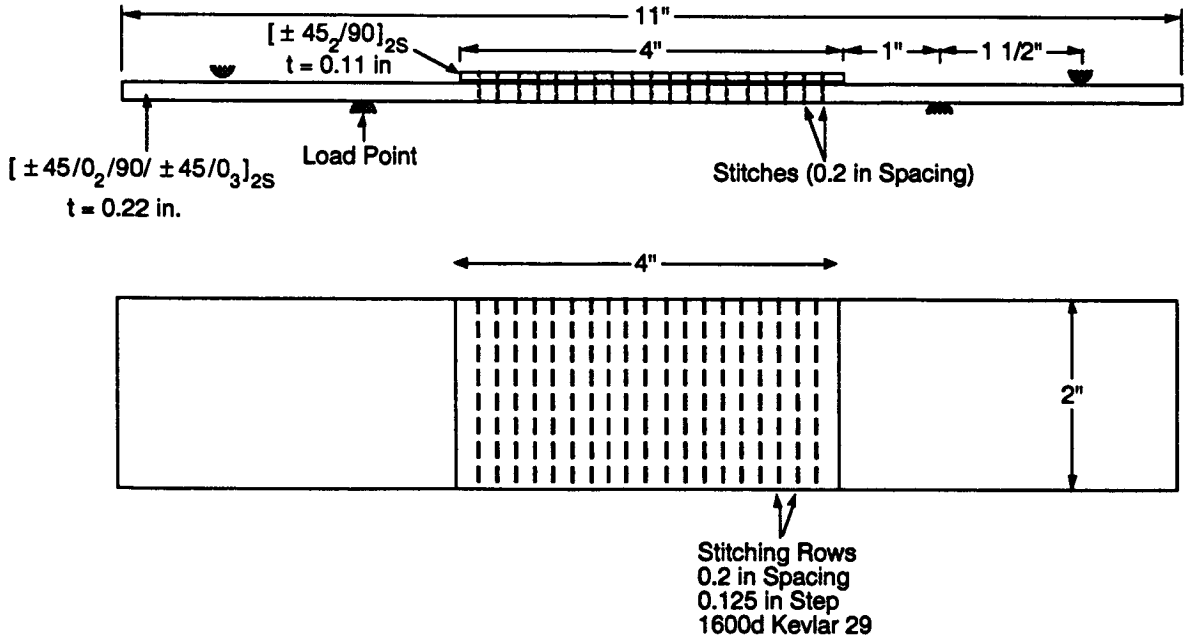

Figure 2. Four-point bending specimen with stitched attached flange.

The fiber volume fractions were 58 to 59 percent. C-Scans of the panels showed very few voids, however, a resin rich area on one side of the flange and bent or displaced fibers on the other

side of the flange were visible on some of the unstitched panels. The flange shifting after closing the mold potentially caused this problem.

Test Procedure

A crosshead rate of 0.02 inches per minute loaded the bending specimens while the load, displacement and crack growth were monitored. The load cell on the hydraulic load frame measured the load and a displacement transducer measured the center span displacement. The edges of the specimens were painted with white paint to make the crack clearly visible. A rule with 0.1 inch spacing was drawn on the side of the specimen to record the crack length as a function of the load. The crack length and load were manually recorded nominally every 0.1 inches of crack length . When the crack reached the center of the specimen the 3-point bend test was stopped. The 4-point bend test was stopped after a crack propagated one inch. The tests did not use any form of starter crack.

Results

A typical pair of load-displacement curves are shown in Fig. 3 for stitched and unstitched 3-point bending specimens. The sudden discontinuities in the curves correspond to sudden extensions of the crack. The curves also show that the stitched specimen is stiffer than the unstitched, beginning with the initial linear portion of the curve. The average stiffness for the stitched 3-point specimens was 15% greater than for the unstitched specimens, while the stitched 4-point specimens were 9% stiffer than the corresponding unstitched version. Using properties for AS4/3501-6 Uniweave taken from Ref. 5, the stiffness was calculated using both finite elements and SUBLAM. The calculated values were 9% and 7% greater than the experimental values for the 3-point and 4-point stitched specimens, respectively. The analysis requires the interlaminar shear stiffnesses, G_{13} and G_{23}. These values were not available, and therefore typical Gr/Ep values (G_{13} = 0.8 Msi, G_{23} = 0.5 Msi) were used in the original analysis. One hypothesis for the discrepancies in stiffness is that the actual transverse shear stiffnesses of this material are less than the assumed values, perhaps due to the uniweave form. Consequently, the values in the analysis were adjusted downward (G_{13} = 0.4 Msi, G_{23} = 0.25 Msi) to obtain a better correspondence between the test and analysis.

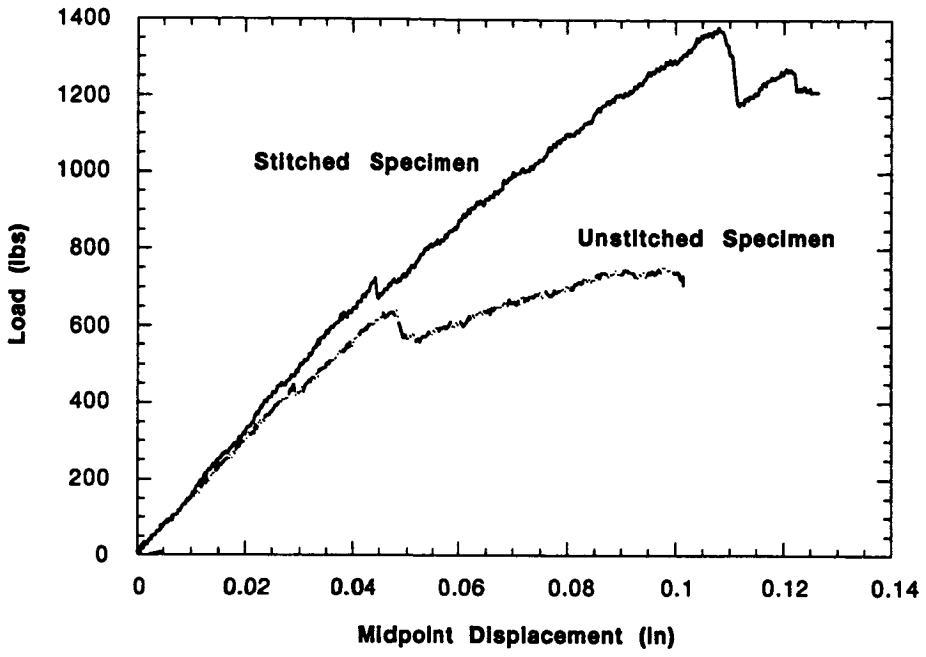

Figure 3. Typical force-displacement curves for stitched and unstitched 3-point bending specimens

From the load versus crack length data for the unstitched specimens, the strain-energy-release-rate can be back-calculated. The results of this calculation are shown in Fig. 4 for the mode I and mode II components. In these plots, "a" is the crack length. Ideally, the values obtained from the 3-point and 4-point specimens should overlap. However, the results show that the 3-point specimens tend to have a lower value of G. The plots also indicate that G increases with crack length. The increase in G with the crack length is frequently associated with bridging of fibers. The initial G_I is greater than would normally be expected for 3501-6 resin. This may be due to the lack of a starter crack, or to the uniweave material form. Finally, we note that the 4-point specimens number 4 and 5 appear to be outliers, although there was no obvious difference in these specimens.

The stitching analysis requires both the critical G_I and G_{II} ($G_{Icrit}$and G_{IIcrit}). The unstitched specimens are mixed-mode, but do not provide sufficient information to determine both values. Based on typical Gr/Ep properties, we assumed that $G_{IIcrit} = 4\ G_{Icrit}$. The following linear mixed mode crack growth criteria was also assumed.

$$\frac{G_I}{G_{Icrit}} + \frac{G_{II}}{G_{IIcrit}} = 1$$

Using these two assumptions, G_{Icrit} was determined so that a good fit to the initial crack extension load for the unstitched specimens was obtained. This yielded a G_{Icrit} of 2.2 in-lb/in^2.

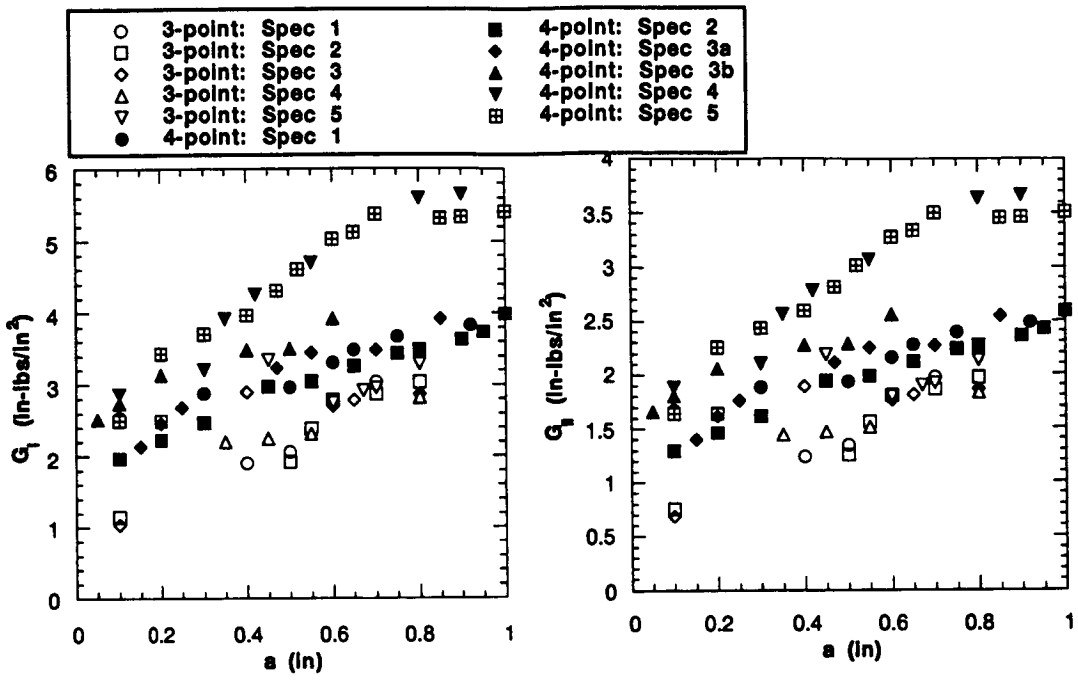

Figure 4. Experimental values of G_I and G_{II} versus crack length.

The predicted and experimental loads for crack growth are given in Fig. 5 and 6. Two values of the stitched spring stiffness were used. The first, k=1.2 x 10^5 lb/in^2, assumes that the stitch is fully debonded. The second, k = 4.7 x 10^5 lb/in^2, assumes that the stitch is bonded, but that the matrix behaves as an elastic-plastic material, calculated using the methods given in Ref. 4. Both curves for the stitched cases fall below the experimental data. The change in assumed stitch stiffness affects how rapidly the stitches begin to suppress the crack growth, but has little effect on the maximum load that may be applied. The predictions use the initial values of G, and do not take the observed crack resistance curve into account. Therefore, in Fig. 5, the unstitched predicted load goes down with increasing crack length (unstable growth), while the experimental values increase with crack length.

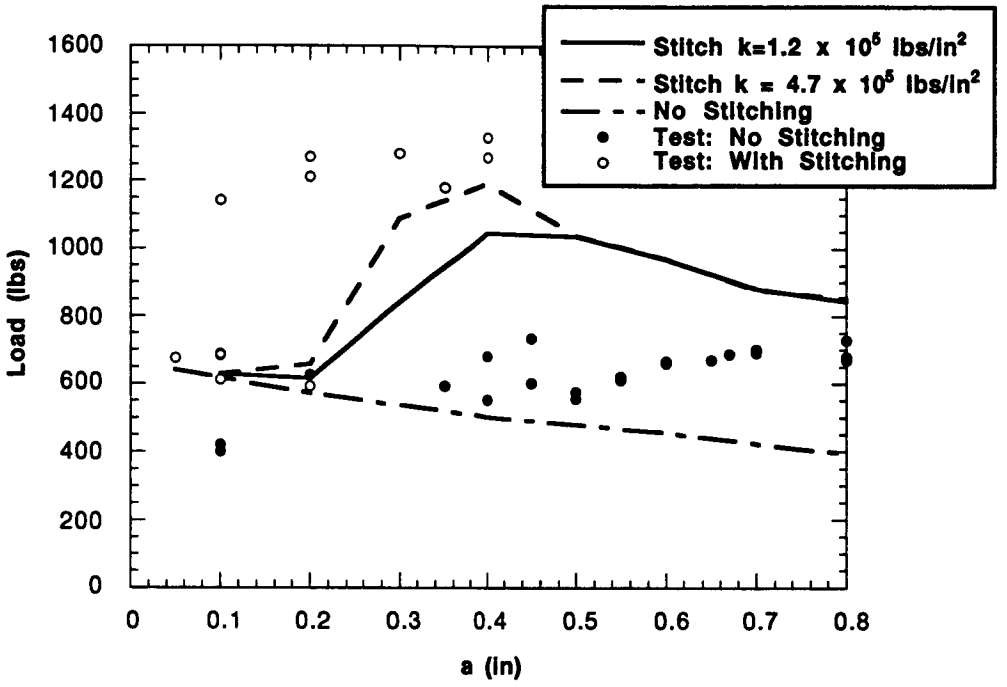

Figure 5. Predicted and measured loads required for crack extension. Three-point bending case.

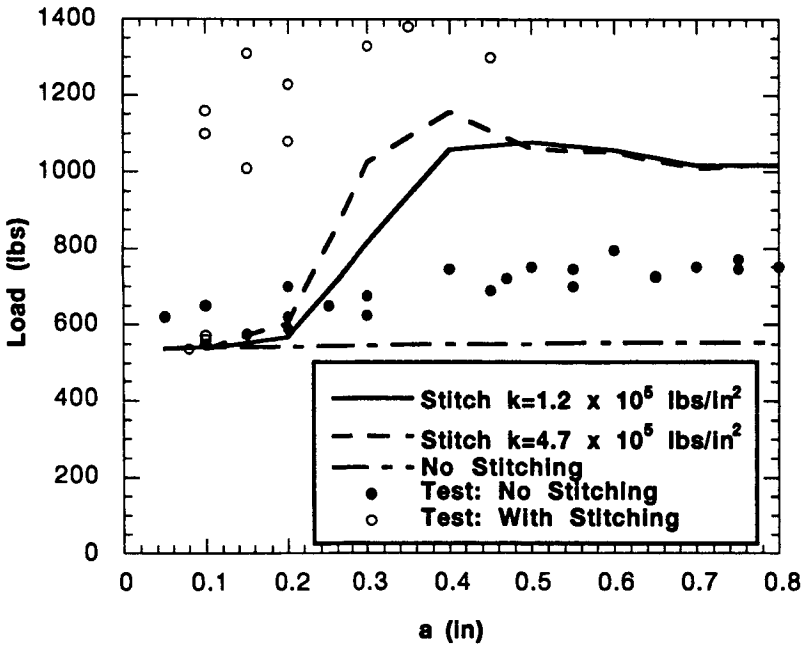

Figure 6. Predicted and measured loads required for crack extension. Four-point bending case.

The failure of the analysis to predict the full effect of the stitches may be related to the simple model in which the stitch only resists through-thickness stretching. In this model, the stitch does nothing to suppress mode II crack growth. In the analysis of the stitched specimens, the stitching was sufficiently stiff to completely suppress mode I crack growth. The results indicate that stitches also reduce mode II growth. Fig. 7 shows the sliding displacement that occurs at the stitch locations in the 3-point bending specimens. Stitches may resist this sliding motion either by shearing, or by local large rotations.

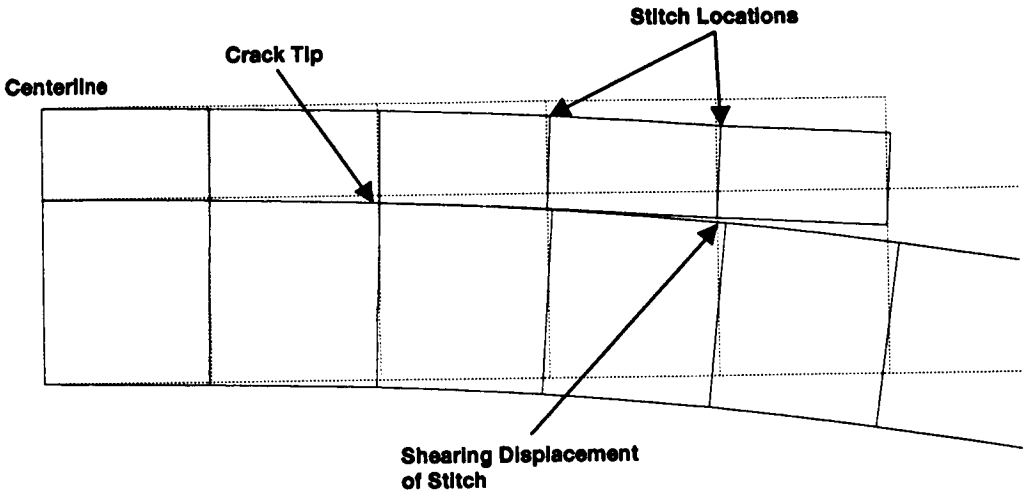

Figure 7. Deformed three-point bending specimen from SUBLAM analysis

PARAMETRIC STUDIES

The inherent design flexibility of composite structures makes it difficult to create generic design graphs. Consequently, design with composite invariably involves computer software. However, some highly idealized configurations can be treated in a parametric manner to give a feel for the mechanics involved, and to give order-of-magnitude estimates for the stitch parameters needed to stop delamination growth. Such idealizations have been examined using the SUBLAM program in order to create a series of design charts.

A number of simplifications had to be made to create problems that can be nondimensionalized. One simplification is that we treat plates made from a homogeneous, orthotropic material, instead of laminates. This removes stacking sequence considerations from the problem. For the problems

studied, we have further assumed the orthotropic material has the properties of a quasi-isotropic layup of graphite/epoxy.

Another simplification involves our treatment of delamination growth. A general analysis would involve tracking the growth of a delamination until either unstable growth occurs, or the structure collapses. The simplified approach is to determine the strain-energy-release rate for a delamination of a predetermined size. Furthermore, we assume the delamination size is smaller than the spacing between stitches. Thus, the models include only a single row of stitches. The approach being presented implies that the through-thickness reinforcement should be selected to stop a delamination within a single row of stitches; a conservative criterion.

The stiffness of the stitch is an independent parameter in the design charts. Our models assume that the cross-section of the structure is constant. Consequently, a row of stitches is actually treated as a 2-dimensional sheet. The spring stiffness, k, of such a sheet is defined by the force-displacement relation

$$k = N/\delta$$

where δ is the displacement, and N is a running load with units lb/in. Therefore, the units of k are lb/in^2, and k can be estimated by the relation

$$k = 6.222 \times 10^{-9} \frac{E\, n\, w}{\rho\, l} \quad lb/in^2$$

where E is the modulus of the stitching material (lb/in^2), n is the stitch pitch along the row (penetrations/in), w is the weight of the stitch in Denier, ρ is the volume density of the stitch material (lb/in^3), and l is the effective length of the stitch (in). The constant represents a unit conversion from Denier to lb/in. A lower bound on the stiffness can be determined by assuming the stitch is fully debonded. In which case, l is the total thickness of the laminate. If the stitch does not fully debond, the effective length is smaller, and the stitch acts as a stiffer spring.

The design charts give running load, f_S (lb/in), for the row of stitches. This load can be used to estimate the applied load needed to fail the row of stitches. The strength of the row can be estimated from

$$f_s^{ult} = 6.222 \times 10^{-9} \frac{\sigma_s^{ult}\, n\, w}{\rho} \quad lbs/in$$

where σ_s^{ult} is the ultimate strength of the stitching material.

The delamination growth criterion used in our charts is the strain-energy-release-rate (G). The charts give the mode I and II values for G. If G_I and G_{II} are determined for a trial applied load, then, assuming a linear interaction curve, the critical load for delamination growth is given by

$$R = \left(\frac{G_I}{G_{I\,crit}} + \frac{G_{II}}{G_{II\,crit}} \right)^{-1/2}$$

where $G_{I\,crit}$ and $G_{II\,crit}$ are the critical material values for pure mode I and mode II, and R is a scaling factor that multiples the trial applied load (assuming proportional loading). In the design charts, the values of G are given in nondimensional form. The combination of parameters used for nondimensionalization are given on the individual charts.

The first idealized geometry treats a sudden change in thickness for a cantilevered beam (Fig. 8). This problem could represent the attached flange of a stiffener. We have assumed that the initial delamination length is $1.25\ h_1$.

Three load cases can be considered; pure moment, pure normal shear at the crack tip, and axial load. The results for the pure moment case are given in Fig. 9-11 for a range of h_2/h_1 values. If one observes the trends with respect to changes in h_2, there appears to be a sudden change in behavior when $h_2 = 0.2\ h_1$. This jump in the results is being investigated. Note that G_{II} actually increases with increasing stitch stiffness. However, for most brittle composites, the critical mode II toughness for the material is much greater than the mode I value. Therefore, the decrease in G_I is more significant toward suppressing delamination.

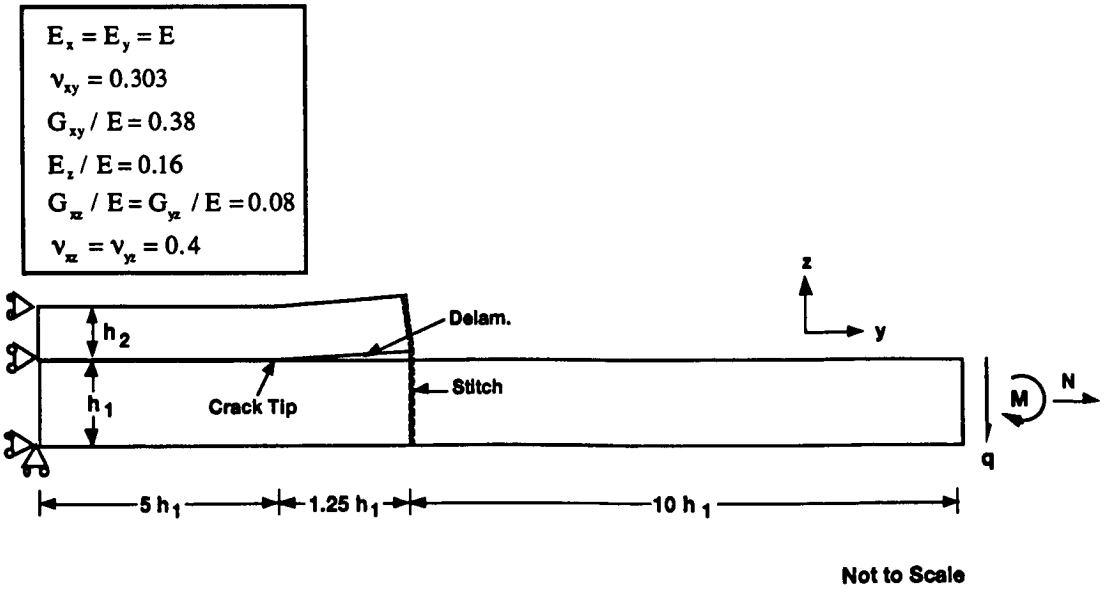

Figure 8. Idealization of attached flange.

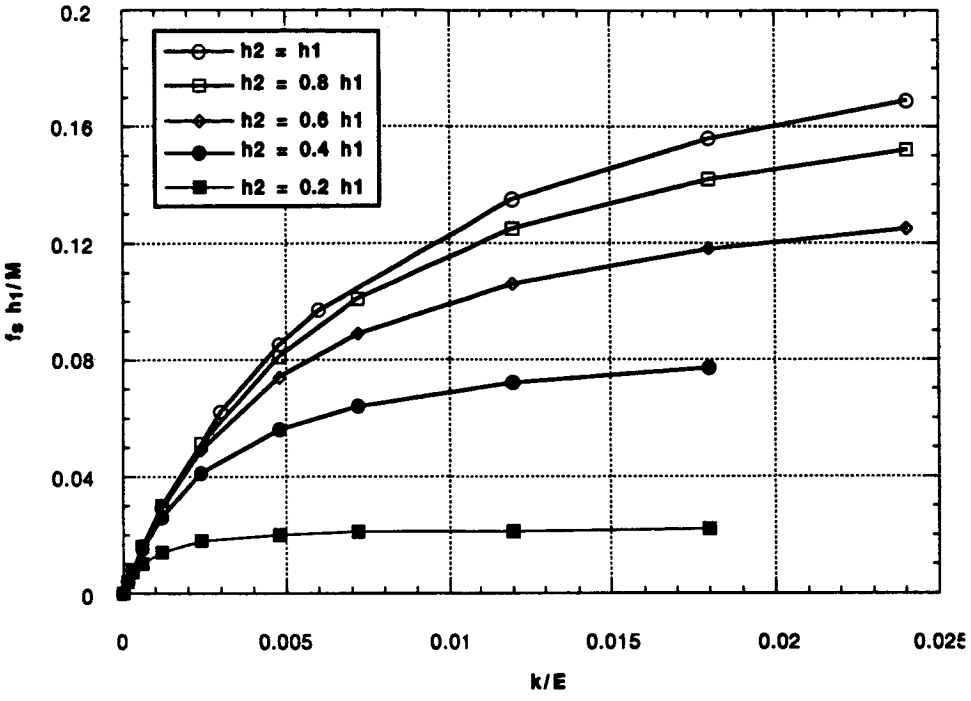

Figure 9. Normalized stitch force for attached flange under moment load.

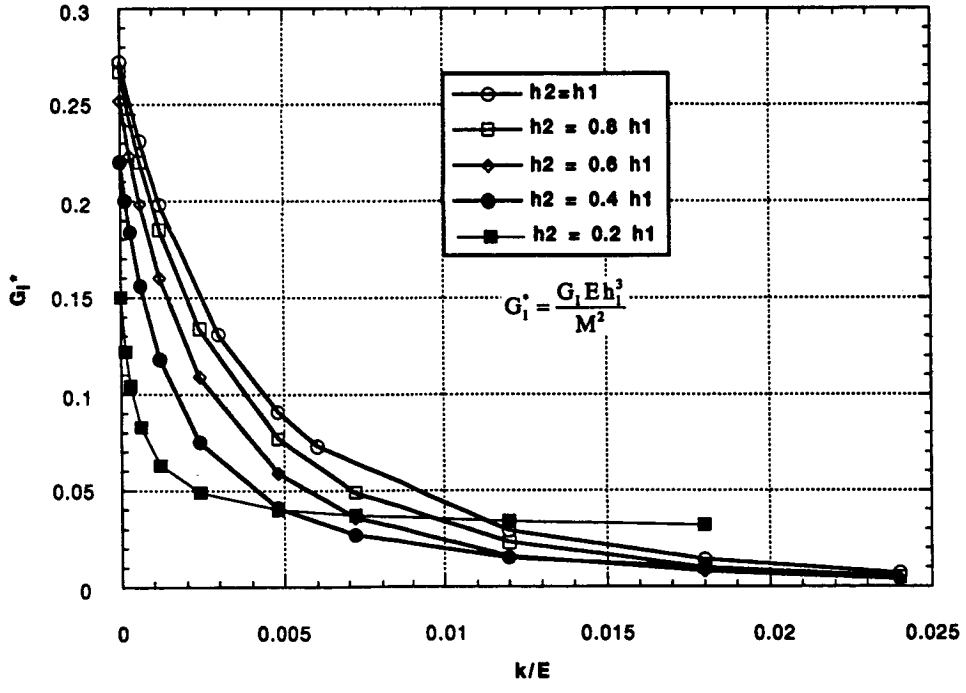

Figure 10. Normalized G_I for attached flange under moment load.

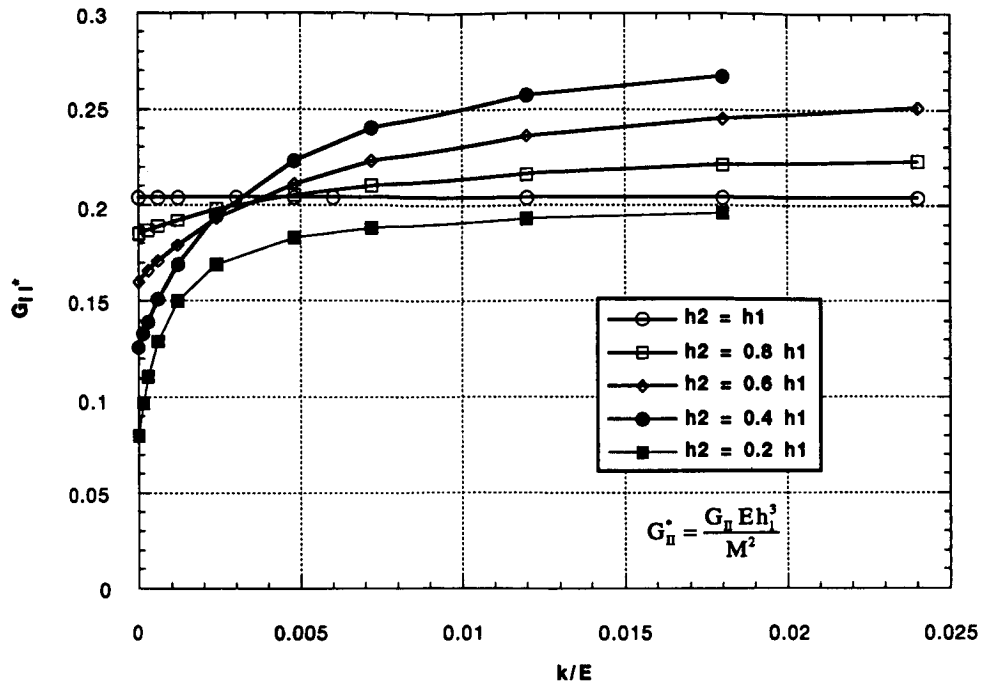

Figure 11. Normalized G_{II} for attached flange under moment load.

To use the charts of this form, it is suggested that the analyst determine the combination of moment, shear and axial load at the crack tip for a particular case. The values of G can be determined from the charts for each load component independently. The individual G's can then be summed, and the interaction equation given above used to determine the load scaling factor (if R is less than 1, then there is a negative margin-of-safety for crack growth). Flanges with gradual tapers can be approximately analyzed by using the local thickness at the stitch row location.

A second idealized problem represents the stiffener pull-off problem (Fig. 12). In this model, we assume that the filler material has already failed. Because the load condition is symmetric, only half of the geometry is modeled, and symmetry boundary conditions are applied. The stitch row is placed at the dividing line between the flat and curved parts of the stiffener laminate. Creating a generic series of plots for this problem is more difficult since the structure is not statically determinant. Thus, the loads at the crack-tip will be affected by the length of the skin segment, and the boundary conditions for the skin. For the idealization, we assume that the skin is clamped at a distance of 50 h_1 from the centerline. The sensitivity of the results to these arbitrary dimensions needs to be investigated. Based on Grumman design practice, the inside radius of the curved laminate is equal to the laminate thickness.

The results for the pull-off problem are given in Fig. 13-15. Curves are not given for $h_2 = h_1$ and $h_2 = 0.8\ h_1$ because the crack was closed for these values, making the stitch ineffective. In these cases, the crack could extend in pure mode II. This behavior may be related to the qualitative observation made in Ref. 6 that stitches placed near the heel of a stiffener appeared to be failing in shear. Figure 14 indicates that G_I approaches a constant value even for large values of the stitch stiffness. Thus, for the assumed delamination length, there is a limit to how effectively the stitches can suppress mode I fracture.

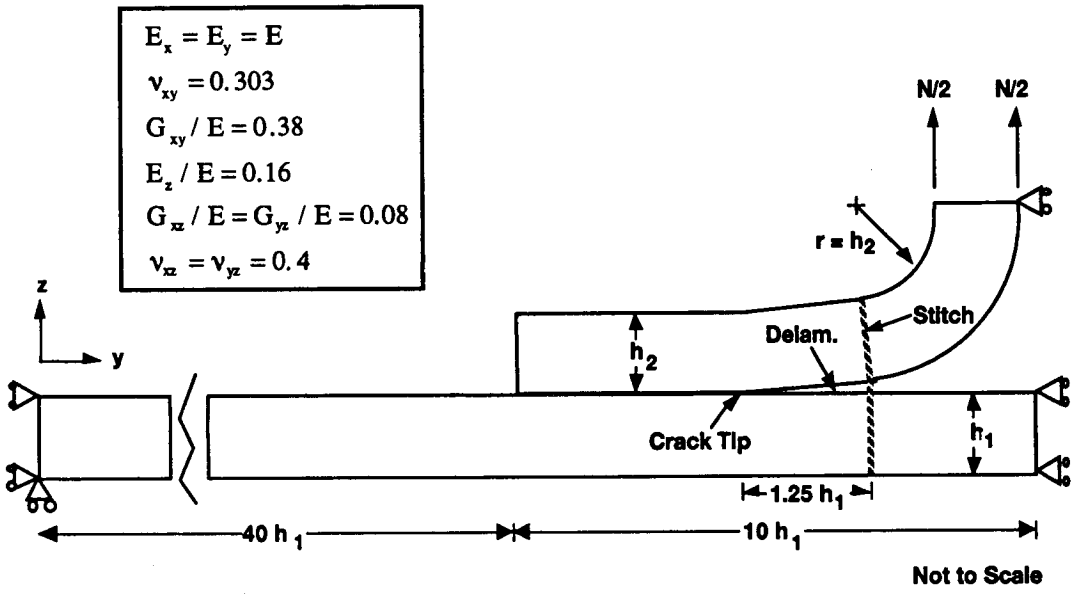

Figure 12. Idealization for stiffener pull-off problem.

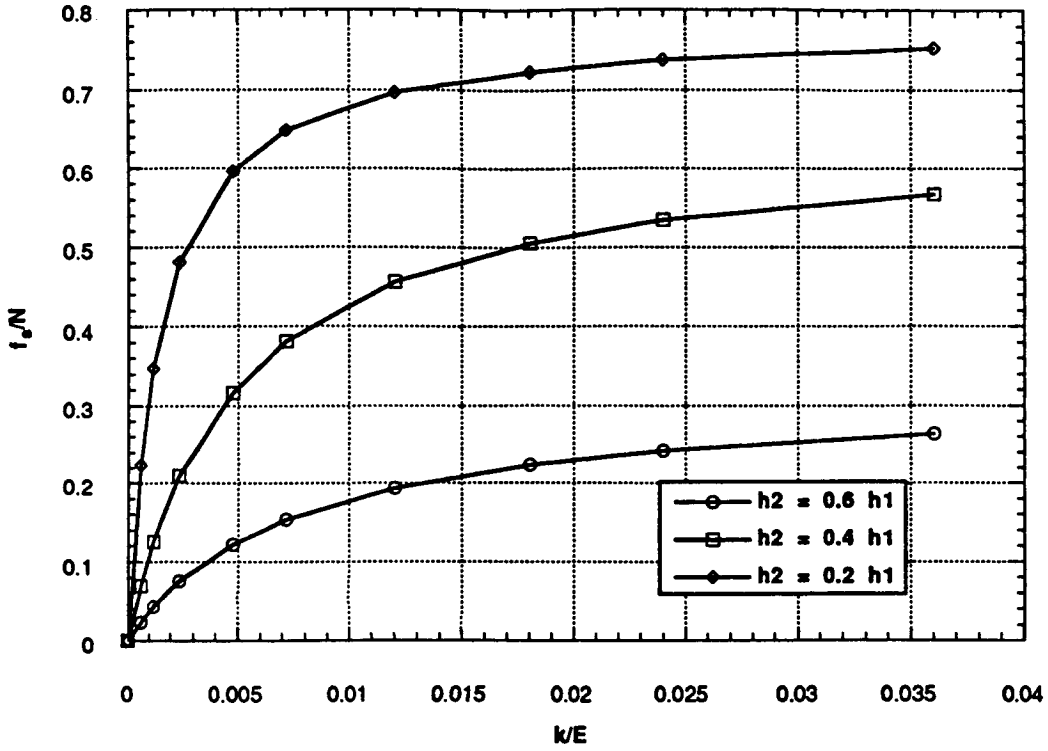

Figure 13. Normalized stitch force for pull-off problem

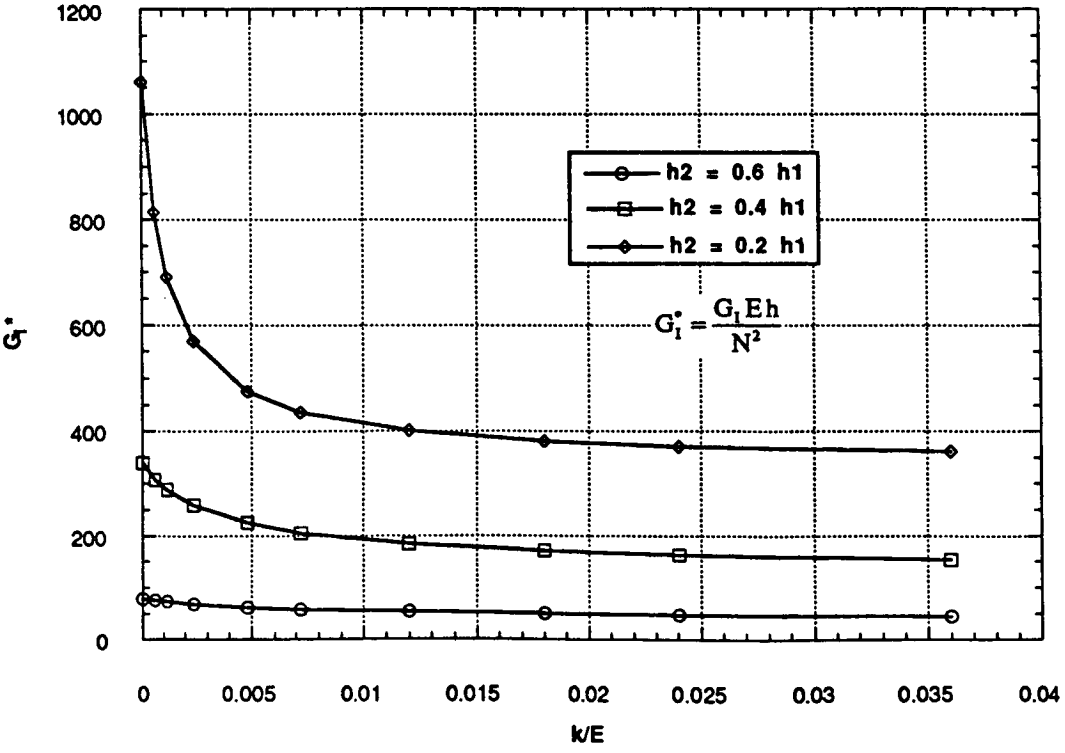

Figure 14. Normalized G_I for pull-off problem

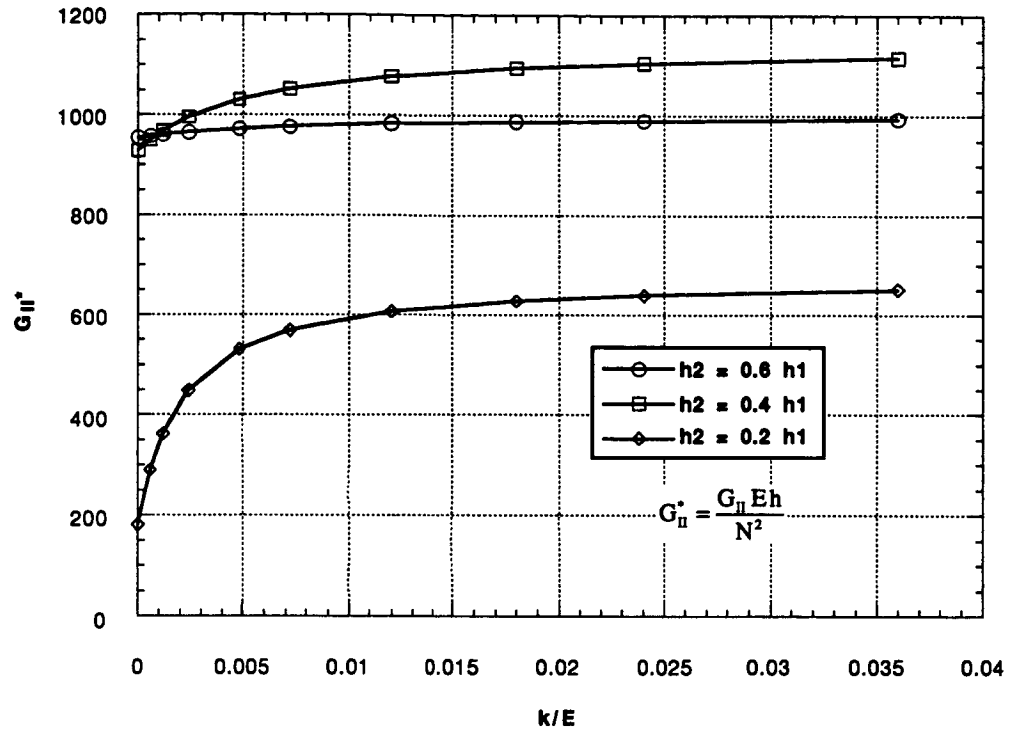

Figure 15. Normalized G_{II} for pull-off problem.

CONCLUSIONS

A methodology has been developed that can be used to select appropriate through-thickness reinforcements. Verification tests of the analysis were somewhat ambiguous because the pure mode I and II fracture toughnesses for the material were not available. The analysis gives conservative results for the amount of additional load a stitched flange can take without delaminating. This conservatism seems to be related to the ability of stitching to suppress mode II fracture, in addition to the mode I behavior included in the model.

The analysis gives us the ability to create non-dimensional curves that help in designing cocured structures with through-thickness reinforcements. Despite the shortcomings revealed in the testing, the analysis provides a conservative method of design, while minimizing the amount of element testing that must be performed.

ACKNOWLEDGMENTS

This work was performed under NASA's Novel Composites for Wing and Fuselage Applications (NCWFA) program, contract No. NAS1-18784, with Mr. H. Benson Dexter as the Contracting Officer Technical Representative. The test specimens were fabricated and tested at NASA/LaRC.

REFERENCES

1. Joon-Hyung Byun, John W. Gillespie, Jr., and Tsu-Wei Chou, "Mode I Delamination of a Three-Dimensional Fabric Composite," J. of Composite Materials, Vol. 24, May 1990, pp 497-518.

2. G. Flanagan, "A Sublaminate Analysis Method for Predicting Disbond and Delamination Loads in Composite Structures," J. of Reinforced Plastics and Composites, Vol. 12, August 1993, pp 876-887.

3. G. Flanagan, "A General Sublaminate Analysis Method for Determining Strain Energy Release Rates in Composites," AIAA Paper 94-1358, 35th AIAA/ASME/ASCE/AHS/ASC Structures, Structural Dynamics, and Materials Conference, Hilton Head, SC, April 18-20, 1994, pp 381-389.

4. G. Flanagan, "Development of Design Guidelines for Stitching Skins to Substructure," presented at the Fourth NASA/DoD Advanced Composites Technology Conference, Salt Lake City, Ut., June 7-11, 1993.

5. "Innovative Composite Aircraft Primary Structures (ICAPS), February 1992 Technical Progress Report," preparted for NASA Langley Research Center under contract NAS1-18862, McDonnell Douglas Corp., pg. 17.

6. C. Cacho-Negrete, "Integral Composite Skin and Spar (ICSS) Study Program - Vol, 1," AFWAL-TR-82-3053, Sept. 1982, pg 269.

FINITE ELEMENT BASED MICRO-MECHANICS MODELING OF TEXTILE COMPOSITES *

E.H. Glaessgen† and O.H. Griffin, Jr.††
Department of Engineering Science and Mechanics
Virginia Polytechnic Institute and State University
Blacksburg, VA 24061

SUMMARY

Textile composites have the advantage over laminated composites of a significantly greater damage tolerance and resistance to delamination. Currently, a disadvantage of textile composites is the inability to examine the details of the internal response of these materials under load. Traditional approaches to the study of textile based composite materials neglect many of the geometric details that affect the performance of the material.

The present three dimensional analysis, based on the representative volume element (RVE) of a plain weave, allows prediction of the internal details of displacement, strain, stress, and failure quantities. Through this analysis, the effect of geometric and material parameters on the aforementioned quantities are studied.

INTRODUCTION

Textile based composite materials have received considerable attention in the literature in recent years [1,2]. These traditional approaches to the study of textiles are typically an extension of proven techniques for the study of laminated materials. They tend to be based on strength of materials and classical lamination theory (CLT), a homogenized finite element approach that uses classical micromechanics or CLT as a basis for material properties, or a spar in a matrix approach [3]. The result is a lack of ability to determine details of the internal response of these materials under load. A macro finite element approach was developed by Whitcomb [4] and Woo and Whitcomb [5] and is a compromise between the previously mentioned models and the type of detailed finite element models developed for the present study. Although the analysis by Whitcomb shows some details of the load distribution within the composite, it may neglect some of the geometric details that affect the performance of the material. Techniques employing conventional finite elements have also been reported [6,7,8]. These have been developed for woven composites under mechanical loads and provide varying degrees of accuracy and details of results.

* Work performed under grant NAG-1-343 at Virginia Polytechnic Institute and State University
† Graduate Research Assistant
†† Professor and Associate Dean

The present finite element based technique allows the interrogation of the internal response of textiles. This approach greatly reduces the geometric simplifications required for modeling, since the finite element models are taken directly from either the Textile Geometry Model (TGM) [9] or from micrographs of manufactured materials. Although originally developed for the analysis of textiles under mechanical loads [6], this technique is easily extended to include response to thermal loading. The present analysis, based on the representative volume element (RVE) of a textile composite, allows prediction of the load, mode, and location of failure initiation within the RVE. Through these models, not only is gross characterization possible, but internal details of displacement, strain, stress, and failure parameters can be studied. Specifically, this discussion focuses on the analysis of a plain weave textile composite. Both mechanical and thermal loading is considered.

GEOMETRIES STUDIED

Although it is desirable to avoid more geometric simplifications than necessary, certain simplifications are unavoidable. Sectioning of manufactured woven textile composites shows that material variances exist throughout the textile. Accounting for the differences between RVEs in a given architecture must be treated as a statistical problem and is beyond the scope of this paper, instead, a "typical" geometry is studied. The yarn center line is assumed to be a smooth (order O2) b-spline while the cross-section is an O2 b-spline of an elliptical shape. The RVE is assumed to repeat both its geometr and response throughout the entire material. Details of the construction of the finite element model are given in an upcoming section.

In the present study, the geometry is determined by sampling points on the yarn centerline and cro: sectional perimeter of a fabricated material [10]. Details of the RVE size and yarn dimensions are given . Table 1. As shown in Figure 1, the geometric rendering of the RVE, the x and z directions are the in-plan

Table 1: Model Geometry

RVE size (in)	a / b, axial yarn (in/in)	a / b, transverse yarn (in/in)
0.275 x 0.050 x 0.1960	0.0787 / 0.0098	0.0866 / 0.00866

directions, while y is the out-of-plane direction.

MATERIAL SELECTION

One unfortunate limitation of the finite element method is that the geometry and material properties must be selected a-priori. As with the geometric parameters, representative values of the material properties commonly found in textile composites are used. The values have been chosen to represent

typical glass/epoxy and carbon/epoxy materials. The material properties are given in Table 2.

Table 2: Material Properties

Material Properties	Epoxy	Glass / Epoxy	Carbon / Epoxy
E_x (E6 psi)	0.5	5.5	23.0
E_y (E6 psi)	0.5	1.43	1.58
E_z (E6 psi)	0.5	1.43	1.58
G_{xy} (E6 psi)	0.1875	0.59	1.00
G_{xz} (E6 psi)	0.1875	0.59	1.00
G_{yz} (E6 psi)	0.1875	0.55	0.60
υ_{xy}	0.33	0.27	0.27
υ_{xz}	0.33	0.27	0.27
υ_{yz}	0.33	0.30	0.30
α_x (E-6 in/in F)	25.0	4.83	0.010
α_y (E-6 in/in F)	25.0	19.6	11.50
α_z (E-6 in/in F)	25.0	19.6	11.50

SOLID MODEL

The response of a fiber reinforced material is dependent on the type of reinforcement, constituent material properties, and physical location and orientation of the reinforcement. In the case of a textile reinforced composite, quantification of the geometrical structure of the of the reinforcement is rather complex. Thus, the first step in a detailed modeling approach is the development of methodologies for predicting the positions and orientation of the yarns contained in the RVE. The details of the Textile Geometry Model and its use in predicting the textile geometry are given in Pastore, et.al. [9].

Once the yarn cross section and spline data are obtained from the TGM, they are directly converted to a format suitable for use in SDRC I-DEAS 6.1, the solid modeling and mesh generation package used for this study. First, the cross section of the yarn is input as a series of discrete points on the yarn surface. These points are fit to a b-spline representing the yarn perimeter. Second, the yarn centerline points are input and fit to a b-spline in a similar manner. The I-DEAS skin group for the yarns is developed by first creating a profile from the b-spline fit yarn cross section. The profile is dragged along the sectional spline to develop the yarn skin group. The logical flow for this process is illustrated in Figure 1c.

The solid modeling routines in I-DEAS are used to translate the yarn skin group to a yarn solid object. Creation of additional yarns proceeds in one of two ways. If an additional yarn is merely a translated or rotated version of the original, the appropriate I-DEAS commands are executed to perform the translation/rotation operation. If the yarn is a unique (not a translated or rotated version of the previous

yarn), the original yarn creation process is repeated beginning with the surface and/or spline points. Once created, all of the yarn solid objects are oriented in three-dimensional space to correspond to their locations within the textile geometry model (TGM), as shown in Figure 1d.

The outer boundaries of the representative volume element (RVE) are represented as a hexahedral shaped solid object oriented with its centroid at the centroid of the RVE. The boolean capabilities within I-DEAS are used to subtract the yarns from the outer block. The object that remains corresponds to the surrounding matrix contained within the RVE as shown in Figure 1a and 1b.

Once the RVE solid containing the details of the interior boundaries of the textile has been developed, the mesh areas and mesh volumes are created. The volume having the same boundaries as the original volume is considered the matrix finite element volume, while the yarn volumes become yarn finite element volumes.

FINITE ELEMENT MODEL

Because of their three-dimensional structure, textiles tend to be computationally expensive to model with finite elements. Thus, it is desirable to model the RVE with as few elements as required for convergence. This leads to consideration of hexahedral elements, in particular to the quadratic hexahedra Models composed of this element tend to converge quickly for a given number of degrees of freedom. However, current mesh generators can use this element only in conjunction with five and six faced volumes. Since the RVE may contain dozens or even hundreds of faces, the process of further subdividin the original single volume of the RVE into an appropriate number of five and six sided subvolumes becomes prohibitively time consuming. Conversely, a mesh composed of quadratic tetrahedral elements can be used to discretize the complete matrix volume into finite elements. The yarn volumes are also discretized as complete volumes. The main disadvantage of tetrahedra-based meshes is the size of the resulting finite element models. Tetrahedra-based meshes are generally much larger than comparable hexahedra-based meshes.

Convergence of a finite element mesh can be determined through several methods. The method used here is perhaps the most straightforward albeit most computationally expensive method. Here, the domain is meshed with an ever increasing level of refinement. If two consecutive refinements yield results that differ by a sufficiently small amount, the former mesh is said to be converged. Typically, a few percent is used as a criterion.

Choice of proper discretization for volumes as complicated as those found in textiles leads to a trade-off between mesh convergence and model size. A typical global element size is approximately 1/20 of the model characteristic dimension, while local refinements are made to ensure convergence in known regions of high stress gradient. Once the finite element discretization of both the matrix volumes and the yarn volumes has been completed and checked for element distortion, a concern considering the complex shape of the mesh volumes, the element coordinate systems of the yarn elements are aligned with the b-spline defining the orientation of the yarn volume. This alignment insures that the yarn finite elements will behave as subdomains within a homogeneous piecewise transversely isotropic material with the properties given in Table 2. Both materials were modeled with 10-node tetrahedron (ABAQUS C3D10) elements.

FINITE ELEMENT MODEL - THERMAL LOADING

In addition to mechanical loading (to be discussed later), complete analysis of any structural material requires that thermal loading be considered. Textile composites may be subjected to thermal loads both during the curing process and during in-service temperature changes.

A uniform temperature change is considered as it is a fundamental case when considering the structural behavior of a material under thermal loading. Typically, textile preforms are layered and are many RVEs wide, thus it is appropriate to consider that a randomly selected RVE may be subjected to virtually any degree of constraint. This becomes important when accounting for the relative position of a RVE within a textile preform. To bound the limits of constraint, five boundary conditions are considered. These are: 1) periodic, 2) out-of-plane symmetry, 3) out-of-plane free, 4) in-plane symmetry, and 5) in-plane free boundary conditions.

The first of these boundary conditions, periodic, represents the upper bound of constraint, a RVE far from any boundary. To simulate this situation, the opposing faces are restrained with multi-point constraints (MPC) to remain uniformly straight and parallel to one another. The second, out-of-plane symmetry, is an intermediate case similar to the behavior of a two layer un-nested textile. Out-of-plane free boundary conditions are representative of the least constrained RVE, that is, a composite that is one RVE thick. While the out-of-plane symmetry case has one free face, the out-of-plane free case has both top and bottom surfaces free to deform from their original planar state.

Of the two in-plane variations, the in-plane symmetry case is an intermediate degree of constraint representing a narrow composite two RVEs wide. The final case, in-plane free, is the lower bound of restraint, a composite one RVE wide. In this last case, the material is assumed to have two edges that are allowed to deform freely.

In all cases, a uniform temperature change of one degree Fahrenheit is applied to each element within the finite element model. Although this represents the steady state loading condition, geometric complexities and material dissimilarities are sufficient to induce the complex behavior shown in the results portion of this paper.

The results that follow are based upon the finite element models discussed in the preceding section. The results are divided into two main sections: 1) displacements, and 2) strain energy density. The later quantity is discussed because it is the basis of many energy based failure criteria and also provides a useful scalar quantity for visualization independent of material coordinate system.

Note that familiar terms are used in describing the geometry of the RVE. For example, "lower" and "upper" refer to the surface having most negative y coordinate (y= -0.025 in.) and the most positive y coordinate (y= +0.025 in.), respectively. Also, numbers in parenthesis correspond to a specific detail on the figure being discussed.

The models have been checked for convergence, and for the idealized geometries considered, are

converged to within a few percent. However, in the figures that follow, it may be more beneficial to consider the qualitative nature of the isosurfaces than it is to compare exact numbers represented by the isosurfaces.

DISPLACEMENT RESULTS - PERIODIC BOUNDARY CONDITIONS

The isosurfaces illustrated in Figure 2a represent the computed internal axial displacements of a well restrained region within plain weave textile composite under a uniform temperature change. As prescribed by the boundary conditions, the exterior boundaries remain planar and parallel. Displacements within this RVE are, as expected, the most uniform. Although not planar, every point on the surface (1) is 12.5% of the maximum value. It can be thought of as representing the average axial strain in that part of the model. Thus, the axial yarn is seen to strain more than the transverse yarn that is just above it in the RVE. Further, recalling elementary elasticity, the angular change in the displacement isosurface (1) can be compared directly to a local shear strain. The sharper the angle, the greater the shear strain. This "shear strain" is seen in both the x-y and x-z planes.

Figure 2b represents the out-of-plane deformation associated with periodic boundary conditions. Note that the maximum value of out-of-plane displacement is 83% larger than the corresponding in-plane displacement for these boundary conditions. This occurs for two reasons: 1) the coefficient of thermal expansion (CTE) of the yarn's transverse direction is much greater than the CTE in the yarn axial direction, and 2) the in-plane stiffness of the axial and transverse yarns restrains the in-plane deformation.

As with the in-plane deformation for this fully restrained case, the top and bottom boundaries are forced to remain straight and parallel from the applied boundary conditions. However, internally, the deformations are as shown (1).

Figure 2c is the baseline of transverse displacement (fully constrained) for the RVE models. Again, the outer boundaries are allowed to deform in a planar fashion only. Although the temperature change is uniform in the x and z directions, as indicated in Table1, the RVE geometry is not uniform. Thus it is reasonable to expect that the internal deformation behavior is not uniform in the two in-plane directions.

DISPLACEMENT RESULTS - OUT-OF-PLANE BOUNDARY CONDITIONS

When the upper surface of the RVE is released to deform out-of-plane, the reduced constraint results in the axial deformation shown in Figure 3a. This case is representative of a layer of a two layer un-nested composite and provides an intermediate condition to the fully restrained case shown in Figures 2, and the unconstrained case that will be seen as Figures 4. Note here that the lower portion of isosurface (1) shows a similar deformation as the lower portion of isosurface (1) in Figure 2a, whereas the free condition on the top surface localizes the axial deformation to the region between the transverse yarns. As before, the local strains associated with isosurface (1) can be visualized as the ratio of the value of displacement

represented by the isosurface (12.5% of $U_{x,max}$) to the distance from the isosurface to the left side boundary. Thus, a disproportionate percentage of the axial deformation occurs in the most axially compliant region of the RVE (2).

Out-of-plane deformations, Figure 3b, are "dish" shaped. Now, the restraint on out-of-plane deformation is relaxed, and the upper surface is allowed to deform freely. Note the isosurface shown is at 50% (1), while the bottom surface is the fixed, or 0%, surface. This surface is concave, and the maximum displacement occurs above the point of maximum concavity. For clarity, isosurfaces other than the one at 50% have been omitted from the plot; however, it is important to note that the maximum value of displacement occurs along a surface that is a function of the local weave geometry.

By further decreasing the constraint on the model to allow for both top and bottom surfaces to freely deform, a situation as shown in Figure 3c results. In the regions of maximum constraint (those regions near the yarns), the axial displacement isosurfaces (1) are similar to those in the fully restrained case (Figure 2a). However, differences are greatest in the more compliant regions away from the yarns. Here, the angular change in isosurface and resulting shear strains are reduced because of the absence of the planar constraint.

An interesting artifact in Figure 3d is (1), the isosurface of 50% of the maximum out-of-plane displacement. Because of the angle from which this image was taken, it appears that considerable out-of-plane deformation occurs at (1), while little occurs at (2). Actually, because of the anti-symmetric geometry, the two regions of the displacement are anti-symmetric. Because of the absence of in-plane constraint, the maximum deformation is 47% larger than for a similar layer embedded within the composite (Figure 2b). Thus, it is possible to conclude that there is a non-uniform displacement gradient not only within the individual RVEs (Figure 3d), but among the several RVEs through the thickness of a typical textile composite, and that it is a function of their position from the center-line of the composite.

DISPLACEMENT RESULTS - IN-PLANE BOUNDARY CONDITIONS

To simulate a free edge, the front boundary of the RVE has been un-constrained in Figure 4a to allow free deformation. Note that the axial deformation along the back, or constrained, surface (1) is similar to the axial deformation in the same region for the fully constrained case. However, a very different condition exists at the free edge. A disproportionately large percentage of the total axial deformation occurs near the compliant center of the front edge (2). Further, increased shear strains develop. For example, the x-y component of shear strain, shown as an angular change in the isosurface, is prominent along the front edge (3).

Figure 4b illustrates the transverse deformation, in particular, the transverse deformation along the free edge. Nominally, only slightly more than 25% of the total deformation in the RVE occurs in the back half (1) of the RVE. Also, the greatest transverse deformation occurs near the center of the RVE. This is the least constrained (transverse) region of the model both because of the domination of the region by axial yarns and by its distance from the stiffening effects of the restraints along the transverse edges (2).

When both the front and back edges of the RVE are released, simulating a composite one RVE wide, the axial deformation is as shown in Figure 4c. The internal deformation is redistributed such that the axial strain varies greatly with position from the x-axis (1). Further, the center of the RVE, the matrix dominated region, is found to be in a state of near constant displacement (2).

Corresponding transverse displacements are shown in Figure 4d. Similar to the transverse displacements shown in Figure 4b, the compliant region away from the front/back edge boundary conditions and the transverse yarns, has the greatest transverse displacement. The combined constraining effect of planar edges and transverse yarns is similar to the thermal expansion case for a plate with cantilevered edges. The center is allowed to displace from the nominal centerline of the edge, however, the displacement is not as large as if the edges were allowed to rotate freely

The largest transverse displacement is 50% larger than for the case of one free edge and over 400% larger than for the fully constrained case. A comparison can be made with the free edge case for laminated composites where the edge displacements are seen to vary as a function of through thickness (y) coordinate along the edge. In contrast to the laminate, the transverse displacements for the textile are also greatly dependent on axial coordinate (1).

STRAIN ENERGY DENSITY RESULTS

Strain energy density (SED) results for the case of periodic boundary conditions are shown in Figure 5a. The SED distributions in this model correspond to the displacement distributions shown in Figures 2 discussed previously. The left and right hand regions shown in (1) are similar. In the figure, the two regions of the isosurface are anti-symmetric as a function of the yarn geometry.

Note that the yarns contain much of the SED in the model (1), while the largest values of SED are found in the regions of the matrix immediately above and below the axial/transverse yarn crossovers (2). Because this architecture is not quite balanced, the maximum values occur at the alternate corners on the top and bottom of the model (3). Checking the stresses and strains in the several regions of interest indicates that a matrix failure primarily due to through-thickness tension at region (3) is the likely first failure.

The centerline paths of the axial yarns are not fully antisymmetric for this geometry. An important result of this geometric artifact is that the distance from the axial yarn outer surface to the horizontal boundary of the RVE is different for adjacent pairs of interstices. Thus, of the eight corner locations in the RVE, there are two pair of four distinct values of SED. A typical pair is shown in (4).

Since SED is a scalar product of strain and stress components in the model, it is always zero or positive for conservative systems. As shown in Figure 5a, it is greater than zero for all locations within the model and reaches a maximum of 6.68E-4 in-lb/in^3 in regions (3).

When the out-of-plane restraints are removed from the top and bottom surfaces, the strain energy distribution is shown in Figure 5b. This figure corresponds to the displacements shown in Figures 3 that have been discussed previously. Large values of SED are found in the corners of the matrix similar to the

fully restrained case (1). However, the largest values of SED in the model are found in alternate inboard locations (2) and (3) and result primarily from the combined effect of through-thickness and axial tension. Thus, while the material exhibiting the maximum SED has not changed, the location has been altered significantly.

When the in-plane restraints are removed from the front and back surfaces, the strain energy distribution is similar to that in Figure 5c and corresponds to the displacements in Figures 4. The largest values of SED are very localized such that the interior cusp regions of the transverse yarns contain all the SED above 30% of the maximum (1). The maximum value of SED is increased by 165% over the fully restrained case. Now, the mode has changed to axial tension in the transverse yarns as determined in the local coordinate system.

In contrast to the mode and location shown in Figure 5a for a carbon/epoxy system, if the material parameters are changed to simulate glass/epoxy, strain energy density values such as those in Figure 5d result. The yarns contain all of the SED above 40% of the maximum value. However, in the glass/epoxy material system, the thermal and mechanical mismatches are not as severe as with carbon/epoxy. The largest values of SED are found near the centerline of the yarns (2) and are primarily the result of axial loads in the local coordinate systems.

FINITE ELEMENT MODEL - MECHANICAL LOADING

A uniform axial extension is the fundamental case when studying the behavior of a material under mechanical loading and will be discussed here. For this load case, the positive x-face (Figure 1) is displaced uniformly by a displacement producing a nominal strain of 1000 micro-strain (0.00275 in. applied axial displacement through 0.275 in.), the negative x-face is restrained from displacement in the axial direction, and the other faces are subjected to restraints simulating extremes of position within the overall structure. As with the case of thermal loading, the following limiting cases are considered: 1) periodic, 2) out-of-plane symmetry, 3) out-of-plane free, 4) in-plane symmetry, and 5) in-plane free boundary conditions.

DISPLACEMENT RESULTS - PERIODIC BOUNDARY CONDITIONS

The isosurfaces shown in Figure 6a represent the computed internal axial displacement of a well constrained region within the plain weave textile composite under uniform axial extension. As with Figure 2a (uniform temperature change), the exterior boundaries remain planar and parallel. Unlike the case of uniform temperature change, the isosurfaces are representative of a near uniform axial displacement gradient (1). Since the axial yarns dominate the axial stiffness of the material, it is evident that, for this case, a state of near planar axial deformation exists.

Out-of-plane deformation of the textile is illustrated in Figure 6b. The magnitude of the maximum value of this displacement component is approximately 1% of the applied axial value. The length to

thickness ratio of the model is 5.5, producing an average through-thickness Poisson's ratio of υ=0.0 The isosurface shown is at 50%, and once again, the internal displacements are a function of the loc yarn geometry (1). In particular, note that since every point on the isosurface has the same displacemen the regions dominated by the transverse yarns show a greater through-thickness contraction than th regions dominated by axial yarns. This, however, is a local effect, and due to the periodic boundar conditions, must sum to the same through-thickness (y) contraction at every x-z location in the model.

The large non-planar character of the transverse displacements shown in Figure 6c indicates that tl transverse strain in the yarns' fiber direction (near the edges of the RVE) is much less than the strain i the yarn transverse direction (1). Once again, the summation of all of these local phenomenon must equ a common value along the restrained edges for this particular set of boundary conditions.

DISPLACEMENT RESULTS - OUT-OF-PLANE BOUNDARY CONDITIONS

When the upper surface of the RVE is released to deform out of plane, the axial deformation shown Figure 7a results. Unlike what is seen in Figure 3a, there is little effect of lack of out-of-plane constr on the distribution of axial displacement in the model under axial loading (Figure 7a). The c differences are minor and are located near the matrix rich center of the RVE (1).

Out-of-plane deformations are, once again, "dish shaped" and localized (1) as seen in Figure 7b. maximum U_y displacement occurs at (2). This maximum U_y is 69% larger than the correspon displacement for the fully restrained case. Unlike the corresponding thermal load case, where the load is induced in all directions resulting in a somewhat uniform concave surface (Figure 3b), isosurface in Figure 7b is preferential to the axial direction.

When the planar constraint is eliminated completely from the model to simulate a material one RV thick, the axial displacement isosurfaces appear as in Figure 7c. Unlike the more restrained cases, t free-free case has very non-planar isosurfaces of axial displacement indicating that the strain distributi within the model has been significantly altered as a function of weave geometry. Further greatly increas shear strains (1) result. These isosurfaces are somewhat similar to those shown for ΔT in Figure 3c.

The corresponding isosurfaces of out-of-plane displacement are given in Figure 7d. The maximum U is 2400% larger than for the fully restrained case and is very irregular. Here, (1) is at the maximum U while (2) is the minimum for the entire model. The shape of (3), the 50% surface, further illustrates th extreme gradient of displacements in this model. If, for example, this surface is considered the neutr surface, then displacements on either side can be considered to be of opposite sense. While the in-plar requirement for the top and/or bottom surface prevented the large U_y in the constrained models with axi loading, and the force in the transverse yarn counterbalanced much of the force in the axial yarns in th case of thermal loading, no such situation exists in this particular case.

DISPLACEMENT RESULTS - IN-PLANE BOUNDARY CONDITIONS

Unlike the case of uniform temperature change, a free edge in an axially loaded RVE has little effect on the axial displacement. This is seen in Figure 8a.

Figure 8b illustrates the transverse deformation for the one edge free case. The isosurface (1) is the region of maximum transverse displacement (dimpling at the edge). Unlike a laminated material, this dimpling is a function of both the local x- and y-coordinate. Of course, the details are a function of the location of the free edge within the RVE. If, for example, the free surface were at the midplane of this RVE (z=0) the local deformation and strain energy states would likely be very different.

The axial displacement for the limiting case of a structure one RVE wide (both front and back edges released) is shown in Figure 8c. Even with no transverse constraint beyond the boundaries of the representative volume element, and unlike the thermally loaded case, there is little dependence on the transverse (z) coordinate.

The isosurfaces of transverse displacement are shown in Figure 8d. Similar to what is shown in Figure 8b, the transversely compliant region near the center of the RVE has the greatest transverse displacement. The maximum transverse displacement is 500% larger than in the fully restrained case. Once again the x-y dependence is seen, as are angular changes representative of large shear strains (1).

STRAIN ENERGY DENSITY RESULTS

Strain energy density (SED) results for the case of periodic boundary conditions and axial loading are shown in Figure 9a. The yarns contain all of the SED in the model above 2.5 in-lb/in^3. Unlike the case of uniform thermal expansion, the product of axial stress and axial strain dominates the behavior of the material. The maximum value of SED is 11.2 in-lb/in^3 and occurs at the axial yarn centerline between the two constraining transverse yarns. Also, since the transverse yarns are considerably stiffer and take more load than the matrix, the SED in the axial yarns is slightly reduced at the regions of transverse yarn cross-over.

Removal of the out-of-plane constraints produces a SED distribution as shown in Figure 9b. Again the axial yarns dominate the energy distribution in the model; however, both the magnitude and location of the maximum values have changed (1). The maximum value is now 7.2 in-lb/in^3 and is a combined result of axial tension and, recalling the displacements in Figure 7d, local bending.

If both in-plane restraints are removed, a strain energy density distribution similar to that in Figure 9c results. The yarns are once again seen to contain most of the SED. Now the distribution of the maximum values of SED is uniform along the centerline of the axial yarns and little effect of the transverse yarns is noted. The maximum value is 10.6 in-lb/in^3. Comparing this value to that for the fully restrained case (11.2 in-lb/in^3) indicates that transverse constraint contributes only slightly to the maximum value of SED in this material under axial load.

SUMMARY OF RESULTS - MAXIMUMS FOR THERMAL LOADING

Table 3: Thermal Loading

Boundary Condition	U_x (in/F)	U_y(in/F)	U_z(in/F)	SED(in-lb/in^3/F)
Periodic	8.89E-7	16.3E-7	9.19E-7	6.68E-4
Free Top	9.08E-7	21.2E-7	**	**
Free Top / Bottom	9.92E-7	23.9E-7	**	5.06E-4
Free Front	11.5E-7	**	31.6E-7	**
Free Front / Back	10.2E-7	**	47.3E-7	17.9E-4

** not discussed

SUMMARY OF RESULTS - MAXIMUMS FOR AXIAL LOADING

Table 4: Axial Loading

Boundary Condition	U_x (in)	U_y (in)	U_z(in)	SED(in-lb/in^3)
Periodic	0.00275	-2.56E-5	-1.31E-5	11.2
Free Top	0.00275	-4.33E-5	**	**
Free Top / Bottom	0.00275	-61.2E-5	**	7.2
Free Front	0.00275	**	-4.40E-5	**
Free Front / Back	0.00275	**	-6.60E-5	10.6

** not discussed

DISCUSSION OF ANALYSIS

General Comments on the Combined TGM-FEM Analysis

The technique that has been used for this analysis allows:
- Consideration of 3D geometry of textiles
- Interrogation of the details of the behavior of complex textile architectures
- Inclusion of general boundary conditions
- Extraction of components of material response

The method does require:
- Large model size and execution time
- Several simplifications that are unavoidable

Thermal Loading

- The response of even simple textile composites such as plain weaves is fully three-dimensional as shown in the figures in this paper
- Stacking of layers restrains in-plane deformation of the weave
- Severe dimpling is characteristic of an (unrestrained) single layer
- Free edge localizes axial/transverse displacement between transverse yarns
- Low levels of SED for ΔT show similar distribution to mechanical load
- Max SED for fully restrained carbon/epoxy is located in the corners and is dependent on corner geometry
- Decreased mechanical mismatch in glass/epoxy changes location of maximum SED to the transverse yarns (fully restrained case)
- Removing out-of-plane restraint initiates greatest SED away from corners
- Free edge condition redistributes SED into transverse yarns

Mechanical (Axial) Loading

- Although axial deformation is well approximated as two-dimensional, transverse and through-thickness deformation are not
- Unlike the case of thermal loading, axial deformation is not significantly affected by width effects
- The effect of no out of plane constraint is very significant in both deformation and SED response
- Free edge effect is very significant and is a function of both x- and y-coordinate
- Maximum SED is always found in the axial yarns and is altered as a function of the RVE's location within the overall material
- RVE's with little through-thickness constraint are subject to considerable bending

REFERENCES

1. Dexter, H.B., Camponeschi, E.T., and Peebles, L., 3D Composite Materials, NASA CP 24020, Hampton, Va., 1985.

2. Raju, I.S., Foye, R.L., and Avva, V.S., "A Review of Analytical Methods for Fabric and Textile Composites", Proceedings of Indo-US Workshop on Composite Materials for Aerospace Applications, 1990.

3. Carter, W.C., Cox, B.N., Dadkhah, M.S., and Morris, W.L., "An Engineering Model of Woven Composites Based on Mircromechanics," pre-publication.

4. Whitcomb, J.D., "Three-Dimensional Stress Analysis of Plain Weave Composites," NASA TM-101672, Nov. 1989.

5. Woo, K., and Whitcomb, J.D., "Global/Local Finite Element Analysis for Textile Composites," 34th AIAA/ASME/ASCE/AHS/ACS Structures, Structural Dynamics and Materials Conference, pp.

1721-1731, La Jolla, Ca., AIAA-93-1506-CP, 1993.

6. Glaessgen, E.H., Pastore, C.M., Griffin, Jr., O.H., and Birger, A., "Modeling of Textile Composites," Proceedings of the First International Conference on Composites Engineering, New Orleans, 1994.

7. Lene, F. and Paumelle, P., "Micromechanisms of Damage in Woven Composite," Composite Material Technology, PD-Vol 45, ASME, 1992, pp. 97-105.

8. Blacketter, D.M., Walrath, D.E., and Hansen, A.C., "Modeling Damage in a Plain Weave Fabric-Reinforced Composite Material," J. Composites Technology and Research, Vol. 15, No. 2, 1993, pp. 136-142.

9. Pastore, C.M., Gowayed, Y.A., and Cai, Y., "Application of Computer Aided Geometric Modeling for Textile Structural Composites," Computer Aided Design in Composite Material Technology, pp. 45-53, Computational Mechanics Publications, Southampton, UK, 1990.

10. Burr, S.T., private communication, Virginia Polytechnic Institute and State University, Blacksburg, Va, Feb. 1994.

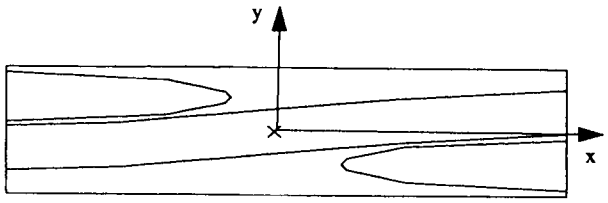

Figure 1a, Side View of RVE

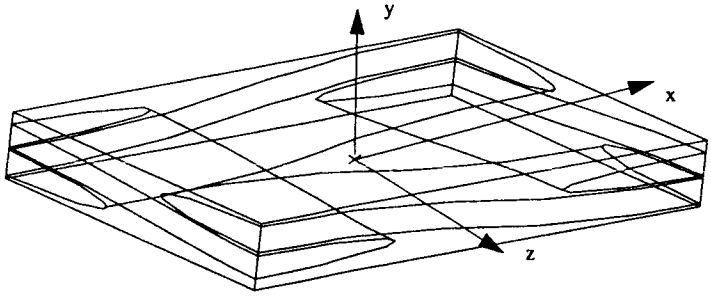

Figure 1b, Isometric View of RVE

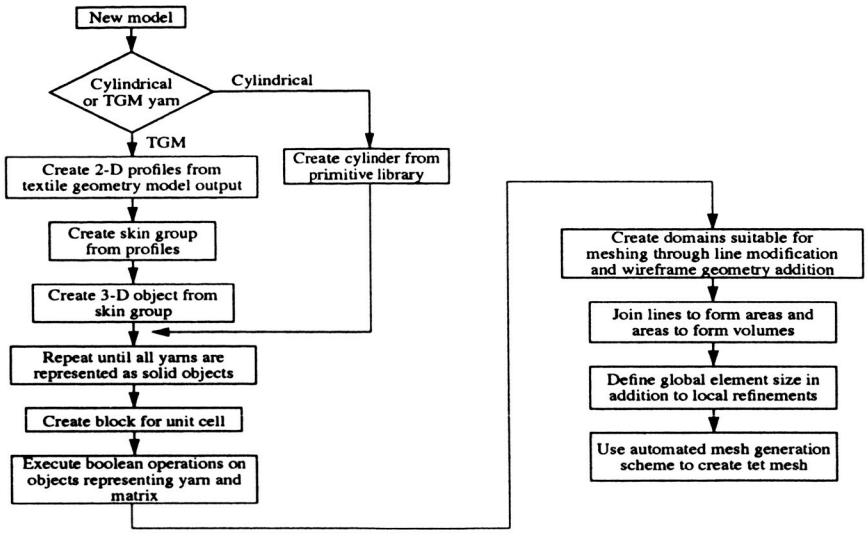

Figure 1c, Model Construction Flowchart

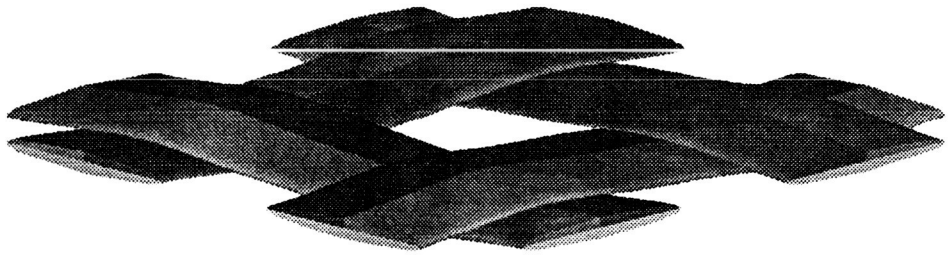

Figure 1d, Yarn Geometry for Plain Weave

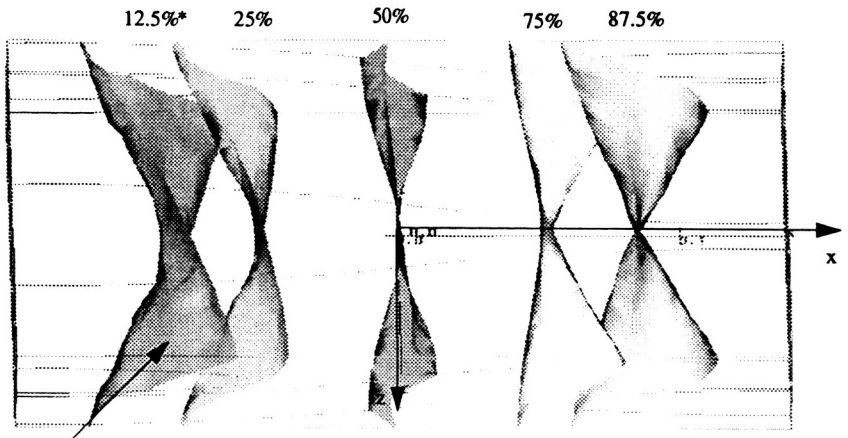

Figure 2a, Axial Displacement, U_x
Periodic Boundary Conditions
$U_{x,\,max}$ = 8.89E-7 in/F

*% of total displacement represented by isosurface

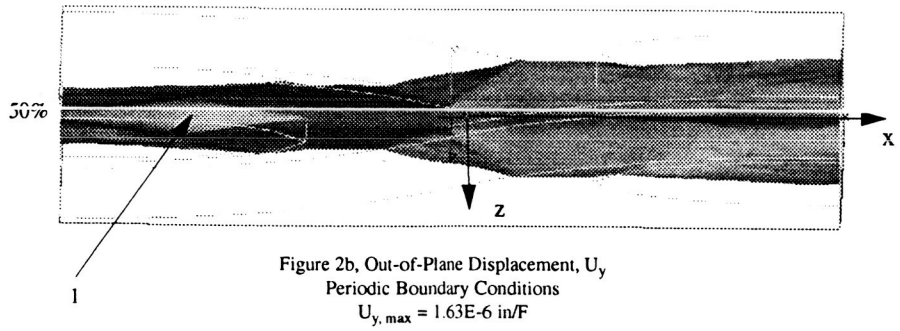

Figure 2b, Out-of-Plane Displacement, U_y
Periodic Boundary Conditions
$U_{y,\,max}$ = 1.63E-6 in/F

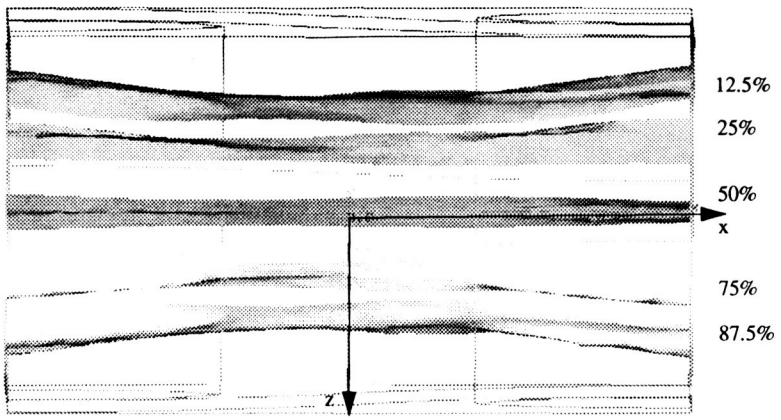

Figure 2c, Transverse Displacement, U_z
Periodic Boundary Conditions
$U_{z,\,max}$ = 9.19E-7 in/F

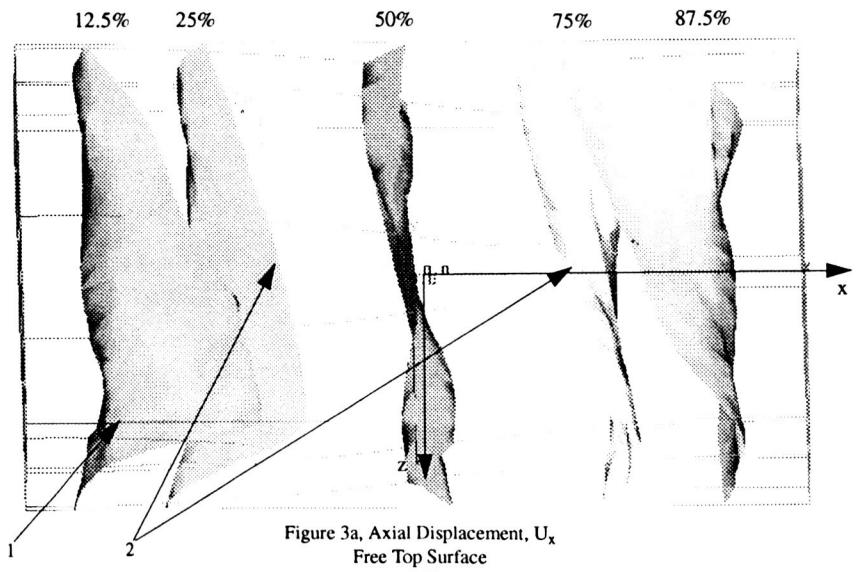

Figure 3a, Axial Displacement, U_x
Free Top Surface
$U_{x,\,max}$ = 9.08E-7 in/F

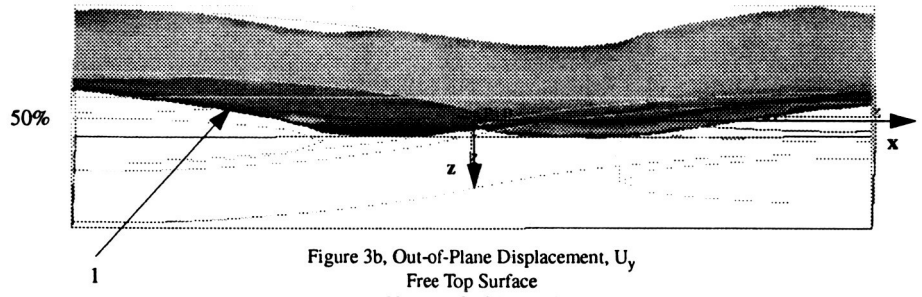

Figure 3b, Out-of-Plane Displacement, U_y
Free Top Surface
$U_{y,\,max}$ = 2.12E-6 in/F

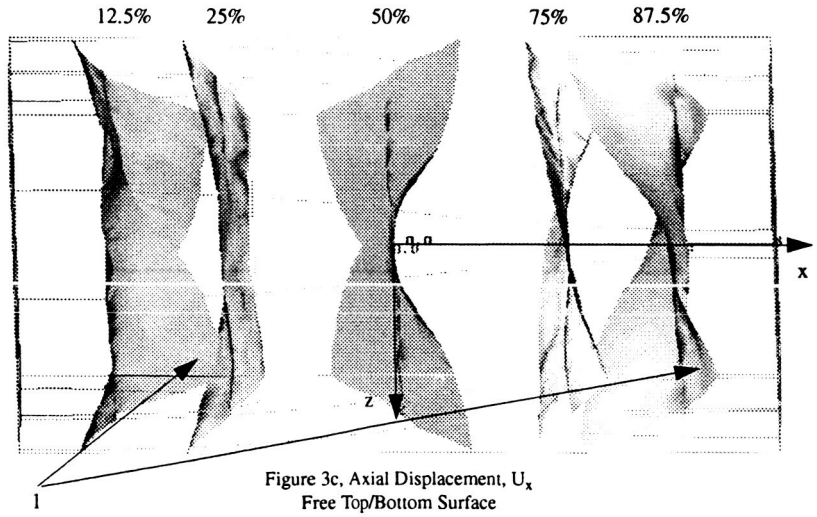

Figure 3c, Axial Displacement, U_x
Free Top/Bottom Surface
$U_{x,\,max}$ = 9.92E-7 in/F

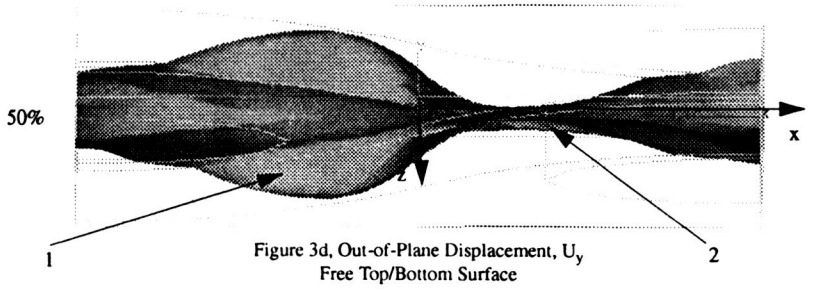

Figure 3d, Out-of-Plane Displacement, U_y
Free Top/Bottom Surface
$U_{y,\,max}$ = 2.39E-6 in/F

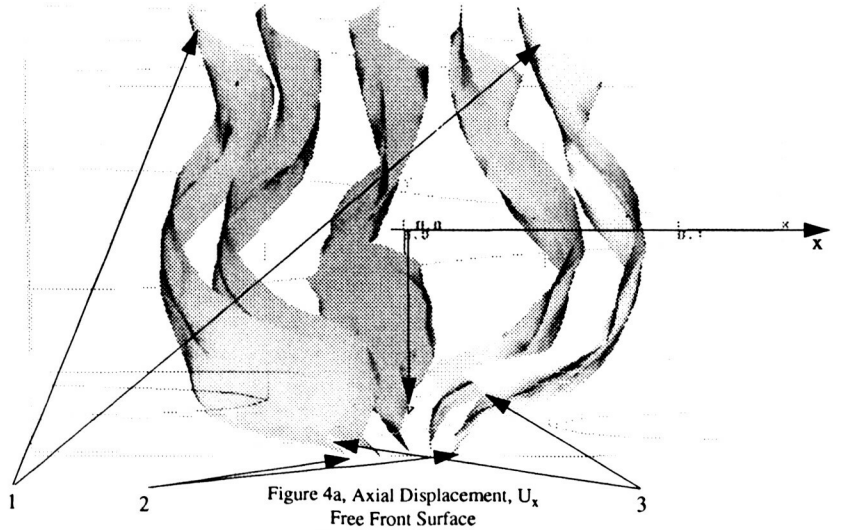

Figure 4a, Axial Displacement, U_x
Free Front Surface
$U_{x,\,max}$ = 1.15E-6 in/F

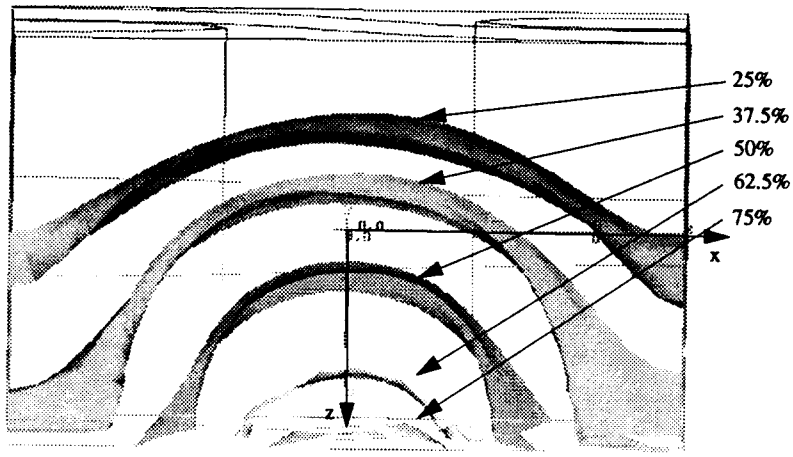

Figure 4b, Transverse Displacement, U_z
Free Front Surface
$U_{z,\,max}$ = 3.16E-6 in/F

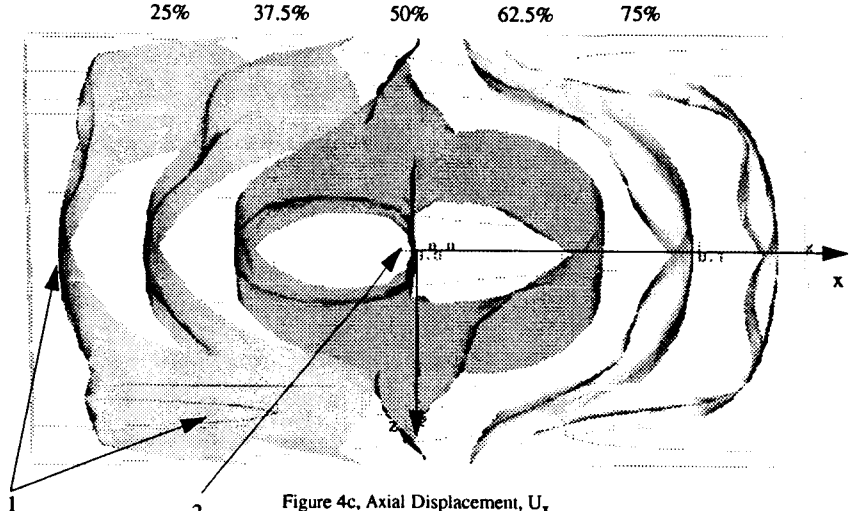

Figure 4c, Axial Displacement, U_x
Free Front/Back Surface
$U_{x,\,max}$ = 1.02E-6 in/F

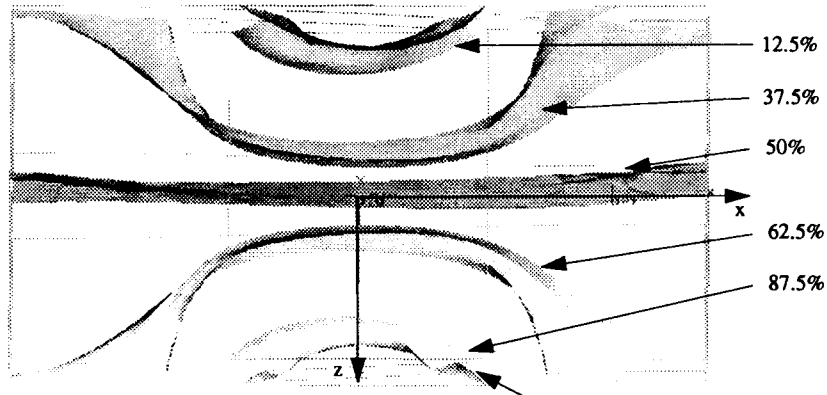

Figure 4d, Transverse Displacement, U_z
Free Front/Back Surface
$U_{z,\ max}$ = 4.73E-6 in/F

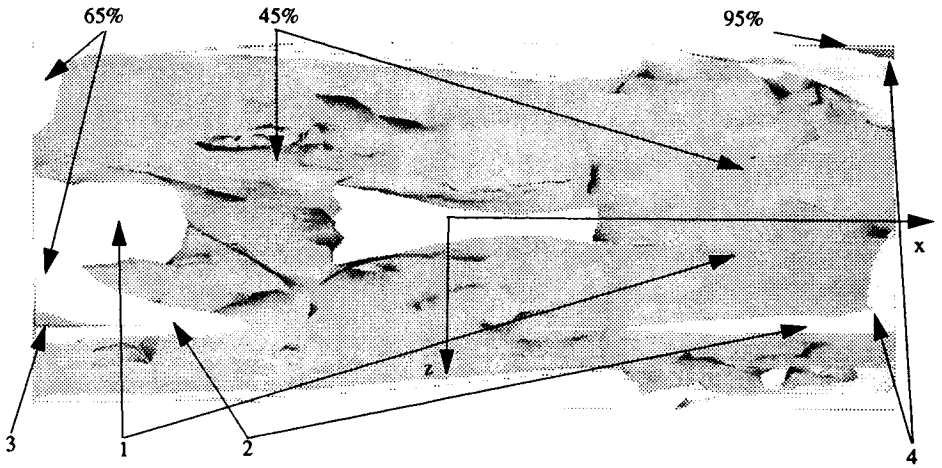

Figure 5a, Strain Energy Density, SED
Periodic Boundary Conditions
0.546E-4<SED<6.68E-4 (in-lb/in^3)/F

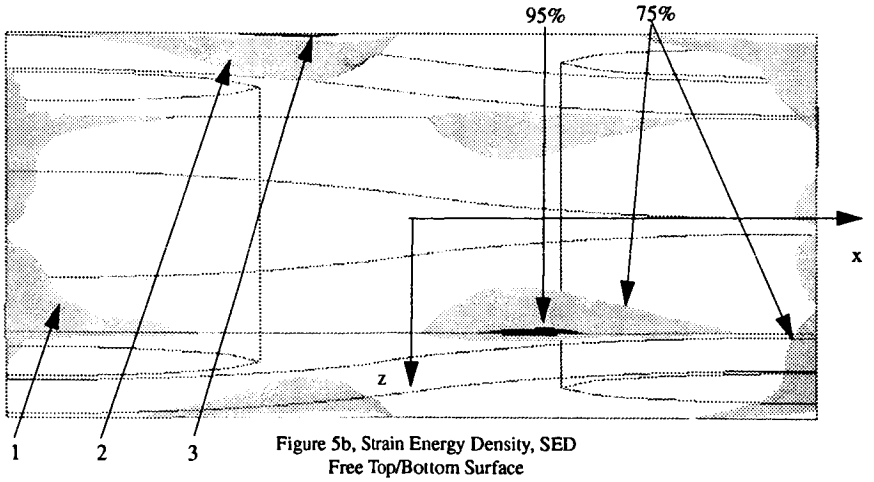

Figure 5b, Strain Energy Density, SED
Free Top/Bottom Surface
0.532E-4<SED<5.06E-4 (in-lb/in^3)/F

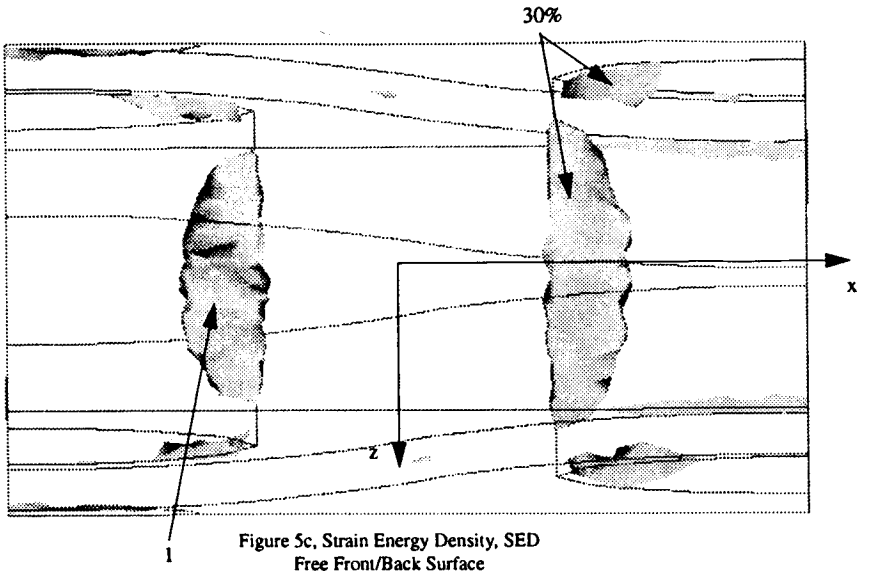

Figure 5c, Strain Energy Density, SED
Free Front/Back Surface
0.248E-4<SED<17.90E-4 (in-lb/in^3)/F

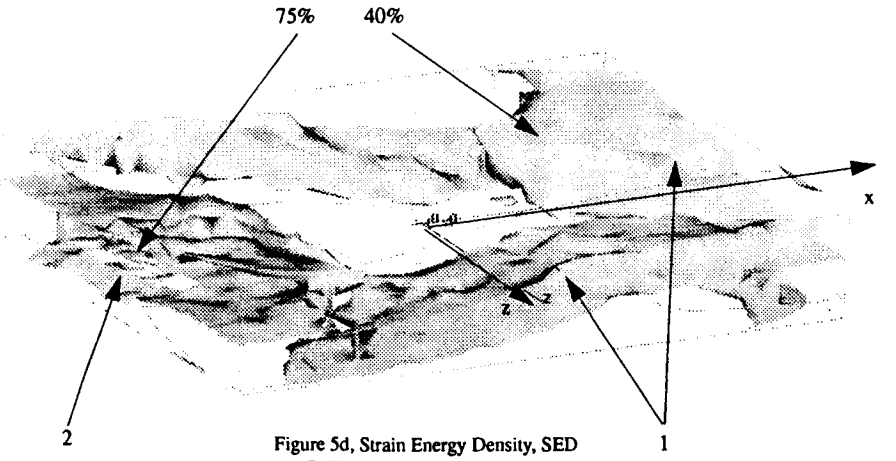

Figure 5d, Strain Energy Density, SED
Periodic Boundary Conditions
Glass/Epoxy Yarns
0.281E-4<SED<4.08E-4 (in-lb/in^3)/F

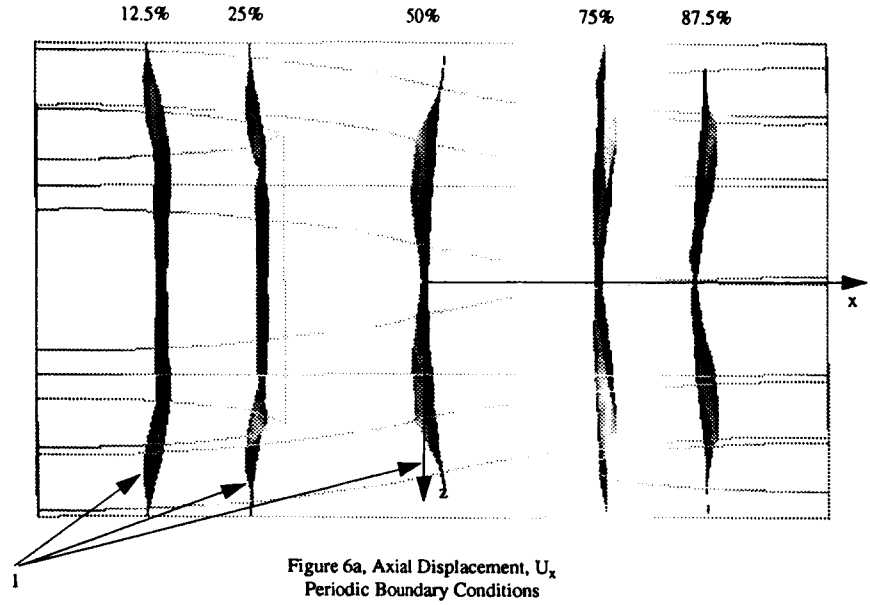

Figure 6a, Axial Displacement, U_x
Periodic Boundary Conditions
$U_{x,\,max}$ = 0.00275 in

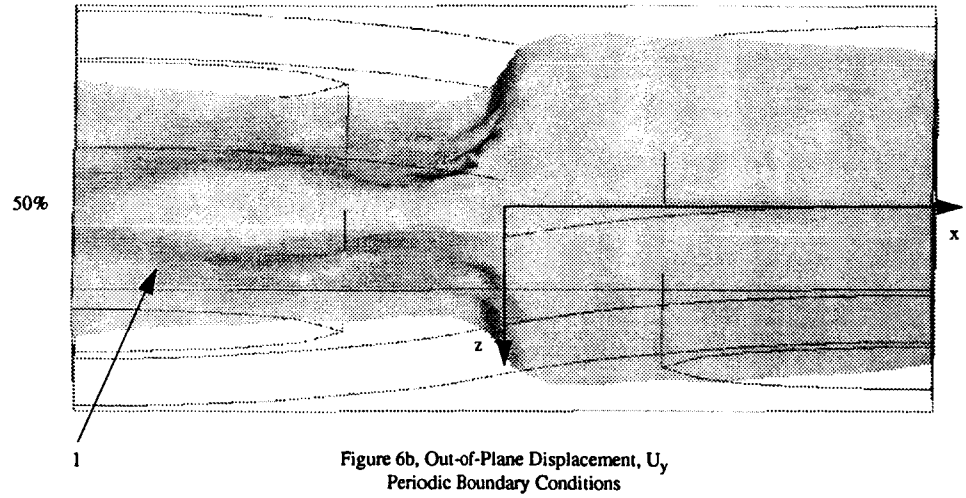

Figure 6b, Out-of-Plane Displacement, U_y
Periodic Boundary Conditions
$U_{y,\,max}$ = -2.56E-5 in

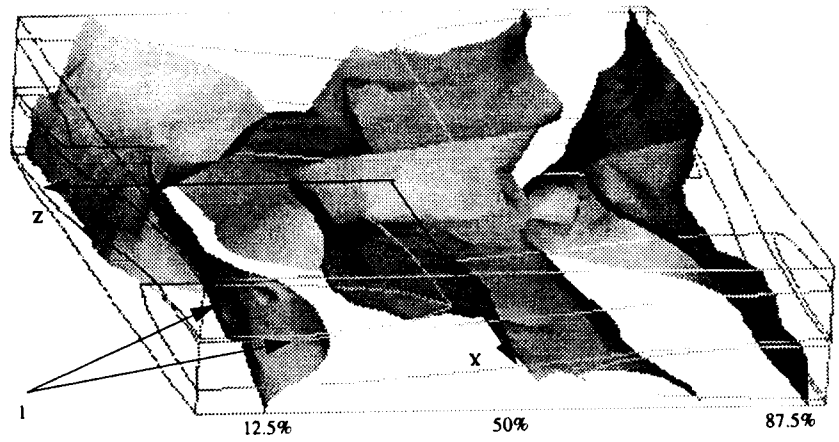

Figure 6c, Transverse Displacement, U_z
Periodic Boundary Conditions
$U_{z,\,max}$ = -1.31E-5 in

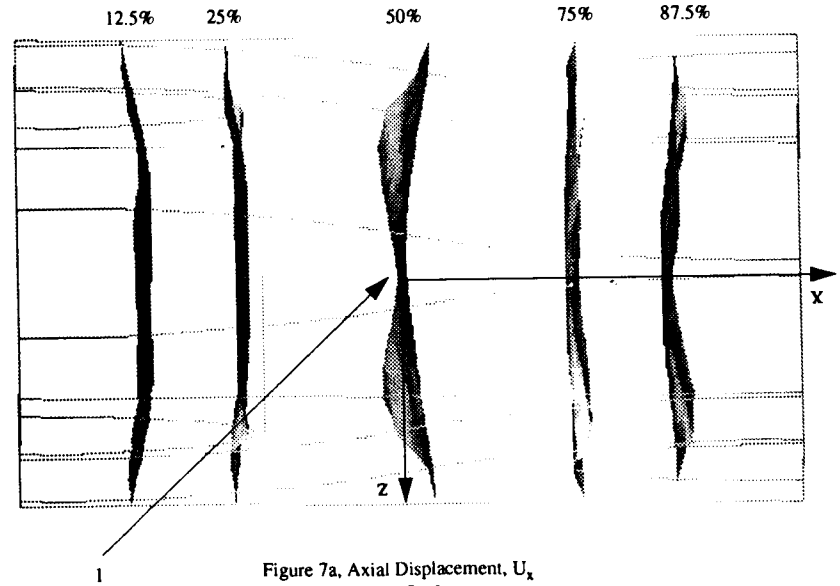

Figure 7a, Axial Displacement, U_x
Free Top Surface
$U_{x,\,max}$ = 0.00275

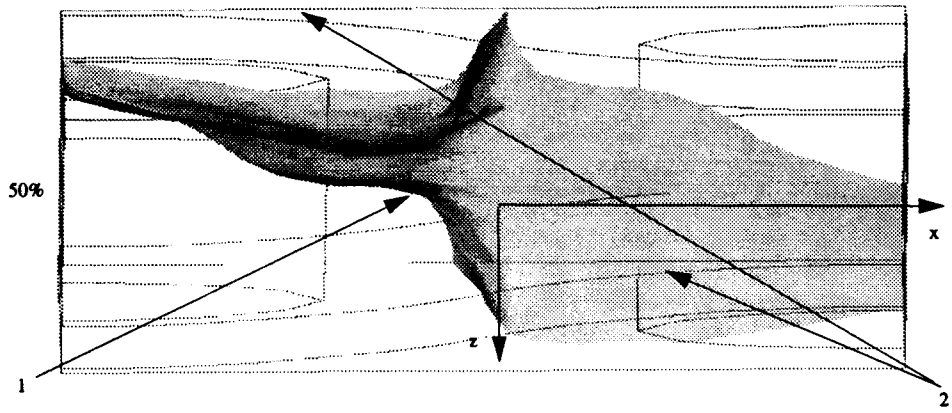

Figure 7b, Out-of-Plane Displacement, U_y
Free Top Surface
$U_{y,\,max}$ = -4.33E-5 in

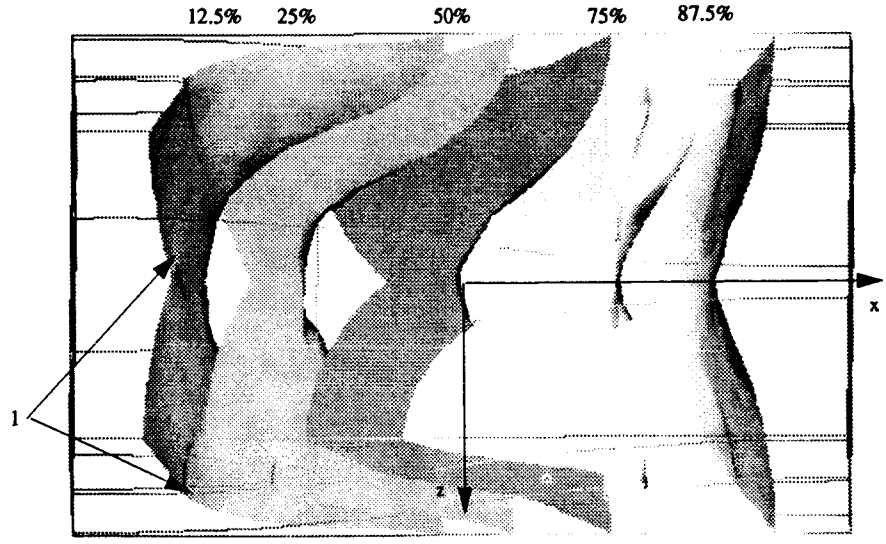

Figure 7c, Axial Displacement, U_x
Free Top/Bottom Surface
$U_{x,\,max}$ = 0.00275 in

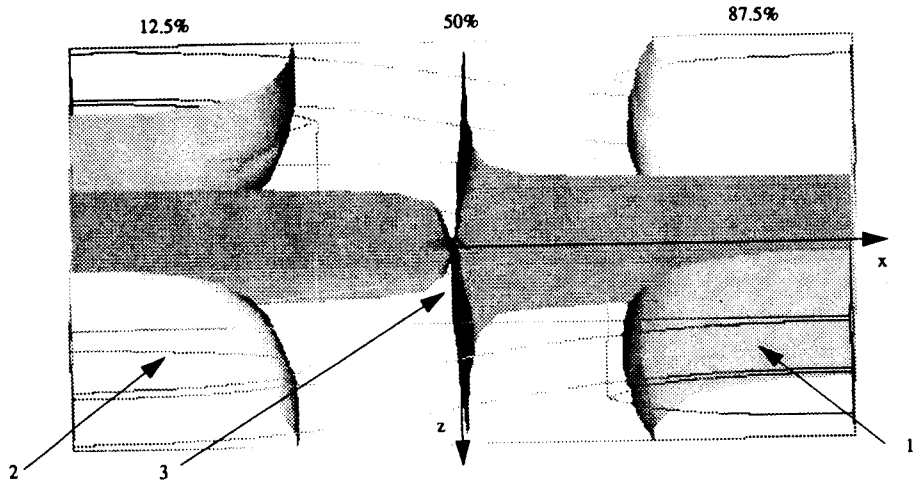

Figure 7d, Out-of-Plane Displacement, U_y
Free Top/Bottom Surface
$U_{y,\,max}$ = -61.2E-5 in

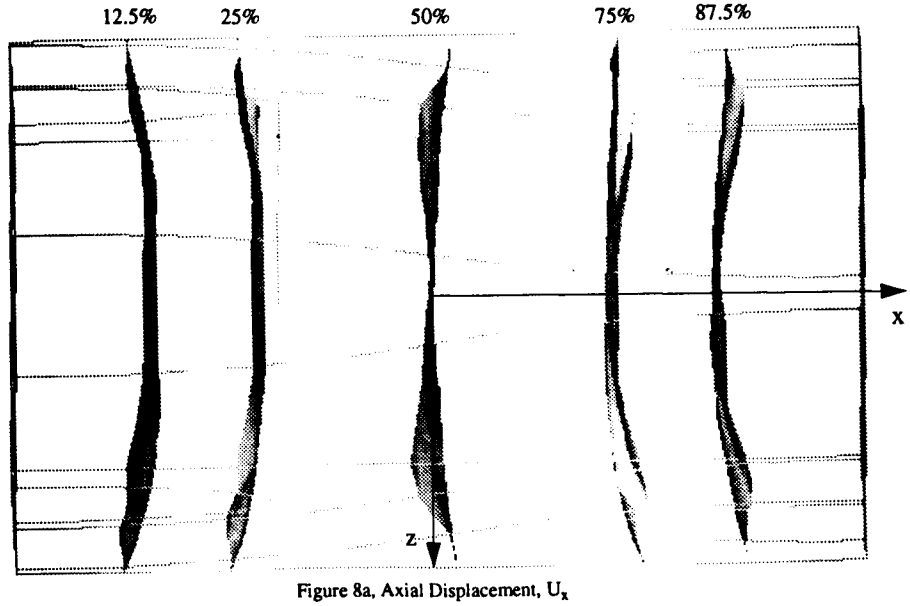

Figure 8a, Axial Displacement, U_x
Free Front Surface
$U_{x,\,max}$ = 0.00275 in

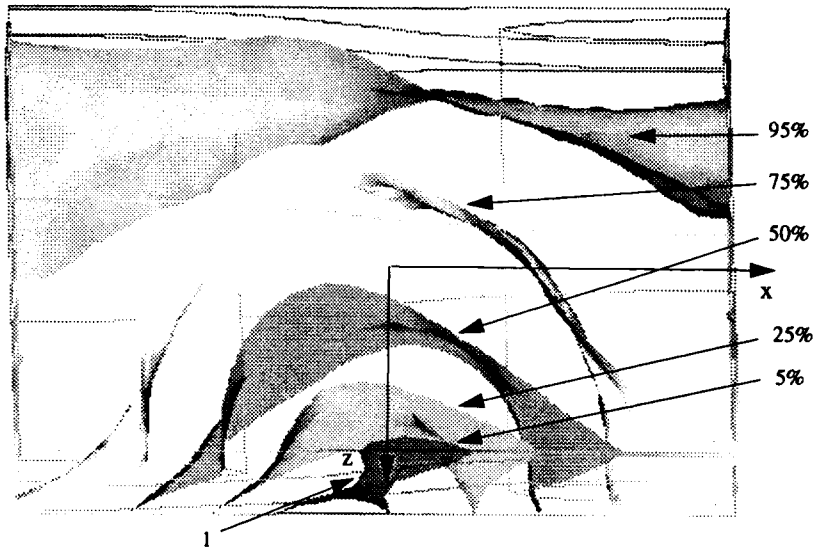

Figure 8b, Transverse Displacement, U_z
Free Front Surface
$U_{z,\,max}$ = -4.40E-5 in

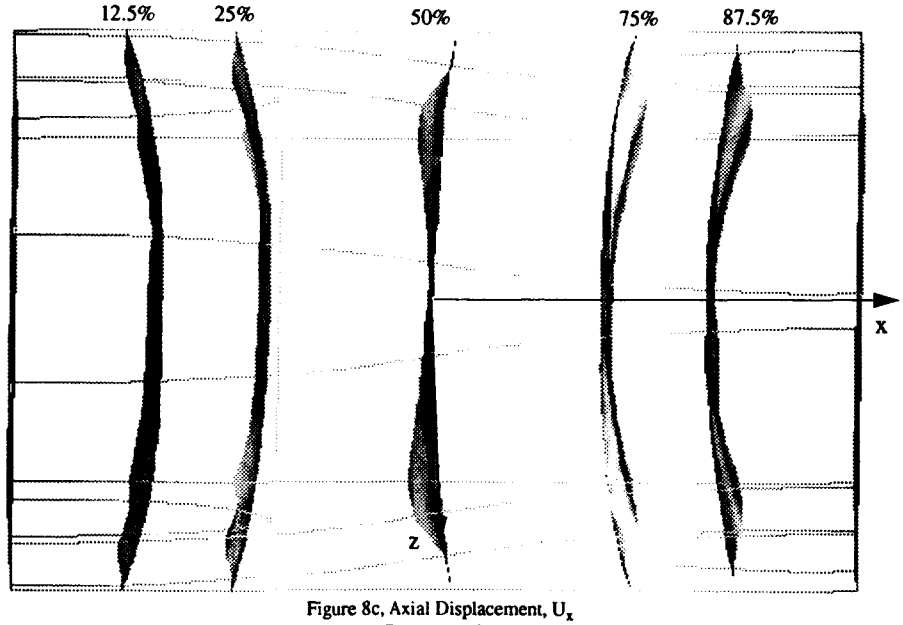

Figure 8c, Axial Displacement, U_x
Free Front/Back Surface
$U_{x,\,max}$ = 0.00275 in

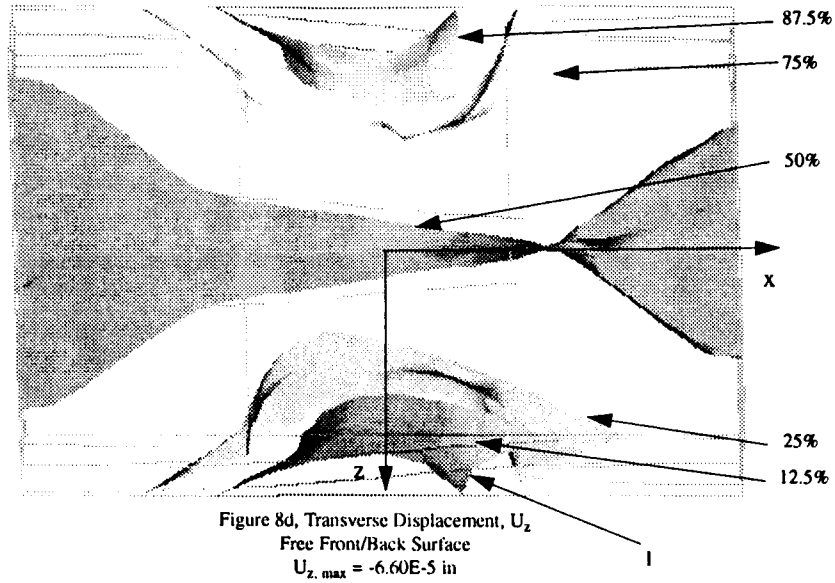

Figure 8d, Transverse Displacement, U_z
Free Front/Back Surface
$U_{z,\,max}$ = -6.60E-5 in

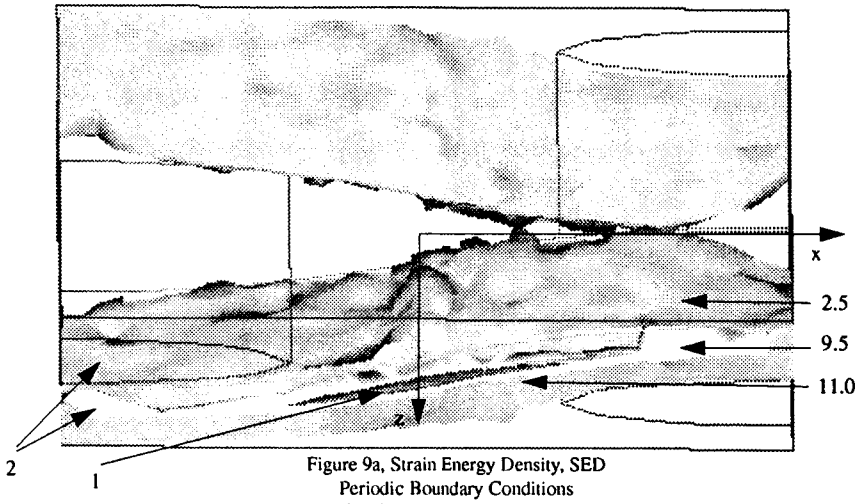

Figure 9a, Strain Energy Density, SED
Periodic Boundary Conditions
0.0035<SED<11.2 in-lb/in^3

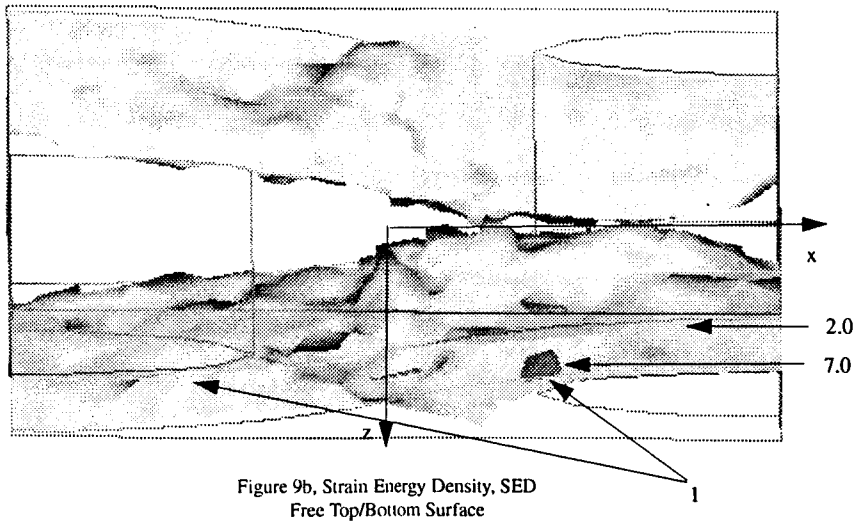

Figure 9b, Strain Energy Density, SED
Free Top/Bottom Surface
0.0545<SED<7.2 in-lb/in^3

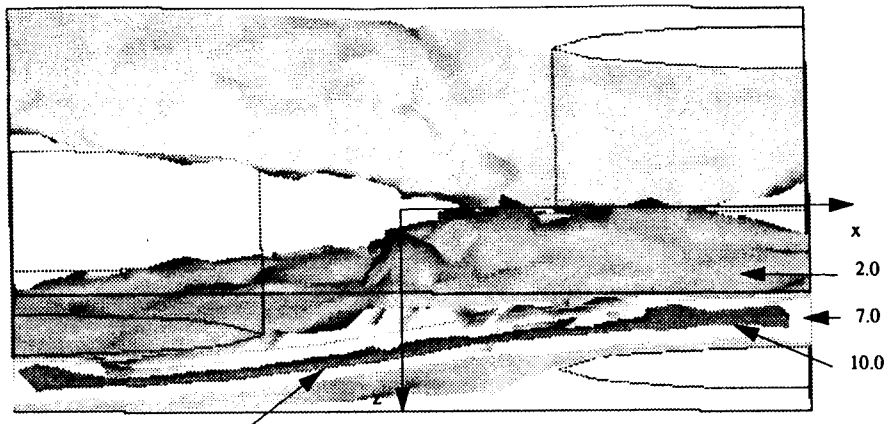

Figure 9c, Strain Energy Density, SED
Free Front/Back Surface
0.0638<SED<10.6 in-lb/in^3

TEXCAD - TEXTILE COMPOSITE ANALYSIS FOR DESIGN[1]

Rajiv A. Naik
Analytical Services and Materials, Inc.
Hampton, Virginia.

INTRODUCTION

The Textile Composite Analysis for Design (TEXCAD) code provides the materials/design engineer with a user-friendly, desktop computer based tool for the analysis of a wide variety of fabric reinforced woven and braided composites. It can be used to calculate overall thermal and mechanical properties along with engineering estimates of damage progression and strength. TEXCAD also calculates laminate properties for stacked, oriented fabric constructions. It discretely models the yarn centerline paths within the textile repeating unit cell (RUC) by assuming sinusoidal undulations at yarn cross-over points and uses a yarn discretization scheme (which subdivides each yarn into smaller, piecewise straight yarn slices) together with a 3-D stress averaging procedure to compute overall stiffness properties. In the calculations for strength, it uses a curved beam-on-elastic foundation model for yarn undulating regions together with an incremental approach in which stiffness properties for the failed yarn slices are reduced based on the predicted yarn slice failure mode. Nonlinear shear effects and nonlinear geometric effects can be simulated. Input to TEXCAD consists of: (i) material parameters like impregnated yarn and resin properties such as moduli, Poisson's ratios, coefficients of thermal expansion, nonlinear shear parameters, axial failure strains and in-plane failure stresses; and (ii) fabric parameters like yarn sizes, braid angle, yarn packing density, filament diameter and overall fiber volume fraction. Output consists of overall thermoelastic constants, yarn slice strains/stresses, yarn slice failure history, in-plane stress-strain response and ultimate failure strength. Strength can be computed under the combined action of thermal and mechanical loading (tension, compression and shear).

A brief overview of the analytical capabilities, program organization and modules, input and output parameters, computer platforms, distribution, and, modifications/extensions of the TEXCAD code is presented here.

[1]This work was performed under Contract Numbers NAS1-19399, NAS1-19708.

Analysis Capabilities

- Three-dimensional Stiffnesses
- Coefficients of Thermal Expansion (CTE's)
- Thermal and Mechanical Stresses
- Progressive Damage
- Nonlinear Geometric and Material Response
- Strengths
  - Tension (longitudinal and transverse)
  - Compression
  - Shear

Textile Architecture Models

- Weaves
  - Plain
  - 5-harness satin
  - 8-harness satin
- Braids
  - 2-D
  - Triaxial (1x1, 2x2)
  - 3-D multi-interlock
  - 3-D, 4-step (under development)
- Custom architectures

TEXCAD Organization and Modules

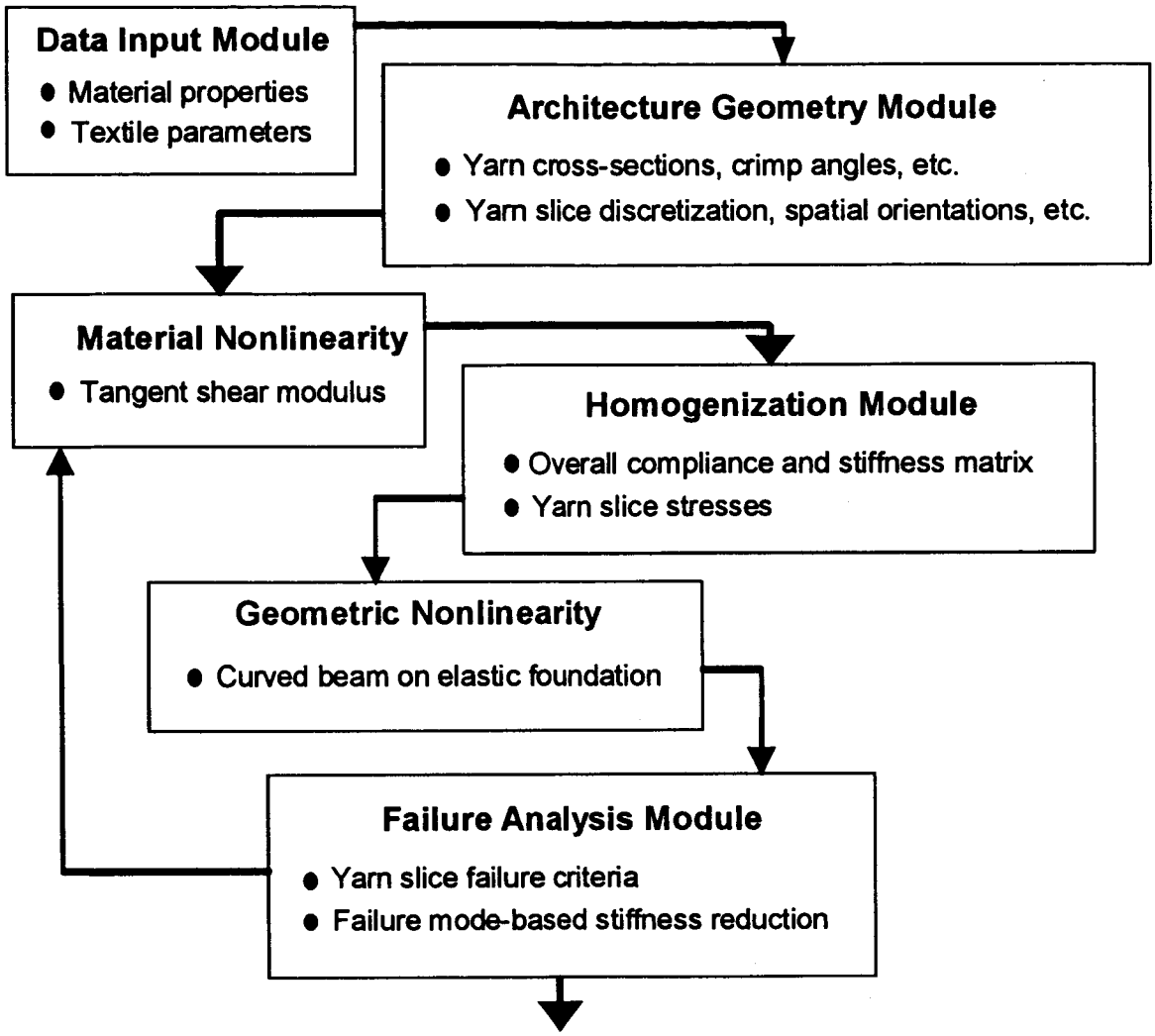

TEXCAD Input Parameters

- **Braid angle**
- **Yarn filament counts**
- **Filament diameter**
- **Yarn packing density**
- **Yarn and resin material properties**
- **Composite fiber volume fraction**

GEOMETRIC MODELING OF YARNS

- Yarn cross-section is a flattened lenticular shape and remains constant along yarn path.
- A yarn is approximated by piecewise straight slices.
- Yarn follows a sinusoidal path at a cross-over point.
- Volume not occupied by yarns is assigned to interstitial matrix.

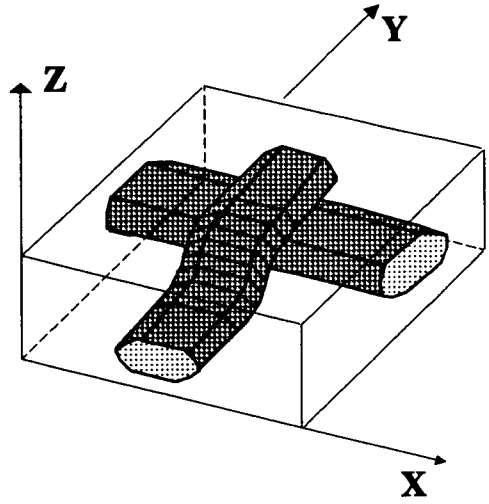

MULTI-DIRECTIONAL COMPOSITE MODEL FOR TEXTILES

- Each yarn slice described by orientation angles θ and β and by its volume fraction.
- RUC assumed to be a multi-directionally reinforced composite.
- Internal stresses calculated by assuming an iso-strain state within RUC.
- Stiffness calculated by volume averaging of internal stresses in yarn slices and interstitial matrix.

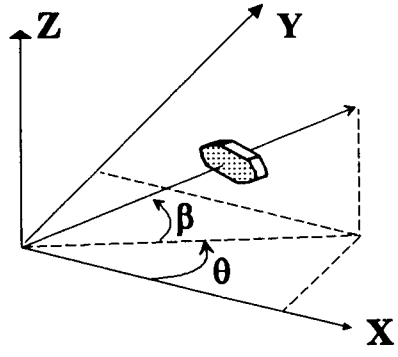

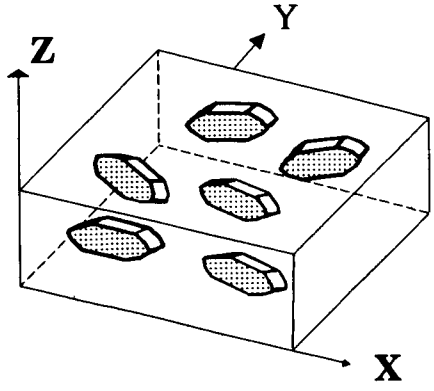

NON-LINEAR SHEAR RESPONSE

- A three parameter equation [Richard and Blacklock, 1969] was used to represent material non-linearity under shear:

$$\tau_{12} = \frac{G_{12}\,\gamma_{12}}{\left[1 + \left(\frac{G_{12}\,\gamma_{12}}{\tau_{12}^{ult}}\right)^{m}\right]^{\frac{1}{m}}}$$

- Based on curve-fits to experimental data $\underline{m = 2.78}$ for AS4/3501-6 tape laminates and $\underline{m = 2.34}$ for 3501-6 resin.

OVERALL THERMO-ELASTIC CONSTANTS

- The overall stiffness matrix $[C_{eff}]$ is determined by volume averaging of the yarn slice stresses and is given by:

$$[C_{eff}] = \sum_{k=1}^{N} \left(V_k [T]_k^T \left[C' \right]_k [T]_k \right)$$

- The effective coefficients of thermal expansion are given by:

$$[\bar{\alpha}] = \left[C_{eff} \right]^{-1} \left\{ \sum_{k=1}^{N} \left(V_k [T]_k^T \left[C' \right]_k \left\{ \alpha' \right\}_k \right) \right\}$$

YARN BENDING ANALYSIS

- Initial Sinusoidal Yarn Path: $w = A_o \sin\left(\frac{\pi x}{L_u}\right)$
- Assumed Deformation: $w = A_1 \sin\left(\frac{\pi x}{L_u}\right)$
- A_1 determined by Min. Potential Energy Theorem:

$$\frac{\partial(U - W)}{\partial A_1} = 0$$

$$\beta = \frac{\pi}{L_u}$$

$$A_1 = \frac{-E_o \beta^2 A_o}{E_{11} I \beta^4 + E_o \beta^2 + k}$$

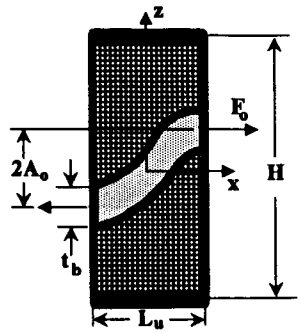

k - from Lee and Harris, 1990

- For Geometric Non-linear Analysis: $A_o^{i+1} = A_o^i + A_1^i$

$$L_u^{i+1} = L_u^i (1 + \varepsilon_x^i)$$

- This model is used only for estimating yarn strains in the x-z plane.

FAILURE CRITERIA

Yarn Failure:

- *Max. stress criterion* to predict following failure modes:
  - Transverse tension (σ_{22}, σ_{33})
  - Transverse shear (τ_{23})
  - Longitudinal shear (τ_{12}, τ_{13})
- *Max. strain criterion*:
  - Axial yarn failure under tension/ compression

Matrix Failure:

- *Maximum principal stress criterion* ($\tau_{12} = 0$).
- *Von Mises octahedral shear stress criterion* ($\tau_{12} \neq 0$).

TEXCAD Output

- Yarn geometry, crimp angles, etc., for each yarn
- Overall stiffness and compliance matrix
- Unit cell three dimensional stiffnesses and CTE's
- Mechanical and thermal stress/strain in all yarns
- Composite stress-strain response
- History of failure stress and mode of failed yarn slices

The TEXCAD user interface under the Microsoft Windows environment

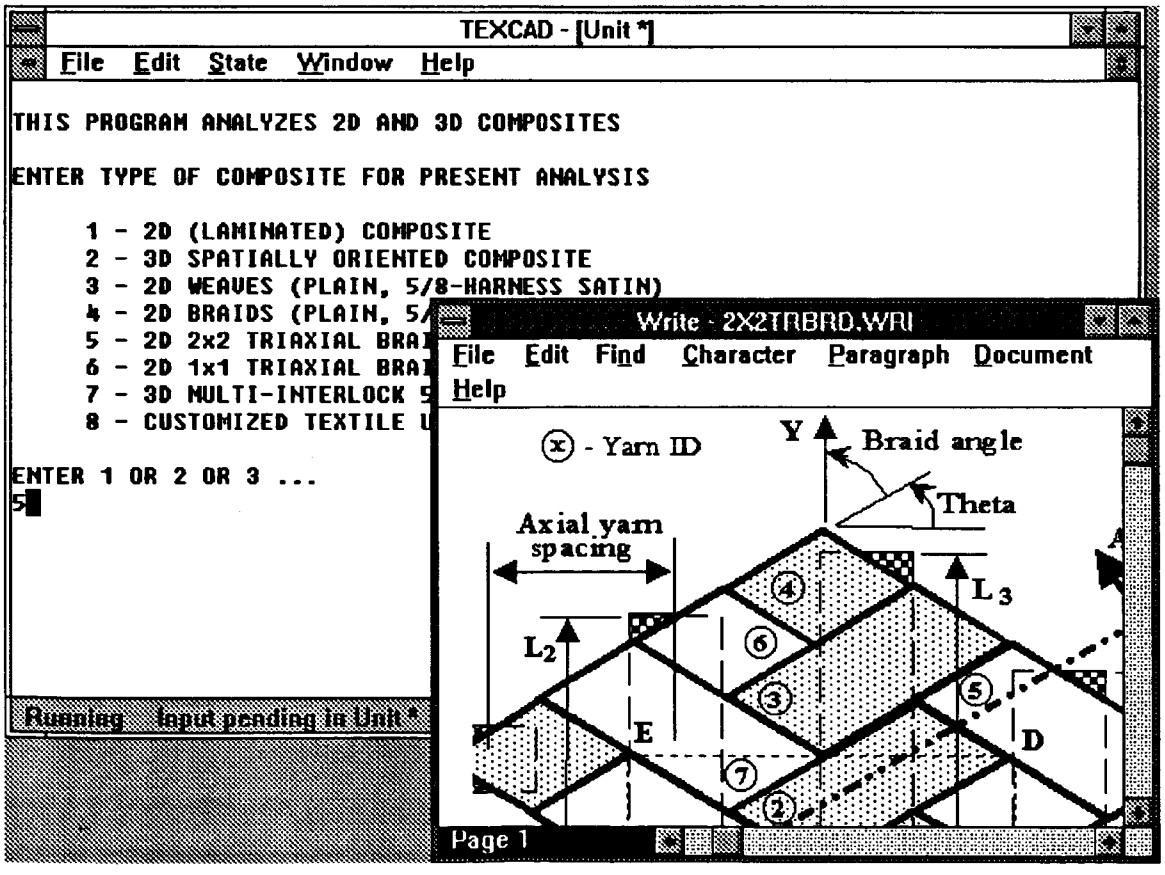

TEXCAD Computer Platforms

- IBM PC compatibles
  - DOS
  - Microsoft Windows
- Apple Macintosh
- UNIX Workstations

TEXCAD Documentation

- TEXCAD User's Manual
- TEXCAD Theory Manual I - NASA CR-194930, June 1994.
- TEXCAD Theory Manual II - NASA CR-194981, Sept. 1994.
- Publication:

  Journal of Composite Materials, Vol. 28, No. 7, 1994
- Presentations:

  NASA/DoD ACT Conference, Salt Lake City, June 1993

  ASTM 12th Symposium on Composite Materials: Testing and Design, May 1994

  NASA/DoD ACT Conference, Seattle, August 1994

Collaborations

- **Lockheed, Georgia - *Bharat Shah, Kwoon Young***
  - Development of TEXCAD for Hybrid 2-D Triaxial Braids.
- **North Carolina A&T State University - *Prof. A. D. Kelkar,*** Graduate Student: ***Dwayne Crawford***
  - Development of a 3-D Finite Element Model for 2-D Triaxial Braids using TEXCAD Geometry Module.
- **North Carolina A&T State University - *Prof. K. N. Shivakumar,*** Graduate Student: ***Kevin Branch***
  - Development of a TEXCAD Geometry Module for 3-D, 4-Step, Circular Braids.
- **University of Florida - *Prof. B. V. Sankar and Prof. P. G. Ifju***
- **Lockheed Engineering and Sciences - *Dr. J. E. Masters***

TEXCAD Distribution

Industry

- **Lockheed, Georgia**
- **GE Aircraft Engines and GE R&D**
- **Pratt & Whitney**
- **Beech Aircraft**
- **Atlantic Research Corporation**
- **Fiber Innovations**
- **Dow United Technologies**
- **Boeing Defense Space Group**
- **Martin Marietta**
- **McDonnell Douglas Helicopter**
- **Alliant Techsystems**

University

- **Virginia Tech**
- **Iowa State University**
- **North Carolina A & T**
- **Wichita State University**
- **Boston University**
- **Florida Atlantic University**

Government

- **Wright Laboratories, WPAFB**

SUMMARY

- A general-purpose analysis for stiffness, damage-progression, and strength of textile composites was developed and implemented in the user-friendly TEXCAD code.

- Documentation in the form of a User's Manual and theory manuals was completed.

- A number of evaluation copies of TEXCAD were distributed to users in industry, government and university.

Geometrical Modelling of Textile Reinforcements

Christopher M. Pastore* Alexander B. Birger Eugene Clyburn

February 24, 1995

SUMMARY

The mechanical properties of textile composites are dictated by the arrangement of yarns contained within the material. Thus to develop a comprehensive understanding of the performance of these materials, it is necessary to develop a geometrical model of the fabric structure. This task is quite complex, as the fabric is made from highly flexible yarn systems which experience a certain degree of compressability. Furthermore there are tremdous forces acting on the fabric during densification typically resulting in yarn displacement and misorientation.

The objective of this work is to develop a methodology for characterizing the geometry of yarns within a fabric structure including experimental techniques for evaluating these models. Furthermore, some applications of these geometric results to mechanical property predictions models are demonstrated.

Although more costly than its predecessors, the present analysis is based on the detailed architecture developed by one of the authors and his colleagues [1, 2] and accounts for many of the geometric complexities that other analyses ignore.

INTRODUCTION

While laminated composite materials have gained wide acceptance in aerospace and other industries, they do have disadvantages. Among these is a significant lack of damage tolerance. Because design allowables necessarily account for the performance of a damaged component, aircraft components made of laminated composites must be designed for maximum stresses or strains that are much lower than the undamaged strength of the materials. Textile composites offer significantly improved damage tolerance compared with traditional laminated materials though they do have decreased in-plane properties. However, since the residual strength of the damaged textile composite is typically higher than that of a corresponding laminate, the design allowables for the parts may actually be higher.

*North Carolina State University, College of Textiles

Traditional approaches to the study of textile based composite materials incorporate a type of volume averaging from the onset. They tend to be based on strength of materials and classical lamination theory, or a homogenized finite element approach [3, 4]. These models have been shown to work well for predicting gross elastic properties for many textile based materials, and, in some cases, provide reasonable estimates of material strength for simple textiles. However, even the finite element models consider the inhomogeneous materials either as voxels or as spars/beams in a matrix. The result is lack of ability to determine details of the internal response of these materials under load. Other failure models tend to be empirical [4], and because of the expense of developing a material database suitable for design, are often not flexible enough for practical use. A macro finite element approach [5] shows some details of load distribution within the composite, but even this analysis neglects many of the geometric details that affect the performance of the material.

As with any structural material, it is necessary to have a good understanding of the mechanical response and failure mechanisms. For textile reinforced composites, this ability has not yet been fully developed. In this paper, a method for analyzing the stress-strain state of a loaded textile composite material is presented. The proposed technique for the analysis of textile composites is based on a finite element discretization of detailed textile architectures.

Unlike previous attempts to determine the response of textile composites, this approach greatly reduces the geometric simplifications required for modeling. The finite element models are taken directly from Textile Geometry Models (TGM) and allow internal details of the response of representative structures to be examined. This paper focuses on the development of the models from the TGM phase through the development of the finite element model of a sample textile composite.

GEOMETRIC MODELLING

Although more costly in terms of computational resources, the present analysis, based on the representative volume element (RVE) of a textile composite, allows prediction of the load, mode, and location of failure initiation within the RVE. Through these models, not only is gross characterization possible, but internal details of displacement, strain, stress, and failure parameters can be studied. Specifically, this discussion focuses on the analysis of a plain weave textile composite. Linear elastic in-plane axial loading is considered.

It is clear that the mechanical response of a reinforced material is dependent upon the

type of reinforcement, constituent material properties, and the physical location and orientation of the reinforcing members. In the case of a textile reinforced composite, quantification of the geometrical properties of the reinforcement is rather complex. Thus, the first step in a detailed modeling approach is the development of methodologies for predicting and reporting the positions and orientation of the yarns contained within the RVE.

Theory and Discussion of TGM

Considering a yarn to contain typically 12,000 or more filaments, it is computationally efficient to consider the yarn as a continuum. The physical and mechanical properties of this yarn can be determined and predicted on the basis of the thousands of filaments, but the RVE analysis will be based on yarns as fundamental elements.

Thus the textile reinforcement can be considered as a collection of prismatic elements which bend, twist and undulate throughout the RVE. Ideally the yarn can also vary its cross-sectional shape (although not area) depending on transverse pressure, etc.

The analytical solution of this problem meets serious difficulties because of the large number of mechanisms involved in the deformation of a fabric, such as crimp exchange; thread shear; extension, bending, twisting and flattening of yarns; friction between yarns and others. Another obstacle is a large number of required parameters. For example, following [6], eleven parameters are needed in order to describe the geometry of a plain weave fabric and four to define the orthogonal components of stress and strain. Thus, the complete analysis of the fabric when considering all the parameters and mechanisms is an extremely complicated task. In order to predict mechanical behavior, varying degrees of simplification have been introduced. For example, in [6], among several other assumptions, the yarns are assumed to be circular.

In the present research, the geometrical and mechanical modeling is carried out on the structural level of the unit cell. The unit cell can be built from the segments of multiple yarns, where the number of yarn segments, their relative location, and the applied forces being entirely determined by fabric design.

Analytical Basis

The yarns forming a unit cell are considered to be elastic bodies interacting with one another and subject to external loads. The center line of every yarn is represented as a Bezier curve interpolating a set of discrete support points. In this study, a continuous Bezier with degree $n-1$ (over n support points per yarn) was used. The location of the support points fully determines the current mechanical state of the unit cell. The yarns are assumed to have elliptical cross sectional shapes.

Lagrange's principle of minimum work is used to determine the mechanical equilibrium of the system. The following expression is used to represent the Lagrangian:

$$L = \sum_{i=1}^{N} (W_t^i + W_b^i + W_\theta^i) + W_{penalty} - A_{extern} \tag{1}$$

where

$$\begin{aligned} W_t^i &= \int C_t^i \varepsilon_i^2 dl_i \\ W_b^i &= \int C_b^i \kappa_i^2 dl_i \\ W_\theta^i &= \int C_\theta^i \theta_i^2 dl_i \end{aligned} \tag{2}$$

C_t^i, C_b^i, and C_θ^i correspond to tension, bending and twist coefficients of i^{th} yarn, ε_i is the longitudinal strain, κ_i is the local curvature, and θ_i is the linear twist of the i^{th} yarn. N represents the number of yarns forming the unit cell, l_i is the arc-length coordinate along the center line of i^{th} yarn, W_p represents a penalty for volumetric intersection of yarns, and A_e is the work of applied external loads.

The Lagrangian (1) does not account for the dissipation of energy in the system. Of course, in the general case friction can be one of the major factors influencing the mechanics of the unit cell. It is important to note that there are no principal difficulties in introducing the corresponding friction term into the model.

The center lines of yarns are represented in the model by Bezier curves [7] interpolating sets of support points. In addition, a number of intermediate points placed on the center lines of yarns are selected. At any of these intermediate points tangent, normal and bi- normal vectors are built [8]. Ellipses located in the planes perpendicular to the center lines and containing intermediate points as their centers represent the surfaces of yarns.

In-plane orientation of axes of the ellipses and all three coordinates of support points are subject to variations in order to minimize L. After every variation and rebuilding of surfaces, all of the yarns are checked for mutual volumetric intersections. For this purpose, the surfaces each pair of yarns are rendered. For every encountered local intersection event extra penalty is added to L, the value of the penalty depending upon the dimensions of intersection volume. By choosing the corresponding penalty function it is possible to account indirectly for the energy of changing of the shape of the yarn cross section of two interacting yarns. For modeling of rigid yarns the penalty term should be equal to some sufficiently large value which will exclude any volumetric intersection of the yarns. The scanning of surfaces is the most complicated and numerically expensive portion of the algorithm. Only by assuming that all the yarns have circular cross-sections is it possible to escape computer scanning of surfaces and to apply some simpler method: scanning of center lines of every couple of yarns forming unit cell. But this assumption cannot be applied in many cases.

The work of external forces is defined as:

$$W_e = \sum_{i=1}^{N} (u_\alpha^i F_\alpha^i + u_\omega^i F_\omega^i) \tag{3}$$

where u_α^i and u_ω^i are displacement vectors of the beginning and the end point of the i^{th} yarn, and F_α and F_ω are the external forces applied to these points.

There is one serious problem which appears when determining mechanical equilibrium of the unit cell. In general, the geometry model leads to mathematical task of finding the minimum of a multi-extremum function. Practically, any numerical algorithm for solving this task can converge to a local extremum which can result in the incorrect prediction of elastic properties of the fabric. In order to increase the probability of finding the state of the system corresponding to the global minimum of L, a number of techniques are known, but none of them can guarantee the convergence to the global minimum. For the problem under consideration the following method proved to be effective: the positions of several support points of different yarns are varied simultaneously during

a single step. In particular, two contacting yarns can be displaced together without penetrating one into another (this situation is one of the origins for local minima of L, and any variation of position of any single support point can be unable to reduce the Lagrangian).

GEOMETRY FROM FABRICATED MATERIALS

Having developed the previously described model for predicting the geometric structure of an arbitrary fabric, it is necessary to consider the quality of the results. This is accomplished by comparing the theoretical predictions with experimental results for a plain weave fabric.

Comparison of Experimental and Theoretical Results

One method of evaluating the effectiveness of this model is to consider the changes that occur to the fabric as a function of applied external load. This also allows the flexibility to incorporate forces associated with molding to the model. For this purpose, a set of data determined at NCSU[1] have been obtained by applying uni-axial tension to a specimen made of woven cloth. The properties of the specimen are described in Table 1.

A number of tensile tests have been performed on warp and weft yarns. The results are shown in Table 2

The parameters of the fabric (dimensions of yarns, distance between the yarns) and the results of testing, characterizing elastic properties of warp and weft yarns (C_t), have been taken as input data for the numerical phase of the geometrical analysis.

In order to simulate the experiment, a model representing four segments of yarns has been used. The geometry of the unit cell indicating the direction of forces applied to the ends of warp yarns in the warp direction are shown in Figure 1.

Initial geometry and applied loads

The minimization of Lagrangian (1) was performed for several different load values. When the applied load F is small (*i.e.* the work on the individual yarns is of the same order of magnitude as

[1]The experiments were performed by S. V. Pullela and Dr. B. S. Gupta of the College of Textiles, North Carolina State University.

the energy of tension for all yarns) the elongation of specimen in the warp direction occurs mostly due to the crimp interchange between warp and weft yarns, the length of warp yarns being almost unchanged. It corresponds to the initial nonlinear segment of stress-strain curve. When the applied loads are high, the warp yarns are almost straight, and the weft yarns are crimped. The elongation of the specimen occurs due to elongation of warp yarns, and the modulus is stiffer and close to linear.

As an example, the unit cell of the plain weave was solved for the case of nominal warp yarn loading (in this case, 25 grams applied to each warp yarn). The results are illustrated in Figure 1. As can be seen, the unit cell is symmetric, as expected.

When a greater load is applied (in this case 1,000 grams per warp yarn), there is tremendous crimp exchange, and much of the strain is due to reorientation of the yarns within the unit cell. The loaded unit cell is illustrated in Figure 2, and the dramatic differences in warp and weft yarn paths can be seen clearly.

During the minimization of L the out-of-plane (z) coordinates of the end points of both weft yarns and both warp yarns were kept unchanged. This allowed simulation of real boundary conditions of the experiment. The Poisson's effect in the specimen, neglected in this formulation of boundary conditions, is believed to be small because of the small distance between the jaws of the testing machine (2.0 cm). In addition, only those variations which do not violate the anti-symmetry of the unit cell with respect to its center were applied to the coordinates of support points.

Both experimental and analytical load-strain curves are shown in Figure 3 The values of applied external forces have been normalized by a number of warp yarns in the specimen. Good agreement between experimental and analytical curves which is seen in Figure 3 demonstrates the validity of the developed geometrical model.

Table 1: Parameters of Plain Weave Fabric Under Consideration

Picks per cm	17.7
Ends per cm	22.0
Crimp in the weft yarn	20%
Crimp in the warp yarn	3%
Denier (Weft)	567
Denier (Warp)	578

Table 2: Tensile properties of warp and weft yarns

Yarn	Number Tests	Average peak Load, (gf)	Average peak Strain (%)
Warp yarn	14	1021	29.64
Weft yarn	10	563.9	23.66

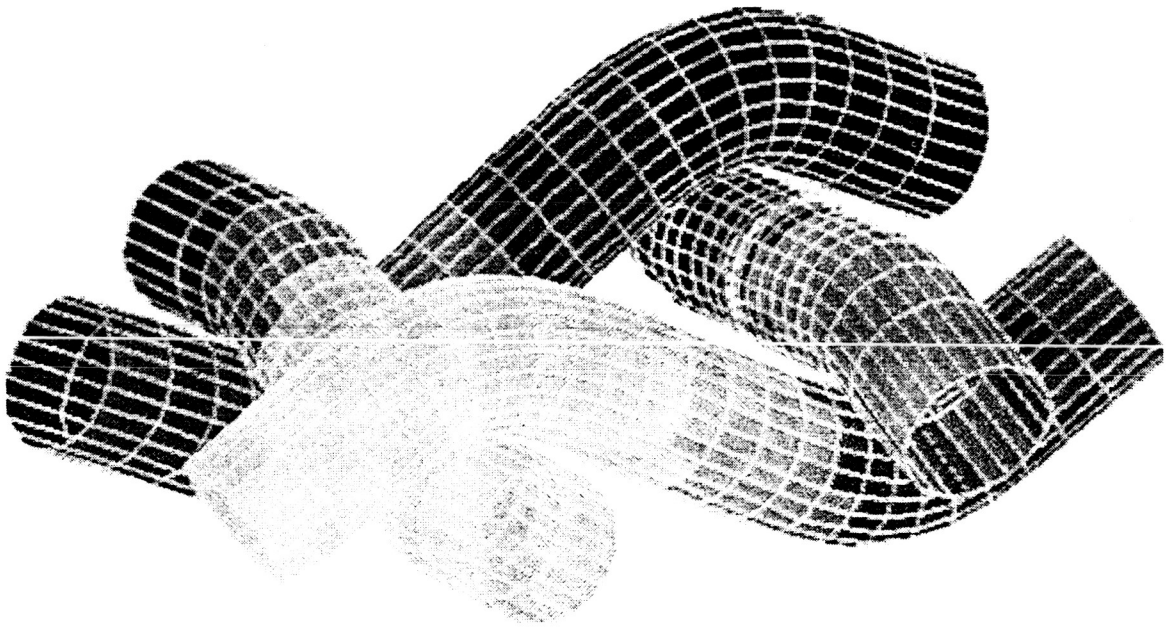

Figure 1: Graphical Rendering of Plain Weave Fabric With Nominal External Load (25 g) at Equilibrium

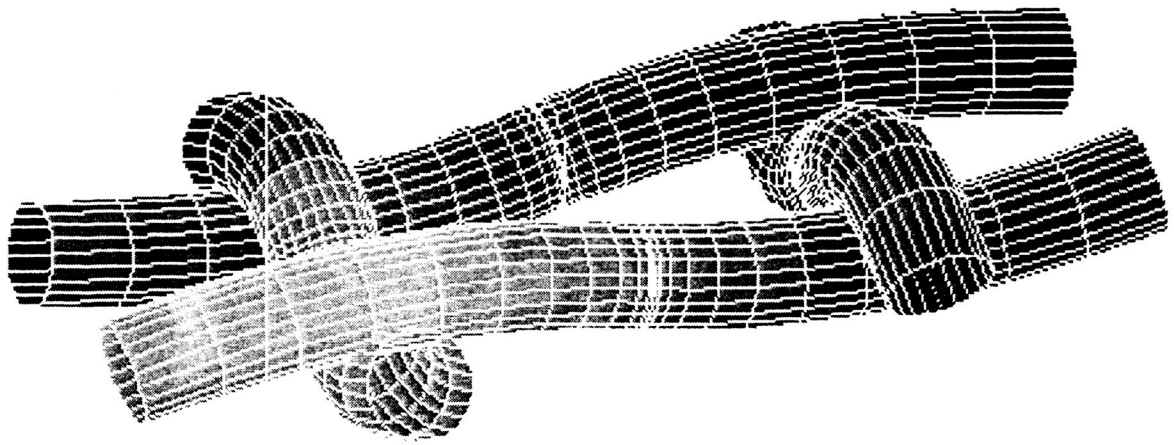

Figure 2: Graphical Rendering of Plain Weave Fabric With 1,000 Gram External Load at Equilibrium

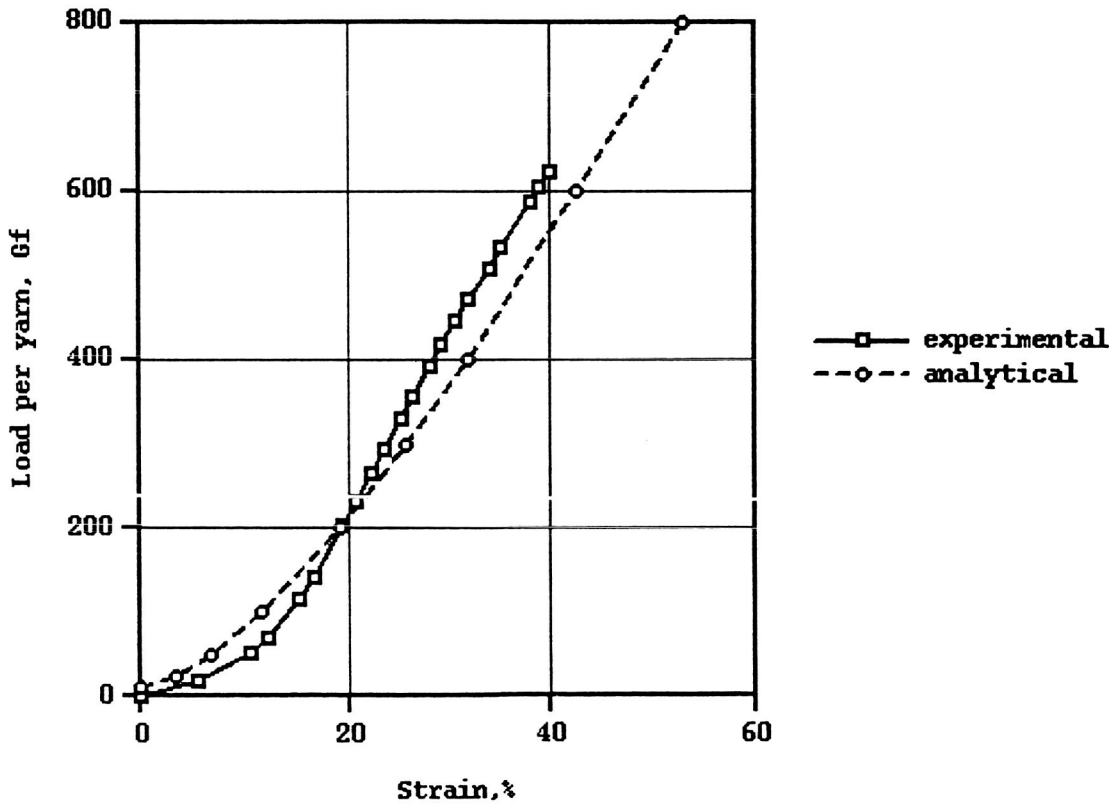

Figure 3: Comparison of Experimental and Predicted Axial Stress-Strain Response of Plain Weave Fabric

Although is can be shown that the model gives a good estimate of the geometrical properties of "dry" fabrics, even when exposed to external loading, for composite applications this fabric will be consolidated or densified with some matrix material. It is during this densification process that various misallignments can occur. Depending on the care taken when processing the material, the resultant composite may have good match with the geometrical predictions, or may have experienced significant skewing during formation.

Additionally, it is not uncommon to find fabrics with defects. A model of an ideal RVE necessarily does not include defects in the modeling. For the purposes of this paper ideal fabrics have been modeled, that is, the fabric structure contains no defects and there is no distortion or skewing of the fabric during densification. Furthermore it is assumed that there is no interlayer nesting in the stacked composite. Only a single layer composite is considered in the subsequent geometrical analysis.

NUMERICAL GEOMETRIC RESULTS

The analysis was performed for the four specific braids that are currently being tested as part of the overall NASA activity. These braids are characterized according to Table 3:

The yarns forming the analized fragment were assumed to have elliptical cross-sections with the ratio:

$$r_{major}/r_{minor} = 3$$

and with the cross-sectional area proportional to number of fibers in the yarn.

These data are represented graphically for LSS in Figures 4 and 5. Braid LLS is illustrated in Figures 6 and 7. Figures 8 and 9 show the geometry predictions for SLL. Braid LLL is not shown, as it is geometrically equivalent to SLL. The master sub-cell of each braid is shown in two different spatial orientations for visualization purposes.

Table 3: Braided Fabric Identification Scheme

ID	Long. Size	θ size	θ	% Long.
LSS	6K	15K	45	12.0
LLS	36K	15K	45	46.0
SLL	30K	6K	70	46.0
LLL	75K	15K	70	46

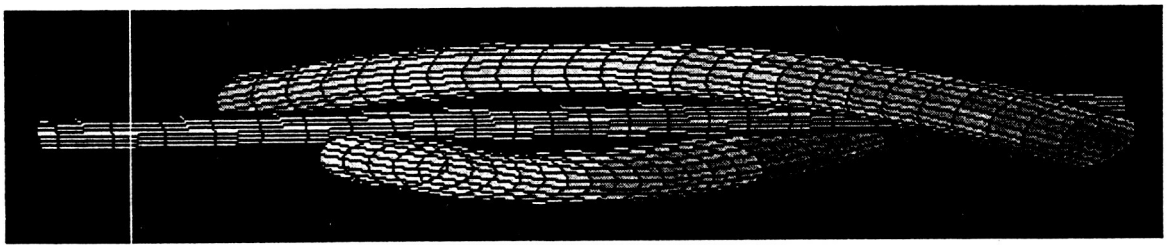

Figure 4: Geometry of Triaxial Braid Model. LSS, Front View.

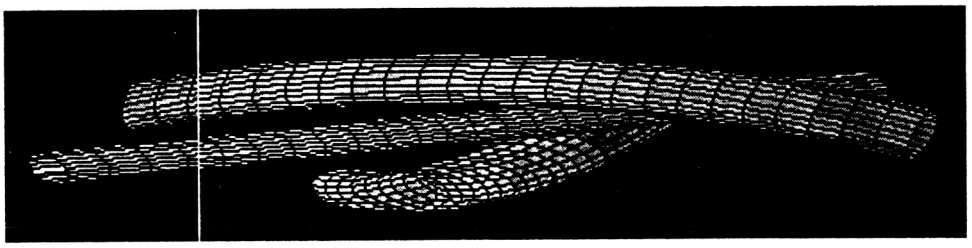

Figure 5: Geometry of Triaxial Braid Model. LSS, Oblique View.

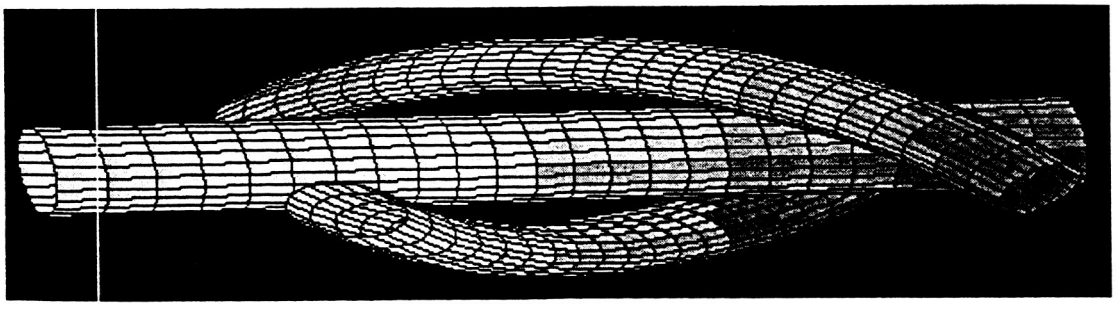

Figure 6: Geometry of Triaxial Braid Model. LLS, Front View.

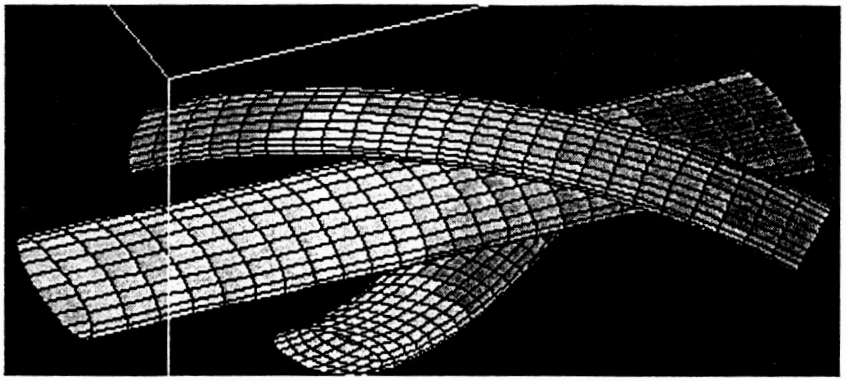

Figure 7: Geometry of Triaxial Braid Model. LLS, Oblique View.

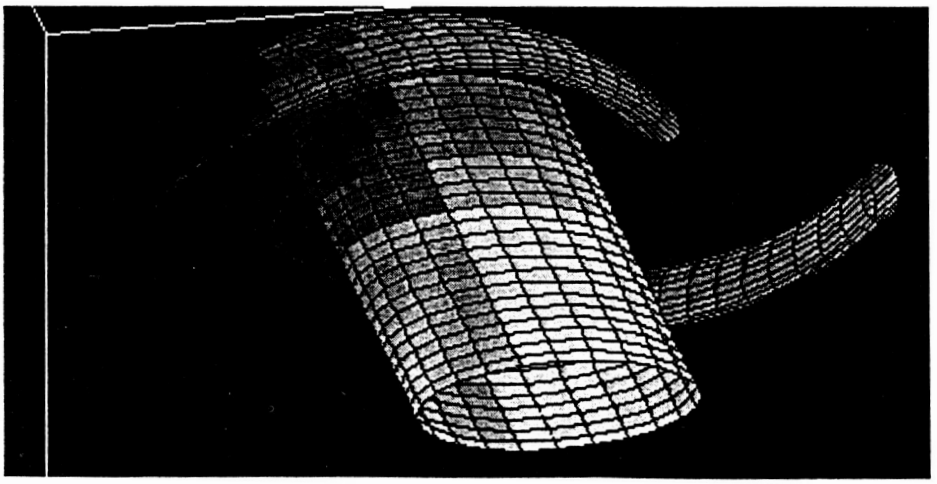

Figure 8: Geometry of Triaxial Braid Model. SLL, Front View.

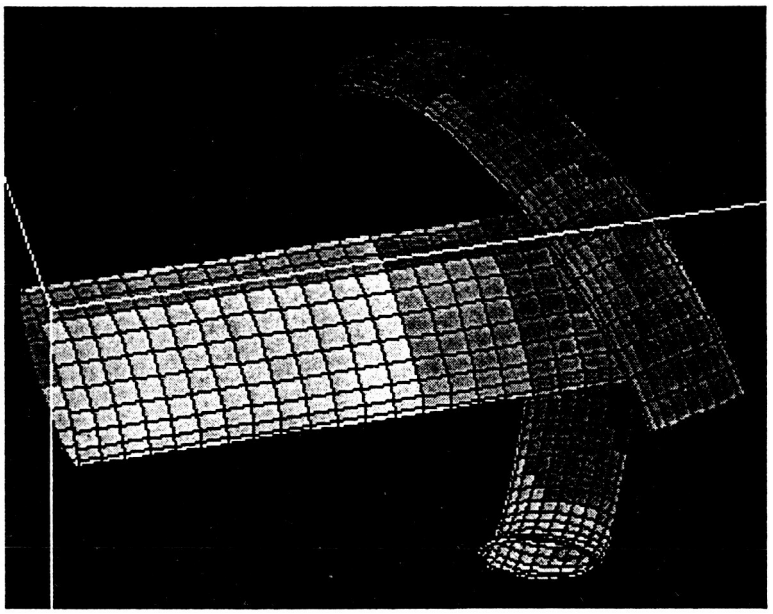

Figure 9: Geometry of Triaxial Braid Model. SLL, Oblique View.

As can be seen from the figures, neither mutual intersection nor gap between the yarns is seen for any of the four braids. Still the analysis of the numerical data shows the presence of a little gap (the biggest one is of about 1/5 of the minor radius length for SLL). The size of the gap depends upon the selection of penalty function imposed on the system in order to prevent mutual intersections of yarns and the number of iteration steps used for convergence analysis. The size of this gap can be controlled by changing the penalty function. For the current results, the penalty function had a "near-field" component acting as a repulsive force when the yarns are close enough. It was introduced in order to reach fast convergence to the equilibrium state. Thus the price for reduction of the slot between the yarns which are supposed to touch one another will always be a slower convergence.

EXPERIMENTAL METHODS FOR DETERMINING GEOMETRIC FEATURES

Experimental methods for evaluating and quantifying geometric features generally fall into two classifications: destructive and non-destructive. Work has been carried out in both of these activities, and a brief description of the techniques and typical results follows.

Material Serial Sectioning

The specimen preparation is carried out by mounting a small sample (1.0 x 1.0 x sample thickness) in a matrix cylinder (2.0 cm in diameter and 2.0 cm in height). Successive manual polishing operations are carried out to prepare the specimen for microscopical observation. The polishing operation is done with increasingly fine sandpaper, finishing with 1μm Al_2O_3 particles.

In order to get useful pictures for the three-dimensional image reconstruction, two main issues should be considered:

i. decreasing the distance between successive physical sections

ii. maintaining the levelness of each sample to ensure taking parallel pictures.

Coding pictures are carried out in two steps: first, Polaroid pictures directly from the microscope then digitizing the acquired pictures on computers using a flat bed scanner. Computer encoding for gray scale images is normally carried out by dividing the screen into small divisions

called pixels. Each pixel can be coded using the available gray scale range between black and white colors. This range can go up to 256 shades of gray. The values of gray can be used to distinguish yarn from surrounding resin.

Numerical Results

Figure 10 shows a stero pair rendering of serial cross-sectioning results from a triaxially braided fabric. For the purposes of clarity, only three yarns have been selected from the entire fabric. The fabric underconsideration was "A-1" from the NASA Langley research project, a triaxially braided carbon/epoxy composite with a nominal braid angle of 65°.

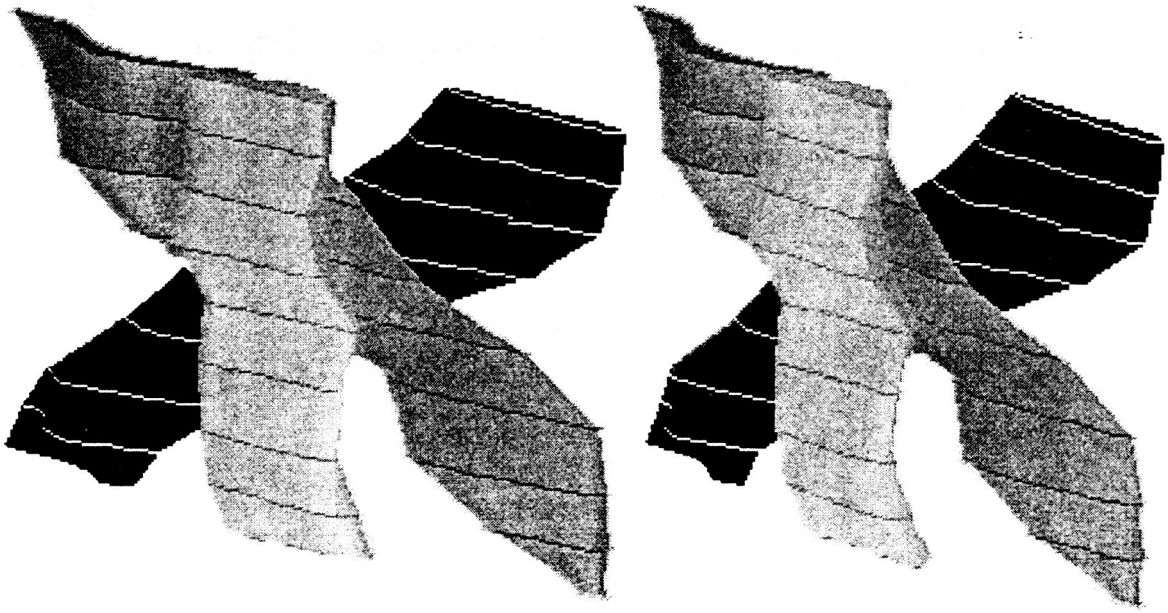

Figure 10: Stero Pair Rendering of Serial Section Imaging of Braid $A-1$ showing Three Yarns in the Fabric

Modelling of the geometrical reinforcement requires some experimental activities to validate the work. The use of established conventional x-radiography is in principle attractive for this purpose but requires enhancement of the yarns since graphite and epoxy are both transparent to standard operating voltages. Investigations into two different methods show that enhancement can be accomplished and yarn detection is possible. One approach attempts to image the entire yarn body via doping with materials of high x-ray attenuation. The other utilizes radiographically opaque tracer fibers in the individual yarns to determine global yarn orientations. The use of doped prepreg fibers and copper magnet wire for tracers produced the best results for each respective method.

The established and low-cost non-destructive imaging techniques of conventional radiography and computed tomography (CT) are attractive for this application, save for some fundamental problems. Graphite and the constituent materials of epoxy have low atomic numbers (¡22) and are basically transparent to the operating voltages of conventional radiography (typically over 50 kV). X-rays exhibit a linear increase in mass attenuation with respect to rising atomic number. This results in denser materials providing greater contrast in a radiograph. In addition, the yarn and matrix have similar x-ray attenuation coefficients (3.22 *barns* for carbon versus 3.50 *barns* for typical epoxies at 80 kV energy) resulting in no visible contrast between the two in a radiograph. The first problem has been overcome via the use of soft, high flux x-rays operating at 10-20 kV which will image graphite-epoxy but require special equipment and dealing with problems such as air becoming a predominant absorber. Even with this technique, the yarns are still difficult to distinguish which prevents the tracing of the yarns with CT.

In order to utilize conventional x-radiography operating levels, it is necessary to enhance the yarns in some fashion to increase their contrast, both to the radiation and to the epoxy matrix. Since the primary concern of this study was to image the yarns, the matrix was not modified and left transparent to the x-rays.

Two approaches were examined to enable the determination of yarn orientation. The first involved the doping of individual yarns with substances possessing high attenuation coefficients. This was aimed at imaging the entire yarn in width and length in a radiograph and in cross-section with tomography. The second approach examined the introduction of radiographically opaque tracer fibers into the graphite yarns. Although the actual yarn would not be imaged, the idea was to determine yarn direction on a global scale.

Samples for this study consisted of six $12K$ graphite yarns unidirectionally woven with a continuous T40 Kevlar fill. Epon 8132 resin with V-40 hardener was used for the matrix at a 1:2.5 mix ratio. Individual yarns were treated before weaving.

Modifications to individual yarns for each sample were as follows:

Sample 1	10% concentration of Gadolinium Oxide powder in RIMline GMR-5000 Polyurethane resin applied to fibers, prepreg formed and undoped Epon resin used to consolidate part.
Sample 2	Yarns sprayed with 3-M 77 adhesive, coated with Gadolinium Oxide powder and overcoated with 77 adhesive.
Sample 3	Yarns sprayed with 3-M 77 adhesive, coated with Boric Acid powder and overcoated with 77 adhesive.
Sample 4	10% concentration of Gadolinium Oxide powder in Acetate solution; yarns immersed for 10 seconds and Acetate dried off; 77 adhesive overcoat applied.
Sample 5	10% concentration of Gadolinium Oxide powder in Acetate solution; yarns immersed for 10 seconds and Acetate dried off; no overcoat applied.
Sample 6	40 AWG copper magnet wire (113 μm diameter) laid with three yarns before weaving.
Sample 7	37 AWG copper magnet wire (78 μm diameter) laid with three yarns before weaving.
Sample 8	100 μm boron fibers laid with three yarns before weaving.
Sample 9	Control

The choices for enhancement substances were made in regard to neutron radiography as well as x-ray radiography, the gadolinium and boron materials being high neutron absorbers. Results from the neutron radiography work will be reported next quarter.

A Picker model F-12 x-ray tube rated at 50-90 kV and 0-15 mA was used for exposures with Kodak SR-5 industrial radiographic film. No back screen was employed. Distance between tube opening and the image plane was 34 inches. Timed step wedges were made at different combinations of voltage and flux to determine a background optical density of 2.5 for the film. The final settings were 80 kV and 4.5 mA for 45 second exposure.

Experimental Neutron Tomography Results

For the first approach of enhancing the entire yarn, Sample 1 produced the best radiograph. The individual yarns are clearly distinguished with good edge and spatial resolution. By prepreging individual yarns, the enhancing material is somewhat constrained within the dimensional boundaries of the yarn and has less of a chance to diffuse into the surrounding matrix, thus blurring the image. However, this method makes yarn-fabric processing difficult since partly cured resin stiffens the yarn and allows less freedom for detailed geometries.

Some demarcation between the yarns and the matrix could be seen in Sample 2 though it is interesting to note that the "thin shell" phenomena exists with the coatings. Whereas the yarns appear lighter than the matrix in Sample 1, in Sample 2 the spacing between the yarns is the lighter area. This is effectively the contact area between the yarns where the thickness of gadolinium oxide is greatest, thus imaging the yarn edges. One thought to this would be to dope the matrix with an enhancer and look for the yarns. Unfortunately, the epoxy already has a slightly higher x-ray attenuation than raw carbon and any further increase would fully mask the presence of the yarns.

Samples 4 and 5 also showed visible contrast of the yarns although soaking the yarns in the acetate solution dissolved the yarn sizing. This allowed the yarn fibers to blossom making the parts difficult to process and resulting in irregular yarn dimensions in the radiographs. The adhesive applied to Sample 4 had no effect in constraining the fibers. The distribution of gadolinium oxide in the yarns is random, probably due to the position of the yarns during draining of the solution. With further development of this technique including the application of sizing after the solution, improved results may be possible.

The boric acid sample and the control did not produce radiographs with sufficient contrast for reproduction. The boron samples (both powder and fibers) hold more potential for contrast with neutrons as the transmission medium.

Tracer Fibers

Both the 40 and 37 AWG magnet wires in Samples 6 and 7 were easily distinguished. Though the yarns were not discerned, their paths and orientations were readily evident. Attractive features of the magnet wire included its ease of processing, size, ductility and low cost. The idea for using

tracer fibers in composites has been investigated for some time though typically plies rather than individual yarns are the topic of interest and the tracer fibers usually have mechanical properties similar to the graphite yarns. In this study, tracers were solely used for imaging purposes and not for mechanical testing.

The boron fibers in Sample 8 were discernible though not nearly to the extent of the copper wires. The contrast was probably due to the tungsten core of the boron fibers. Again, the boron fibers should contrast stronger with neutron radiography though their expense and difficulty in processing may make their application impractical.

MECHANICAL PROPERTY PREDICTIONS

One of the objectives of determining the geometric properties of textile reinforcements is to provide a means to understand the mechanical response of the composite formed from the fabric. Since the mechanical properties of a continuous fiber reinforced composite are clearly highly dependent upon geometric properties, it is necessary to understand the structure of the reinforcement in order to carry out any property predictions.

Two basic approaches to this problem were employed. In one case the geometric data were used as input to a meshing algorithm creating a finite element model of the yarns and surrounding matrix. In the other the geometric data was reduced to simpler orientation parameters and a smearing method was employed.

Application to FEA Methods

Working with Hayden Griffen and Edward Glaesgen from VPI&SU, conversion of the geometric data for finite element modelling was carried out. Once the yarn cross section and spline data are obtained from the TGM, they are directly converted to a format suitable for use in SDRC I-DEAS 6.1[2]. First, the cross section of the yarn is input as a series of discrete points on the yarn surface. These points are fit to a B-spline representing the yarn perimeter [9]. Second, the yarn center line points are input and fit to a B-spline in a similar manner. The I-DEAS skin group for the yarns is developed by first creating a profile from the B-spline fit yarn cross section. This profile is dragged along the cross sectional spline to develop the yarn skin group.

[2]Available from Structural Dynamics Research Corporation, Milford, OH

The solid modeling feature in I-DEAS is used to translate the yarn skin group to a yarn solid object. Creation of additional yarns proceeds in one of two ways. If an additional yarn is merely a translated or rotated version of the original, the appropriate I-DEAS commands are executed to perform the translation/rotation operation. If the yarn is unique (not a translated or rotated version of a previous yarn), the original yarn creation process is repeated beginning with the surface and/or spline points.

The outer boundaries of the representative volume element (RVE) are represented as a hexahedral shaped solid object oriented with its centroid at the centroid of the RVE. The boolean capabilities within I-DEAS are used to subtract the yarns from the outer block. The object that remains corresponds to the surrounding matrix contained within the RVE.

Once the RVE solid containing the details of the interior boundaries of the textile has been developed, the mesh area and mesh volumes are created. The original volume is considered matrix material, while the yarn volumes become yarn finite element volumes.

Stiffness Averaging

Another approach to simple mechanical property predictions is through the use of homogenization techniques for predicting constituitive relations for the material under investigation.

The Fabric Geometry Model (FGM) is a technique for predicting the stiffness of composite materials with spatially oriented reinforcements. This technique, developed by the authors and their colleagues [10] [11] [12], calculates elastic properties from constituent material properties using micromechanics and geometrical properties of textile reinforcement. The objective of this paper is to present a Self-Consistent FGM model which can be easily adopted by researchers in this area. The particulars of the calculations are demonstrated and sample pseudo-code is given for the development of software. The objective of the model is to allow designers to identify composite properties from constituent material properties and the textile processing route. Although lacking the detail of more rigorous finite element techniques, such as those developed by [13] and [14], the FGM provides a quick method for constructing good predictions of elastic behavior. With additions to the approach, strain dependent tensile behavior can be modeled, such as that associated with metal matrix composites (plastic deformation of matrix [15]) and ceramic matrix composites (micro-cracking of matrix [16]).

The basic idea behind the FGM is to treat the fibers and matrix as a set of composite rods having various spatial orientations. The local stiffness tensor for each of these rods is calculated and rotated in space to fit the global composite axes. The global stiffness tensors of all the composite rods are then superimposed with respect to their relative volume fraction to form the composite stiffness tensor. This technique is called a stiffness averaging method [17].

Formulation Of Transformation Tensor

The transformation of the local stiffness matrix to the global stiffness matrix is as follows [18] :

$$C_{global} = T_{\sigma}^{-1} \; C_{local} \; T_{\varepsilon} \tag{4}$$

where C_{global} and C_{local} are the global and local stiffness matrices respectively and T_{σ} and T_{ε} are the stress and strain transformation matrices successively.

We can write [19]:

$$T_{\varepsilon} = \begin{pmatrix} l_1^2 & l_2^2 & l_3^2 & l_2 l_3 & l_1 l_3 & l_1 l_2 \\ m_1^2 & m_2^2 & m_3^2 & m_2 m_3 & m_1 m_3 & m_1 m_2 \\ n_1^2 & n_2^2 & n_3^2 & n_2 n_3 & n_1 n_3 & n_1 n_2 \\ 2m_1 n_1 & 2m_2 n_2 & 2m_3 n_3 & m_2 n_3 + m_3 n_2 & m_1 n_3 + m_3 n_1 & m_1 n_2 + m_2 n_1 \\ 2l_1 n_1 & 2l_2 n_2 & 2l_3 n_3 & l_2 n_3 + l_3 n_2 & l_1 n_3 + l_3 n_1 & l_1 n_2 + l_2 n_1 \\ 2l_1 m_1 & 2l_2 m_2 & 2l_3 m_3 & l_2 m_3 + l_3 m_2 & l_1 m_3 + l_3 m_1 & l_1 m_2 + l_2 m_1 \end{pmatrix} \tag{5}$$

Due to orthogonality, T_{σ} and T_{ε} have the following relation [19]

$$T_{\sigma}^{-1} = T_{\varepsilon}^{T} \tag{6}$$

and we need to determine T_{ε} only.

Although the transformation tensors are well defined, the actual technique of determining the values of the transformation matrices for stresses (T_{σ}) and the strains (T_{ε}) are not consistent in the literature. Furthermore, some formulations are not defined over all possible orientations. The authors recommend the following procedure.

The formation of the transformation matrices depends exclusively on the direction cosines l_i, m_i, and n_i. These direction cosines may be viewed as the components of the unit basis vectors associated with the principal axes of the fibrous reinforcement:

- $\vec{r_1}$ = unit vector associated with the fiber axis = (l_1, l_2, l_3)
- $\vec{r_2}$ = unit vector associated with the #2 direction of the fiber = (m_1, m_2, m_3), and
- $\vec{r_3}$ = unit vector associated with the #3 direction of the fiber = (n_1, n_2, n_3).

In most instances, $\vec{r_1}$ is known. This may be determined by constructing a rectangular parallelepiped which contains the fiber, having dimensions a, b, and c. In this case, $\vec{r_1}$ can be determined as:

$$\vec{r_1} = \frac{a}{\sqrt{a^2+b^2+c^2}}\ \vec{\imath} + \frac{b}{\sqrt{a^2+b^2+c^2}}\ \vec{\jmath} + \frac{c}{\sqrt{a^2+b^2+c^2}}\ \vec{k} \tag{7}$$

Through the use of geometric relationships, it is possible to determine the other two vectors. Since $\vec{r_1}$, $\vec{r_2}$, and $\vec{r_3}$ are mutually orthogonal,

$$\begin{aligned} \vec{r_1} \bullet \vec{r_2} &= 0 \\ \vec{r_2} \bullet \vec{r_3} &= 0 \\ \vec{r_1} \bullet \vec{r_3} &= 0 \end{aligned} \tag{8}$$

where $\vec{x} \bullet \vec{y}$ = inner product (dot product) of vectors $\vec{x}$ and $\vec{y}$. As they are all direction cosine vectors, they have modulus of unity:

$$\begin{aligned} \|\vec{r_1}\| &= 1 \\ \|\vec{r_2}\| &= 1 \\ \|\vec{r_3}\| &= 1 \end{aligned} \tag{9}$$

Since the unidirectional fiber is transversely isotropic, there is one degree of freedom in the determination of $\vec{r_2}$ and $\vec{r_3}$. This degree of freedom was employed by the authors as:

$$m_1 = \sqrt{1 - l_1^2} \tag{10}$$

Since l_1 is the direction cosine of the fiber with the x-axis ($cos(1, x)$), the definition of m_1 corresponds with $m_1 = sin(1, x)$. This places the 2-axis of the fiber in the plane made with the fiber and the x-axis of the composite. The remaining 5 terms can be solved from 8 and 9. Of course, it is important to use the relationships in 8 for the determination of the last term in each vector and to account for the radical term introduced by 10. A sample pseudo-code solution algorithm for determining the numerical value of these three vectors is given in Figure 11.

Then, for each system of reinforcing fibers, the global stiffness C_{global_i} is calculated and the total composite stiffness is determined as:

$$C_{comp} = \sum_{i=1}^{n} k_i C_{global_i} \tag{11}$$

where C_{comp} is the composite final stiffness matrix and k_i is the relative volume fraction of the i^{th} reinforcing system.

This technique is called a "stiffness averaging" method [17]. Alternatively, one may use the "compliance averaging" method, in which case the composite stiffness is determined by :

$$C_{comp}^{-1} = \sum_{i=1}^{n} k_i C_{global_i}^{-1} \tag{12}$$

Conclusions

The quantification of the geometric structure of a fabric can be accomplished for an idealized system. The incorporation of defects, deformations, and distortions raises the complexity of the problem tremendously.

The availability of the geometric data provides a mechanism for developing analytical methodologies to predict mechanical properties of the reinforced structure. Even in the event of idealization of the reinforcing geometry, such an approach has a significant pedagogical value to research.

References

[1] Frank K. Ko and Christopher M. Pastore. Cim of braided preforms for composites. In C. A. Brebbia, W. P. deWilde, and W. R. Blain, editors, *Computer Aided Design in Composite Materials Technology*. Springer-Verlag, 1990.

[2] Christopher M. Pastore, Yasser A. Gowayed, and YunJia Cai. *Applications of Computer Aided Geometric Modelling for Textile Structural Composites*, pages 45–53. Computational Mechanics Publications, Southampton, UK, 1990.

[3] I.S. Raju, R. L. Foye, and V. S. Avva. A review of analytical methods for fabric and textile composites. In *Proceedings of Indo-US Workshop on Composite Materials for Aerospace Applications*, July 1990.

[4] H. B. Dexter, E. T. Camponeschi, and L. Peebles. 3-d composite materials. NASA Conference Pubvlication 24020, Hampton, VA, November 1985.

[5] K. Woo and J. D. Whitcomb. Global/local finite element analysis for textile composites. In *34th AIAA/ASME/ASCE/AHS/ACS Structures, Structural Dynamics and Materials Conference*, pages 1721–1731, La Jolla, CA, 1993. AIAA/ASME/ASCE/AHS/ACS.

[6] F. T. Pierce. The geometry of cloth structures. *Journal of the Textile Institute*, 28, 1937.

[7] P. Bézier. *Essay de définition numérique des courbes et des surfaces expérimentales.* PhD thesis, University of Paris VI, 1977.

[8] P. E. Bezier. A computer aided system for car body design. In K. B. Evans and E. M. Kidd, editors, *Proceedings of Graphics Interface '82*, pages 131–152, 1982.

[9] A. W. Tiller. Rational B-splines for curve and surface representation. *IEEE Computer Graphics and Applications*, pages 61–69, September 1983.

[10] Dennis W. Whyte. *On the Structure and Properties of 3-D Braided Composites.* PhD thesis, Drexel University, Philadelphia, PA, June 1986.

[11] Christopher M. Pastore. *A Processing Science Model of Three Dimensional Braiding.* PhD thesis, Drexel University, Philadelphia, PA, March 1988.

[12] Frank K. Ko and Christopher M. Pastore. Design of complex shaped structures. In *Textiles: Product Design and Marketing*, pages 123–135. The Textile Institute, The Textile Institute, May 1987.

[13] R. L. Foye. Finite element analysis of unit cells. In J. Buckley, editor, *Fiber Tex '90*, pages 45–53, Hampton, VA, May 1992. NASA Langley Research Center, NASA Langley Research Center.

[14] J. D. Whitcomb. Three dimensional stress analysis of plain weave composites. In *3rd Symposium on Composite Materials: Fatigue and Fracture*, Philadelphia, PA, Oct. 1989. American Society for Testing and Materials, ASTM.

C-5.

[15] Frank K. Ko, Christopher M. Pastore, Charles Lei, and Dennis W. Whyte. A fabric geometry model for 3-D braid reinforced FP/Al-Li composites. In *1987 International SAMPE Metals Conference: Competitive Advances in Metals/Metal Processing*, Cherry Hill, NJ, Aug. 1987. American Society for Testing and Materials, ASTM.

[16] Christopher M. Pastore, Eileen Armstrong, and Frank K. Ko. A fabric geometry model for brittle matrix composites. In *Ceramic Matrix Composites*, Indianapolis, IN, April 1989. American Ceramic Society, ACerS.

[17] A. F. Kregers and G. A. Teters. Use of averaging methods to determine the viscoplastic properties of spatially reinforced composites. *Polymer Mechanics*, 15(4):617–624, July-August 1979.

[18] George E. Dieter. *Mechanical Metallurgy.* McGraw-Hill Book Co., New York, third edition, 1986.

[19] A. E. H. Love. *A Treatise on the Mathematical Theory of Elasticity.* Dover Publications, New York, 4 edition, 1944.

MICROMECHANICAL MODELS FOR TEXTILE COMPOSITES*

Bhavani V. Sankar
and
Ramesh V. Marrey
Center for Studies of Advanced Structural Composites
University of Florida
Gainesville, FL

1. SUMMARY

Numerical and analytical micromechanical models are presented to predict the thermo-elastic behavior of a textile composite. In the numerical model, the unit-cell is discretized with finite elements, and periodic boundary conditions are imposed between opposite faces of the unit-cell. For a thin textile composite, stress gradients effects through the thickness are demonstrated. The consequent difference in the stiffness and strength behavior of thick and thin composites are discussed. The numerical model is implemented to predict the 3-D thermo-elastic constants for a thick textile composite, and the plate thermo-mechanical properties for a thin textile composite. The numerical model is extended to compute the thermal residual microstresses due to processing and to predict the composite failure envelopes. An analytical model - Selective Averaging Method (SAM) - is proposed, which is based on a judicious combination of stiffness and compliance averaging to estimate the 3-D elastic constants. Both the models are tested and verified for several examples by comparing the stiffness properties with elasticity solutions and available results.

2. INTRODUCTION

The increasing demand for lightweight yet strong and stiff structures has lead to the development of fiber reinforced composites. These materials are not only used in the aerospace industry but also in variety of commercial applications like automobile, marine and biomedical applications. However the manufacture of fibrous laminated composites from prepregs is labor intensive. Besides, fibrous laminated composites lack through the thickness reinforcement, and hence have poor interlaminar shear strength. Recent developments in textile technology shows some promise in overcoming the above limitations. Three-dimensional woven and braided composites provide multidirectional reinforcement, thus enhancing the strength and stiffness in the thickness direction. Textile manufacturing processes such as weaving and braiding in conjunction with resin transfer molding are also suitable for the production of intricate structural forms at a reduced turn-round time.

***Work done on grant at the University of Florida, NAG-1-1226.**

With the advancements in aforementioned technologies there is a need to develop scientific methods of predicting the performance of the composites made using the above processes. There are numerous variables involved in textile processes besides the choice of the fiber and matrix materials. This, for example, includes the number of filaments in the yarn specified by the yarn linear density and the yarn architecture within the unit-cell determined by the type of weaving or braiding processes. Thus there is a need for analytical/numerical models to study the effect of these variables on the textile composite behavior. Ideally a structural engineer would like to model textile composites as a homogeneous anisotropic material - preferably orthotropic - so that the structural computations can be simplified, and also the existing computer codes can be used in the design. This would require the prediction of the effective (macroscopic) properties of the composites from the constituent material (microscopic) characteristics such as fiber and matrix properties, fiber-matrix interface characteristics and the fiber architecture. This is possible if we assume that there is a representative volume element (RVE) or an unit-cell that repeats its self throughout the volume of the composite, which seems to be true in the case of textile composites. Ishikawa and Chou (1982; 1983a; 1983b), Yang and Chou (1987), Ma, Yang and Chou (1986), have proposed several models for estimating the thermoelastic and mechanical properties of woven and braided composites. Yoshino and Ohtsuka (1982), Dasgupta et al. (1990) and Whitcomb (1991) analyzed the unit-cell of textile composites using three-dimensional finite elements to predict the overall macroscopic behavior of the composites. Their models can be used to predict both stiffness and strength properties. In the present paper, we have demonstrated numerical models to predict the stiffness and strength behavior of textile composites. An approximate analytical method is also described to estimate the stiffness properties of a textile composite.

3. FINITE ELEMENT MODELS FOR THERMO-MECHANICAL PROPERTIES

In this section, we demonstrate micromechanical models utilizing finite elements to predict the effective stiffness properties and coefficients of thermal expansion (CTE's) for a textile composite. The macroscopic properties of the composite are determined at a scale much larger than the dimensions of the unit-cell, but comparable to the dimensions of the structural component. The average stresses at a point at the structural scale will be called the macroscopic stresses or macrostresses. The actual stresses at a point at the continuum level will be called the microscopic stresses or microstresses.To distinguish the macroscopic deformations and stresses from their microscale counterparts - a superscript "M" will be used to denote the macroscopic deformations and stresses.

3.1 Unit-Cell Analysis for Three-Dimensional Elastic Constants

The unit-cell analysis assumes that the material is subjected to a uniform state of strain in the macroscopic sense. The average stresses required to create such a state of strain is computed from the finite element model of the unit-cell. In the microscale, all unit-cells have

identical stress and strain fields. Continuity of stresses across the unit-cell then requires that tractions be equal and opposite at corresponding points on opposite faces of the unit-cell. Since the displacement gradients are constant for a homogeneous deformation, the displacements at corresponding points on opposite faces of the unit-cell differ only by a constant.

Consider a rectangular parallelepiped as the unit-cell of the three-dimensional textile composite. The edges of the unit-cell are assumed to be parallel to the coordinate axes x_1, x_2 and x_3, with unit-cells repeating in all three directions. The length of the unit-cell in the x_i direction is defined as L_i. On the macroscale the composite is assumed to be homogeneous and orthotropic and the composite behavior is characterized by the following constitutive relation :

$$\begin{Bmatrix} \sigma_{11}^M \\ \sigma_{22}^M \\ \sigma_{33}^M \\ \tau_{23}^M \\ \tau_{31}^M \\ \tau_{12}^M \end{Bmatrix} = \begin{bmatrix} C_{11} & C_{12} & C_{13} & C_{14} & C_{15} & C_{16} \\ & C_{22} & C_{23} & C_{24} & C_{25} & C_{26} \\ & & C_{33} & C_{34} & C_{35} & C_{36} \\ & \textit{symm.} & & C_{44} & C_{45} & C_{46} \\ & & & & C_{55} & C_{56} \\ & & & & & C_{66} \end{bmatrix} \left\{ \begin{Bmatrix} \epsilon_{11}^M \\ \epsilon_{22}^M \\ \epsilon_{33}^M \\ \gamma_{23}^M \\ \gamma_{31}^M \\ \gamma_{12}^M \end{Bmatrix} - \begin{Bmatrix} \alpha_1^s \\ \alpha_2^s \\ \alpha_3^s \\ \alpha_{23}^s \\ \alpha_{31}^s \\ \alpha_{12}^s \end{Bmatrix} \Delta T^M \right\} \tag{1}$$

where $\{\sigma^M\}$ and $\{\varepsilon^M\}$ are the macroscale stresses and strains respectively; $\{\alpha^s\}$ and $[C]$ are the macroscale CTE's and orthotropic elasticity matrix to be determined; ΔT^M is a uniform temperature difference throughout the unit-cell.

3.1.1 Periodic Boundary Conditions

The periodic BC's consist of the periodic displacement boundary conditions which ensure the compatibility of displacements on opposite faces of the unit-cell, and the periodic traction boundary conditions to enforce the continuity of stresses. A macroscopically homogeneous deformation can be represented as

$$u_i^M = H_{ij} x_j \qquad i,j=1,2,3 \tag{2}$$

where H_{ij} are the displacement gradients. Then the periodic displacement boundary conditions to be imposed on the faces $x_i=0$ and $x_i=L_i$ are

$$\begin{aligned} u_i(L_1,x_2,x_3) - u_i(0,x_2,x_3) &= H_{i1}L_1 \\ u_i(x_1,L_2,x_3) - u_i(x_1,0,x_3) &= H_{i2}L_2 \\ u_i(x_1,x_2,L_3) - u_i(x_1,x_2,0) &= H_{i3}L_3 \end{aligned} \tag{3}$$

The traction boundary conditions to be imposed on the faces $x_i=0$ and $x_i=L_i$ are

$$\begin{aligned} F_i(L_1,x_2,x_3) &= -F_i(0,x_2,x_3) \\ F_i(x_1,L_2,x_3) &= -F_i(x_1,0,x_3) \\ F_i(x_1,x_2,L_3) &= -F_i(x_1,x_2,0) \end{aligned} \tag{4}$$

The above periodic BC's are imposed in the finite element model by using multi-point constraint elements or by using transformation equations to eliminate the constrained displacements (Cook et al., 1989). Both methods require a finite element model with corresponding nodes on opposite faces of the unit-cell.

3.1.2 Determination of Three-Dimensional Elastic Constants and CTE's

The unit-cell is discretized with three-dimensional finite elements such that opposite faces of the unit-cell have identical nodes. Periodic displacement and traction boundary conditions are enforced between the corresponding nodes. The periodic displacement BC's are imposed such that only one of the components of the macroscopic strains is non-zero; and the uniform temperature difference ΔT^M is set to zero. Then, the difference in displacements between corresponding points on opposite faces of the unit-cell will be equal to that in a homogenous continuum subject to the same deformation. The average stresses (macroscopic stresses) required to create such a deformation are obtained from the finite element results. Substituting the macroscopic stresses and strains in the composite constitutive relation Eqn. (1) the stiffness coefficients in the column corresponding to the non-zero strain can be evaluated. This procedure is repeated for other macroscopic strain components (keeping the temperature difference zero) to obtain the entire stiffness matrix $[C]$. The orthotropic elastic constants of the composite material can be easily determined by inverting the stiffness matrix, and comparing the compliance coefficients with that of an orthotropic material.

To compute the six CTE's, a finite temperature change T_o is applied to all the elements in the unit-cell; and periodic displacement BC's are imposed such that all the macroscopic strain components are zero. Then the composite constitutive relation Eqn. (1) will reduce to

$$\{\sigma^M\} = -[C]\{\alpha^s\}\, T_o \tag{5}$$

The macroscopic stresses for such a deformation are computed as described below. Knowing the stiffness matrix $[C]$, the composite CTE's are found as

$$\{\alpha^s\} = -\frac{1}{T_o}[C]^{-1}\{\sigma^M\} \tag{6}$$

Table 1 presents the non-zero displacement BC's imposed on the unit-cell to obtain $[C]$ and the CTE's $\{\alpha^s\}$.

The macroscale stresses for a given deformation state can be found by one of the following two methods. In the first method, the macroscale stresses are obtained by averaging the nodal forces on each face of the unit cell. For example, the macroscale $\sigma_{11}{}^M$ can be

obtained as

$$\sigma_{11}^{M} = \frac{1}{L_2 L_3} \Sigma_n F_1^{(n)}(L_1, x_2, x_3) \tag{7}$$

where $F_1^{(n)}$ is the nodal force in the x_1 direction at the nth node, and Σ_n denotes summation over all nodes on the face $x_1=L_1$. Alternately, the macroscopic stresses can be computed by volume-averaging the corresponding microstress component in the unit-cell. Then the macroscale σ_{11}^{M} is obtained as

$$\sigma_{11}^{M} = \frac{1}{V}\int_V \sigma_{11}(x,y,z)\,dV \tag{8}$$

where V is the volume of the unit-cell. The microstresses are computed at the quadrature points, and numerically integrated over the volume in each element of the unit-cell.

3.1.3 Results and Discussion for 3-D Elastic Constants and CTEs

The above procedure was demonstrated for the following materials:

Example 1. isotropic material
Example 2. bimaterial medium - both materials are assumed isotropic
Example 3. unidirectional composite with identical poisson ratios for fiber and matrix - fiber and matrix materials are isotropic
Example 4. unidirectional composite with different poisson ratios for fiber and matrix - fiber and matrix materials are isotropic
Example 5. plain-weave textile composite (yarn geometry and properties obtained from Dasgupta et al., 1990)
Example 6. plain-weave textile composite (yarn geometry and properties obtained from Naik, 1994)
Example 7. 5-harness satin weave (yarn geometry and properties obtained from Naik, 1994)

For the textile composite examples, i.e, examples 5-7, the yarn is assumed to be transversely isotropic and the matrix material is assumed isotropic. The constituent material properties for the examples are listed in Table 2.

A 3-D finite element code called $\mu TE\chi$-20 (pronounced as *mutech*) was written and implemented for the seven examples to compute the homogeneous elastic constants and CTE's. The unit-cell was divided into uniform eight noded hexahedral elements. The element stiffness matrix (K^e) was formulated as

$$\begin{aligned} K^e &= \int_{V^e} B^T C B \, dV^e \\ &= \int_{-1}^{+1}\int_{-1}^{+1}\int_{-1}^{+1} B^T C B \, |J| \, d\xi \, d\eta \, d\zeta \\ &\approx \sum_{i=1}^{N}\sum_{j=1}^{N}\sum_{k=1}^{N} W_i W_j W_k B^T C(\xi,\eta,\zeta) B \, |J| \end{aligned} \tag{9}$$

where V^e is the domain of the element, B is the strain-displacement transformation matrix, C

is the elasticity matrix, N is the number of Gauss points used for integration, W is the Gaussian integration weight factor and $|J|$ is the determinant of the Jacobian. The material property at each Gauss point (ξ,η,ζ) was determined, and the corresponding elasticity matrix was used to perform the volume integration. The element stiffness matrix thus represented the averaged properties of the constituent materials in that element. The computed elastic constants for the seven examples are listed in Tables 3-5.

The bimaterial medium consisted of two different layers of equal thickness in the xy-plane alternating in the z-direction (Fig. 1). The effective Youngs moduli, Poisson ratios and CTE's of the bimaterial medium were derived exactly as described below. The constitutive relation (considering only the normal stresses) for each layer was defined as

$$\begin{Bmatrix} \sigma^i_{xx} \\ \sigma^i_{yy} \\ \sigma^i_{zz} \end{Bmatrix} = \begin{bmatrix} C^i_{11} & C^i_{12} & C^i_{13} \\ C^i_{12} & C^i_{22} & C^i_{23} \\ C^i_{13} & C^i_{23} & C^i_{33} \end{bmatrix} \begin{Bmatrix} \epsilon^i_{xx} \\ \epsilon^i_{yy} \\ \epsilon^i_{zz} \end{Bmatrix} \qquad i=1,2 \tag{10}$$

where the superscript refers to the layer number. To derive C_{11}, C_{12} and C_{13} for the bimaterial medium, $\varepsilon_{xx}{}^M$ was assumed as one; and $\varepsilon_{yy}{}^M$ and $\varepsilon_{zz}{}^M$ as zero.The assumption of $\varepsilon_{zz}{}^M=0$ implied that $\varepsilon_{zz}{}^1 = -\varepsilon_{zz}{}^2$. The following constraints were, in addition, imposed across the bimaterial interface :

$$\begin{aligned} \epsilon^1_{xx} &= \epsilon^2_{xx} = \epsilon^M_{xx} \\ \epsilon^1_{yy} &= \epsilon^2_{yy} = \epsilon^M_{yy} \\ \sigma^1_{zz} &= \sigma^2_{zz} = \sigma^M_{zz} \end{aligned} \tag{11}$$

From the above interfacial constraints and Eqn. (10), the stresses in each layer were computed. The stresses in the layers were volume-averaged to yield the corresponding macroscopic stresses, i.e, $\sigma_{xx}{}^M$, $\sigma_{yy}{}^M$ and $\sigma_{zz}{}^M$. Since $\varepsilon_{xx}{}^M$ was equal to unity, the computed macroscopic stresses were identical to the stiffness coefficients C_{11}, C_{12} and C_{13}. A similar procedure was followed to find the remaining stiffness coefficients and CTE's for the bimaterial medium. The inplane shear modulus of the bimaterial medium was computed as $G_{xy}= (G_1+ G_2)/2$ knowing that the shear strain was uniform in both layers. The isostress assumption was used to derive the transverse shear modulus as $G_{xz}= 2G_1G_2 / (G_1+G_2)$. It was found that $\mu TE\chi$-20 results were identical to the elasticity results for the bimaterial medium (Table 3).

Table 4 presents the elastic constants and CTE's for the two unidirectional composite examples. The unidirectional composite unit-cell is shown in Fig. 2. The unidirectional composite properties were compared with available analytical solutions. The rule of mixtures formulae were used to predict E_L and ν_{LT} ; the Halpin-Tsai equations (Halpin and Tsai, 1969) for E_T, G_{LT} and ν_{TT} and Schapery's expressions (Agarwal and Broutman, 1990) for the thermal

coefficients α_L and α_T. The relations for E_L, ν_{LT} and α_L are exact when the poisson ratios are identical for the fiber and the matrix. The reason for the discrepancy in example 3 is that a point-location subroutine in $\mu TE\chi$-20 identified a fiber volume fraction of 0.595, whereas the actual fiber volume fraction was 0.6.

The elastic constants for the three textile composite examples are presented in Table 5. Figures 3 & 4 illustrate the weave patterns for the plain-weave (examples 5 & 6) and the 5-harness satin weave (example 7) respectively. The properties for example 5 were compared with Dasgupta's results for an overall fiber volume fraction (V_f) of 0.26. The yarn properties were not specified in Dasgupta et al. (1990). So the rule of mixtures and Schapery's expressions were used to obtain the yarn properties from the given fiber and matrix properties. The $\mu TE\chi$-20 results for examples 6 and 7 were compared with TEXCAD - an approximate analytical method developed by Naik (1994). In both the examples the overall fiber volume fraction was 0.64. It must be noted that $\mu TE\chi$-20 will marginally under-predict the stiffness moduli - since the yarn cross-section in the numerical model is approximated as a polygon inscribed within the actual cross-sectional area. Consequently the yarn/fiber volume fraction in the numerical model will always be lesser that the theoretical volume fraction.

3.2 Stress Gradient Effects

The methods explained in Section 3.1 assume that the unit-cells exist in all the three directions. This will be true in the case of thick textile composites. However there are many applications in which thin composites are used. In fact in order to take advantage of the properties of composites, the structures have to be made of thin plate like members with stiffeners for load transfer. In such cases there will be fewer unit-cells in the thickness direction. Thus the free surface effects will be predominant. There will be severe stress gradients through the thickness, and they will have an influence on the apparent stiffness and strength of the structure.

The following simple example will illustrate the stress gradient effects on stiffness. Consider a layered medium consisting of alternating layers of materials of equal thickness with Young's moduli E_1 and E_2 respectively (Fig. 5a). Any micromechanical model would predict that the medium can be considered as a homogeneous orthotropic material at macroscale and also the effective Young's modulus in the longitudinal direction is $(E_1+E_2)/2$, and there would not be any bending-stretching coupling in the principal material direction. However, if we consider a bimaterial beam consisting of the same two materials (Fig. 5b), we will find that there is a bending-stretching coupling, and also the flexural rigidity cannot be predicted from the Young's modulus of the homogeneous orthotropic medium and the total beam thickness. The bimaterial beam has properties and behavior different from the corresponding infinite medium. This phenomenon is observed in the transverse shear behavior also (Sankar and Marrey, 1993). A similar behavior is also expected in thin textile composites where there are fewer unit-cells in the thickness directions, and the unit-cells are not subjected to a macroscopically homogeneous state of deformation as assumed in Section 3.1. The effect of stress gradients on stiffness and strength of thin textile composites are discussed

in Marrey and Sankar (1993a).

One method of overcoming the above difficulties in thin textile composites is to model the composite as a plate/beam, and compute the structural stiffness properties (eg., [A], [B] and [D] of the plate) directly from the unit-cell analysis instead of the continuum stiffness properties (Young's modulus, shear modulus etc.). In the following sub-sections we illustrate these concepts - first for a thin textile composite modeled as a beam, and then for a textile composite plate. The purpose of the beam model is to present the issues involved in computing the structural stiffness coefficients. Further the periodic BC's are different from those in the continuum model.

3.3 Unit-Cell Analysis for Beam Thermo-Mechanical Coefficients

The textile composite beam is assumed to be in the xz-plane with unit-cells repeating in the x-direction. A state of plane strain parallel to the xz-plane is assumed. On the macroscale it is assumed that the beam is homogeneous and its behavior can be characterized by the following beam constitutive relation :

$$\begin{Bmatrix} P \\ M \\ V \end{Bmatrix} = \begin{bmatrix} K_{11} & K_{12} & K_{13} \\ K_{12} & K_{22} & K_{23} \\ K_{13} & K_{23} & K_{33} \end{bmatrix} \left\{ \begin{Bmatrix} \epsilon_0^M \\ \kappa^M \\ \gamma_0^M \end{Bmatrix} - \begin{Bmatrix} \alpha_P \\ \alpha_M \\ \alpha_V \end{Bmatrix} \Delta T^M \right\} \tag{12}$$

where P, M and V are the axial force, bending moment and transverse shear force resultants respectively; $[K]$ is the symmetric matrix of beam stiffness coefficients; ϵ_0^M, κ^M and γ_0^M are the midplane axial strain, curvature and transverse shear strain respectively; α_P, α_V and α_M respectively are the thermal expansion, thermal shear and thermal bending coefficients. The midplane deformations are related to the midplane axial displacement u_0, transverse displacement w, and rotation ψ as:

$$\epsilon_0^M = \frac{\partial u_0}{\partial x}, \quad \kappa^M = \frac{\partial \psi}{\partial x}, \quad \gamma_0^M = \psi + \frac{\partial w}{\partial x} \tag{13}$$

Actually K_{11}, K_{12}, K_{22} and K_{33} are similar to the laminate stiffness coefficients A_{11}, B_{11}, D_{11} and $\kappa^2 A_{55}$ respectively. The beam constitutive relation in Eqn. (12) can also be expressed in terms of compliance coefficients as

$$\begin{Bmatrix} \epsilon_0^M \\ \kappa^M \\ \gamma_0^M \end{Bmatrix} = \begin{bmatrix} S_{11} & S_{12} & S_{13} \\ S_{12} & S_{22} & S_{23} \\ S_{13} & S_{23} & S_{33} \end{bmatrix} \begin{Bmatrix} P \\ M \\ V \end{Bmatrix} + \begin{Bmatrix} \alpha_P \\ \alpha_M \\ \alpha_V \end{Bmatrix} \Delta T^M \tag{14}$$

As discussed earlier, the unit-cell analysis assumes that all the unit-cells are subjected to identical stress and strain fields, for a given state of loading. This is true in the case of constant axial force (P) and constant bending moment (M) in the beam. However, when a shear force (V) is applied to the beam, the shear force will give rise to the building up of bending moment at every cross-section, such that $V = -(dM/dx)$. This situation created difficulties in estimating the shear stiffness of the beam accurately.

The detailed procedures for evaluating [K] and the beam CTE's are explained in Sankar and Marrey (1993) and Marrey and Sankar (1993b). However the principles involved in finding the beam stiffness matrix [K] are described briefly for the sake of completion. Three linearly independent deformations are applied to the unit-cell namely,

Case (i) unit axial strain ($\varepsilon_0 = 1,\ \kappa = 0,\ \gamma_0 = 0$)

Case (ii) unit curvature accompanied by transverse deflection such that the transverse shear strain was zero ($\varepsilon_0 = 0,\ \kappa = 1,\ \gamma_0 = 0$)

Case (iii) unit transverse shear strain ($\varepsilon_0 = 0,\ \kappa = 0,\ \gamma_0 = 1$)

The periodic displacement boundary conditions for the three unit deformations are given in Table 6. The temperature change, ΔT, is assumed to be zero. The top and bottom surfaces of the unit-cell are considered as free surfaces. For each case, the axial force P, the bending moment at the center of the unit cell M, and the shear force V are computed. Since the bending moment varies linearly along the unit cell, the bending moment at the center will be the average of the bending moments at the left and right ends of the unit cell. By substituting the values of P, M and V in Eqn. (12), one can evaluate the stiffness coefficients.

3.3.1 Beam Results and Discussion

The procedures to obtain the beam coefficients were implemented for the following cases:
(a) an isotropic beam; (b) a bimaterial beam with isotropic layers of equal thickness; (c) a plain weave textile composite beam where the yarn is assumed to be transversely isotropic and the matrix is isotropic. The properties of the constituent materials for all the cases are listed in Table 7. The dimensions of the unit-cell and the yarn architecture for the textile beam were taken from Yoshino and Ohtsuka (1982). The same unit-cell dimensions (length of 3.6 mm and height 1.8 mm) were also used for the isotropic and bimaterial cases.

The unit-cell of the beam was discretized using eight-noded isoparametric plane strain finite elements. The finite element mesh for the isotropic unit-cell and the plain weave unit-cell were identical except that different material properties were used. The deformed plain weave unit-cell under various independent loading conditions is shown in Fig. 6.

The stiffness and thermal coefficients for the three beams examples are shown in Table 8. The results for the isotropic and bimaterial beams were compared to exact beam theory solutions. Exact shear correction factors - 0.833 for the isotropic beam and 0.555 for bimaterial beam were used in the beam theory solution to compute the shear stiffness (Whitney, 1973). It can be seen that the beam unit-cell analysis is able to predict the axial and bending stiffness coefficients (K_{11} and K_{22}) very accurately. As expected the shear stiffness (K_{33} or A_{55}) predictions have errors, but they are very minimal. The textile beam

stiffness coefficients were also estimated using a procedure similar to the mosaic model (Ishikawa and Chou, 1982). They are compared with the coefficients obtained from the unit-cell analysis as shown in Table 8. It can be seen that the mosaic model predicts K_{33} reasonably well. The reason for the lack of agreement in K_{11} and K_{22} can be attributed to the fact that a major portion of the yarn is modeled as a 0° laminate in the mosaic model, which tends to over-predict the axial and flexural stiffness.

The shear modulus of the plain-weave beam G_{xz} was found by imposing periodic boundary conditions between the top and bottom surfaces, and left and right ends of the unit-cell. This would yield the apparent shear stiffness as $G_{xz}h$=5.53 x 10^6 Nm^{-1} - whereas the actual shear stiffness is 9.21 x 10^6 Nm^{-1} (K_{33} in Table 8). The Young's modulus of the textile beam E_x may be extracted from K_{11}, as K_{11}/h, which would yield E_x=15.42 GPa. If this value of E_x were used to predict the homogeneous flexural stiffness as $D_{11}=E_x h^3/12$, we would obtain D_{11} as 7.50 Nm - whereas the actual flexural stiffness is equal to 5.41 Nm. The same idea holds for the beam thermal coefficients also. The beam CTE's ,*i.e*, α_P, α_M and α_V cannot be predicted from the corresponding continuum CTE's. Table 9 shows the disagreement for the plain-weave example between the beam CTE's obtained directly, and the beam CTE's predicted from the corresponding continuum CTE's. It may be noted that the continuum model would always predict the thermal expansion coefficient α_P as α_x, and the thermal bending coefficient α_M as zero. This underscores the importance of the present analysis for predicting the beam stiffness properties for a thin textile composite directly.

3.4 Unit-Cell Analysis for Plate Thermo-Mechanical Coefficients

In this section we describe a procedure to find the stiffness and thermal properties of a textile fabric modeled as a structural composite plate. The textile composite plate is assumed to be in the *xy*-plane with unit-cells repeating in the *x* and *y* directions. The lengths of the unit-cell in the *x*- and *y*-directions are assumed to be *a* and *b* respectively and the unit-cell thickness as *h*. On the macroscale the plate is assumed to be homogeneous and the plate behavior is characterized by the plate constitutive relation:

$$\begin{bmatrix} A_{11} & A_{12} & A_{16} & B_{11} & B_{12} & B_{16} \\ A_{12} & A_{22} & A_{26} & B_{12} & B_{22} & B_{26} \\ A_{16} & A_{26} & A_{66} & B_{16} & B_{26} & B_{66} \\ B_{11} & B_{12} & B_{16} & D_{11} & D_{12} & D_{16} \\ B_{12} & B_{22} & B_{26} & D_{12} & D_{22} & D_{26} \\ B_{16} & B_{26} & B_{66} & D_{16} & D_{26} & D_{66} \end{bmatrix} \left(\begin{Bmatrix} \epsilon^M_{x0} \\ \epsilon^M_{y0} \\ \gamma^M_{xy0} \\ \kappa^M_x \\ \kappa^M_y \\ \kappa^M_{xy} \end{Bmatrix} - \begin{Bmatrix} \alpha^p_x \\ \alpha^p_y \\ \alpha^p_{xy} \\ \beta^p_x \\ \beta^p_y \\ \beta^p_{xy} \end{Bmatrix} \Delta T \right) = \begin{Bmatrix} N_x \\ N_y \\ N_{xy} \\ M_x \\ M_y \\ M_{xy} \end{Bmatrix} \quad (15)$$

where ε_{i0}^{M}, γ_{i0}^{M} and κ_i^{M} are the midplane axial strain, shear strain and curvature; α_i^{P} and β_i^{P} are the plate thermal expansion and bending coefficients; N_i and M_i are the axial force and bending moment resultants respectively in the homogeneous plate. The midplane strains and curvatures are related to the midplane displacements and rotations as:

$$\epsilon_{x0}^{M} = \frac{\partial u_o}{\partial x}, \quad \epsilon_{y0}^{M} = \frac{\partial v_o}{\partial y}, \quad \gamma_{xy0}^{M} = \frac{\partial u_o}{\partial y} + \frac{\partial v_o}{\partial x} \tag{16}$$

$$\kappa_x^{M} = \frac{\partial \psi_x}{\partial x}, \quad \kappa_y^{M} = \frac{\partial \psi_y}{\partial y}, \quad \kappa_{xy}^{M} = \frac{\partial \psi_x}{\partial y} + \frac{\partial \psi_y}{\partial x} \tag{17}$$

3.4.1 Unit-Cell Boundary Conditions

The plate thermo-mechanical properties were obtained by modeling the unit-cell with eight-noded brick elements and subjecting the unit-cell to linearly independent deformations. The unit-cell was subjected to minimum support constraints to prevent rigid body rotation and translation. The top and bottom surfaces of the plate were assumed to be free of tractions. The faces $x=0$ and $x=a$ had identical nodes in the finite element model, and so did the pair of faces $y=0$ and $y=b$. The identical nodes on opposite faces of the unit cell were constrained to enforce the periodic BC's. The traction boundary conditions on the lateral faces of the unit-cell were:

$$F_i(a,y,z) = -F_i(0,y,z), \quad F_i(x,b,z) = -F_i(x,0,z), \quad i = x,y,z \tag{18}$$

The periodic displacement BC's enforced for the deformations are presented in Table 10.

3.4.2 Determination of Plate Stiffness Coefficients and CTE's

Linearly independent deformations are applied to the unit-cell such that only one of the six components of deformation is non-zero (first six cases in Table 10). The temperature difference is set to zero for all six cases. It must be noted that the applied deformations must ensure that the transverse shear strains, γ_{xz}^{M} and γ_{yz}^{M} are zero where

$$\gamma_{xz}^{M} = \psi_x + \frac{\partial w}{\partial x}$$

$$\gamma_{yz}^{M} = \psi_y + \frac{\partial w}{\partial y} \tag{19}$$

The force and moment resultants can be obtained by averaging the nodal forces on each face

of the unit cell. For example, on the face $x=a$ the force and moment resultants are computed using the relations:

$$N_x = \left(\frac{1}{b}\right) \sum_{i=1}^{n} F_x^{(i)}(a,y,z), \quad N_{xy} = \left(\frac{1}{b}\right) \sum_{i=1}^{n} F_y^{(i)}(a,y.z) \tag{20}$$

$$M_x = \left(\frac{1}{b}\right) \sum_{i=1}^{n} z\, F_x^{(i)}(a,y,z) , \quad M_{xy} = \left(\frac{1}{b}\right) \sum_{i=1}^{n} z\, F_y^{(i)}(a,,y,z) \tag{21}$$

where $F_x^{(i)}$ and $F_y^{(i)}$ are the nodal forces in the x and y directions at the i^{th} node and 'n' is the total number of nodes on the face. The force and moment resultants can also be computed by averaging the microstresses over the unit-cell volume. Then the resultants on the face $x=a$ are obtained as

$$N_x = \frac{1}{ab}\int_V \sigma_{xx}(x,y,z)dV \quad N_{xy} = \frac{1}{ab}\int_V \tau_{xy}(x,y,z)dV \tag{22}$$

$$M_x = \frac{1}{ab}\int_V z\,\sigma_{xx}(x,y,z)dV \quad M_{xy} = \frac{1}{ab}\int_V z\,\tau_{xy}(x,y,z)dV \tag{23}$$

Substituting the values of the deformation and the force resultants in the plate constitutive relation, Eqn. (15), the stiffness coefficients in the column corresponding to the non-zero deformation can be computed. This procedure is repeated for other deformation components to obtain all the stiffness coefficients.

To predict the CTE's, the plate unit cell is subject to a uniform temperature difference, given by $\Delta T = T_0$. In the finite-element model, periodic displacement BC's are applied such that all six components of the deformation are zero (seventh case in Table 10). The force and moment resultants are computed using one of the procedures described above. The thermal expansion coefficients α^p, and thermal bending coefficients β^p are then obtained from the relation:

$$\begin{Bmatrix} \alpha^p \\ \beta^p \end{Bmatrix} = -\frac{1}{T_0} \begin{bmatrix} A & B \\ B & D \end{bmatrix}^{-1} \begin{Bmatrix} N \\ M \end{Bmatrix} \tag{24}$$

3.4.3 Results for Plate Stiffness Coefficients

The plate [A], [B], [D] matrices and CTE's were found for the seven examples listed in Table 2 by implementing the finite element code $\mu TE\chi$-20. The plate properties for the isotropic and bimaterial cases are presented in Tables 11 and 12 respectively. The bimaterial plate properties were also computed using the lamination theory for two plies, and from the 3-D elastic constants (Table 12). For example the coefficient D_{11} is obtained from the 3-D elastic constants as

$$D_{11} = \frac{E_x^M h^3}{12(1-\nu_{xy}^{M^2})}$$

The finite element results for the bimaterial case were exact, *i.e,* identical to the results obtained with the two-ply lamination theory. The [*A*] and [*D*] matrices computed from the bimaterial 3-D constants were found to be in good agreement with the two-ply lamination theory only because both the layers were equal in thickness. In-general, however the plate properties obtained from the 3-D elastic constants would be different from the two-ply lamination theory results. The plate properties for the unidirectional composite examples are presented in Table 13 and for the textile examples in Table 14. In all the examples it was found that the plate properties, especially [*B*], D_{11} , $\{\alpha^p\}$ and $\{\beta^p\}$ could not be predicted from the corresponding 3-D elastic constants.

4. FINITE ELEMENT MODELS FOR STRENGTH PROPERTIES

In the previous sections, we had demonstrated methods to model a general textile composite either as a three-dimensional material or as a thin plate/beam to predict their corresponding thermo-mechanical coefficients. In this section we extend the same numerical models to compute the thermal residual stresses due to processing in the yarns and the matrix. Then the numerical models are used to study the strength behavior of the composite by predicting the failure envelopes for thin and thick textile composites.

4.1 Thermally Induced Residual Microstresses

The mismatch in the CTE's for the constituent materials in the composite induces the residual microstresses in the yarn and matrix. The difference between composite curing temperature and room temperature then serves as the driving force to create these microstresses.The microstresses in the vicinity of the yarn-matrix interface are particularly important as they could lead to failure due to debonding. Since composites designed for high temperature applications are fabricated at higher temperatures, the residual microstresses become particularly relevant in the strength considerations of such composites.

4.1.1 Determination of Residual Microstresses

Let T_o be the difference between room temperature and the composite fabrication temperature. Since the composite is stress free at the fabrication temperature, which is above the room temperature, T_o is generally negative. The residual microstresses in the yarn and the matrix are obtained by superposing the microstresses due to the two load cases as explained below. In the first load case, the unit-cell is constrained from expanding by fixing the corner nodes of the unit-cell and enforcing zero displacement difference between corresponding nodes on opposite faces of the unit-cell (periodic displacement BC's). A temperature difference T_o is applied to all elements in the finite element model. This is exactly the same problem we solve for finding the three-dimensional CTE's. The applied boundary conditions mean that all the macroscopic strain components are equal to zero ($\{\varepsilon^M\} = 0$, $\Delta T^M = T_0$). Then the corresponding macroscopic stresses required to restrain the unit-cell expansion are

given by

$$\{\sigma^M\} = -[C]\{\alpha^s\}T_o \tag{26}$$

In the second load case, deformations are applied so as to reverse the macroscopic stresses developed in the first load case. This can be accomplished by imposing the deformations $\{\varepsilon^M\} = \{\alpha^s\}\ T_o$ and $\Delta T^M=0$. It can be noted that the macroscopic stresses developed in the second loading case $[C]\{\alpha^s\}T_o$ are equal and opposite to the macrostresses in Eqn. (26). The microstresses from both load cases are superposed to obtain the residual stresses due to free thermal expansion.

The same idea can be extended to finding the residual microstresses in the plate model. Then the deformations to be applied in the first load case are $\{\varepsilon^M\} = 0$, $\{\kappa^M\} = 0$ and $\Delta T^M = T_o$; and the deformations in the second load case are $\{\varepsilon^M\} = \{\alpha^p\}\ T_o$, $\{\kappa^M\} = \{\beta^p\}\ T_o$ and $\Delta T^M = 0$. The residual microstresses were computed for the plain-weave textile beam at the Gaussian center of the elements in the unit-cell. Figure 7 shows the thermal stress contours for σ_{xx}, σ_{zz} and τ_{xz}. The composite curing temperature was assumed to be 150°C above room temperature.

4.2 Strength Modeling of Textile Composites

There are many failure criteria or strength theories for unidirectional fiber composites. This for example includes (Agarwal and Broutman, 1990) maximum stress theory, maximum strain theory, Tsai-Hill theory. Even though failure of a material is a very complex phenomenon, engineering strength theories such as mentioned above have been found to be useful in design. The interpretation of strength values obtained from such theories are different for different materials. For example in metal matrix composites the failure envelope obtained using the above theories will correspond to the initial yield surface (Dvorak et al., 1973). In graphite/epoxy composites the failure theories can be used to predict fiber or matrix failure. In the present study our intent is to explore the possibility of developing such failure criteria for textile composites.

4.2.1 Determination of Composite Failure Envelope

Our approach is similar to that used by Dvorak et al. (1973). A state of homogeneous deformation, corresponding to each of the six macrostrain components, are independently applied to the unit-cell by imposing the boundary conditions explained in Section 3.1. For each case, the various stress components are computed in the elements in the unit-cell - typically at the element Gaussian integration points. These stresses will be referred to as microstresses. Assuming linear elastic behavior, the microstresses can be computed for any arbitrary combination of the macrostrain components. Since we know the macroscopic elastic constants, we can find a relation between microstresses at a point and any arbitrary state of

macrostress as:

$$\{\sigma\} = [F]\{\sigma^M\} \tag{27}$$

$[F]$ can be considered as a matrix of influence coefficients, which is evaluated at the integration points of all the elements in the unit-cell. We also assume that the failure behavior of the matrix material and the yarn is known. For instance, let the failure criterion of the matrix be given by $[H]\{\sigma\}_{matrix} = 1$. Then the failure criterion for the composite is obtained from Eqn. (27) as $[H][F]\{\sigma^M\} = 1$. The same idea also applies for the yarn. The textile composite is assumed to have failed, if there is failure on the microscale in any one of the constituent materials - either matrix or the yarn. By varying the macrostresses using a numerical simulation, failure envelopes can be obtained for the idealized homogeneous material. It might be noted that Eqn. (27) can be modified to include the thermal residual stress field in the unit-cell as

$$\{\sigma\} = [F]\{\sigma^M\} - \{\sigma_T\}T_o \tag{28}$$

where $\{\sigma_T\}$ is the matrix of thermal microstresses computed at the element integration point for a temperature difference of T_o.

4.2.2 Effect of Stress Gradients on Strength

The strength analysis for a three-dimensional composite can extended for thin composites using the plate model. As mentioned in Section 3.2, the macroscopic stresses will not be homogeneous thorough the thickness in such composites. Then the composite failure will be determined by the stress gradients through the thickness, represented by the averaged force resultants (F) and moment resultants (M). The composite failure criterion will be of the form

$$[H][F]\begin{Bmatrix} N \\ M \end{Bmatrix} = 1 \tag{29}$$

Thus the failure envelope of the composite will be in the six-dimensional space of the force resultants and the moment resultants. The above procedure was demonstrated using the beam model, for the case of a plain-weave textile composite.

4.2.3 Beam Failure Envelope Results

The strength properties used for the constituent materials in the beam are as follows:
Yarn: σ_L^T=1725 MPa, σ_L^C=1366 MPa, σ_T^T=42 MPa, σ_T^C=230 MPa, τ_{LT}=95 MPa
Matrix: σ^T=70 MPa, σ^C=100 MPa
where the superscripts 'T' and 'C' refer to the tensile and compressive strengths respectively. The maximum principal stress criterion was used to determine the matrix failure and the maximum strain theory for unidirectional fiber composite was used for the yarn. Both continuum and structural failure envelopes were developed. Figures 8 and 9 depict the

structural failure envelopes in the *P-M* space. If we assume that the beam is made of a homogeneous but orthotropic material with properties as predicted by the continuum model, then one can derive structural failure envelopes from the continuum failure envelopes using simple beam theories. The derived structural failure envelopes are compared with that obtained from direct micromechanical analyses in Figs. 10 and 11 respectively. One can note that the continuum failure criteria are very conservative for the case of a thin beam.

5. ANALYTICAL MODELS FOR STIFFNESS PROPERTIES

The complex yarn architectures in a textile composite make numerical modeling of the unit-cell extremely difficult. Analytical methods are popular because they are easy to model and suitable for performing parametric analysis. However these methods are approximate because they assume a certain state of stress or strain in the unit-cell. Averaging the stiffness or compliances of the matrix and the inclusion has been used to estimate the bounds of effective elastic properties of the composite. Essentially the stiffness averaging assumes a state of uniform strain in the composite (isostrain), and compliance averaging assumes a state of uniform stress (isostress) in the matrix and inclusion. In fact the rule of mixtures expressions for estimating the effective properties of a unidirectional composite is based on such averaging schemes. These methods are too simplistic, because the state of stress/strain in a textile composite under a uniform macrostress is much more complex. We propose a scheme of selective averaging in which both stiffness and compliance coefficients can be averaged selectively depending on a more realistic assumption of either isostress or isostrain.

5.1 Selective Averaging Method (SAM)

Consider a rectangular parallepiped of dimensions $a \times b \times c$ as the unit-cell. To find the first column of the effective stiffness matrix, the unit-cell is divided into slices (mesolevel) of thickness d parallel to the yz-plane (Fig. 12a). Each slice is further sub-divided into elements (microlevel) as shown in Figs. 12(b) and 12(c). In this section, to distinguish between the macrolevel, mesolevel and microlevel properties, an over-tilde is used to denote the mesolevel properties, and a superscript "M" is used to denote the macrolevel properties. For example, $[C^M]$, $[\tilde{C}]$ and $[C]$ will represent the macrolevel, mesolevel and microlevel stiffness respectively. The unit-cell is subjected to a deformation such that all macrostrains except ε_{xx}^M are equal to zero and $\varepsilon_{xx}^M = 1$. It is assumed that the mesolevel and microlevel strains, corresponding to the zero macrostrains, are negligible.

$$\epsilon_i^M = \tilde{\epsilon}_i = \epsilon_i = 0 \qquad i \neq 1 \tag{30}$$

The average stiffness of a slice can be obtained based on the isostrain assumption within the slice ($\varepsilon_{xx}(x,y,z) = \tilde{\varepsilon}_{xx}(x)$) as :

$$\tilde{C}_{11}(x)=\frac{1}{bc}\int\int C_{11}(x,y,z)\,dy\,dz \tag{31}$$

where $C_{11}(x,y,z)$ is the element stiffness coefficient transformed to the unit-cell coordinates. The stiffness of the slices are averaged on the macrolevel based on the isostress assumption, *i.e.*, $\sigma_{xx}(x) = \sigma_{xx}^{M}$. Thus the first column of the effective stiffness matrix can be computed using the following relations:

$$\frac{1}{C_{11}^{M}}=\frac{1}{a}\int\frac{1}{\tilde{C}_{11}(x)}dx$$

$$C_{i1}^{M}=\frac{1}{abc}\int\int\int\frac{C_{11}^{M}}{\tilde{C}_{11}(x)}\,C_{i1}(x,y,z)\;dx\,dy\,dz \quad (i=2,\ldots,6) \tag{32}$$

A similar procedure can be implemented to determine the second and third columns of the homogenous stiffness matrix $[C^{M}]$.

A slightly different averaging scheme is used when the unit-cell is subjected to shear strains on the macrolevel. Consider the case where the unit-cell is subjected to unit γ_{yz}^{M} at macroscale. Assume that all the other components of strain at the macrolevel, mesolevel and microlevel are zero, *i.e.*,

$$\epsilon_i^{M} = \tilde{\epsilon}_i = \epsilon_i = 0 \qquad i\neq 4 \tag{33}$$

where $\varepsilon_4 = \gamma_{yz}$. We also assume that the shear stress is constant in a slice such that $\tau_{yz}(x,y,z) = \tau_{yz}(x)$. The shear compliance of a slice can then be obtained by averaging the shear compliances of all the elements in the slice as:

$$\frac{1}{\tilde{C}_{44}(x)}=\frac{1}{bc}\int\int\frac{1}{C_{44}(x,y,z)}dy\;dz \tag{34}$$

The fourth column of the stiffness matrix C_{i4}^{M} is obtained under the assumption that all the slices are under a state of constant shear strain:

$$C_{i4}^{M}=\frac{1}{abc}\int\int\int\frac{\tilde{C}_{44}(x)}{C_{44}(x,y,z)}C_{i4}(x,y,z)\;dx\,dy\,dz \quad (i=1,\ldots,6) \tag{35}$$

A similar procedure is used to determine the fifth and sixth columns of $[C^{M}]$.

5.2 SAM Results

A code was written in FORTRAN to implement SAM. The code ($\mu TE\chi$-10) was used to predict the elastic constants for the seven examples, whose constituent material properties are listed in Table 2. Input to the code were the unit-cell dimensions, yarn/fiber geometry, constituent material properties, and the number of divisions required to discretize the unit-cell in the x, y and z directions. The element stiffness matrix $[C]$ was computed by finding the constitutive stiffness matrix for the point at the center of the element, and transforming it to the unit-cell coordinate system.

The results for the bimaterial medium (example 2) are given in Table 15. The bimaterial medium consisted of two layers of isotropic materials stacked alternately in the z-direction (Fig. 1). It can be observed that SAM marginally under-predicts the bimaterial longitudinal and transverse Youngs moduli, while the inplane and transverse shear moduli are exact. Table 16 presents the SAM results for two cases of unidirectional composite (examples 3 and 4). The fiber and matrix had identical poisson ratios in example 3, and different poisson ratios in example 4. The elastic constants from SAM were compared with the finite element results from Section 3.1 and with analytical solutions for a unidirectional composite (the rule of mixtures formulae and the Halpin-Tsai equations). Table 17 compares the SAM properties for three textile composites (examples 5, 6 and 7) with the previously computed finite element results and other available results. In all three cases the elastic constants obtained by implementing SAM were in good agreement with the available results.

6. CONCLUSIONS

Micromechanical models were demonstrated to predict the stiffness and strength behavior of textile composites. In thin textile composites, the stress gradients through the thickness were significant, and hence the composite was modeled as a homogeneous plate/beam rather than homogeneous continua. The beam model was first discussed to present the issues involved in computing the structural stiffness and strength properties. Then the plate model was presented for computing the plate stiffness and plate CTE's, and to predict the failure envelope for a thin textile composite. The failure envelope for a thin textile composite was described in the space of the force and moment resultants instead of the space of the macroscopic stresses. It was shown for various examples, that the plate properties could not be predicted from the corresponding continuum properties.

In the models using finite elements (Section 3), the periodic BC's were enforced for continuity of tractions and displacements across the unit-cell boundaries. Therefore the finite element results for the stiffness properties could be expected to be very accurate. However due to difficulties in mesh generation, the unit-cell for the 3-D continuum and the plate models were discretized into inhomogeneous finite elements (elements with one or more constituent materials). Thus the stresses in the vicinity of the yarn-matrix interface for the above models may be approximate. For the beam model, however, the unit-cell was

discretized into homogeneous elements.

The Selective Averaging Method (SAM) discussed in Section 6 was based on a combination of isostress and isostrain assumptions. The method was fast and easy to implement and suitable for parametric studies such as yarn preform selection. Extension of SAM to predict the continuum CTE's, plate stiffness and plate CTE's is straightforward and is underway.

REFERENCES

Agarwal, D. A.; and Broutman, L. J.: *Analysis and Performance of Fiber Composites.* John Wiley and Sons Pub., 1990.

Cook, R. D.; Malkus, D. S.; and Plesha, M. E.: *Concepts and Applications of Finite Element Analysis.* John Wiley and Sons Pub. Third Edition, 1989, pp. 272-274.

Dasgupta, A.; Bhandarkar, S.; Pecht, M.; and Barkar, D.: Thermo-elastic Properties of Woven-fabric Composites using Homogenization Techniques. *Proceedings of the American Society for Composites. Fifth Technical Conference.*, 1990, pp. 1001-1010.

Dvorak, G. J.; Rao, M. S. M.; and Tarn, J. Q.: Yielding in Unidirectional Composites under External Loads and Temperature Changes. *J. Comp. Materials*, 1973, Vol.7, pp. 194-216.

Halpin, J. C.; and Tsai, S. W.: Effects of Environmental Factors on Composite Materials. *AFML-TR -67-423*, June 1969.

Ishikawa, T.; and Chou, T. W.: Elastic Behavior of Woven Hybrid Composites. *J. Comp. Mater.*, 1982, Vol. 16, pp. 2-19.

Ishikawa, T.; and Chou, T. W.: One Dimensional Mircomechanical Analysis of Woven Fabric Composites. *AIAA J.*, 1983a, Vol. 21, pp. 1714-1721.

Ishikawa, T.; and Chou, T. W.: In-plane Thermal Expansion and Thermal Bending Coefficients of Fabric Composites. *J. Comp. Mater.*, 1983b, Vol. 17, pp. 92-104.

Ma, C. L.; Yang, J. M.; and Chou, T. W.: Elastic Stiffness of Three Dimensional Braided Textile Structural Composites. *Composite Materials: Testing and Design (Seventh Conference),* ASTM STP 893, 1986, pp. 404-421.

Marrey, R. V.; and Sankar, B. V.: Stress Gradient Effects on Stiffness and Strength of Textile Structural Composites. *Composite Materials and Structures, 1993 ASME Winter Annual Meeting,* AD-Vol. 37/AMD-Vol. 179, 1993a, pp. 133-148.

Marrey, R. V.; and Sankar, B. V.: Thermo-mechanical Properties of and Residual Stresses in

Textile Structural Composites. *Proc. Am. Soc. Composites. VIII Tech. Conference* , 1993b, pp. 499-508.

Naik, R. A.: Analysis of Woven and Braided Fabric Reinforced Composites. NASA CR-194930, 1994.

Sankar, B. V.; and Marrey, R. V.: A Unit-cell Model of Textile Composite Beams for Predicting Stiffness Properties. *Composites Science and Technology*, 1993, Vol. 49, pp. 61-69.

Whitcomb, J. D.: Three Dimensional Stress Analysis of Plain Weave Composites. *Composite Materials Fatigue and Fracture (Third Volume),* ASTM STP 1110, 1991, pp. 417-438.

Whitney, J. M.: Shear Correction Factors for Orthotropic Laminates under Static Load. *J. Appl. Mech.*, 1973, Vol. 40, pp. 302-304.

Yang, J. M.; and Chou, T. W.: Performance Maps of Textile Structural Composites. *Sixth International Conference on Composite Materials (ICCM VI).*, 1987, Vol. 5 , pp. 579-588.

Yoshino, T.; and Ohtsuka, T., 1982: Inner Stress Analysis of Plane Woven Fiber Reinforced Plastic Laminates. *Bulletin of the JSME*, Vol. 25-202, pp. 485-492.

Table 1. Non-zero BC's Imposed to Obtain 3-D Thermo-Elastic Constants

stiffness coefficients to be obtained	**non-zero BC's**
first column of $[C]$ ($\varepsilon_{11}^M = 1$)	$u_1(L_1, x_2, x_3) - u_1(0, x_2, x_3) = L_1$
second column of $[C]$ ($\varepsilon_{22}^M = 1$)	$u_2(x_1, L_2, x_3) - u_2(x_1, 0, x_3) = L_2$
third column of $[C]$ ($\varepsilon_{33}^M = 1$)	$u_3(x_1, x_2, L_3) - u_3(x_1, x_2, 0) = L_3$
fourth column of $[C]$ ($\gamma_{23}^M = 1$)	$u_2(x_1, x_2, L_3) - u_2(x_1, x_2, 0) = L_3/2$ $u_3(x_1, L_2, x_3) - u_3(x_1, 0, x_3) = L_2/2$
fifth column of $[C]$ ($\gamma_{13}^M = 1$)	$u_1(x_1, x_2, L_3) - u_1(x_1, x_2, 0) = L_3/2$ $u_3(L_1, x_2, x_3) - u_3(0, x_2, x_3) = L_1/2$
sixth column of $[C]$ ($\gamma_{12}^M = 1$)	$u_1(x_1, L_2, x_3) - u_1(x_1, 0, x_3) = L_2/2$ $u_2(L_1, x_2, x_3) - u_2(0, x_2, x_3) = L_1/2$
CTE's ($\Delta T^M = 1$)	$\Delta T = 1$

Table 2. Properties of Constituent Materials for Examples 1-7

Example 1		E = 10 GPa, ν=0.3, α=10x10^{-6} / °C
	unit-cell size:	0.500×0.500×0.256 mm
Example 2	**layer 1 (E-glass):**	E_1=70 GPa, ν_1=0.200, α_1= 5x10^{-6} / °C, V_1=0.5
	layer 2 (epoxy):	E_2=3.50 GPa, ν_2=0.350, α_2= 60x10^{-6} / °C, V_2=0.5
	unit-cell size:	0.500×0.500×0.256 mm
Example 3	**fiber:**	E_f=100 GPa, ν_f=0.300, α_f= 10x10^{-6} / °C, V_f=0.6
	matrix:	E_m=10 GPa, ν_m=0.300, α_m= 100x10^{-6} / °C
	unit-cell size:	10×10×10 μm
Example 4	**fiber (E-glass):**	E_f=70 GPa, ν_f=0.200, α_f= 5x10^{-6} / °C, V_f=0.6
	matrix (epoxy):	E_m=3.50 GPa, ν_m=0.350, α_m= 60x10^{-6} / °C
	unit-cell size:	10×10×10 μm
Example 5	**yarn properties (glass-epoxy):**	
	E_L=58.61 GPa, E_T=14.49 GPa, G_{LT}=5.38 GPa, ν_{LT}=0.250	
	ν_{TT}=0.247, α_L=6.15x10^{-6} / °C, α_T=22.64x10^{-6} / °C, V_f=0.26	
	matrix properties (epoxy):	
	E=3.45 GPa, ν=0.37, α=69x10^{-6} / °C	
	unit-cell size:	1.680×1.680×0.228 mm
Examples 6, 7	**yarn properties (graphite-epoxy):**	
	E_L=144.80 GPa, E_T=11.73 GPa, G_{LT}=5.52 GPa, ν_{LT}=0.230	
	ν_{TT}=0.300, α_L= -0.324x10^{-6} / °C, α_T=14.00x10^{-6} / °C, V_f=0.64	
	matrix properties (epoxy):	
	E=3.45 GPa, ν=0.35, α=40x10^{-6} / °C	
	unit-cell size:	2.822×2.822×0.2557 mm (Example 6)
		7.055×7.055×0.2557 mm (Example 7)

Table 3. 3-D Properties for Examples 1 and 2 using Finite Elements

		E_x, E_y (GPa)	E_z (GPa)	G_{xz}, G_{yz} (GPa)	G_{xy} (GPa)	ν_{xz}, ν_{yz}	ν_{xy}	α_x^s, α_y^s x 10^{-6}/°C	α_z^s x10^{-6} /°C
Example 1 (isotropic medium)	***μTEχ*-20 (FEA)**	10	10	3.85	3.85	0.300	0.300	10	10
	exact solution	10	10	3.85	3.85	0.300	0.300	10	10
Example 2 (bimaterial medium)	***μTEχ*-20 (FEA)**	36.79	9.79	2.48	15.23	0.312	0.208	8.19	59.60
	exact solution	36.79	9.79	2.48	15.23	0.312	0.208	8.19	59.60

Table 4. 3-D Properties for Examples 3 and 4 using Finite Elements

		E_L (GPa)	E_T (GPa)	G_{LT} (GPa)	G_{TT} (GPa)	ν_{LT}	ν_{TT}	α_L x10^{-6} /°C	α_T x10^{-6} / °C
Example 3 (unidirect. composite)	***μTEχ*-20 (FEA)**	63.55	36.48	12.93	9.94	0.300	0.232	15.74	40.79
	rule of mixt./ Halpin-Tsai eqns.	64	34.55	11.26	-	0.300	0.300	15.63	55.11
Example 4 (unidirect. composite)	***μTEχ*-20 (FEA)**	43.12	18.15	5.59	3.92	0.242	0.222	7.40	25.44
	rule of mixt./ Halpin-Tsai eqns.	43.40	14.79	4.45	-	0.260	0.252	6.77	34.24

Table 5. 3-D Properties for Examples 5, 6 and 7 using Finite Elements

		E_x, E_y (GPa)	E_z (GPa)	G_{xz}, G_{yz} (GPa)	G_{xy} (GPa)	ν_{xz}, ν_{yz}	ν_{xy}	α_x^s,α_y^sx 10^{-6}/°C	α_z^sx 10^{-6}/°C
Example 5 (plain-weave)	***μTEχ-20* (FEA)**	11.55	6.26	1.94	2.12	0.399	0.186	29.75	75.82
	Dasgupta results	14.38	6.25	1.94	3.94	0.463	0.167	22.5	86
Example 6 (plain-weave)	***μTEχ-20* (FEA)**	58.27	10.92	4.32	4.84	0.363	0.097	1.47	23.15
	TEXCAD	64.38	11.49	5.64	4.87	0.396	0.027	1.33	20.71
Example 7 (5-harness weave)	***μTEχ-20* (FEA)**	62.51	11.02	4.45	4.80	0.349	0.047	1.58	23.18
	TEXCAD	66.33	11.51	4.93	4.89	0.342	0.034	1.46	21.24

Table 6. Periodic Displacement BC's for Beam Stiffness Coefficients

	$u(L,z)-u(0,z)$	$w(L,z)-w(0,z)$	ΔT
Case i. unit axial strain ($\varepsilon_0^M=1$)	L	0	0
Case ii. unit curvature ($\kappa^M=1$)	Lz	$-L^2/2$	0
Case iii. unit shear strain ($\gamma_0^M=1$)	0	L	0

Table 7. Constituent Material Properties for Beam Examples

isotropic beam	E = 10 GPa, ν = 0.30, α = 10x10^{-6} /°C
bimaterial beam	E_1 = 70 GPa, ν_1 = 0.33, α_1 = 23x10^{-6} /°C E_2 = 3.5 GPa, ν_2 = 0.35, α_2 = 60x10^{-6} /°C
plain-weave textile beam	**yarn:** E_1 = 159 GPa, E_2 = 10.9 GPa, G_{12} = 6.4 GPa, ν_{12} = 0.38, ν_{23} = 0.38, α_1 = 0.045x10^{-6} /°C, α_2 = 20.2x10^{-6} /°C where the yarn direction is parallel to the *1*-axis and *23*-plane is the plane of isotropy. **matrix:** E_m = 3.5 GPa, ν_m = 0.35, α_m = 60x10^{-6} /°C.

Table 8. Comparison of Beam Stiffness Coefficients and CTE's (SI Units)

		K_{11}	K_{12}	K_{22}	K_{33}	α_P /°C	α_M /°C
isotropic beam	unit-cell analysis	19.78×10^{6}	0	5.35	5.96×10^{6}	10×10^{-6}	0
	beam theory	19.78×10^{6}	0	5.34	5.77×10^{6}	10×10^{-6}	0
bimaterial beam	unit-cell analysis	74.29×10^{6}	30.20×10^{3}	20.06	8.47×10^{6}	30.73×10^{-6}	-14.62×10^{-3}
	beam theory	74.29×10^{6}	30.20×10^{3}	20.06	8.62×10^{6}	30.74×10^{-6}	-14.63×10^{-3}
plain-weave textile beam	unit-cell analysis	27.76×10^{6}	0	5.41	9.21×10^{6}	12.66×10^{-6}	-24.12×10^{-6}
	mosaic model	71.48×10^{-6}	0	8.13	8.14×10^{6}	4.39×10^{-6}	0

K_{13}, K_{23} and α_V are zero for all cases

Table 9. Comparison of Beam CTE's for Plain-weave Textile Beam

	CTE's from beam model	CTE's from continuum model	% error
α_P x 10^{-6} °/C	12.66	11.30	-10.46
α_M x 10^{-6} °/C/m	-24.12	0	100
α_V °/C	0	0	-

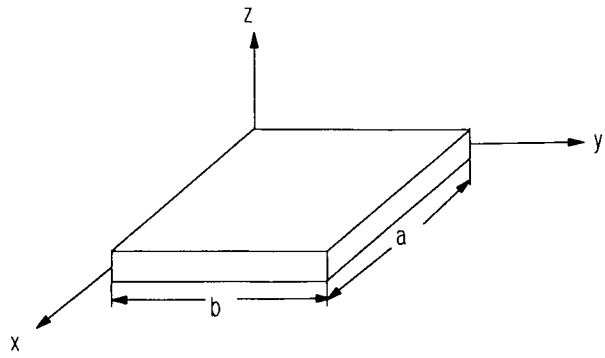

Table 10. Periodic Displacement BC's Imposed on the Lateral Faces of the Plate Unit-cell

		$u(a,y)-u(0,y)$	$v(a,y)-v(0,y)$	$w(a,y)-w(0,y)$	$u(x,b)-u(x,0)$	$v(x,b)-v(x,0)$	$w(x,b)-w(x,0)$	ΔT
1.	$\varepsilon_{x0}^{M}=1$	a	0	0	0	0	0	0
2.	$\varepsilon_{y0}^{M}=1$	0	0	0	0	b	0	0
3.	$\gamma_{xy0}^{M}=1$	0	a/2	0	b/2	0	0	0
4.	$\kappa_{x}^{M}=1$	az	0	$-a^2/2$	0	0	0	0
5.	$\kappa_{y}^{M}=1$	0	0	0	0	bz	$-b^2/2$	0
6.	$\kappa_{xy}^{M}=1$	0	az/2	-ay/2	bz/2	0	-bx/2	0
7.	$\Delta T^{M}=1$	0	0	0	0	0	0	1

Table 11. Non-zero [*A*], [*B*] and [*D*] Coefficients for Example 1 (Isotropic Plate) using Finite Elements

	A_{11} x10^6	A_{12} x10^6	A_{22} x10^6	A_{66} x10^6	D_{11} x10^{-3}	D_{12} x10^{-3}	D_{22} x10^{-3}	D_{66} x10^{-3}	α_x^p, α_y^p x10^{-6}/°C
***μTEχ*-20 (FEA)**	2.810	0.843	2.810	0.983	15.320	4.606	15.320	5.358	10
lamination theory	2.810	0.843	2.810	0.983	15.310	4.593	15.310	5.358	10

[*A*], [*B*] and [*D*] coefficients in SI units

Table 12. Non-zero [*A*], [*B*] and [*D*] Coefficients for Example 2 (Bimaterial Plate) using Finite Elements

	A_{11}, A_{22} x10^6	A_{12} x10^6	A_{66} x10^6	B_{11}, B_{22} x10^3	B_{12} x10^3	B_{66} x10^{-3}
***μTEχ*-20 (FEA)**	9.832	2.043	3.895	- 0.563	- 0.108	- 0.228
lamination theory for two plies	9.832	2.043	3.895	- 0.563	- 0.108	- 0.228
lamination theory using 3-D elastic constants	9.844	2.048	3.899	0	0	0

	D_{11}, D_{22} x10^{-3}	D_{12} x10^{-3}	D_{66} x10^{-3}	α_x^p, α_y^p x10^{-6} /°C	β_x^p, β_y^p /°C/m
***μTEχ*-20 (FEA)**	53.590	11.149	21.220	17.800	0.170
lamination theory for two plies	53.573	11.131	21.220	17.814	0.170
lamination theory using 3-D elastic constants	53.762	11.183	21.293	8.190	0

Table 13. Non-zero [*A*], [*B*] and [*D*] Coefficients for Examples 3 and 4 (Unidirectional Composite) using Finite Elements

		A_{11} x10^6	A_{12} x10^6	A_{22} x10^6	A_{66} x10^6
Example 3	***μTEχ*-20 (FEA)**	0.690	0.149	0.496	0.177
	Halpin-Tsai eqns. and lamination theory	0.673	0.109	0.363	0.113
Example 4	***μTEχ*-20 (FEA)**	0.452	0.062	0.285	0.114
	Halpin-Tsai eqns. and lamination theory	0.444	0.039	0.151	0.045

		D_{11} x10^{-6}	D_{12} x10^{-6}	D_{22} x10^{-6}	D_{66} x10^{-6}	α_x^px 10^{-6}	α_y^px 10^{-6}
Example 3	***μTEχ*-20 (FEA)**	3.589	0.596	1.980	0.947	15.489	26.184
	Halpin-Tsai eqns. and lamination theory	5.606	0.908	3.026	0.939	15.625	55.112
Example 4	***μTEχ*-20 (FEA)**	2.256	0.224	0.873	0.568	7.378	13.188
	Halpin-Tsai eqns. and lamination theory	3.702	0.328	1.262	0.371	6.774	34.239

[*A*], [*B*] and [*D*] coefficients in SI units

Table 14. Non-zero [*A*], [*B*] and [*D*] Coefficients for Examples 5, 6 and 7 using Finite Elements

		A_{11}, A_{22} x10^6	A_{12} x10^6	A_{66} x10^6	B_{11} x10^3
Example 5	***μTEχ*-20 (FEA)**	2.630	0.598	0.511	0
	lamination theory using 3-D constants	2.728	0.508	0.483	0
Example 6	***μTEχ*-20 (FEA)**	12.750	3.332	1.237	0
	lamination theory using 3-D constants	15.040	1.461	1.237	0
Example 7	***μTEχ*-20 (FEA)**	15.362	1.065	1.228	0.515*
	lamination theory using 3-D constants	16.020	0.756	1.228	0

		D_{11}, D_{22} x10^{-3}	D_{12} x10^{-3}	D_{66} x10^{-3}	α_x^p, α_y^p x10^{-6} /°C	β_x^p /°C/m
Example 5	***μTEχ*-20 (FEA)**	8.564	1.555	2.142	28.310	0
	lamination theory using 3-D constants	11.816	2.203	2.093	29.752	0
Example 6	***μTEχ*-20 (FEA)**	53.912	0.413	4.421	1.418	0
	lamination theory using 3-D constants	81.948	7.962	6.740	1.471	0
Example 7	***μTEχ*-20 (FEA)**	107.390	2.072	5.814	2.191	-0.018*
	lamination theory using 3-D constants	87.283	4.122	6.691	1.580	0

* In example 7, $B_{22} = -B_{11}$ and $\beta_y^p = -\beta_x^p$

[*A*], [*B*] and [*D*] coefficients in SI units

Table 15. SAM Results for Examples 1 and 2

		E_x, E_y (GPa)	E_z (GPa)	G_{xz}, G_{yz} (GPa)	G_{xy} (GPa)	ν_{xz}, ν_{yz}	ν_{xy}
Example 2 (bimaterial medium)	**$\mu TE\chi$-10 (SAM)**	36.03	8.72	2.48	15.23	0.599	0.183
	exact solution	36.79	9.79	2.48	15.23	0.312	0.208

Table 16. SAM Results for Examples 3 and 4

		E_L (GPa)	E_T (GPa)	G_{LT} (GPa)	G_{TT} (GPa)	ν_{LT}	ν_{TT}
Example 3 (unidirectional composite)	**$\mu TE\chi$-10 (SAM)**	64	40.51	11.17	8.36	0.245	0.300
	$\mu TE\chi$-20 (FEA)	63.55	36.48	12.93	9.94	0.300	0.233
	rule of mixt./Halpin-Tsai eqns.	64	34.55	11.26	-	0.300	0.300
Example 4 (unidirectional composite)	**$\mu TE\chi$-10 (SAM)**	43.23	22.11	4.43	3.06	0.159	0.237
	$\mu TE\chi$-20 (FEA)	43.12	18.15	5.59	3.92	0.242	0.222
	rule of mixt./Halpin-Tsai eqns.	43.40	14.79	4.45	-	0.260	0.252

Table 17. SAM Results for Examples 5, 6 and 7

		E_x, E_y (GPa)	E_z (GPa)	G_{xz}, G_{yz} (GPa)	G_{xy} (GPa)	ν_{xz}, ν_{yz}	ν_{xy}
Example 5 (plain-weave)	***μTEχ*-10 (SAM)**	11.52	6.48	1.60	1.60	0.396	0.171
	***μTEχ*-20 (FEA)**	11.55	6.26	1.94	2.12	0.399	0.186
	Dasgupta results	14.38	6.25	1.94	3.94	0.463	0.167
Example 6 (plain-weave)	***μTEχ*-10 (SAM)**	64.49	11.37	3.97	4.26	0.398	0.027
	***μTEχ*-20 (FEA)**	58.27	10.92	4.32	4.84	0.378	0.098
	TEXCAD	64.38	11.49	5.64	4.87	0.396	0.027
Example 7 (5-harness weave)	***μTEχ*-10 (SAM)**	65.61	11.14	3.66	4.44	0.363	0.032
	***μTEχ*-20 (FEA)**	62.51	11.02	4.45	4.80	0.349	0.047
	TEXCAD	66.33	11.51	4.93	4.89	0.342	0.034

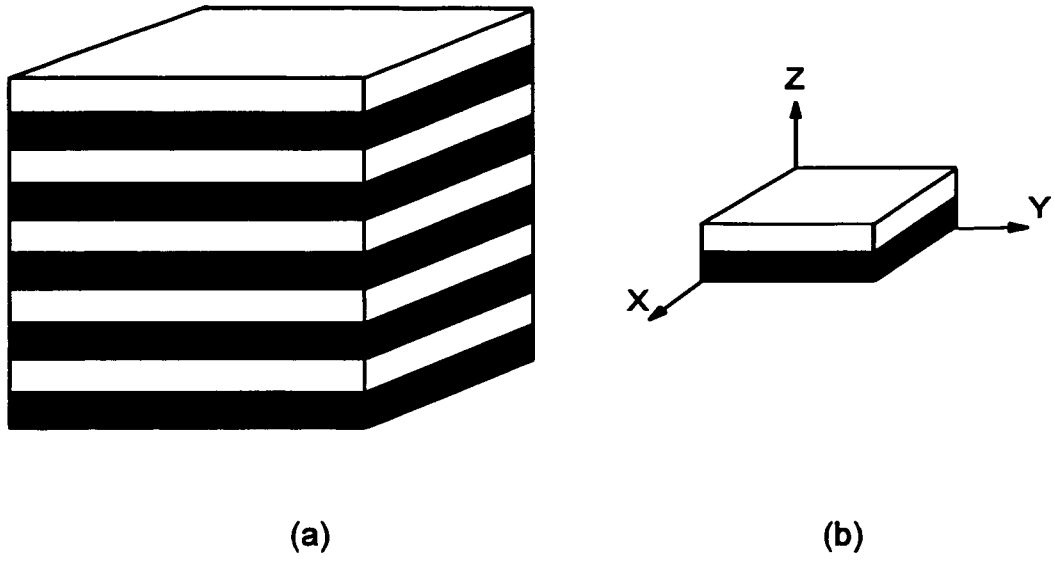

Figure 1. (a) bimaterial medium; (b) bimaterial unit-cell.

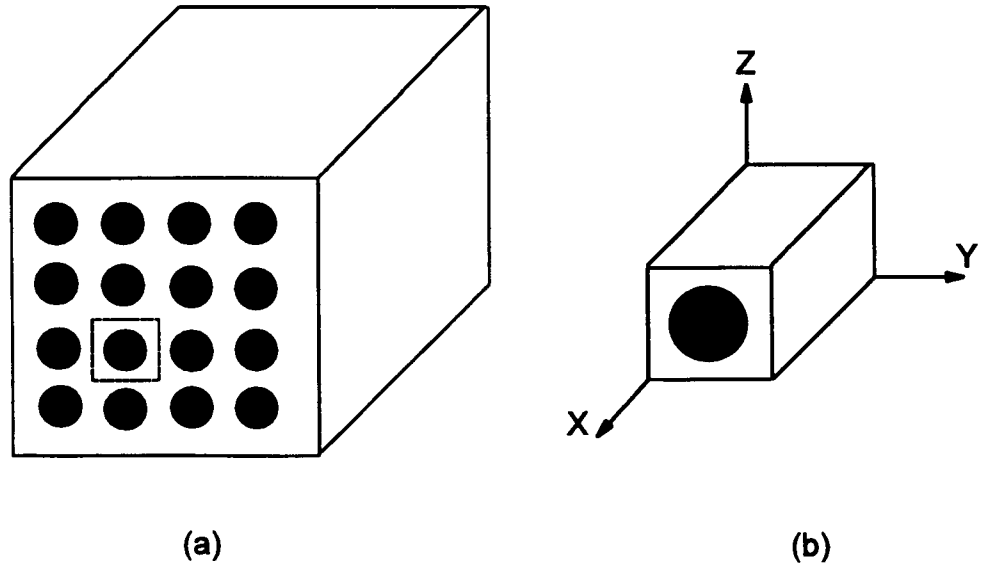

Figure 2. (a) unidirectional composite; (b) unit-cell for the composite.

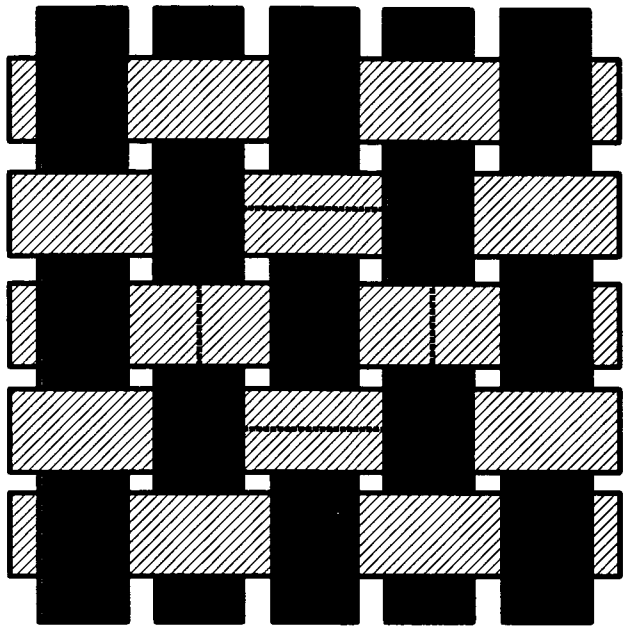

Figure 3. Yarn pattern in a plain weave preform (unit-cell boundary in dotted lines).

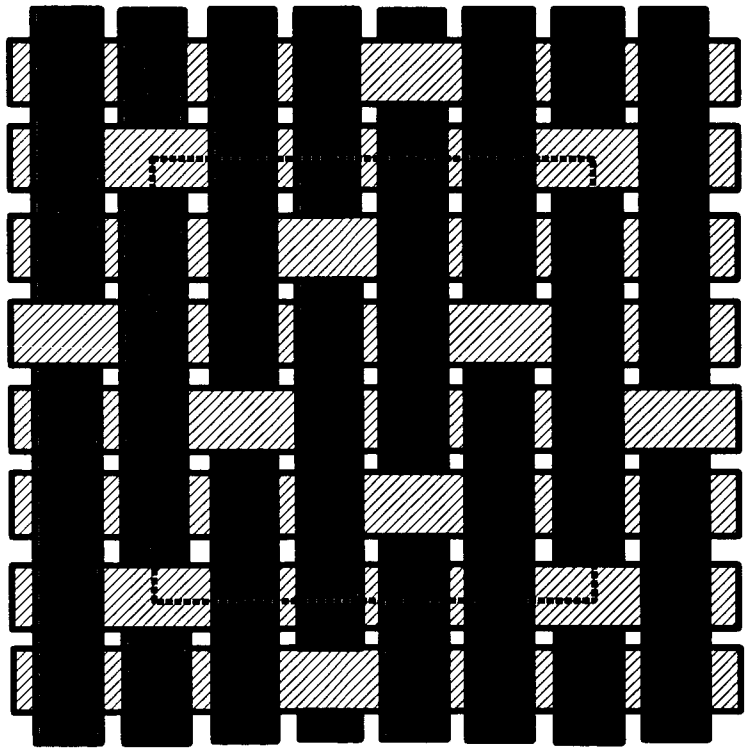

Figure 4. Yarn pattern in a 5-harness satin weave preform (unit-cell boundary in dotted lines).

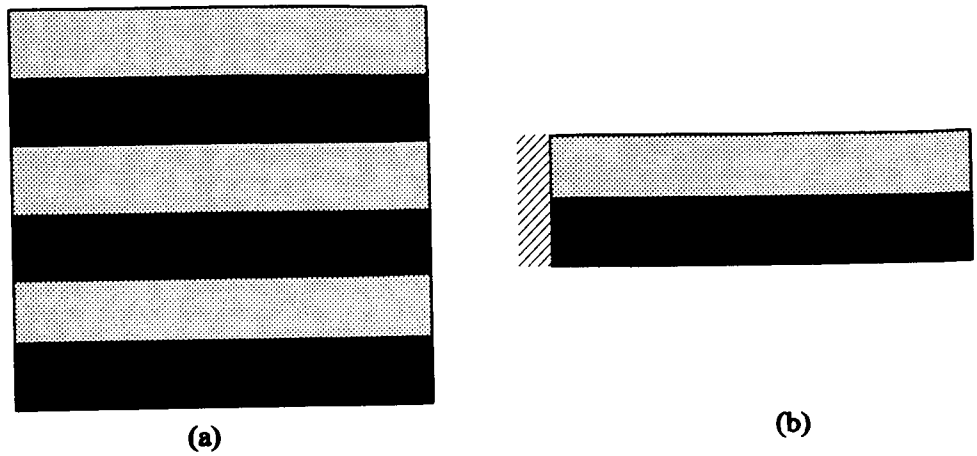

Figure 5. (a) Layered medium; (b) bimaterial beam.

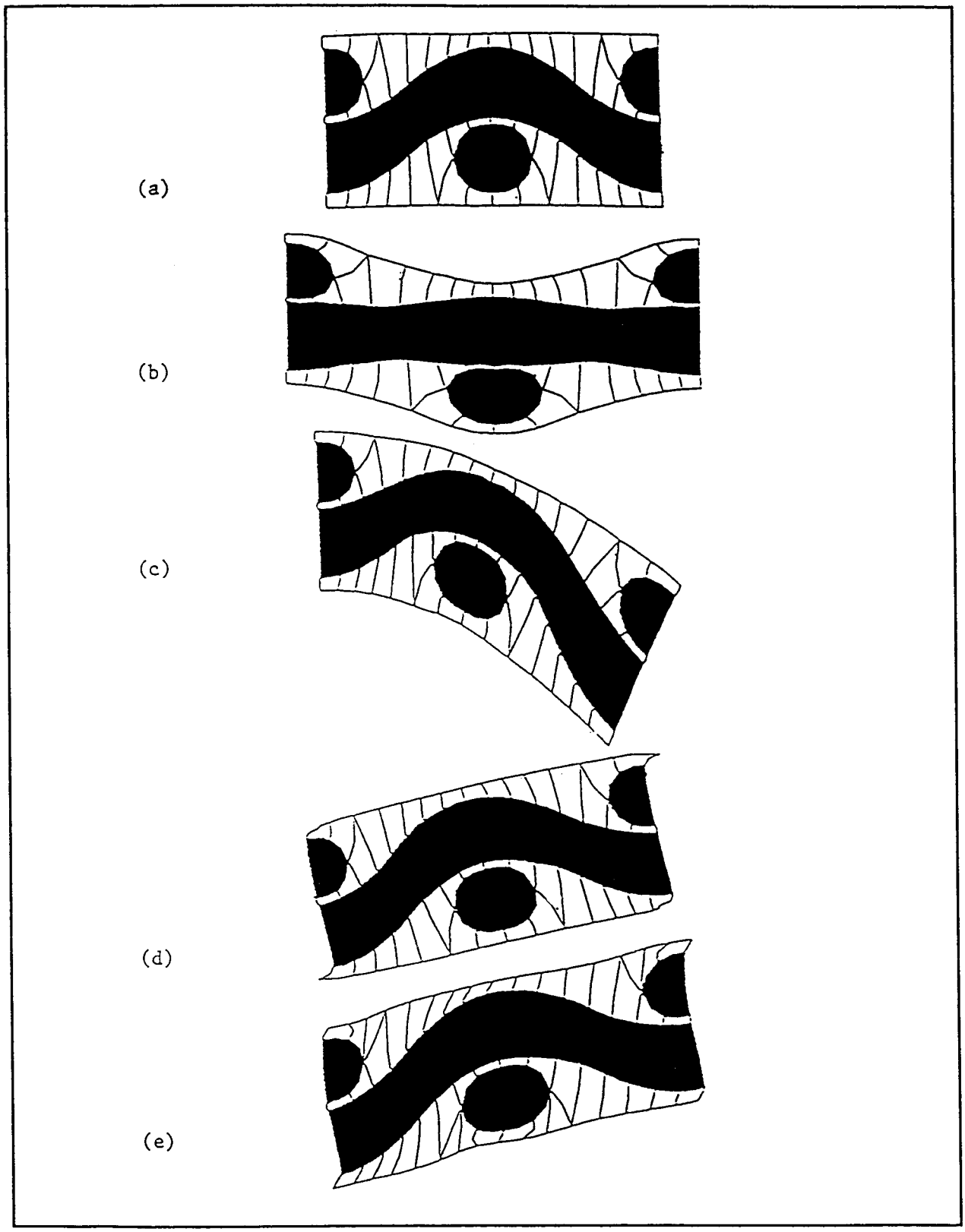

Figure 6. Textile beam: (a) undeformed unit-cell and deformation under: (b) unit extensional strain; (c) unit curvature; (d) unit shear strain, top and bottom surfaces are traction free; (e) unit shear strain, tractions allowed on top and bottom surfaces. (not to scale)

(a)

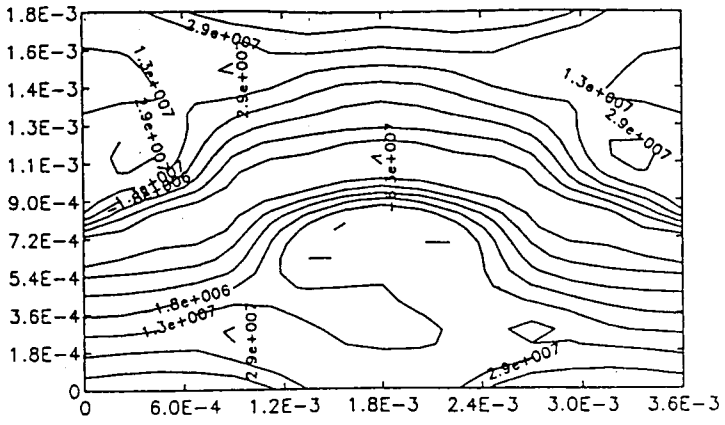

(b)

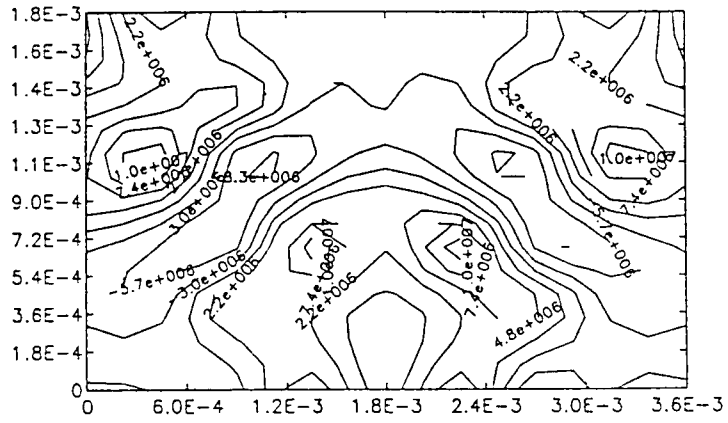

(c)

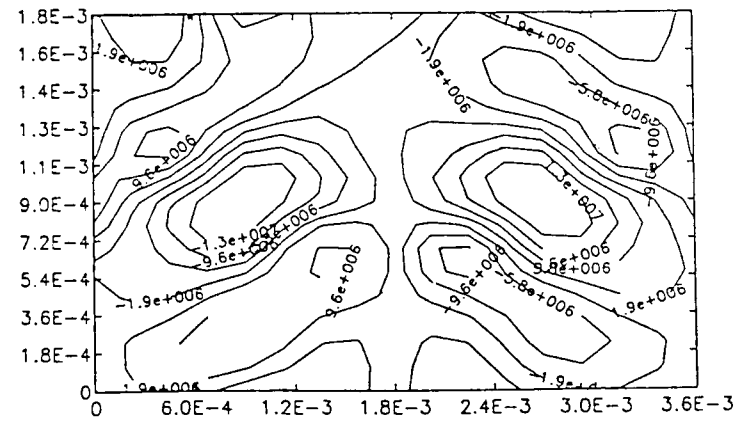

Figure 7. Thermal microstress contours in a plain weave beam for ΔT= -150°C: (a) σ_{xx}; (b) σ_{zz}; (c) τ_{xz}.

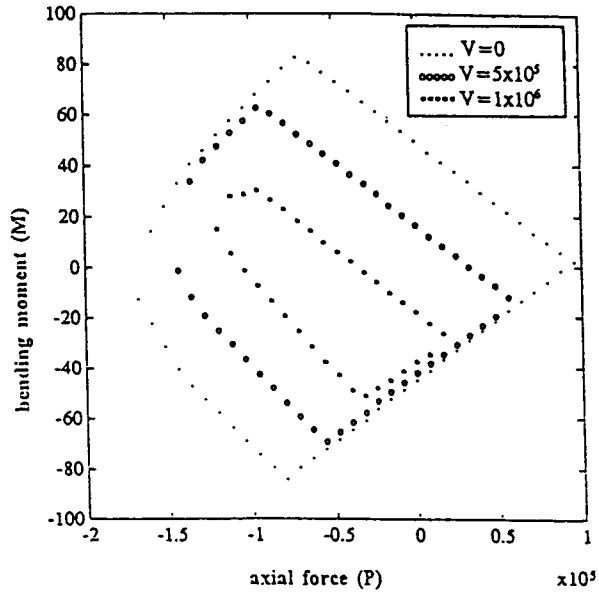

Figure 8. Beam failure envelope based on yarn failure.

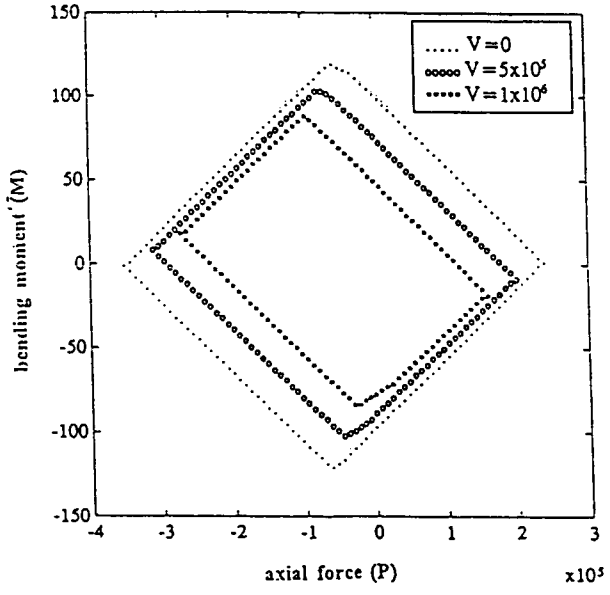

Figure 9. Beam failure envelope based on matrix failure.

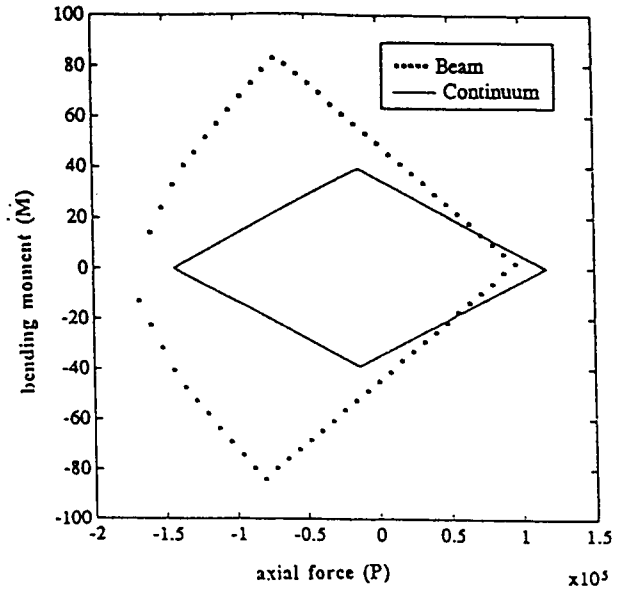

Figure 10. Comparison of failure envelopes based on yarn failure.

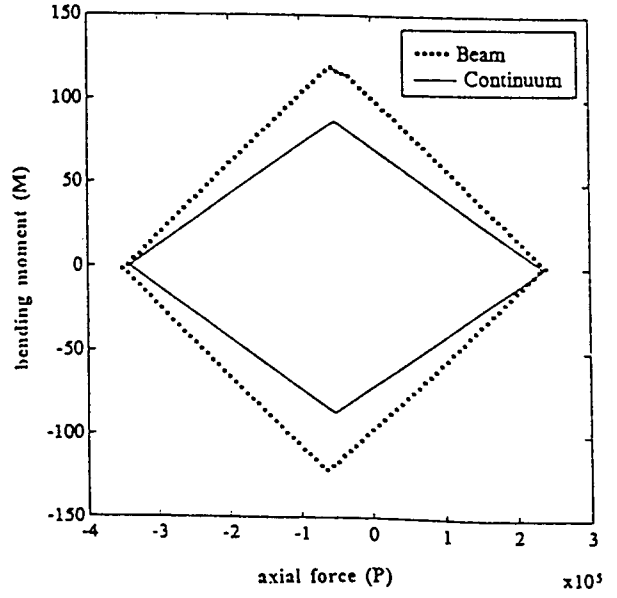

Figure 11. Comparison of failure envelopes based on matrix failure.

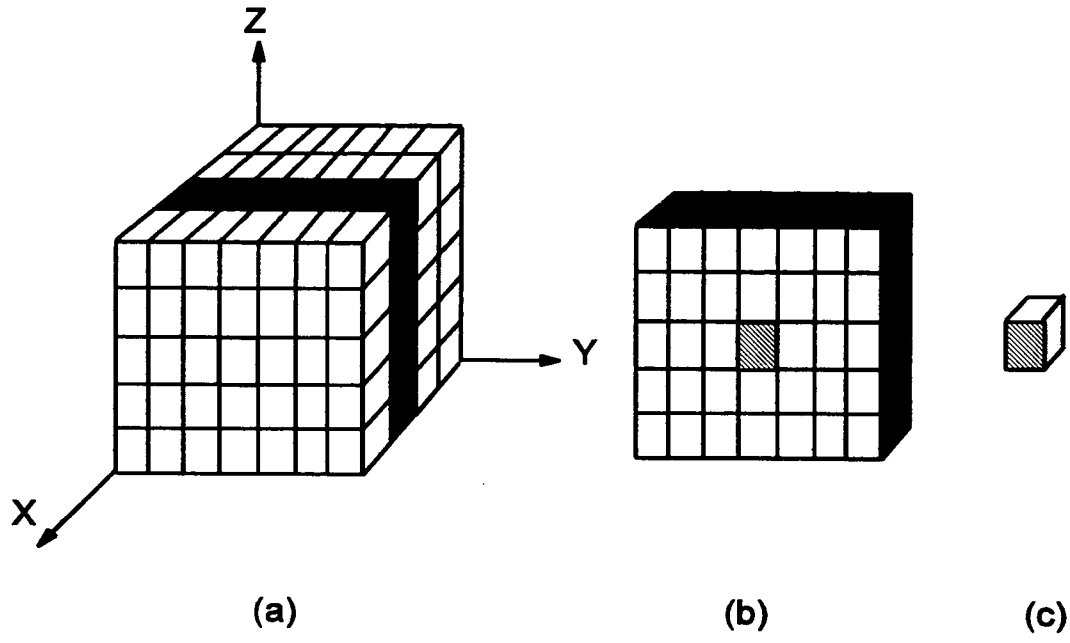

Figure 12. Hierarchy of discretization for a unit-cell to implement SAM: (a) unit-cell (macrolevel); (b) slice (mesolevel); (c) element (microlevel).

Effect of Various Approximations on Predicted Progressive Failure in Plain Weave Composites

John Whitcomb
Kanthikannan Srirengan
Aerospace Engineering Department
Texas A&M University
College Station, Texas

Abstract

Three-dimensional finite element analysis was used to simulate progressive failure of a plain weave composite subjected to in-plane extension. The loading was parallel to one of the tow directions. The effects of various characteristics of the finite element model on predicted behaviour were examined. The predicted behavior was found to be sensitive to quadrature order, mesh refinement and the material degradation model. Also the sensitivity of the predictions to the tow waviness was studied. The predicted strength decreased considerably with increased waviness. More numerical studies and comparisions with experimental data are needed to establish reliable guidelines for accurate progressive failure prediction.

Introduction

Textile composites consist of interlaced tows (fiber bundles) which are then impregnated with a matrix material and cured. Figure 1 illustrates the architecture for a plain weave composite. The interlacing of the tows offers the potential for increased through-thickness strength. There is also the potential for reduced fabrication costs, since fairly complicated shapes can be formed using textile machinery. One disadvantage of textiles is the difficulty in predicting their performance. The complex geometry makes detailed stress analysis quite challenging. The early analyses were based on modified laminate theory. (eg. References 1,2) In recent years there have been a few attempts to discretely model the fiber bundle architecture and predict internal stress states (eg. References 3-11) Reference 11 presented a particularly interesting progressive failure analysis of a plain weave composite. The results in Reference 11 consisted of nominal stress strain curves. The response of the composite was almost linear for in-plane extension and highly nonlinear for in-plane shear. The nonlinearity was primarily a result of progressive damage. However, little information was provided on damage evolution and load redistribution within the composite during the loading process. Also, there was no indication of the sensitivity of the predictions to

mesh refinement or other approximations inherent in such analyses.

This paper has two objectives. The first is to evaluate the sensitivity of predicted progressive failure to quadrature order, mesh refinement, and choice of material degradation model. The second objective is to describe the nature of the progressive failure process for two weaves with very different waviness. Loading consisted of a nominally uniaxial stress along one of the fiber tow directions. Only mechanical loads were considered in this study. To simplify the response the composite was assumed to consist of an infinite number of identical unit cells in all three coordinate directions.

The following sections begin with a description of the basic theory used for progressive damage modelling. Then the configurations will be described. Finally the results from the numerical simulations will be discussed.

Theory

There is no "right" way to model damage evolution in a textile composite that is also practical. It is not feasible to discretely model all of the damage, so approximation is unavoidable. Perhaps the simplest procedure to account for damage in a finite element model is to modify the constitutive matrix at the quadrature points of a numerically integrated finite element. If history effects are not included, the analysis of the loading becomes a series of elastic analyses. Of course, there are many possibilities for how to modify the constitutive matrix. Three techniques were used herein. The first method considered the material totally failed (ie. the entire constitutive matrix was reduced to essentially zero) when any allowable stress component was exceeded. This method will be refered to as the non-selective discount method. The second technique selectively reduced the rows and columns of the constitutive matrix according to the particular stress allowable which was exceeded. For example, if the third stress component exceeded the allowable, the third row was set to essentially zero to eliminate that stress component. To keep the constitutive matrix symmetric, the third column would also be set to zero. Zeroing the column has the undesirable side effect of stiffening the material with respect to the other stresses. This degradation method will be referred to as the selective RC method. The third technique selectively reduced the engineering moduli according to the particular stress allowable which was exceeded. Except as noted, this technique was used in the analyses. This technique will be referred to as the Blackketter method.

The progressive failure analysis begins with a linear analysis of the undamaged configuration. Based on the calculated stresses, the initial load was scaled back so that failure would occur only at points which were within two percent of the maximum normalized stress. (The stresses were normalized by the respective strengths.) The constitutive matrix was modified at the failure points. Residual forces were calculated and used to determine the incremental displacements required to restore equilibrium. The total displacements were updated and used to determine the new stresses. If no further failures occured at the current nominal strain state, the nominal strain was incremented to cause failure. This procedure was repeated until the nominal strain exceeded one percent.

Configurations

The fiber bundles or tows in the models were generated by translating a lenticular cross-section along a sinusoidal path. The waviness ratio is defined to be the ratio of the woven mat thickness to the wavelength. The weave consists of warp and fill tows oriented perpendicular to each other. In general, the warp and fill tows could be different in terms of material and shape. In

this study they were assumed to be identical. More details about the mesh geometry can be found in Reference 9. The following subsections describe the finite element meshes, the boundary conditions, and the material properties.

Finite Element Meshes

Symmetry in the material and loading was exploited so that only 1/32 of a unit cell had to be modeled. A wide range of mesh refinements were used, as shown in Figure 2. The crude mesh had only 4 elements and 42 nodes. The most refined mesh had 192 elements and 1049 nodes. The elements were 20-node hexahedral elements. Since only 1/32 of the unit cell was modeled, these refinements correspond to full cell models with 128 to 6144 elements.

Boundary Conditions

The periodic boundary conditions for a complete unit cell are quite simple. The appropriate boundary conditions for a 1/32 unit cell are a bit more complicated. Derivation of the periodic boundary conditions is somewhat tedious, so details will not be given here. Details can be found in Reference 9. The periodic conditions are listed below. Figure 2 shows the coordinate system assumed.

$u(a/2,y,z) = u_0$	$v(x,a/2,z) = \text{constant}$	$w(x,y,c/2) = \text{constant}$
$u(0,y,z) = -u(0,y,-z)$	$v(0,y,z) = v(0,y,-z)$	$w(0,y,z) = -w(0,y,-z)$
$u(x,0,z) = u(x,0,-z)$	$v(x,0,z) = -v(x,0,-z)$	$w(0,y,z) = -w(0,y,-z)$

The load was controlled by specifying the magnitude of u_0. This corresponds to uniaxial loading in the warp tow direction.

Material Properties

The unit cell contains two "types" of materials: the tows and the matrix pockets. Relative to the material coordinate system, the properties of the tows are invariant (before damage occurs). Of course, the properties of the tows are needed in the global coordinate system. Fourth order tensor transformation formulas were used to perform the required calculations. The rotation angles to be used in these formulas were specified at each quadrature point by using interpolation. This procedure was shown in References 8 and 9 to be preferable to using a single angle for the entire element. The particular properties used are listed below. These properties, which are

representative of AS4/3501-6 graphite/epoxy, are from Reference 13.

	Tow properties		Matrix properties	
	Modulus	Strength	Modulus	Strength
E_{11}	154.27 GPa	2342.0 MPa	3.45 GPa	84.85 MPa
E_{22}	10.80 GPa	56.6 MPa	3.45 GPa	84.85 MPa
E_{33}	10.80 GPa	56.6 MPa	3.45 GPa	84.85 MPa
G_{12}	7.47 GPa	48.7 MPa	1.28 GPa	101.00 MPa
G_{13}	7.47 GPa	48.7 MPa	1.28 GPa	101.00 MPa
G_{23}	3.33 GPa	48.7 MPa	1.28 GPa	101.00 MPa
ν_{12}	0.28		0.35	
ν_{13}	0.28		0.35	
ν_{23}	0.34		0.35	

Results and Discussions

Most of the results in this paper illustrate the effects of characteristics of the finite element model on the progressive failure prediction. The effects of quadrature order, mesh refinement, and material degradation strategy will be considered first. Then the effect of the tow waviness on failure behavior be discussed. Except where indicated otherwise, the results will be presented for a waviness ratio of 1/3 and for the material degradation strategy in Reference 11, (the "Blackketter method").

Figure 3 shows the effect of quadrature order on the stress-strain curve. The peak stress obtained using 8 quadrature points (2x2x2) is 4 percent higher than that obtained using 64 points. The peak stresses obtained using 27 and 64 quadrature points differ by 1 percent. Damage initiation is predicted 3 percent earlier when 64 points are used. After the large stiffness loss which occurs at about 0.3 percent strain, there is even larger differences in the predictions. In Reference 12, non-selective discount was used for the same configuration. The difference in the peak stress obtained using 8 and 64 point quadratures was 10 percent. Hence, the sensitivity of the predictions to quadrature depends on the degradation model. The sensitivity to quadrature order is not suprising. For example, when more quadrature points are used, the more extensive sampling is more likely to find the extremes in the stress field. One might expect a refined mesh to exhibit less sensitivity to quadrature order than a coarse mesh. For the meshes considered in this study, this was the case. Also, when failure occurs within an element, and the constitutive matrix is modified, the element becomes inhomogeneous. The numerical integration effectively fits a polynomial function to the variation of the material properties. Since the material properties are very different in the failed and unfailed parts of the element, it is difficult to obtain a good fit. In fact, there is a concern as to whether the assumed quadratic displacement functions for a 20-node element are sufficient to obtain a reasonable approximation regardless of the integration order.

Figure 4 shows the effect of mesh refinement on the predicted stress-strain curve for the two waviness ratios. The 4 element model predicts the correct trends, but is quite inaccurate. The error in the peak stress is much worse for larger waviness ratio. The peak stress and corresponding strain for a coarse mesh is larger than for a refined mesh, but the peak stress and corresponding strain for a moderately refined mesh are not necessarily bound by the extreme cases of mesh refinement. (see Figure 4b) The peak stress and the corresponding strain, decrease with increased waviness. The ratio of the initial damage stress to the peak stress and the corresponding ratio of strains increase with decrease in waviness ratio. That is, not only is the strength reduced by the

waviness, but there is also earlier damage initiation relative to the peak stress.

Figure 5 shows damage volume versus the nominal strain for the warp and fill tows for four mesh refinements. Damage volume for the resin is not shown since there is almost no damage. The curves are quite close for the 108 and 192 element meshes, which suggests that the curves might be close to convergence. As the mesh is refined, the increments in damage volume become smaller , but more numerous. The damage volume at the peak stress decreases with mesh refinement for both the warp and fill tows. This is not surprising since the corresponding stress is also smaller. After the peak stress is reached, there is a large increase in damage volume without an increase in strain (of course, the stress drops). The damage volume after this sudden increase is sensitive to mesh refinement for the warp tow but insensitive to mesh refinement for the fill tow. The curve for the 192 element mesh in Figure 5a has points labeled A and B. From A to B the damage initiation and growth was dominated by the inter-tow normal stress σ_{33}. The sudden increase in damage at point B was due to the stress component σ_{13} (the x_1 direction is parallel to the fibers),

The damage volumes just after the peak stress is reached is as follows

Waviness Ratio	Warp	Fill	Percent Stiffness Loss
1/6	.51	.39	41
1/3	.33	.35	60

Interestingly, the damage volume is larger for the 1/6 waviness ratio, but the percentage stiffness loss is less.

Figure 6 and 7 show the effect of mesh refinement and waviness ratio on damage accumulation during loading. The black region indicates the damage zone. The stress-strain curve for a particular mesh is shown above that mesh. The points labeled A,B and C indicate the correspondence between the strain level and the damage contours. The damage zone corresponding to point A indicates the initial damage. The damage zones corresponding to points B and C indicate the pre- and post- collapse damage states, where collapse refers to the large stress drop just after the peak stress is reached. Also indicated are the stress components which contributed to the damage. The 4-element mesh does not model the initial failure well for the two waviness ratios of 1/3 and 1/6. The 32 element model performs reasonably well for obtaining qualitative results. Further numerical studies are needed to determine how close the 192 element results are to convergence. For the 1/3 waviness ratio σ_{33} dominates the initial failure. This initial failure appears to be an inter-tow failure resembling delamination in laminated composites. The collapse is characterized by σ_{13} failure in the warp tows. For the 1/6 waviness ratio, the collapse is due to a significant failure of the warp tow due to σ_{13} and cracking of the fill tow due to σ_{22}.

Figure 8 shows the stress-strain curves obtained using the three degradation models described earlier: non-selective, selective RC, and the Blackketter method. The non-selective method predicts 22% lower peak stress than the Blackketter method. Selective reduction of rows and columns in the constitutive matrix results in a much larger residual stiffness after the peak stress than the other two methods. Selective reduction of rows and columns in the constitutive matrix also does not result in a large sudden drop in the stress after the peak stress is reached. Concomitantly, for the selective RC method there is also no sudden increase in the damage volume after the peak stress is reached. (This is not shown on the plot.) It should be noted that if variability in the strength of the constituents from one unit cell to another was included, there

would also be less severe jogs in the stress-strain curve.

Concluding Remarks

Simulation of progressive failure in a plain weave composite is extremely complex. Consequently, only approximate treatment is practical at this time. One of the goals of this paper was to examine the effect of several approximations on predicted behaviour. One obvious conclusion from this study is that the predictions are quite sensitive to a number of decisions which must be made when assembling a finite element model. Further numerical experiments and comparisons with experimental data are needed to establish guidelines for accurate analysis of progressive failure.

Another objective of this paper was to describe the effect of tow waviness on damage accumulation. The results suggest that the degree of waviness not only affects the stress at which damage initiates, but also the type of damage which occurs. Also, the stress component responsible for damage changed during the progressive failure process.

Acknowledgements

This research was supported by NASA Grant NAG-1-1324. James Reeder was the technical monitor. This support is gratefully acknowledged.

References

1. Ishikawa, T. and Chou.T.W.: "Stiffness and Strength Behavior of Woven Fabric Composites," Journal of Material Science, 17:3211-3220, 1982.

2. Ishikawa.T. and Chou T.W.: "Elastic Behavior of Woven Hybrid Composites," Journal of Composite Materials, 16:2-19, January 1982.

3. Paumelle, P., A. Hassim, and F. LÁnÁ.: "Composites with Woven Reinforcements: Calculation and Parametric Analysis of the Properties of the Homogeneous Equivalent," La Recherche AÁrospatiale, 1:1-12, 1990.

4. Paumelle, P., A. Hassim, and F. LÁnÁ.: "Microstress Analysis in Woven Composite Structures," La Recherche AÁrospatiale, 6:47-62., 1991.

5. Whitcomb, J. D.: "Three-Dimensional Stress Analysis of Plain Weave Composites," Composite Materials: Fatigue and Fracture , ASTM STP 1110, T. K. O'Brien, Ed., Philadelphia: American Society for Testing and Materials, 3:417-438., 1991.

6. Woo, K.: "Stress and Failure Analysis of Textile Composites," Ph.D. Dissertation, Department of Aerospace Engineering, Texas A&M University, 1993.

7. Dasgupta, A. and Bhandarkar, S.: "Effective Thermomechanical Behavior of Plain-Weave Fabric-Reinforced Composites Using Homogenization Theory," Journal of Engineering Materials and Technology, 116 :99-105, January 1994.

8. Avery, William B. and Carl T. Herakovich. 1987. "A Study of the Mechanical Behavior of a 2D Carbon-Carbon Composite," Virginia Polytechnic Institute and State University, Interim

Report 66.

9. Chapman, C.: "Effects of Assumed Tow architecture on the Predicted Moduli and Stresses in Woven Composite," MS thesis, Department of Aerospace Engineering, Texas A&M University, 1993.

10. Guedes J.M. and Kikuchi N.,"Preprocessing and Postprocessing for Materials Based on the Homogenization Method with AdaptiveFinite Element Methods," Computer Methods in Applied Mechanics and Engineering, 83 :143-198, 1990.

11. Blackketter, D.; Walrath, D.; and Hansen, A.: "Modeling Damage in a Plain Weave Fabric-Reinforced Composite Material," Journal of Composites Technology and Research, 15 :2 : 136-142, Summer 1993.

12. Whitcomb, J.D. and Srirengan, K.: Simulation of Progressive Failure in Plain Weave Composites. Proceedings of the Symposium on Mechanics of Textile Composites at the ASME International ME'94 Congress & Exposition, November, 1994.

13. Naik, R.: "Micromechanical Combined Stress Analysis-MICSTRAN, A User Manual NASA Contractor Report 189694, Oct. 1992.

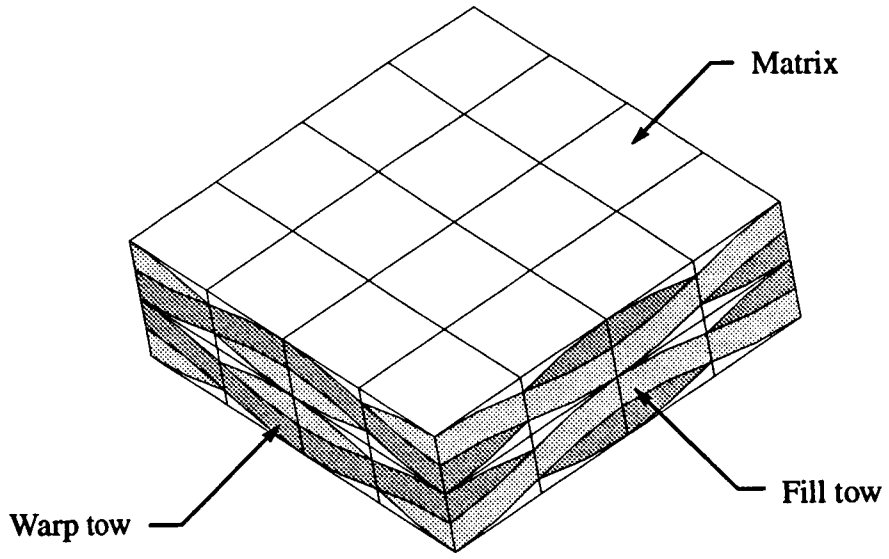

(a) Full unit cell.

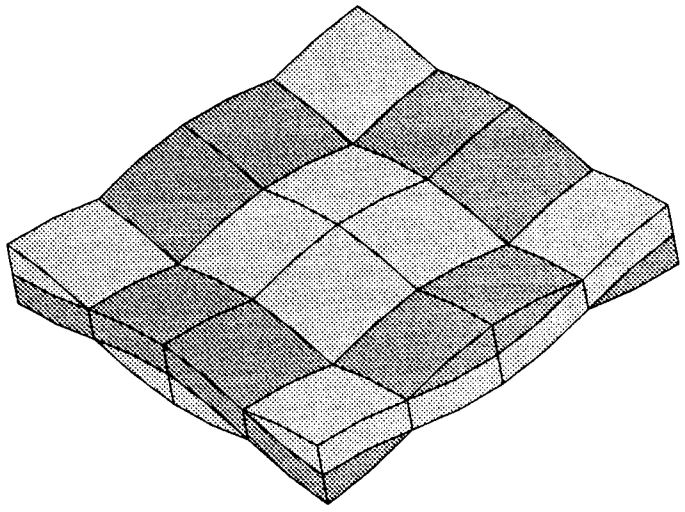

(b) Single mat with matrix pockets removed.

Figure 1 Schematics of plain weave composite.

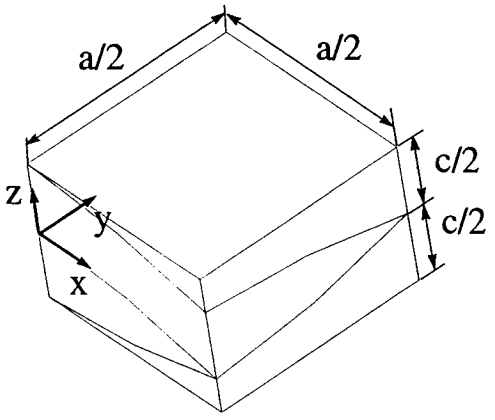

Mesh 1 :
4 elements and 42 nodes

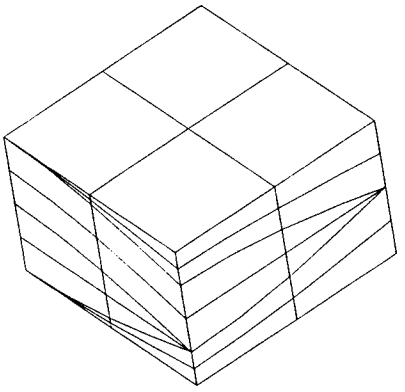

Mesh 2 :
32 elements and 221 nodes

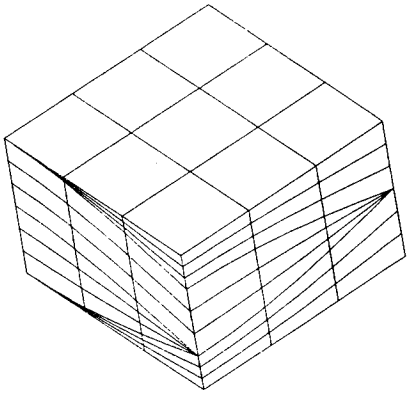

Mesh 3 :
108 elements and 634 nodes

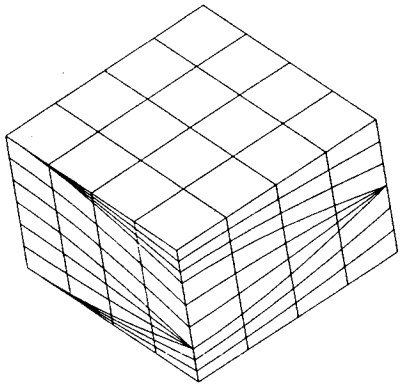

Mesh 4 :
192 elements and 1049 nodes

Figure 2 Finite element meshes used to determine the effect of mesh refinement on failure prediction.

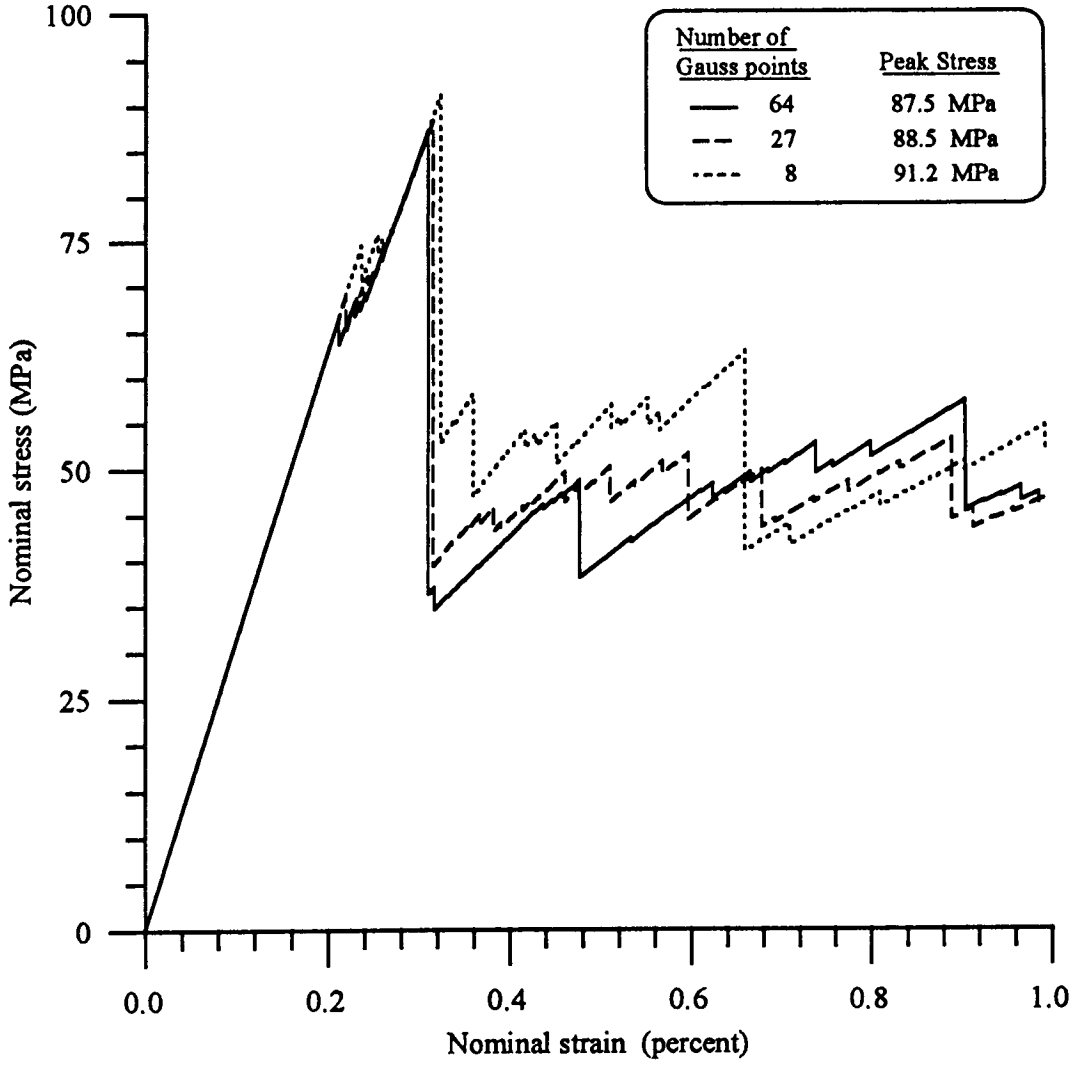

Figure 3 Effect of quadrature order on nominal stress-strain curve. Waviness ratio = 1/3. Blackketter discount method was used. The model had 192 elements and 1049 nodes.

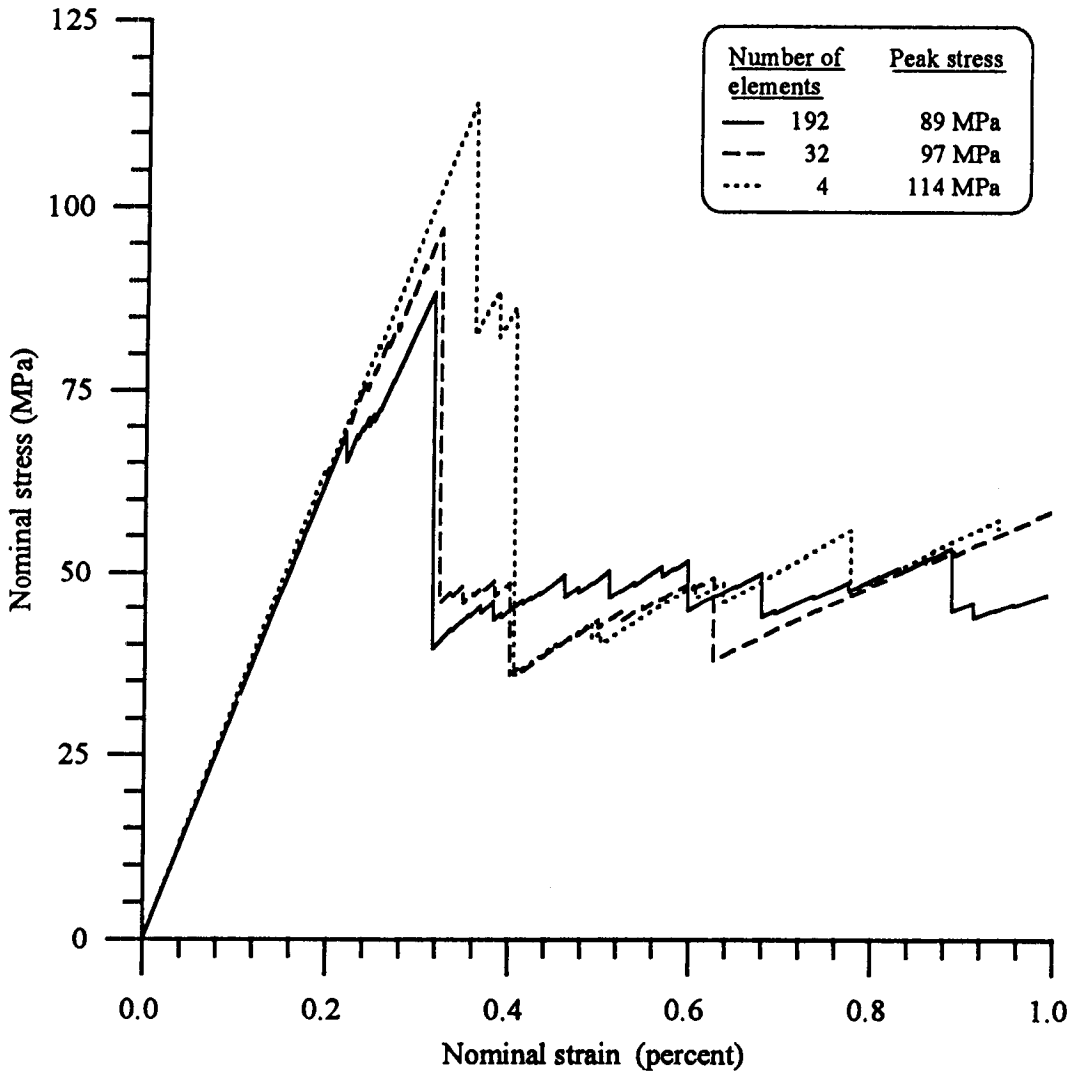

(a) Waviness ratio = 1/3

Figure 4 Effect of mesh refinement on nominal stress-strain curve. Blackketter discount method was used.

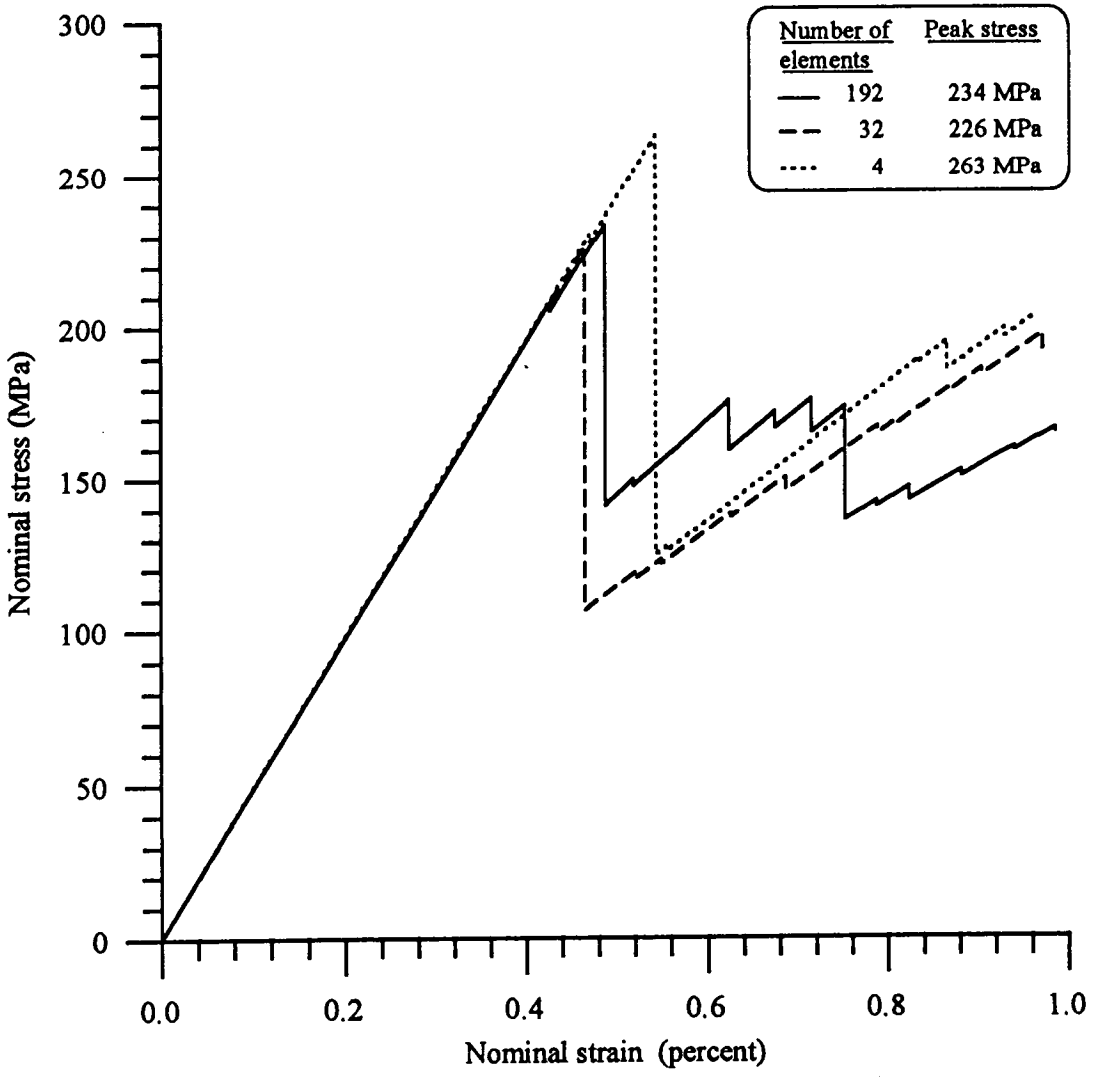

(b) Waviness ratio = 1/6

Figure 4, Cont'd.

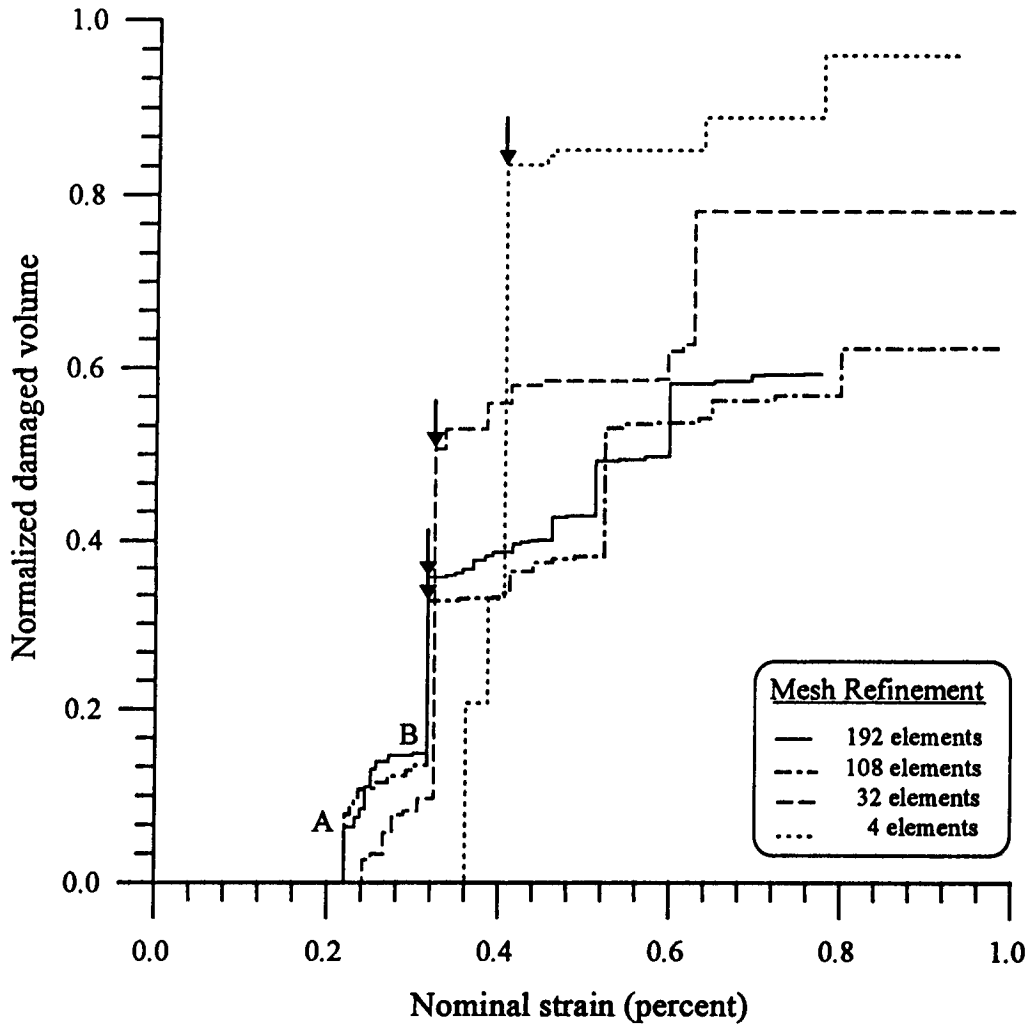

(a) Warp tow

Figure 5 Effect of mesh refinement on damage volume.
Waviness ratio = 1/3. Blackketter discount method was used.
↓ indicates strain at which collapse occured.

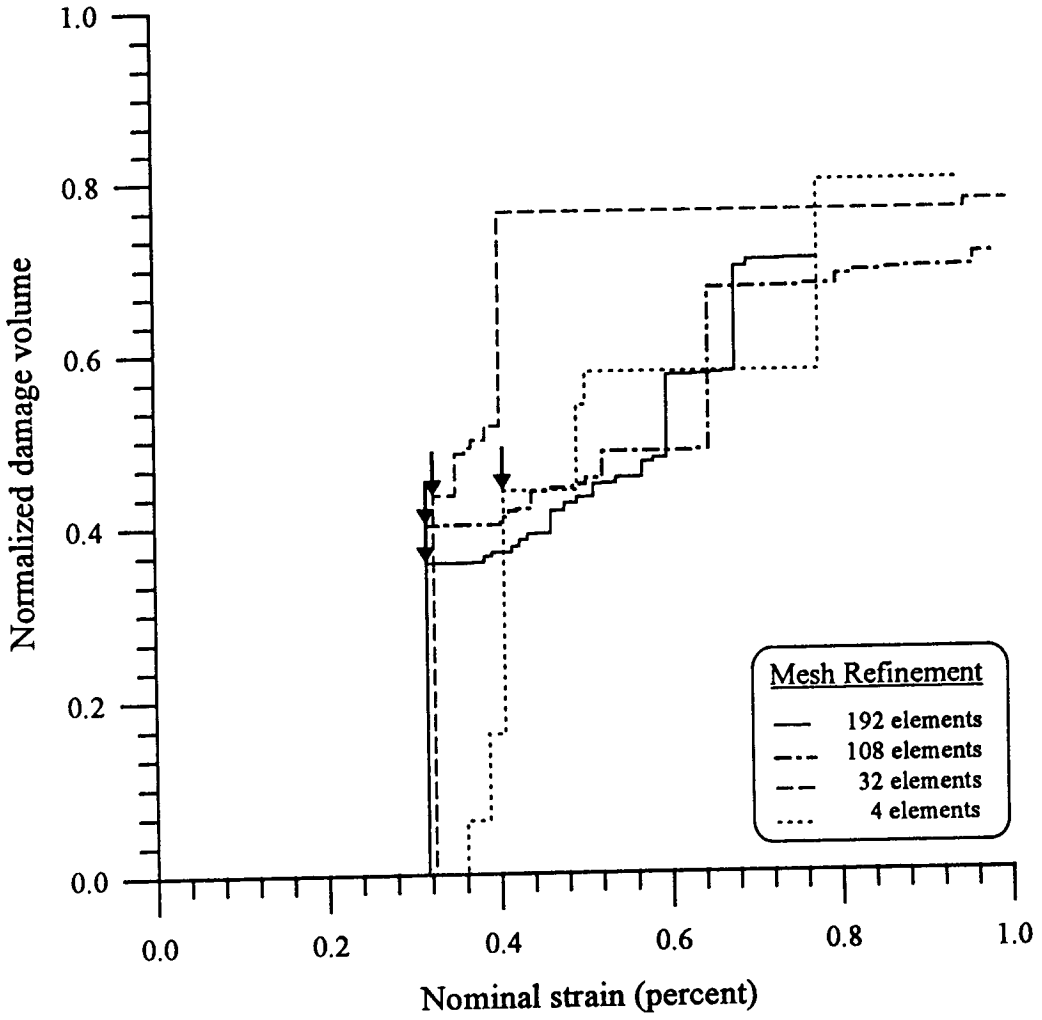

(b) Fill tow

Figure 5, Cont'd.

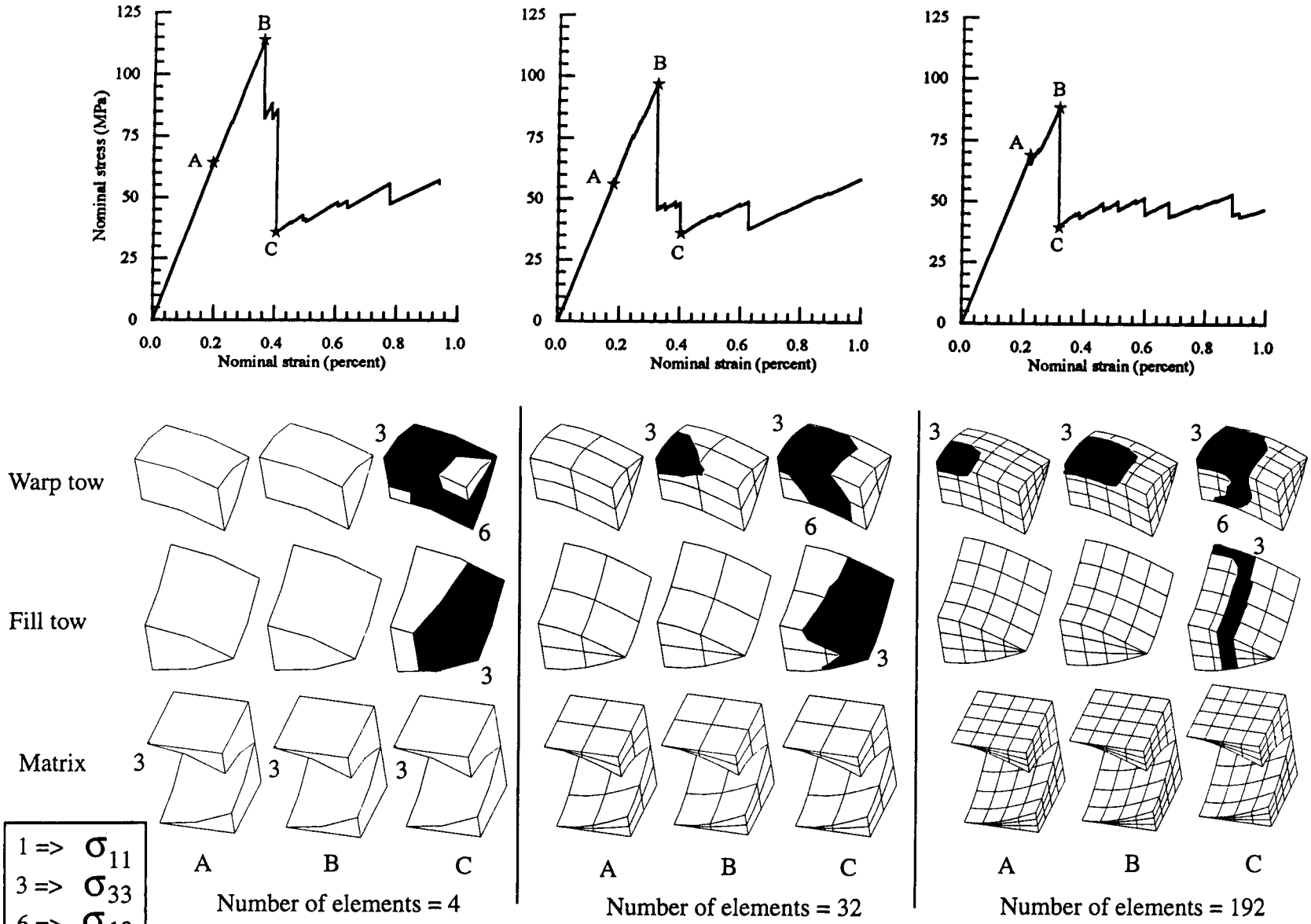

Figure 6 Effect of mesh refinement on damage development for waviness ratio = 1/3. Blackketter discount method was used.

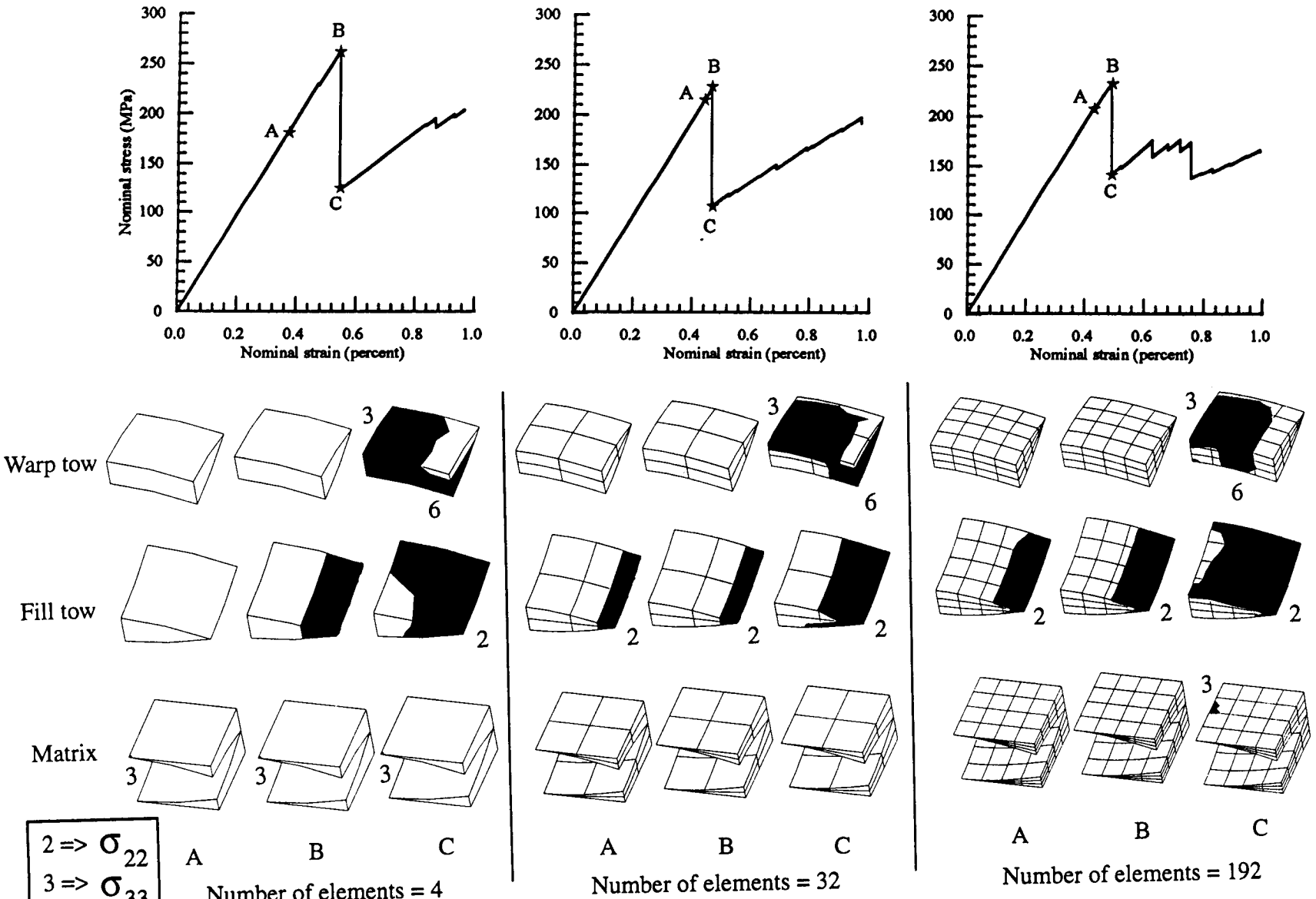

Figure 7 Effect of mesh refinement on damage development for waviness ratio = 1/6 Blackketter discount method was used.

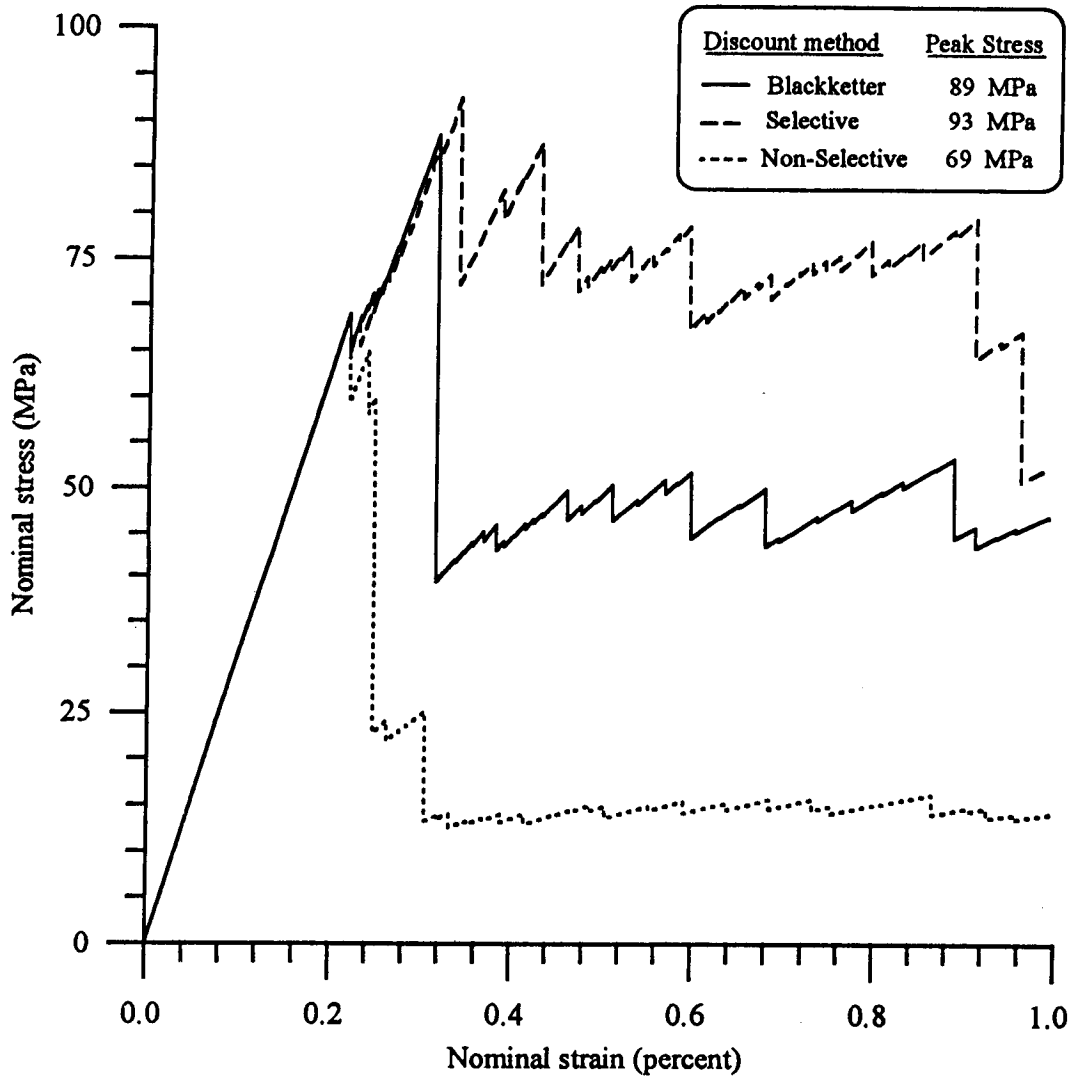

Figure 8 Effect of discount method on nominal stress-strain curve. Waviness ratio = 1/3. The model had 192 elements and 1049 nodes.

REPORT DOCUMENTATION PAGE

Form Approved
OMB No. 0704-0188

1. AGENCY USE ONLY *(Leave blank)*	2. REPORT DATE	3. REPORT TYPE AND DATES COVERED
	October 1995	Conference Proceedings

4. TITLE AND SUBTITLE
Mechanics of Textile Composites Conference

5. FUNDING NUMBERS
WU 510-02-1107

6. AUTHOR(S)
Clarence C. Poe, Jr. and Charles E. Harris

7. PERFORMING ORGANIZATION NAME(S) AND ADDRESS(ES)
NASA Langley Research Center
Hampton, VA 23681-0001

8. PERFORMING ORGANIZATION REPORT NUMBER
L-17532B

9. SPONSORING/MONITORING AGENCY NAME(S) AND ADDRESS(ES)
National Aeronautics and Space Administration
Washington, DC 20546-0001

10. SPONSORING/MONITORING AGENCY REPORT NUMBER
NASA CP-3311
Part 2

11. SUPPLEMENTARY NOTES

12a. DISTRIBUTION/AVAILABILITY STATEMENT
Unclassified–Unlimited
Subject Category—24

12b. DISTRIBUTION CODE

13. ABSTRACT *(Maximum 200 words)*
This document is a compilation of papers presented at the Mechanics of Textile Composites Conference in Hampton, Virginia, December 6–8, 1994. This conference was the culmination of a 3-year program that was initiated by NASA late in 1990 to develop mechanics of textile composites in support of the NASA Advanced Composites Technology Program (ACT). The goal of the program was to develop mathematical models of textile preform materials and test methods to facilitate structural analysis and design. Participants in the program were from NASA, academia, and industry.

14. SUBJECT TERMS
Weave; Braid; Stitch; Textile; Composite; Resin transfer molding; Test methods; Strengths; Thermo-elastic constants; Failure modes; Analysis

15. NUMBER OF PAGES
438

16. PRICE CODE
A19

17. SECURITY CLASSIFICATION OF REPORT	18. SECURITY CLASSIFICATION OF THIS PAGE	19. SECURITY CLASSIFICATION OF ABSTRACT	20. LIMITATION OF ABSTRACT
Unclassified	Unclassified		

NSN 7540-01-280-5500

Standard Form 298 (Rev. 2-89)
Prescribed by ANSI Std. Z39-18
298-102